Organised By:

THE HONG KONG INSTITUTION OF ENGINEERS 香港工程師學會
Geotechnical Division 岩土分部

Supported By:

HONG KONG GEOTECHNICAL SOCIETY 香港岩土工程學會
THE HONG KONG INSTITUTION OF ENGINEERS 香港工程師學會 Civil Division 土木分部
THE HONG KONG INSTITUTION OF ENGINEERS 香港工程師學會 Structural Division 結構分部

The HKIE Geotechnical Division 46th Annual Seminar

Fundamentals and First Principles :

Bridging Theory & Practice in Geotechnical Engineering

12 May 2026

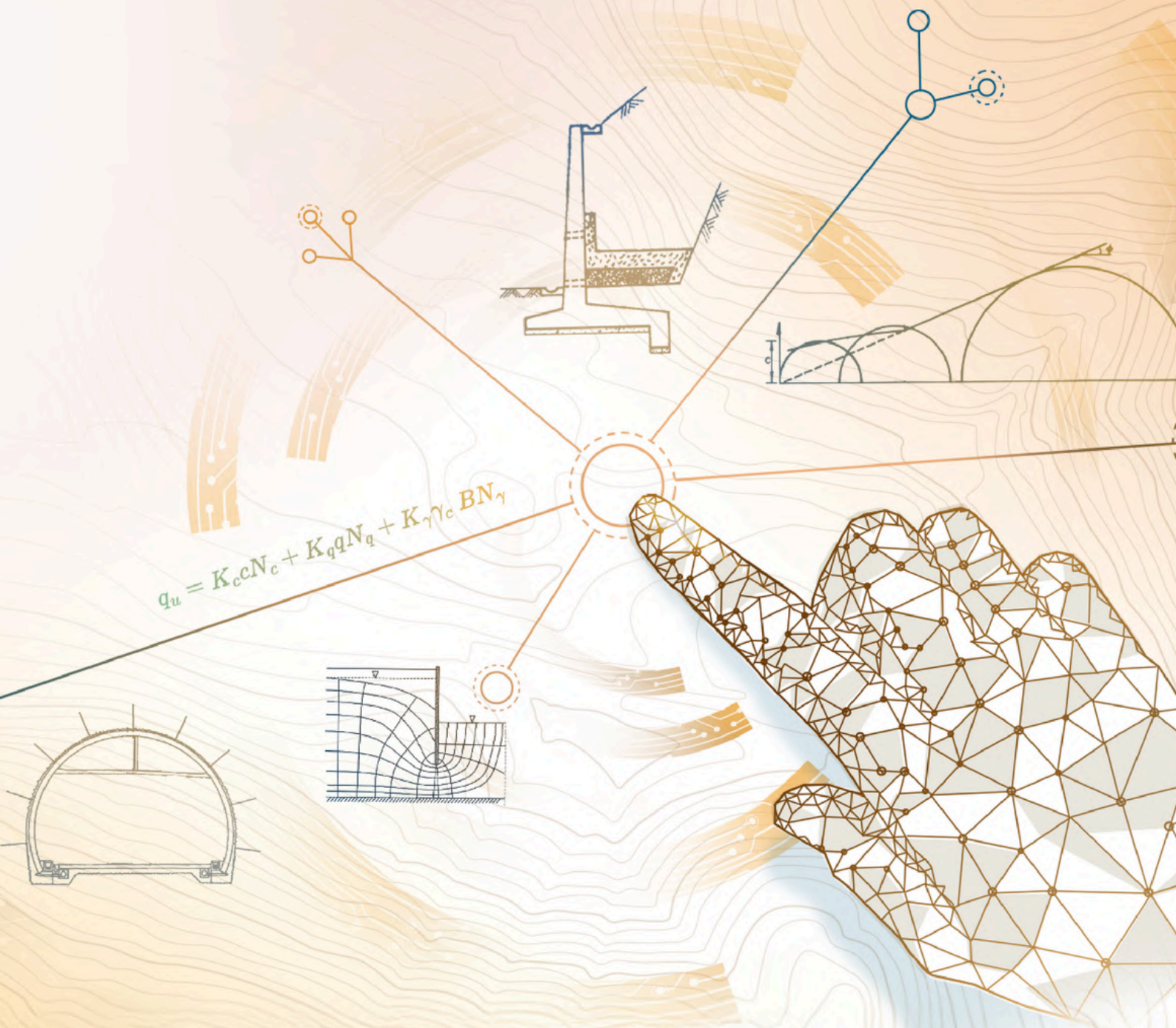

AECOM

Unlocking Cavern Potential with Geotechnical Engineering Innovations

AECOM is pioneering Hong Kong's first non-infrastructure cavern project for the Joint Cavern Development at Anderson Road Quarry Site. This innovative initiative will free up land for housing and waterfront open space development in East Kowloon.

To address the various constraints of building inside the caverns, particularly site logistics and the transportation of construction materials, a 4D BIM model is adopted to enhance buildability and ensure safe site operations.

*Reference design in investigation stage

aecom.com

Learn more

DELIVERING A BETTER WORLD.

ADRIAN CONSTRUCTION LIMITED

毅源建築有限公司

我們主要業務包括：

Our Business includes:

樓宇拆卸（煙囪拆卸）

Demolition of Building (Demolition of Chimney)

污泥及污水淨化（生化堆）

Land and Water Decontamination (Biochemical Mound)

污泥及污水淨化（重金屬污泥處理）

Land and Water Decontamination (Treatment for Heavy Metal)

斜坡鞏固及工地平整

Slope Stabilisation and Site Formation Works

香港新界葵涌葵昌路50號葵昌中心11樓1106室

Unit 1106, 11/F, Kwai Cheong Centre, 50 Kwai Cheong Road, Kwai Chung, NT, Hong Kong

Tel : +852 2428 8923 Fax : +852 2484 1622

aurecon

ENGINEERING HONG KONG TRANSPORT CONNECTIONS

Supporting Northern Metropolis Growth with advanced civil, geotechnical, highway and tunnel engineering

Aurecon helps deliver resilient, efficient transport and land infrastructure in Hong Kong, combining local insight with advanced design and assessment to manage complex ground, underground interfaces and delivery constraints. We act as a design and build designer, supporting projects from feasibility and approvals through detailed design and construction, bringing a practical, safety-led approach to buildability, staging and long-term performance.

- **Civil engineering:** multidisciplinary integration; construction-stage design support and interface management
- **Geotechnical:** ground models and risk-based design; ELS/retaining solutions and monitoring strategies
- **Highway & transportation:** optioneering and assessments; corridor/junction design and traffic staging
- **Tunnels & engineering geology:** tunnel/cavern design and support systems; engineering geology for ground risk

Explore our portfolio or connect with our transport & land team.

aurecongroup.com

C M WONG & ASSOCIATES LTD
黃志明建築工程師有限公司

11/F Universal Trade Centre
3-5A Arbuthnot Road, Hong Kong
Tel: (852)2522-1068
Fax: (852)2526-3111
www.cmwal.com
cmwal@cmwal.com

C M Wong & Associates Ltd is a Hong Kong based consulting engineer in providing a full range of professional services including feasibility studies, planning, design and supervision in relation to building and infrastructure projects. Our clients include various Hong Kong Government departments, institutions and major developers.

We adopt a flexible approach to suit clients' needs. We are also renowned for providing innovative engineering solutions for challenging projects especially for those with difficult ground conditions.

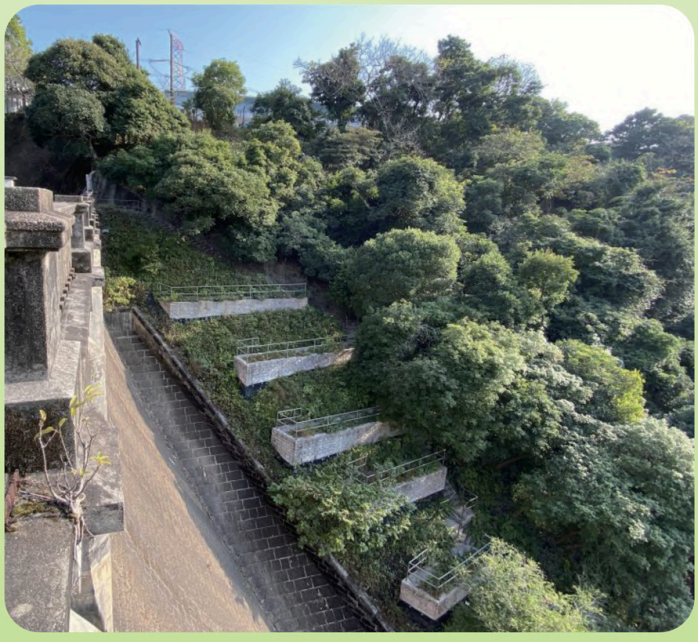

ISO 9001 : 2015
Certificate No.: CC 801

ISO 14001 : 2015
Certificate No.: CC 5408

ISO 45001 : 2018
Certificate No.: CC 7033

中國建築工程(香港)有限公司
CHINA STATE CONSTRUCTION ENGINEERING (HONG KONG) LIMITED

慎微篤行　精築致遠

EXERCISE CAUTION IN DETAILS AND IMPLEMENTATION
BUILD A STRONG FOUNDATION TO SEEK GREATER SUCCESS

www.cscechk.com

新界西堆填區擴建計劃
West New Territories Landfill Extension

將軍澳海水化淡廠第一階段
First Stage of Tseung Kwan O Desalination Plant

香港國際機場三跑道系統項目-北跑道改建工程
Hong Kong International Airport Three Runway System Project - North Runway Modification Works

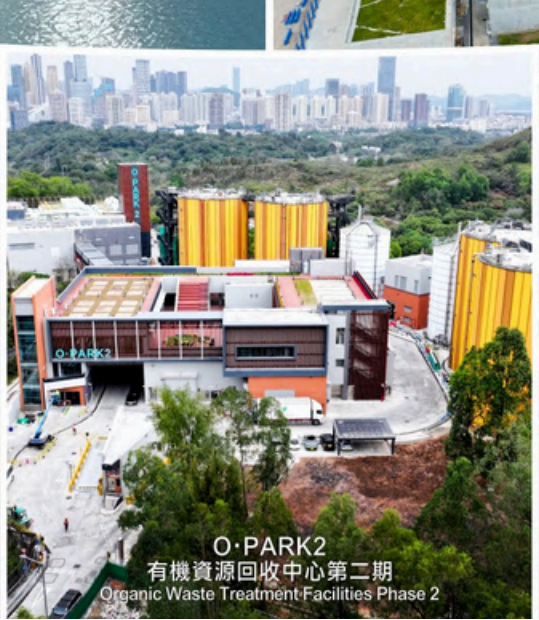
O·PARK2
有機資源回收中心第二期
Organic Waste Treatment Facilities Phase 2

元朗防洪霸及明渠改善計劃
Yuen Long Barrage and Nullah Improvement Schemes

G&E

Geosynthetic Specialist

The Company has a strong vision of geosynthetics advancement with technological evolution and towards a more achievable sustainable construction by working closely with renowned manufacturers, design engineers, academic and research institutions, and worldwide groups of interest. For more than four decades, the mission to broaden the versatility and diversification of geosynthetics applications has never found a slowdown.

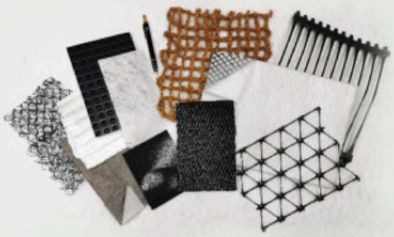

G&E ENGINEERING Since 1984

G AND E COMPANY LIMITED

14/F Kiu Yin Commercial Building
361 – 363 Lockhart Road, Wanchai, Hong Kong
Tel: 2570 0103 Fax: 2570 0089
e-mail: info@g-and-e.com
website: www.g-and-e.com

AGS (HK) igs ACT UKAS MANAGEMENT SYSTEMS 0273

geoquest

www.geoquest-group.com.hk

RETAIN

- MSE & precast retaining walls
- Reinforced soil slopes
- Dams, dikes, reservoirs and canals
- Quays, jetties & river training

CROSS

- Bridge abutments
- Buried bridge structures
- Box bridges
- Tunnels and underground structures

PROTECT

Natural & industrial risks protection

- Erosion
- Rockfall & debris flow
- Slope stabilization
- Floods & coastal
- Waste storage

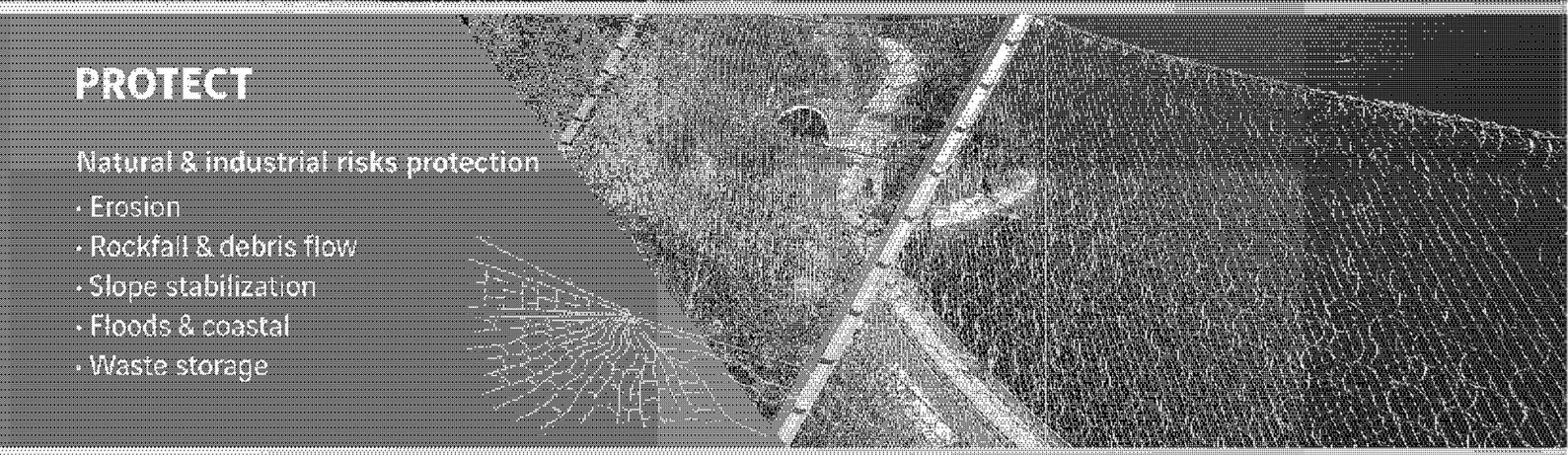

STRENGTHEN

- Embankments over soft soils, piles & subsidence
- Soil reinforcement
- Geosynthetic solutions

Products supply: geogrids, geotextiles, geocells, drainage geocomposites

GEOQUEST HONG KONG LIMITED

Unit 705-706, 7/F, Tower 1, Cheung Sha Wan Plaza, 833 Cheung Sha Wan Road, Kowloon, Hong Kong

Tel: +852 2794 0322 Email: infohongkong@geoquest-group.co.hk

VSL A member of Bouygues Construction | INTRAFOR

DELIVERING COMPLEX UNDERGROUND SOLUTIONS IN HONG KONG

Circular Shaft
MTR NOL 1635 Works Package 1

KEY CAPABILITIES

Low headroom construction
Efficient work in highly constrained spaces using specialized equipment.

Irregular shapes - circular & peanut shafts
Optimized design for complex deep shaft construction.

Diaphragm walls
Advanced D-wall execution in Hong Kong's challenging ground conditions.

Low Headroom Cutter

Intrafor.com

Empowering the Next World Class Developments

With a proven track record in delivering complex developments, Arup brings deep geotechnical expertise through a fully integrated, multidisciplinary approach to help clients turn bold, ambitious visions into safe, buildable, and innovative realities, unlocking groundbreaking solutions that transform the New Central Harbourfront into a next world class destination.

arup.com

盼記建設有限公司

Pan Kee Construction Limited

建造香港

BUILD HONG KONG FUTURE

+852 9745 9676 info@pankee.com.hk Unit 7,3/F , Block 2, Tak Fung Industrial Centre , No.168, Texaco Road,Tsuen Wan,N,T

隧道股份

香港北角英皇道 510 號港運大廈 2306-08A
Unit 06-0SA, 23/F., Island Place Tower,
510 King's Road, North Point, Hong Kong.
+852 2187 3680

Shanghai Smart City Operations Platform
上海城市智慧運營平臺

Planning 規劃	Consultation 咨詢	Investment 投資
Operation 運營	Construction 建設	Design 設計

承載城市夢想　建築美好生活
Carrying the city's dream　building a better life

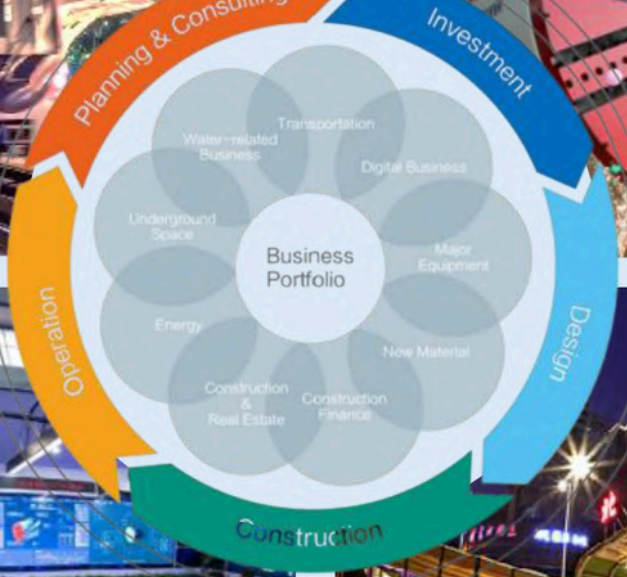

VIBRO 惠保

周大福創建集團成員
Member of CTFS Group

COMMITTED
PROFESSIONAL
UNITED

Zones 2A, 2B & 2C
of the West Kowloon
Cultural District

Development of
ex-Cha Kwo Ling
Kaolin Mine Site
(Phase 2)

Pak Shing Kok
Ventilation Building
Property Development

WWW.VIBRO.COM.HK

YWL

EXCEPTIONAL SOLUTION FROM INNOVATIVE & PASSIONATE ENGINEERS

PASSION
Exceptional solution by visionary and dedicated engineer

EXPERTISE
Leading infrastructure consultant with robust research and development support

INNOVATION
Redefine excellence with continual innovation, offering design that are safe, efficient, eco-friendly and highly buildable

SUPPORT
One stop solution to all your engineering needs

YWL is a leading bridge and structural engineering consultancy with a distinguished focus on integrating design with construction. With over two decades of international experience, we specialize in providing innovative and economical solutions for permanent and temporary works, from value engineering and construction methodology to the custom design and supply of heavy lifting equipment. Our team is renowned for tackling complex challenges across the region, backed by our own engineering software development, such as one of the widely-used geometry control software (GeomPro) for precast segmental bridge works. YWL has successfully completed many significant bridge projects located in Hong Kong, Singapore, Malaysia, Thailand, Brunei, Vietnam, Sri Lanka, India, United Arab Emirate, Kuwait, Bahrain, Australia, Ecuador and many major cities in mainland China.

We extend our sincere congratulations to the HKIE Geotechnical Division 46th Annual Seminar 2026. Our recent landmark projects demonstrate our commitment to advancing industry standards: the specialised design of Hong Kong's first S960 ultra-high-strength steel footbridge for the Fanling bypass development; the creation of a bespoke tilting table system enabling the transport of a record-breaking 7.3-meter super-wide module; and a Safety Award-winning rotating bridge design at the same serious of development project. We are proud to support the Association and look forward to collaborating on future engineering challenges.

OUR FOOTPRINT AND SERVICES

- Consultancy and project management services for infrastructure works
- Design and supply of major temporary works
- Design and supply of erection equipment and segment moulds
- Structural health monitoring system development
- Value engineering
- VDC.IDD – 3D, 4D, 5D, BR, AR

Bridging Lives

Fanling bypass S960 Footbridge

Skybridge

Airport City Link (Marine)

Fanling bypass Tilting Table

Airport City Link (Land)

Fanling bypass Bridge Rotation

Fanling bypass S960 Footbridge

Hong Kong- Zhuhai- Macao Bridge HK Link Road 2

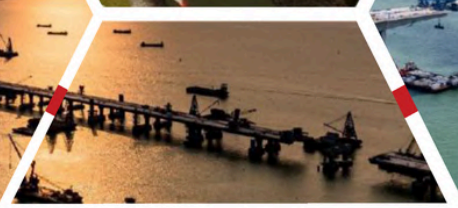

Hong Kong- Zhuhai- Macao Bridge HK Link Road 2

contact@ywlgroup.com (852) 2217 3099 www.ywlgroup.com

Innovative Solutions for Resilient Geotechnical Foundations

At Asia Infrastructure Solutions Limited, we lead the way in geotechnical engineering excellence across Asia. With over 90 years of collective experience, our expert team excels in bridging theory and practice for complex ground engineering challenges — from deep excavations and tunnel construction to the application of Self-Propelled Modular Transporters for precision heavy-lift operations. By integrating fundamental soil mechanics with advanced construction methodologies, we deliver safe and resilient foundations for all kinds of major civil infrastructure and built environments.

- 1600+ Clients
- 900+ Employees
- 90+ Years of Experience
- 8,000+ Projects

asia infrastructure solutions
a GISI Consulting Group company

Asia Infrastructure Solutions Limited
23/F, Two Harbour Square, 180 Wai Yip Street, Kwun Tong, Kowloon, Hong Kong
T: +852 3619 9400 | E: info-hk@asiainfrasolutions.com | W: asiainfrasolutions.com

AtkinsRéalis

Our Markets

Buildings & places · Defense · Industrial · Minerals & metals · Nuclear · Power & renewables · Transportation · Water

Our Services

Consulting, strategy & advisory · Engineering & design · Project & program management · Project delivery · Operations & maintenance · Capital · Decommissioning

Sustainably progressing the way we are all housed, connected, powered & protected

Engineering a better future for our planet and its people

Explore our how we're shaping Asia

中國路橋工程有限責任公司
CHINA ROAD AND BRIDGE CORPORATION

Build Smarter
Greener
and Faster

www.CRBC.com.hk
crbchk@crbc.com.hk
2283 1688 2283 1689

Decoding earth

Tremors, shifts, currents.
We map, model and monitor the built and natural environment to unlock insights from Geo-data. So you can predict what's coming.

for a resilient future

FUGRO

Gammon LAMBETH

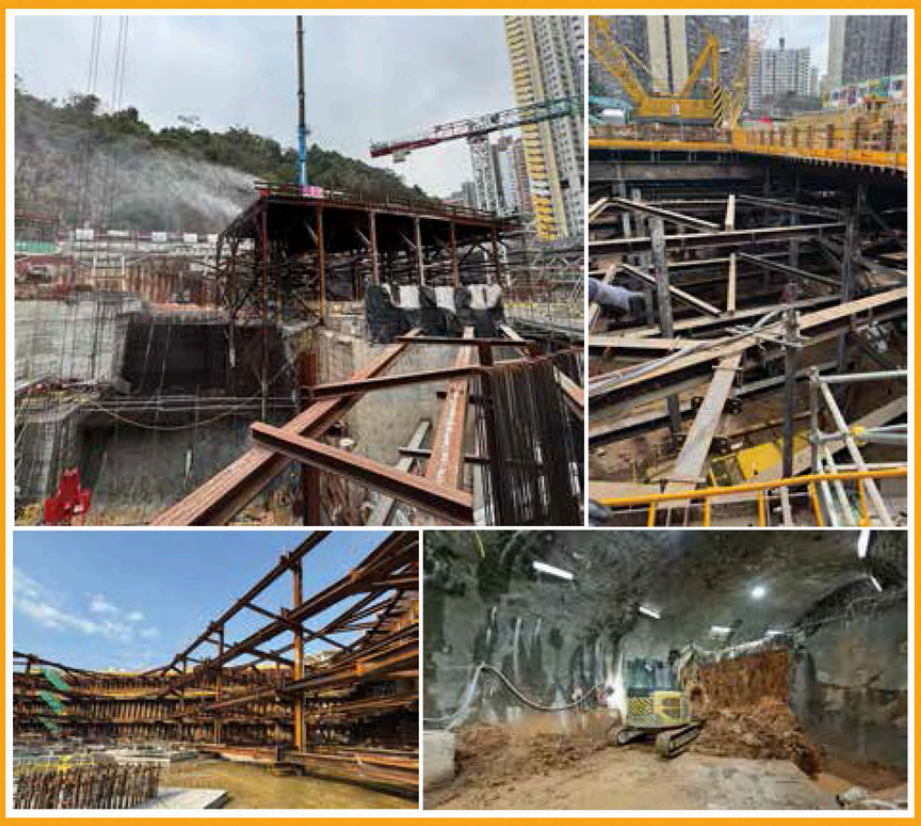

Gammon Construction and **Lambeth Associates** bring together the diverse experience of operations, planning, commercial, and design professionals – ensures it remains at the forefront of new techniques and new thinking in Geotechnical and Foundation Engineering Excellence. We are fully committed to building a better quality of life and living environment in a safe and sustainable manner.

22/F, Tower 1, The Quayside, 77 Hoi Bun Road, Kwun Tong, Kowloon, Hong Kong Tel: 2516 8790 Fax: 2516 6352

力盛工程有限公司
LIK SHING ENGINEERING COMPANY LIMITED

Room 3010, 30/F., Cable TV Tower, 9 Hoi Shing Road, Tsuen Wan, New Territories
新界荃灣海盛路9號有線電視大樓30樓3010室
Tel.(電話): (852) 2278 0039 Fax.(傳真): (852) 3577 8129
Email(電郵): info@likshingeng.com

MEINHARDT
Consulting Engineers . Planners . Managers

Over 60 Offices Worldwide

your FIRSTCHOICE | Innovative • High-quality • Value-added Solutions

Trunk Road T2

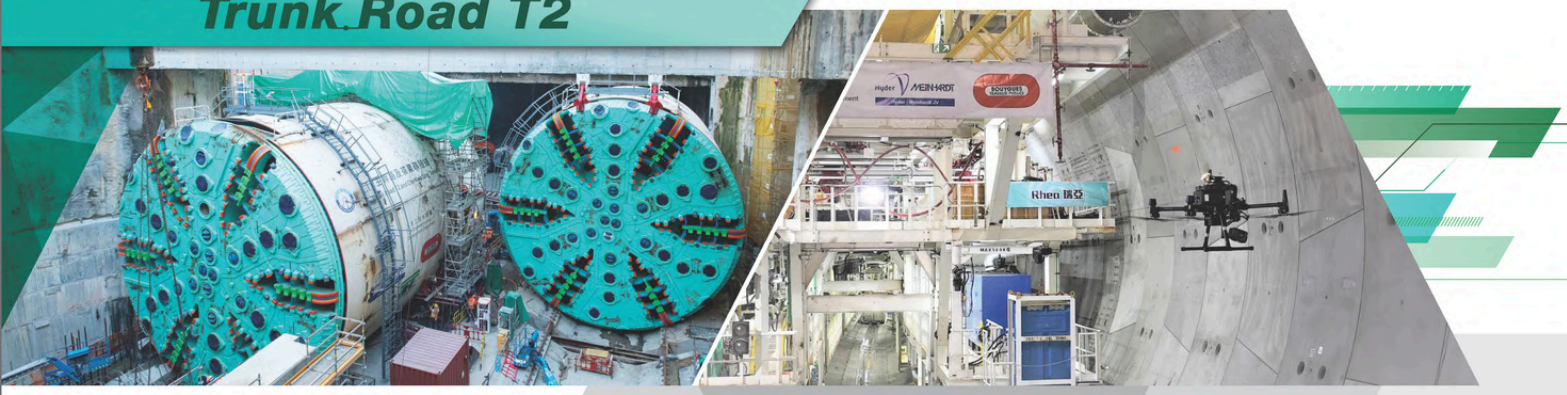

East Coast Boardwalk

Facebook

LinkedIn

Instagram

10/F, Genesis, 33-35 Wong Chuk Hang Road, Wong Chuk Hang, Hong Kong

www.Meinhardt-china.com I www.meinhardtgroup.com
mcehk@meinhardt.com.hk

MTR
心繫生活每一程

Go smart
Go beyond
載向綠色未來

致力節能減排及加強車站綠化，推動環保低碳生活！
Committed to energy saving, emissions reduction and greening of stations, to promote a green and low-carbon lifestyle!

sixense

Understanding Ground and Structures Through Data

- Subsurface investigation & modeling
- Risk management solutions for climate-affected environments
- Ground, structural and environmental monitoring & inspection

contact.asia@sixense-group.com
https://asia.sixense-group.com

Transforming your infrastructure into living assets

Tony Gee

Tung Chung East New Town Extension – Contract 1 Reclamation and Contract 3 Infrastructure
Temporary works and geotechnical design for the construction of the HK$12bn reclamation project which will provide 40,000 units of housing

Design once, engineer right

For enquiries on our specialist services contact:

+852 2377 2765 hongkong@tonygee.com

tonygee.com

泰 昇 集 團
TYSAN GROUP

泰昇地基工程有限公司
TYSAN FOUNDATION LIMITED

泰 昇 地 基 土 力 工 程 有 限 公 司
TYSAN FOUNDATION GEOTECHNICAL LIMITED

香港黃竹坑香葉道2號 One Island South20樓
20/F One Island South, 2 Heung Yip Road, Wong Chuk Hang, Hong Kong
電話 Tel: (852) 2882 3632 傳真 Fax: (852) 2808 0565
網址 Website: http://www.tysan.com

ISO 9001:2015
Certificate No.: CC111 Tysan Foundation Limited
Certificate No.: CC2852 Tysan Foundation Geotechnical Limited

ISO 14001:2015
Certificate No.: CC3315 Tysan Foundation Limited
Certificate No.: CC5565 Tysan Foundation Geotechnical Limited

ISO 45001:2018
Certificate No.: CC6837 Tysan Foundation Limited
Certificate No.: CC6836 Tysan Foundation Geotechnical Limited

ISO 50001:2018
Certificate No.: CC5697 Tysan Foundation Limited
Certificate No.: CC5861 Tysan Foundation Geotechnical Limited

泰昇地基工程有限公司
泰昇地基土力工程有限公司

業務覆蓋香港及澳門，專注地基工程，主要提供設計及建造服務，包括地盤勘察、海陸鑽孔樁／打樁、迷你樁、鑽孔工程、地腳、樁帽及地庫工程、地盤平整、泥釘及斜坡之防護工程。

Tysan Foundation Limited
Tysan Foundation Geotechnical Limited

spcialise in foundation works with businesses covering Hong Kong and Macau area. We provide services on design and construction which include site investigation, land & marine bored / driven piling, mini-piling, preboring work, footing, pile cap & basement construction, site formation, soil nail and slope protection work.

Proceedings of the 46th Annual Seminar
Geotechnical Division, The Hong Kong Institution of Engineers

Fundamentals and First Principles: Bridging Theory and Practice in Geotechnical Engineering

12 May 2026
Hong Kong

Organised by:
Geotechnical Division, The Hong Kong Institution of Engineers

Supported by:
Hong Kong Geotechnical Society
Civil Division, The Hong Kong Institution of Engineers
Structural Division, The Hong Kong Institution of Engineers

ORGANISING COMMITTEE

Chairman
Ir Lai Chi Kin, Kenneth

Members
Ir Chan Wai Keung, Ray
Ir Hung Kin Chung, Roy
Dr Wong Ngai Yuen, Louis
Ir Wong Wing Lung, Victon
Ir Lee Jo Wah, Roger
Ir Tam Wing Man, Grace
Ir To Sai Shun
Ms Chan Tsz Tung, Krista
Mr Ho Yuk Pui, Daniel

Any opinions, findings, conclusions or recommendations expressed in this material do not reflect the views of the Geotechnical Division, Hong Kong Institution of Engineers.

Published by:
Geotechnical Division
The Hong Kong Institution of Engineers
9/F., Island Beverley, 1 Great George Street, Causeway Bay, Hong Kong

Tel: 2895 4446
Fax: 2577 7791
Prepared in Hong Kong

FOREWORD

It is my great pleasure to welcome you to the 46th Annual Seminar of the Hong Kong Institution of Engineers (HKIE) Geotechnical Division.

With the theme "Fundamentals and First Principles: Bridging Theory and Practice in Geotechnical Engineering," this year's Seminar highlights the enduring importance of fundamental concepts in guiding sound engineering judgement and effective practice. In an era of rapid technological advancement and increasing project complexity, revisiting first principles enables us to better integrate theoretical understanding with field experience, ensuring that innovation remains grounded in robust engineering fundamentals.

Geotechnical engineering continues to play a pivotal role in supporting Hong Kong's infrastructure development, site formation works, and sustainable urban growth. As our city faces challenges arising from climate change, land supply constraints, and the need for resilient infrastructure, it is essential that we strengthen our foundation of knowledge while embracing new methodologies and technologies. By bridging theory and practice, we can enhance our capability to deliver safe, efficient, and sustainable engineering solutions.

This Seminar brings together practitioners, academics, and young professionals to exchange insights, share experience, and present research that demonstrates how fundamental principles continue to shape and advance our profession. I am particularly honoured to have Ir Professor Philip Chung and Ir Dr Victor K S Li as our keynote speakers, who will share their valuable perspectives and expertise. In addition, a series of technical papers will further enrich the discussions and contribute to the collective advancement of geotechnical knowledge.

I would like to express my sincere gratitude to the Organising Committee, led by Ir Kenneth Lai, for their dedication and hard work in putting together this Seminar. My appreciation also extends to all speakers, authors, sponsors, and participants for their invaluable contributions and continuous support to the Geotechnical Division.

I wish you all a fruitful and rewarding experience at the Seminar, and I trust that the knowledge and insights gained will inspire further innovation and excellence in geotechnical engineering practice.

Thank you.

Ir Terence YAU Lap Yan
Chairman, Geotechnical Division
Hong Kong Institution of Engineers (2025/26 Session)

ACKNOWLEDGEMENTS

The Organising Committee would like to acknowledge the support of the following sponsors for their generous support of the Seminar:-

Adrian Construction Limited
AECOM Asia Co Limited
Asia Infrastructure Solutions Limited
AtkinsRealis Asia Limited
Aurecon Hong Kong Limited
C M Wong & Associates Limited
China Road and Bridge Corporation
China State Construction Engineering (HK) Limited
Fong On Geotechnics Limited
Fugro (Hong Kong) Limited
G and E Co Limited
Gammon Construction Limited (Foundations and Lambeth)
Geoquest Hong Kong Limited
Intrafor Hong Kong Limited
Lik Shing Engineering Co Limited
Meinhardt Consulting Engineers
MTR Corporation Limited
Ove Arup & Partners Hong Kong Limited
Pan Kee Construction Limited
Shanghai Tunnel Engineering Co Limited
Sixense Limited
Tony Gee and Partners (Asia) Limited
Tysan Foundation Limited
Vibro (HK) Limited
YWL Engineering Limited

2026 HKIE Geotechnical Paper Award

The 2026 HKIE Geotechnical Paper Award has received 22 nominations. With the endorsement of the Geotechnical Division Committee (GDC), a 5-member Assessment Board is formed to search for the winning papers. It comprises Ir Terence Yau (Chairman), Ir Dr S W Lee (Coordinator), Ir Dr C K Lau, Ir Dr Daman Lee and Ir Dr Gavin Toh. Ir Terence Yau is an ex-officio member of the Board, who is Chairman of the GDC. The other four members are selected from the 15-member Assessment Board Panel taking account of the subject nature of the contending papers and the need to avoid potential conflicts of interest.

The Assessment Board follows the practices set up since inauguration in 2014 to ensure the confidentiality of participants and fair but critical judgment on the contending papers. Hence, the Board members would receive information on a need-to-know basis, and only the winning papers are made known publicly. They share views through a hub that removes identity tags. Deciding winners in the Assessment Board meeting is by ballot.

I am pleased to announce that the Assessment Board has decided at a meeting held on 8 April 2026 to confer the 2026 Awards on two papers:

"Advancements in design and construction practice for deep excavation (2024)"

Shum, L.K.W., Cheung, S.P.Y., Koo, R.C.H., Li, I. and Liu, J.C.

Citation: For a seminal contribution to geotechnical practice through the modernisation of deep excavation design, this paper presents the rationale and technical advancements underpinning the new GEO Publication No. 1/2023. It harmonises design approaches across public and private sectors, introduces refined limit-state methods, and proposes an innovative five-level ground deformation control mechanism that enhances both safety and constructability. By addressing long-standing challenges in urban excavation, such as groundwater level estimation, ground settlement prediction, and stakeholder coordination, the work provides a balanced framework that improves cost-effectiveness without compromising safety. This paper exemplifies how thoughtful revision of engineering guidance can have a profound and lasting impact on an entire industry.

and

"Experimental investigation of major rocks in Hong Kong as potential sensible thermal energy storage medium (2024)"

Liu Zihan, Louis Wong Ngai Yuen and Chang Su-chin

Citation: For an outstanding contribution to the field of energy geotechnics, this paper presents a comprehensive experimental characterisation of 15 rock types from Hong Kong as potential sensible thermal energy storage media. Through systematic measurements of thermophysical and mechanical properties up to 1000 °C, coupled with detailed mineralogical and chemical analyses, the work establishes a robust framework for selecting locally sourced rocks for high-temperature thermal energy storage. The identification of basalt as an optimal candidate, with clear guidance on maximum working temperatures (e.g. 850 °C for basalt), offers a practical and sustainable pathway for integrating rock-based storage systems into renewable energy infrastructure. The paper provides a rigorous and comprehensive evaluation that has already become a foundational reference for both researchers and practitioners.

The Prize presentation ceremony is to be held at the HKIE Geotechnical Division 46th Annual Seminar on 12 May 2026. The authors of the winning papers will be presented with a trophy, and a certificate each. The authors will be invited to give a 10-min presentation each on the key findings of their respective papers.

For further information on the HKIE Geotechnical Paper Award, please visit “https://hkieged.org/public/geotechnical-paper-award” at the HKIE Geotechnical Division website.

Ir Dr S W Lee
Coordinator, Assessment Board
2026 HKIE Geotechnical Paper Award

TABLE OF CONTENTS

PAPERS	Page No.
1. Some Thoughts on Bridging Research and Practice in Geotechnical Engineering Victor Li	1 - 16
2. A Simple Method for Calculating Consolidation Settlements of Clayey Soils and Settlement Prediction-Control J.H. Yin, Z.J. Chen, P.C. Wu & Z.Y. Yin	17 - 28
3. A Creative Approach for Cable Upgrading Works in Challenging Conditions Roger Lee, Karuppasamy Kalimuthu, Arthur KO So, Brian Mok, Tony Yau, Derrick Leung, Kelvin Chan	29 - 39
4. Fundamentals and First Principles of Point Load Test in Rock Mechanics Zhaonan Wang, Louis Ngai Yuen Wong	40 - 52
5. An Engineering Geological Model for Kaolin-rich Zones and Soil-Pipe Cavities in Volcanics C.D. Shardlow, R.A. Evans, Ricky C.P. Wong, Mike W.H. Cho, Andrew W.C. Lee	53 - 64
6. Comparative Study on In-Line Orthogonal and Staggered Arrangements of DCM Columns: Stress Distribution, Deformation Characteristics of Two Cases Ming-min Wang, Pan Liu, Ting-hao Mao, Alvin Lam	65 - 75
7. Analysis on Earth-pressure Imbalance on a Deep Excavation L.W. Wong	76 - 85
8. Development of Sprayable Engineered Cementitious Composites (SECC) for Tunnel Lining Applications S.N. Goh, K.L. Lo, Ivan H.H. Chan, Roy K.C. Hung, T. Wang, H. Wu, Christopher K.Y. Leung & Victor C. Li	86 - 97
9. Three-Dimensional Analysis of Stress Interaction between Closely-Spaced Bored Piles in Rock James ZJ Ruan, Anthony TT Chuang & Sammy PY Cheng	98 - 111
10. Proposed Methodology for Evaluating the Allowable Peak Particle Velocity Limit of Stabilized Rock Slopes with Rock Dowels Subject to Blasting Vibration Ivan H.H. Chan, Stanley Y.T. Cheung, Daniel Y.P. Ho, Guy Bridges,	112 - 120

Genie C.Y. Nip, Matthew W.H. Fong

11. Predicting Tunnel Overbreak in Drill and Blast Operations Using Random Forest Regression: A Case Study in Hong Kong Granitic Rock 121 - 133
Jason T.Y. Chin

12. New State-of-the-art Design Guidelines for Deep Cement Mixing: Global Review and Benchmarking Study 136 - 147
Leo C.Y. Shu, Sunny T.C. So, Anthony H.K. Wong, S.W. Lee, Z. Xu2 & Lawrence K.W. Shum

13. Recent Advancement in the Estimation of Design Debris Volume for Natural Terrain Hazard Mitigation Measures 148 - 156
R.W.M. Cheung, I. Li, C. Lam, A.C.Y. Fu & E.Y.C. Zeng

14. Application of the Circucore Pro Method in the Boardwalk underneath Island Eastern Corridor Project 157 - 166
C.K. Tse, Kenneth, S H Chung, Vincent L T Chan, Philip Daynes

15. From Heterogeneous Borehole Data to City-Scale 3D Geological Modelling Supporting Seismic Response Studies for Northern Metropolis in Hong Kong 167 - 179
K.I.M Ismail & G. Wang

16. Assessment of Foundation and Excavation and Lateral Support (ELS) Works for a Footbridge near MTR Structure in Admiralty, Hong Kong 180 - 190
Y.T. Shang, L.M. Wei, Y. Chen

17. SmartLog: Transforming Ground Investigation Records and Applications 191 - 203
Caleb Sang, Stuart W. Millis, Regis L.G. Chee, Rachel W.Y. Lau, Eric H.Y. Sze, Anthony C.T. So

18. Exploring a Cost-Effective and Sustainable Design Solution for Rock Tunnels in Hong Kong – the Rock Reinforcement Approach (RRA) and Norwegian Method of Tunnelling (NMT) 204 - 215
Franklin K. L. To, Clayton Y. K. Chan, Nick R. Barton

19. AI-Enabled Slope Upgrading Works: From Static Archives to Operational Intelligence 216 - 228
I.H.H. Chan, K.S.T. Kwong, B.J. Jiang, T.M. Ma, C.S. Sun, I.W. Wong, C.T.L. Lee, H.H.L. Cheng

20. Rainfall-Induced Loose Fill Slope Failure: New Insights from MPM Analysis 229 - 238
Z.Q. Zhan & C. Zhou

21. An Unprecedented Incident of Concrete Contamination by Marine Deposits in Bored Pile Construction Leading to Abandonment of the Piles in a Hong Kong Building Project 239 - 251
Thomas S.K. Lam

22. Implementing the 5A Control Framework: Case Studies Demonstrating Economic and Safety Benefits in Deep Excavation Design 252 - 257
Terence L Y Yau & Rachel Y K Chan

23. Integrating Design Theory to Practical Construction of Reinforced Fill Slope 258 - 266
Clifford W.C. Phung, K.F. Yeung, Penny K.C. Choy & Ben M.H. Wong

24. Application of First-Principles Sequential Inversion in Geotechnical Engineering:An Engineering Framework for Predicting Tunnel-Induced Ground Deformation 267 - 278
Zhengyong Wei

25. AI-Enhanced Detection of Untrained Compound Damage and Scour in Wind Turbines 279 - 289
De-Jie Song, Li Long, Zohreh Mousavi, Wei-Qiang Feng

26. Sustainable Design Approaches for Large Span Rock Caverns in Hong Kong 290 - 299
Jacky W.H. Tsun, Jitendra Kumar Soni, Max L.Y. Ngok, Genie C.Y. Nip, Hermann H.M. Suen

27. Case Study of Mohr–Coulomb and Hardening Soil Models in PLAXIS Using Field Monitoring Data for Excavation and Lateral Support Works 300 - 310
Gavin S.H. Toh, S.S. To, T.S. Ho, Y.L. Yeung, M.C. Fok

28. Subsurface Diagnosis Method for Undergrounds Using Distributed Acoustic Sensing with Ambient Noise Tomography 312 - 320
Wu Ju-Yang, Zhang Tian-Yu, Ma Jun-Wei, Luo Bin &
Feng Wei-Qiang

29. Geotechnical Design with Rhino and Grasshopper: Reinforcing First Principles in Hong Kong Practice 321 - 331
E. Alnaqdy

30. The Application of Multi-Temporal Unmanned Aerial Vehicle ("UAV") Imagery for Automated Landslide Identification 332 - 341
Leslie W. H. Tsang, Eugene Y. M. Tam, Danny Yung

31. Back-analysis of Excavation-Induced Ground Settlement in Hong Kong Using Mohr-Coulomb and Hardening Soil Models 342 - 353
P.O. Tang, A.K.M. Lam, Y.X Huo, W. Cheang; S. Rajbhandari

32. Design of SFRC Segmental Tunnel Linings: A Practical Framework for Wider Implementation in Hong Kong 354 - 365
T.H. Lee, T.C. Choi, C.O.A. Leung, K.H. Chan & Z.Y. Li

33. Design and Construction for the Largest Rock Cavern in Asia – A Case Study on the Relocation of Sha Tin Sewage Treatment Works to Caverns 366 - 378
Franklin K.L. To, Bridges D.C. Guy, Andrew K.W. Seto, Stephen L.C. Tam, Michael W.K. Choi & Steve C.H. Leung

34. Test and Analysis of Confined Compressive Strength and Average Elastic Modulus of Metasedimentary Rocks in the Northern Metropolis of Hong Kong 379 - 390
Zhiqian Liu, Qi Zhao,Guoxu Chen, Pan Hu, Andy Y. F. Leung, Maggie H.Y. Suen & Cyrus C.F. Chow

35. Effective Health Diagnosis System for Underground Pipeline Networks Using Distributed Fiber Optic Sensing 391 - 399
Yang Wen-Tao, Zhang Tian-Yu, Ngai Kwok-Leung, Cheung Hoi-Yan

36. Geotechnical Instrumentation Monitoring – A Transition from 3A to 5A Approach 400 - 412
Arthur K O So & Roger J W Lee

37. From Simplified Assumptions to Soil–Structure Interaction: A Paradigm Shift in Raft and Piled Raft Foundation Design 413 - 425
Ted Tse, Ryan Cheung and Bryan Zhu

Some Thoughts on Bridging Research and Practice in Geotechnical Engineering

Victor Li
Victor Li & Associates Ltd.

ABSTRACT

The behaviours of soils are too complex to be modelled without simplifying assumptions. Despite the limitations, there are still many useful albeit approximate geotechnical theories that can be relied upon to assist engineers in developing innovative schemes for design and to guide them in making rational decision for solving problems on site. The importance of the construction effects cannot be overemphasized when trying to understand or predict geotechnical behaviours. The paper discusses the nature and value of geotechnical theory, the state-of-play of design practices and make suggestions on bridging theory and practice. Examples are presented to illustrate how knowledge in theory can be used to improve the design practice and vice versa.

1 INTRODUCTION

Young graduates who are fresh out of universities may be deeply impressed by powerful computer software available for analyzing almost everything in geotechnical engineering. After running geotechnical programs day in and day out for a few years in their training, they may build up confidence on geotechnical analysis, believing that actual geotechnical structures should and will behave as predicted by computer analyses. This is far from being true in reality. Engineers seldom realize that the method of construction can have a huge impact on the behaviours of a geotechnical structure. If the analyses fail to replicate the correct procedures of construction, the prediction can be wrong by a big margin.

Geotechnical engineering, like many other branches of civil engineering, is often experienced-based. The design rules and practices established based on past experiences are seldom challenged. But the harsh fact is that prevailing design rules and practices are in many instances expedient guidelines without a sound technical basis.

This paper presents some observations on why geotechnical theories can be so wide of the mark and give examples of how some of the prevailing design practice can lead to nonsensical outcomes. Some suggestions for narrowing the gap between theory and practice will also be presented.

2 NATURE OF GEOTECHNICAL THEORY

Soils and rocks are non-homogeneous materials with high innate variability in field. Geomaterials are generally three-phase materials comprising air, water and solid. Their behaviors are complex, often time-dependent, influenced by pore-air pressure and pore-water pressure, and dependent on stress history, stress/strain path and stress level. Naturally, the behaviours of a geotechnical structure supported by geomaterials are equally complex and affected by factors such as construction method and equipment used for construction. The complex behaviours of geomaterials lead to the following characteristics of geotechnical theories:

- Significant simplifications or idealization are needed to make geotechnical theories simple and manageable for routine design.
- Theories which fail to capture the influence of construction method on geotechnical behaviours are often highly misleading and harmful.
- Predictions are often poor due to variability of soil properties, inaccuracy of theory and difficulties in obtaining representative input parameters for analysis.

2.1 Limitation of geotechnical theory

The classical theory of consolidation developed by Terzaghi (1925, 1943) is a good example to illustrate the simplification used in a geotechnical theory. The coefficient of consolidation c_v, defined as $k/(\gamma_w m_v)$ where k and m_v = the permeability and coefficient of compressibility of soil respectively and γ_w = unit weight of water, is assumed to be constant in the governing differential equation. With this assumption, an analytical solution can be obtained for the relationship between the degree of consolidation and the time factor. Although k and m_v both decrease with void ratio, they do not diminish in a linearly proportional manner. c_v is therefore not constant and changes as consolidation progresses. c_v cannot be treated as a fundamental property of soils and its magnitude is expected to be scale-dependent. In simple terms, it is a fudge factor which forces agreement between theory and observed data. Strictly speaking, the value of c_v inferred from an oedometer test of a thin clay sample may not be representative of a clay layer much thicker than a test specimen.

In the wetting band theory developed by Lumb (1962), the governing differential equation for vertical infiltration flow of water into an unsaturated slope depends on the parameters *k* and diffusivity *D* defined by $k\frac{\partial U}{\partial w}$ where *U* = potential (or suction head) and *w* = volumetric water content of soil. By assuming *D* and *k* to be constant, an analytical solution can be obtained for predicting the rate of rain infiltration into the slope. In actuality, *k* and *U* are both non-linear functions of *w*. The accuracy of the wetting band theory hinges on whether good representative design parameters for *D* and *k* can be obtained by field measurements.

Because of the need for simplification and idealization, most if not all geotechnical theories are at best approximate theories.

2.2 Influence of construction

Geotechnical engineers including renowned researchers often fail to appreciate the influence of construction on the behaviours of geotechnical works.

In most textbooks on foundation, the shaft resistance τ of pile is predicted using the following deceptively simple equation.

$$\tau = \sigma_h \tan\delta = K\,\sigma_v \tan\delta = \beta\,\sigma_v \quad (1)$$

where δ = friction angle soil at the pile/soil interface, σ_h and σ_v = horizontal and vertical stress respectively, *K* = coefficient of horizontal pressure and β = shaft friction coefficient. Eq.1 involves a series of simplifications. Textbook authors often mislead readers into misbelieving that there is a sound soil mechanics basis for Eq.1. In fact, none of the quantities in Eq.1 can be known with certainty except perhaps for σ_v. The horizontal stress σ_h and the friction angle δ depends significantly on the construction method and do not necessarily relate to the soils in the original soil profile.

When the temporary steel casing is used for construction of a bored pile, the soils outside casing will be subjected to different modes of shear movement depending on whether a vibrator, an oscillator or a rotator is used for installing the casing (Li 2026). The soils outside the casing will also be densified to a differing degree depending on the equipment used for sinking the casing and this will affect the magnitude of both σ_h and δ.

If a permanent liner is provided for a bored pile, there will be an annular gap between the liner and the temporary steel casing (Li 2026). When the casing is extracted, the soils outside the casing will displace towards the liner. If the arching effect of soils is significant enough, the pile bore is stable and an open void will remain, giving $\sigma_h = 0$. Otherwise, the soils will continue to move and close up the gap. Figure 1 shows a photograph of a stable gap observed outside the permanent liner after extraction of temporary casing for a project in Yuen Long (Li 2026) and a graph for the measured depth of a similar stable deep annular void for another bored pile in a project at Tseung Kwan O (Lam & Li 2023). Note that the depth of stable void was deeper than 40m in the first day after extraction of temporary casing.

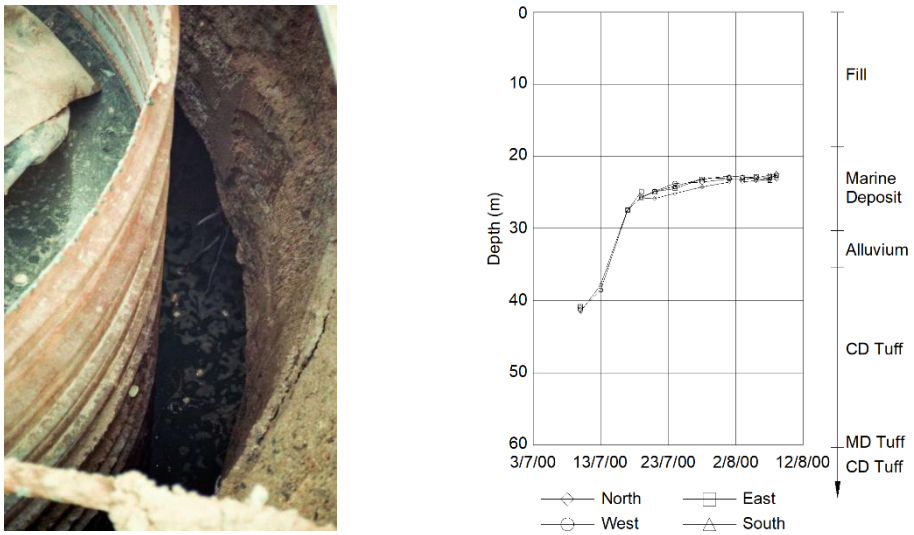

Figure 1: Annular void outside permanent liner (Li 2026; Lam & Li 2003)

If the arching effect is not sufficient to maintain a stable pile bore after extraction of casing, σ_h will drop from a higher value corresponding to its initial state to a smaller but non-zero value after closing the gap. According to the study by Lo et al. (2001), the final horizontal stress is small and well below the pressure under the at-rest condition.

When a permanent liner is provided, the interface friction angle δ may have no relationship to the soils located next to the bored pile in the original soil profile. If the annular void is stable after extraction of casing, the materials filling up the gap may come from soils sloughing off the stable pile bore from higher levels or fill materials placed by the contractor before constructing the pile cap. The interface friction angle δ also depends on the nature of the permanent liner. If a thin steel casing is used, δ may be smaller due to the smooth surface of the casing. If a spiral corrugated liner is used (see Figure 1), δ is expected to be higher due to the undulating surface of the liner.

If no permanent liner is used, the pile bore will be in direct contact with the tremie concrete. The horizontal stress σ_h along the pile bore will simply be the pressure of wet concrete. If one knows how to predict the pressure profile of wet concrete, he may obtain a better prediction of the shaft resistance than using soil mechanics theories.

The prediction of shaft friction of a driven H-pile is by no means a simpler task than that for a bored pile. The author recalls a technical talk delivered by a Rankine lecturer some years ago. The speaker presented the results of a study in which he had used an analysis model developed by his team to obtain accurate predictions of the behaviour of an H-pile. Like most engineers would have done, the soil layers used in his analysis model was based on the original soil profile inferred from boreholes. The Rankine lecturer failed to recognize the important phenomenon that when an H-pile is driven or jacked into the ground, the soils on both sides of the web of the pile will be dragged downwards. Vertical voids will be formed below the ground surface as shown in Figure 2. The soils in contact with the H-pile will be quite different from those inferred from the original soil profile. The vertical voids outside the H-piles are usually backfilled by contractor using whatever fill materials they can find on site after completion of pile installation. It is puzzling why a good prediction of pile response can be obtained by the Rankine lecture using the original soil profile without knowing the depth of voids and the materials used for backfilling the voids. Again, Eq.1 seems to be of little use in helping us to predict the shaft resistance of an H-pile.

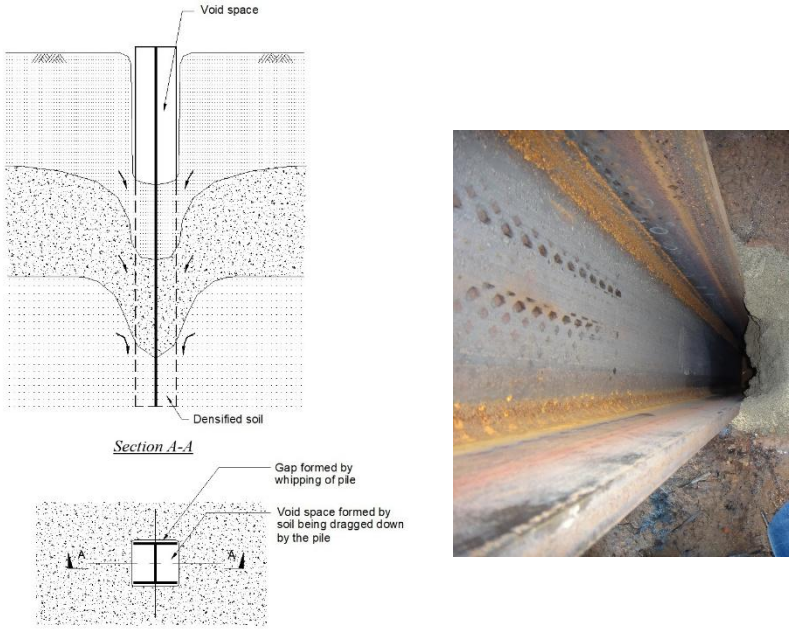

Figure 2: Voids formed during installation of H-pile (Li, 2026)

The influence of construction is equally important for assessing the pullout resistance of soil nails. Chu & Yin (2004) presented pullout test results of soil nails measured in the laboratory. The vertical pressure was applied after the test soil nail had been installed inside the test apparatus. Based on this test arrangement, Chu & Yin (2004) observed a linear relationship between pullout resistance and applied vertical pressure. In the discussion to their paper, the author argued that the test procedures adopted by Chu & Yin was inappropriate (Li & Lo 2007). The overburden pressure of an existing slope should be in existence before the soil nails are installed. After the drillhole for a soil nail has been formed, the arching effect of soil will be mobilized to resist the overburden pressure such that the radial stress acting at the surface of the drillhole must be zero if the drillhole is stable. The overburden pressure sensed by the soil nails is practically zero, not the initial existing overburden pressure. The pullout resistance of soil nails should be attributed to other factors not related to the overburden pressure of soils, such as normal stress induced by constrained dilatancy, interface dilatancy due to overbreaks in the drillhole and/or physical bonding between cement grout and soils. To obtain the real behaviour of soil nails, Li & Lo (2007) argue that the drillhole for test soil nail should be formed after the vertical pressure has been applied to the soils in the test apparatus. Such a test arrangement has indeed been adopted later by Su et al. (2008). The new results indicate that the pullout resistance of soil nails is now largely independent of overburden pressure.

2.3 Uncertainty of prediction

Geotechnical predictions are subject to large uncertainties due to inaccuracy caused the simplifying assumptions made in the theory, use of meaningless formulas, innate variability of soil properties/input parameters, failure to account for effect of construction or a combination of these factors. As remarked by Terzaghi (1963), '*in soil mechanics, the accuracy of computer results never exceeds that of a crude estimate*'. As a norm, it is unrealistic to expect a very good prediction to be obtained from a geotechnical theory.

Table 1 shows the shaft resistance coefficient β for different pile types and soil types inferred from instrumented test piles in Hong Kong (GEO 2006). The ranges of β are so wide that Eq.1 is of little practice use in assessing the shaft resistance of piles because shaft resistance is highly dependent on construction methods and many other factors.

Table 1: Typical values of β (GEO 2006)

Type of piles	Type of soils	Shaft resistance coefficient β
Driven small displacement piles	Saprolite Loose to medium dense sand	0.1 – 0.4 0.4 – 0.5
Driven large displacement piles	Saprolite Loose to medium dense sand	0.8 – 1.2 0.2 – 1.5
Bored piles and barrettes	Saprolite Loose to medium dense sand	0.1 – 0.6 0.2 – 0.6
Shaft-grouted bored piles & barrettes	Saprolite	0.2 – 1.2

Figure 3(a) which shows the bearing capacity factor N_q for the toe resistance of a solid pile developed by various renowned researchers. The variations in N_q are large purely due to the differences in assumptions or simplifications used in different bearing capacity theories. Figure 3(b) presents the data and design lines marked with A, D, K, M, P, T and W recommended by various researchers for the adhesion factor used for assessing the shaft resistance of piles in clayey soils. Again, there are large differences amongst the various design lines likely to be due to innate variability of soil properties and dependence of α on construction methods.

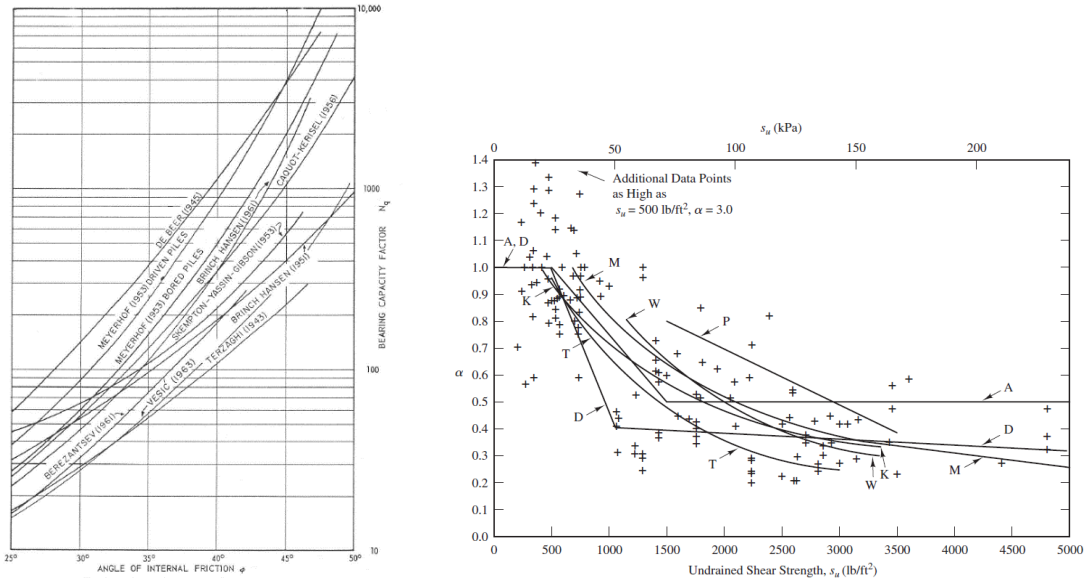

(a) (b)

Figure 3: (a) Bearing capacity factor N_q for toe resistance of pile (after Vesic 1967) and (b) Adhesion factor α for clay (after Coduto et al. 2016)

3 DESIGN PRACTICE – THE STATE OF PLAY

3.1 From control to over-control

With the introduction of design codes, technical guidance notes, practice notes and design guidance documents promulgation by various government departments, geotechnical design has become increasingly codified and regulated in Hong Kong. Design rules and practices will emerge to deal with the restrictions arising from formal or de facto regulatory requirements. As discussed by Li (2026), such design rules and practices possess the following general characteristics.

a. They are simple and usually conservative.
b. Deemed-to-satisfy guidelines are specified to avoid dealing with the analysis and checking of otherwise more complicated actual situations.

c. Design rules or practices are often ad-hoc or expedient suggestions. They are not necessarily sound and can sometimes be nonsensical.
d. They are rigid requirements. There are penalties for not following the design rules, such as a longer period for obtaining approval, the need for trial pile and etc. Otherwise, design engineers will change the design rules frequently and design approval will no longer be a straight forward task for regulators.

Design rules and practices are created to make checking of design submissions easier and to prevent designers from being too aggressive in their designs. Geotechnical engineers who want to be innovative and have more freedom in design often find it frustrating when trying to deviate from established rules and practices. The author shared some of his frustrations in design submissions in Li & Lo (2008). The following are some more cases to be shared.

In Hong Kong, foundations are customarily designed as either footings or pile foundations. Also, computer programs need to be pre-approved by the Buildings Department before they can be used for engineering analysis for design submissions to the department. An internationally renowned professor and foundation expert has once told the author the following story. He was appointed as a consultant to develop a pile-raft design for a project in Hong Kong. Obviously, it would not be an easy task to secure the approval of such an 'innovative' design even though pile-raft foundations are not uncommon outside Hong Kong. The professor initially carried out the design using design charts and manual calculations. The design was rejected on the ground that a more rigourous analysis should be used to justify the design. He then re-submitted the design using a well-known program he had developed himself. The design was again rejected on the ground that the program was not a pre-approved program. The professor finally gave up.

Some years ago, the author prepared a simple design for government approval. It involved some minor temporary cut slopes with a sheetpile cofferdam. The proposed cut slopes had a gradient of 30º and a maximum height not exceeding 0.75m. The author did not prepare any slope stability calculations for the proposed temporary cut slopes, thinking that such calculations would not be necessary because the proposed cuttings were minor and would not a safety threat to the public. The author's judgement was wrong. After submission, full slope stability analyses were required and the slope gradient needed to be further reduced to 26º to make sufficiently safe to meet the prevailing design standard.

In the early 2000s, a contractor was awarded a foundation contract for installing jacked piles for a government project. There was practically no experience on how jacked pile could be installed to meet the pile acceptance criteria at the time. The contractor managed to negotiate the residual settlement criterion to be waived in the contract and there was also no contract specification to dictate how jacked piles should be installed. The author was appointed by the contractor as consultant for the project. Since there was no contract specification controlling the method of construction, the author had the free hand to develop his own method for installing the jacked piles. Fortunately, some simple methods were developed by the author that enabled the jacked to be installed successfully and could also meet the residual settlement criterion as a bonus. After this successful project, the residual settlement criterion could no longer be waived by the government department for subsequent projects. In addition, a particular specification was developed to control the installation of jacked piles. Additional requirements related to regular calibration of pile jacking machine and re-jacking of installed piles to confirm the performance of completed jacked piles were gradually introduced in the specification. With the many requirements introduced in the specification, jacked piles have become an unattractive foundation option to contractor for future projects.

3.2 McDonaldization of design work

From a commercial point of view, design consultants may actually prefer geotechnical design to be codified, highly regulated and conservative. There are good reasons for this. First, a conservative design has a lower probability of failure and will hence reduce the consultant's professional liability and risk exposure. Second, the consultant can give a good excuse to his client not to adopt an innovative design because of the smaller chance of getting the approval from regulatory authorities although the real reason is probably to save the man-hours needed for developing and defending an unconventional design. Third, McDonaldization of design work, a term borrowed from Ritzer (2000), can be developed when design codes and rigid design guidelines are enforced by regulators.

McDonaldization of design work is important to consultants to remain competitive in their business. It is normally done with the help of standard worksheets for calculations and standard typical details to be used in

design drawings. Once the design process has been McDonaldized, the design work can be performed by technicians, inexperienced graduate engineers or perhaps equally well by non-technical staff to reduce staff cost and to achieve higher productivity and profit margin.

McDonaldization has important side effects. People involved in performing McDonaldized design may not need to know or understand the basic concepts or details behind the black-box tools they use for the calculations. They are trained to become proficient engineers, not professional engineers. Engineers trained in this manner may have little interest to learn the fundamentals of geotechnical engineering when the criterion for job promotion is based on proficiency. The author had once the opportunity in a professional interview to ask an engineer who seemed to be quite experienced in geotechnical engineering according to his resume the question: 'What is a marine deposit?'. The author was shocked to hear the answer : 'It is accumulation of rubbish on the seabed'.

4 VALUE OF THEORY

Geotechnical theories are useful despite their limitations provided that they are able to capture certain fundamental behaviours of soils even in an approximate manner. Theories are important in explaining and understanding geotechnical behaviours, assisting designers in developing innovative schemes and guiding engineers in making rational decisions to solve problems on site as illustrated below.

a. Although the classical consolidation theory involves the incorrect assumption of a constant c_v, it can usefully explain the gradual settlement of a clay layer under loading.

b. The wetting band theory involves the big assumptions of constant *D* and *k*, but it can beautifully explain why a deeper wetting front can develop for the less permeable volcanic soils in Hong Kong.

c. It is well established that preloading can reduce primary and secondary settlement of soils although such effects cannot be predicted accurately using available geotechnical theories. The same behaviour is expected to be applicable to pile. Although the approach of subgrade reaction in modelling soils as soil springs is subject to criticism, it does demonstrate that buckling of pile is not an issue even when the pile is embedded in loose sand with a low constant of horizontal subgrade reaction n_h. Given these theoretical findings, a construction method can be successfully developed for installation of jacked H-piles using the technique of preloading to reduce residual pile settlement and sand filling for preventing buckling of pile during jacking (Li 2026).

d. The shear strength τ of an unsaturated soil can be represented using the following equation (Fredlund & Rahardjo (1993).

$$\tau = c' + (\sigma - \sigma_a)\tan\phi' + (\sigma_a - \sigma_w)\tan\phi^b \qquad (2)$$

where σ = normal stress, σ_a = pore air pressure, σ_w = pore water pressure, ϕ' = angle of internal friction relative to $(\sigma - \sigma_a)$ and ϕ^b = angle related to shear strength relative to matric suction $(\sigma_a - \sigma_w)$. The matric suction of soils in a slope can be very high and exceed 100 kPa during a dry season or when the surface of the slope is protected by a hard surface (e.g. Sweeney 1982). The apparent cohesion represented by the term $c' + (\sigma_a - \sigma_w)\tan\phi^b$ may be significant enough to maintain stability of a steep slope. This can explain when old steep chunam slopes can remain stable for decades. The shear strength of soils can drop quickly when the soil suction is lost due to rain infiltration and this can explain when rain-induced shallow failures of slope often occur suddenly without warning.

e. The factor of safety *F* of a dry slope with a planar slip surface is given by the following expression.

$$F = \frac{c'L}{W\sin\alpha} + \frac{\tan\phi'}{\tan\alpha} \qquad (3)$$

where c' and ϕ' = effective strength parameters of soils, L = length of slip surface, W = weight of soil wedge and α = slope angle. L is proportional to the slope height h. W is related to the area of the soil wedge and is hence proportional to h^2. The second term of Eq.3 is constant and the first term is inversely proportional to slope height h. Some important implications on slope design can be made from just the simple equation of Eq.3. For large slopes, i.e. when h is large, the first term is insignificant and an increase in factor of safety can only be achieved by having a gentler slope. For a steep slope, a high factor of safety can only be achieved when the slope height is small and the first term of Eq.3 becomes more significant. Despite its simplicity, Eq.3 is extremely useful for preliminary design of slopes and making the decision on whether more rigourous slope stability analyses need to be carried out. This equation is also a useful quick tool for checking the 'reasonableness' of the results obtained from more detailed computer slope stability analyses.

f. A useful design scheme can often be developed based on some very basic soil mechanics concepts or theories. The retaining wall schemes discussed by Li & Chung (2013) can be used to illustrate this point and they involve a few basic textbook theories regarding earth pressure, stability of retaining wall and bearing capacity. The earth pressure acting on a retaining wall can be estimated using various theories in the literature such as the Coulomb's theory. Figure 4 shows the variation of coefficient of active pressure K_a with the inclination angle of wall back α for a cohesionless sand with angle of shearing resistance $\phi = 35^o$ and wall friction angle of $\delta = 0$ based on the formula in GEO (1982, Figure 17). As compared with a retaining wall with a vertical wall back (i.e. $\alpha = 0$), K_a is larger i.e. ($\alpha < 0$) when the wall back slope forward and smaller when the wall leans backward (i.e. $\alpha > 0$) according to Figure 4.

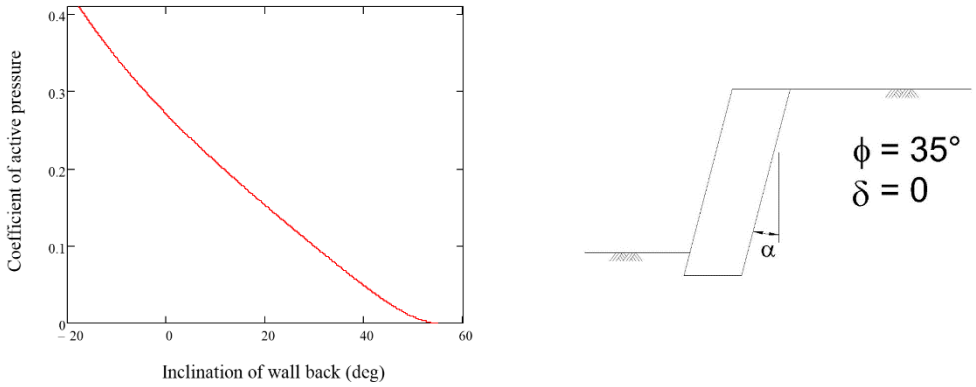

Figure 4: Variation of active earth pressure coefficient K_a with inclination of wall back α

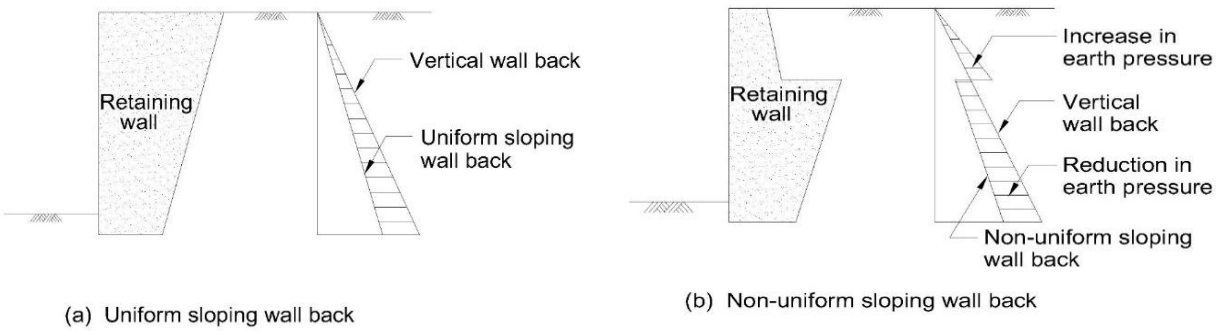

Figure 5: Retaining wall with sloping wall back

Since the earth pressure can be reduced using an inclined wall back, a higher factor of safety against sliding for a gravity wall can be achieved using the wall geometry shown in Figure 5(a). As earth pressure increases with overburden pressure and depth, the highest reduction in earth pressure occurs at the lower portion of the retaining wall. The wall geometry in Figure 5(a) is not efficient because the upper portion of the wall occupies a larger proportion of the total area (hence a higher material cost) with only a small

reduction in active earth pressure. A more efficient geometry can be obtained by a vertical or forward leaning wall back for the top part of the wall as shown in Figure 5(b). It can substantially reduce the cross-sectional area of the wall without significantly increasing the earth pressure.

The cross-sectional area of the retaining wall can be further minimized by reducing the wall width and constructing part of the wall using reinforced concrete as shown in Figure 6. Again, textbook soil mechanics theories are useful in guiding us in modifying the design scheme. The wall base needs to be sufficiently wide to achieve an adequate factor of safety against overturning about the wall toe. The bearing capacity of a shallow foundation depends on its width according to bearing capacity theory. The wall base should be wide enough to achieve the required factor of safety against bearing failure. Higher factors of safety for overturning and bearing failure can be achieved by extending the wall toe as shown in Figure 6.

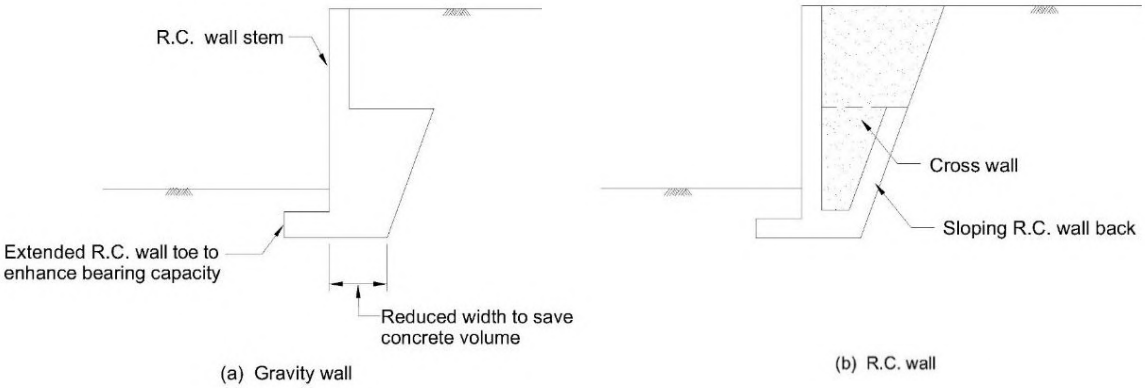

Figure 6: Additional schemes of retaining wall with sloping wall back

Geotechnical design is in many ways like cooking a meal. A good chef (the geotechnical engineer) should have a good knowledge of a wide range of food ingredients and seasonings (fundamental geotechnical theories). He should be able to distinguish good ingredients that can enhance the food from those (the useless theories like Eq.1 for predicting shaft resistance) that can ruin the dish. The chef should be able to choose the right combination of ingredients in preparing a good recipe (the design). A good dish can often be produced just using simple ingredients, like a nice salad prepared from fresh vegetables and a special dressing. The discussions above for a retaining wall with sloping wall back demonstrate that one can go a long way in developing useful design schemes by just a few basic textbook concepts.

5 BRIDGING THEORY AND PRACTICE

The skills needed in bridging theory and practice evolve with time. In the past, site experiences must be gained from spending time on site. In this internet age and new era of artificial intelligence, knowledge site experience can be gained by sitting in front of the computer and using imagination. The following are some suggested ways for bridging theory and practice based on the author's past experiences.

5.1 To keep learning

A good knowledge of theory and practice is an essential requirement for being a competent geotechnical engineer. It is therefore useful to develop a habit of continuous learning as new and useful theories, ideas and practices are constantly developed by others.

There are many useful theories that can capture the fundamental behaviours of soils and geotechnical structures, but one should be careful that there are equally many theories which are useless. Eq.1 is a good example of a useless theory. The β value is largely based on past experience. It is like having the answer before doing the prediction. There are also many theories that are toxic. The Asaoka method is a good example of this. It is a deceptively simple and powerful method for predicting the ultimate settlement of a clay layer. On closer examination, it is purely a curve and extrapolation tool. It can be used to fit almost all data and produce a prediction that can be seriously wrong (Li 2006, 2026). It is often extremely boring to study theories in the

beginning. With time, one becomes sharper in identifying theories that are useless or misleading. The study of technical information will then become a much more challenging and interesting exercise.

Information on construction methods in the form of company brochures and youtube videos is widely available on the internet. One can learn how reverse circulation drilling is performed for construction of bored piles comfortably in an air-condition room without having to endure the burning sun on site. However, one must be careful in filtering the information on the internet. Manufacturers who develop the video, for instance, for a particular equipment or construction technique may be biased and do not mention the problems that may occur.

There is no excuse for an engineer not to keep learning unless he is content with being a proficient engineer. There are good incentives for doing extensive reading. Civil engineering, of which geotechnical engineering is a branch, is a very old profession. There must be numerous civil engineering papers written on case histories of interesting projects, innovative design schemes, failures, problems encountered with solutions, and etc. There must be some good things in these publications which you can copy, adapt and improve for use in your own projects. The author often says jokingly to his staff, 'don't invent if you can copy (可以抄便不要創作)'. The advantages of copying are well discussed by Earls (2015). Copying enables you to become a geotechnical guru faster because you can develop a better scheme much more easily by improving innovative solutions already developed by others. You can learn about and avoid problems which others have taken many years to discover the hard way.

Figure 7 presents an innovative solution developed by the author based on copying. In 1999, the author read an interesting paper published by Powrie et al. (1999). The paper described a retaining wall scheme (Scheme 1 in Figure 7) involving a contiguous bored pile wall with a stabilizing base. To construct the stabilizing base, a temporary slope berm needs to be maintained initially in front of the wall. A raking prop is then installed to support the bored pile wall before removing the slope berm for construction of the stabilizing base. The raking prop can be removed upon completion of stabilizing base.

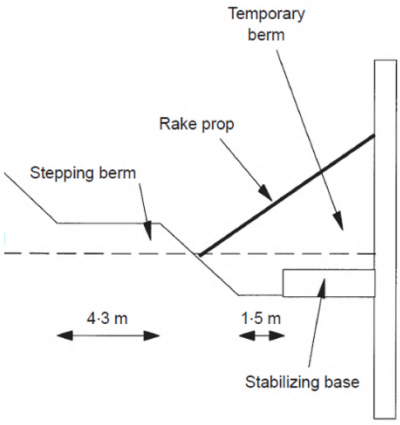

Scheme 1: Powrie et al. 1999

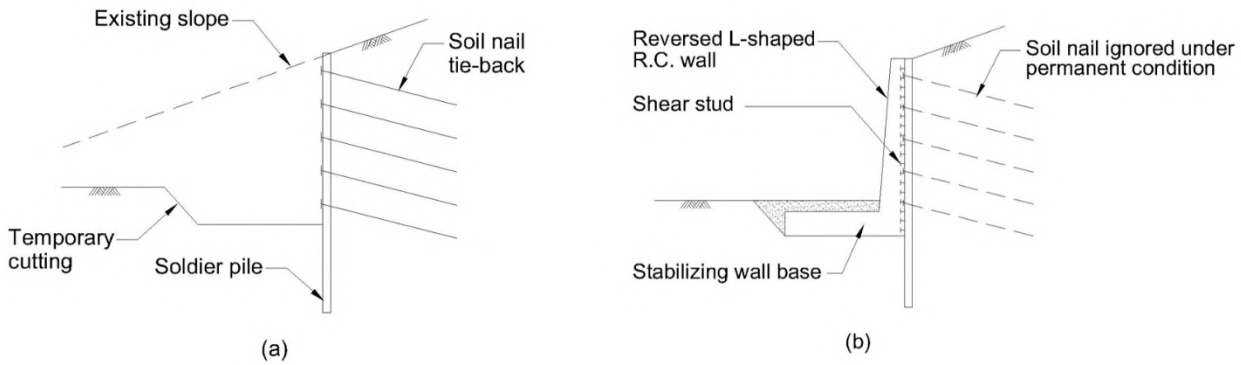

Scheme 2: Li & Chung (2013)

Figure 7: Retaining wall with stabilizing base

The concept of a stabilizing base is useful in increasing the height of a retaining wall, but the author does not like Scheme 1 for two main reasons. First, the construction of bored piles on a slope is not an easy task and usually requires a major steel temporary working platform. If a temporary working platform has to be built, it may be easier to adopt a simpler scheme of a cantilever bored pile wall with larger piles. Second, the connection of a new concrete base to the completed bored pile wall is a troublesome task. The author has built on the concept of Scheme 1 and developed Scheme 2 in Figure 7 which is much easier to construct. Steel soldier H-piles supported by tie-backs are used the lateral support system. The soldier piles can be constructed on sloping ground using crawler cranes with a telescopic boom. A reversed L-shaped reinforced wall can then be constructed and integrated with the steel soldier pile wall to form a composite retaining wall. Scheme 2 has now been used for several major projects in Hong Kong with retaining height exceeding 20m in some projects (Li & Chung, 2013; Choi et al. 2021).

5.2 To develop a critical mind

When acquiring new knowledge, one should develop a critical mind in reviewing the information he has learned. He should separate the wheat from the chaff and keep only useful new knowledge in the precious storage space of his brain. One can develop a critical mind by forming a habit of asking 'why', 'why not' and 'what-if' questions in a learning process described as mental Q&A by Li (2026).

By asking 'why', you are trying to make sure that you do understand the technical paper you are reading or to query if there are any mistakes in the paper. You should not accept the information you have learned as useful until you have satisfactory answers to your 'why' questions.

By asking 'why not', you are challenging or deviating from the current practice. Very often, the 'why not' question can lead to a useful outcome. There is a good story to be told about asking 'why not'. A contractor was awarded the contract for the Happy Valley Underground Stormwater Storage Scheme project. The site was located within the Happy Valley Race Course. The original design involved over 500 rock socketed H-piles to resist the flotation of the underground water storage box- structures. To maintain uninterrupted horse racing activities on Wednesdays or Saturdays, the contractor had to remove or relocate the piling equipment before any racing day so as not to obstruct the view of the horse racings. The author was invited by the contractor to attend a meeting to advise on whether the number of tension piles could be reduced. After listening to a short briefing on the project by the contractor, the discussion began by my question of 'why not delete all the piles'. The reason for this question is simple. If there is indeed a method that can be used to reduce the number of piles, it is likely that the same method can be enhanced to enable all piles to be deleted. In the end, subsoil drains were used to reduce the upthrust and all the piles were deleted.

The 'what-if' questions are also useful because it can often spin off to some new ideas and potential issues not discussed or considered in the original research paper, geotechnical design or technical proposal.

5.3 To design for construction effects

The behaviour of a geotechnical structure is significantly influenced by the method of construction as already discussed earlier. One must cater for the likely outcomes in his design. If an annular void around the pile is expected to be formed when constructing a bored pile with a permanent liner, one must make sure that the bored pile is still structurally adequate when the lateral subgrade reaction is expected to be small or close to zero along the permanent liner.

5.4 To be imaginative

Mental simulation is a technique that involves visualizing in the mind about possible outcomes that will occur for a given event. The author finds this technique very useful. When reading a technical paper, one can often get a fair idea of whether the paper is technically sound using this technique. The same technique can also be used to guess the plausible root cause of a problem occurring on site.

When reading the paper by Chu & Yin (2004), one can simulate the construction of soil nails on an existing slope in his mind. One can easily visualize and expect that there will be no radial stress acting on the surface of a stable drillhole. If so, the initial normal stress acting on the soil nails after installation must be small and close to zero. If the test procedures in a experimental cannot replicate the actual initial loading conditions of soil nails,

the results are likely to be misleading. Therefore, one can put a big question on the findings by Chu & Yin (2004) simply on the basis of a mental simulation.

Mental simulation can help to identify the likely cause of ground settlement during excavation within a pipe pile cofferdam. Figure 8(a) and (b) show the typical details of a pipe pile wall. Lagging walls are installed across adjacent pipe piles and sealed by welding. A grout curtain is usually installed behind the pipe pile wall to provide an impermeable barrier to reduce the drawdown and associated ground settlement outside the cofferdam. The voids between the excavated surface and the lagging wall are to be sealed by cement mortar.

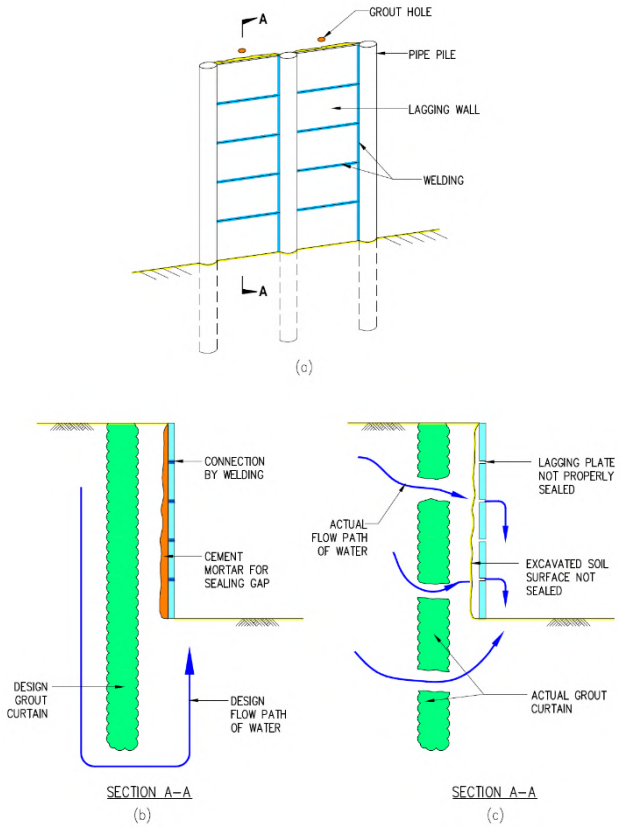

Figure 8: Performance of a pipe pile cofferdam

Proficient engineers who are well trained in producing reports for design submissions often suffer from the problem of tunnel vision. When a problem of ground settlement next to a pipe pile cofferdam occurs, they will often jump to the conclusion that the grout curtain is not deep enough, the struts are not stiff or close enough and so on. It is understandable because these are the issues which they are familiar with and need to deal with day in and day out in their shoring designs in the office. Additional grouting works and/or reduction of vertical spacing of future struts are often specified as the remedial measures for controlling further ground movement. Grouting works require drillholes to be sunk before grouting can be carried out. The drilling operation itself will cause relaxation of ground and hence further ground settlement. The remedial works of additional grouting works often lead to more ground settlement, not less.

Based on the author's experience, the root cause of the problem is usually completely different. If one imagines being the contractor, he can ask himself whether he will diligently carry out the welding to seal the lagging wall and to fill the voids behind the lagging walls with cement mortar. The answer is obvious – 'No'. If one carries out further mental simulation, one can foresee that the actual situation is likely to be similar to what is described in Figure 8(c). The grout curtain may not be continuous due to difficulty in ensuring a perfect continuous grouted zone, deterioration of chemical grout with time or simply poor workmanship. The voids behind the lagging wall are left open and the lagging wall is not sealed by continuous welding. All these will lead to uncontrolled flow of water through the lagging wall and a rapid drawdown of groundwater table outside cofferdam. One can easily verify the finding of the mental simulation by a single visit to the site or asking the contractor to send him a photograph of the lagging wall to see if there is water emerging from the lagging wall.

If the finding of the mental simulation is right, the most effective remedial works will be to seal the lagging walls quickly by welding and fill up the voids behind the lagging wall using a suitably thick cement grout.

The author has recently been asked by a contractor to provide technical advice on proposing some precautionary measures for minimizing potential ground movement of a deep excavation in Central, Hong Kong. The site is surrounded by several live MTR tunnels. Bored piles with left-in steel casings are used as the embedded wall for the cofferdam. Temporary steel lagging walls were to be installed between adjacent bored piles and welded onto the left-in casings in a manner similar to that described in Figure 8(a). The penalty for delay was extremely high for the project. The contractor could not afford any loss of time caused by suspension of works if the observed ground movements were to exceed the allowable limit. Amongst various suggestions made by the author to the contractor, the strongest advice was to limit the construction of lagging walls within a smaller zone each time. The lagging walls must be completely sealed by welding and the voids behind them have to be completely filled up by cement grout. According to feedback from the contractor, the suggestion was effective in preventing leakage of water through the lagging walls. The excavation for the project was completed successfully with very small ground settlements within just a few millimetres.

5.5 To defy convention

With extensive McDonaldization of design work, on-the-job training is focused on producing proficient engineers whose mindset are deeply shaped by the prevailing design rules and practices. They become insensitive to deficiencies which may exist in such rules and practices.

Pile sleeving is a standard technique used to prevent transfer of lateral load from piles onto slopes. The allowable lateral deflection of piles is small, typically 25mm or less. For a sizable slope, failure is unlikely to cannot be triggered by such a small lateral movement. If so, pile sleeving serves no function other than using it as a trick to avoid having to deal with the problem. If pile sleeving has to be used, a more practical approach is to still treat the pile as sleeved in the analysis but do not actually provide the sleeving in construction (Li 2026).

The residual settlement criterion for pile loading test has been used for decades and few will question its usefulness. As discussed by Li (2024), full unloading of piles will not occur for a real structure until the structure is demolished. It is therefore meaningless to impose a residual settlement criterion as part of the pile acceptance criteria. The residual settlement criterion can lead to the absurd outcome that a well performing pile is rejected while a pile with poor performance will pass the loading test (Li 2024).

Geotechnical engineers should critically evaluate the prevailing design rules and practices and be bold to point out the deficiencies. A flawed design rule/practice is more likely to be changed when there is a higher awareness about its deficiency within the geotechnical profession.

5.6 To think out of the box

The constraints for geotechnical designs depend on site conditions. There are no simple rules for tackling the design problems that are applicable to all sites. An innovative design often calls for thinking out of the box.

It is usually thought that deep foundations must be installed using pile equipment, but it is not always the case. Li (2026) discussed a case study in which pipe pile cofferdams are used to support the excavations to reach the bedrock. Rectangular concrete piers resting on the bedrock are then constructed within the cofferdams as foundations for supporting the tall building. The pile cap and the piers are like a wooden stool supported by four rectangular legs with unequal length.

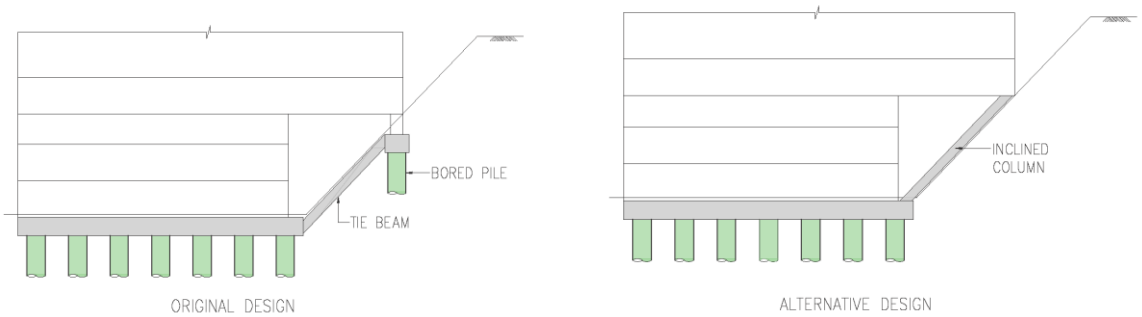

Figure 9: Foundation for building above existing slope

Based on the author's experience, it is often easier to solve a geotechnical problem using a structural solution if feasible. Figure 9 shows a building structure located partially above an existing slope (Li 2026). The original design of foundation involves the use of bored piles to be installed on the slope for supporting the columns along the building edge. A much simpler alternative is to introduce new inclined columns for supporting the edge columns. It is much easier to erect falsework on a slope to construct the inclined columns than to build a major steel temporary platform for the construction of bored piles.

Figure 10 shows another example in which the problem of shoring works is tackled using a structural solution. The structural design of the building requires a screen wall/shear wall to be constructed right along the site boundary as shown in Figure 10(a). It is not easy to develop a conventional shoring scheme for the cofferdam which is water-tight and can enable the boundary screen wall/shear wall to be constructed within the cofferdam. In the end, a special scheme as shown in Figure 10(b) and (c) is developed to enable the screen wall/shear wall to be constructed along the site boundary above ground to meet the design requirement. In this scheme, the pile cap is set back from the site boundary, providing space for sheetpiles to be installed as a water-tight embedded wall to support the excavation for construction of the pile cap. Deep corbels located between the sheetpiles are constructed on the side of the pile cap to support the screen wall/shear wall. The lower part of the screen wall/shear wall is designed as a deep beam serving as the capping beam for the corbels. The remaining part of the screen wall/shear wall will be supported on the deep beam.

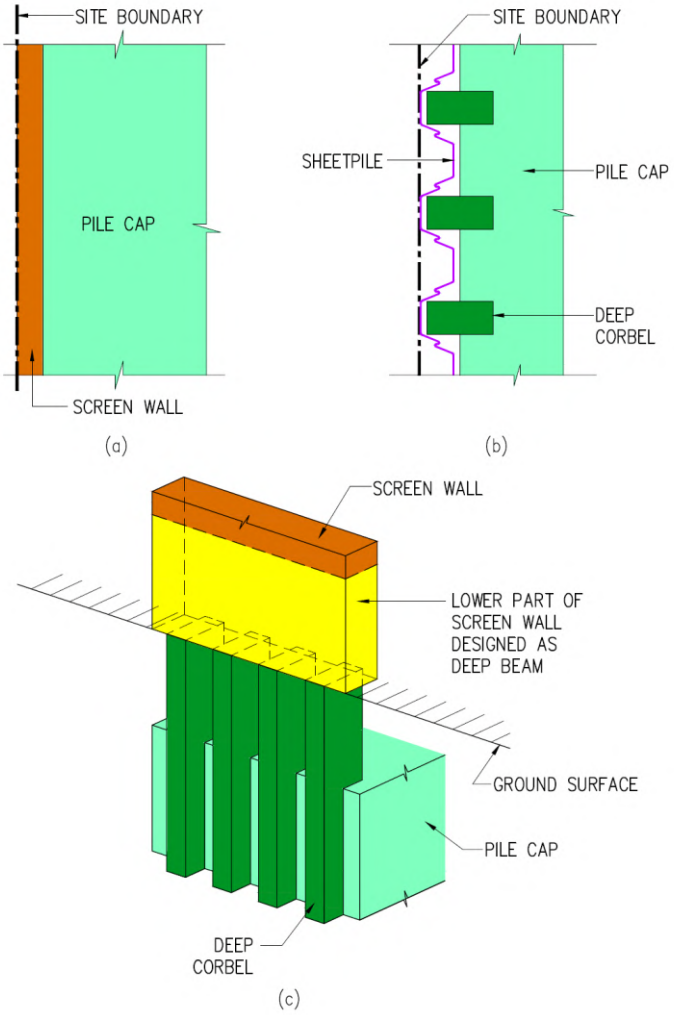

Figure 10: A design scheme for shoring works and pile cap construction

6 CONCLUSIONS

Geotechnical theories cannot have the same precision as laws in physics. They are at best approximations. It is not realistic to expect geotechnical theories to give accurate predictions of the real behaviours of soils and geotechnical structures. One has to make decisions under uncertainty in respect of design, construction and solving problems on site based on imprecise theories and predictions. This makes geotechnical engineering a difficult discipline to master, but at the same time a rewarding profession if one can get a handle on dealing with the uncertainties. Fortunately, there are many useful albeit imperfect theories that can guide geotechnical engineers in formulating sensible design schemes and site engineers in taking the right actions in averting problems on site.

One should not be content with just being a proficient engineer, but aim at becoming a professional engineer. To attain this goal, he should be diligent physically in spending time on continuous learning. There are far more good ideas, theories, design method and solutions for solving problems readily available in books and on the internet than one can use in his entire professional career. Geotechnical engineers should also be diligent in his mind to critically review the geotechnical knowledge he has learnt, and accept only those theories, idea, and design methods that can capture the real behaviours of soils and geotechnical structures. One should also be aware of the important effects of construction on geotechnical behaviours.

Given the complex nature of soils, the use of a sophisticated program will not necessarily produce a more reliable prediction if the theories or assumptions used in the software are unreal or if the analysis model developed by the engineer cannot reflect the actual method of construction. It is fitting to end this paper by quoting the following insightful remarks made almost half a century ago by Lumb (1980), which are still very true today.

> *In the soil engineering world it is all too easy to spend time on calculating what can be calculated rather than on what should be calculated, to give an overprecise answer to the wrong question.*

REFERENCES

Choi, K.Y.M., Li, V. & Tam, A.Y.S. 2021. An innovative design of retaining wall in Lung Shan Tunnel construction. *Proc. HKIE Geotechnical Division Annual Seminar*, 31-39.

Chu, L.M. & Yin, J.H. 2005. Comparison of interface shear strength of soil nails measured by both direct shear box tests and pullout tests. *Journal of Geotechnical and Geoenvironomental Engineering*, 131(9): 1097-1107.

Coduto, D.P., Kitch, W.A. and Yeung, M-C. R. 2016. *Foundation Design Principles and Practices*, 3rd Edition. Pearson Education, Inc.

Earls, M. 2015. *Copy*, *Copy*, *Copy*: *How to do smarter marketing by using other people's ideas*, John Wiley & Sons Ltd.

Fredlund, D.G. & Rahardjo, H. 1993. *Soil Mechanics for Unsaturated Soils*, John Wiley & Sons, Inc.

Geotechnical Engineering Office (GEO). 1982. *Geoguide 1 – Guide to Retaining Wall Design, 2nd Edition.*

Geotechnical Engineering Office (GEO). 2006. *Foundation Design and Construction*, GEO Publication 1/2006.

Lam, J. & Li, K.S. 2003. Influence of construction method on shaft friction of bored pile – a case study. *Proc. HKIE Geotechnical Division Annual Seminar*, 142-152.

Li, K.S. & Lo, S.R. 2007. Discussion on 'Comparison of interface shear strength of soil nails measured by both direct shear box tests and pullout tests'. *Journal of Geotechnical and Geoenvironomental Engineering*, 133(3): 344-346.

Li, V. 2006. Analysis of geotechnical data. *Proceedings of Symposium on Hong Kong Soils and Rocks*, Editor: R.P. Martin & K.S. Li, Centre for Research & Professional Development, IMMM and Geological Society of London, Hong Kong Regional Group, 163-196.

Li, V. 2024. A critical review of pile acceptance criteria. *Proc. HKIE Geotechnical Division Annual Seminar*, 189-200.

Li, V. 2026. *Bridging Research and Practice – the VLA Experience, Vol.4 – Foundation Engineering*, Victor Li & Associates Ltd.

Li, V. & Chung, E. 2013. Some useful schemes for retaining wall design for forming building platforms. *Proc. HKIE Geotechnical Division Annual Seminar*, 133-138.

Li, V. & Lo, S-C. 2008. Obstacles to innovative technologies in geotechnical works in Hong Kong. *Proc. HKIE Geotechnical Division Annual Seminar*, 191-195.

Lo, S-C.R., Gnanendran, C.T. & Li, K.S. 2001. The application of numerical analysis to geotechnical engineering projects. *Proc. 14th Southeast Asian Geotechnical Conference – Geotechnical Engineering Meeting Society's Needs*, 3: 383-388.

Lumb, P. 1962. Effect of rainstorms on slope stability. *Symposium on Hong Kong Soils*. Hong Kong Joint Group of The Institution of Civil, Mechanical and Electrical Engineers, 73-87.

Lumb, P. 1980. Thirty years of soil engineering in Hong Kong, Rupert H Myers Lecture, Leura, Australia.

Powrie, W., Chandler, R.J., Carder, D.R. & Watson, G.V.R. 1999. Back-analysis of an embedded retaining wall with a stabilizing slab. *Proc. ICE – Geotechnical Engineering*, 137, April, 75-86.

Ritzer, G. 2000. *The McDonaldization of Society*, Pine Forge Press.

Su, L.J., Chan, T.C.F., Yin, J.H., Shiu, Y.K. & Chiu, S.L. 2008. Influence of overburden pressure on soil-nail pullout resistance in a compacted fill. *Journal of Geotechnical and Geoenvironomental Engineering*, 134(9): 1339-1347.

Sweeney, D.J. 1982. Some in situ soil suction measurements in Hong Kong's residual soil slopes. *Proc. 7th Southeast Asian Geotechnical Conference*, Hong Kong, 91-106.

Terzaghi, C. 1925. Principles of soil mechanics: IV – settlement and consolidation of clay. Engineering News-Record, Nov., 874-878.

Terzaghi, K. 1943. *Theoretical soil mechanics.* John Wiley and Sons, Inc.

Terzaghi, K. 1963. Karl Terzaghi's last writings on soils. *Engineering News-Record*, Nov., 39-40.

Vesic, A.S. 1967. Ultimate loads and settlements of deep foundation in sand. *Proc. Symposium on Bearing Capacity and Settlement of Foundations*, (Editor: A.S. Vesic), 53-68.

A Simple Method for Calculating Consolidation Settlements of Clayey Soils and Settlement Prediction-Control

J.H. Yin, Z.J. Chen, P.C. Wu & Z.Y. Yin
The Hong Kong Polytechnic University, Hong Kong

ABSTRACT

Large settlements of foundations or artificial islands on soft soil grounds such as the Tower of Pisa, Japan Kansai Airport Reclamations, and Hong Kong reclamations, are caused by viscous behaviour (creep) of clayey soil skeleton. The paper then presents (i) Hypothesis A and Hypothesis B methods for calculating consolidation settlements of clayey soils and (ii) the history and equations of the two methods, explaining the inherent logical mistakes of Hypothesis A method. A simplified Hypothesis B method, namely simple method, is presented for calculating consolidation settlements of one-layer and multi-layers of clayey soils with or without vertical drains. Verifications of the simple method by comparison with lab data and values from fully coupled numerical methods are presented. The fully coupled numerical methods and simple method presented in this paper have been adopted in the 5th edition of "Canadian Foundation Engineering Manual" (2023). The control of post-construction settlement is important and can be achieved by over-surcharging soft soils beyond the designed vertical pressure and making the soft soils overconsolidated. The simple method can be used to predict and control the settlement of soils during and after construction.

1 INTRODUCTION

In many coastal cities, the long-term serviceability and structural integrity of critical infrastructure, including embankments and foundations, and large-scale artificial islands, are frequently significantly challenged by the time-dependent settlement of clayey soils. Lessons have been learned through a series of historical and modern engineering stories. For instance, the Leaning Tower of Pisa's precarious tilt was triggered by the differential long-term settlement of underneath soft clay layers with uneven thickness, which cost massive stabilisation efforts (Burland et al., 2003). Similarly, the Kansai International Airport in Japan, built on thick marine clay, has seen settlements exceeding 10 meters, with several meters occurring post-construction. The excessive settlement has been attributed to the compressibility, especially the creep of Osaka marine clay (Rocchi et al., 2006). In Hong Kong, reclamation constituted a significant portion of the land supply for urban development. Traditional reclamation in Hong Kong relied on the dredging method. Due to environmental concerns, non-dredging reclamation has become mainstream, which involves the improvement of in-situ soft soil layers. The long-term settlement of these soft soil layers in reclaimed areas is a major concern in geotechnical design.

Soil consolidation involves the increase of effective stress as excess porewater pressure dissipates under load increment, whereas creep represents the visco-plastic compression that continues even under constant effective stress. More broadly, the visco-plastic compression behaviour of clayey soil not only results in secondary compression during effective stress variations, but also causes other time-dependent phenomena like strain rate effects and stress relaxation. The underlying cause of this visco-plasticity is largely attributed to the diffuse electrical double layer of bound water surrounding negatively charged clay particles (Borja & Choo, 2016; Le et al., 2012; Mitchell & Soga, 2005; Yin, 2015; Zeevaert, 1986). Because this bound water behaves differently from free water, its viscous movement drives the creep motion among particle contacts and therefore the creep deformation of the soil skeleton.

To avoid unexpected long-term settlement as experienced by Kansai Airport, modern geotechnical design requires sufficient consideration of soft soil creep. Different theoretical models or methods have been developed in the past decades, including the two Hypotheses (A and B) for calculating the creep settlement of soils with different thicknesses (Degago et al., 2011; Jamiolkowski et al., 1985; Kavazanjian, 1988; Ladd et al., 1977; Leroueil, 2006; Mesri & Choi, 1985). However, there exist significant confusing issues in the use of creep models. Traditional design relied on Hypothesis A for its simplicity, while recent studies have suggested

that Hypothesis B reflects the more factual behaviour of soils and stands on a safer side, which should replace Hypothesis A in modern design guidelines. One of the major concerns of adopting Hypothesis B lies in the difficulty of implementing an elastic visco-plastic model in consolidation analysis, which is a coupled process of pore pressure dissipation and creep compression. To address this issue, simplified Hypothesis B methods have been proposed and developed in the past several years (Yin et al., 2022; Yin & Feng, 2017). With the development of computation tools, Hypothesis B has been adopted internationally, from UK, Norway, to Canada. Specifically, the Canadian Foundation Engineering Manual (CGS, 2023) has adopted both fully coupled numerical methods and the simplified Hypothesis B method for calculating the settlement of soils with viscous compression behaviour. It is expected that Hypothesis B will be adopted by technical guidelines in more and more countries and regions.

In this paper, the fundamental differences between Hypotheses A and B will be clarified. The importance of adopting Hypothesis B, which considers creep effects during the primary consolidation process, is highlighted. The simple Hypothesis B method with an elastic visco-plastic model is presented and applied in the analysis of different cases. Following that, the post-construction settlement control of clayey soils through over-surcharge is discussed based on Hypothesis B and elastic visco-plastic model. The paper will illustrate the efficiency and accuracy of the Hypothesis B method, providing a modernised tool for future geotechnical projects concerning soft soil improvement and settlement risk management.

2 Discussion of different hypotheses and models

2.1 History of Hypothesis A and Hypothesis B

The first attempt to account for soil creep during consolidation can be dated back to Taylor and Merchant (1940), who described the compression of soils considering the void ratio evolving with both effective stress and time:

$$\frac{de}{dt} = \frac{\partial e}{\partial t} + \frac{\partial e}{\partial \sigma'}\frac{\partial \sigma'}{\partial t} \tag{1}$$

where e is the void ratio, t is time, σ' is the effective stress. The equation indicates that time-dependent consolidation settlement is contributed not only by the increasing of effective stress ($\partial\sigma'/\partial t$), but also the "viscous flow or creep" ($\partial e/\partial t$). However, at that time, the exact mathematical expression of $\partial e/\partial t$ and $\partial e/\partial \sigma'$, and their possible coupling way was not fully understood.

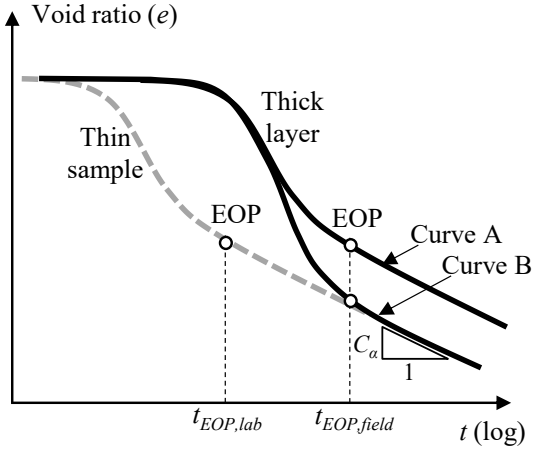

Figure 1: Illustration of Hypotheses A and B

Ladd et al. (1977) pointed out that there existed two different ways in considering the creep compression of soils under consolidation settlement, as represented by the two curves in Figure 1. "Curve A" indicated that there exists a unique void ratio (or strain) at end-of-primary consolidation (EOP). Therefore, for soils with different thicknesses, despite their different time of EOP (t_p or t_{EOP}) and different rates of effective stress increment, they always exhibit the same EOP strain followed by parallel creep curves (secondary compression curves). In this theory, settlements before and after EOP can be solved separately. It was therefore popularly used in traditional design. In contrast, "Curve B" was interpreted by rheological theories, which believed that

creep is a separate phenomenon happening before and after EOP. Such creep will affect the void ratio at EOP, mostly, causing the settlement curves to converge after EOP. Jamiolkowski et al. (1985) further defined the two curves as "Hypothesis A" and "Hypothesis B". In their interpretation, "Hypothesis A" indicates no creep during primary consolidation (as it has no influence on the EOP strain), while "Hypothesis B" contains creep during primary consolidation.

2.2 Key issues related to Hypotheses A versus B

In Hypothesis A, "primary consolidation" and "secondary consolidation" are separated by the "EOP". As the EOP is unique, the settlement before EOP is only dependent on the dissipation of pore pressure. After EOP, the secondary consolidation settlement is controlled by the creep:

$$S = S_{primary} + S_{secondary} = UH_0\Delta\varepsilon_{EOP} + \frac{C_\alpha}{1+e_0}H_0 \log\frac{t}{t_p} \tag{2}$$

where C_α is the secondary consolidation coefficient, e_0 is the initial void ratio, H_0 is the initial thickness of the soil layer. Hypothesis A was mainly massively used in engineering design due to its simplicity, without the need to consider creep during primary consolidation.

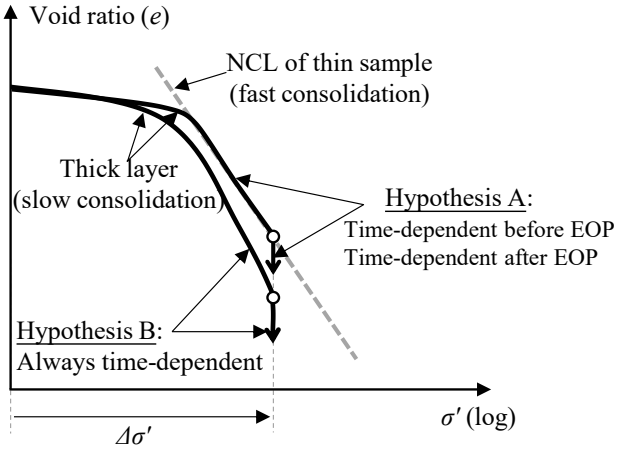

Figure 2: Illustration of the $e-\log\sigma'$ paths for Hypotheses A and B

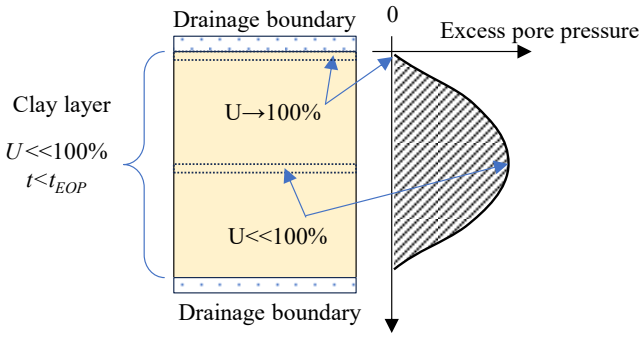

Figure 3: Illustration of the non-uniform distribution of degree of consolidation in a soil layer

However, there are two major contradictions about Hypothesis A. Firstly, comparing Equations (2) to (1), we can find that $\partial e/\partial t$ is not coherent in Hypothesis A. The soil behaviour is time-independent before EOP but becomes time-dependent after EOP. In the $e-\log\sigma'$ space, Hypothesis A causes a unique compression curve before EOP, and a non-unique compression curve after EOP, as shown in Figure 2. Therefore, Hypothesis A is considered to violate continuum mechanics theories (Kavazanjian, 1988; Leroueil, 2006). Secondly, the degree of consolidation is not uniform in a thick soil layer. The elements near the drainage boundary will achieve EOP when the whole layer has not attained EOP, as shown in Figure 3. According to Hypothesis A, the elements achieving EOP will develop creep compression, while the whole layer does not,

which exhibits an obvious contradiction. Some supporters of Hypothesis A suggested that creep before EOP follows a complex evolving mechanism, which interacts with the rate of consolidation and somehow causes the unique EOP strain (Mesri & Funk, 2015; Mesri & Vardhanabhuti, 2005). However, there is no physics proof for such claims.

<table>
<tr><th></th><th>Hypothesis</th><th>1D Model / Theory</th><th colspan="2">Behaviour</th></tr>
<tr><th></th><th></th><th></th><th>e-logt curves</th><th>e-logσ' curves</th></tr>
<tr><td>Hypothesis A</td><td>• Separation of primary and secondary compression by EOP
• t_p as a parameter</td><td>Unique EOP theory
(Mesri et al.)</td><td> 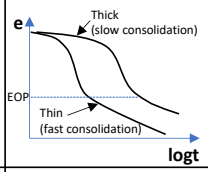
</td><td> 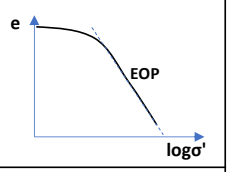
</td></tr>
<tr><td rowspan="2">Hypothesis B</td><td rowspan="2">• Creep as a constitutive behaviour due to soil viscosity
• No separation of primary and secondary compression
• t_p not as a parameter</td><td>Isotache EVP model
(e.g., Šuklje, Bjerrum, Yin and Graham, Vermeer and Neher, Leroueil et al., etc.) (“equivalent time”)</td><td> 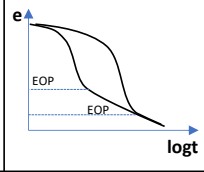
</td><td> 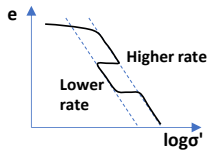
</td></tr>
<tr><td>Non-isotache EVP model
(e.g., Yuan and Whittle)</td><td> 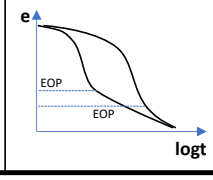
</td><td> 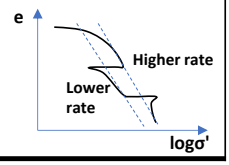
</td></tr>
</table>

Figure 4: Illustration of the Hypotheses A and B in $e-\log\sigma'$ relations

As a result, Hypothesis B is now supported by the majority of experts in soil mechanics (Degago et al., 2011; Grimstad et al., 2022; Leroueil, 2006; Yin & Feng, 2017). As pointed out by Ladd et al. (1977), Hypothesis B is based on the rheological theory of soft soils, which considers that the straining of the soil skeleton naturally contains a viscous part. The viscous straining causes soil to exhibit not only creep, but also strain rate effect and stress relaxation. Since Taylor and Merchant (1940), researchers have been developing mathematical expressions for the viscous behaviour of soils in different ways. Šuklje (1957) proposed an “isotache” concept to describe the rate-dependent $e-\log\sigma'$ curves in 1D consolidation, which associates the $\partial e/\partial t$ and $\partial e/\partial\sigma'$ with rate-dependent preconsolidation pressure σ'_p and $\partial e/\partial\sigma'$. In the 7th Rankine Lecture, Bjerrum (1967) introduced the concept of “instant compression” and “delayed compression” concepts of soils, and indicated that creep of soil leads to an increase of σ'_p and undrained shear strength. Based on Šuklje and Bjerrum’s concepts, a series of constitutive models have been proposed to account for the creep effects of soils (Adachi & Oka, 1982; Vermeer & Neher, 1999; Yin & Graham, 1989; Yin et al., 2010; Yuan & Whittle, 2018). These constitutive models can be classified as “Elastic Visco-Plastic (EVP) model” (Yin & Graham, 1994), in which the total strain rate of soils is divided into two parts: the elastic part and the visco-plastic part. The evolution of elastic and visco-plastic strain is controlled by effective stress and the hardening rules, respectively. With the EVP models, there is no need to separate “primary consolidation” and “secondary compression” during the settlement calculation. The major differences between Hypotheses A and Hypotheses B, along with different constitutive models, are summarised in Figure 4.

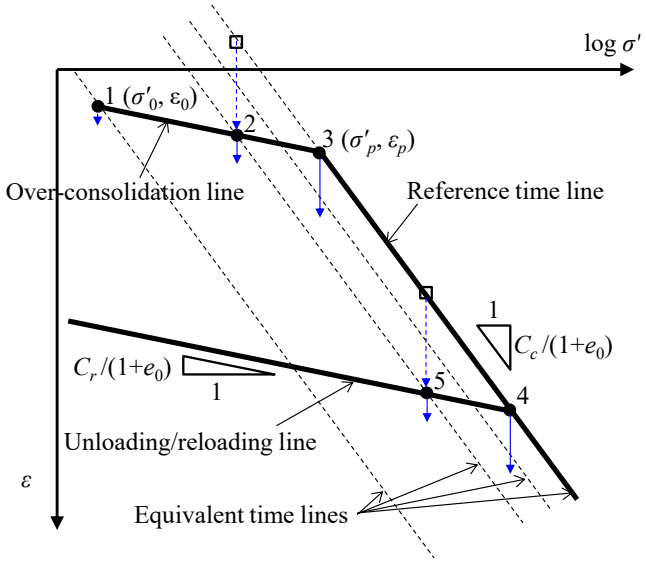

Figure 5: Illustration of the Yin and Graham's 1D EVP model

In Yin and Graham's (1989, 1994) 1D Elastic Visco-Plastic model, the strain of a clayey soil at any stress history can be expressed as:

$$\varepsilon = \varepsilon_p + \frac{C_c}{V}\log\frac{\sigma'}{\sigma'_p} + \frac{C_\alpha}{V}\log\frac{t_0 + t_e}{t_0} \tag{3}$$

where $\left(\sigma'_p, \varepsilon_p\right)$ is the pre-consolidation stress and the corresponding strain which should be a fixed point at the reference time line (the normal consolidation line, *i.e.,* NCL under reference time t_0 from oedometer test), C_c is the normal compression index, $V = 1 + e_0$ is the initial specific volume, t_0 is the reference time (usually 24 hours), C_α is the creep coefficient (secondary compression coefficient from oedometer test), t_e is the equivalent time. Based on the equivalent time framework, the viscoplastic strain rate at any stress-strain state $\left(\sigma', \varepsilon\right)$ can be derived as:

$$\dot{\varepsilon}^{vp} = \frac{d\varepsilon}{dt_e} = \frac{C_\alpha}{V t_0 \ln 10}\exp\left[-\left(\varepsilon - \varepsilon_p\right)\frac{V\ln 10}{C_\alpha}\right]\left(\frac{\sigma'}{\sigma'_p}\right)^{\frac{C_c}{C_\alpha}} \tag{4}$$

The elastic strain rate can be calculated as:

$$\dot{\varepsilon}^{e} = \frac{C_r}{V\ln 10}\frac{\dot{\sigma}'}{\sigma'} \tag{5}$$

where C_r is the re-compression index. The conceptual diagram of this EVP model is presented in Figure 5.

3 A SIMPLE HYPOTHESIS B METHOD

Hypothesis A has been found to underestimate the settlement of clayey soil ground by many researchers (Degago et al., 2011; Szavits-Nossan, 2015). To use Hypothesis B, the most rigorous way is to fully couple the elastic visco-plastic behaviour with the consolidation process of soils. Such coupled methods require a numerical program, so that the nonlinear partial differential equation from Terzaghi/Biot consolidation theories and the constitutive model can be solved simultaneously. There is a series of available numerical codes for fully coupled analysis based on Hypothesis B, such as PLAXIS. However, consolidation analysis by numerical algorithms could be time-consuming and computationally demanding.

A question arises regarding whether Hypothesis B can offer the same operational convenience as Hypothesis A. To address this issue, Yin and his co-workers have developed a simple Hypothesis B method

combining the simple consolidation solutions and the EVP model (Yin et al., 2022; Yin & Feng, 2017). In this method, the total settlement of a clayey soil layer can be expressed as:

$$S = S_{primary} + S_{creep} = \begin{cases} US_f + \alpha U^{\beta} S_{creep,f} & for \;\; t_0 \le t \le t_{EOP,field} \\ US_f + \left[\alpha U^{\beta} S_{creep,f} + \left(1 - \alpha U^{\beta}\right) S_{creep,d} \right] & for \;\; t \ge t_{EOP,field} \end{cases} \quad (6)$$

where U is the average degree of consolidation for the soil layer, S_f is the "final" consolidation settlement without considering creep effect, $S_{creep,f}$ is the "final" creep settlement without considering the delay by excess pore pressure dissipation, $S_{creep,d}$ is the "delayed" creep settlement due to excess pore pressure dissipation. α and β are empirical coefficients to consider the effect of consolidation on the creep settlement. It has been suggested that $\alpha = 0.8$ and $\beta = 0.3$ are suitable for many typical clayey soils (Chen et al., 2021, 2023, 2024; Yin et al., 2022, 2024). These clayey soils were reported in different regions including Japan, Malaysia, Sweden, and Hong Kong, with natural water contents of 70% to 120, high compressibility and significant creep effects.

S_f can be calculated from the $e - \log\sigma'$ relations (Figure 5), which is:

$$S_f = \begin{cases} H \dfrac{C_r}{1+e_0} \log \dfrac{\sigma'_f}{\sigma'_0} & for \;\; \sigma'_0 < \sigma'_f \le \sigma'_p \\ H \dfrac{C_r}{1+e_0} \log \dfrac{\sigma'_p}{\sigma'_0} + H \dfrac{C_c}{1+e_0} \log \dfrac{\sigma'_f}{\sigma'_p} & for \;\; \sigma_0 \le \sigma'_p < \sigma'_f \\ H \dfrac{C_c}{1+e_0} \log \dfrac{\sigma'_f}{\sigma'_0} & for \;\; \sigma'_p \le \sigma'_0 < \sigma'_f \end{cases} \quad (7)$$

where $\sigma'_0, \sigma'_p, \sigma'_f$ represent the initial effective stress, preconsolidation stress, and final effective stress after consolidation, *H* represents the thickness of the soil layer.

The *U* can be analyzed by different analytical or semi-analytical methods. For 1D consolidation without vertical drains, *U* is calculated by Terzaghi's 1D consolidation equation. For consolidation with vertical drains, *U* is calculated by Hansbo's unit cell theory (Hansbo, 1981). For multi-layered soils with and without vertical drains, *U* of each layer can be calculated by Walker and Indraratna's spectral method (Walker & Indraratna, 2009). In the consolidation analysis, the compressibility and the coefficient of consolidation can be obtained as follows:

$$\begin{cases} m_v = \dfrac{S_f}{H\left(\sigma'_f - \sigma'_0\right)} \\ C_v = \dfrac{k_v}{\gamma_w m_v} \\ C_h = \dfrac{k_h}{\gamma_w m_v} \end{cases} \quad (8)$$

where C_v, C_h represent coefficients for vertical and horizontal consolidation, k_v, k_h represent vertical and horizontal permeabilities, γ_w represents the unit weight of water.

$S_{creep,f}, S_{creep,d}$ are calculated by the following equations:

$$\begin{cases} S_{creep,f} = H \dfrac{C_\alpha}{1+e_0} \log \dfrac{t_{ef} + t}{t_{ef} + t_0} & for \;\; t_0 \le t \le t_{EOP,field} \\ S_{creep,d} = H \dfrac{C_\alpha}{1+e_0} \log \dfrac{t_{ef} + t}{t_{ef} + t_{EOP,field}} & for \;\; t > t_{EOP,field} \end{cases} \quad (9)$$

where t_{ef} is the equivalent time at σ'_f, such as the Points 2~5 in Figure 5. If the final state is on the normal consolidation line (e.g., Points 3 and 4), t_{ef} is equal to zero. If the final state is on the over-consolidation or unloading-reloading line (e.g., Points 2 and 5), t_{ef} is non-zero, which can be calculated by:

$$t_{ef} = \exp\left[-\left(\varepsilon_p - \varepsilon_f\right)\frac{1+e_0}{C_\alpha}\ln 10\right]\left(\frac{\sigma'_f}{\sigma'_p}\right)^{-\frac{C_c}{C_\alpha}} - t_0 \tag{10}$$

where $\varepsilon_f = \varepsilon_0 + S_f / H$ is the strain corresponding to σ'_f. It can be found that t_{ef} is dependent on the effective stress and strain of the soil.

A major procedure of the simple Hypothesis B method is summarized in the flow-chart of Figure 6.

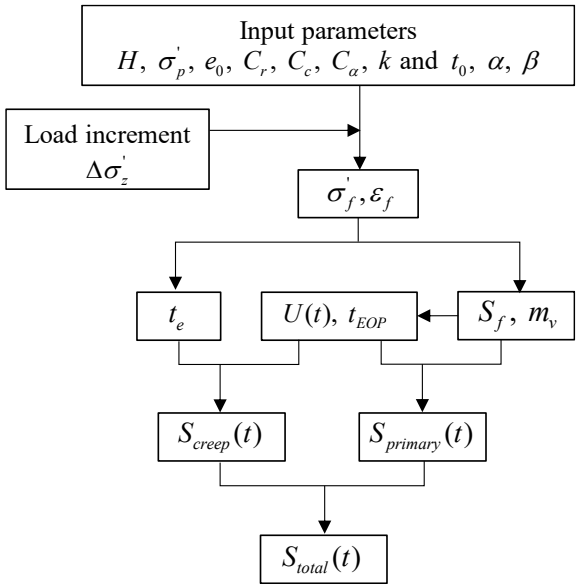

Figure 6: Flowchart of the simple Hypothesis B method for settlement calculation

4 SETTLEMENT CALCULATION AND CONTROL

4.1 Verification of the simple Hypothesis B method

A test embankment was constructed as part of the reclamation project of Chak Lap Kok International Airport of Hong Kong (Zhu et al., 2001). In this paper, this well-documented embankment will be used to demonstrate the effectiveness of the simple Hypothesis B method. The ground investigation indicated four different soil materials, namely upper marine clay, upper alluvium, lower marine clay, and lower alluvium, with an impermeable rock bed at the bottom. The detailed parameters of each soil layer had been reported in the literature (Koutsoftas et al., 1987; Yin et al., 2022). Three stages of surcharge fills were constructed over the soft soil layers, equivalent to three different vertical pressures. Vertical drains were installed for the acceleration of consolidation. Settlement plates were installed at four different depths to monitor the layered settlement with time.

The consolidation analysis is conducted through the Spectral Method. After calculating the average degree of consolidation for each layer, the total settlement is obtained by the summation of the settlement of all layers. Three loading stages are calculated independently, and their settlement accumulations are considered by summation.

Figure 7 shows the calculation results of the embankment using the simple Hypothesis B method. Comparisons between measurements and calculations confirm the effectiveness of the proposed method. The settlement curve from the Hypothesis A method is also plotted for comparison, which obviously underestimates the real settlement of the soils.

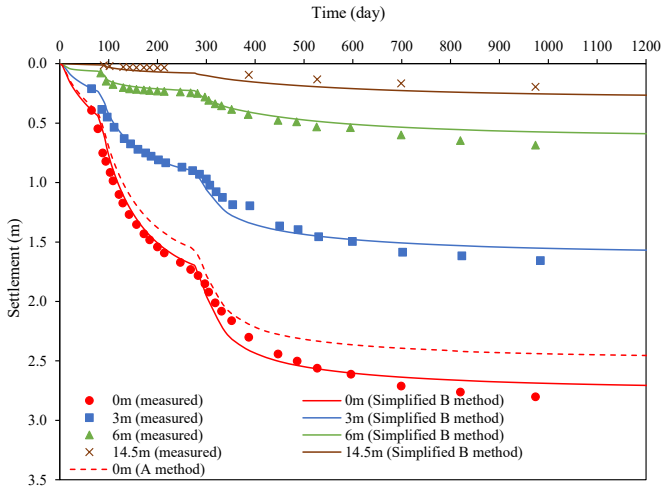

Figure 7: Settlements of the test embankment from calculations and measurements

4.2 Settlement prediction for soils with different OCR

To further illustrate the importance of considering creep with Hypothesis B, Figure 8(a)-(c) plot the settlement curves for a clayey soil layer with different initial over-consolidation ratios (OCR). The parameters of the clayey soil follow (Feng & Yin, 2018). The thickness is 4m, with vertical drains installed at a spacing of 1.5 m. A uniform vertical pressure of 20 kPa is applied on the top of the soil layer for consolidation. Three different methods are used for settlement analysis: (1) Hypothesis A method; (2) the simple Hypothesis B method; (3) the fully coupled finite element method (FEM), which is conducted by PLAXIS with the Soft Soil Creep model. The curve "B/A" indicates the ratio between settlement by Hypothesis A and settlement by Hypothesis B method.

It can be found from Figure 8 that the proposed simple Hypothesis B method agrees well with the fully coupled FEM with an EVP model. The ratio between settlements by Hypothesis B and Hypothesis A (B/A) could be more than 1.6. Furthermore, it can be found that with the same stress increment (20kPa) and the same initial stress, the B/A ratio increases with OCR. This can be explained by the $e-\log\sigma'$ paths as presented in the figures. As the final stress-strain points fall on the NCL, similar creep settlements are developed for all cases. With a larger initial OCR, the total void ratio change is smaller, so the relative contribution by creep will be larger. Therefore, the underestimation of Hypothesis A grows with OCR as it neglects parts of the creep settlement. Finally, it is also worth noting that the value of B/A is even higher before the EOP, which indicates that considering creep is important for both short-term and long-term consolidation settlement assessment.

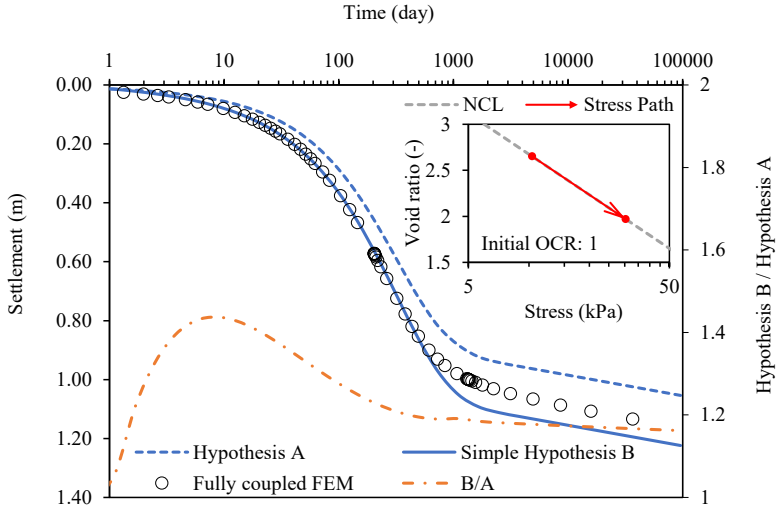

(a)

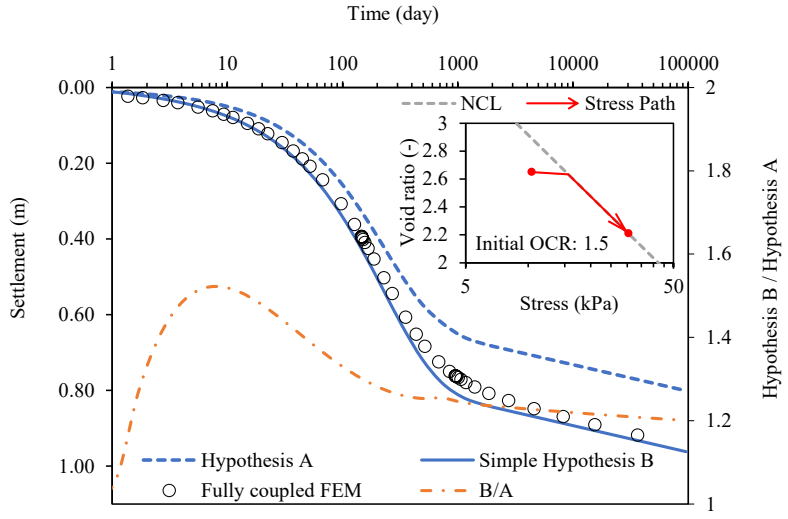

(b)

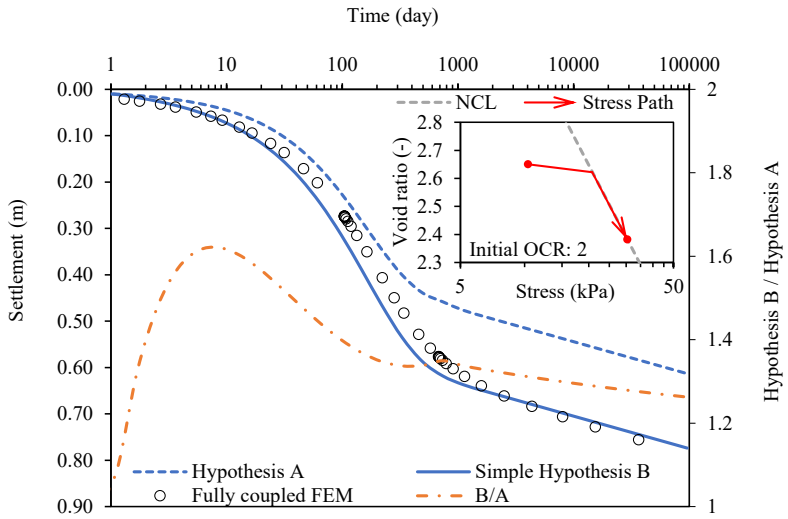

(c)

Figure 8: Settlement of a clayey soil layer with vertical drains by different methods

4.3 Post-construction settlement control based on Hypothesis B

According to Equation (9), the creep settlement decreases as equivalent time increases. Therefore, to reduce the long-term settlement due to creep, such as the excessive settlement of Kansai Airport, it is important to increase the equivalent time under the normal working load. As shown in Figure 9, Point 5 at the reference time line (NCL) has zero equivalent time, and its creep is significant. However, if there is an over-surcharge from Point 5 to Point 6', followed by an unloading to Point 5', the soil becomes over-consolidated. The equivalent time of Point 5 will be much larger, and the creep rate will be much lower. In fact, the stress-strain state under 5 (by path 5'-6'-6) is equivalent to a long-time creep from 5 to 5'. Both creep and over-consolidation cause plastic compression and hardening of the soil skeleton.

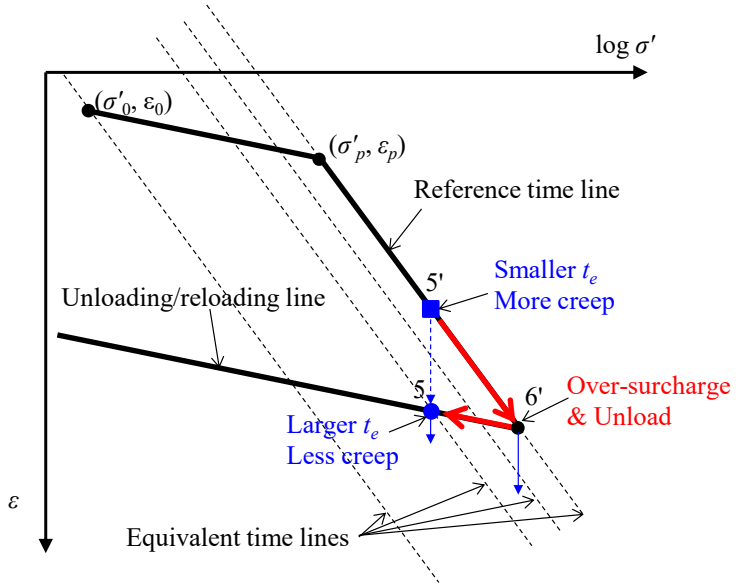

Figure 9: Illustration of the over-surcharge effect on creep

The excessive post-construction settlement of Kansai International Airport can be attributed to the significant creep compression of the marine clay layers, which were not properly over-surcharged. To illustrate the effectiveness of over-surcharge on reducing the post-construction settlement, a parametric study is carried out on the same clayey soil layer as section 4.2. The working load is still 20kPa, but the soil is subject to different historical maximal loads (20, 30, 40, 50 kPa). The ratio between historical load and current working load is defined as "over-surcharge ratio", which ranges from 1, 1.5, 2, to 2.5. The post-construction settlement is calculated as the settlement after EOP of the soil layer, as plotted in Figure 10. According to Figure 10, the over-surcharge ratio has a significant influence on the post-construction settlement. When over-surcharge is not conducted (ratio=1), the post-construction settlement is significant, with 0.18m in 50 years. With the over-surcharge ratio increased to 1.5, the settlement at 50 years is reduced by 40%. With an over-surcharge ratio of 2 and above, the settlements under 20 kPa at 50 years become negligible.

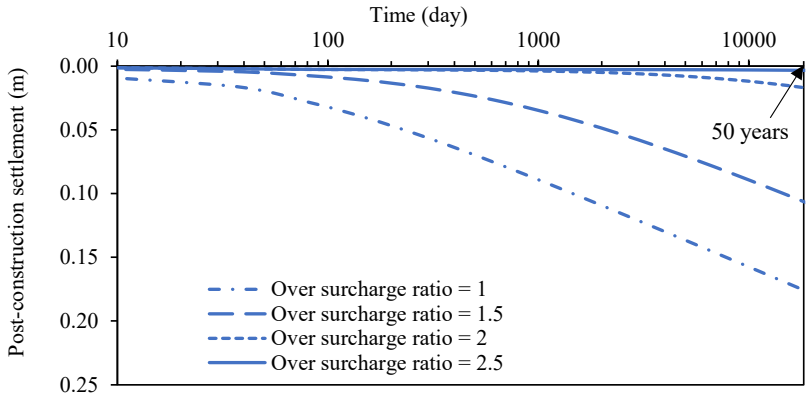

Figure 10: Post-construction settlement of a clayey soil layer with different over-surcharge ratio

5 CONCLUSIONS

This paper revisits Hypotheses A and B for the consolidation and creep settlement analysis of clayey soils. A simple Hypothesis B method applicable for single/multiple layered soils with/without vertical drains is introduced, with verifications by field test data and fully coupled finite element analysis. Parametric studies are presented to reveal the consolidation settlement of clayey soils under different circumstances and the control method by over-surcharge. The following conclusions are made from this study.

(a) Hypothesis A is an outdated method with logical contradictions and underestimations of settlements.

(b) The simple Hypothesis B method shows high reliability as compared with field-monitored settlement and numerical simulations.

(c) The creep settlement during primary consolidation could be significant in both short-term and long-term settlement analysis with vertical drains.
(d) According to the Hypothesis B and EVP model, the long-term post-construction settlement of clayey soil ground can be effectively reduced by over-surcharge.

REFERENCES

Adachi, T., & Oka, F. (1982). Constitutive equations for normally consolidated clay based on elasto-viscoplasticity. *Soils and Foundations*, *22*(4), 57–70.

Bjerrum, L. (1967). Engineering geology of Norwegian normally-consolidated marine clays as related to settlements of buildings. *Géotechnique*, (17), 81–118. https://doi.org/10.1680/geot.1967.17.2.83

Borja, R. I., & Choo, J. (2016). Cam-Clay plasticity, Part VIII: A constitutive framework for porous materials with evolving internal structure. *Computer Methods in Applied Mechanics and Engineering*, *309*, 653–679. https://doi.org/10.1016/j.cma.2016.06.016

Burland, J. B., Jamiolkowski, M., & Viggiani, C. (2003). The stabilisation of the Leaning Tower of Pisa. *Soils and Foundations*, *43*(5), 63–80.

CGS. (2023). Section 7.9.2. Methods for consolidation analyses of clayey soils exhibiting viscous compression. In *Canadian Foundation Engineering Manual (CFEM)* (5th ed., pp. 228–232). The Canadian Geotechnical Society (CGS).

Chen, Z. J., Feng, W. Q., & Yin, J. H. (2021). A new simplified method for calculating short-term and longterm consolidation settlements of multi-layered soils considering creep limit. *Computers and Geotechnics*, *138*, 104324. https://doi.org/10.1016/j.compgeo.2021.104324

Chen, Z. J., Feng, W. Q., Yin, J. H. & Shi, X. S. (2023). Finite element model and simple method for predicting consolidation displacement of soft soils exhibiting creep underneath embankments in 2-D condition. *Acta Geotechnica*, *18*, 2513–2528 (2023). https://doi.org/10.1007/s11440-022-01741-z

Chen, Z., Li, P., Wu, P., Yin, J., & Song, D. (2024). Study of the one-dimensional consolidation and creep of clays with different thicknesses using different hypotheses and three elastic visco-plastic models. *Acta Geotechnica*, *19*(11), 7329–7347. https://doi.org/10.1007/s11440-024-02405-w

Degago, S. A., Grimstad, G., Jostad, H. P., Nordal, S., & Olsson, M. (2011). Use and misuse of the isotache concept with respect to creep hypotheses A and B. *Geotechnique*, *61*(10), 897–908. https://doi.org/10.1680/geot.9.P.112

Feng, W., & Yin, J. (2018). A new simplified Hypothesis B method for calculating the consolidation settlement of ground improved by vertical drains. *International Journal for Numerical and Analytical Methods in Geomechanics*, *42*(2), 295–311. https://doi.org/10.1002/nag.2743

Grimstad, G., Karstunen, M., Jostad, H. P., Sivasithamparam, N., Mehli, M., Zwanenburg, C., den Haan, E., Ghoreishian Amiri, S. A., Boumezerane, D., Kadivar, M., Ashrafi, M. A. H., & Rønningen, J. A. (2022). Creep of geomaterials – some finding from the EU project CREEP. *European Journal of Environmental and Civil Engineering*, *26*(7), 2521–2536. https://doi.org/10.1080/19648189.2016.1271360

Hansbo, S. (1981). Consolidation of fine-grained soils by prefabricated drains. *Proceedings of the International Conference on Soil Mechanics and Foundation Engineering*.

Jamiolkowski, M., Ladd, C. C., Germaine, J. T., & Lancellotta, R. (1985). New development in field and laboratory testing of soils. *Proceedings of the 11th International Conference on Soil Mechanics and Foundation Engineering*, *1*, 57–153.

Kavazanjian, E. (1988). Discussion: The occurrence of creep during consolidation. *Proceedings of the 11th International Conference on Soil Mechanics and Foundation Engineering*, *5*, 2625.

Koutsoftas, D. C., Foott, R., & Handfelt, L. D. (1987). Geotechnical investigations offshore Hong Kong. *Journal of Geotechnical Engineering*, *113*(2), 87–105. https://doi.org/10.1061/(ASCE)0733-9410(1987)113:2(87)

Ladd, C., Foott, R., Ishihara, K., Schlosser, F., & Poulos, H. (1977). Stress-deformation and strength characteristics. *State of the Art Report, Proceeding 9th of ISMFE*, *2*, 421–494.

Le, T. M., Fatahi, B., & Khabbaz, H. (2012). Viscous Behaviour of Soft Clay and Inducing Factors. *Geotechnical and Geological Engineering*, *30*(5), 1069–1083. https://doi.org/10.1007/s10706-012-9535-0

Leroueil, S. (2006). The isotache approach. Where are we 50 years after its development by Professor Šuklje? (2006 Prof. Šuklje's Memorial Lecture). *Proceedings of the 13th Danube-European Conference on Geotechnical Engineering; Ljubljana*, *2*, 55–88.

Mesri, G., & Choi, Y. K. (1985). Settlement analysis of embankments on soft clays. *Journal of Geotechnical Engineering*, *113*(9), 1076–1085. https://doi.org/10.1061/(ASCE)0733-9410(1987)113:9(1076)

Mesri, G. & J. R. Funk. (2015). Settlement of the Kansai International Airport Islands. *Journal of Geotechnical and Geoenvironmental Engineering*, *141*(2), 1–16. https://doi.org/10.1061/(ASCE)GT.1943-5606.0001224

Mesri, G., & Vardhanabhuti, B. (2005). Secondary Compression. *Journal of Geotechnical and Geoenvironmental Engineering*, *131*(3), 398–401. https://doi.org/10.1061/(asce)1090-0241(2005)131:3(398)

Mitchell, J. K., & Soga, K. (2005). *Fundamentals of soil behavior*. Wiley.

Rocchi, G., Vaciago, G., Fontana, M., & Plebani, F. (2006). Enhanced prediction of settlement in structured clays with examples from Osaka Bay. *Geomechanics and Geoengineering*, *1*(3), 217–237. https://doi.org/10.1080/17486020600986793

Šuklje, L. (1957). The analysis of the consolidation process by the isotache method. *Proceedings of the 4th International Conference on Soil Mechanics and Foundation Engineering*, *1*, 200–206.

Szavits-Nossan, V. (2015). Consolidation and creep: Hypotheses A and B revisited. *Geotechnical Engineering for Infrastructure and Development*, 3765–3770.

Taylor, D. W., & Merchant, Wilfred. (1940). A theory of clay consolidation accounting for secondary compression. *Journal of Mathematics and Physics*, *19*(4), 167–185.

Vermeer, P. A., & Neher, H. P. (1999). A soft soil model that accounts for creep. *Beyond 2000 in Computational Geotechnics. Ten Years of PLAXIS International. Proceedings of the International Symposium, Amsterdam, March 1999*. https://doi.org/10.1201/9781315138206-24

Walker, R., & Indraratna, B. (2009). Consolidation analysis of a stratified soil with vertical and horizontal drainage using the spectral method. *Géotechnique*, *59*(5), 439–449. https://doi.org/10.1680/geot.2007.00019

Yin, J., & Graham, J. (1994). Equivalent times and one dimensional elastic viscoplastic modelling of time-dependent stress strain behaviour of clays. *Canadian Geotechnical Journal*, *31*, 42–52. https://doi.org/10.1139/t94-005

Yin, J.-H. (2015). Fundamental Issues of Elastic Viscoplastic Modeling of the Time-Dependent Stress–Strain Behavior of Geomaterials. *International Journal of Geomechanics*, *15*(5), 1–9. https://doi.org/10.1061/(asce)gm.1943-5622.0000485

Yin, J.-H., Chen, Z.-J., & Feng, W.-Q. (2022). A general simple method for calculating consolidation settlements of layered clayey soils with vertical drains under staged loadings. *Acta Geotechnica*, *17*(8), 3647–3674. https://doi.org/10.1007/s11440-021-01318-2

Yin, J.-H., Chen, Z.-J., Wu, P.-C., & Liu, K. (2024). Fully Coupled Numerical Methods and a Simple Method for Calculating Settlements of Foundations and Reclamations on Clayey Soils. *Proceedings of The HKIE Geotechnical Division 44th Annual Seminar - Elevating Geotechnical Excellence: Novel Practices & Innovative Solutions, Hong Kong, 2024*

Yin, J.-H., & Feng, W.-Q. (2017). A new simplified method and its verification for calculation of consolidation settlement of a clayey soil with creep. *Canadian Geotechnical Journal*, *54*(3), 333–347. https://doi.org/10.1139/cgj-2015-0290

Yin, J.-H., & Graham, J. (1989). Visco-elastic-plastic modelling of one-dimentional time-dependent behaviour of clays. *Canadian Geotechnical Journal*, *26*(2), 199–208.

Yin, Z. Y., Chang, C. S., Karstunen, M., & Hicher, P. Y. (2010). An anisotropic elastic-viscoplastic model for soft clays. *International Journal of Solids and Structures*, *47*(5), 665–677. https://doi.org/10.1016/j.ijsolstr.2009.11.004

Yuan, Y., & Whittle, A. J. (2018). A novel elasto-viscoplastic formulation for compression behaviour of clays. *Géotechnique*, *68*(12), 1044–1055. https://doi.org/10.1680/jgeot.16.P.276

Zeevaert, L. (1986). Consolidation in the intergranular viscosity of highly compressible soils. In *Consolidation of soils: Testing and evaluation*. ASTM International.

Zhu, G., Yin, J.-H., & Graham, J. (2001). Consolidation modelling of soils under the test embankment at Chek Lap Kok International Airport in Hong Kong using a simplified finite element method. *Canadian Geotechnical Journal*, *38*(2), 349–363. https://doi.org/10.1139/cgj-38-2-349

A Creative Approach for Cable Upgrading Works in Challenging Conditions

Roger Lee, Karuppasamy Kalimuthu and Arthur KO So
Meinhardt Infrastructure & Environment Limited, Hong Kong

Brian Mok and Tony Yau
The Hongkong Electric Company Limited, Hong Kong

Derrick Leung and Kelvin Chan
Yee Hop Engineering Company Limited, Hong Kong

ABSTRACT

Multiple approaches were adopted for upgrading of cable circuits in Kennedy Town, Hong Kong, to address the challenging site constraints. These included the construction of a cable shaft beneath an existing hillside building to facilitate excavation of a connecting Adit Tunnel by a Tunnel Boring Machine (TBM), which links to an existing Air-Raid Precaution (ARP) tunnel network, as well as the construction of a temporary connection tunnel.

The proposed cable route runs from the Davis 275-kV Switching Station (DAX) through a 48-mdeep, 5-mdiameter shaft down to the existing circuit network at Belcher's Street. The existing DAX is a reinforced concrete structure founded on piles and was constructed in the 1980s at the crest of the slope adjacent to Pok Fu Lam Road. The works area was located beneath the existing DAX, between the piles, on a 30-degree slope. Headroom was constrained to approximately 3 m due to the existing tie beams within the DAX structure. Site logistics were also challenging, as plant and equipment had to be mobilised from Pok Fu Lam Road to a 16-mhigh suspended platform equipped with a gantry crane, before being transferred to a temporary steel working platform at the base of the DAX.

The ground conditions comprised approximately 2 m of fill underlain by about 6.5 m of weathered granite, followed by rockhead, with the groundwater level located approximately 3 m above the rockhead. Temporary works for the cable shaft consisted of pipe piles socketed into rock above the final excavation level, together with a perimeter grout curtain to provide groundwater cut-off. The permanent shaft-ring lining was installed following phased excavation carried out in 4-m lifts. Below the rockhead level, temporary rock dowels were installed to stabilize the rock-face down to the junction structure. A TBM was then deployed to excavate the Adit Tunnel from the junction structure to the repurposed ARP tunnel network, followed by improvement works within the ARP tunnel.

This paper presents an overview of the approach adopted for the upgrading of the cable circuits, including the construction of the cable shaft and Adit Tunnel, the improvement works to the ARP tunnel section, and the construction of the temporary connection tunnel.

1 INTRODUCTION

The cable circuits between the Davis 275-kV Switching Station (DAX) in Kennedy Town and the Sai Ying Pun Zone Substation on Hong Kong Island have to be upgraded. The cable shaft at DAX and the associated connecting tunnels required bespoke underground solutions to address the challenging site constraints.

The cable circuit commences at a deep cable shaft at DAX to facilitate vertical cable transition to the Adit Tunnel, before connecting to a repurposed section of an existing Air-Raid Precaution (ARP) tunnel network. The proposed alignment of the cable route strategically utilises the ARP tunnel to mitigate impacts on adjacent structures and sensitive receivers, including the underlying Mass Transit Railway (MTR) West Island Line, by

minimising construction works. Excavation by a Tunnel Boring Machine (TBM) was adopted for the Adit Tunnel to ensure minimal vibration and to reduce the risk of ground loss during construction. The final section of the cable route comprises permanent improvement works within the existing ARP tunnel.

This paper describes the upgrading works of the cable circuits, including the construction of the deep cable shaft using a phased excavation method, TBM excavation of the Adit Tunnel, and the works carried out within the ARP tunnel network and the connection tunnel.

2 THE SITE

2.1 Site Setting

The top level of the cable shaft is located on sloping terrain dipping towards the northwest, along a hillside descending from approximately +60.0 mPD at DAX to about +5.0 mPD at Belcher's Street. DAX is a reinforced concrete structure constructed in the 1980s on a slope adjacent to Pok Fu Lam Road.

The proposed cable shaft is situated directly beneath and within the footprint of the existing DAX substructure, positioned between existing piles founded on rock. It was critical that continuous operation of DAX had to be maintained while the construction works were carried out.

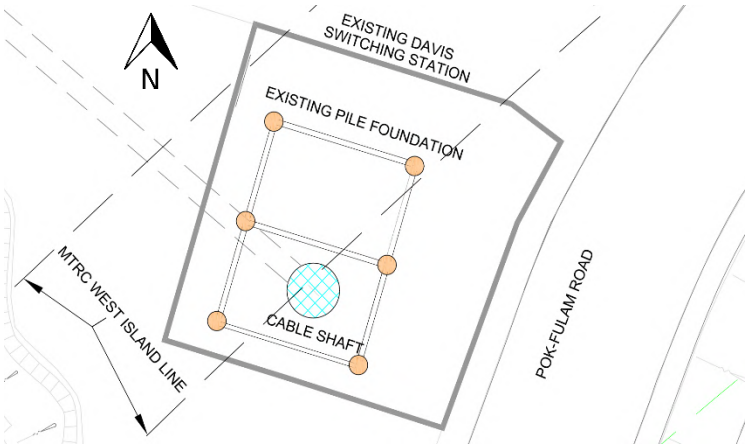

Figure 1: Cable Shaft Site Layout Plan

From the cable shaft and the junction structure, an Adit Tunnel was proposed to connect to an existing ARP tunnel network adjacent to Belcher's Street. Repurposing the existing ARP tunnel network for the cable upgrading works provides a sustainable solution by minimising additional rock excavation and resulting in negligible disruption to the public.

The ARP tunnel was constructed in the late 1930s as an air-raid shelter and was discreetly integrated into the hillside in close proximity to densely populated urban areas. The ARP tunnel network incorporates multiple access points to facilitate safe evacuation and to reduce the risk of entrapment during air raids.

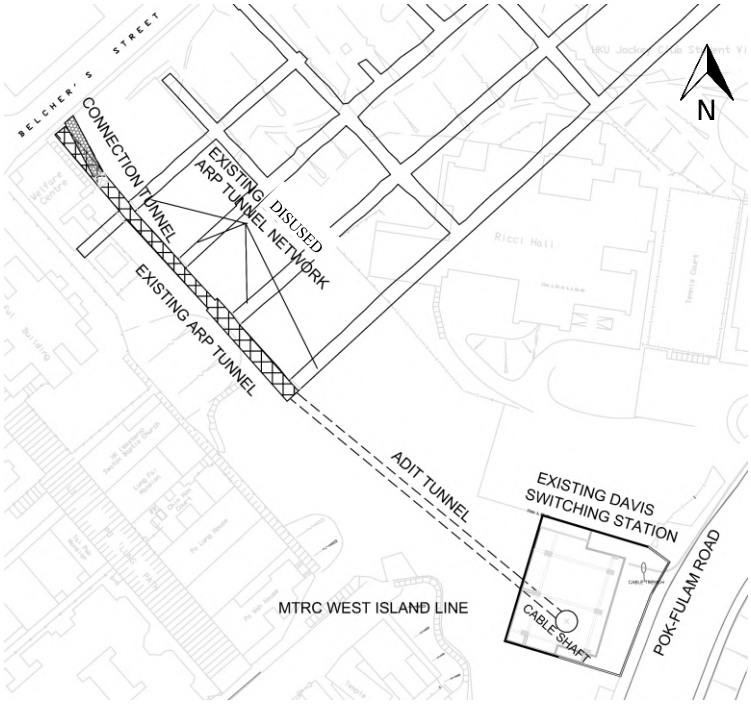

Figure 2: Key Plan

According to the second-stage investigation of Disused Tunnel Network No. 14 at Belcher's Street (South) conducted in 1982, the invert levels of the utilised tunnel section range from approximately +7.1 mPD at the portal to about +8.2 mPD at the proposed Adit Tunnel connection. The existing ARP tunnel comprises partially lined precast concrete lintel crowns with masonry sidewalls, forming an internal profile of approximately 2.4 m to 3.5 m in width and 2.0 m to 2.4 m in height.

Other sections of the tunnel are lined with sidewalls only, with the remaining surfaces formed by exposed rock where rock conditions were assessed to be sound.

Figure 3: ARP Tunnel

2.2 Sensitive Receivers and Site Constraints

The proposed cable route alignment commences beneath DAX and descends through a 48-m deep, 5-m diameter cable shaft. From the base of the shaft, the cable alignment continues northwest via a 73-m long Adit Tunnel to connect with an existing ARP tunnel network.

The works area was located on a slope with an average gradient of approximately 30° and was constrained by limited headroom of about 3 m beneath the DAX tie beams. The bottom of the proposed cable shaft is situated approximately 23 m above the existing MTR West Island Line tunnel structure and lies within the Railway Protection Boundary, where special requirements apply.

Immediately to the north of DAX is the existing Pok Fu Lam Zone Substation, which was required to remain fully operational throughout the works, including the maintenance of access for operation and maintenance activities. In addition, existing electrical cables are present in the vicinity of the proposed cable shaft and were required to be protected during construction.

3 DESIGN

3.1 Geology

A site-specific ground investigation was undertaken, comprising six drillholes, trial pits, sampling, and groundwater monitoring, to establish the ground model and to provide data for the derivation of geotechnical design parameters and groundwater levels. The ground profile comprises approximately 1.0 m to 3.5 m of fill, consisting of loose to medium-dense yellowish-brown sandy clayey silt to silty sandy gravel, underlain by about 2.0 m to 3.5 m of colluvium comprising firm clayey silt to medium-dense sandy gravel. This is followed by weathered gneiss and completely to highly decomposed meta-granite. Moderately decomposed or better bedrock was encountered at approximately +53.0 mPD.

Groundwater was observed within the superficial deposits and decomposed rock, with perched groundwater levels recorded up to approximately 3 m above the rockhead.

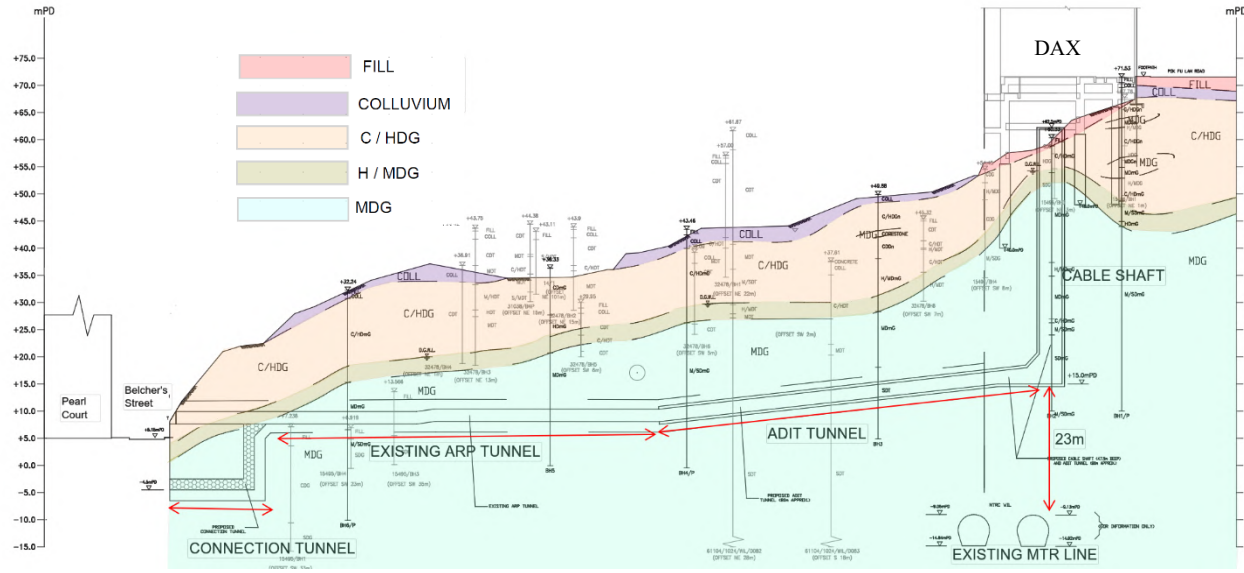

Figure 4: Geological Profile

3.2 Design

The proposed cable shaft is circular in plan with an internal diameter of 4.2 m. A 400-mm thick reinforced concrete ring lining is proposed as the permanent lining for the shaft in both the soft ground and rock sections. At the base of the shaft, a junction structure is provided to facilitate the connection between the cable shaft and the Adit Tunnel.

The design groundwater pressure takes into account both the observed groundwater level, which is approximately 3 m above the rockhead, and the provision for porewater pressure relief between the ring lining segments. The imposed live loading on the shaft structure considers the existing DAX foundation using a 45° load-dispersion approach, together with an additional surcharge of 20 kPa. The reinforced concrete lining was designed for a cast-in-situ construction method, with the shaft constructed in sequential sections of 3 m segmental height following phased excavation.

To enable construction of the cable shaft, a temporary pipe pile wall was designed to support and retain the surrounding ground beneath the permanent ring lining during phased excavation. The pipe pile wall comprises 273-mm diameter pipe piles installed at 460 mm centre-to-centre spacing, socketed into rock and terminating approximately 20.5 m above the final excavation level. A perimeter grout curtain was proposed around the external face of the pipe pile wall to provide groundwater cut-off and to temporarily support the gaps between piles and the soil–rock interface at the rockhead. The temporary pipe pile wall was designed with due consideration of ground movement control, changes in earth and groundwater pressures, and potential impacts on the existing DAX structure. As the steel pipe pile sections are not interlocked, the control of groundwater ingress during phased excavation highly relies on the performance of the surrounding grout curtain.

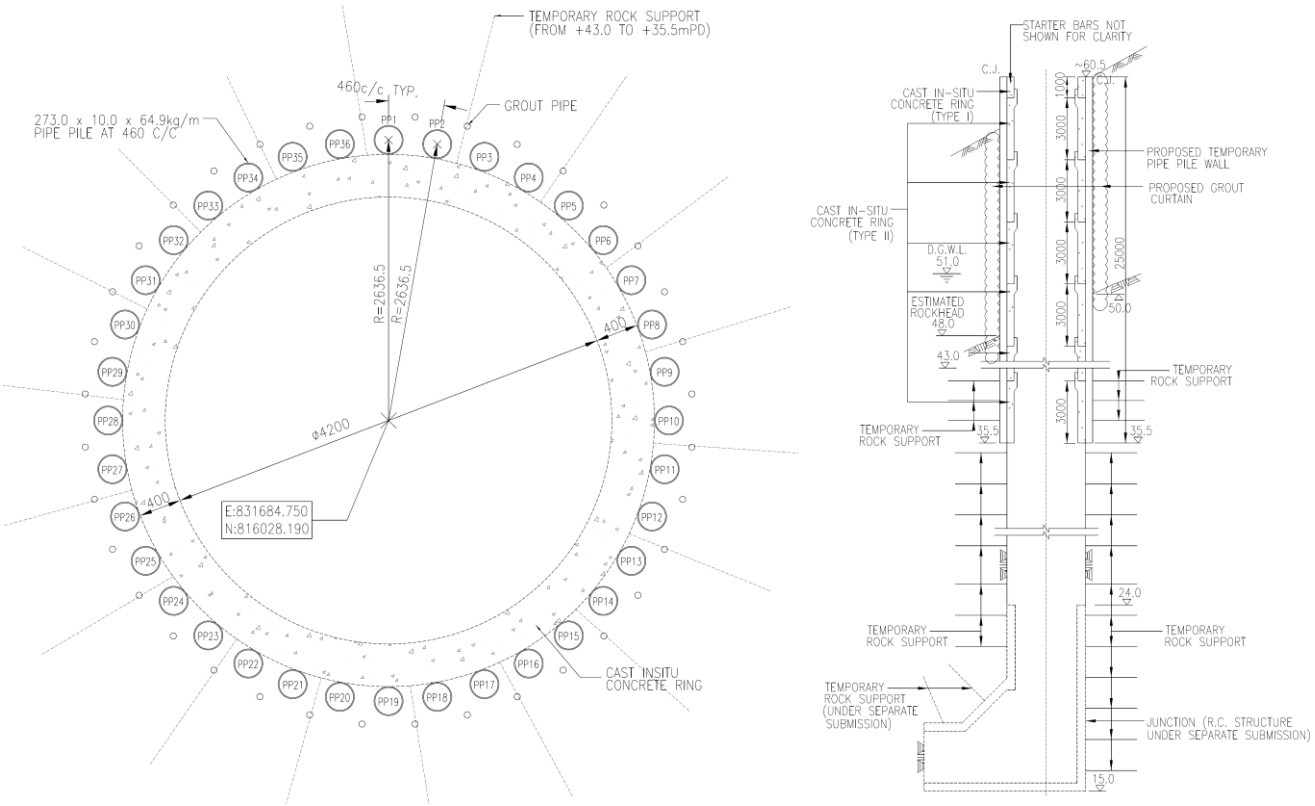

Figure 5: Pipe Pile Wall Layout Plan and Section

For the lower portion of the cable shaft between +50 mPD and +15 mPD, a Q-system was adopted to classify the rock mass for assessing the stability of the shaft excavation below the rockhead. The initial rock mass classification was derived from drillhole logging data at the centre of the shaft and was subsequently verified through systematic mapping of the exposed rock at 1.6 m depth intervals. All exposed rock surfaces were inspected, scaled, and surveyed, with particular attention given to groundwater seepage. Although the rock mass

was generally of very good quality, occasional rock dowels were installed to address uncertainties associated with suspected adverse jointing. Temporary rock support comprised 3-m long T25 dowels together with 55-mm thick shotcrete and mesh. Given that the proposed shaft lies outside the geotechnical influence zone of the underlying MTR facilities, and considering the competent nature of the rock mass, negligible impacts on the MTR tunnel were anticipated in terms of pressure changes, ground movements, and vibrations.

The proposed Adit Tunnel connects the junction structure to the disused ARP tunnel network and follows a downward gradient from approximately +15.0 mPD to +8.17 mPD. The Adit Tunnel was designed with a D-shaped cross-section providing internal dimensions of 2.0 m in width and 2.5 m in height. Temporary steel sleeve pipe lining was proposed following excavation of the Adit Tunnel under an overburden of approximately 48 m to 28 m. The temporary lining design took into account imposed loads from rock pressure, surcharge, hydrostatic pressure, and loadings from the existing DAX foundations.

The design intent for utilising the ARP tunnel was to retain its existing condition as far as practicable, with minimal alterations, while upgrading the structure with the necessary permanent stabilisation measures. Rock face mapping was carried out and the existing tunnel condition was surveyed. Where required, the proposed works included the application of 150-mm thick shotcrete with mesh to the crown and sidewalls, together with spot dowels installed at the rock face in accordance with the tunnel mapping results. A 150-mm wide flat drainage channel was proposed along the tunnel invert to collect and convey seepage from weep holes in the wall lining.

The final section comprises the connection tunnel extending the ARP tunnel to Belcher's Street. A temporary vertical shaft with plan dimensions of 2.0 m by 3.5 m was excavated downwards to a depth of 6.7 m below the ARP tunnel invert to facilitate cable installation works. From this connection shaft, a 15.5-m long temporary rock tunnel was constructed along an alignment selected to avoid existing underground utilities at Belcher's Street.

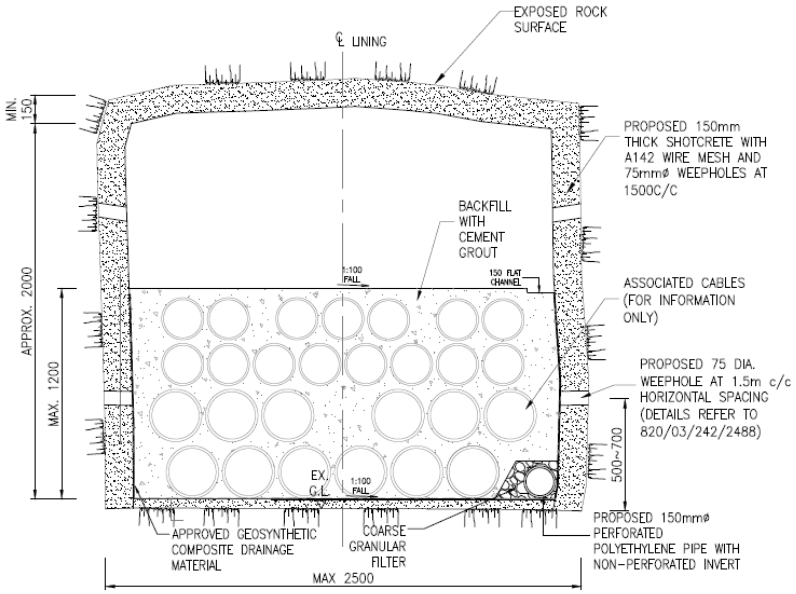

Figure 6: Proposed Upgrading Works for the Existing ARP Tunnel

The D-shaped tunnel, measuring 2.2 m in width and 2.5 m in height, comprised temporary shotcrete applied to the exposed rock face together with continuous steel segmental panels for support. A temporary strutted pipe pile cofferdam was provided at the ARP tunnel invert to act as a safety barrier, protecting workers from falling debris and preventing surface water inflow into the temporary shaft. Upon completion of the cable installation works, the connection shaft and connection tunnel were permanently backfilled with cement grout.

4 CONSTRUCTION

4.1 Construction Method

In addition to the pipe pile wall, other temporary works were implemented to facilitate construction of the cable shaft. Materials and equipment, including the TBM components, were transported from Pok Fu Lam Road to the works area located approximately 16 m beneath DAX by means of a suspended steel platform and gantry crane secured to the existing structures.

At the sloping ground where the shaft was located, a level working area required for shaft construction was formed by constructing a temporary steel platform on the downslope side and a temporary concrete retaining wall on the upslope side. Protective steel plates were also installed around the existing reinforced concrete tie beams and columns of DAX to prevent damage during construction.

Figure 7: Temporary Gantry Crane and Working Platform

Figure 8: Pipe Pile Installation

A phased excavation method was adopted as the most suitable and safe solution in view of the limited access and headroom constraints. Major risks, including surface spalling of the excavated face, hydraulic failure, and groundwater drawdown, were mitigated through the use of the temporary pipe pile wall, perimeter grout curtain, and associated pumping tests. Comprehensive safety precautionary measures were implemented throughout the shaft excavation to ensure worker safety, including the provision of ventilation systems.

Key advantages observed from adopting the phased excavation method included the ability to carry out real-time inspection of exposed ground conditions, minimal site setup requirements, the use of compact plant, and reduced over-break. The approach also resulted in negligible vibration levels and minimised the risk of adverse impacts on the existing DAX structure and the underlying MTR line.

Figure 9: Exposed Rock Face of Cable Shaft

For the excavation of the cable shaft, manual methods and a compact excavator were adopted for soil excavation, while the drill-and-break method was used for rock excavation to minimise vibration and dust generation. The construction sequence was as follows:

1. Install the pipe pile wall together with a perimeter grout curtain.
2. Carry out pumping tests to verify the effectiveness of the groundwater cut-off.
3. Excavate the shaft in a phased, lift-by-lift sequence.
4. Install the permanent reinforced concrete lining following each excavation cycle.
5. Repeat Steps 2 to 4 until the toe level of the temporary pipe pile wall was reached.
6. Excavate rock in a phased, lift-by-lift sequence.
7. Undertake rock mapping and rock face stabilisation at each excavation stage.
8. Upon reaching the bottom of the cable shaft at +15 mPD, construct the reinforced concrete junction structure using a bottom-up method.
9. Construct the shaft top cover and reinstate the ground at the top of the shaft.

To ensure that the concrete lining rings remained secure and stable during subsequent excavation below, temporary shear studs were installed along each pipe pile, together with socket details and dowel bars between adjacent concrete ring segments. At locations where rock was exposed during excavation, temporary rock dowel bars were provided to support the permanent concrete ring segments.

Figure 10: Cable Shaft

The Adit Tunnel excavation was carried out using a TBM launched from the junction structure at the base of the cable shaft. During tunnelling, roof probing of 10 m length at an inclination of 45°, together with face probing of 25 m length, was undertaken to confirm the presence of adequate competent rock cover and to ensure tunnel stability during the temporary works stages. As the TBM advanced, temporary steel sleeve pipe lining was installed to provide interim ground support.

Upon completion of the tunnel excavation, the TBM was dismantled and removed through the existing ARP tunnel prior to commencement of the cable installation works. The Adit Tunnel was permanently backfilled following completion of the works.

Figure 11: TBM Breakthrough Within the Disused Air-Raid Precaution (ARP) Tunnel Network

Within the ARP tunnel, improvement works were carried out, including rock mapping, installation of rock dowels for stabilisation, and application of shotcrete with wire mesh to the crown and sidewalls. Feature dowels were installed at the crown to provide additional localised stabilisation. Mass concrete walls were constructed at four existing tunnel junctions to isolate the repurposed ARP tunnel section, enhance overall tunnel stability, and permanently decommission the interfaces with the unused tunnel branches.

For the connection tunnel shaft, a temporary pipe pile wall was installed at the invert level of the ARP tunnel. Drilling and excavation of the connection tunnel shaft were undertaken within the ARP tunnel under constrained working space and limited headroom, necessitating the use of manual methods and compact plant.

Figure 12: Pipe Pile Works in the existing ARP Tunnel for the Connection Tunnel

4.2 Instrumentation and Monitoring

A comprehensive instrumentation and monitoring scheme was implemented in the vicinity of the proposed cable shaft, including ground settlement markers, standpipes and piezometers, building settlement points, and real-time monitoring of tilt and vibration. Throughout the excavation of the cable shaft, construction of the junction structure, and Adit Tunnel excavation works, the maximum monitoring response was located within close vicinity to the works and indicated negligible ground movement (<5 mm), building movement (~0 mm) and tilt (<1:6000) at the DAX.

The key measure contributing to effective control of ground response was the adoption of a phased excavation method for the cable shaft. With permanent reinforced concrete rings installed in a top-down manner following each excavation cycle, the temporary pipe pile wall and perimeter grout curtain were required to retain a maximum exposed excavation height of only 1.6 m at any time. As a result, relatively small-diameter pipe piles of 273 mm were sufficient for the shaft excavation, thereby reducing the risk of ground loss associated with pile installation. Furthermore, rock excavation was carried out using compact plant and manual drill-and-break methods, which avoided rock overbreak and further contributed to limiting ground vibration and movement.

Figure 13: Tilt and Vibration Monitoring Instrumentation

5 CONCLUSIONS

The deep cable shaft, junction structure, Adit Tunnel, ARP Tunnel, and connection tunnel were successfully constructed within a highly constrained environment, particularly at the cable shaft location, through the adoption of a phased excavation method combined with a site-specific retaining structure design. The works were completed safely and effectively in close proximity to the existing DAX substructures founded on piles, directly above the operational MTR tunnels, and while maintaining uninterrupted DAX operations throughout the construction period.

Instrumentation and monitoring data consistently demonstrated negligible ground movement, vibration, groundwater response, and impacts on surrounding structures, utilities, and adjacent roads. The temporary works adopted for the cable shaft, including the pipe pile wall, perimeter grout curtain, and rock stabilisation measures, proved to be effective in supporting lateral earth pressures during construction of the permanent shaft lining.

The use of a TBM for excavation of the Adit Tunnel and breakthrough into the repurposed ARP tunnel network represented an innovative and sustainable approach, enhancing construction safety while maintaining negligible impacts on sensitive receivers. Only minimal upgrading works were required within the ARP tunnel, further reducing the potential for adverse impacts on adjacent sensitive receivers.

Fundamentals and First Principles of Point Load Test in Rock Mechanics

Zhaonan Wang[a,b], Louis Ngai Yuen Wong[a,b]
[a] *The University of Hong Kong Shenzhen Institute of Research and Innovation (HKU-SIRI), China*
[b] *Department of Earth and Planetary Sciences, The University of Hong Kong, Hong Kong, China*

ABSTRACT

The point load test (PLT) is a widely used index test for rapid rock strength assessment because of its simplicity, low specimen-preparation requirements, and applicability to core, block, and irregular lump specimens. This paper presents a comprehensive review of the origin, development, standardization, interpretation, and future prospects of the PLT. The historical evolution of the PLT is traced from its early empirical formulation in the 1960s to its subsequent theoretical development and formal standardization by ISRM, ASTM, and Recommended National Standard of China. The review highlights that, although the size-corrected point load strength index, $I_{s(50)}$, is commonly correlated with uniaxial compressive strength (UCS) and sometimes tensile strength, these relationships are not universal. Reported index to strength conversion factors vary substantially with lithology, weathering grade, anisotropy, specimen geometry, and loading contact conditions. Evidence from Hong Kong indicates that the commonly adopted conversion factor of 24 may overestimate the UCS of several local rock types, with locally derived values generally lower. The paper further reviews analytical and numerical studies on PLT failure mechanisms, showing that stress concentration, local crushing, and tensile splitting jointly govern failure, while current models remain limited by simplifying assumptions or computational cost. Finally, future research priorities are identified.

1 INTRODUCTION

Rock is a mechanically complex and heterogeneous geomaterial that exhibits a wide spectrum of strength and deformation behaviors. Reliable characterization of its geomechanical properties, particularly uniaxial compressive strength (UCS) and tensile strengths, is fundamental to rock mass classification, excavation design, slope stability assessment, and underground construction. Because direct laboratory determination of these properties is often time-consuming, costly, and specimen-dependent, indirect index tests remain widely employed in both field and laboratory practice.

Among these methods (Figure 1), the point load test (PLT) has become one of the most commonly adopted index tests because of its operational simplicity, low specimen-preparation requirements, and rapid execution. The PLT is covered by three major standards referred to in this study: the International Society for Rock Mechanics (ISRM, 1985), American Society of Testing Materials (ASTM D5731-16, 2016), and Recommended National Standard of China (GB/T 50266-2013, 2013). In the PLT, a rock specimen is loaded to failure between a pair of coaxial truncated conical platens (cones), and the peak load is used to calculate the point load strength index (PLSI) I_s. Unlike the UCS test or the Brazilian tensile strength (BTS) test, which generally require more regular specimen geometry and greater testing control, the PLT can be conducted on core, block, and irregular lump specimens, making it particularly attractive for site investigations and construction-stage decision-making. Its principal engineering purpose is to determine the I_s or the size-corrected index $I_{s(50)}$, which is then correlated empirically with UCS and, in some standards, tensile strength.

Nevertheless, the applicability of the PLT is not without limits. ASTM D5731-16 (2016) states that this method is intended for medium strength or stronger rock (UCS > 15 MPa), and is not suitable for very weak rock. By contrast, Geoguide 3 (GEO, 2017), which classifies rock material strength using UCS, PLSI, and field identification tests, implies that the PLT may also be applicable to moderately weak or stronger rock with UCS values ≥ 5 MPa. This discrepancy highlights an important practical issue. The lower strength boundary of PLT applicability remains somewhat context-dependent and may vary with testing standard and engineering practice (UCS ≥ 5 MPa).

However, the practical appeal of the PLT is also the source of its main scientific limitation: it is an index test rather than a direct strength test. It was emphasized by ISRM (1985) that “an index test needs to be simple”. Yet the simplicity of the procedure contrasts with the complexity of the failure process. A large body of research

has shown that the relationship between $I_{s(50)}$ and UCS is not universal. Reported index to strength conversion factors (hereafter referred to as conversion factors) vary substantially among lithologies, weathering states, anisotropy conditions, and geological settings. These discrepancies arise from at least two broad causes. First, geological history, including mineralogical composition, diagenesis, metamorphism, weathering, and microcrack development, strongly influences the failure behavior of rock under concentrated loading. Second, the PLT is highly sensitive to specimen size, shape, loading configuration, platen penetration, and contact geometry, all of which introduce scatter into measured values. As a result, routine adoption of a single conversion factor to estimate UCS from PLT data can be misleading, especially for rocks outside the lithological range on which the factor was originally calibrated. This limitation is explicitly acknowledged in ASTM D5731-16 (2016), which cautions that "the test results should not be used for design or analytical purposes".

Methods	Measured Parameters	Schematic	Advantages	Disadvantages
Uniaxial compressive strength test	Uniaxial compressive strength		○ Fundamental test method ○ High reliability ○ Wide applicability ○ Straightforward result interpretation	○ Careful and sophisticated specimen preparation ○ Time-consuming and labor-intensive ○ High equipment requirement ○ Sensitive to end effects
Brazilian tensile strength test	Indirect tensile strength	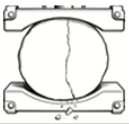	○ Relatively simple specimen preparation ○ Simple test setup	○ Sensitive to loading jaw-specimen contact condition ○ An indirect estimation of tensile strength
Point load test	Point load index strength		○ Fast and simple ○ Minimum specimen preparation ○ Equipment portability - suitable for field use	○ High result dispersion ○ Strong influence of loading point location ○ Frequent test invalidity due to chipping and slippage of specimen

Figure 1: Comparison of common rock strength tests.

Compared with the extensive literature on UCS and BTS, mechanistic studies of rock failure under point loading remain relatively limited. Existing work can be broadly divided into analytical and numerical approaches, supported by a substantial body of laboratory and field-obtained PLT data. Analytical studies have provided important closed-form or semi-analytical solutions for stress distributions in idealized geometries under point loading (e.g., Hiramatsu and Oka, 1966; Chau, 1998; Chau and Wei, 1999; Russell and Wood, 2009; Serati et al., 2013; Wei and Chau 2013). These studies have significantly improved understanding of how contact geometry, specimen dimensions, and elastic properties govern the internal stress fields. Nevertheless, most analytical solutions are built on assumptions of homogeneity, linear elasticity, and ideal specimen geometry, which limit their ability to represent crack initiation, damage accumulation, and unstable fracture in natural rock.

Numerical methods have therefore become increasingly important for investigating PLT failure mechanisms. Most published numerical studies have employed discontinuum-based approaches, especially the Discrete Element Method (DEM), to model crack initiation and propagation under point loading (Ren et al., 2018; Haeri et al., 2017; Shi et al., 2023; Wang et al., 2024). These simulations have yielded valuable insights into the effects of loading indenter radius, specimen shape, and loading configuration. However, they also reveal a methodological gap. Due to the inherent computational expense of DEM, constructing highly refined numerical models (e.g., with millions of particles) for three-dimensional (3D) point load problems remain challenging. Consequently, the stress-transfer process from local contact to global tensile splitting remains incompletely understood.

This limitation is especially relevant in regions where PLT is routinely used for rapid strength assessment, but where local calibration remains insufficient. In Hong Kong, the expansion of major infrastructure and urban development, including projects associated with the Northern Metropolis, has generated, and will continue to generate, a substantial volume of rock engineering data and demand rapid rock strength characterization across diverse lithologies. Yet much of the widely cited PLT conversion framework was developed for relatively intact, isotropic igneous and volcanic rocks, whereas Hong Kong and the wider Guangdong–Hong Kong–Macao Greater Bay Area (GBA) also include sedimentary and metasedimentary rocks with more variable fabric, weathering profiles, and mechanical response. Although local practice often adopts a conversion factor 24

between $I_{s(50)}$ and UCS (GEO, 2017), studies over the past four decades suggest that this value may overestimate UCS for several important local rock types. This issue is not merely academic: an inappropriate conversion factor can bias preliminary rock classification and create inconsistency between field-based screening results and laboratory-derived design parameters.

Against this background, this paper reviews the development of the PLT from its origins in the 1960s to current analytical, experimental, and numerical research, with particular emphasis on Hong Kong experience and prevailing PLT standards. The review has two objectives. First, it critically evaluates the extent to which existing PLT knowledge supports reliable rock strength estimation across different geological settings. Second, it identifies research priorities for improving interpretability, regional calibration, and digital integration of PLT in future rock engineering practice.

2 ORIGIN AND DEVELOPMENT OF PLT

2.1 Historical Overview

The PLT evolved through a series of studies that progressively improved its practicality, theoretical basis, and standardization. Its development was not linear; rather, it reflects a continuing attempt to balance two competing goals: maintaining the test as a simple field index while improving its reliability as a proxy for fundamental rock strength parameters.

As the conceptual pioneer, Protodyakanov (1960) in Russia proposed the first PLT on irregular lumps. Adopted by the International Bureau for Rock Mechanics (IBRM), this work established the core premise of PLT as a standard technique using irregular "egg-shaped" rock lumps (≈100 cm³, axis ratio 1.5:1). The specimens are obtained by breaking lumps of rock using any suitable method and rounding off suitable specimens by light hammer blows. The importance of this work lies in its practicality. It demonstrated that rock fragments obtained directly in the field could be tested without the extensive specimen preparation required for conventional strength tests. However, the method remained largely empirical and lacked a rigorous mechanical interpretation.

A major advance was made by Hiramatsu and Oka (1966), who validated PLT theoretically and experimentally by comparing stress states in spherical, cubic, and rectangular prism specimens via 3D photoelasticity. They confirmed that near the loading axis, irregular specimens exhibit stress equivalence to diametrically compressed spheres. Critically, they derived practical tensile strength S_t:

$$S_t \approx \frac{0.9F_0}{d^2} \quad \text{or} \quad S_t \approx 1.4\frac{F_0}{2\pi a^2} \tag{1}$$

where F_0 represents the critical load, $2a$ or d is the distance between the points of loading, replacing cumbersome volume measurements with a simple distance parameter. Experiments on marble, sandstone, and andesite showed good agreement with disk diametral tests, proving irregular specimens could yield reliable tensile strength data. This study was significant because it moved the PLT beyond empirical field practice and gave it a preliminary mechanics-based foundation. At the same time, the analysis was based on idealized geometry and elastic behavior, limitations that would remain a recurring issue in later PLT interpretation.

Reichmuth (1967) further advanced PLT standardization through the development of a universal testing jig. This jig accommodated various specimen geometries, including cores, prisms, half-cores, and disks, utilizing spherical-ended rods/rollers to ensure consistent load application. He addressed size and shape effects by proposing a modified strength formula:

$$S_t = K_s P / h^2 + K_b P \tag{2}$$

where P denotes applied load, h is distance between loading points, K_s is the shape factor, K_b is the brittleness index. These factors (K_s and K_b) were introduced to characterize the material's behavior, particularly its brittleness. Furthermore, his work provided a correlation for compressive strength, $S_c \approx -16S_t$, thereby establishing a direct link between PLT results and compressive strength, which was crucial for practical engineering design applications. As shown in Figure 2, the fracture morphology analysis further revealed Hertzian conical cracks in brittle materials, significantly enhancing the understanding of PLT failure mechanisms. This was a crucial mechanistic insight because it showed that PLT failure is not a pure tensile

process; rather, local compressive damage and global tensile splitting coexist. This mixed failure mechanism partly explains why empirical correlations between PLT and UCS are inherently variable.

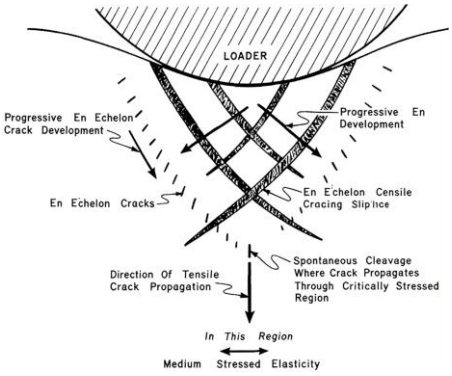

Figure 2: Schematic illustration of rock failure caused by a point loader (Reichmuth, 1967).

Broch and Franklin (1972) formalized PLT as a practical and widely applicable field-applicable index test. They standardized diametral and axial protocols and derived size-correction curves to normalize results to a 50 mm reference diameter $I_{s(50)}$, resolving strength reduction with specimen size. They also introduced the anisotropy index for bedded/schistose rocks and demonstrated a strong correlation between $I_{s(50)}$ and uniaxial compressive strength. Their work laid the practical foundation for large-scale use of the PLT and became the basis for the ISRM suggested method issued in 1972. The importance of this contribution lies in its balance between field usability and procedural consistency. Nevertheless, the standardization of procedure did not resolve a more difficult question: whether a standardized index can be converted to UCS using a standardized factor across different geological contexts.

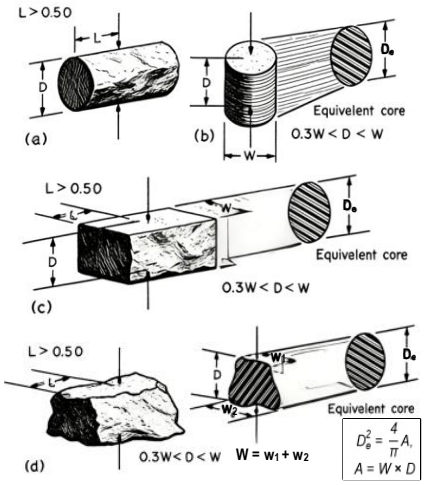

Figure 3: Specimen shape requirements for (a) the diametral test, (b) the axial test, (c) the block test, and (d) the irregular lump test (revised from ISRM (1985)).

A major refinement came with Brook (1985), who introduced the "equivalent core diameter" D_e to unify testing of irregular lumps, blocks, and cores (Figure 3). This innovation simplified shape correction and greatly improved the operational flexibility of the test. The revised ISRM (1985) "*Suggested Method for Determining Point Load Strength*" incorporated this concept, formalized procedures for different specimen types, and refined the treatment of water condition and anisotropy. This caveat is significant. It shows that even at the stage of formal standardization, the limitations of a universal conversion factor were already recognized.

Taken together, the historical development of the PLT shows clear progression. Early work focused on feasibility, later work on standardization, and more recent work on interpretation. What remains unresolved is not how to conduct the test, but how confidently its index value can be translated into fundamental strength properties under varying geological and loading conditions. ISRM (1985) established a fundamental

consensus within the geotechnical community, profoundly influencing the development of subsequent national and international standards, including ASTM D5731-16 (2016) and GB/T 50266-2013 (2013).

2.2 Calculation of the point load strength index (PLSI)

Following Broch and Franklin (1972) and ISRM (1985), the point load strength index I_s is determined from the maximum load P recorded at specimen failure according to Equation (3):

$$I_s = \frac{P}{D_e^2} \tag{3}$$

where P represents the maximum load recorded during the test, and D_e is the equivalent core diameter. As illustrated in Figure 3, the equivalent diameter squared D_e^2 is defined by:

$$D_e^2 = \begin{cases} D^2, & \text{for diametral cone tests without peneration} \\ \dfrac{4A}{\pi}, & \text{for axial, block and lump tests} \end{cases} \tag{4}$$

where $A = W \times D$ represents the minimum cross-sectional area of a plane through the platen contact points as shown in Figure 3.

ASTM D5731-16 (2016) further note that "If significant platen penetration occurs in the test, such as when testing weak sandstone, the value of D should be the end value of the separation of the loading points, D'[1]. Measurements of core diameter D or specimen width W made perpendicular to the line joining the loading points are not affected by this platen penetration and should be retained at the original values. The modified values of D can be calculated from:

$$\begin{cases} D_e^2 = D \times D' & \text{for cores} \\ D_e^2 = \dfrac{4W \times D'}{\pi} & \text{for other shapes} \end{cases} \tag{5}$$

This is a practical but often underappreciated issue. Penetration alters the local contact condition and effectively changes the geometry used in strength normalization. The implication is that weak rocks are not only more difficult to test consistently, but also more vulnerable to procedural uncertainty in index calculation. This helps explain why PLT-based UCS estimates tend to be less reliable at the lower end of the rock strength spectrum.

To compare tests conducted on specimens of different sizes, measured I_s values are corrected to a reference equivalent diameter of 50 mm, yielding the $I_{s(50)}$ value.

$$I_{s(50)} = F \times I_s \tag{6}$$

The size correction factor F can be determined either graphically from the chart presented in Figure 4 (ASTM, 2016) or analytically using the expression given in Equation (4):

$$F = \left(\frac{D_e}{50}\right)^{0.45} \tag{7}$$

For tests conducted on specimens with equivalent diameters close to 50 mm, a simplified approximate expression for F may be used, introducing only a slight error:

$$F = \sqrt{D_e / 50} \tag{8}$$

[1] According to ISRM(1985), D' is measured at the instant of failure.

Although these size corrections are well established, they remain empirical. Their continued use is justified operationally, but they should not be interpreted as universally valid mechanical laws. Several studies have shown that size effects in PLT are influenced not only by geometry but also by lithology, contact condition, and heterogeneity. Therefore, while the correction procedure improves comparability, it does not fully remove scale dependency.

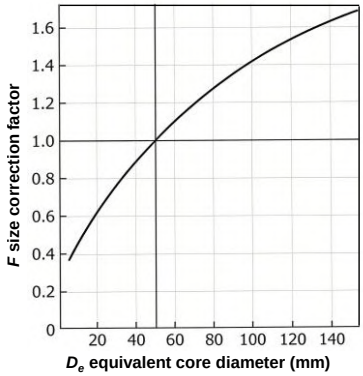

Figure 4: Size correction factor chart (revised from ASTM D5731-16, 2016)

3 EXPERIMENT, THEORY AND NUMERICAL INVESTIGATIONS

3.1 Characterization of PLT behavior in Hong Kong

PLT results are well known to exhibit significant scatters. To reduce the influence of outliers and specimen-to-specimen variability, current standards recommend repeated testing. ASTM D5731-16 (2016) recommends at least 10 specimens for core or block, and 20 for irregular-shaped specimens obtained by other means. GB/T 50266-2013 (2013) recommends 5–10 specimens for core/block tests and 15–20 for block and irregular lump tests. ISRM (1985) and GB/T 50266-2013 (2013) also suggest removing the two highest and two lowest values when ten or more valid tests are available, and averaging the remaining results. These recommendations are useful for quality control, but they also highlight a fundamental feature of PLT. Variability is intrinsic to the PLT. Accordingly, the use of a single PLT result, or of a UCS value converted directly from a single PLT result, as a design parameter is unsafe and difficult to justify.

In Hong Kong, the relationship between $I_{s(50)}$ and UCS has been examined in several studies, and the collective evidence indicates that the commonly adopted conversion factor of 24 (GEO, 2017) is not universally representative of local rocks (Table 1). Lumb (1983), in one of the earliest systematic studies on Hong Kong igneous rocks, showed that the conversion coefficient varies markedly with weathering grade, dropping from about 22 for intact rock to about 10 for decomposed material. This finding has major practical implications. It suggests that weathering state may influence the UCS–PLSI relationship as strongly as lithology itself and that a single conversion factor can substantially overestimate strength in decomposed rock.

Subsequent studies reached broadly similar conclusions. Chau and Wong (1996) reported a lower conversion factor of 12.5 for granite and tuff, while Tham et al. (1999) proposed a factor of 21.3 for granite, limestone, marble, and tuff. Basu and Aydin (2006) found a final strong correlation for granite with a factor of about 18.0. Yin et al. (2017), based on diametral, axial, and irregular lump tests on Hong Kong granite, reported factors ranging from 21.6 to 22.3. Taken together, these studies suggest that for fresh to moderately weathered granitic rocks in Hong Kong, a conversion factor around 21–22 may be more realistic than 24. More importantly, they show that the variation is systematic rather than random: different specimen forms and weathering conditions may yield different correlations, but most locally derived values still cluster below the conventional factor adopted in practice.

Table 1: Relationship between UCS and $I_{s(50)}$ for different PLTs and rock types of Hong Kong

References	Rock type	PLT type	Decomposition grades	Correlation equation	R^2
Lumb (1983)	Igneous rocks	Not differentiated[2]	Fresh	UCS = 22.0×$I_{s(50)}$	Not stated
			Decomposed	UCS = 10.0×$I_{s(50)}$	
Gamon (1984)	Granite	Axial & Irregular lump	Moderately to slightly decomposed	UCS = 14.0×$I_{s(50)}$	Not stated
Chau and Wong (1996)	Granite and Tuff	Axial	Fresh to moderately decomposed	UCS = 12.5×$I_{s(50)}$	0.73
Tham et al. (1999)	Granite, Limestone, Marble and Tuff	Diametral	Moderately and highly decomposed	UCS = 21.3×$I_{s(50)}$	Not stated
Basu and Aydin (2006)	Granite	Diametral & Axial	Moderately to highly decomposed	UCS = 18.0×$I_{s(50)}$	0.97
Yin et al. (2017)	Granite	Diametral	Moderately to slightly decomposed	UCS = 21.6×$I_{s(50)}$	0.7361
		Axial		UCS = 21.7×$I_{s(50)}$	0.8044
		Irregular lump		UCS = 22.3×$I_{s(50)}$	0.8189

This body of work is valuable, but it also has limitations. First, most local studies have focused on granitic rocks, whereas the engineering geology of Hong Kong and the wider GBA includes a wider range of lithologies, including volcanic, sedimentary, metasedimentary, and weathered materials. Second, most reported relationships are simple linear regressions with limited discussion of the underlying mechanics or uncertainty bounds. Third, the datasets are generally modest in size and often drawn from specific projects or lithological subsets. Therefore, while local evidence clearly questions the blanket use of a factor of 24, it is not yet sufficient to justify a single replacement value for all geological conditions. The key implication is that regional calibration should move from one-factor practice toward lithology- and condition-specific frameworks.

3.2 Analytical models for PLTs

Because the PLT is governed by a highly non-uniform three-dimensional stress field, influenced significantly by specimen geometry and size (Broch and Franklin, 1972; Masoumi et al., 2018), analytical modelling has played a central role in clarifying the mechanics of failure. These models are especially important for interpreting what the measured index actually represents. If the PLT is to be used as more than a purely empirical tool, then the relationship between local contact damage, internal stress development, and macroscopic splitting must be understood.

In a pioneering effort, Hiramatsu and Oka (1966) utilized photoelastic tests to investigate the stress distribution in both spherical and disc-shaped samples subjected to point loads. Their research not only elucidated these complex stress fields but also provided a closed-form solution for the stress distribution within a sphere under such loading conditions. Building on this fundamental work, a specific formula for calculating the tensile strength of spherical rock specimens was proposed as detailed in Equation (1). Wijk (1978) provided a critical re-evaluation of the analytical solution for the PLT (Hiramatsu and Oka, 1966), demonstrating that accurate stress convergence requires summing many more terms in the series expansion than previously used, and revealed that the actual maximum tensile stress is significantly higher than the "plateau value" conventionally taken as the tensile strength measure. This was a critical intervention because it questioned whether the commonly adopted stress measure in PLT theory accurately represents controlling failure stress.

A more comprehensive body of analytical work was subsequently developed by Chau and co-workers (Chau, 1998; Chau and Wei, 2001; Wei et al, 1999, 2019). These studies derived stress solutions within specimens for different specimen geometries and loading configurations, encompassing diametral, axial, and irregular types. The results show that the central tensile zone is accompanied by severe local stress concentration near the

[2] Original wording in Lumb (1983): "Point load index tests were occasionally performed on portions of discarded core, using a simple loading jig. Some additional point load test results will be quoted which were obtained in the field, using a commercial testing device, on irregularly-shaped hand specimens (M.K. Millar, personal communication, 1981)."

loading points. They also demonstrated that the peak tensile stress is influenced by Poisson's ratio, specimen size, contact area, and indenter geometry.

This body of work was important because it established that PLT failure cannot be interpreted solely in terms of nominal load and specimen size; contact mechanics matters. Of particular merit, Wei et al. (1999) concurrently leveraged their analytical solutions to propose a simplified model as presented in Figure 5(a). This model aimed to analyze the grain crushing zone that forms within the specimen due to intense stress concentrations adjacent to the loading platens. As shown in Figure 5(b), the predictions generated by this model demonstrated commendable consistency with experimental observations (Zhang et al., 1990).

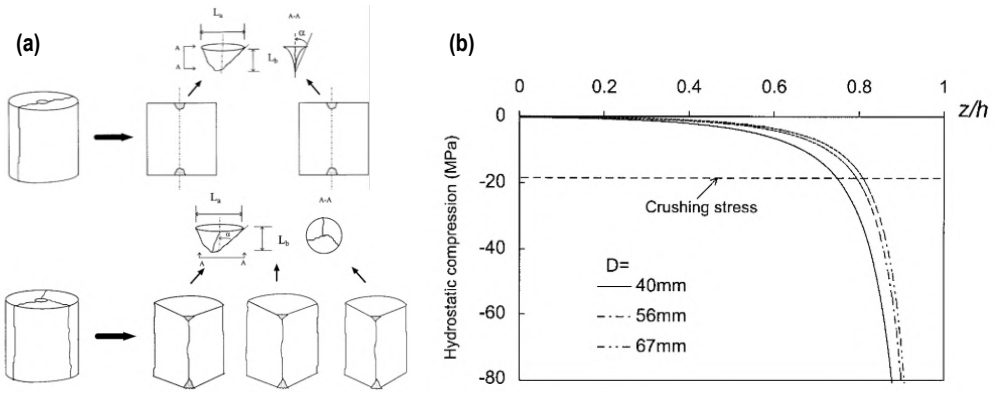

Figure 5: Depiction of localized grain comminution zones beneath the loading indenter, as conceptualized by the axial point load analytical theory proposed by Wei et al. (1999): (a) Representative failure patterns. (b) Theoretical predictions for the distribution of hydrostatic stress as a function of normalized distance for various indenter diameters.

As shown in Figure 6, the observed pattern of tensile stress distribution (Chau, 1998; Chau and Wei, 2001) along the loading line bears resemblances to those identified in spheres subjected to diametral PLT and cylinders tested under axial/diametral PLT conditions. The analytical model ascertained that the peak tensile stress diminishes with an increase in Poisson's ratio of the rock, contact area between the loading indenter and rock, and indenter ball radius, yet conversely escalates with an increase in the cylinder's diameter (Chau and Wei, 2001).

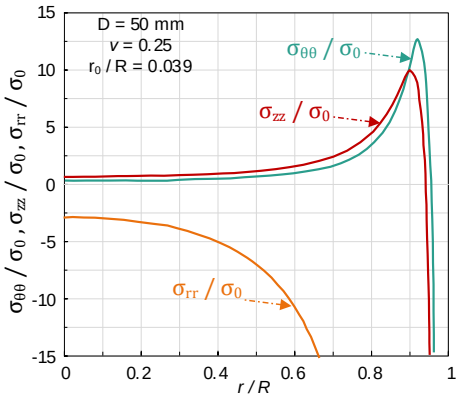

Figure 6: Analytical solution of the diametral PLT A typical stress distribution of the normalized stresses $\sigma_{\theta\theta}/\sigma_0$, σ_{zz}/σ_0 and σ_{rr}/σ_0 versus r/R, where $r_0 = P/D^2$ is the load stress under the constant P; ν represents the Poisson's ratio, r_0 denotes a nominal radius for the elliptical contact area between the spherical heads of the indenters (revised from Chau and Wei (2001)).

Russell and Wood (2009) took a different but complementary approach by deriving a theoretical relationship among the PLSI, compressive strength, and the tensile strength for brittle spheres. A theoretical expression for the correlation coefficient C was proposed to involve the effect of the contact angle between the loading platen and rock, the characteristics of the loading device, and the inherent properties of the rock material. The theoretical predictions derived from their model exhibited strong agreement with experimental measurements

of both compressive strength and tensile strength. This was a notable contribution because it attempted to move beyond empirical regression and toward a physically reasoned conversion framework.

Serati et al. (2013) further extended analytical capability by developing a general 3D elastic solution for circular cylinders under arbitrary lateral loading using a double Fourier series and the Papkovich-Neuber displacement potential to analyze the stress field and specifically applied this method to model the BTS test and PLT. Their work is particularly useful because it highlights the close but not identical mechanical relationship between these two indirect loading tests.

Despite these advances, analytical models share several limitations. Almost all assume linear elasticity, material homogeneity, and idealized specimen geometry. These assumptions are useful for isolating stress mechanisms, but they also constrain applicability to natural rock, which is anisotropic, microcracked, and often strongly heterogeneous. Most analytical solutions are therefore better understood as mechanistic benchmarks than as full predictive tools. Their greatest value lies in revealing why PLT is sensitive to contact geometry, size, and material properties, not in removing the need for empirical calibration. The practical implication is that analytical studies support caution rather than simplification: they explain the sources of variability that empirical conversion factors often obscure.

3.3 Numerical models for PLTs

Numerical modelling is increasingly used to bridge the gap between idealized analytical stress solutions and the observed fracture processes in real rock specimens. This is particularly important for the PLT because failure typically involves a coupled sequence of localized contact crushing, tensile stress redistribution, crack initiation, crack coalescence, and unstable splitting. These processes are difficult to capture analytically, especially in irregular or heterogeneous specimens.

Unlike UCS test or BTS test where outputs of compressive or indirect tensile strengths are generally attainable through numerical modeling, PLT simulations offer reduced diagnostic value if the primary goal is merely the inference of the UCS. Additionally, the computational replication of PLT inherently presents greater complexities than other standard rock mechanics tests, given the imperative for precise 3D representation of the interface between the loading platen and the rock sample. The highly localized nature of point loading, characterized by an exceptionally diminutive circular contact zone, precludes the validity of simplifying assumptions such as a two-dimensional (2D) plane strain model.

In a notable contribution, Li and Zhao (2021) utilized a four-dimensional lattice spring model (4D LSM) to conduct simulations of PLTs across various rock lithologies. Their methodology involved employing a Newton–Raphson algorithm to align the computational outputs with empirical observations, thereby enabling the prediction of rock's UCS. Although the 4D LSM exhibited considerable proficiency in replicating rock failure phenomena during PLT scenarios, the principal thrust of their investigation was the expedited determination of rock UCS via a digital twin paradigm, consequently dedicating less attention to a comprehensive elucidation of the underlying failure mechanisms specific to point loading conditions.

In contrast, several research (e.g., Haeri et al., 2017; Ren et al., 2018; Shi et al., 2023; Wang et al., 2023; Zhao et al., 2023) has leveraged the DEM to explore the impact of loading indenter geometry (specifically, curvature radius) and specimen configuration on the observed rock failure modes. Nonetheless, the substantial intrinsic computational burden linked with DEM frequently impedes high-resolution modeling, especially within the highly localized region directly adjacent to the loading platen. Figure 7 shows the numerical results for the 4D LSM and DEM(PFC^{3D}) for the formal (diametral, axial and irregular) and sphere specimens respectively.

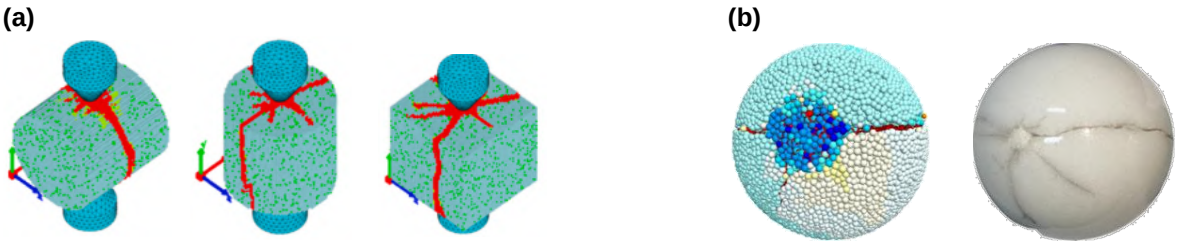

Figure 7: Numerical simulations of the PLT using discontinuous techniques: (a) Results from 4D LSM (Li and Zhao, 2021), and (b) Results from PFC^{3D} (Zhao et al., 2023).

A key limitation of the current numerical literature is its emphasis on reproducing observed failure patterns rather than quantifying uncertainty or testing transferability across lithologies. In other words, many studies demonstrate that a numerical model can match one experiment, but fewer show that the model can robustly explain why a correlation factor should differ from one rock type or geological setting to another. This is a critical gap if numerical methods are to contribute meaningfully to PLT standardization or regional calibration.

Overall, current numerical work has improved understanding of PLT failure processes, but it has not yet resolved the central interpretive problem: how to convert an index measured under a geometry-sensitive loading condition into a reliable estimate of fundamental rock strength across varied geological materials.

4 OUTLOOK FOR FUTURE INVESTIGATIONS

The existing literature suggests that the next phase of PLT research should move beyond repeated confirmation of empirical correlations and toward integrated, regionally calibrated, and mechanics-informed frameworks. This need is especially pressing in Hong Kong and the GBA, where rapid infrastructure development will require fast but defensible rock strength assessment across diverse geological conditions.

A first priority is the systematic development of a regional PLT database. Current Hong Kong practice still relies heavily on conversion factors derived from relatively limited datasets, often dominated by igneous rocks. A more robust framework would require large, curated datasets extended to other rock types, linking PLT results with UCS, BTS, weathering grade, mineralogical composition, porosity, and non-destructive indicators such as ultrasonic pulse velocity. Such a database would not merely refine regression coefficients; it would allow the uncertainty and domain of applicability of each correlation to be quantified. This is essential if PLT results are to support preliminary design, ground investigation interpretation, and construction-stage decision-making in a transparent and defensible way.

A second priority is methodology. Simple linear regressions between PLSI and UCS remain useful for engineering screening, but they are unlikely to capture the full nonlinearity and heterogeneity of natural rock. Machine learning models trained on sufficiently large and well-structured datasets may offer improved predictive performance by incorporating multiple descriptors simultaneously. However, the adoption of such methods should be approached critically. Their value will depend not only on predictive accuracy but also on interpretability, data quality, and geological representativeness. In other words, machine learning should not become a black-box replacement for mechanics; it should be used to complement, rather than replace, physically meaningful understanding.

A third priority concerns specimen geometry. In Hong Kong, due to the availability of cylindrical rock cores obtained from ground investigation, most controlled research still focuses on core specimens, whereas many field applications involve irregular blocks or lumps obtained directly from excavation. This mismatch is significant because irregular geometry intensifies uncertainty in stress concentration, edge effects, and failure interpretation. Advances in 3D scanning now make it feasible to digitally reconstruct irregular specimens before testing or after sampling. Coupled with numerical simulation, this creates an opportunity to study how real specimen morphology affects PLT outcomes and to develop geometry-aware correction or interpretation schemes. Figure 8 schematically depicts a hypothetical workflow, from mobile phone-based rock specimen scanning to its reconstruction within a finite element environment.

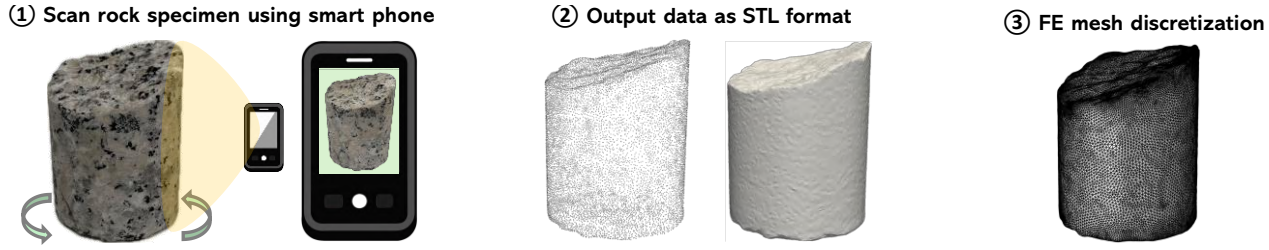

Figure 8: Conceptual workflow for the digital reconstruction of irregular specimens from 3D scanning data and their subsequent integration into numerical simulations.

Once an irregular rock specimen has been digitally rendered, the selection of an appropriate numerical simulation technique becomes paramount. For PLT simulations, two critical aspects demand meticulous attention: (1) the accurate representation of 3D crack initiation and subsequent propagation within the rock matrix, and (2) the robust formulation of contact algorithms governing the interaction between the 3D loading indenter and the rock specimen.

A fourth priority lies in numerical modelling. As reviewed in Section 4.2, previous numerical investigations into PLT have predominantly employed discontinuous mechanics. However, a comprehensive and fine-grained exploration of the intrinsic failure mechanisms under point loading often renders these discontinuous theories computationally prohibitive due to their immense resource demands. Conversely, contemporary advancements in continuum mechanics, notably exemplified by Phase Field (Miehe et al., 2010; Wang and Wong, 2025, 2026) and peridynamics (Sun and Fish, 2021; Sun et al., 2024) methods, have seen their integration into commercial software platforms. These methods are increasingly capable of efficiently solving fracture mechanics problems involving millions of degrees of freedom on standard personal computing systems. Furthermore, hybrid approaches, such as the Finite-Discrete Element Method (FDEM) (Liu and Wong, 2024), offer a compelling capability to simulate the entire continuum-to-discontinuum transition in 3D rock engineering scenarios Their real potential for PLT lies not simply in reproducing failure patterns, but in enabling systematic exploration of how contact geometry, heterogeneity, anisotropy, and scale jointly control the measured index. If developed carefully, irregular field specimens are scanned, reconstructed, simulated, and interpreted in near real time.

More broadly, future PLT research should not aim only to improve prediction of UCS. It should also clarify what PLT measures reliably, under what conditions, and with what uncertainty. This shift, from correlation seeking to interpretive robustness, is likely to be the most important step toward more defensible use of the PLT in modern geotechnical engineering.

5 CONCLUSIONS

This paper reviews the origin, evolution, standardization, interpretation, and future development of the PLT as an efficient indirect method for rock strength assessment. The historical progression is delineated into several key developmental stages: from the early “Russian method” to Broch & Franklin’s seminal systematization of experimental protocols, which ultimately culminated in the formal standardization of the PLT as a suggested method by the ISRM. Subsequent revisions to the ASTM standard further refined the test procedure and broadened its practical application.

Although international standards commonly cite ranges of the conversion factors, the literature consistently shows that the UCS–PLSI relationship varies with lithology, weathering, anisotropy, specimen geometry, and loading contact conditions. This variability is not a statistical inconvenience but a consequence of the mechanics of point loading. GEO (2017) put forward a correlation factor of 24 for isotropic igneous and volcanic rocks. Furthermore, a retrospective analysis of PLT research in Hong Kong reveals that empirically derived conversion factors between the point load strength index $I_{s(50)}$ and UCS are typically lower than this value.

Analytical models have clarified the role of tensile stress concentration, contact mechanics, and specimen geometry, yet they typically rely on ideal assumptions of elasticity, homogeneity, and regular geometry. Their main contribution is mechanistic interpretation rather than universally applicable strength conversion. Existing DEM and lattice-based simulations have provided useful insight into crack evolution and contact effects, but computational cost and model complexity have limited broader mechanistic and parametric exploration. Numerical investigations into the fundamental failure mechanisms remain disproportionately scarce compared to those dedicated to the BTS or the UCS. Newer fracture-capable numerical methods offer a promising path forward.

For Hong Kong and the GBA, progress will depend on the establishment of regional big-data repositories, combining PLT with complementary geological and geophysical descriptors, exploring the implementation of machine learning-driven predictive models, and the integration of 3D reconstruction for irregular specimens with high-fidelity numerical simulations.

ACKNOWLEDGEMENTS

The work is supported by the National Natural Science Foundation of China (Grant No. 42377149) and the Research Grants Council of Hong Kong (General Research Fund Project No. 17202423).

REFERENCES

ASTM D5731-16, 2016. *Test Method for Determination of the Point Load Strength Index of Rock and Application to Rock Strength Classifications*, American Society for Testing and Materials, West Conshohocken, PA, USA.

Basu, A. & Aydin, A. 2006. Predicting uniaxial compressive strength by point load test: significance of cone penetration. *Rock Mechanics and Rock Engineering*, 39(5): 483-490.

Broch, E. & Franklin, J. A. 1972. The point-load strength test. *International Journal of Rock Mechanics and Mining Sciences & Geomechanics Abstracts*, 9(6): 669-676.

Brook, N., 1985. The equivalent core diameter method of size and shape correction in point load testing, International *Journal of Rock Mechanics and Mining Sciences & Geomechanics abstracts*, 22(2): 61-70.

Chou, K.T. & Wong, R.H.C. 1996. Uniaxial compressive strength and point load strength. *International Journal of Rock Mechanics and Mining Sciences*, 33(2): 183-188.

Chau, K.T. 1998. Analytic solutions for diametral point load strength tests. *Journal of engineering mechanics*, 124(8): 875-883.

Chau, K.T. & Wei, X.X. 2001. A new analytic solution for the diametral point load strength test on finite solid circular cylinders. *International Journal of Solids and Structures*, 38(9): 1459-1481.

Gamon, T.I. 1984. The use of the point load test for the determination of strength of weathered rocks in Hong Kong. *Geological Society of Hong Kong Newsletter*, 2(4): 9-16.

GB/T 50266-2013, 2013. *Standard for test methods of engineering rock mass (in Chinese)*. Ministry of Housing and Urban-Rural Development of the PRC & General Administration of Quality Supervision, Inspection and Quarantine of the PRC. Beijing: China Architecture & Building Press.

GEO, 2017. *Guide to Rock and Soil Descriptions (Geoguide 3)*. Hong Kong: Geotechnical Engineering Office, Civil Engineering Department, Hong Kong Government.

Haeri, H., Sarfarazi, V., Shemirani, A. B. & Hosseini, S. S. 2017. Experimental and numerical investigation of the effect of sample shapes on point load index. *Geomechanics and Engineering*, 13(6): 1045-1055.

Hiramatsu, Y. & Oka, Y. 1966. Determination of the tensile strength of rock by a compression test of an irregular test piece. *International Journal of Rock Mechanics and Mining Sciences & Geomechanics Abstracts*, 3(2): 89-90.

ISRM, 1985. Suggested method for determining point load strength. *International Journal of Rock Mechanics and Mining Sciences & Geomechanics Abstracts*, 22(2): 51-60.

Li, Y.M. & Zhao, G.F. 2021. A numerical integrated approach for the estimation of the uniaxial compression strength of rock from point load tests. *International Journal of Rock Mechanics and Mining Sciences*, 148: 104939.

Liu, Z. & Wong, L. N. Y. 2024. A new thermomechanical coupled FDEM model for geomaterials considering continuum-discontinuum transitions. *Journal of Rock Mechanics and Geotechnical Engineering*, 16(11): 4654-4668.

Lumb, P. 1983. Engineering properties of fresh and decomposed igneous rocks from Hong Kong. *Engineering Geology*, 19(2): 81-94.

Masoumi, H., Roshan, H., Hedayat, A. & Hagan, P. C. 2018. Scale-size dependency of intact rock under point-load and indirect tensile Brazilian testing. *International Journal of Geomechanics*, 18(3): 04018006.

Miehe, C., Hofacker, M. & Welschinger, F. 2010. A phase field model for rate-independent crack propagation: Robust algorithmic implementation based on operator splits. *Computer Methods in Applied Mechanics and Engineering*, 199: 2765-2778.

Protodyakonov, M. M. 1960. New methods of determining mechanical properties of rock. *Proceedings of the international conference on strata control*, 187-195.

Reichmuth, D. R. 1967, . Point load testing of brittle materials to determine tensile strength and relative brittleness. *ARMA US Rock Mechanics/Geomechanics Symposium*, ARMA-67.

Ren, F., Liu, H., He, R., Li, G. & Liu, Y. 2018. Point load test of half-cylinder core using the numerical model and laboratory tests: size suggestion and correlation with cylinder core. *Advances in Civil Engineering*, 2018(1): 3870583.

Russell, A. R. & Wood, D. M. 2009. Point load tests and strength measurements for brittle spheres. *International Journal of Rock Mechanics and Mining Sciences*, 46(2): 272-280.

Serati, M., Alehossein, H. & Williams, D. J. 2014. 3D elastic solutions for laterally loaded discs: generalised Brazilian and point load tests. *Rock mechanics and rock engineering*, 47(4): 1087-1101.

Shi, Q., Ouyang, Z., Mishra, B. & Zhao, Y. 2023. A self-confined compression model of point load test and corresponding numerical and experimental validation. *Computers and Concrete*, 32(5): 465.

Sun, W. & Fish, J. 2021. Coupling of non-ordinary state-based peridynamics and finite element method for fracture propagation in saturated porous media. *International Journal for Numerical and Analytical Methods in Geomechanics*, 45(9): 1260-1281.

Sun, W., Wang, R. & Zhang, J.M. 2024. Coupled peridynamics modelling of liquefaction-induced shear strain localisation and delayed failure. *Géotechnique*, 74(13): 1815-1828.

Tham, L.G., Lee, P.K.K., Tsui, Y. & Chiu, C.K. 1999. Hardness, point load indices and strength of Hong Kong rocks (in Chinese). *Rock and Soil mechanics*, 20: 52–56.

Wang, Z., Ouyang, Y. & Yang, Q. 2024. Numerical simulation on effect of indenter radius during point load test. *Journal of Shanghai Jiaotong University (Science)*, 29(5): 909-918.

Wang, Z. & Wong, L. N. Y. 2025. A material point finite element method for thermo-hydro-mechanical modeling in poro-elastic media with brittle fracturing. *Journal of Rock Mechanics and Geotechnical Engineering*, 17(6): 3299-3315.

Wang, Z. & Wong, L. N. Y. 2026. Effects of rock cavern fires on the interaction behavior and thermal spalling fracturing of rock support system. *Tunnelling and Underground Space Technology*, 170: 107386.

Wei, X.X., Chau, K.T. & Wong, R.H.C., 1999. Analytic solution for axial point load strength test on solid circular Wei, X. X., Chau, K. T., & Wong, R. H. C. 2019. Theoretical and experimental validation of point load strength test for irregular lumps. *Journal of Engineering Mechanics*, 145(9): 04019065.

Wijk, G. 1978. Some new theoretical aspects of indirect measurements of the tensile strength of rocks. *International Journal of Rock Mechanics and Mining Sciences & Geomechanics Abstracts*, 15(4): 149-160.

Yin, J. H., Wong, R. H., Chau, K. T., Lai, D. T. & Zhao, G. S. 2017. Point load strength index of granitic irregular lumps: Size correction and correlation with uniaxial compressive strength. *Tunnelling and Underground Space Technology*, 70: 388-399.

Zhang, J., Wong, T. F. & Davis, D. M. 1990. Micromechanics of pressure-induced grain crushing in porous rocks. *Journal of Geophysical Research: Solid Earth*, 95(B1): 341-352.

Zhao, R., Tao, M., Cao, W., Du, K. & Zhu, J. 2023. Strength and failure characteristics of marble spheres subjected to paired point loads. *Journal of Rock Mechanics and Geotechnical Engineering*, 15(9): 2280-2290.

An Engineering Geological Model for Kaolin-rich Zones and Soil-Pipe Cavities in Volcanics

C.D. Shardlow & R.A. Evans
Ove Arup & Partners Hong Kong Limited
Ricky C.P. Wong, Mike W.H. Cho, Andrew W.C. Lee,
Civil Engineering Office, Civil Engineering and Development Department, of the HKSARG

ABSTRACT

During the project for Site Formation and Infrastructure Works for Public Housing Developments at Pok Fu Lam South, the major soil slope cutting works discovered two sub-parallel natural cavities up to 5m³ and 50m³. The cavities were found deep in altered saprolite and below large corestones of coarse-ash crystal Tuffs within the Repulse Bay Volcanic Group. Associated with these were multiple persistent kaolin-rich zones along relict sheeting joints, each up to 15cm thick. Remote 3D LiDAR scanning was used to show the detailed geometry of the cavities, and no evidence of recent man-made activity or recent groundwater flow was seen.

The cavities were backfilled by cement grout and additional ground investigation (GI) works were carried out to verify further the engineering implications to the geotechnical design model. This paper concludes the investigation, findings, and characterization for the local area, and provides recommendations and insights on the distribution of kaolin-rich zones and formation of soil pipe structures.

1 INTRODUCTION

1.1. Site Formation Project at Pok Fu Lam South

The Site Formation and Infrastructure Works for Public Housing Developments at Pok Fu Lam South (Contract No. CV/2020/01) includes the provision of approximately 7 ha. of housing development platforms and associated infrastructure on mostly disturbed steep terrains. The Kai Lung Wan South (KLWS) site shown in Figure 1 comprises a major 60m high cut slope, with a 35m upper soil portion of weathered saprolite with corestones reinforced by soil nails, and a 25m lower rock portion of extremely strong eutaxitic welded Tuff.

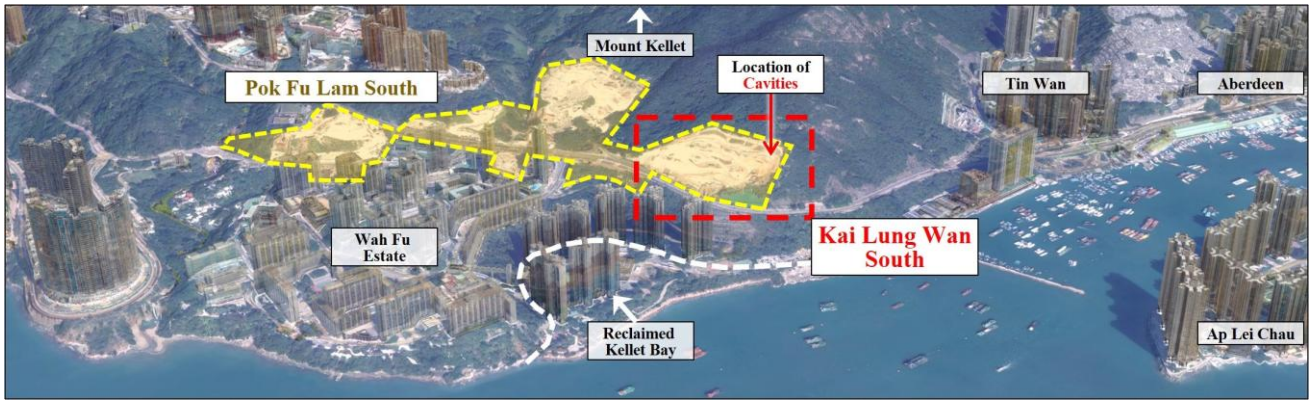

Figure 1: Site Formation Works at Pok Fu Lam South.

Given the complex ground and extreme groundwater conditions encountered at Kai Lung Wan South, the major slope cutting for site formation works involved the broad reprofiling of the slope with surface drains, extensive installation of approx. 1,400 nos. of soil nails to reinforce the 35m high soil cut portions, 350 nos. of

raking drains to relieve groundwater pressures, and nearly 100 groundwater monitoring instruments installed at different stages during the contract works from 2018 to 2025.

1.2. Discovery of Natural Cavities

Two cavities were discovered in December 2023 during the excavation for soil nail heads at the Kai Lung Wan South area shown in Figure 1. Both cavities were tabular and sub-parallel, up to 5m³ and 50m³, and found beneath moderately decomposed (Grade III) corestones in highly decomposed (Grade IV) saprolite of dacitic coarse-ash crystal TUFF. As shown in Figure 2, multiple persistent and sub-parallel kaolin-rich seams (≈10 to 15 cm) were exposed with no signs of recent inflow or seepage evident inside the cavities. The internal geometry shown in Figure 3 was measured remotely using 3D LiDAR scanning to determine the approx. volume and apparent dip/dip direction (14°/140° and 21°/165°). The orientation was consistent with the local outcrops of relict sheeting joints and rock joints, dipping south-south-east as shown in Figure 4. After the liaison with GEO, the cavities were subsequently backfilled with cement grout, and additional GI works and Category II Geotechnical Supervision were implemented to verify and assess the extent of any potential changes to the geotechnical design model and propose further stabilisation measures as necessary.

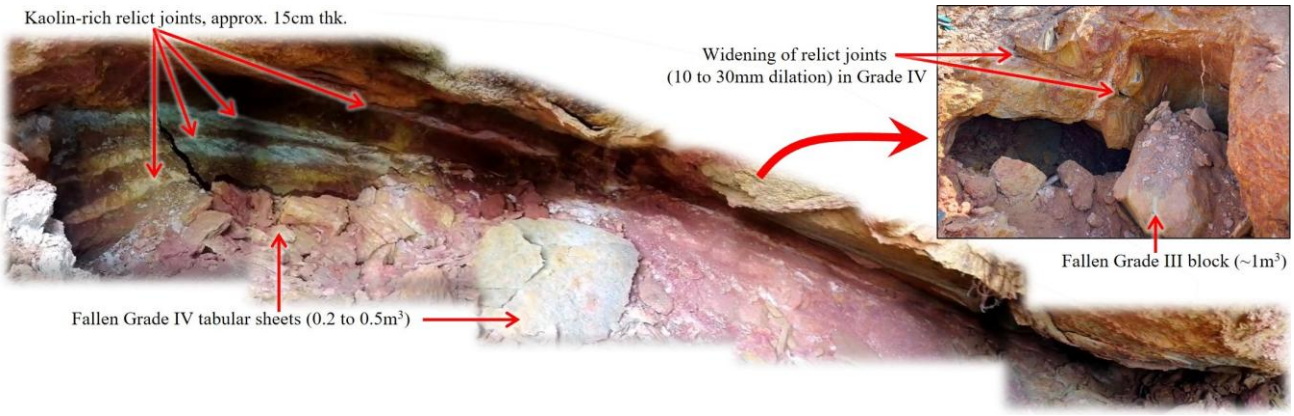

Figure 2: View Inside the Main Cavity with Kaolin-Rich Relict Joints (Inset: Cavity Opening with Grade III Blocks).

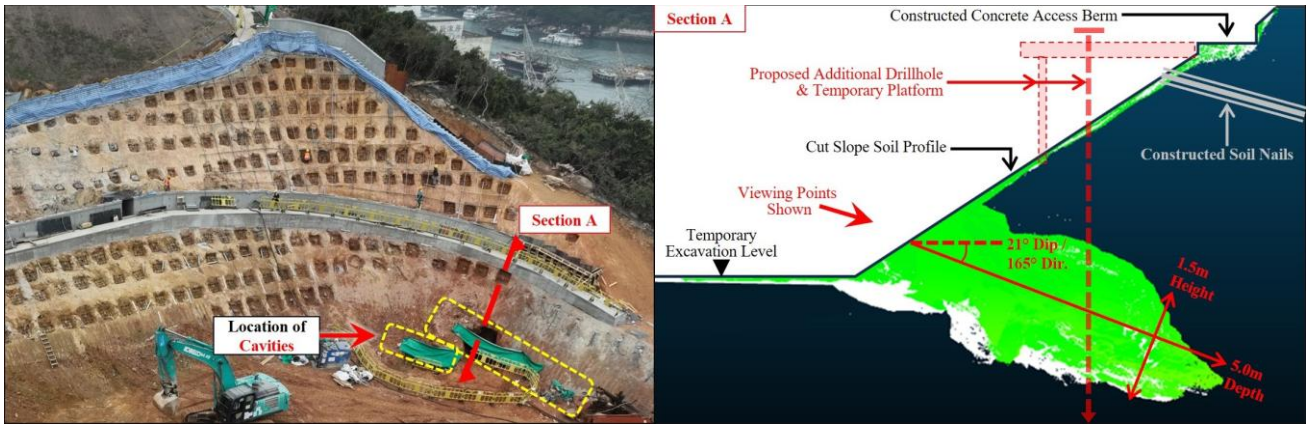

Figure 3: Views of the Cavities (Left: External Location, Right: Section A Generated from Internal LiDAR Scan).

Figure 4: Views of Large Grade II Corestones in Saprolite during Site Formation and Excavation Works.

2 VERIFICATION OF THE GROUND MODEL

2.1. Background of Kaolin and Soil Pipes

Studies by the Geotechnical Engineering Office (GEO) have identified that both kaolin infills and thick kaolin-rich zones are significant factors in slope stability. Kaolin is an aluminum silicate white clay formed by the chemical disintegration of k-feldspar minerals, where the platy mineral structure is susceptible to hydration, plastic anisotropy and weak shear strengths (φ_p' = 19° - 31°, φ_r' = >12°) (GEO, 2002a). In hydrothermal mineral systems, kaolin alteration may occur in saturated volcanics that overlie calc-alkaline intrusions such as Quartz Monzonite porphyries (Corbett, 2009). The correlation of many major landslide and mineral alteration localities adjacent to intrusions of Quartz Monzonite is shown in Figure 5. These intrusions are often associated with deeply weathered faults and buried valley terrains at the present day. In contrast, near-surface weathering of saprolite may also form kaolin at higher elevations, as discussed in Section 2.4.

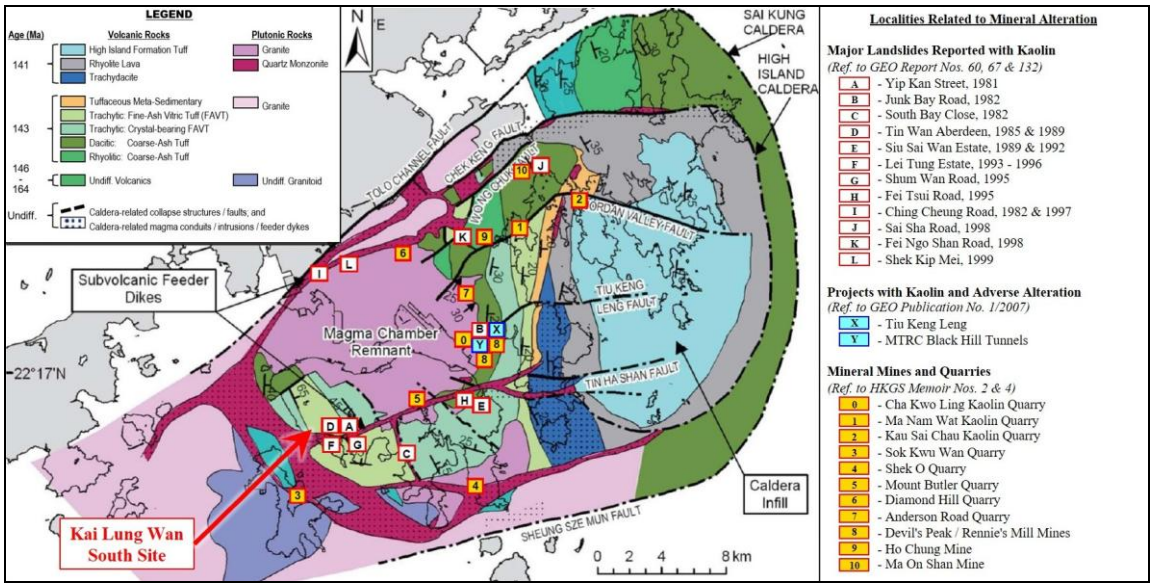

Figure 5: Distribution of Major Landslides and Alteration (Left: after Sewell, Tang & Campbell, 2012, Right: Localities).

Many case studies of landslides with adverse kaolin features also identified localised soil pipe networks as well, such as the complex landslides at Ching Cheung Road of 1954 and 1997. The reactivated 1997 landslide was attributed to an increased groundwater head due to the collapse or blockage of soil pipes below a

topographic depression at the slope crest (GEO, 2007). The combination of findings support that kaolin-rich zones may enable both soil pipe erosion (eluviation) and the transportation of clayey infills (illuviation).

The distribution and influence of relict discontinuities on groundwater flow in soils are challenging to represent during early preliminary design models, yet these may direct the local flow paths along relict features in soils or the build-up of cleft water pressures at permeable discontinuities in rock (GEO, 2002b). Such features may further dynamically evolve over time, forming soil pipes by preferentially eroding and removing weaker materials, transporting sediments, and potentially choking or damming with infill deposits that redirects seepage (Hencher, 2000).

For kaolin-rich zones, TGN No. 4 (GEO, 2004) notes "During the initial phase of ground investigation, emphasis should be directed to developing a representative geological and hydrogeological model rather than testing.". This is similarly stated for relict joints (GEO, 2002b), and is applied herein for assessing soil pipe cavities as well, to provide meaningful context and verification of the design model during construction.

2.2. Applied Engineering Geology

The available GI records, desk study findings and design model assumptions were revisited for the new site-specific context, and the major geological factors affecting the local weathering history were identified as:

- The site is underlain by the Ap Lei Chau Formation, but includes occasional Mount Davis Formation and mudstones, with north-east trending geological boundaries and fold-axis (incl. eutaxitic fabrics);
- A single stress-relief joint set is extremely persistent across all rock types as relict or sheeting joints;
- The steep topography is bounded by eroded intrusions (presently offshore) of Tei Tong Tsui Quartz Monzonite, comprising margins of latite cooling outwards to minor rhyolitic or basaltic dykes locally;
- The dacitic coarse-grained rock types have very widely-spaced joints that favour partial weathering into reddish orange saprolite with large corestones or boulders; and
- The trachyte to rhyolitic and tuffaceous fine-grained rock types have frequent very closely-spaced joints that favour faster mass weathering into lighter greyish soils, that may channel valley erosion and re-direct groundwater flow over time.

The conceptual ground model using Aerial Photograph Interpretation (API) was refined using site-specific insights during construction. Shown in Figure 6, the surface boulder fields are associated with the corestone forming coarse-ash crystal tuff, and major topographic depressions are associated with photolineament boundaries and tuffites (tuffaceous siltstone). The coarse tuffs are eutaxitic and extremely strong with typical Point Load Strength Index ($I_{s(50)}$) values of 10 MPa to 20 MPa. The orientation of extremely persistent relict joint sets consistent with the cavities (~20°/150°) were also reviewed against field mapping and acoustic borehole televiewer surveys. A projection plane of the key sheeting joint set is shown in Figure 6b daylighting at a historic pre-1964 landslide scar identified by API. The basal slip surface of the scar was noted in the Stage 3 Study Report of the feature, and was reprofiled with extensive stabilization measures completed in 2000.

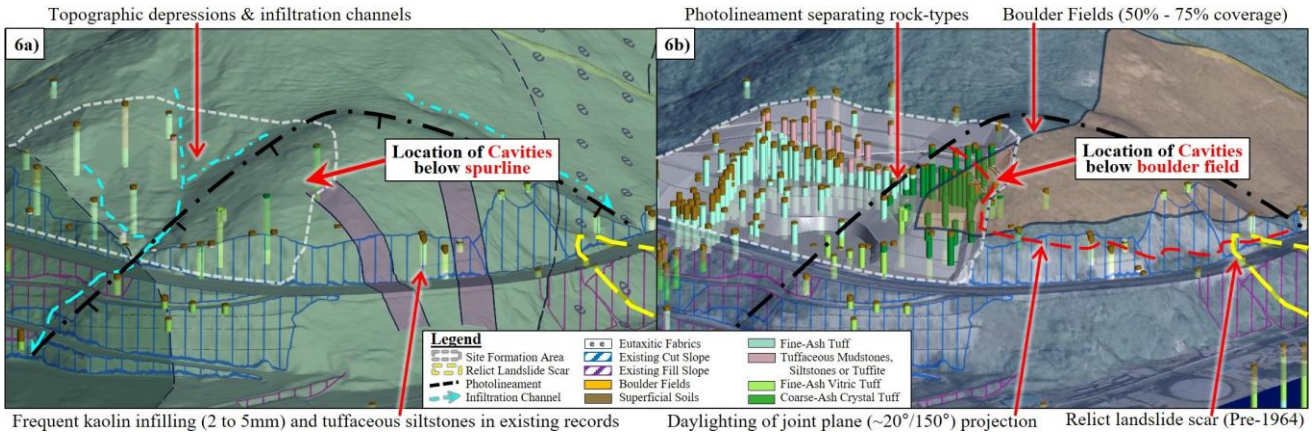

Figure 6: Surface Features Identified by Desk Study (left), and Sub-Surface Geology Found by GI (right).

2.3. Enhanced Ground Investigation

To verify the design and differentiate any artificially induced core-loss (by wash-boring or water-flushing drillhole methods) from low recovery at soil pipe cavities, 4 nos. of additional drillholes were carried out near the cavities (within 0-15m) and 4 nos. broadly across site at other zones with low recovery. The targeted GI included triple-tube coring with air-foam flushing, continuous mazier sampling, and permeability tests at major weathered joints with core-loss. For nearly all cases, these successfully recovered quality mazier samples of kaolin-rich soils and soil pipe infill deposit. 4 nos. of mazier samples were used for triaxial compression tests and direct shear box tests, and 14 nos. were split for inspection.

In practice, the constant or falling head, and packer permeability tests carried out were only indicative of the soil permeability, as outflow was often observed from the raking drains installed nearby. Permeability tests are still recommended for any insights on direction of flow and effectiveness of the in-situ drainage. At suspected soil pipes, downhole CCTV cameras were deployed for inspection and automatic vibrating-wire piezometers were installed for continuous groundwater monitoring.

The Figures 7 and 8 help to compare the coarse-grained saprolite and fine-grained soils. Thin (<3mm) mottled light grey alteration halos or kaolin infills (often limonite-stained yellowish orange) were found in both soil types, but thick (50-200mm) kaolin-rich zones were only found in coarse-grained saprolite. Large lateral soil pipes (100-250mm thick) associated with relict joints were only found in mazier samples of coarse-grained saprolite, typically with poorly-graded and normally-sorted fine SAND to angular quartz GRAVEL infill (Figures 7c and 7e). In contrast, small vertical soil pipes (40-50mm dia.) were only found in mazier samples of weakly cemented fine-grained soils and near to major topographic drainage channels, with infill deposits typically well-graded with reverse-sorting of fine to coarse SAND to clayey SILT. These fine-grained soils included completely decomposed (Grade V) to Grade IV light grey silty fine-ash TUFF (Figures 8a to 8c) and soft to firm light brown clayey SILTS with occasional black clasts of very friable tuffaceous mudstone, derived from the weathering of a tuffaceous TUFFITE layer (Figures 8d to 8f).

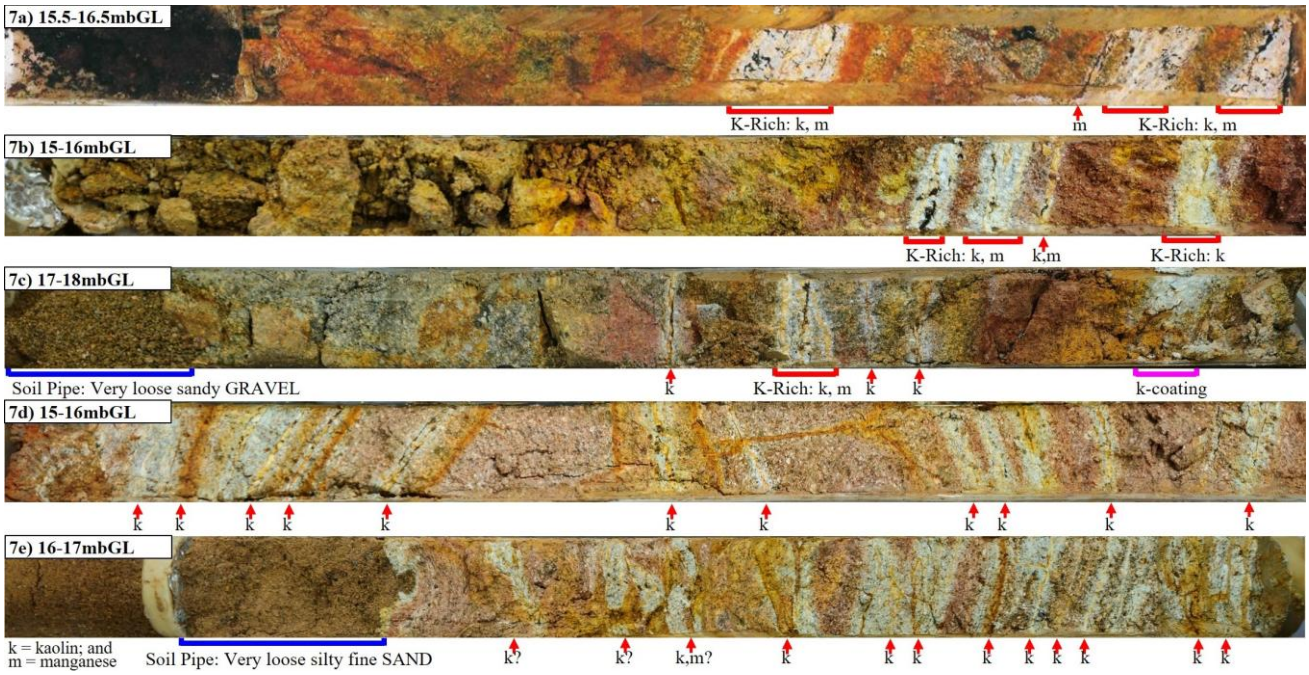

Figure 7: Split Mazier Samples of Kaolin Features and Soil Pipes in Saprolite of Coarse-Ash Crystal TUFF.

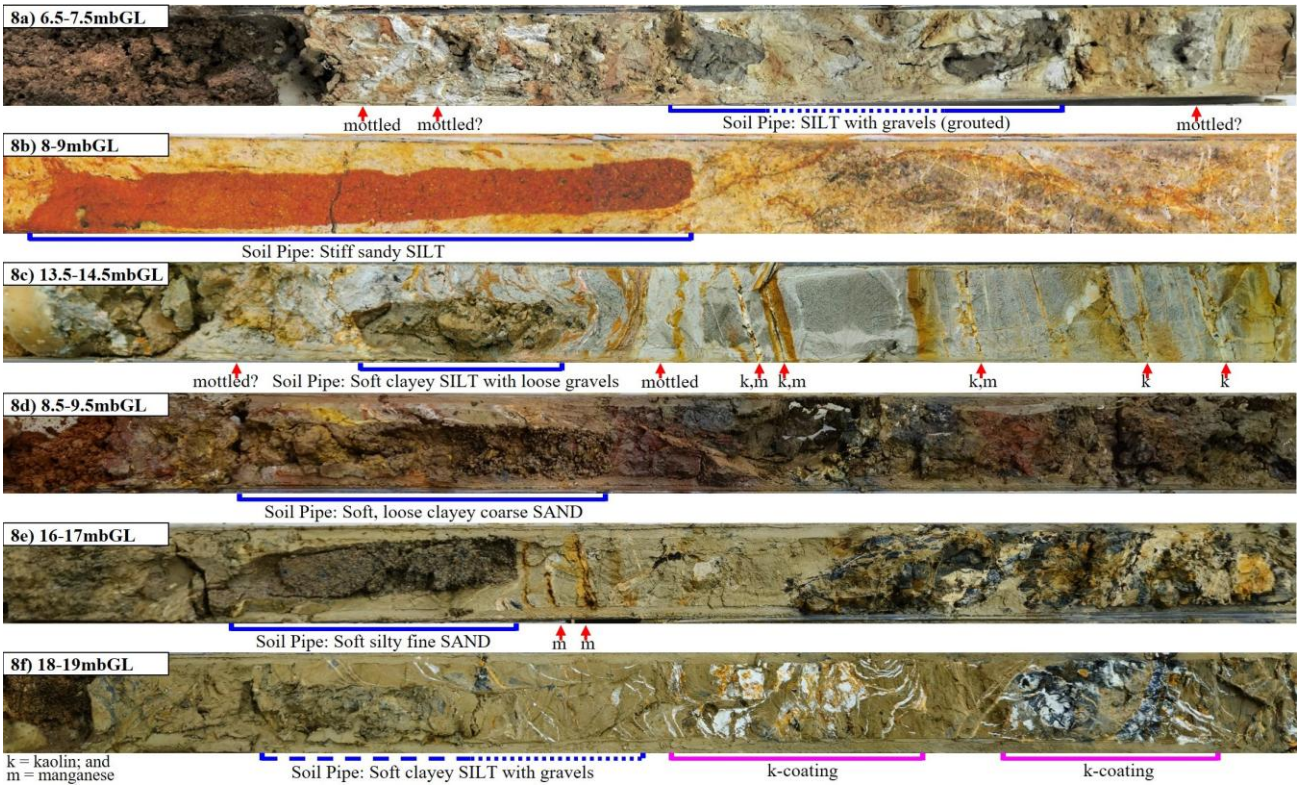

Figure 8: Split Mazier Samples of Kaolin Features and Soil Pipes in weathered Fine-Ash TUFF and tuffaceous SILTS.

2.4. Field Verification of Features

Engineering geological field mapping and discontinuity surveys of all cut slopes during construction were used to iteratively validate the working geotechnical model or specify further numerical stability assessments.

A broad web of kaolin-rich zones was exposed in the Figure 9 (photo taken after a rainstorm) showing extremely persistent (5-75m) sub-parallel relict sheeting joints, mottled white clayey SILT (often 150-250mm) in yellowish orange and brownish red saprolite (Grade IV/V) of coarse-ash crystal tuff with corestones. The yellowish orange and brownish red colours indicate oxidation of iron and aluminum in an unsaturated near-surface saprolite. However, when saturated, oxygen reduction instead locally leaches metal-oxides to form kaolin with manganese that leaves a mottled grey alteration halo, indicating the local saturation extent of seasonally high groundwater percolation in a normally unsaturated saprolite (GEO, 1996). Lateral kaolin-rich zones were abundant in the lower-half of the PW 30/50 profile, corelating with a typical Groundwater Level (GWL) measured from rockhead. They were less frequent in the upper-half of the PW 30/50 profile, which only reached the highest measured GWL rise during extreme or intense rainfall events. As no relict features are preserved close to ground level, none were found in Residual Soils or the immediate Grade V soils.

Fresh exposures were only evident in the coarse-grained saprolite during field mapping, shown in Figure 9. The potential variability of these weathered features across depth and distance is shown in Figure 10, and is consistent with the inspected split mazier samples shown in Figure 7, and characterized by:

- Firm to stiff, mottled grey to white sericite alteration halos of clayey to sandy SILTS (<250mm) hosting nodules or coatings of manganese (1-10mm) with lenses or stringers of kaolin clay (1-10mm);
- Secondary yellowish orange limonite-staining of cohesive kaolin clay is more likely than the surrounding silts, identifying continued seepage at the original discontinuity that is now infilled;
- Below the GWL, areas of higher hydraulic gradients are associated with increased eluviation (depletion of fine clays or cementation), leaving residual brown sandy matrixes. Later infilling may still occur;
- Slickensided or sheared lenses were typically less than 0.5m from impermeable rockhead or Grade III corestones, likely due perched groundwater flow and excess porewater pressures;
- Soil pipe infill deposits were loose, light brown, fine SANDS to GRAVELS of angular quartz; and
- The PW 50/90 zone is mostly missing on sloping rockhead as the hydraulic gradients may be higher.

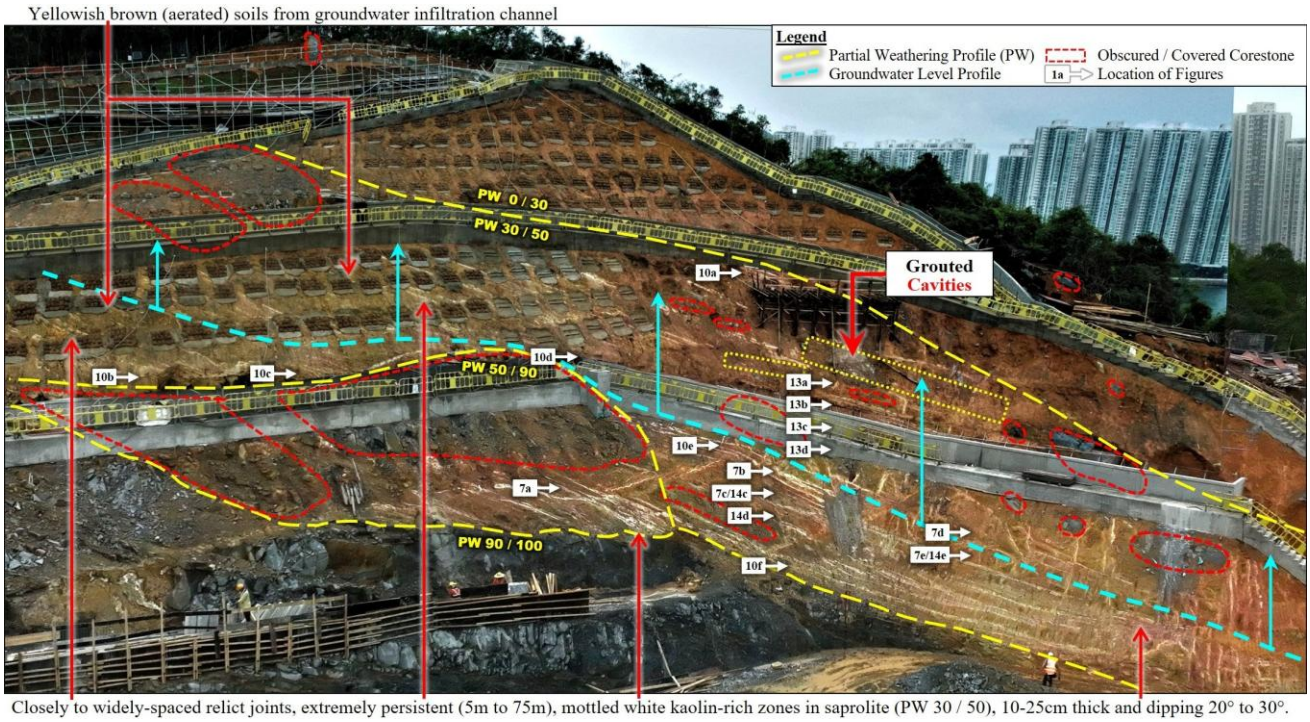

Figure 9: Zonal Weathering of Numerous Kaolin-Rich Relict Sheeting Joints in Saprolite with Removed Corestones.

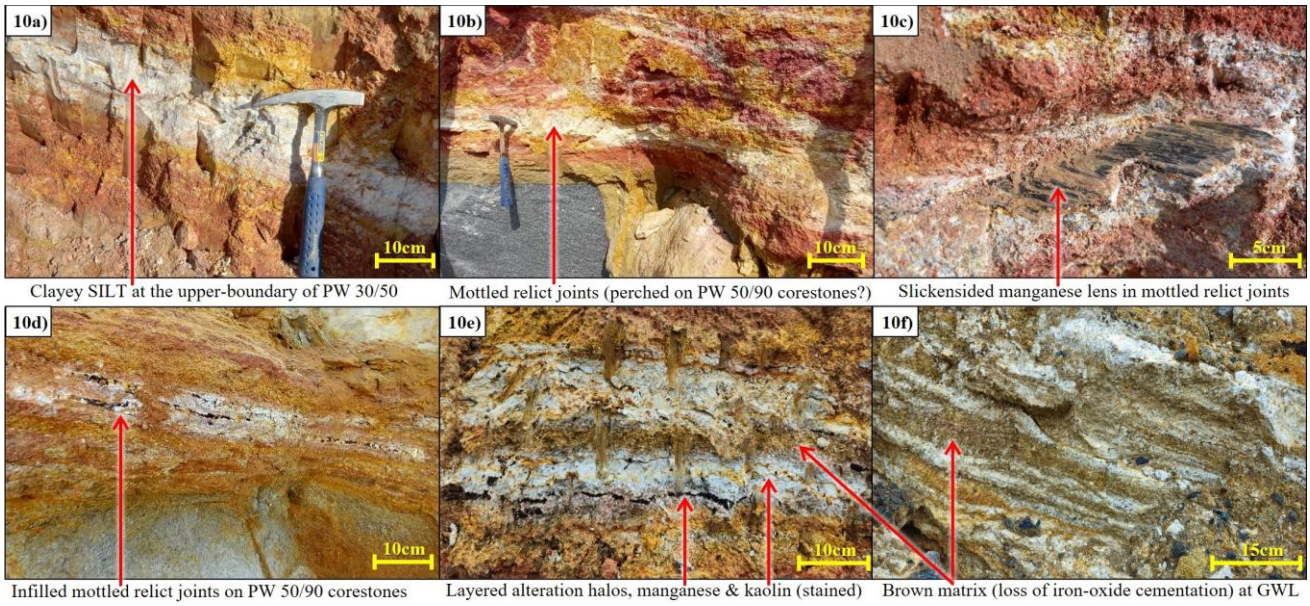

Figure 10: Fresh Exposures of Kaolin-Rich Features in Weathered Saprolite of Coarse-Ash Crystal TUFF.

Thick kaolin-rich zones were not found in the fine-ash tuff or tuffite. This is generally attributed to the lack of preservation in thin near-surface soil profiles on open hillslopes, as fine-grained and closely jointed masses naturally prefer mass weathering (and mass erosion) instead of partial weathering (supported by corestones). However, where the weathering profile is deeply channelised, such as at large topographic depressions, the mass erosion may instead be constrained leading to accumulation of poorly cemented weathered soils. In these topographic depressions, soil pipe eluviation and kaolin coatings in fine-grained soils are more common.

2.5. Laboratory Shear Strength Testing

Mazier samples closest to the cavities were inspected after removing the mazier casings to specify 4 nos. of single-stage and multi-stage consolidated undrained (CUS/CUM) triaxial compression tests with 6 nos. of small-sized (20mm) direct shear box (DSB) tests. The DSB testing found inclusions of manganese nodules (Figure 12c), and the DSB results indicated early max. shear stresses and contraction consistent with medium dense sandy SILTS, a relatively high effective cohesion (c'=5kPa), and friction angle (ϕ'=45°). The CUS/CUM testing indicated a lower effective cohesion (c'=3kPa) and friction angle (ϕ'=33°) that were consistent with the lower-bound of Grade V Tuffs in the KLWS site. A plot of the results is shown in Figure 11 which combines the normal and effective shear stresses for ease, and comparisons are plotted from the historical Stage 3 Study Report of a nearby downhill slope (existing Feature No. 11SW-C/C5) and from the back-analysis of major landslides in the district at Tin Wan Hill, Aberdeen and Shum Wan Road, Wong Chuk Hang where kaolin infilling was a major contributing factor in fine-ash tuffs.

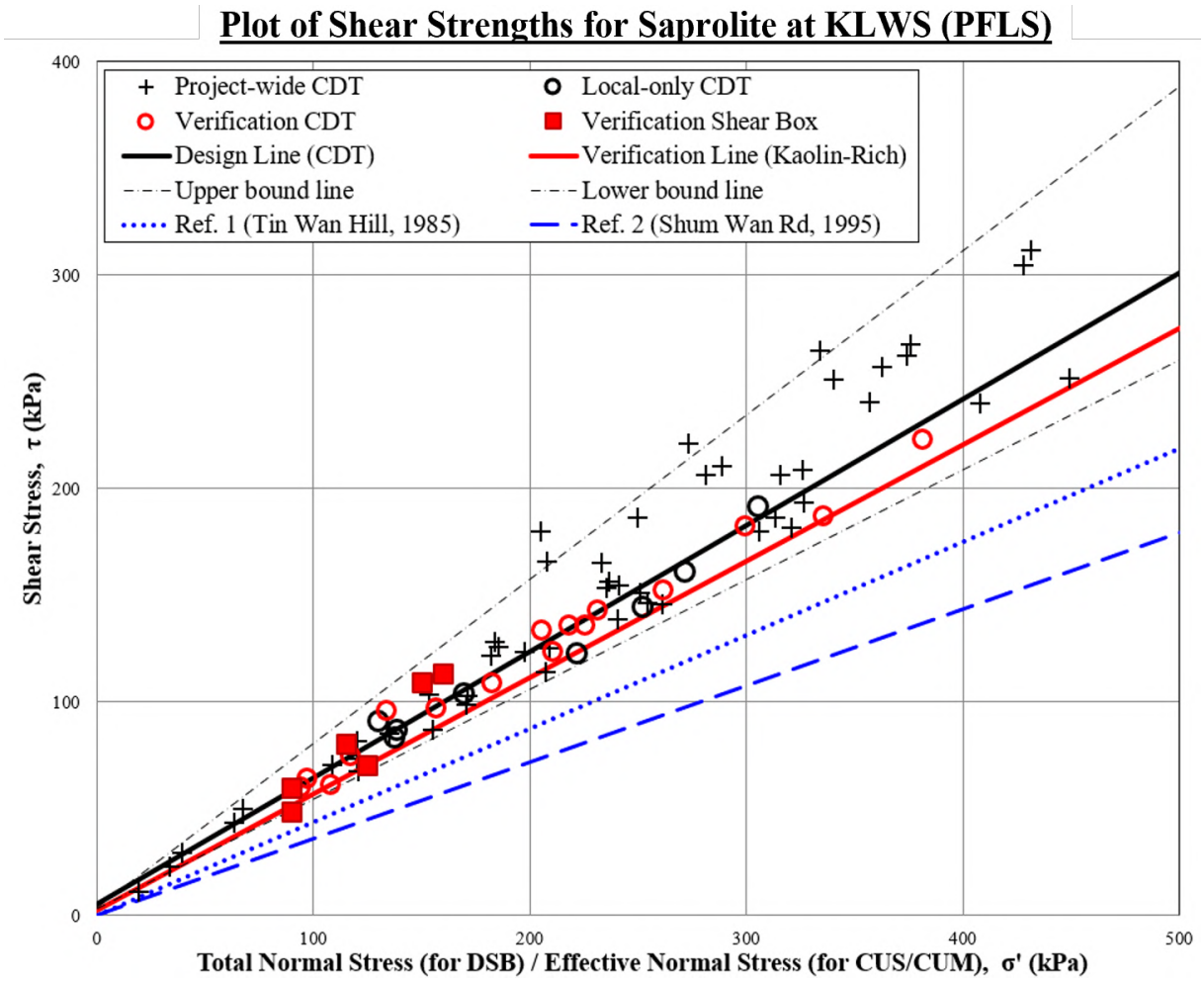

Figure 11: Review of Shear Strengths for Kaolin-Rich CDT During Verification Works.

The coarse-ash crystal tuff saprolite shown in Figure 12 is on average fine-grained sandy SILT with minor clays or gravels (3% clay, 72% silt, 23% sand and 2% gravel), with a Liquid Limit of 49%, Plastic Limit of 28%, Plasticity Index of 21% to Non-Plastic, and porosity of 32%.

Overall, kaolin-rich zones in altered relict joints of coarse-ash crystal tuff are in-line with the intergranular shear strengths of confined medium dense sandy SILTS and the mature unconfined soil pipe deposits of loose fine SAND to GRAVEL of angular quartz. Discretion is still recommended where any transient groundwater flow or soil pipe end-points are suspected of significant clayey solutes infilling adversely orientated features.

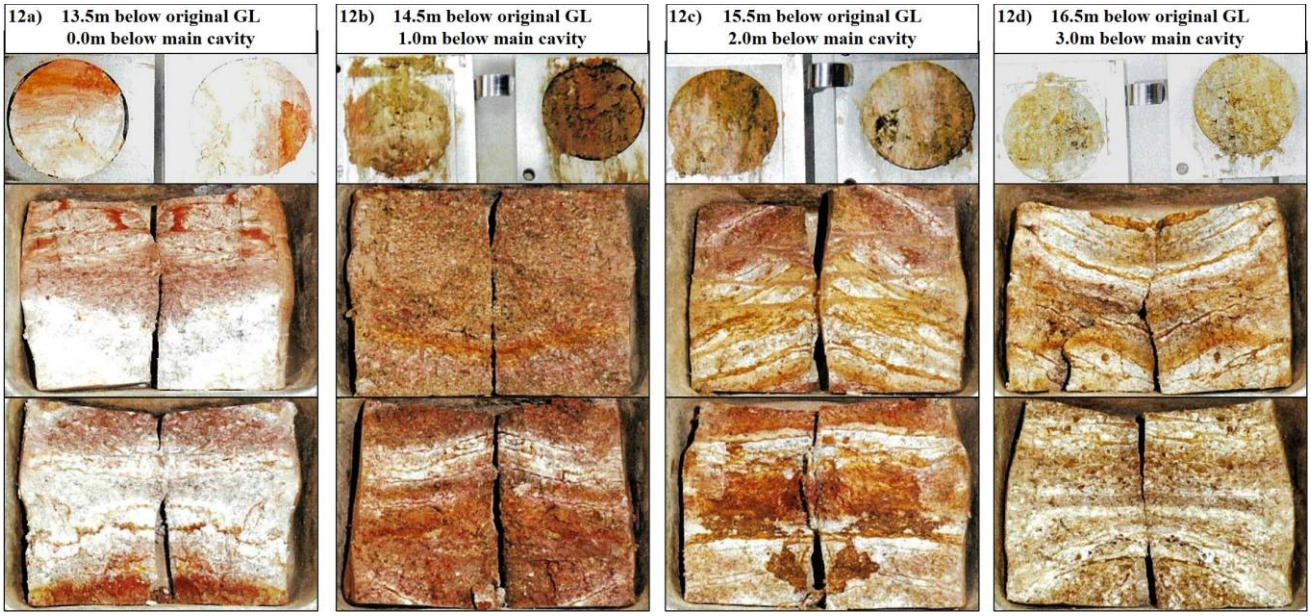

Figure 12: Samples of Kaolin-Rich CDT after Direct Shear Box Testing (top) and Triaxial Testing.

Table 1: Summary of Soil Strength Parameters with Typical Field Classifications.

Soil Type or Kaolin Related Feature	Bulk Density, γ'	Effective Cohesion, c'	Friction Angle, ϕ'
Highly Decomposed Tuff (HDT) (1) Mass weathered (equivalent to PW 0/30), closely jointed fine-grained silty Tuffs.	19 kN/m³	**B: 10 kPa**	**B: 38 °**
Completely Decomposed Tuff (CDT) (1) Mass weathered (equivalent to PW 0/30), with sporadic and non-persistent white or limonite-stained 1-3mm thick kaolin veinlets, typically without coatings of manganese or shearing fabrics in relict-joints. Often closely jointed fine-grained silty Tuffs	19 kN/m³	U: 6 kPa	U: 50 °
		B: 5 kPa	**B: 36 °**
		L: 3 kPa	L: 31 °
Kaolin-Rich CDT/HDT (1)(2)(3) For zonal use (typically PW 30/50) in complex kaolin-rich altered saprolite of coarse-grained Tuffs. E.g., with frequent widely-spaced and extremely persistent kaolin-rich relict joints, with 10-25cm mottled white halos to brown, clayey SILT to SAND, with clasts or lenses of white to yellowish limonite-stained kaolin clay, and black manganese nodules.	18 kN/m³	U: 5 kPa (2)	U: 45 ° (2)
		U: 3 kPa (3)	U: 37 ° (3)
		L: 0 kPa (3)	L: 35 ° (3)
		L: 3 kPa (1)	**L: 33 ° (1)**
Kaolin-Infilled Features (4)(5) For specific use at identified kaolin clayey features. E.g. infilled or coated adverse rock joints or relict joints, slickensided or soapy-smooth kaolin clay (white or limonite-stained).	-	L: 0 kPa (4)	L: 26 ° (4)
		B: 0 kPa (5)	**L: 21 °** (5)

Notes:
(U) Upper-Bound Limit; (B) Best-Fit Line; (L) Lower-Bound Limit; (1) Project-specific Undrained Triaxial Tests of HDT or CDT saprolite; (2) Project-specific Direct Shear Box tests of CDT saprolite; (3) Direct Shear Box tests of the nearby feature 11SW-C/C 5 (Stage 3 Study Report S3R233-97); (4) Back-analysis of the nearby Tin Wan Hill, Aberdeen landslide (GEO Report No. 132, 2002); (5) Direct Shear Box tests of the nearby Shum Wan Road, Wong Chuk Hang (GEO Report No. 132, 2002).

2.6. Monitoring and Design Verification

The Kai Lung Wan South site installed nearly 100 nos. of GWL monitoring instruments since late-2018 as the site works progressed, including standpipes with Halcrow buckets or automatic vibrating-wire piezometers (VWP). VWPs provide excellent remote data logging at 5-min. intervals and automated notification of water levels reaching a defined trigger level. During the 7th – 8th September 2023 extreme rainstorm events (with a 1,000yr return period), the recorded GWLs in the saprolite of coarse-ash crystal tuff measured a rapid piezometric GWL rise of up to 6m which fully dissipated within approx. 24hrs. A typical GWL between 2m above impermeable rockhead and 1/3rd of soil height is shown in Figure 9, where a further 6m rise during extreme rainfall correlates with the upper PW 30 / 50 profile. In contrast during the same extreme rainfall in 2023, the recorded GWL below the central topographic channel of fine-grained weathered soils recorded a piezometric GWL rise of 18m which required 8-10 weeks to return to the measured long-term average. During later intense rainfalls in 2024, the GWL response was reduced to an 11m rise which mostly dissipated in 1 week and returned to the long-term average after a further 2-3 weeks. Despite the very frequent intense rainstorms during 2025, the recorded GWL response was limited to a 4m rise which fully dissipated in 1-2 weeks. The significant improvements reflect the on-going site formation works advancing each year from

2023 to 2025. The initially high piezometric head of the topographic channel is likely a driving factor in the original development of soil pipes, as seen at each project stage summarized below:

- Topographic depressions directing surface water infiltration were identified by API (Figure 6a);
- Preferential weathering along more permeable geological boundaries assumed by broad GI (Figure 6b);
- Deep flow paths in small vertical soil pipes (at up to 19m depth) sampled by GI (Figures 8d to 8f); and
- Converging large lateral soil pipes (7m deeper) at the weathered base, where groundwater may perch on impermeable rockhead and induce basal shearing, exposed during the slope cutting (Figure 13).

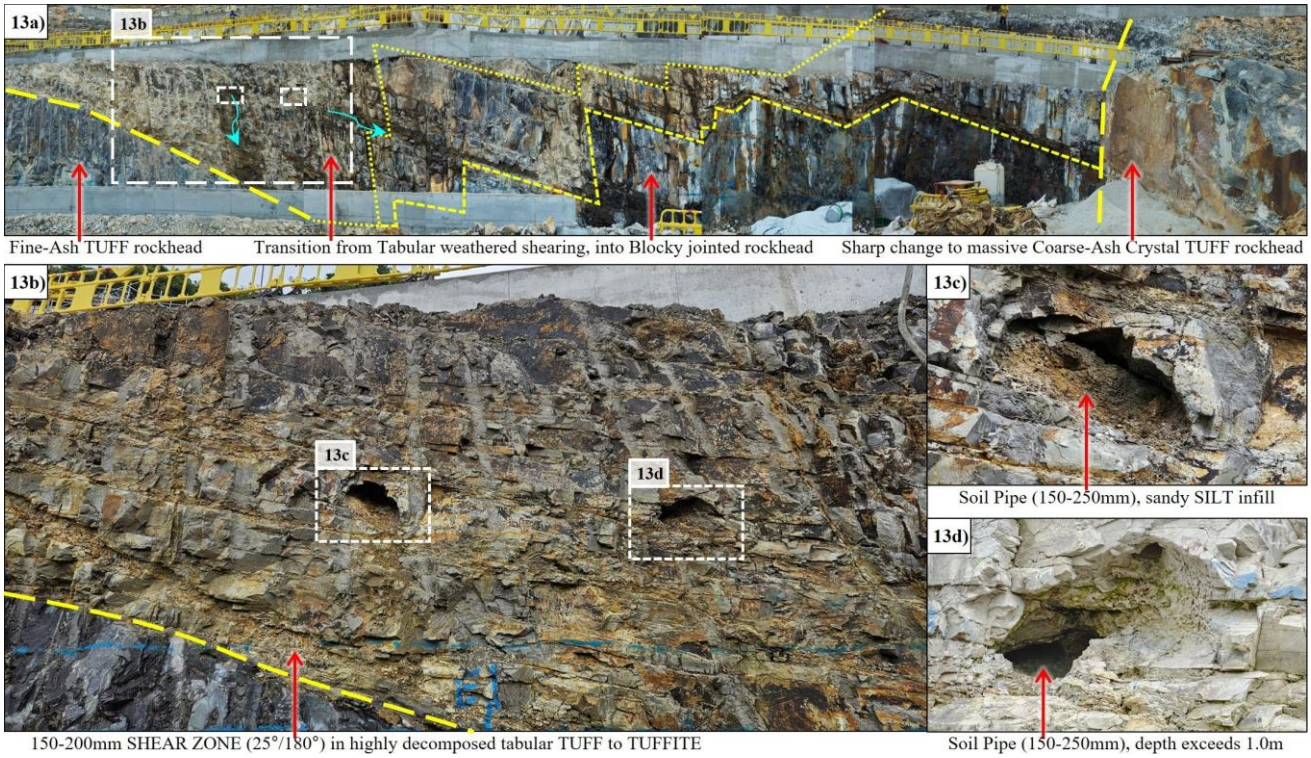

Figure 13: Cut Face Exposing Soil Pipes in Weathered TUFF to TUFFITE Overlying Rockhead.

The design verification review incorporated the field mapping of kaolin-rich CDT and all adversely kaolin infilled features, revised soil parameters, revised rainfall intensities and the highest measured GWLs for both the extreme rainfall events and standard cases. The frequency and lengths of soil nails and raking drains increased up to 24m and 20m length respectively, and the surface channel sizes of the feature were increased.

3 RECOMMENDATIONS

3.1. Engineering Geological Model

Schematic models of the geological and hydrogeological characteristics in the broader area are shown in Figures 14a and 14b. These aim to provide contextual understanding of the initial kaolin-rich alteration found deep within the partially weathered saprolite hosting corestones, and derive the key stages of soil pipe development associated with the cavities found below large corestones.

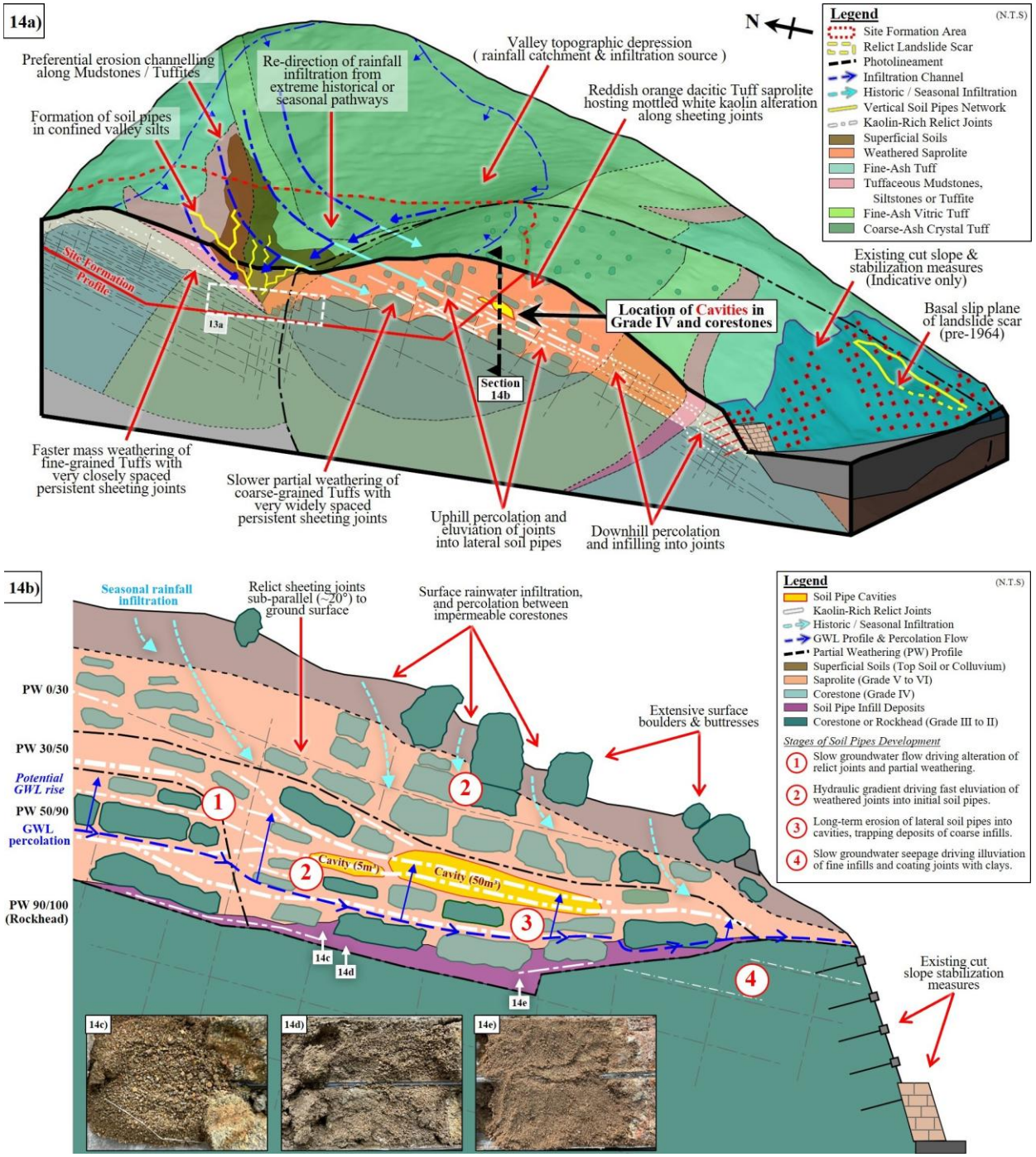

Figure 14: Schematic Models Showing the Development of Kaolin-Rich Zones and Soil Pipes in Volcanics.

3.2. Implications During Design and Construction

The recommendations of TGN No. 4 (GEO, 2004) proved to be fundamentally sound during the major geotechnical verification of kaolin-rich zones. Given the significance of soil pipe cavities also found at KLWS site, further apparent factors are provided in Table 2.

All soil nail drilling and grouting records were reviewed to ensure their constructability and performance. The actual grout in-take was not excessive compared to the theoretical volumes expected and within acceptable limits. However, it is still beneficial to review with consideration to the working geological model, as soil nail clusters of re-drilled drillholes and higher grout in-take were typically found below the major topographic drainage channels, such as the area associated with yellowish brown soils shown in Figure 9.

Table 2: Summary of Key Factors for Kaolin-Rich Zones and Soil Pipes (Further to TGN No. 4 (GEO, 2004)).

	Recommended Factors for Adverse Geological (G), Hydrogeological (H), and Anthropogenic (A) Features	G	H	A
Desk Study	The different nature of jointing and weathering in coarse-grained lithologies from fine-grained lithologies.	✓		
	Presence of spurlines capped with coarse-ash crystal tuff, large corestones, or dense boulder fields	✓		
	The history of any obscured topographic infiltration channels, geological boundaries and instabilities.		✓	✓
Ground Investigation	Thick Grade IV saprolites (particularly in reddish coarse saprolite) with corestones or steep hydraulic gradients.	✓	✓	
	Large lateral soil pipes with loose granular infills may be misrepresented as low recovery zones below corestones.			✓
	Permeability testing of the above and any thick zones of mottled white silt or clay in reddish coarse saprolite.		✓	
	The orientation of persistent joints intercepting key sources of groundwater infiltration, percolation, or seepage.	✓	✓	
	Revisit zones of low recovery or gaps aligning with the above joints that may be conducive to soil pipe eluviation.		✓	
	Presence and nature of in-situ altered silts or sands, manganese nodules, and stained clays, vs. illuviation or infill.	✓		
	Small vertical soil pipes underlying weathered topographic depressions may be missed by vertical drillholes.			✓
	Splitting and logging of continuous mazier samples. For sensitive soils or infills, air-foam flushing is preferred.	✓		✓
Design & Review	Groundwater risks associated with upslope eluviation (e.g. mottled white sheeting joints in coarse saprolite and corestones) may differ to those associated with downslope illuviation (e.g. mobilised clayey infilling and coating).		✓	
	Stability during extreme rainfall events (e.g., 1:1,000yrs) and updated rainfall intensities should be reviewed.		✓	
	Presence of deeply weathered valleys or channels, soil pipe infill deposits, or adverse grouting works that may block seepage or build-up high groundwater pressure heads. The effect of any historical channels is also relevant.	✓		✓
	Corrosion protection measures of reinforcement and concrete is likely where soil alteration (leaching) is apparent.		✓	✓
	Iterative field mapping of the above by Engineering Geologists is required for refined numerical design models.	✓	✓	✓
Construction	Presence or clusters of anomalies in drilling / grouting records of soil nails / raking drains should be reviewed.			✓
	Subsurface drainage (e.g. Type 3 raking drains) is likely for relieving obstructed seepage and GW pressure heads.		✓	✓
	Category II supervision of the GI and geotechnical works is recommended for sensitive cases.	✓	✓	✓

ACKNOWLEDGEMENTS

This paper is published with the permission of the Head of the Civil Engineering Office and the Director of the Civil Engineering and Development Department of the Hong Kong Special Administrative Region, and with special thanks to China Harbour – China Geo Joint Venture.

REFERENCES

GEO. 1986. *Geology of Hong Kong Island and Kowloon (HKGS Memoir No. 2)*. Geotechnical Control Office, CEDD of HKSAR Government.

GEO. 1996. *Mineralogy and Fabric Characterization of Weathered Granitic Rocks in Hong Kong (GEO Report 41)*. Geotechnical Engineering Office, CEDD of HKSAR Government.

GEO. 1998. *Assessment of Geological Features Related to Recent Landslides in Volcanic Rocks of Hong Kong Phase 2A – Chai Wan Study Area (GEO Report 60).* Geotechnical Engineering Office, CEDD of HKSAR Government.

GEO. 1999. *Assessment of Geological Features Related to Recent Landslides in Volcanic Rocks of Hong Kong Phase 2B – Aberdeen Study Area (GEO Report 67).* Geotechnical Engineering Office, CEDD of HKSAR Government.

Hencher, S. 2000. *Engineering Geological Aspects of Landslides. Proceedings of the Conference on Engineering Geology*. Institution of Mining and Metallurgy, Hong Kong Branch, pp 93-115.

GEO. 2002a. *Report on the Investigation of Kaolin-rich Zones in Weathered Rocks in Hong Kong (GEO Report 132).* Geotechnical Engineering Office, CEDD of HKSAR Government.

GEO. 2002b. *Enhancing the Reliability and Robustness of Engineered Slopes (GEO Report 139)*. Geotechnical Engineering Office, CEDD of HKSAR Government.

GEO. 2004. *Guidelines on Recognition of Geological Features Hosting, and Associated with, Silt- and Clay-rich Layers Affecting the Stability of Cut Slopes in Volcanic and Granitic Rocks (GEO Technical Guidance Note No. 4 (TGN 4))*. Geotechnical Engineering Office, CEDD of HKSAR Government.

GEO. 2007. *Engineering Geological Practice in Hong Kong (GEO Publication No. 1/2007).* Geotechnical Engineering Office, CEDD of HKSAR Government.

Corbett, G. 2009. *Anatomy of porphyry-related Au-Cu-Ag-Mo mineralized systems: Some exploration implications*. Proceedings of the Australian Institute of Geoscientists North Queensland Exploration Conference June 2009, AIG Bulletin 49, pp 33-46.

Sewell, R.J., Tang, L.K.D., & Campbell, S.D.G. 2012. *Volcanic-plutonic connections in a tilted nested caldera complex in Hong Kong*. Geochem. Geophys. Geosyst., 13, Q01006, doi:10.1029/2011GC003865.

Comparative Study on In-Line Orthogonal and Staggered Arrangements of DCM Columns: Stress Distribution, Deformation Characteristics of Two Cases

Ming-min Wang, Pan Liu, Ting-hao Mao, Alvin Lam *Ove*
Arup & Partners Hong Kong Ltd, Hong Kong

ABSTRACT

Deep Cement Mixing (DCM) method has been increasingly adopted in site formation and ground improvement projects in Hong Kong. The planar arrangement of DCM columns directly influences the bearing performance, stress distribution, and deformation characteristics of composite foundations. This paper systematically compared the differences between in-line (square/orthogonal) and staggered (triangular/quincunx) arrangements of DCM columns. The three-dimensional (3D) finite element method is adopted to analyse the mechanical response of two cases in Hong Kong. One case is a deep trench excavation in column-type DCM treated ground. Another case is a building sitting on DCM improved ground. By comparing the stress distribution and deformation characteristic of the in-line orthogonal and staggered DCM column layout, the engineering benefits of staggered DCM column arrangement in excavation and foundation projects are provided.

1 INTRODUCTION

In recent years, the deep cement mixing (DCM) method has been increasingly adopted in site formation and ground improvement projects in Hong Kong. Compared with dredged method or preloading ground improvement, the DCM technique offers advantages including a relatively short construction period, high treated soil strength, controllable quality, and environmental sustainability.

The Port Works Design Manual (PWDM) published by Civil Engineering Department of Hong Kong Government presented the fundamental design philosophies of DCM (CEO, 2002a, 2002b, 2003). In July of 2025, Island Division of Geotechnical Engineering Office of the Civil Engineering and Development Department published an Interim Design Guide to Deep Cement Mixing for Reclamation Works (IDG), which has adopted recent local projects technical details and advancements in DCM works (S.T.C. So 2025). The IDG focuses on the design methodology and construction specifications of DCM supporting seawalls, breakwaters and land reclamation, the use of DCM beyond those maritime applications are not covered by both the PWDM and IDG documents. Wang (2019) presented the characteristics of cement-soil mixture in the laboratory environment as well as performance of the field mixed soil using the same binder material. The relationship of strength between laboratory mixed soils and field mixed soils were provided. Cheung (2021) provided a review of deep cement mixing treatment for non-dredged seawall in Hong Kong. He (2022) summarized the application of offshore deep cement mixing method in the main reclamation works of Hong Kong International Airport three runway system project. Cheung (2022) described the usage of DCM in Tung Chung East Reclamation project. Chu (2023) provided test method and typical results of unconfined compressive strength of cement stabilised soil cores in Hong Kong. ZHENG (2023) provided detailed description of land four-shaft deep cement mixing rig and key construction technology used in the Hong Kong International Airport three runway project. Recently, DCM technique also applied in the context of earth retaining system in Hong Kong. DCM retaining wall has been successfully adopted in a box culvert construction in Tung Chung East reclamation area.

Successful applications of DCM in foundation system for buildings, roads and important utilities are springing out in Chinese mainland. Fu (2009) studied the soil squeezing effect of DCM pile and its application to subway tunnel. Chen (2019) studied the settlement of soft foundation under seawall reinforced by DCM piles by Plaxis3D software. Xu (2023) studied on the reasonable layout form of DCM pile composite foundation for immersed tunnel of Shenzhen-Zhongshan Link. Zhu (2024) studied the influence of DCM plane layout on slope stability based on 3D finite element analysis. Cao (2024) did model tests to study 3D soil arching in pile-supported embankments with and without geotextile. Chen (2025) provided research

outcomes on lateral load reduction mechanism of anchored sheet pile wall by DCM piles in active zone. Zhang (2025) did research on cement mixing pile reinforcement for soft soil foundations based on numerical simulation.

Since the column-type DCM arrangement is a discontinuous pattern in plane, the loads transfer route in the DCM treat ground will be controlled by the differential stiffness between DCM column and soil. The arching effect is a crucial mechanism of DCM pile-soil interaction in column type DCM treated ground. Liu (2014) studied the soil arching effect by numerical simulation. Wang (2015) studied the arching effect for soil behind soldier piles under horizontal loads. Liu (2018) proposed a calculation method for the arching effect in square and triangular pile configurations. Wang (2024) provided a literature review of load-transferring mechanism in a pile-supported embankment, and it reduces the even settlement on the embankment surface.

For DCM improved ground, conditions involving excavation or localized surcharge have emerged, while detailed research outcomes are not sufficient to deal with challenges related to stress distribution and deformation behaviour of DCM treated ground under complex engineering practices. For the commonly used column-type DCM improvements, planar arrangement of DCM columns is one of the key factors affecting composite foundation performance. Planar arrangements of DCM columns primarily include two basic forms: in-line (squared/orthogonal) arrangement and staggered (triangular/quincunx) arrangement (Figure 1). Different arrangements alter the pile-soil interaction mechanism, directly influencing the stress transfer path, deformation mode, and overall stability of the foundation.

This study employs the three-dimensional (3D) finite element method to analyse the mechanical response of two cases in Hong Kong. One case is a deep trench excavation in column-type DCM treated ground. Another case is a building sitting on DCM improved ground. By comparing the stress distribution and deformation characteristic of the in-line (squared/orthogonal) and staggered (triangular/quincunx) DCM column arrangement, the engineering benefits of staggered DCM column arrangement are provided.

2 Overview of Column-type DCM Pile Arrangement

Currently, the DCM used in Hong Kong are mainly formed by two or four overlapping DCM columns (Zheng, 2023). A DCM column/cluster/panel produced in one single operation is collectively termed as “DCM element”. Typical DCM improvement patterns include column, wall, grid, and block-type stabilisation. In Chinese mainland and Macau, other kinds of DCM patterns like three-axis cement mixing pile or five-axis cement mixing pile are widely used.

In engineering practice, DCM pile arrangements include column-type, wall-type, grid-type and block-type. Even though research show that wall-type, grid-type, and block-type arrangements significantly improve the overall stability of DCM treated ground, pile-type arrangements are widely used due to its relative low cost and reasonably settlement control effectiveness. For column-type DCM arrangements, the plan arrangements of DCM columns are important in design stage.

2.1 In-Line (Squared/Orthogonal) Arrangement

DCM column positions are arranged in a regular grid pattern on the plane. The pile spacings in longitudinal and transverse directions can be the same or different. This arrangement is simple to construct and easy to control, but the continuous linear soft gap between DCM rows may cause soil squeeze out problem, and stress distribution in the soil between DCM columns is uneven. The Three-runway System, Tung Chung New Town Extension (East), and the Integrated Waste Management Facilities have adopted the in-line (squared) DCM arrangement (He, 2022).

2.2 Staggered (Triangular/Quincunx) Arrangement

DCM pile positions are arranged in triangles on the plane. This arrangement provides more sufficient pile-soil interaction, but construction control is relatively more complex.

Wu (2019) proposed staggered arrangement for DCM piles in foundation reinforcement of slope cofferdam of artificial island. Zhang (2025) compared the in-line (square) arrangement and staggered arrangement of DCM columns for the subgrade of a highway project. He indicated that the staggered arrangement is more effective than the square arrangement. The maximum settlement of staggered arrangement is 20mm smaller

than in-line (square) arrangement, which accounts for 8% of the maximum settlement of the triangular arrangement.

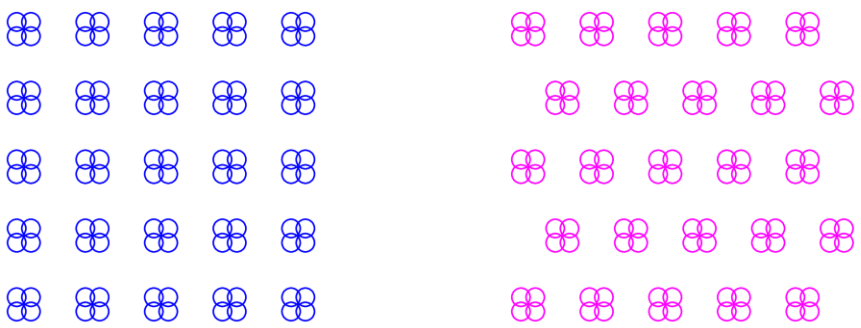

Figure 1: In-Line (Left) and Staggered (Right) Arrangements of DCM Columns

This paper compared the differences between in-line (square/orthogonal) and staggered (triangular/quincunx) arrangements of DCM columns in Hong Kong ground condition. Plaxis3D is adopted to analyse the mechanical response of two cases. One case is a deep trench excavation in column-type DCM treated ground. Another case is a building sitting on DCM improved ground.

3 Case One: A Deep Trench Excavation in Column-type DCM Treated Ground

3.1 General Information

This case is a cut-cover tunnel built on a reclamation area in Hong Kong. The reclamation adopted non-dredged methods where soft muds remain in place under the reclamation fill. Ground improvement works in form of DCM were involved across the soft layers with embedment into the competent stratum. The cut and cover tunnel was built after the DCM ground improvement.

The existing ground strata of the site generally include reclamation fill on top of the existing quaternary deposits forming the land area (FILL); soft unlaminated SILT/CLAY (Marine Deposit); Medium dense, fine to coarse SAND (Alluvium); completely and highly decomposed granite (C/HDG) and moderately to slightly weathered GRANITE.

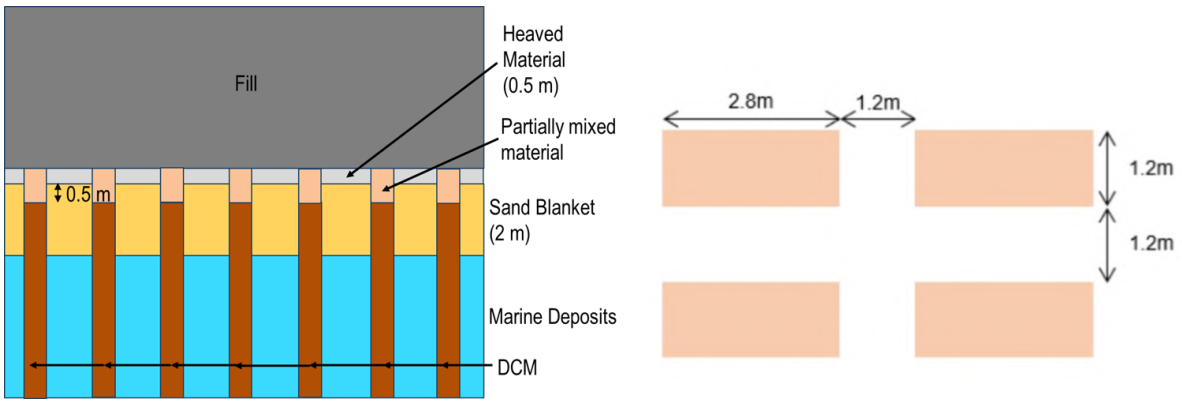

Figure 2: Typical Section (Left) and Plan (Right) Arrangement of DCM

Table 1: Material Parameters

Soil Stratum	Bulk Unit Weight (kN/m^3)	Friction Angle, φ (kPa)	Cohesion, c' (kPa)	Elastic Modulus, E (MPa)
Sand Fill	20	33	0	13
Heaved Material	18	-	15 ($C_u^{\#}$)	5.2
Sand Blanket	20	33	0	13
Marine Deposit	15.5	-	120	E=6.2 (Z*≤15m)

Alluvium firm & stiff undrained	17.5	-	($C_u^{\#}$) 55 ($C_u^{\#}$)	E=6.2+(Z-15)*0.355 (Z* > 15m) E=19.1 (Z*≤25m) E=19.1+(Z-25)*0.870 (Z* > 25m)
Completely Decomposed Granite	19.5	35	5	100
Moderately Decomposed Granite	21	100	45	2500

Note: * Depth below the ground level.
Soil undrained shear strength.

For DCM parameters in the Plaxis 3D models, C_u is 500 kPa, E is 200 MPa, tensile strength is 100 kPa and friction angle is 0°. Cut off level of DCM column is +3 mPD. Toe level of DCM column is -21 mPD (1m below Marine Deposit). Two kinds of DCM plan arrangements are illustrated in Figure 3, representing the in-line orthogonal arrangement (Case 1a) and staggered arrangement (Case 1b).

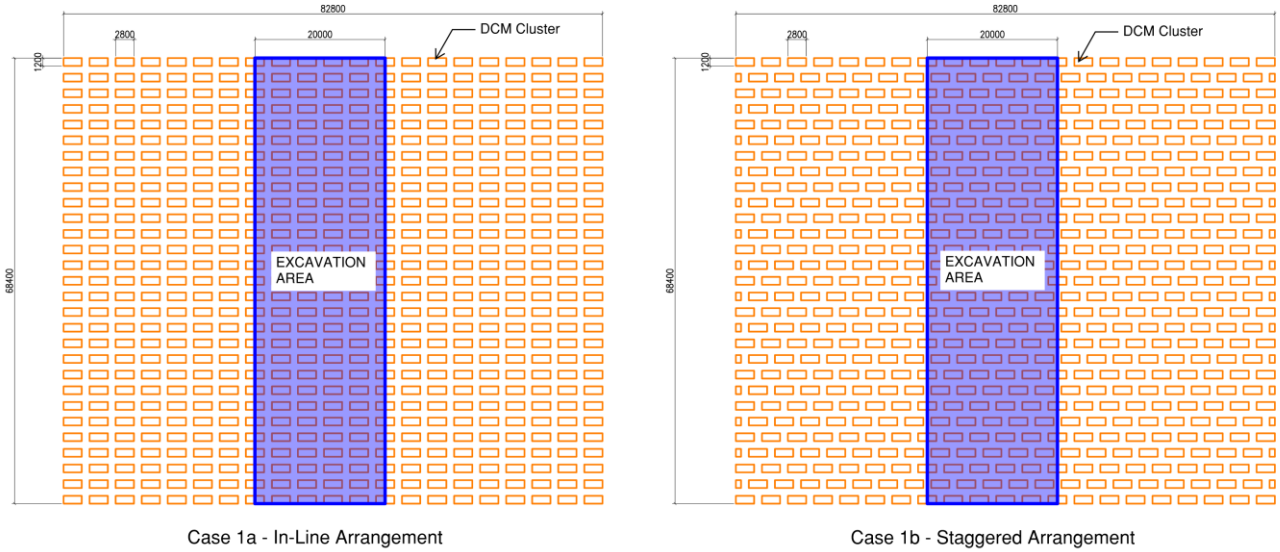

Figure 3: DCM Plan Arrangement for Case 1a and Case 1b

The final excavation level of excavation area is -12.00 mPD. Pipe pile wall with strut is adopted as ELS scheme. The pipe pile wall is made by CHS 813mm steel pipes with 20mm thickness. Cut off level of the pipe pile wall is +3 mPD. Toe level of pipe pile wall is -40 mPD. The Plaxis3D model size is 82.8m × 68.4m × 73m.

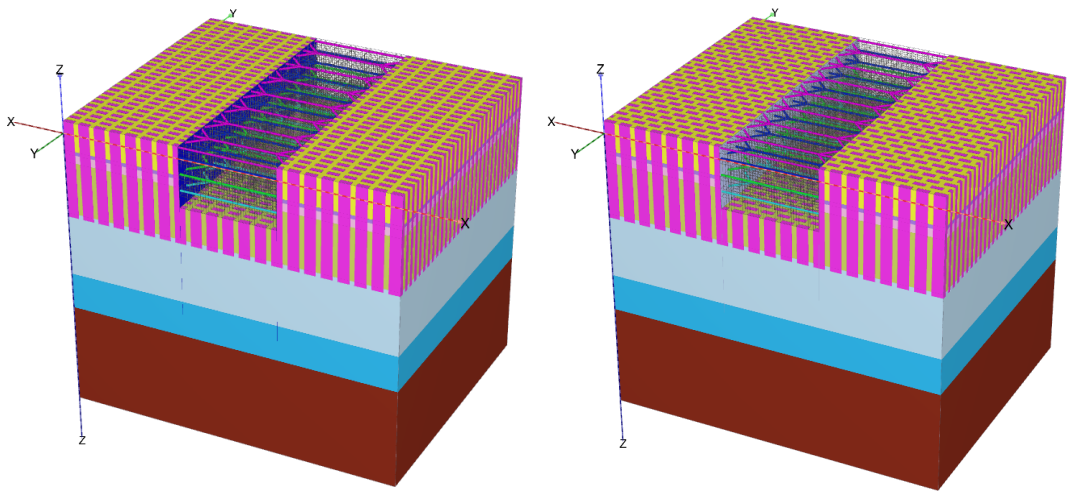

Figure 4: 3D View of Plaxis3D model for Case 1a (left) and Case 1b (right)

3.2 Horizontal Stress Distribution

Figure 5 presented the plastic points distribution at -4mPD for Case 1a and Case 1b. It can be seen that for the in-line orthogonal arrangement, almost all untreated soil in the row gap between DCM have enter plastic condition. While for staggered arrangement, the plastic points are located in the zigzag gap between DCM columns.

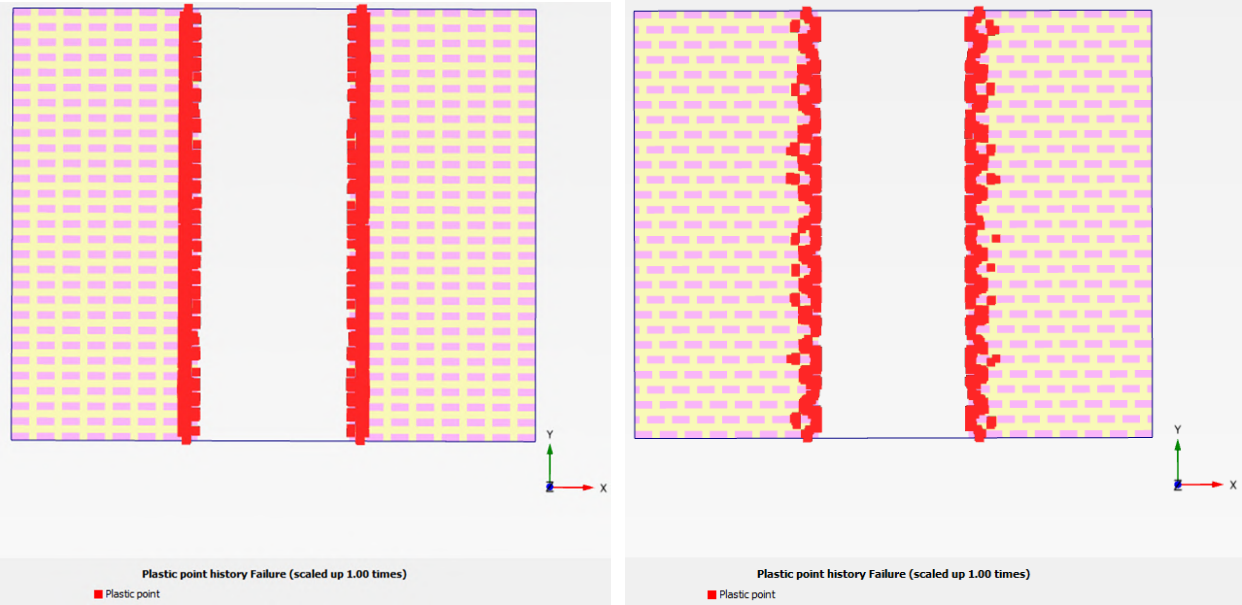

Figure 5: Soil Plastic Point Distribution at -4mPD for Case 1a (left) and Case 1b (right)

3.3 Displacement Characteristics

Figure 6 presents the horizontal displacement at -4 mPD. Different arrangements of DCM columns formed influence on the displacement of soil, DCM and pipe piles. Compared with in-line orthogonal arrangement, staggered arrangement reduced the horizontal displacements by 16.4%.

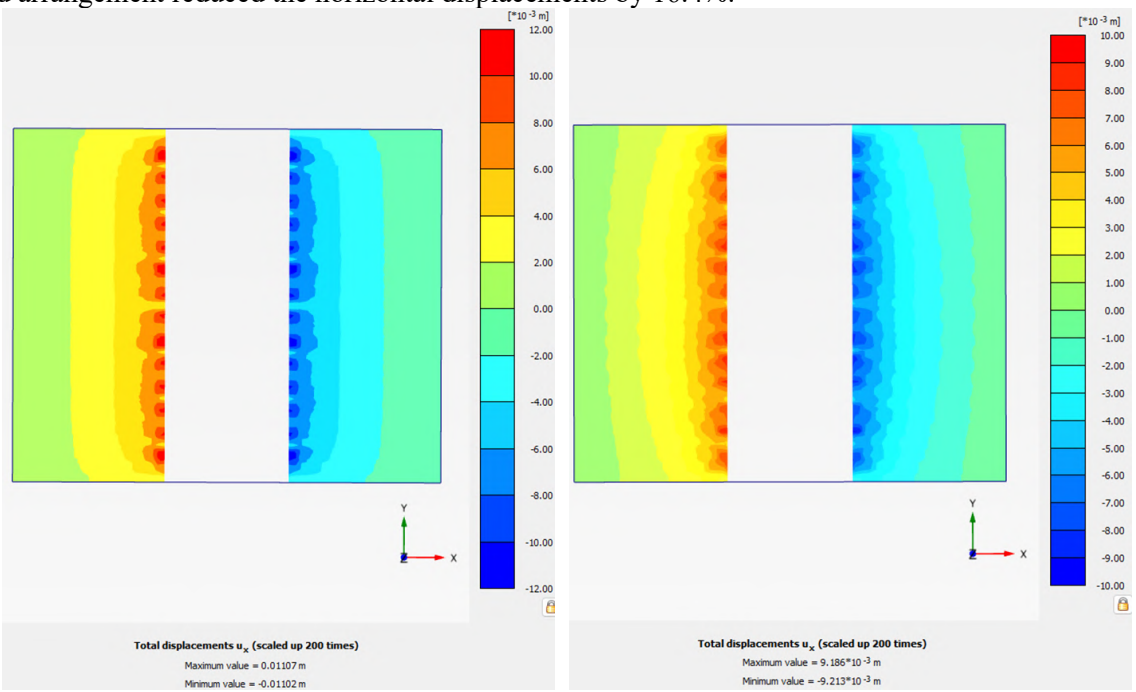

Figure 6: Soil Horizontal Displacement at -4mPD

3.4 Soil Rebound Caused by Excavation

Excavation is a process of unloading for the soil under the bottom of the pit. Soil under the bottom of the pit will rebound due to the reduce of stress level. The three-dimensional finite element models shown the rebounding phenomenon (Figure 7).

Compared with in-line orthogonal arrangement, staggered arrangement reduced the maximum soil rebound displacement by 9%. The rebounding displacement of the soil below the excavation surface is greatly affected by the rebounding modulus of the soil layers and the excavation depth of the foundation pit. DCM piles installed before the excavation will move upward during the excavation progress. Even though the elastic Mohr-Coulomb material used in this analysis may overestimate the rebound displacement, but the rebound phenomenon of deep excavation and its impacts can not be ignored in real projects (Wang 2019).

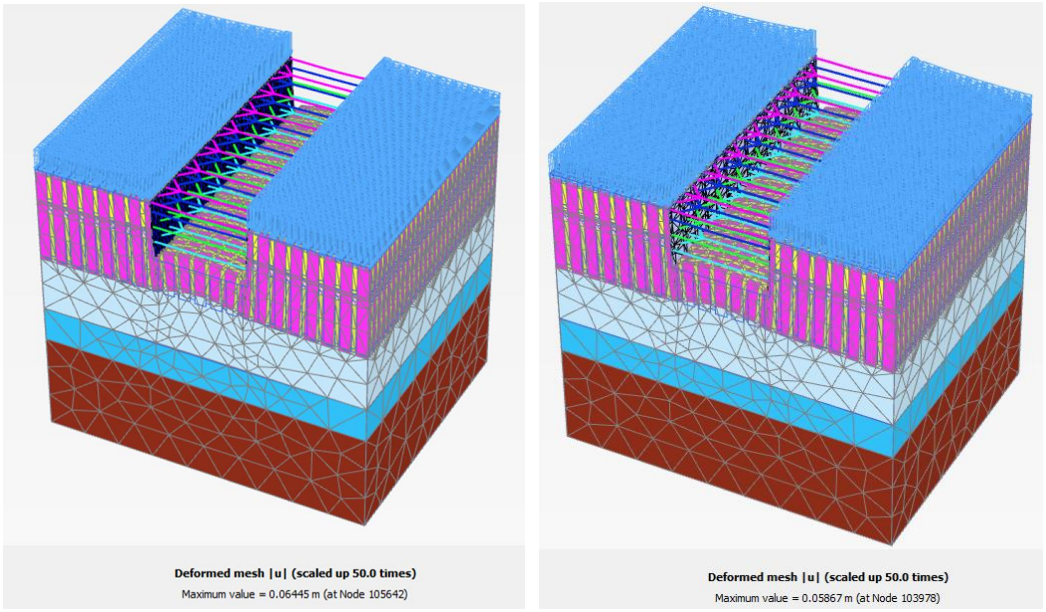

Figure 7: Soil Rebound after Excavation

4 Case Two: A Building with Raft Foundation Sitting on DCM Improved Ground.

4.1 General Information

This case is a building with raft foundation and sitting on a DCM treated ground in Hong Kong. The strata of this site include Fill, Estuarine Deposits, Alluvium, completely and highly decomposed granite (C/HDG) and moderately to slightly weathered GRANITE. Due to the existing of Estuarine Deposit Clay will cause relatively large consolidation settlement, column-type DCM is proposed to treat the soft and compressible Estuarine Deposit Clay beneath the footprint of the building.

Figure 8 presents the typical section of the DCM improved subgrade. 1m thick sand blanket is recommended between the base slab of the building and DCM columns for loads distribution purpose.

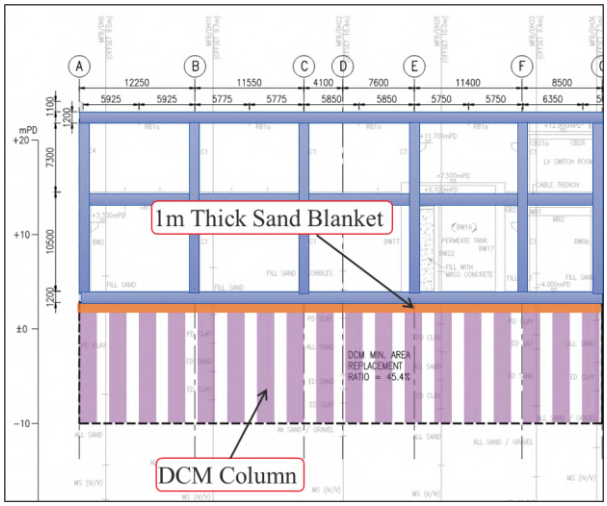

Figure 8: Typical Section of DCM Treated Subgrade

Table 2: Material Parameters

Soil Stratum	Bulk Unit Weight (kN/m^3)	Friction Angle, φ (kPa)	Cohesion, c' (kPa)	Elastic Modulus, E (MPa)
Silt (Fill)	19	28	2	7
Clay (Estuarine Deposit)	17	28	3	E=3.5(Z*≤6m) E=3.5+(Z-6)*0.455 (Z* > 6m)
Sand blanket	19	35	0	20
DCM treated area	24	-	875(C_u#)	350
Sand (Alluvium)	19	36	0	E=15(Z*≤14m) E=15+(Z-6)*0.839 (Z* > 14m)
Completely Decomposed Phyllite	19	33	0	50
Moderately Decomposed Phyllite	24	100	45	1500

Note: * Depth below the ground level.
Soil undrained shear strength.

For DCM parameters in Plaxis 3D, C_u is 875 kPa, E is 350 MPa, tensile strength is 175 kPa and friction angle is 0°. Cut off level for DCM column is +4.3 mPD. Toe level of DCM is -5 mPD (2.5m below Estuarine Deposit). Two kinds of DCM plan arrangements are illustrated in Figure 9, representing the in-line squared arrangement (Case 2a) and staggered arrangement (Case 2b). Figure 10 presents the 3D view of the Plaxis3D models.

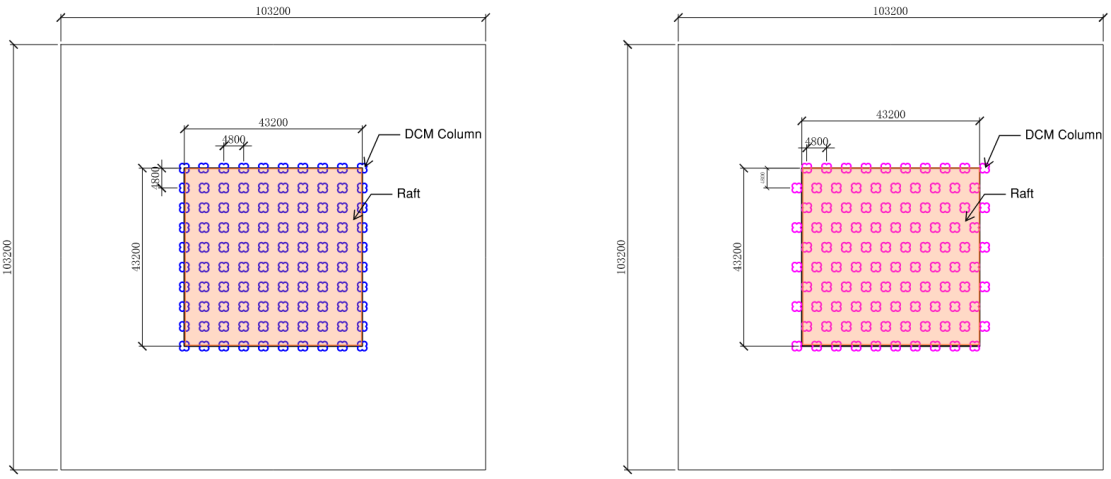

Figure 9: DCM Plan Arrangement for Case 2a (left) and Case 2b (right)

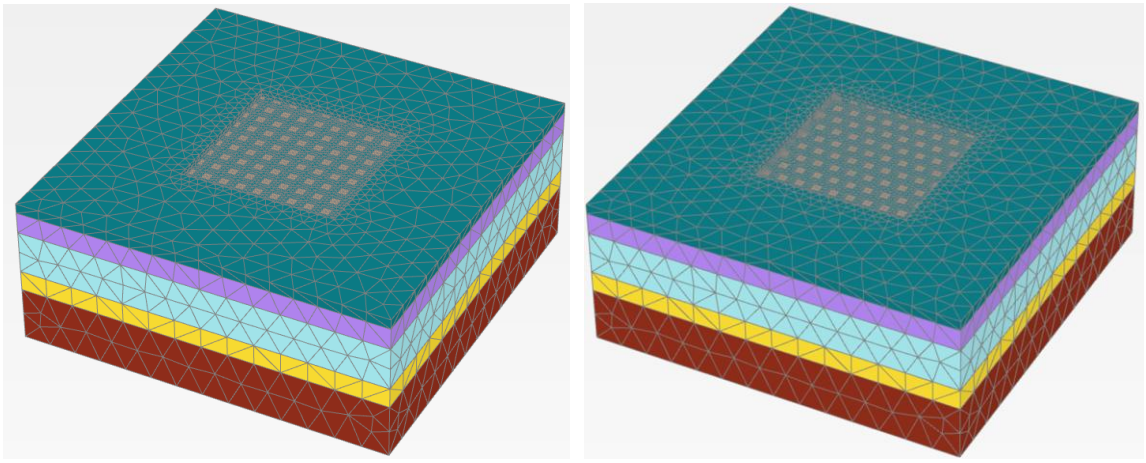

Figure 10: 3D View of Plaxis3D model for Case 2a (left) and Case 2b (right)

4.2 Vertical Stress Distribution

Figure 11 shows the soil stress distribution at 1m below sand blanket. It can be seen that the characteristics of vertical stress variation in DCM treated subgrade with square and staggered pile arrangements are similar. With a staggered pile arrangement, maximum compression stress is 6.6% lower than in-line squared arrangement. The staggered arrangement, due to interlocking pile positions, results in a more uniform stress distribution.

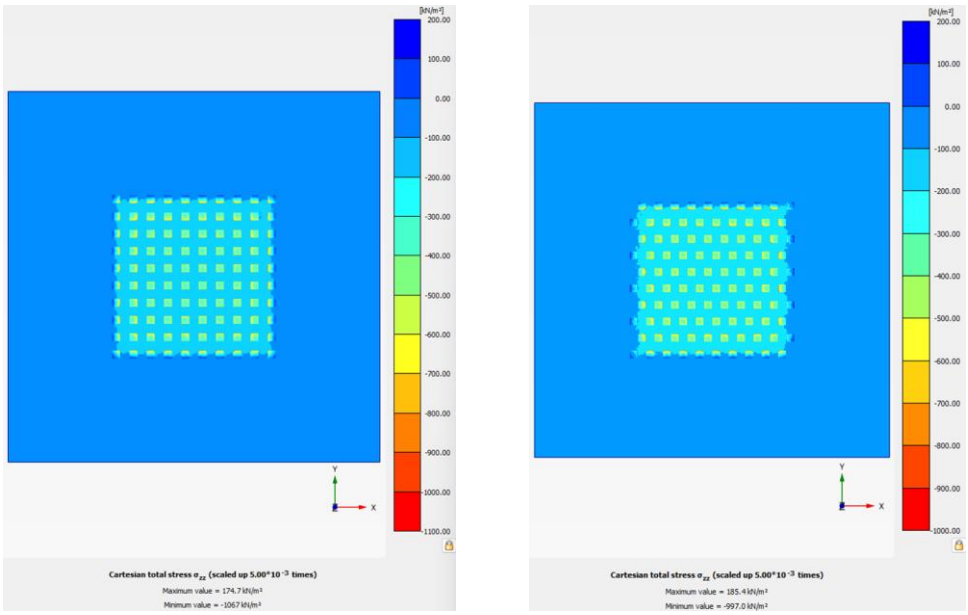

Figure 11: Soil Stress Distribution at 1m below sand blanket for Case 2a (left) and Case 2b (right)

Figure 12 presents the stress distribution in DCM columns. Due to the raft is not cover all DCM columns, there are stress concentrations in both the in-line squared arrangement and staggered arrangement. It is recommended to extend the base slab and sand blanket to cover full section of boundary DCM columns.

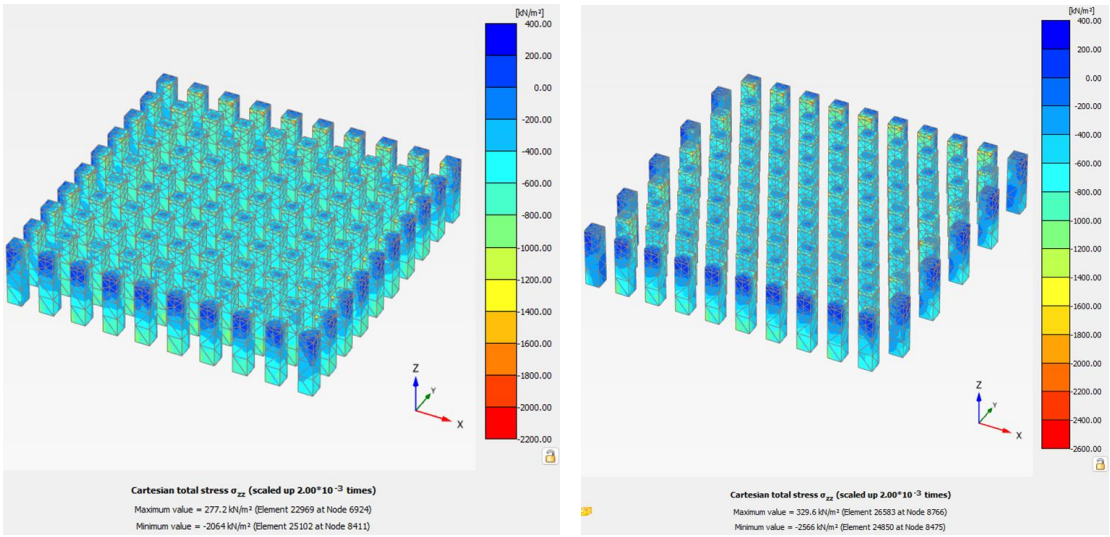

Figure 12: DCM Stress Distribution for Case 2a (left) and Case 2b (right)

4.3 Displacement Characteristics

Figure 13 shows the displacement of raft sitting on in-line squared DCM arrangement and staggered DCM arrangement. It can be seen the maximum displacements are almost the same (1% difference). From Figure 11 we can see that 10 DCM columns are out of the footprint of raft in Case 2b. Since those 10 DCM columns do not contribute to the settlement control for the raft, they can be deleted for cost saving purpose. Hence the staggered DCM arrangement can reduce the cost by about 10%.

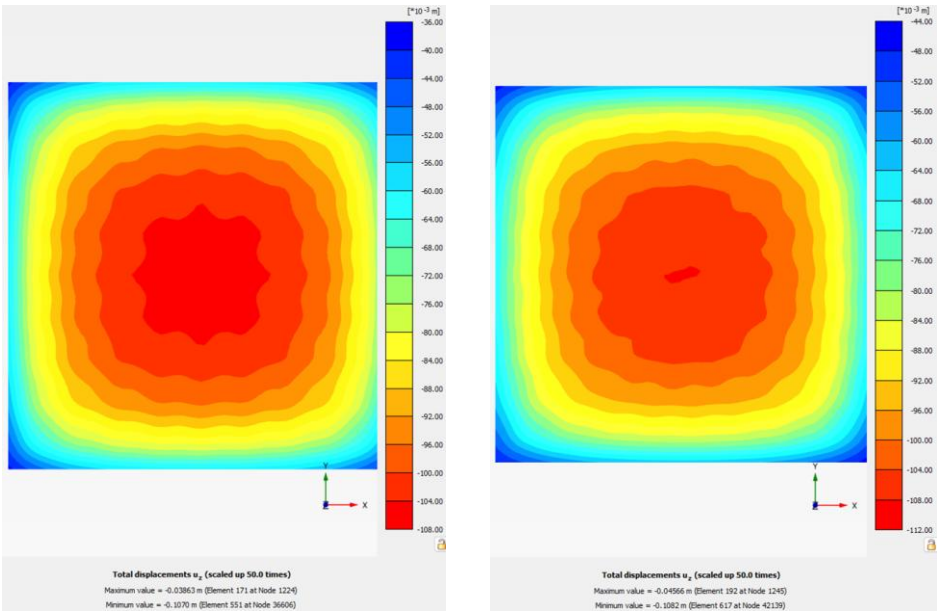

Figure 13: Raft Displacement for Case 2a (left) and Case 2b (right)

5 Conclusion

By the analysis of two cases, it can be seen that there are differences in stress distribution and deformation characteristics between in-line (squared/orthogonal) arrangement and staggered (triangular/quincunx) arrangement of DCM piles.

For Case one which represents the excavation and unloading in column-type DCM treated ground, staggered (triangular/quincunx) arrangement of DCM piles provides better displacement control effects.

For Case two which represents the local surcharge on the column-type DCM treated ground, staggered (triangular/quincunx) arrangement of DCM piles provides lower maximum compression stress than in-line

squared arrangement. With the same calculated vertical displacement, the staggered DCM arrangement provided a possibility of reducing the cost by about 10%.

For column-type DCM design, no matter the in-line (squared/orthogonal) arrangement or staggered (triangular/quincunx) arrangement is adopted, the DCM pile spacing and replace ratio are the most significant two parameters to control the stress and displacement of the treated ground. DCM-Soil stiffness ratio also has influence on the stress distribution between DCM pile and soil.

In engineering applications, the arrangement form should be selected carefully based on specific project conditions, load characteristics, and geological environment. Generally, for potential excavation and local surcharge projects, staggered DCM columns arrangements provided some benefits than in-line square arrangements of DCM columns arrangements.

REFERENCES

Cao Weiping, Xie Zedong, Yue Yaxin, et al. 2024. Model tests on 3D soil arching in pile-supported embankments with and without geotextile, Case Studies in Construction Materials, 20: 3-15.

CEO. 2002a. Port Works Design Manual – Part 1: General Design Considerations for Marine Works. Civil Engineering Office, HKSAR Government, 219 p.

CEO. 2002b. Port Works Design Manual – Part 3: Guide to Design of Reclamation. Civil Engineering Office, HKSAR Government, 130 p.

CEO. 2003. Port Works Design Manual – Part 4: Guide to Design of Seawalls and Breakwaters. Civil Engineering Office, HKSAR Government, 168 p.

Chen Liang-zhi, Zou Peng-xu, Peng Zhi-hao. 2019. Numerical simulation of semi-rigid cement soil mixing pile for soft soil foundation reinforcement. Port & Waterway Engineering. 551: 156-162.

CHEN Shengyuan, DAI Jiqun, GUAN Yunfei, et al. 2025. Research on lateral load reduction mechanism of anchored sheet pile wall by deep cement mixing pile in active zone. *Chinese Journal of Geotechnical Engineering*, 47(10): 2026-2035.

Cheung, C.K.W., Wong, A.H.K., Cheung, H.K.T & So, S.T.C. 2021. Design of deep cement mixing treatment for non-dredged seawall in HKSAR Government. Proceedings of DFI Deep Mixing Conference 2021, pp 28-38.

Cheung, H., Yan, C.H., Cheung, C. & Wong, A. 2022. Deep Cement Mixing – The Experience in Tung Chung East Reclamation and Challenges Ahead. AIJR Proceedings, pp 348-360.

Chu, F.L.F. & Chung, P.W.K. 2023. Test Method for Unconfined Compressive Strength of Cement Stabilised Soil Cores (TN 2/2023). Geotechnical Engineering Office, HKSAR Government, 69 p.

Fu Yanbin, Liao Shaoming, Zhu Hehua. 2009. Soil squeezing effect of DCM pile and its application to subway tunnel. Rock and Soil Mechanics, 30(7), 2005-2010.

He Hong-tao, WANG Zheng-liang, et al. 2022. Application of offshore deep cement mixing method in the main reclamation works of Hong Kong International Airport three runway system project. China Harbour Engineering. 42(2): 38-42.

Wang Kangyu, Ye Jiahuan, Wang Xinquan, et al. 2024. The Soil-Arching Effect in Pile-Supported Embankments: A Review. Buildings. 14(126): 1-27.

Liu Feicheng, ZHANG Jianjing, YAN Shijie. 2018. Simplified Method for Analysing Pile-Supported Embankment Settlements over Soft Soil. *Journal of Southwest Jiaotong University*. 53(2): 272-278.

Liu Zhaohui, Wang Xin. 2014. Numerical simulation on soil arching effect of piled low embankment[J]. *Journal of Shenzhen University Science and Engineering,* 31(5):8.

S.T.C. So, A.L. Wong & L.C.Y. Shu. 2025. Interim Design Guide to Deep Cement Mixing for Reclamation Works. Geotechnical Engineering Office, HKSAR Government.

Zheng Shao-he, CHEN Yue, ZHOU Xiao-ke. 2023. Development of land four-shaft deep cement mixing rig and key construction technology. *Journal of Ground Improvement*. 5(3): 239-247.

Wang Ming-min. Wang Gui-lin. Wu Shu-guang. 2015. Stability analysis of soil behind a vertical free-face between supporting piles. *Engineering Geology.* 195:155-163.

Wang Ming-min, Sun Guang-yu, Zhu Li-gang, et al. 2019. A Simplified Calculating Method for Calculating Bearing Capacity Loss of Pile Foundation and Additional Tension Force in Piles Caused by Deep Foundation Pit Excavation. *Building Structure*. 49(22): 53-58.

Wang Yanhua, Xie Geng and Dou Huaren. 2019. Stabilisation of soft clay by deep cement mixing (DCM) method – A case study. *HKIE Transactions*. 26(3): 115–125.

Wu Jiawu. 2019. Application of DCM Piles in Foundation Reinforcement of Slope Cofferdam of Artificial Island. Journal of Water Resources and Architectural Engineering. 17(3): 164-167.

Xu Yu, Xu Guoping, Chen Weile, et al. 2023. Study on Reasonable Layout Form of Deep Cement Mixing Pile Composite Foundation for Immersed Tunnel of Shenzhen-Zhongshan Link. Tunnel Construction, 43(11), 1944-195.

Zhang Feng-feng, Du Peng-gang, Yao Meng-fei, et al. 2025. Cement Mixing Pile Reinforcement Analysis Effects for Soft Soil Foundations based on Numerical Simulation. Architecture Technology. 56(14). 1760-1764.

Zhu Xingke, Xie Wandong. 2024. Influence of DCM Plane Layout on Slope Stability Based on 3D Finite Element Analysis. Port & Waterway Engineering. 003.

Analysis on Earth-pressure Imbalance on a Deep Excavation

L.W. Wong
SMEC Asia Limited

ABSTRACT

An undersea vehicular tunnel was constructed by using the cut-and-cover method. The cofferdam comprised intermittent pipe pile walls of 50 m maximum in depth. The maximum excavation depth was 35 m below the high tide level. The struts were preloaded to as large as 16.4 MN. It was observed that the earth-pressure imbalance effect wall deflections caused 92 mm inward wall movement on one side and 67 mm outward wall movement on the opposite side. A 2-Dimensional numerical analysis using the Hardening-Soil with Small-strain stiffness constitutive soil model has been conducted to study the mechanism of the outward wall movements. The analysis shows that the earth pressure imbalance is attributable to the difference in wall lengths on the opposite side of the excavation trench. The preloading effect and the loss of the applied strut loads due to wall movements plays a crucial role on the performance of wall deflections.

Keywords: Wall deflections, Cut-and-cover tunnel, Earth-pressure imbalance, struts preloading.

1 INTRODUCTION

The earth-pressure imbalance effect causing difference in wall deflections of deep excavation cases have been reported by the researchers. Moh & Hwang (1997) reported the asymmetrical wall deflections at a basement excavation case located at the northern rim of the Taipei basin. Wong & Yong (2013) reported the earth-pressure imbalance effects for an excavation case for the Central Wanchai Bypass cut-and-cover tunnel. Based on the wall deflection profiles observed in inclinometers installed on opposite sides of the excavation trench of 35 m deep, Wong & Ho (2025) reported the earth-pressure imbalance effect. The issue is very complicated and can only be sorted out by numerical analysis. To understand the mechanism causing the asymmetrical wall deflections and to improve the effectiveness on the design and construction of the infrastructure works, the undersea tunnel case on earth pressure imbalance that Wong & Ho (2025) reported is critically studied.

2 HYDROGEOLOGICAL CONDITIONS

2.1 Extent of undersea tunnel

The undersea tunnel accommodating a dual-3 carriageways is located on the north shore of the Victoria Harbour. Descending from the ground level of 5 mPD at the at-grade section, the undersea tunnel section has the lowest formation level around -32 mPD. As depicted in Figure 1, the undersea tunnel presented in this paper is 50 m in width and 230 m in length. Eight inclinometers were installed immediately behind the pipe pile walls along 4 monitoring sections. The piezometers were installed near Sections 11 and 12.

The subsoils along the tunnel route mainly comprise the marine deposits, the alluvium, the granitic saprolites and the granite bedrock. The seabed level was around -5 mPD. The rockhead levels along the route alignment vary from -22 mPD to -50 mPD. Along the shoreline, there is a fill layer of approximately 7 m in thickness. Figure 2 depicts the soil and rock profiles along the transverse Section 11. The fill layer is underlain by the Quaternary alluvial silty sand of 12 m average in thickness at Section 11. The alluvium is underlain by the saprolite of completely decomposed granite (Granite V) of 13 m average in thickness.

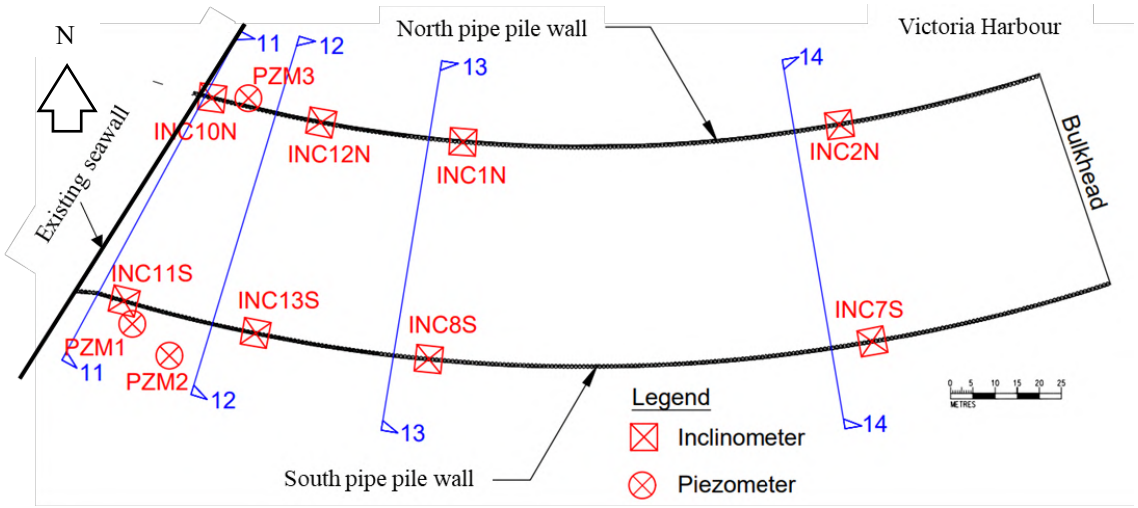

Figure 1: Plan of undersea tunnel showing the locations of the instruments (after Wong & Ho 2025).

Underlying the Granite V is the highly decomposed granite (Granite IV) of 10 m maximum in thickness. The bedrock of moderately decomposed to slightly decomposed granite (Granite III/II) is encountered at the elevations ranging from -33 mPD to -68 mPD. The soil and rock conditions at the project site is summarized in Table 1. The mean sea level is 1.2 mPD. The high tide level of 2.8 mPD was allowed for the cut-and-cover tunnel construction.

Table 1. Summary of soil profile along the undersea tunnel

Soil strata	Top level, mPD	N value	Description
Fill	4	5 to 12	Greyish silty SAND
Marine deposits	-5	5	Dark grey silty CLAY
Alluvium	-10	11 to 40	Stiff yellowish brown silty SAND
Granite V	-20	28 to 80	Yellowish to reddish brown silty SAND
Granite IV	-50 to -60	90 to 160	Yellowish brown sandy GRAVEL and cobbles
Granite III/II	-33 to -68	-	Pink to brown medium to coarse-grained Granite

2.2 Cofferdam for cut-and-cover construction

As depicted in Figure 2, the tunnel was constructed by using the bottom-up method. The excavation was supported by the intermittent pipe pile walls on the north and the south sides. The pipe piles had interlocking joints like those for the sheet piles. The intermittent pipe pile walls were composed of tubular steel sections of 813 mm in diameter, 25 mm in thickness and spacing at 900 mm.

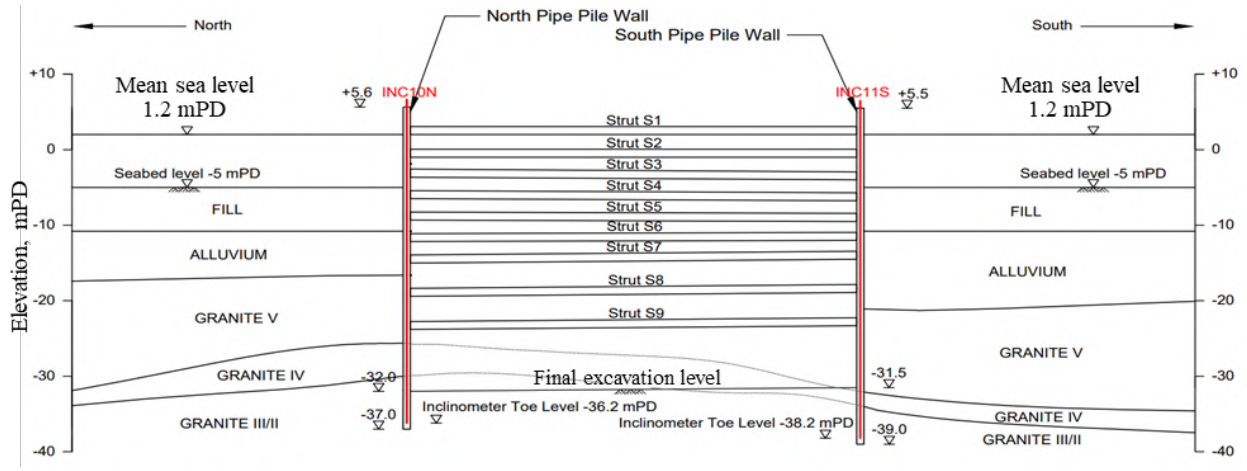

Figure 2: Soil and rock profile along Section 11 of the cut-and-cover tunnel (after Wong & Ho 2025).

At Section 11, where the excavation depths below the high tide level exceeding 35 m, the pipe piles were strengthened by inserting steel H-piles of 305x305x238 kg/m UB. The void between the tubular pipe and the H-pile was filled with cement grout. The stiffness of the pipe pile wall, the EI values, was 5,860 MNm^2/m with the H-pile. Such stiffness is equivalent to the EI value of 5,900 MNm^2/m for the concrete diaphragm wall of 1.5 m in thickness allowing a 0.7 reduction factor for cracks in concrete with the Young's modulus of 30 GPa.

The cofferdam was supported with 9 levels of steel struts along Section 11. The width of the excavation was 49 m. The wall top level was around 5.5 mPD. The toe levels of the pipe pile walls, embedded 5 m in Granite III/II, were at -37 mPD and -39 mPD on the north and the south pipe pile walls respectively. The final excavation levels on the north and the south sides along Section 11 were -32.0 mPD and -31.5 mPD respectively.

2.3 Groundwater conditions

As shown in Figure 1, piezometers PZM1 to PZM3 were installed behind the north and the south pipe pile walls in the vicinity of Section 11. Two piezometers were installed at each location. The upper piezometers were installed in the alluvium and the lower piezometers were in the Granite V stratum. Figures 3a and 3b present the variation of the piezometric levels on the south and the north sides of the excavation respectively. The daily readings show that the piezometric levels were under tidal influence with the average level around 1.2 mPD in the beginning stage of excavation.

Figure 3a shows that on the south side of the cofferdam, the average piezometric levels in the alluvium layer were lowered from 1.5 mPD in the excavation stage to 1.0 mPD at the end of the tunnel structure construction stage. In the Granite V stratum, the average piezometric levels were lowered from 1.5 mPD to 0.5 mPD during that period. The piezometric levels as high as 4.0 mPD observed in PZM21 were likely caused by the installation of the grout curtain behind the south pipe pile wall, where sensitive structures were in the vicinity.

Figure 3b shows that on the north side of the cofferdam, the average piezometric levels in the alluvium layer were lowered from 1.2 mPD in the excavation stage to -1.0 mPD at the end of the tunnel structure construction stage. In the Granite V stratum, the average piezometric levels were lowered from 1.2 mPD to 0 mPD during that period.

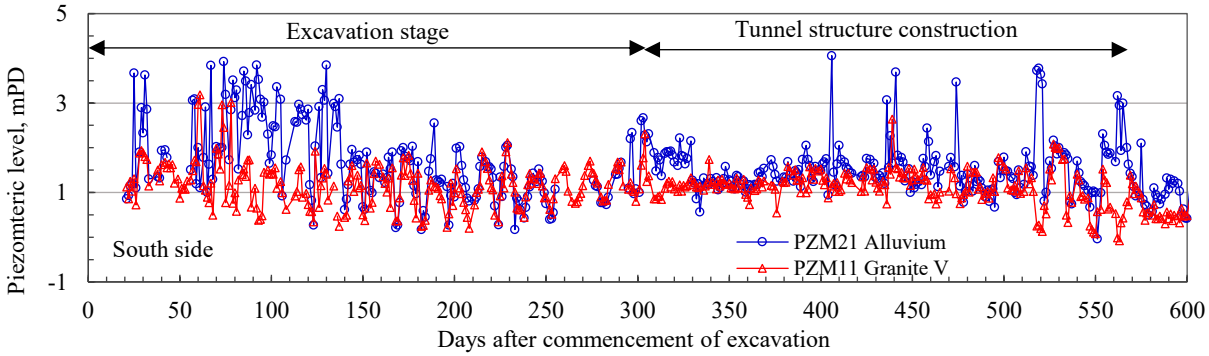

(a) Variation of piezometric levels behind the south pipe pile wall

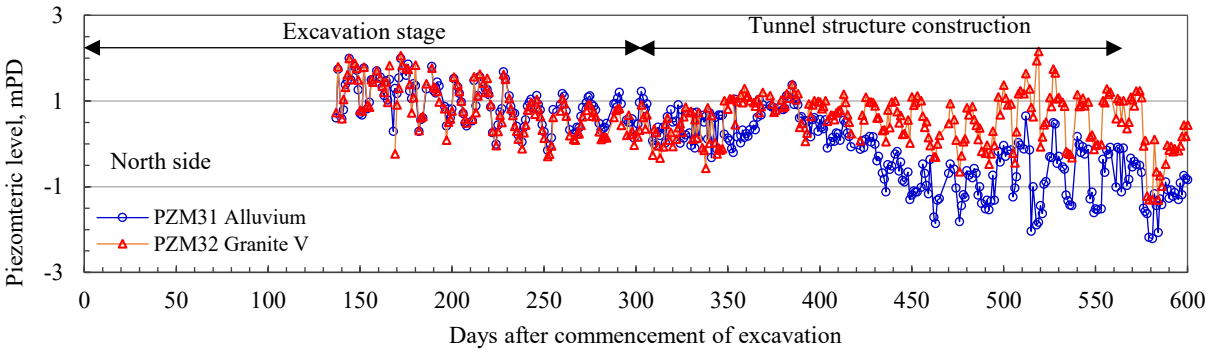

(b) Variation of piezometric levels behind the north pipe pile wall

Figure 3: Variation of the piezometric levels on both sides of Section 11 (after Wong & Ho 2025).

2.4 Struts preloading

Except the level 1 struts S1 was composed of twin-strut of 914x305x289 UB, the level 2 to level 9 struts were composed of twin-steel struts of 914x419x388 UB. These struts had the typical length of 12 m per segment. The twin-struts were installed by connecting the 12 m length modular segments with bolted joints. For the lowest struts S8 and S9 at Section 11, the twin struts were strengthened with steel plates of 25 mm in thickness.

Table 2 summarizes the properties of the struts supporting the excavation at Section 11. The struts of 46 m in length were typically composed of 3 segments of 12 m in length and 2 segments with the knee braces at the strut-waling connections. Struts preloading was applied to the levels 2 to 9 struts. Four hydraulic jacks were used for applying the design strut loads ranging from 11 MN to 16.4 MN. Although the struts were applied to 110 % during the preloading operation, the strut loads were locked-off to around 100 % of the design loads after releasing the applied loads.

Table 2: Strut properties along Section 11

Strut levels	Elevation mPD	Depth below wall top , m	Steel member	Horizontal spacing, m	Preload MN	Stage
S1	2.50	3.3	2-914x305x289 UB	7.0	-	1
S2	-0.50	6.3	2-914x419x388 UB		11.0	2
S3	-3.14	8.9	2-914x419x388 UB		13.7	3
S4	-5.98	11.8	2-914x419x388 UB		15.8	4
S5	-8.82	14.6	2-914x419x388 UB		15.8	5
S6	-11.66	17.5	2-914x419x388 UB		15.8	6
S7	-14.50	20.3	2-914x419x388 UB		15.8	7
S8	-18.90	24.7	2-914x419x388 UB & Plates		16.4	8
S9	-23.30	29.1	2-914x419x388 UB & Plates		16.4	9
Excavation	-32.00	34.5			-	Final

2.5 Observed wall deflections

Figure 4 presents the wall deflection profiles observed at inclinometers INC10N and INC11S, which were immediately behind the north and the south pipe pile walls respectively. The inward wall movements occurred on both sides in the initial stages. In Stage 4, the wall deflections were symmetrical with the maximum inward wall deflections of 43 mm and 42 mm at the north and the south walls respectively.

Starting from Stage 6, the north wall was pushed backward stage by stage. As a results, the net outward wall movements occurred in the later stages. In the final stage, the maximum northward wall deflections at the north and the south walls were -66.8 mm and -91.6 mm respectively. The north wall was pushed outward by the multi rows of struts under the active earth pressures acting behind the south wall. The earth pressure imbalance effect is studied by numerical analysis in Sections 3 and 4. It is noted that in Figure 4, the wall deflections in positive and in negative values denote the southward and the northward wall movements respectively.

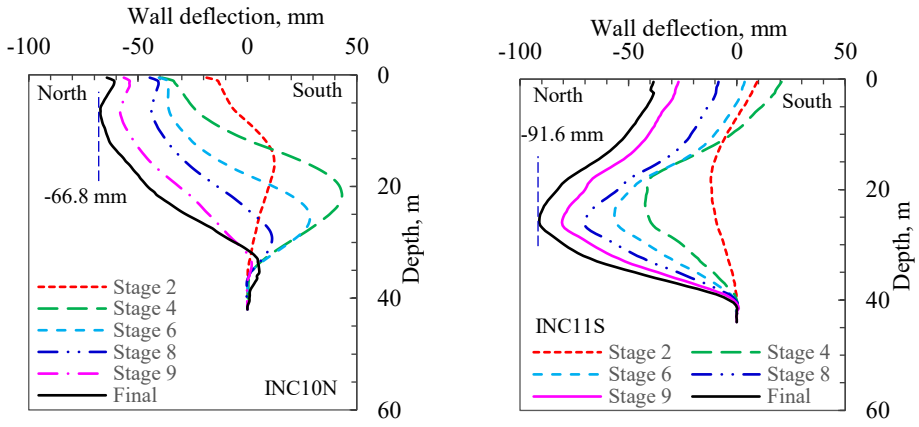

(a) North wall (b) South wall

Figure 4: Observed wall deflection profiles at Section 11 (after Wong & Ho 2025).

3 Numerical Analysis

3.1 Finite element mesh

The 2-Dimensional finite element model for the numerical analysis is depicted in Figure 5. The width of the excavation is 50 m. The excavation is carried out to a depth of 33 m below mean sea level of 1.2 mPD in the analysis. The lateral extent of the finite element model reaches 150 m from the central axis of the trench along the north-south direction. The ground model has the base level of -60 mPD and the diaphragm walls are located at 25 m from the axis of the trench.

The PLAXIS-2D finite element software developed by PLAXIS BV (2013) has become a very popular tool in geotechnical analysis and design. The Hardening-Soil with Small-strain stiffness (HSS) constitutive soil model, an extension of the Hardening-Soil model (Benz 2006, Schanz & Vermeer 1998, Schanz et al. 1999) introduced in the PLAXIS program, is adopted herein to simulate the non-linear stress-strain relationship of soils under loading and unloading conditions.

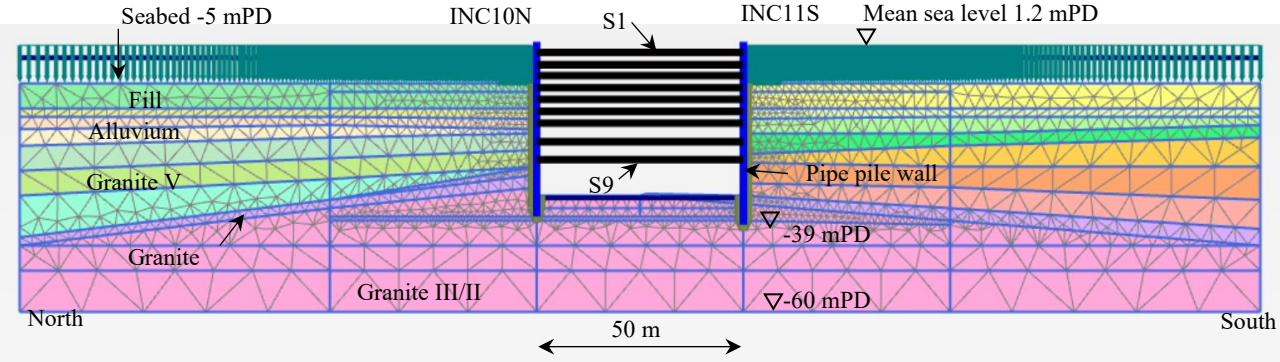

Figure 5: Finite element mesh for the analytical section for 10 stages of excavation.

3.2 Small-strain stiffnesses of soils

As depicted in Figure 2, the excavation trench for the underwater tunnel is supported by fill, alluvium and the granitic saprolite of various degree of decomposition. Ng & Wang (2001) reported the small-strain stiffness for the granitic saprolites measured by the cross-hole seismic tests, the self-boring pressuremeter tests and by the bender element tests. The shear moduli that Ng & Wang (2001) reported are reproduced in Figure 6. The shear moduli obtained by the cross-hole seismic tests are presented in Figure 6a, showing the trend of increase in the shear moduli of the saprolites with depths. The shear moduli measured by the self-boring pressuremeter tests are presented in Figure 6b, showing the degradation of the shear moduli with shear strains.

The shear moduli values for the completely decomposed granite presented in Figure 6b are normalized with the maximum shear moduli obtained by the cross-hole seismic tests and the results are shown in Figure 7. Santos & Correia (2001) recommended that the stress-strain curve for small-strains can be described as:

$$G / G_0 = 1 / (1+ 0.385\, \gamma / \gamma_{0.7}) \quad (1)$$

where the G_0 is the maximum small-strain shear modulus and the $\gamma_{0.7}$ is the threshold shear strain. The G values are the shear moduli mobilizing at various shear strain values of γ. The threshold $\gamma_{0.7}$ values assessed by Equation 1 ranging from 0.8×10^{-3} to 1×10^{-3} are shown in Figure 7. The $\gamma_{0.7}$ value of 0.9×10^{-3} is adopted in this study.

Lu (2021) reported the results of effective shear strength parameters for the completely decomposed granite determined by isotropically consolidated drained triaxial compression tests conducted on Mazier samples. The effective friction angles, the ϕ' values, ranging from 37 degrees to 48 degrees, were obtained. The dilation angles, the ψ' values, range from 4 degrees to 5 degrees. In this study, the lower bound ϕ' values of 37 degrees and the dilation angle ψ'of 4 degrees are adopted. The effective shear strength parameters adopted in the numerical analysis are summarized in Table 3.

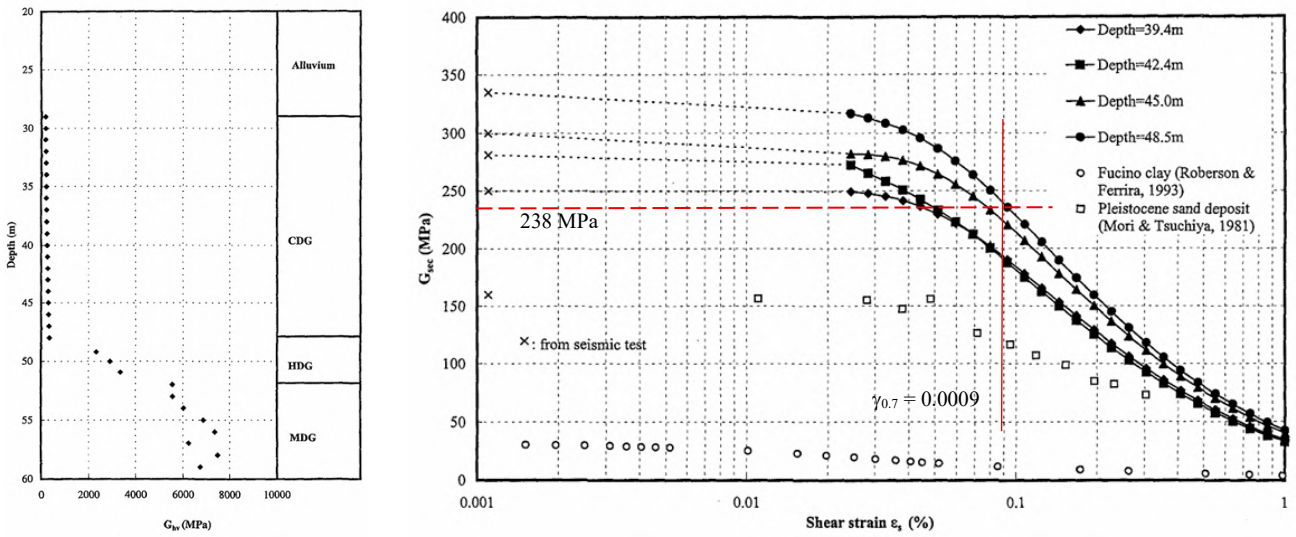

(a) Cross-hole seismic test (b) Self-boring pressuremeter tests

Figure 6: Variation of shear moduli with shear strains for completely decomposed granite. (a) Measured by cross-hole seismic test. (b) Measured by self-boring pressuremeter tests (after Ng & Wang 2001).

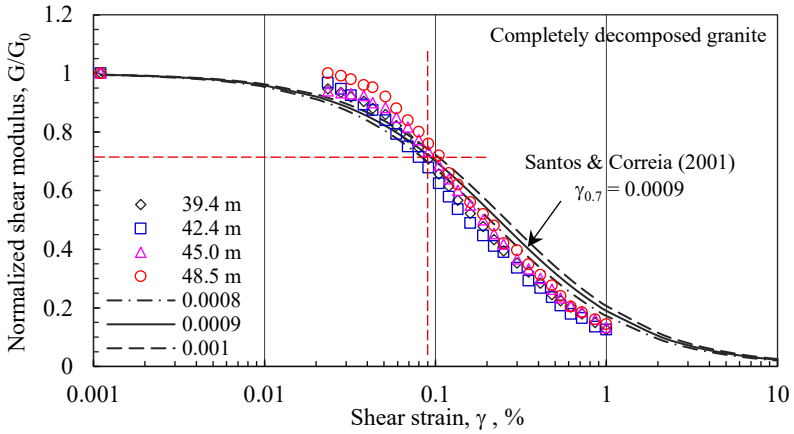

Figure 7: Interpretation for the threshold shear strain by Santos & Correia (2001).

Table 3: Soil parameters for the HSS model adopted in the PLAXIS analyses

Soil strata	Mid depth below seabed m	Unit weight kN/m3	Average N value	Effective shear strength			Reference stiffnesses		Threshold shear strain $\gamma_{0.7}$
				Cohe-sion c', kPa	Friction angle ϕ', deg	Dilation angle ψ', deg	E^{ref}_{50}, E^{ref}_{oed} MPa	E^{ref}_{ur}, G^{ref}_{0} MPa	
Fill	3	18.5	12	1	34	3	16	80	0.0009
Alluvium	8	18.5	14	1	35	3	16	80	0.0009
	11		25	1	35	3	20	100	0.0009
	14		28	1	35	3	24	120	0.0009
Granite V	19	19.0	33	1	37	4	24	120	0.0009
	23		58	1	37	4	27	135	0.0009
	27		80	1	37	4	30	150	0.0009
Granite IV	30	19.6	120	1	39	4	120	600	0.0009
Granite III/II	> 30	20.0	-	50,000	50	4	1,200	6,000	0.0009

The reference shear moduli, the G^{ref}_0 values, adopted for the Granite V, IV and III strata for this study are assessed from the cross-hole test results presented in Figure 6a according to the depths from the seabed. The G^{ref}_0 values for the alluvium and the sand fill strata are assessed by extrapolating the trend line in Figure 6a to the shallow depths.

3.3 Modeling of the retaining structures

The excavation scheme and the retaining structures are depicted in Figure 2. The intermittent steel pipe pile wall is simulated by plate element and an E_s value of 205,000 MPa is adopted. The estimated flexural rigidity (denoted as E_sI_s where I_s is the moment of inertia) and the axial stiffness (denoted as E_sA_s where A_s is the sectional area) of the pipe pile wall of 813 mm in diameter and 25 mm in thickness with the H-pile of 305x305x238 kg/m UB are 5,860 MNm^2/m and 21,000 MN/m respectively.

3.4 Modeling of the earth and water pressures imbalance

In the case histories that Moh & Hwang (1997) and Wong & Yong (2016) reported, the earth-pressure imbalance were caused by the inclined rockhead. During the preliminary analysis of this study adopting the inclined rock head of Granite III-II, it was found that the inward wall movements were computed both at the north and at the south walls. The outward wall movements observed at the north wall in various stages that shown in Figure 4a could not be obtained by the analysis.

The earth-pressure imbalance and the outward wall movements could be attributed to the difference in the lengths of the north and the south pipe pile walls along the longitudinal direction. Figure 1 shows that the horizontal alignment of the north and the south walls measuring from the existing seawall to the bulkhead have the radius of curvature of 310 m and 360 m respectively. The chord lengths of the north and the south walls are 190 m and 225 m respectively. The earth and water pressures that could be mobilized along the north wall would be 84 % of that develop along the south wall.

The curved alignment of the excavation trench may be analyzed by the 3-Dimensional model. However, modeling the inclined rockhead has been challenging. In this study, the 2-Dimensional finite element model is adopted to analyze the curved trench excavation. To simulate the difference in pressures between the north and the south walls, the earth and water pressures along the north wall is reduced to 84 % by using the equivalent unit weight of 11.9 kN/m^3 for the fill and the alluvium strata on the north side of the trench. For the completely decomposed and the highly decomposed granite, the unit weight of 12.1 kN/m^3 is adopted for these strata on the north side of the trench.

3.5 Cases studied

As reported in Section 2.4, the strut loads ranging from 11 MN to 16.4 MN were applied to the level 2 to level 9 struts. The struts preloading would cause backward wall movements and loss of the applied loads for the nearby preloaded struts. Based on the observed field performance of an excavation case history, Hwang & Wong (2018) suggested that 50 % of the applied strut loads shall be adopted in analysis. The Author further observed in this case history that during struts preloading, gaps around 10 mm in width occurred between the waling and the pipe pile wall at the nearby struts on the same level and on the upper level.

In this study, 4 cases have been computed to analyze the effect of loss of applied strut loads. Case 1 adopts 10 % of the applied preloads that presented in Table 2. Case 2, Case 3 and Case 4 adopt 70 %, 50 % and 30 % of the applied preloads respectively.

4 Analysis Results

4.1 Case 1

The computed wall deflections for Case 1 adopting 10 % of the applied preloads for the north and the south walls are presented in Figure 8. The computed deflection profiles show that the maximum outward movements are larger than the maximum inward movements at the north wall starting from Stage 6. It is noted that the positive and the negative deflections denote the southward and the northward wall movement respectively.

Figure 8(g) shows that the computed maximum wall deflection for the north wall in the final stage is -68.1 mm, which is close to the observed maximum deflection of -66.8 mm, with the deviation of 1.3 mm. For the south wall, Figure 8(h) shows that the computed maximum deflection in the final stage is -89.9 mm, which deviates from the observed value of -91.6 mm by 1.7 mm. The computed maximum wall deflections, which deviate within 2 % of those observed, are in close agreement with the field observations.

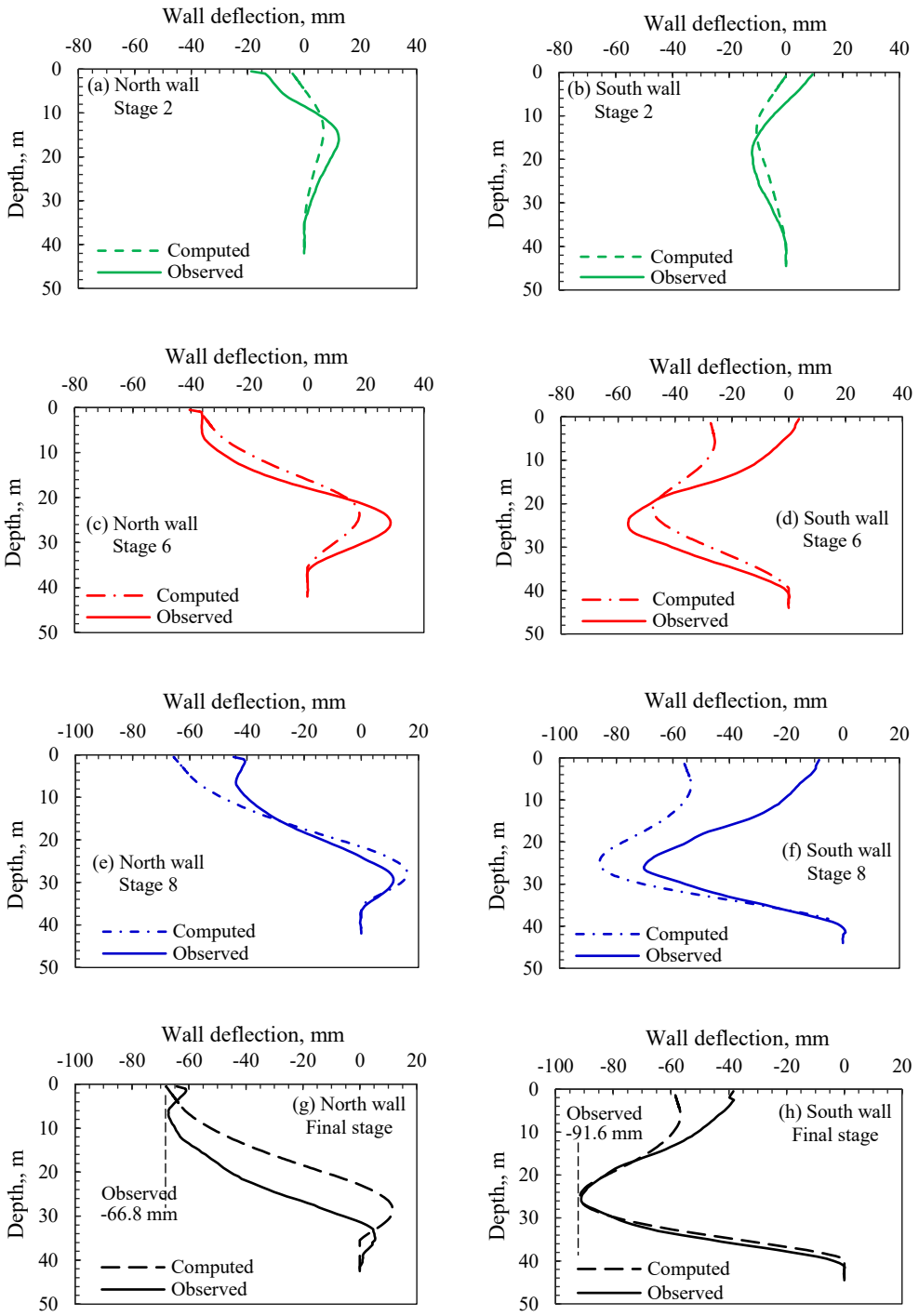

Figure 8: Computed and observed wall deflection profiles for north and the south walls in various stages for Case 1.

4.2 Loss of applied strut loads

The computed wall deflections in the final stage for Case 1, Case 2, Case 3 and Case 4 adopting 10 %, 70 %, 50 % and 30 % of the applied preloads respectively are presented in Figure 9, which shows the development of the wall deflections in the north and the south walls. Figure 9(a) shows that at the north wall, the -66.8 mm observed maximum deflection would occur at around 60 % of the applied strut loads in the final stage. On the other hand, Figure 9(b) shows that the 10 % applied strut loads would induce the observed maximum wall deflection of -91.6 mm at the south wall in the final stage.

It is inferred that the 60 % of the applied strut loads pushed the north wall backward to the maximum deflection of -66.8 mm in the final stage. The backward movements of the north wall reduced the strut loads

acting on the south wall from 60 % to around 10 %. The loss of the applied strut loads caused the maximum inward movements of -91.6 mm at the south wall in the final stage.

Based on the wall deflection profiles observed in the inclinometers, Wong & Ho (2025) reported that the inclined rockhead level induced the earth-pressure imbalance effect. In this study, the numerical analysis results demonstrate that the phenomenon of outward wall movements is mainly attributable to the difference in the chord lengths of the north and the south walls along the longitudinal direction of the excavation trench.

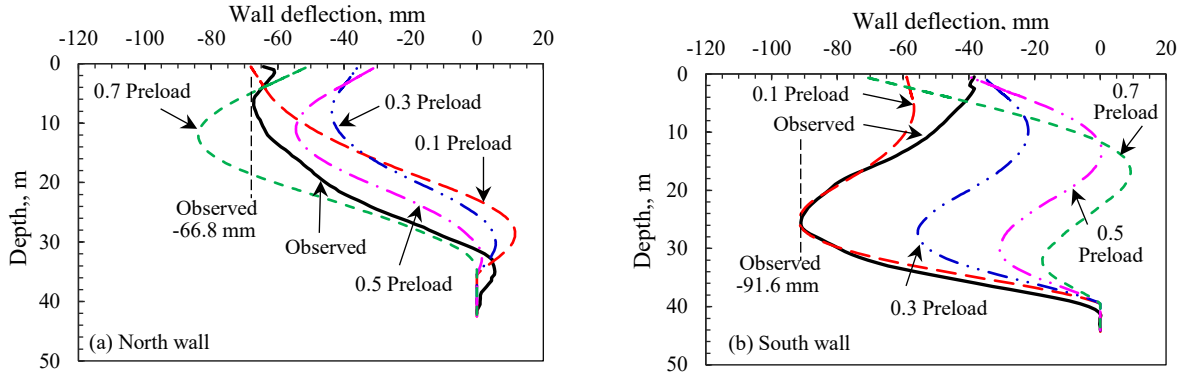

Figure 9: Preloading effect to wall deflections for the north and the south walls in the final stage.

5 CONCLUSIONS

Based on the wall deflection profiles measured in inclinometers installed on the opposite sides of the excavation trench of a cut-and-cover tunnel, the earth-pressure imbalance effect has been observed. This issue is very complicated and can only be sorted out by numerical analyses. Results of 2-Dimensional analysis have the following findings:

(1) In addition to the effect of inclined rockhead, the difference in the chord lengths of the walls on both sides of the curved excavation trench induced the earth-pressure imbalance effect and the outward wall movements.

(2) The wall with the longer chord length pushed back the wall on the opposite side and caused the outward movements of the wall with the shorter chord length.

(3) The preloading effect and the loss of the applied strut loads due to wall movements play a crucial role on the performance of wall deflections. Due to the outward wall movements occurring on one side, the strut loads could be reduced to as low as 10 % of the applied preloads.

(4) The soil stiffness parameters for the granitic saprolites adopted in this study were measured by the cross-hole seismic tests and the self-boring pressuremeter tests reported in literature. The close agreement between the observed and the computed wall deflections validates the set of stiffness parameters.

This study employs the method of reduction in soil unit weights to simulate the difference in earth and water pressures between two sides of the excavation trench. In the next study, the axisymmetric model could be established to analyze the walls with curved alignment and to verify the 84 % reduction in earth and water pressures on one side that adopted in this study. For walls under earth-pressure imbalance conditions, loss of preloads to as low as 10 % of the specified strut loads shall be allowed in the wall deflections estimation. Proper understanding the mechanism causing the asymmetrical wall deflections and outward wall movements, the design and construction of underground infrastructures could be refined and the cost-effective solutions to engineering challenges could be formulated.

REFERENCES

Bentley. 2022. *PLAXIS 2D-Reference Manual*. CONNECT Edition V22.02, Bentley Advancing Infrastructure, August 2022.

Benz, T. 2006. Small-strain stiffness of soils and its numerical consequence. *Dissertation of thesis*, the Institute of Geotechnics, University Stuttgart.

Hwang, R.N. and Wong, L.W. 2018. Effects of preloading of struts on retaining structures in deep excavations. *Geotechnical Engineering Journal of the SEAGS & AGSSEA* ,Vol. 49, No. 2, June 2018: 104-114. ISSN 0046-5828.

Lu, K.K. 2021. Experimental study and constitutive modelling of the stress-strain behaviour of Hong Kong soils. *Thesis for the degree of Doctor of Philosophy*. The Hong Kong Polytechnic University, Department of Civil and Environmental Engineering. June 2020. 329 pages.

Moh, Z.C. & Hwang, R.N. 1997. Geotechnical problems related to design and construction of the Taipei Transit Systems. *Proc. of Keynote Speech, Professor Chun Fung Kee Memorial Lecture*, September 6, 1997, Kuala Lumpur, Malaysia.

Ng, C.W.W. & Wang, Y. 2001. Field and laboratory measurements of small strain stiffness of decomposed granites. *Soils and Foundations*, Japanese Geotechnical Society, Vol. 451, No. 3, 57-71, June 2001: 57-71.

PLAXIS B.V. 2013. *PLAXIS Reference Manual*. PLAXIS, BV, Delft, the Netherlands.

Santos J.A. & Correia, A.G. 2001. Reference threshold shear strain of soil. Its application to obtain a unique strain-dependent shear modulus curve for soil. *In 15th Int. Conf. SMGE*, Volume 1, Istanbul, A.A. Balkema: 267-270.

Schanz, T. & Vermeer, P.A. 1998. On the stiffness of sands. *Geotechnique,* 46, No. 1: 145-151.

Schanz, T., Vermeer, P.A. & Bonnier, P.G. 1999. The hardening soil model: formulation and verification. *Beyond 2000 in Computational Geotechnics*. Rotterdam, the Netherlands: 281-290.

Wong, L.W. & Yong, C.C. 2013. Earth pressure imbalance on deep excavation. *Advance in Geotechnical Infrastructure, 18th Southeast Asian Geotechnical Conference*, May, Singapore: 275-281.

Wong, L.W. and Ho, Y.N. 2025. Influence of imbalance of earth-pressure on wall deflections on a deep excavation. *Proceedings*, 45th HKIE Geotechnical Division Annual Seminar, Hong Kong, May 2025: 320-331.

Development of Sprayable Engineered Cementitious Composites (SECC) for Tunnel Lining Applications

S.N. Goh, K.L. Lo, Ivan H.H. Chan & Roy K.C. Hung
Geotechnical Engineering Office, Civil Engineering and Development Department

T. Wang & H. Wu
Formerly Department of Civil and Environmental Engineering, The Hong Kong University of Science and Technology

Christopher K.Y. Leung
Department of Civil and Environmental Engineering, The Hong Kong University of Science and Technology

Victor C. Li
Department of Civil and Environmental Engineering, University of Michigan

ABSTRACT

Engineered cementitious composites (ECC), pioneered by Li & Leung (1992) and Li (1993), are characterised by tensile strain-hardening, multi-cracking response and self-healing capacity, delivering exceptional ductility, durability and sustainability for civil infrastructure. A study was launched in 2021 by the Geotechnical Engineering Office (CEDD) to develop a sprayable ECC (SECC) for tunnel lining in mixed ground and hard rock conditions. This paper outlines the theoretical basis, mix design, and mechanical performance of SECC, with emphasis on findings from the scale-up production and site spray trials at the Joint Cavern Development, Anderson Road Quarry Site, in Phase II. Results confirm SECC's feasibility and highlight key process-control considerations, with recommendations for optimising mixing and spraying methods to enhance its suitability for tunnel lining in Hong Kong. As ECC's ductile, strain-hardening behaviour extends beyond the linear-elastic–perfectly-plastic framework codified in local practice, its full utilisation will depend on progressive refinements in structural design methodology, ensuring future frameworks evolve to capture its potential.

1 INTRODUCTION

1.1 Background of the study

Engineered Cementitious Composites (ECC) refers to a class of ultra-ductile fibre-reinforced cementitious composites characterised by tensile strain-hardening, multi-cracking and self-healing properties. Unlike common fibre-reinforced concrete (FRC), ECC is designed using fundamental principles of fracture mechanics and micromechanics to analyse and utilise the fibre bridging property, thereby controlling the formation of steady-state flat microcracks across the matrix (Li, 2003). Meticulous calibration of the fibre-matrix-interface characteristics is often required to design and manufacture an ECC mix (Li, 2003). These engineered attributes have enabled widespread applications of ECC in infrastructure projects across the United States, Japan, and the Chinese Mainland, as well-documented by (Li, 2019), demonstrating its contributions to more resilient, durable and sustainable urban development.

In sprayed concrete applications for tunnel linings, ECC would be applied as a thinner overlay on the rock substrate when comparing to traditional cast-in-situ concrete structures. Depending on the ground conditions, the lining may need to withstand bending arising from earth loads and local instabilities (e.g. rock wedges, fault zones, etc.), inducing primarily flexural tensile stresses. This demands tailored mix formulations to ensure sprayability while maintaining structural integrity under bending. Self-controlled, tight crack width of ECC is advantageous for water impermeability in underground facilities. Further, dimensional stability and vibration resistance are necessary for the successful deployment of ECC in tunnel lining applications.

1.2 Objectives of the study and structure of this paper

Motivated by the limited adoption of ECC in Hong Kong—primarily in a housing project as repair mortar (see (Li, 2019), Chapter 9, Section 9.2.3.1)—and the unique challenges of tunnel and cavern environments, the Geotechnical Engineering Office (GEO) of the Civil Engineering and Development Department (CEDD) initiated a developmental project on Sprayable Engineered Cementitious Composites (SECC) that preserve core ECC properties while meeting tunnelling-specific demands. This study has two primary objectives: (i) to conceptualise, design and produce suitable SECC mixes using locally available materials; and (ii) to evaluate end-to-end logistics from scale-up production at a concrete batching plant to on-site spraying. This paper presents key findings addressing both objectives, emphasising the benefits of SECC linings, while discussing study limitations, potential challenges and practical recommendations for future large-scale, routine applications.

2 DESIGN OF SECC MIXES

2.1 Mix conceptualisation and formulation

This study adopted a performance-oriented, iterative approach to SECC design for tunnel linings, targeting balanced sprayability, early-age build-up, mechanical performance, self-healing, and self-stressing, building on knowledge gained from prior research on self-stressing ECC (Zhu et al, 2021). Self-stressing is induced by the controlled expansion of the ECC mix (during curing) restrained by a structural boundary or a rock substrate. Baseline ECC formulations were first developed in the laboratory to achieve fresh-state deformability, setting, and tensile strain-hardening. Key parameters—calcium sulfoaluminate (CSA)/binder ratio, water-to-binder ratio, sand content, and superplasticizer dosage—were systematically adjusted to optimise deformability, penetration resistance, and strength development, capitalising on CSA's high early-age reactivity. OPC served as the primary binder, with CSA added for early hydration and self-stressing control, while ground granulated blast-furnace slag (GGBS) or pulverized fly ash (PFA) and mesh 80–120 quartz sand were incorporated to enhance durability, sustainability and cost-effectiveness. Addition of polyvinyl alcohol (PVA) fibres (Kuraray, Japan; properties in Table 1) ensured composite tensile ductility, fibre dispersion, and tight crack-width control.

Selected mixes were then subjected to laboratory trials, with further modifications including expansion agents, anhydrite, shrinkage-reducing agents, viscosity-modifying admixtures, and retarders to improve volume stability, crack control, build-up thickness, and spraying operability under practical conditions.

For laboratory mixing, all mixes were prepared in a Hobart mixer following a standardised procedure: (i) dry mixing of solid materials for 5 minutes; (ii) addition of water and mixing for 2 minutes; (iii) fibre incorporation and mixing for 3 minutes; and (iv) addition of superplasticizer and mixing for 2 minutes. For chemical admixtures, other than super-plasticisers, hydroxypropyl methylcellulose (HPMC; Alfa Aesar, viscosity 7500–14,000 mPa·s) was added at 0.1% to 0.3% of binder for viscosity modification.

Table 1: Nominal properties of polyvinyl alcohol (PVA) fibre

Length (mm)	Diameter (μm)	Aspect ratio	Elastic Modulus (GPa)	Fibre strength (MPa)	Fibre density (g/cm3)
12	39	308	40	1600	1.30

The final SECC mixes–one with GGBS and another with PFA–are summarised in Table 2 below. The selected mixes exhibited satisfactory sprayability, controlled stiffening suitable for build-up, 28-day mean compressive strength in the approximate range of 45 MPa to 55 MPa, tensile strain-hardening performance with strain capacities exceeding 1.5-2.0%, and tight crack-width control conducive to self-healing.

Table 2: Mix proportions of the final selected SECC (mass ratio, PVA fibre vol. ratio 0.02)

Mix ID	OPC	CSA	SCM*	Water	Sand	HPMC	SP
GGBS-ECC	0.65	0.35	1.0	0.90	0.72	0.003	0.002
PFA-ECC	0.70	0.30	2.0	0.80	0.80	0.001	0.002

* SCM means supplementary cementitious materials, referring to either GGBS or PFA.

2.2 Functional mechanisms of SECC for tunnel lining applications

In principle, SECC shall maintain structural integrity subject to impact loading, while simultaneously limiting crack-induced durability degradation (Khandelwal & Singh, 2009, Koo et al., 2013, Ding et al., 2020). Self-healing and self-stressing behaviours are thus introduced as complementary functional mechanisms, targeting long-term durability and early-age crack control, respectively. These mechanisms are discussed below to elucidate their engineering implications in tunnel lining applications.

2.2.1 Self-healing mechanism

During tunnelling construction, impact loading from blasting or mechanical excavation, together with early-stage tunnel convergence, may induce cracking in lining materials, accelerating water and chemical ingress and compromising durability. While residual mechanical capacity is essential for structural safety, the ability to autonomously seal cracks after damage is equally critical for long-term performance. Impact tests were performed using pendulum loading (drop heights 0.92 m to 1.28 m) and Split Hopkinson Pressure Bar (SHPB) (impact speeds from 2 m/s to 6 m/s) calibrated through numerical modelling of tunnel blasting. Owing to ECC's strain-hardening behaviour and multiple microcracking, most induced cracks remained narrow (in μm) and exhibited satisfactory residual performance in compression, tension, bending and bonding. Crack-width evolution was subsequently monitored under continuous moisture exposure and wet–dry cycling (two days per cycle, with wet curing as the initial step).

Figure 1(a) below presents the evolution of average crack width with curing age under different exposure conditions. Under continuous moisture exposure, crack widths remain nearly unchanged even after prolonged curing, indicating negligible self-healing. In contrast, specimens subjected to wet – dry cycling exhibit pronounced crack closure, with fine cracks (initial widths ⩽ ~127 μm) being fully sealed after several cycles. Representative visual observations of crack evolution are shown in Figure 1(b) to (d), which illustrates the absence of visible healing under moisture exposure and effective crack sealing achieved under wet–dry cycling.

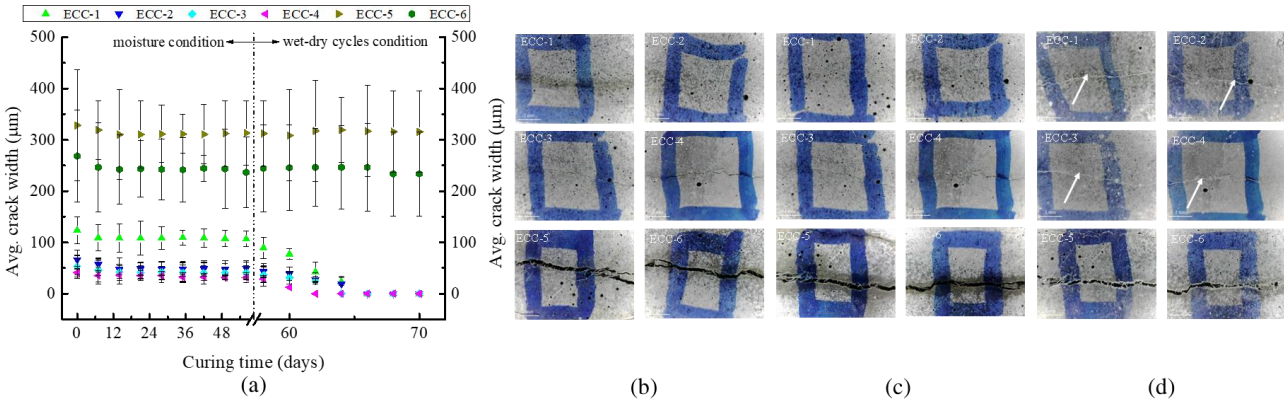

Figure 1: (a) Variations of average crack width with curing ages; and self-healing phenomenon of cracked ECC-specimens (b) 7-day in moisture exposure, (c) 56 days in moisture exposure, and (d) 7 cycles in wet-dry exposure

The underlying self-healing mechanisms were further examined through microstructural characterisation. Scanning electron microscopy (SEM) images of healed cracks (Figure 2(a)) revealed that healing products densely fill the crack surfaces and progressively bridge opposing crack faces. Energy-dispersive X-ray (EDX) analysis of the healing products (Figure 2(b)) indicated that Ca, Si, C, and O are the dominant elements, confirming that the primary healing phases consist of calcium silicate hydrate (C–S–H) and calcium carbonate. These products originate from continued hydration of unreacted cementitious materials and carbonation-induced precipitation during wet–dry cycling.

The concentration of healing products near the crack surface explains why surface crack closure is dominant, while deeper crack regions remain largely unhealed. Nevertheless, sealing of surface-connected cracks is sufficient to significantly reduce permeability and limit water and ion ingress, thereby enhancing durability. The high ductility, multiple micro-cracking behaviour, and tight crack width control of ECC strongly facilitate this

autogenous self-healing process, as narrower cracks require fewer healing products and enable more efficient crack closure (Ghosh, 2009; Van Tittelboom & De Belie, 2013, Yang et al., 2011).

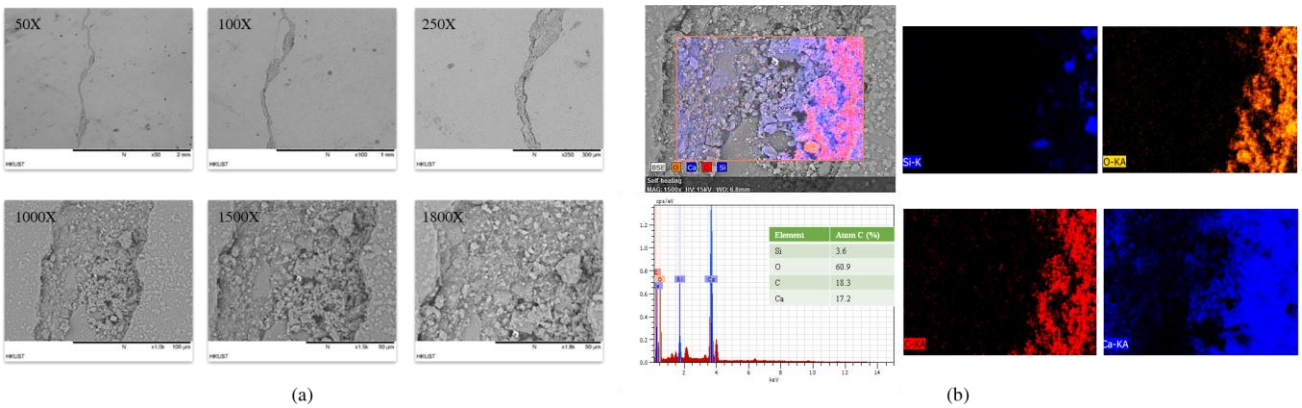

Figure 2: (a) SEM images of self-healed crack (magnification from 50 to 1800 times); and (b) EDX analysis on the self-healing materials

2.2.2 Self-stressing mechanism and volume stability control

In addition to self-healing, self-stressing behaviour was introduced to mitigate shrinkage-induced cracking and improve early-age structural integrity of SECC. The design of self-stressing SECC followed established approaches using CSA-based expansive components (Zhu et al., 2021). Figure 3 illustrates the typical free expansion behaviour of self-stressing ECC mixes with varying CSA contents. Increasing CSA content led to enhanced early-age expansion, with most expansion occurring within the first few days.

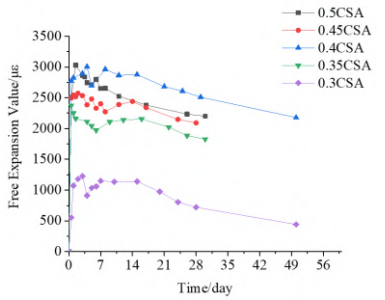

Figure 3: Free expansion/shrinkage measurement of ECC mixes

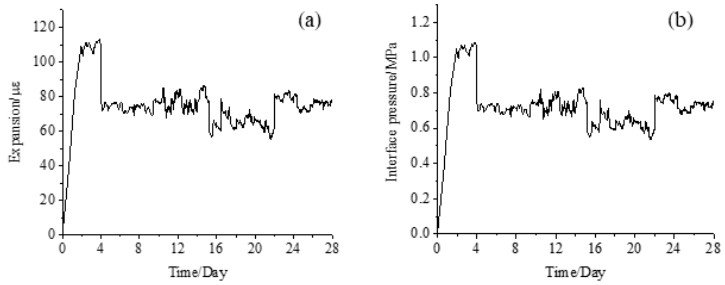

Figure 4: (a) Expansion and (b) interface pressure in the steel ring tests

To evaluate the effectiveness of expansion under restrained conditions, ECC was cast inside a steel ring. Figure 4 above shows the measured expansion of the steel ring and the corresponding interface pressure generated by the expansive ECC. The results confirmed that the early-age expansion translated into beneficial compressive pressure at the ECC–steel interface, indicating improved contact and load transfer under restraint. This phenomenon effectively serves as a self-induced mechanical coupling between the sprayed ECC layer and the surrounding restraint. Importantly, the incorporation of expansive components did not compromise the strain-hardening behaviour of ECC, demonstrating that self-stressing and tensile ductility could be achieved simultaneously.

2.3 Mix refinement for sprayability and build-up capacity

Beyond functional mechanisms, practical application of SECC requires adequate sprayability and build-up capacity during construction. Figure 5 compares the maximum achievable build-up thickness before and after mix refinement. The optimised SECC exhibits a one-time build-up thickness exceeding 60 mm, compared with

approximately 25 mm for the unmodified mix. According to Qian et al. (2025), tunnel lining materials should achieve a minimum one-time build-up thickness of 40–50 mm to ensure construction efficiency and structural integrity. The refined SECC mixes therefore satisfy practical construction requirements and are suitable materials for spray-applied tunnel lining applications. Sprayability and build-up capacity were further assessed in the scale-up production trial and site spray trial as discussed in Section 3 and Section 4 respectively.

Figure 5: Improvement of sprayability and build-up capacity through laboratory trials

3 SCALE-UP PRODUCTION AT A CONCRETE BATCHING PLANT

To test and verify the quality and consistency of the two SECC mixes in a large-scale production, two scale-up production trials were conducted at Shunde Lunjiao Quon Hing Construction Material Company (Figure 6(a)).

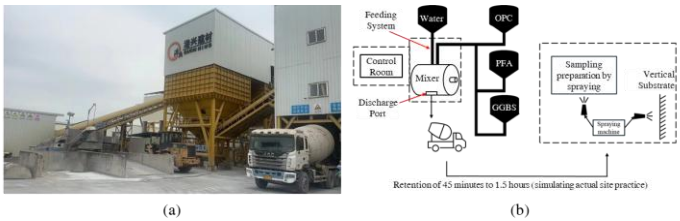

Figure 6: (a) Quon Hing concrete batching plant in Foshan; and (b) schematics of scale-up production

Table 3: Mix proportions (mass ratio, PVA fibre vol. ratio 0.02), each in a volume of 1.2 m^3

Mix ID	OPC	CSA	SCM	Water	Sand	HPMC	SP
GGBS-ECC	0.65	0.35	1.00	0.90	0.72	0.003	0.002
PFA-ECC	0.70	0.30	1.20	0.80	0.80	0.001	0.002

The scale-up production consists of two stages: (i) plant mixing of two SECC mixes developed at HKUST Concrete Laboratory; and (ii) an investigation of the mechanical and applicational properties of the SECC mixes produced. The previous mix design and constituent material proportions in the SECC mixes were further optimised and calibrated based on laboratory performance. All materials were sourced from Foshan, the Chinese Mainland, and supplied by Quon Hing. These constituent materials demonstrated equivalent physical and chemical properties to those employed in the laboratory mix design stage (Section 2) and the site trial stage (Section 4).

The mix compositions are summarised in Table 3 above. For chemical admixtures, a shrinkage-reducing agent (SRA from Sobute, shrinkage reduction rate 30%) and an expansion agent (EA from TUNIU), which mainly consist of CSA and anhydrite (from LeiXin, with $CaSO_4$ content of over 95% and water content of less than 0.5%), were employed.

The schematic diagram of the scale-up production is shown in Figure 6(b) above. The OPC, GGBS, and PFA are in stock at the concrete batching plant and can be fed into the mixer through the feeding system. The other dry materials including sand, PVA fibre and various additives are manually added into the mixer. The moulds for sample preparation through spraying method are placed in an orderly manner on site (Figure 7(a)). The vertical substrates used to simulate practical spraying work are shown in Figure 7(b).

(a) (b)

Figure 7: (a) Moulds for test specimens and (b) vertical wall substrates

3.2 Flexure and energy absorption (toughness) performance

Flexure tests were performed in accordance with ASTM C1609. A Shanghai SUNS UTM2502 Electromechanical Universal Testing Machine was used for this test. The load-central deflection curves for the two SECC mixes are shown in Figure 8. Multiple cracks were observed across the test specimens as shown in Figure 11(a) below.

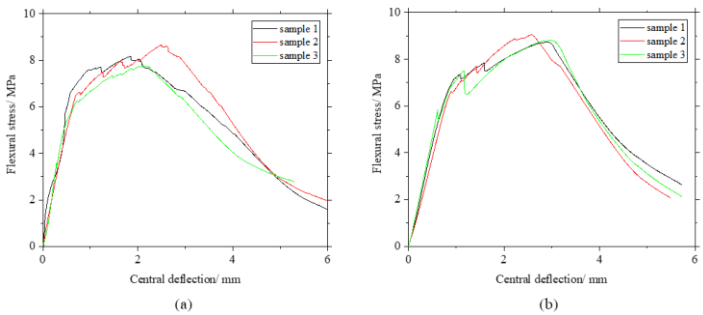

Figure 8: Flexural stress versus central deflection curves for (a) GGBS-ECC and (b) PFA-ECC beams

Table 4 shows the comparison of mean values of the flexural parameters of SECC samples prepared in laboratory and at the concrete batching plant. The plant specimens exhibited higher first-peak load (P_1) and peak load (P_p) than the laboratory specimens. The residual strength at deflections of L/600 and L/150 were also higher for the plant specimens. The toughness parameters, which is the area under the load-deflection curve up to L/150, T_{150}^{D} for the plant specimens are approximately 97.4% and 90.3% of their corresponding laboratory samples' values. This indicates comparable flexural performance between the scale-up production and the laboratory production of the two SECC mixes.

Table 4: Flexural performance comparison between laboratory and scale-up production (plant)

Test Items	Mean value of GGBS-ECC(plant)	Mean value of PFA-ECC(plant)	Mean value of GGBS-ECC(lab)	Mean value of PFA-ECC(lab)
$\boldsymbol{P_P}$, N	27298.7	29545.8	26101.67	25852.41
$\boldsymbol{f_P}$, MPa	8.19	8.86	7.83	7.75
$\boldsymbol{\delta_P}$, mm	2.16	2.81	2.47	2.05
$\boldsymbol{P_1}$, N	22644.33	23919.40	20088.88	18674.02
$\boldsymbol{f_1}$, MPa	6.79	7.17	6.03	5.60
$\boldsymbol{\delta_1}$, mm	0.81	1.05	0.41	0.35
$\boldsymbol{P_{600}^{D}}$, N	18135.23	14326.47	21093.34	20369.27
$\boldsymbol{f_{600}^{D}}$, MPa	5.44	4.30	6.33	6.11
$\boldsymbol{P_{150}^{D}}$,MPa	26409.4	27273.6	22806.32	24993.12
$\boldsymbol{f_{150}^{D}}$, N	7.92	8.18	6.84	7.50
$\boldsymbol{T_{150}^{D}}$, J	40.8	38.35	41.90	42.45

For energy absorption capacity, the SECC samples were tested in accordance with BS EN 14488-5. A single portal frame with maximum load of 50 tons from Hangzhou POPWIL was used in this test. Test results, including load-deflection curves and energy absorption capacity-deflection curves , are shown in Figure 9 and Figure 10 below. The peak loads for PFA-ECC square panels ranged from 101.3 kN to 108.5 kN, while absorbed energy up to 25 mm deflection was 1722 J to 1904 J (1.7–1.9 times the EFNARC Class C/NGI Class E1000 value of 1000 J). For GGBS-ECC panels, peak loads were 96.9 kN to 99.2 kN, with absorbed energy of 1382–1786 J (1.4–1.8 times Class C).

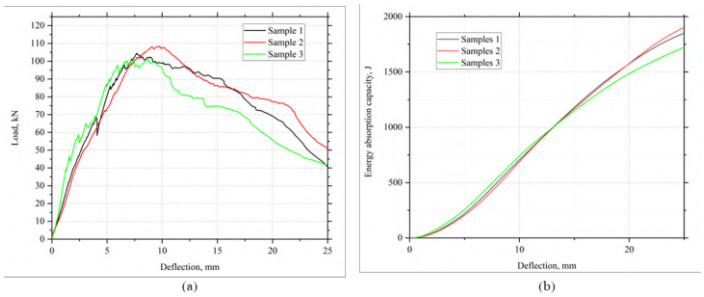

Figure 9: (a) Load versus deflection curves and (b) energy absorption capacity versus deflection curve for PFA-ECC

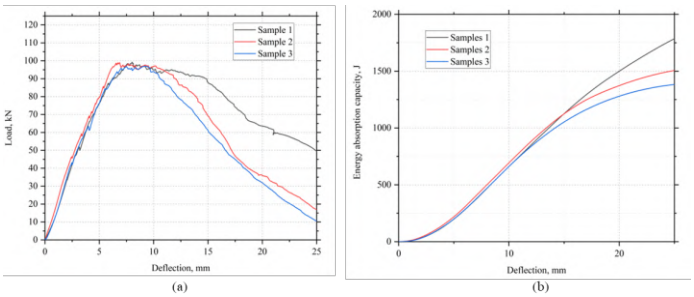

Figure 10: (a) Load versus deflection curves and (b) energy absorption capacity versus deflection curves for GGBS-ECC

Multiple cracks can be seen on all side-faces of the ECC square panels during and after the test (Figure 11(b)). There were no obvious cracks on the compressed surface, but several large cracks appeared on the backside, surrounded by numerous small radial cracks. However, these cracks did not penetrate through the specimen, and the specimen did not break into multiple pieces even after unloading, allowing the panels to withstand a certain load before loss of stability and retain load-bearing capacity.

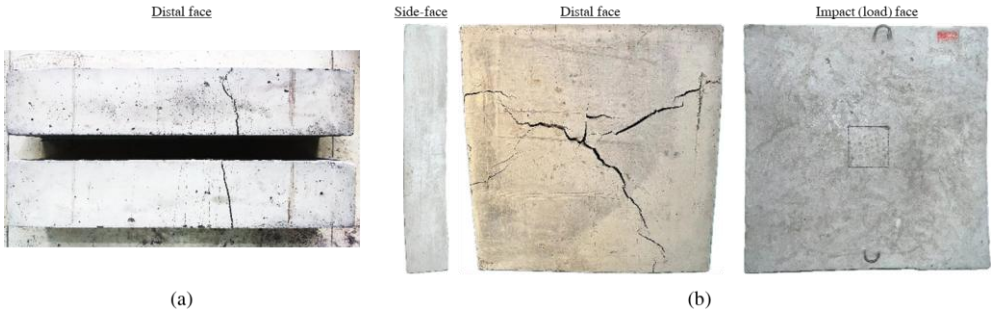

Figure 11: Multiple cracks in (a) flexure test specimens, and (b) panel test specimens in the scale-up production trial

As shown in Figure 12(a) below, test results indicate that plant-produced GGBS-ECC and PFA-ECC panels exhibited strong energy absorption, achieving EFNARC Class C/NGI Class E1000. Average energy absorption capacities were 1558 J for GGBS-ECC (plant) and 1825 J for PFA-ECC (plant), exceeding laboratory samples by 17.7% and 26.8%, respectively. Overall, it shows that the scale-up production trial preserved the designed SECC mixes' performance with notable enhancement.

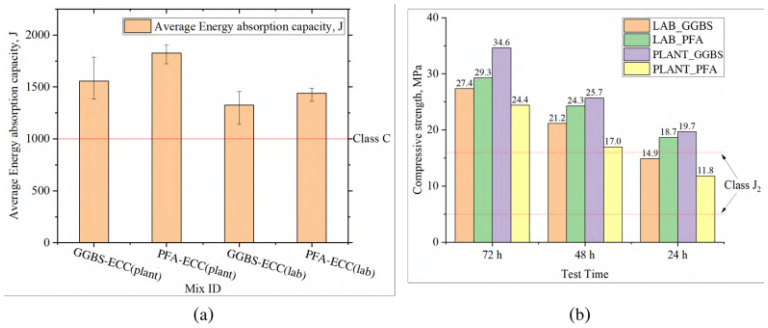

Figure 12: (a) Average energy absorption capacities, and (b) early-age compressive strength results

3.3 Early-age compressive strength

Cube samples were tested at the ages of 1 day, 2 days and 3 days in accordance with BS EN 12390. A Shanghai SUNS YAW-2000 hydraulic testing machine was used for this test. Figure 12(b) above compares compression test results between laboratory and plant specimens. Plant GGBS-ECC specimens showed notably higher compressive strength than laboratory ones, while plant PFA-ECC specimens were slightly lower. Variations may have arisen from cube casting workmanship, mixing quality or related factors. Overall, all specimens met Class J2 requirements per BS EN 14487-1 based on 1-day compressive strength.

4 SITE SPRAY TRIAL

4.1 Site spray trial at the Joint Cavern Development project site

Considering the foreseen shortage of PFA supply in Hong Kong, only one site spray trial was conducted for the GGBS-ECC mix inside the caverns of the Joint Cavern Development at the Anderson Road Quarry Site Project. Glorious Concrete Ltd (Glorious) supplied the required GGBS-ECC mixes for this trial. The concrete batching plant is located in Tuen Mun (Figure 13), with a production capacity of 3000 cubic metres per day.

Figure 13: Concrete batching plant of Glorious Concrete Ltd in Tuen Mun

The proportions of the GGBS-ECC mix used in this trial are summarised in Table 5. To refine the mix design suited to the use of local constituent materials supplied by Glorious, the transportation time (roughly 50 minutes) and the use of an accelerator (BASF SA167 in a mass ratio of 0.06 for fast-setting and expansion control) in the spraying machine were also considered, and an additional laboratory trial was conducted before scale-up production.

Table 5: Mix proportions of GGBS-ECC (mass ratio, PVA fibre vol. ratio 0.02) in a volume of 3 m^3

ID	OPC	CSA	GGBS	Water	Sand	HPMC	SP
GGBS-ECC	0.95	0.05	1.00	0.81	0.72	0.001	0.007

4.2 Set-up of the site spray trial

The site spray trial was designed primarily for testing sprayability and uniformity, as well as adhesiveness of the GGBS-ECC lining to rock substrates up to a certain design thickness (e.g., 10 cm, Table 5). A rock surface panel (representing a wall scenario) and a steel frame with a set of two vertical panels, a set of two inclined panels at

45 degrees to the horizontal and a set of two overhead panels (representing a tunnel crown scenario) were adopted to simulate a full tunnel/cavern setting as shown in Figure 14(a). In practice, the actual thickness varies with overall profile roughness and unevenness. The Normet Spraymec 8100 VC used in routine industrial operation was adopted for this trial, as shown in Figure 14(b).

Table 5: Dimensions of spraying test set-up

Test Set-up	Panel Dimensions
Rock surface panel	4500 × 1500 × 100 mm
Steel frame	1200 × 1200 × 300 mm

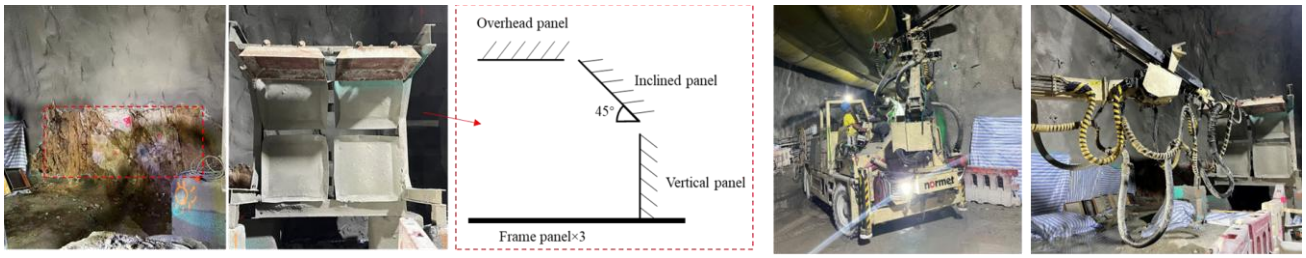

(a) (b)

Figure 14: (a) Spraying test setup with a rock surface panel and a steel frame and (b) Normet Spraymec 8100 VC

Other than the spraying test mentioned above, cube, prism and square panel samples were prepared for the routine quality production tests. All specimens were demoulded after 24 hours from casting in the site spray trial and transported to HKUST Concrete Laboratory for air curing. The required testing ages varied according to the specific test requirements as described in the subsequent sections.

Finally, structural integrity was assessed through two-week deformation monitoring and field survey to see if the lining was affected by shrinkage and blast vibration caused by further construction work. Five monitoring points (MT1, MT2, MT3, MT4, and MT5) were installed on the rock panel surface and the adjacent portions of the cavern wall. Results suggested no observable deformation trend, with movement within 2 mm, indicating adequate structural integrity in this setting.

4.3 Verification of mechanical performance

Mechanical performance of the GGBS-ECC mix in the site spray trial was evaluated through testing of compressive strength, flexural strength, energy absorption capacity and bond strength. Early-age compressive strength performance was verified through a penetration needle test (at 1 hour) and a stud-driving test (at 8 hours) on rock surface panels, in accordance with BS EN 14488-2. Conventional cube tests at ages beyond 8 hours according to CS1:2010 / BS EN 12390-3 were also performed for long-term strength verification. The satisfactory test results are shown in Table 6.

Table 6: Test results of compressive strength for GGBS-ECC samples

Age of SECC	Compressive strength			
	Test values (MPa)			Mean value (MPa)
	Sample 1	Sample 2	Sample 3	
1h (Penetration needle)	0.42	0.55	0.51	0.5*
8h (Stud driving)	2.80	2.30	2.50	2.5*
1d	12.50	13.40	14.70	13.5
7d	37.30	41.20	40.70	39.7
28d	48.00	50.10	46.80	48.3

* Both 1h and 8h compressive strength performance achieved Class J2 as per BS EN 14487-1.

According to BS EN 14487-1, the early-age compressive strength of the GGBS-ECC mix reached the J_2 strength class. The 28-day mean compressive strength of 48.3 MPa was similar to the laboratory and scale-up production trial results (45 MPa to 55 MPa). In particular, due to the strain-hardening of ECC, a grade strength is not specified in this study. The current strength performance may be viewed as similar to the standard strength performance of grade 40 concrete.

For flexural strength performance, prisms were sawn from the test panels and tested according to ASTM C1609 as discussed in Section 3. The flexural stress against central deflection curves of the ECC specimens at ages of 7 days and 28 days are shown in Figure 15 below. Calculated flexural parameters are summarised in Table 7.

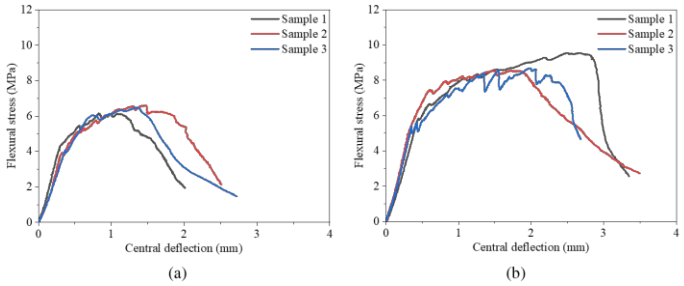

Figure 15: Flexural stress versus central deflection curve of (a) 7-day and (b) 28-day GGBS-ECC beams

The 7-day and 28-day mean first peak flexural strength values of the GGBS-ECC mix are 4.1 MPa and 6.2 MPa, respectively, while the 7-day and 28-day mean peak flexural strength values are 6.4 MPa and 9.0 MPa, respectively. Similar to the results of the scale-up production trial, multiple cracks can be observed on the 28-day GGBS-ECC beam specimen as shown in Figure 16(a). Overall, central deflection values ranged from 2 mm to 4 mm, which varied with sample compactness. Test results were satisfactory and comparable to the laboratory and scale-up production performance.

In addition to directly examining the flexural test results, Table 7 also shows the comparison with the minimum and maximum results according to a database from BS EN 14488-3 and ASTM C1609, composed of 26 sets of three or four replicate test specimens that were cast in laboratory and tested by one operator using a closed-loop, servo-controlled hydraulic universal-testing machine. Except for the deflection, which was slightly smaller than the maximum value, all other test results demonstrated close resemblance to or better performance than the maximum values in the said database.

Table 7: Flexural parameters of ECC samples and test results from a database

Test Items	Mean value of GGBS-ECC (7d)	Mean value of GGBS-ECC (28d)	From the database of BS EN 14488-3 and ASTM C1609	
			Minimum value	Maximum value
P_P, N	21366.3	29759.7	9869	27071
f_P, MPa	6.4	9.0	2.44	7.46
δ_P, mm	1.3	2.1	0.03	2.44
P_1, N	13749.6	20787.9	9868	27071
f_1, MPa	4.1	6.2	2.44	7.12
δ_1, mm	0.4	0.5	0.03	0.06
P_{600}^D, N	16157.1	20572.7	4828	24076
f_{600}^D, MPa	4.9	6.2	1.20	7.00
P_{150}^D,MPa	13884.2	28374.1	5193	18588
f_{150}^D,N	4.2	8.5	1.29	5.41
T_{150}^D, J	32.0	45.2	10	42

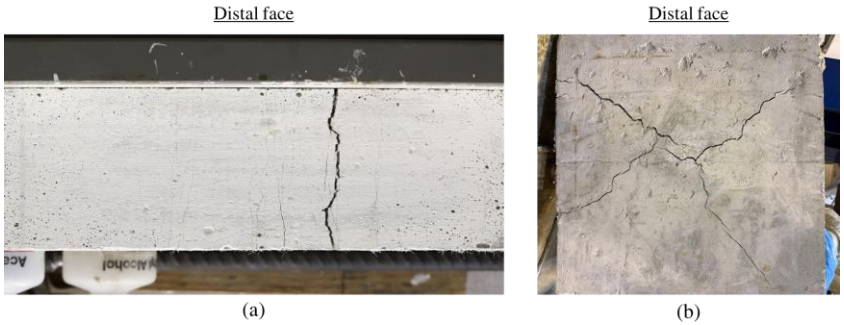

Figure 16: Multiple cracks in (a) flexure test specimens and (b) square panel test specimens for GGBS-ECC

For energy absorption capacity, square panel specimens were tested in accordance with BS EN 14488-5. The load-deflection curves and the energy absorption capacity-deflection curves are shown in Figure 17(a) and Figure 17(b), respectively. Table 8 summarises the peak loads and energy absorption capacities. Thickness correction was performed as the on-site sprayed panels measured approximately 100 mm at the edges with a slight rise to around 120 mm toward centre. As shown in Figure 16(b) above, the test panel typically failed with a formation of cross cracks. Overall, test results achieved EFNARC Class C/NGI Class E1000 (1000 J), which was satisfactory and comparable to the scale-up production performance.

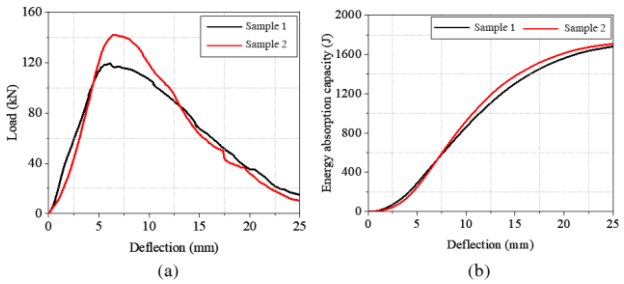

Figure 17: (a) Load versus deflection curves and (b) energy absorption capacity versus deflection curves for GGBS-ECC

Table 8: Summary of energy absorption capacities

Mix ID	Sample ID	Peak Load (kN)	Energy absorption capacity	
			Test value (J)	Corrected value (J)
GGBS-ECC	1	119.1	1680.0	1104.6 (t = 115 mm)
	2	142.0	1706.5	1038.6 (t = 118mm)

Finally, in-situ bond performance was assessed through in-situ coring for further laboratory pull-off / Brazilian test. While a few attempts were made, the coring results showed failure either within the cracked rock substrate or at the glue between the dolly and the GGBS-ECC surface. These results suggested that the bond strength between GGBS-ECC and rock may well exceed the adhesion of the testing glue. Given consistent outcomes from the attempts and further field observations, the spraying process appeared to have no adverse impact on bond strength performance. It should be noted that, however, bond strength performance is more sensitive to spraying technique and workmanship as well as preparation of the rock substrate surface beforehand.

4.4 Spraying performance and final appearance of applied GGBS-ECC

Figure 18 shows the spraying process and the final appearance of GGBS-ECC applied to the rock surface panel. Despite the demonstrated minimal rebound and satisfactory mechanical performance, the applied GGBS-ECC surface appeared nodular and irregular, with some localised cavities. These imperfections are likely attributable to concentrated spraying over a limited area, the long (approximately 1 hour) interval between plant mixing and on-site application, and the lack of calibrated spraying parameters and operator technique specific to ECC. Refinement of the mix design together with improved spraying procedures and crew training will be required to achieve a smoother and more uniform finish.

(a) (b)

Figure 18: (a) Spraying of steel frame panels and (b) final appearance of GGBS-ECC applied to the rock surface panel

5 CONCLUSIONS AND WAY FORWARD

This study developed two feasible SECC mixes using locally available materials, with the GGBS-ECC mix selected for the site spraying trial. Mechanical tests confirmed the characteristic strain-hardening behaviour under flexure, high energy absorption capacity, and consistent quality across laboratory, plant, and field conditions. Certain aspects warrant further investigation, including self-healing and self-stressing in the field, surface texture refinement through adjustments to mix & spraying, and crew training (e.g. nozzlemen).

Overall, this work provides fresh insights into SECC for tunnel lining applications in Hong Kong. Leveraging its self-healing, self-stressing, high ductility, and residual mechanical properties, SECC offers significant potential to enhance water tightness, reduce maintenance costs, and enable more cost-effective design solutions in tunnelling applications. Wider adoption will require streamlined ECC production logistics and a progressive refinement of structural design methodologies to fully capture ECC's potential.

ACKNOWLEDGEMENTS

The authors gratefully acknowledge the collaboration of the Joint Cavern Development at Anderson Road Quarry Site project team in facilitating the site spraying trial, as well as the support of the two ready-mix suppliers in producing the materials. This paper is published with the permission of the Head of the Geotechnical Engineering Office and the Director of Civil Engineering and Development, the Government of the Hong Kong Special Administrative Region.

REFERENCES

Ding, Z., Wen, J., Li, X., Fu, J. & Ji, X. 2020. Mechanical behaviour of polyvinyl alcohol-engineered cementitious composites (PVA-ECC) tunnel linings subjected to vertical load. Tunnelling and Underground Space Technology, 95: 103151.

Ghosh, S.K. 2009. Self-Healing Materials: Fundamentals, Design Strategies, and Applications. Wiley-VCH.

Khandelwal, M. & Singh, T.N. 2009. Prediction of blast-induced ground vibration using artificial neural network. International Journal of Rock Mechanics and Mining Sciences, 46: 1214–1222.

Li, V.C. 1993. From micromechanics to structural engineering — the design of cementitious composites for civil engineering applications. Doboku Gakkai Ronbunshu, 1993(471): 1–12.

Li, V.C. 2019. Engineered cementitious composites (ECC): bendable concrete for sustainable and resilient infrastructure. Springer.

Li, V.C. 2003. On engineered cementitious composites (ECC). A review of the material and its applications. Journal of Advanced Concrete Technology, 1: 215–230.

Li, V.C. & Leung, C.K.Y. 1992. Steady-state and multiple cracking of short random fiber composites. Journal of Engineering Mechanics, 118(11): 2246–2264.

Qian, C., Zhao, Y.C., Sun, M.G., Chen, J.X., Luo, Y.B. & Li, Z. 2025. Study on safety distance of pedestrian cross passages in single-tube four-lane highway tunnels. Chang'an Daxue Xuebao (Ziran Kexue Ban)/Journal of Chang'an University (Natural Science Edition), 45(5): 81–91.

Van Tittelboom, K. & De Belie, N. 2013. Self-Healing in Cementitious Materials—A Review. Materials, 6(6): 2182–2217.

Yang, Y., E.H. Yang, and V.C. Li 2011. Autogenous Healing of Engineered Cementitious Composites at Early Age. Cement and Concrete Research, 41(2), 176-183.

Zhu, H., Zhang, D., Wang, Y., Wang, T. & Li, V.C. 2021. Development of self-stressing Engineered Cementitious Composites (ECC). Cement and Concrete Composites, 118: 103936.

Three-Dimensional Analysis of Stress Interaction between Closely-Spaced Bored Piles in Rock

James ZJ Ruan, Anthony TT Chuang & Sammy PY Cheung

Geotechnical Engineering Office,
Civil Engineering and Development Department,
Government of the Hong Kong Special Administrative Region,
Hong Kong SAR, China

ABSTRACT

Large-diameter bored piles founded on rock are prevalent in Hong Kong. Where the piles are positioned at close spacing, there is a concern regarding the overlapping of bearing stress between adjacent piles that would overstress the rock formation. A conventional 45° stress-dispersion envelope is commonly adopted to estimate the stress distribution and assess the interaction of bearing stress. Some practitioners surmise that the overstressing condition could be avoided by restricting the foundation level of adjacent piles to below a 45° envelope projected upward from the deepest pile. However, the imposition of this envelope may force adjacent piles to be extended to deeper depths, which has a significant impact on the cost and complexity of the piling works. This paper presents a study that critically examines the interaction and stress distribution between closely spaced piles at different founding levels, with the aid of three-dimensional numerical analyses. The Hoek-Brown failure criterion was adopted in the analyses to characterize the engineering properties of the rock formation. The study findings reveal that the stressed zone beneath a pile base is more localized than conventionally assumed, and it is more accurate to adopt a stress-dispersion angle of 26.5° for estimating stress increments with depth. Numerical results also confirm that interaction of bearing stress is minimal and does not lead to an exceedance of the applied bearing pressure, even when piles are spaced as close as 0.5 m apart. The analyses are applicable to end-bearing piles and piles mobilizing shaft and end-bearing resistance. The study also assessed the effect of inclined rockhead surfaces on the mobilization of shaft resistance. Based on the study findings, improved design practices are recommended when placing piles at levels higher than adjacent piles, which include (a) eliminating the check on overlapping bearing stress and the 45° envelope used to restrict founding levels between adjacent piles, and (b) focusing on the stability of plausible wedge failure under the foundation load from closely spaced piles and the load-transfer effect on the structural capacity of closely spaced piles. These improved practices contribute to optimizing the cost and constructability of bored piles while safeguarding safety standards.

1 INTRODUCTION

In Hong Kong, large-diameter bored piles socketed into rock are a prevalent foundation solution for high-rise buildings and infrastructure projects. Where these piles are constructed in close proximity, a long-standing concern is that the overlapping end-bearing stress bulbs from adjacent piles may overstress the underlying rock mass. To address this concern in practice, a simple rule-of-thumb has been adopted: a 45° stress dispersion angle is assumed from the pile base, and adjacent piles are required to be founded below a 45° envelope projected upward from the deepest pile.

The imposition of the 45° envelope from the deepest pile may force adjacent piles to be extended to deeper depths, which has a significant impact to cost and complexity of the foundation works. There are many factors that need to be considered when confirming the founding levels of pile on site. For examples, the founding level may be deepened due to discovery of a weathered seam during excavation, strict assessment by site personnel of the quality of rock excavated, or the presence of sensitive underground structures. Strict adherence to the 45° envelope can have major practical consequences, especially if a pile has to be excavated to a deeper depth after an adjacent pile has already been cast.

Despite its prevalence, the 45° stress-dispersion assumption lacks strong theoretical justification for rock masses that exhibit approximately elastically behaviour under service stress levels. Therefore, it is warranted to investigate the actual extent of the stressed zone beneath pile bases, quantify stress interactions between adjacent piles, and evaluate whether overlapping stresses may exceed the adopted allowable bearing pressure under typical Hong Kong rock conditions.

A three-dimensional numerical study of stress interactions between closely spaced large-diameter bored piles founded on rock is conducted, complemented by elastic solutions for circular loaded areas. The study also assesses the influence of inclined rockhead surfaces on shaft resistance mobilization. The findings provide enhanced understanding of stress overlap beneath closely spaced piles and a sound technical basis for determining founding levels for piles placed in close proximity.

2 CURRENT PRACTICE ON DETERMINING FOUNDING LEVELS

2.1 Simplified Assumption on 45° Stress Dispersion

The conventional approach for assessing stress interaction between adjacent piles assumes a 45° stress-dispersion angle from the pile base to estimate vertical stress increments with depth. Based on this, a 45° envelope projected upward from the deepest pile is sometimes used to restrict founding levels of adjacent piles, requiring them to be socketed below this envelope to prevent overlapping bearing stresses. While intended as a conservative measure, this practice lacks theoretical foundation for competent rock masses and can lead to unnecessarily deep sockets, increasing construction cost and complexity, particularly when variable ground conditions are encountered during excavation.

2.2 Presence of steep bedrock profile and current code provisions

The Hong Kong Code of Practice for Foundations (BD, 2024) provides guidance on the design and construction of large-diameter bored piles. It stipulates that, where a steep bedrock profile is present, the founding levels of adjacent piles should not differ by more than the clear distance between pile bases unless the stability of the rock beneath the piles has been checked using recognised engineering principles, taking into account adverse joints. This provision is intended to address potential rock wedge instability in situations where piles are founded on steep rockhead surfaces intersected by persistent, unfavourably oriented discontinuities. It is not intended to address issues related to overlapping end-bearing stresses between adjacent piles.

3 EXTENT OF VERTICAL STRESS INCREMENTS UNDERNEATH A CIRCULAR PILE

For large-diameter bored piles founded on rock, local practice typically positions the pile bases on competent rock formations that behave approximately as linear elastic materials at service stress levels. Under these conditions, elastic theory may be applied to calculate stress increments within the rock mass due to the imposed foundation loads. The distribution of stress increments in an elastic half-space arising from a point load is given by Boussinesq (1885), and the corresponding vertical stress beneath a uniformly loaded circular area of radius r and pressure q can be obtained by integrating the point-load solution over the loaded area. Using a polar coordinate of r', θ, the vertical stress increase below a circular loaded area can be computed using the following equation:

$$\Delta\sigma_z = \frac{3qz^3}{2\pi}\int_0^{2\pi}\int_0^{r}\frac{r'}{(r'^2 + d^2 - 2r'd\cos\theta + z^2)^{2.5}}\,dr'\,d\theta$$

where d, z and r are defined in Figure 1.

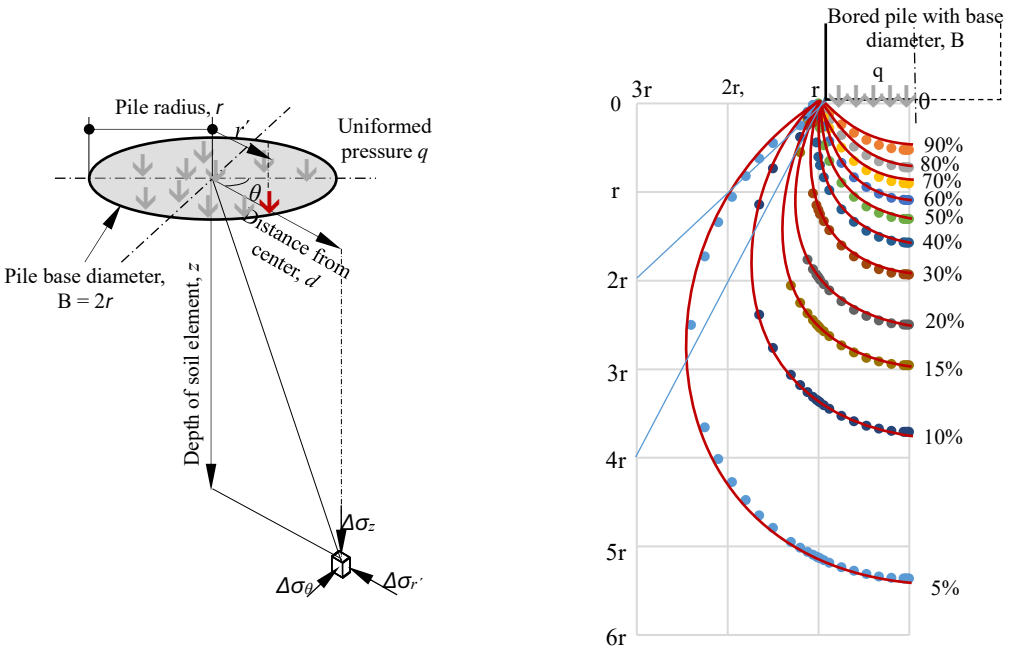

Figure 1: Stress Distribution beneath a Circular Loaded Area

Evaluation of this expression shows that vertical stress increments beneath a uniformly loaded circular area decay rapidly with radial distance and depth. At the pile base, the vertical stress increment directly beneath the centre equals the applied pressure q, while at the edge of the loaded area the vertical stress increment reduces to approximately 0.5q. Beyond the edge, the vertical stress diminishes to negligible levels at a radial distance of about one base diameter B from the pile edge. In the vertical direction, significant stress increments (e.g. greater than 0.1q) are confined to depths of approximately 2.5B below the pile base. These results indicate that the stressed zone induced by pile end-bearing pressure is effectively limited to a region extending laterally up to B from the base edge and vertically to about 2.5B below the base. The envelope of vertical stress increments with depth is more accurately represented by a stress-dispersion angle of about 26.5° measured from the vertical axis through the pile centre, corresponding to an approximate 1:2 (horizontal : vertical) spread from the base edge, rather than the commonly assumed 45°. This narrower dispersion angle provides a more realistic basis for assessing stress interaction between adjacent pile bases in rock. Poulos (1971) and subsequent researchers established that pile-soil interaction diminishes rapidly with spacing, with interaction factors approaching zero when stress increments fall below approximately 20% of the applied load (i.e. 0.2q). This forms the basis for many practical pile group design.

4 THREE-DIMENSIONAL NUMERICAL MODELLING

4.1 Model Configuration

The interaction of vertical stresses between adjacent piles founded at varying depths was investigated using three-dimensional finite element models implemented in PLAXIS 3D version CE V22. Figure 2 illustrates the basic geometric arrangement, comprising two bored piles of diameter B embedded in a soil overlaying competent rock in dry condition. A half-space model was adopted, exploiting symmetry along the longitudinal axis between the piles to improve computational efficiency. The model domain extended around 20m horizontally from the pile centres and 15m vertically below the deepest pile base. Roller boundaries were applied on the lateral faces (preventing horizontal displacement while allowing vertical settlement) and basal face. A 15-node tetrahedral mesh was used with local refinement around pile bases and rock sockets, achieving mesh convergence with < 2% variation.

To achieve the objective of this study, three analysis suites of progressive complexity were designed, as detailed in Table 1. Suite 1 adopts weightless conditions with end-bearing resistance only, serving as a reference case for validation against classical elastic solutions (Boussinesq, 1885) and establishing baseline stress distribution patterns. Suite 2 incorporates full overburden weight of soil and rock and combined shaft (700 kPa over 2B)

and end-bearing resistance (7500 kPa), representing typical design field stress conditions. Suite 3 isolates the effect of rockhead geometry by modelling inclined rockhead surfaces (45° and 60°) under weightless soil conditions, focusing specifically on shaft resistance mobilization without confounding effects from overburden or base resistance. Collectively, these suites progress from theoretical validation through realistic representation to geometric sensitivity analysis, providing comprehensive insight into pile stress interaction mechanisms. Figures 3 & 4 present the configuration of the model suites analysed.

In all cases, the rock socket diameter was assumed equal to the pile shaft diameter B. This simplification has negligible influence on stress distribution and pile-rock interaction. Differences in founding levels between adjacent piles were taken as 0B (same level), 1B, and 2B, as illustrated in Figure 3. Interface elements surrounded the bored piles has been assigned to control mobilization of shaft resistance.

Prior to pile loading, the initial stress field was established using the K_0 or gravity load procedure, subject to the soil-rock geometry. For the soil layer (saprolite), the coefficient of lateral earth pressure at rest was calculated using the Jaky's formula. For the rock mass, a conservative isotropic stress state of $K_h = K_v = 1$ was adopted, assuming initial horizontal effective stress equals vertical effective stress at any given depth. This assumption is justified as it provides a reasonable lower-bound estimate of horizontal stresses in Hong Kong rock masses and consistent with the assessment by Kwong and Wong (2013), who reported the in-situ rock stress ratios typically ranging from 1.4 to 2.5, based on hydraulic fracturing tests conducted in Hong Kong region.

A sequential loading procedure was adopted in Suite 1 &2 analysis: the deeper pile was first loaded to a target end-bearing pressure of 7500 kPa, representing the typical allowable bearing stress for a pile founded on Category 1(c) rock or better according to the GEO Technical Guidance Note (TGN) No. 53 (GEO, 2023). After equilibrium was achieved, the shallower pile was loaded to the same target pressure. This sequence enables direct assessment of how additional loading from a neighbouring pile influences the existing stress field. For Suite 3 analysis, only the deeper pile was loaded to the target end-bearing pressure of 7500 kPa for investigating the inclined rockhead effect.

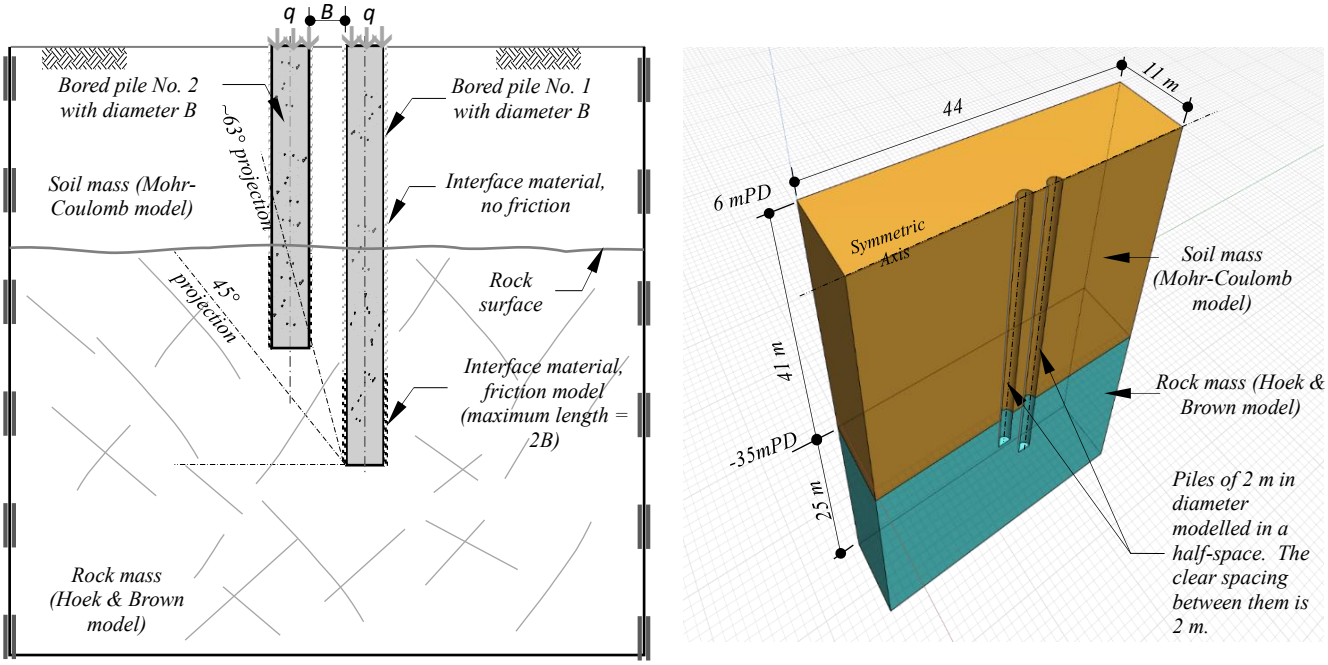

Figure 2 – FE Models for Analysing Interaction Between Adjacent Piles

Table 1. Model Suites Analysed

Model Suite	Self-weight of Soil & Rock	Shaft resistance	Pile spacing	Pile Level difference	Key objective
Suite 1	Weightless ($\gamma = 0$)	None (end-bearing only)	1B, 0.5m	0B, 1B, and 2B	Validate against elastic solution; assess stress interaction

Suite 2	Full weight γ_{soil} = 19 kN/m^3 γ_{rock} = 25 kN/m^3	Rock socket: 700 kPa over 2B	1B, 0.5m	0B, 1B, and 2B	Typical design conditions with shaft and base resistance
Suite 3	γ_{soil} = 0 kN/m^3 γ_{rock} = 25 kN/m	Rock socket: 700 kPa over 2B	1B	1B	Inclined rockhead effect on shaft resistance

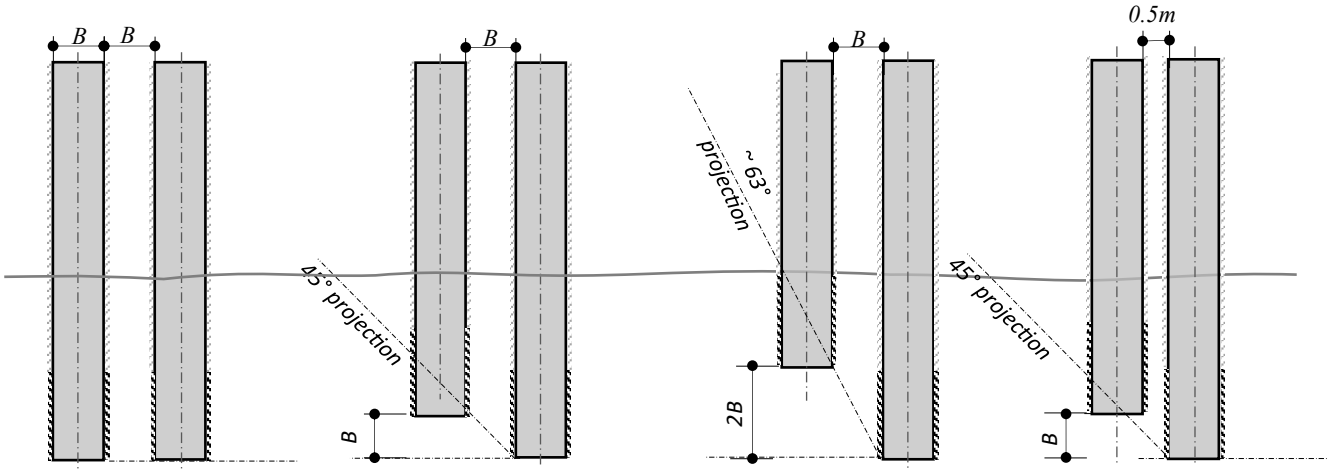

Case 1: Piles at Same Elevation | Case 2: Piles at 45° Projection | Case 3: Piles at ~63° Projection | Case 4: Piles at Same Elevation but with closer spacing

Figure 3 - Basic Geometry of Numerical Models for Suite 1&2 Analysis

4.2 Constitutive Models

Cat 1(c) rock is usually defined as rock mass with a TCR greater than 85% of the designated grade which has a minimum uniaxial compressive strength of the rock not less than 25 MPa. Hoek-Brown (HB) failure criterion (Hoek et *al.*, 2002), is used in the numerical models to represent the stress-strain behaviour of the jointed rock mass. The HB failure criterion is expressed as:

$$\sigma_1' = \sigma_3' + \sigma_c \left(m_b \frac{\sigma_3'}{\sigma_c} + s\right)^a$$

where σ_c' represents the UCS of the intact rock,

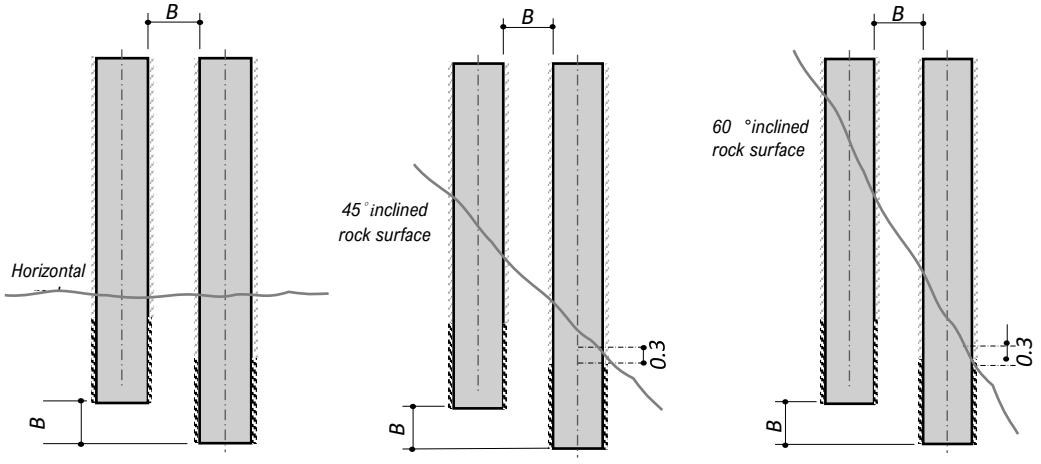

Case 5: Horizontal Rock Surface (Reference Case) | Case 6: 45° Inclined Rock Surface | Case 7: 60° Inclined Rock Surface

Figure 4 – Basic Geometry of Numerical Models for Suite 3 Analysis

σ'_1 and σ'_3 represents the major and minor principal stresses respectively, and
m_b and s represents the material parameters based on the Geological Strength Index (GSI).

$$m_b = m_i \, e^{\left(\frac{GSI-100}{28}\right)}$$

$$s = e^{\left(\frac{GSI-100}{9}\right)}$$

$$a = 0.5 + 0.166 \, (e^{\frac{GSI}{15}} - e^{-6.667})$$

where m_i represents the material parameter of the intact rock.

In the numerical analyses, the GSI is set to 60, that represents rock mass ranging from intact to very blocky, fresh to moderately weathered joint surfaces interlocked by orthogonal discontinuity sets (Hoek and Marinos, 2000). The material parameter m_i reflects the influence of lithology, including the texture and mineralogy of the intact rock. An average value of 24 is assumed that represents variety of igneous rocks and metasedimentary rocks. The parameter m_i is not sensitive to the rock strength characteristics within the range of end-bearing pressures allowed in the foundation design, which is at a maximum of 12.5 MPa for Cat 1(a) rocks. No dilatancy is considered in the HB failure criterion. Figure 5 illustrates the HB failure criterion for different types of Categories 1 and 2 rock with different m_i, as defined in the CoP for Foundations (BD 2024). For Category 2 rocks, a GSI of 40 is usually adopted to account for the higher density of discontinuities typically encountered in these formations. Within the range of the applied bearing pressures, the relationship between the principal stresses σ'_1 and σ'_3 can be approximated as linear across various rock types, although their deformation

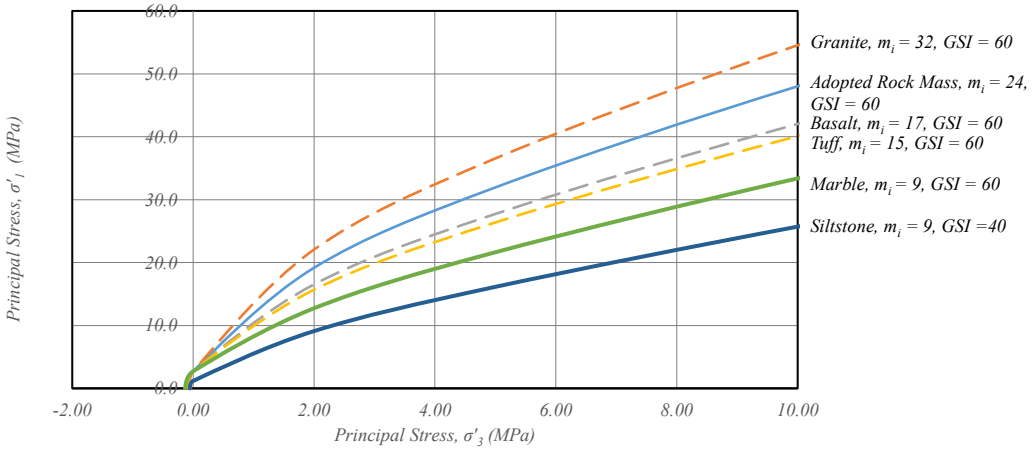

Figure 5 – HB Failure Criterion for Different Categories of Rock

modulus differs.

The theory of elasticity is widely applied in rock mechanics to predict how rock masses respond to applied loads. The theory assumes that the rock mass behaves elastically and remains a continuum under loading. These fundamental principles form the basis for determining the presumed allowable bearing pressure for foundations on different rock categories. Consequently, the results of the numerical models are also applicable to other categories of rock, although the differing rock mass modulus will result in different magnitude of deformation under the same bearing pressure. The soil behaviour is modelled using a linear elastic, perfectly plastic constitutive model with the Mohr-Coulomb failure criterion. The strength parameters for the soil layers (typical saprolites) are defined as effective cohesion, c′ = 10 kPa and effective friction angle, φ′ = 37°. Table 2 below summarize the adopted soil and rock parameters.

Table 2. Summary of Soil and Rock Parameters Adopted in Numerical Models

Material	Model	Unit weight, γ (kN/m³)	E (MPa)	c′ (kPa)	φ′ (°)	Other parameters
Soil (saprolite)	Mohr-Coulomb	19	50	10	37	-
Rock Cat 1(c)	Hoek-	25	7950	-	-	GSI = 60, m_i = 24, σ_{ci} = 25 MPa,

	Brown					m_b = 5.752, s = 0.0117, a = 0.503
Pile	Linear elastic	25	25100	-	-	-
Pile-rock interface	Interface	-	-	-	-	R_{inter} = 1 (rock socket), τ_{max}=700 kPa over 2B
Pile-soil/rock interface	Interface	-	-	-	-	R_{inter} = 0.01 (no shaft resistance)

5 RESULTS AND DISCUSSIONS

5.1 Piles with End-bearing Resistance Only

In the first suite of numerical analyses, the soil and rock were idealised as weightless to isolate the vertical stress increments induced purely by the foundation loads. Omitting the self-weight removes in-situ stresses, so that the computed effective vertical stress directly represents the load-induced stress increment. This approach highlights the stress concentration beneath the pile base and facilitates direct comparison with elastic solutions.

In the initial model, only one bored pile was loaded to an end-bearing pressure of 7500 kPa to examine the dispersion of vertical stress within the rock mass and to compare the results with the elastic half-space solution. Figure 6 shows the contours of vertical stress increment $\Delta\sigma_z$ obtained from the numerical analyses together with the corresponding elastic solution. The numerical contours align closely with the elastic prediction and confirm that vertical stress increments are strongly concentrated beneath the pile base. The main stress increase is confined within an approximate 1:2 (horizontal: vertical) envelope from the base edge, with $\Delta\sigma_z$ reducing to around 0.1q at a depth of about 2B below the pile base. The principal stress increments remain confined to within approximately one pile diameter B from the pile edge.

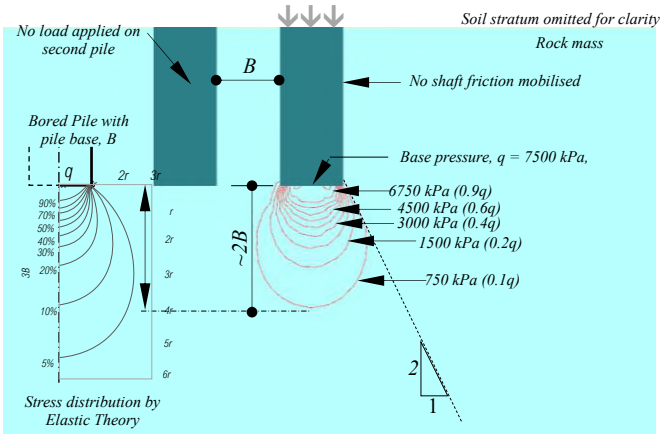

Figure 6 – Vertical stress increments due to loading on a single pile

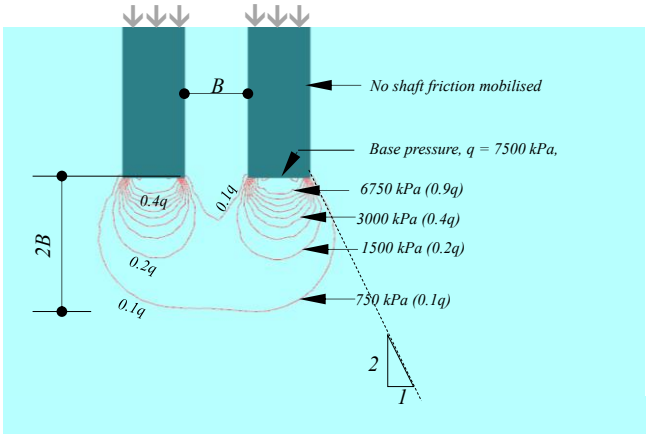

Figure 7 – Vertical stress increments due to loading at both piles with same founding level

Figures 7, 8 and 9 present the contours of $\Delta\sigma_z$ for piles founded at the same level, at a level difference of 1B and 2B, respectively, where both piles have been loaded to the targeted pressure. Figures 7 and 8 show that the vertical stress increments beneath each pile base remain localised, with only partial overlap of the 0.1q contour between adjacent piles. When the piles are vertically separated by 2B at their founding levels (Figure 9), the stress fields beneath each base remain essentially distinct and non-interacting. In all cases, the maximum vertical stress increment does not exceed the applied base pressure of 7500 kPa. This indicates that, for piles spaced one diameter apart, interaction of vertical stress increments is minimal, even when the founding levels differ by more than one diameter.

The Code of Practice for Foundations (BD, 2024) permits a minimum clear spacing of 0.5 m between adjacent bored piles. To assess this more critical arrangement, an additional analysis was conducted for two piles with a clear spacing of 0.5 m and a founding level difference of B. Figure 10 illustrates the resulting vertical stress increments between the two pile bases. The contours show partial overlap at a magnitude of about 0.2q between the pile bases, but the vertical stress remains below the applied base pressure of 7500 kPa at all points. This confirms that the rock mass is not overstressed even when piles are placed at the minimum clear spacing allowed by the Code. In such cases, it is prudent to investigate the cause of differing founding levels between closely spaced piles. For example, the shallower pile may be founded on an isolated corestone, or the rockhead profile may exhibit a steep incline that influences wedge stability in case adverse discontinuities are present.

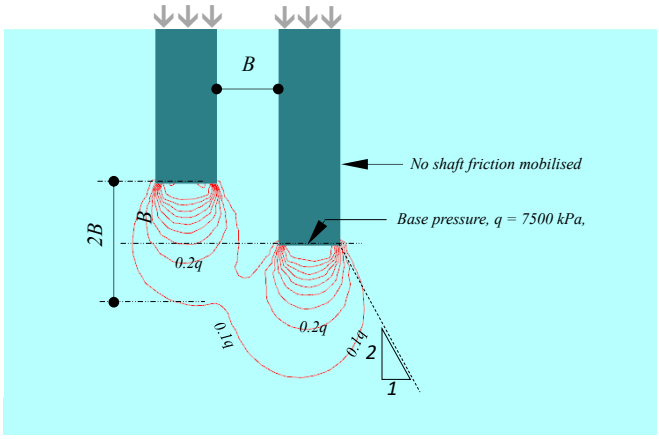

Figure 8 – Vertical stress increments due to loading at pile bases with level difference of 1B

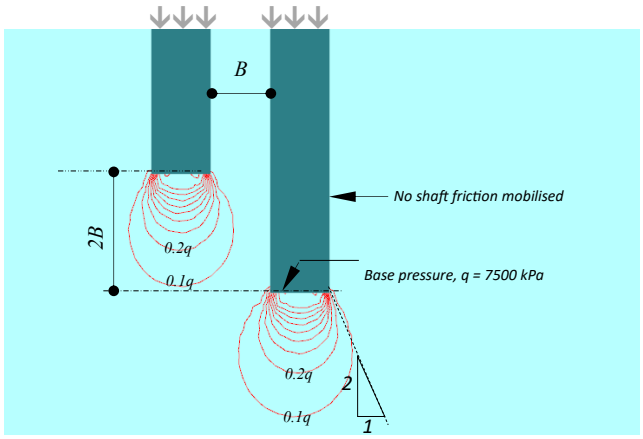

Figure 9 – Vertical stress increments due to loading at pile bases with level difference of 2B

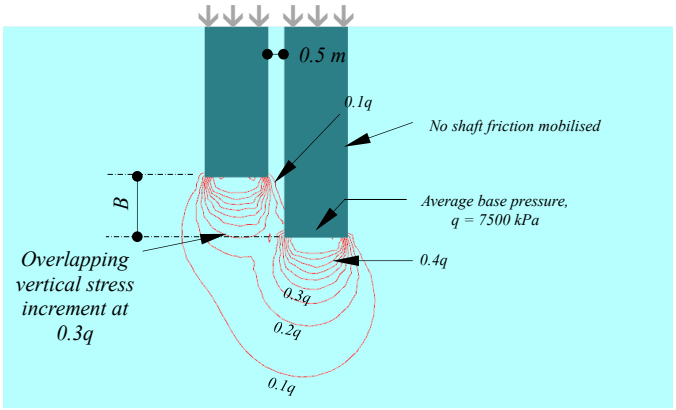

Figure 10 – Vertical stress increments due to loading at pile bases that are 0.5 m apart and with level difference of 1B

The close agreement between the numerical results and the classical elastic solution confirms that, under the applied bearing pressures and the strength characteristics of Category 1(c) rock, the rock mass responds in an essentially linear elastic manner. For a homogeneous, linear elastic medium, the Boussinesq solution demonstrates that the vertical stress distribution beneath a uniformly loaded circular area is independent of the elastic constants. While this idealization provides a robust framework for competent rock, it assumes that the rock mass remains within its linear elastic range and possesses uniform stiffness characteristics. In Hong Kong practice, the adopted foundation bearing pressures incorporate a substantial factor of safety, such that the principal stress at the pile base remains well below the peak strength at which micro-cracking and non-linear behaviour of rock would initiate. Consequently, the rock mass can be assumed to respond in an essentially linear elastic manner under working stress conditions. Accordingly, the 26.5° dispersion envelope is considered also applicable to competent rock masses, ranging from fresh to moderately weathered grades, as typically encountered in local foundation practice.

5.2 Piles with Shaft and End-bearing Resistance

In many instances, large-diameter bored piles are socketed into rock mass to increase their load-carrying capacity, with the design typically allowing for the mobilization of both shaft and end-bearing resistance. It is therefore important to examine the interaction between adjacent piles when shaft resistance is mobilised, and to assess whether stress overlap could lead to overstressing of the rock mass.

In Hong Kong practice, the shaft resistance of large-diameter bored piles founded on rock is limited to a prescribed value, and the maximum socket length for piles without bell-out is restricted to 2D or 6 m, whichever is smaller (BD, 2024). For Category 1(c) rocks, the allowable shaft resistance is 700 kPa. These constraints were adopted in the Suite 2 numerical models, although the actual shaft resistance along the full socket length would generally be higher. For the 2 m diameter piles analysed, full mobilization of the allowable shaft resistance of 700 kPa over the 4 m socket length (2B) generates a shaft resistance of approximately 17600 kN. This corresponds to an equivalent reduction of about 5600 kPa in the stress transmitted to the pile base. To achieve an end-bearing pressure comparable to the previous suite, the pile loads were increased so that the base pressure again reached approximately 7500 kPa.

Figure 11 shows the contours of effective vertical stress, $\Delta\sigma_z$, when only one pile is loaded with both shaft and base resistance mobilised. In this suite of analyses, the self-weight of the soil and rock was included to represent in-situ stress conditions for piles with shaft resistance. As PLAXIS outputs only gross effective vertical stresses, the vertical stress increment $\Delta\sigma_z$ due to the applied load was estimated by subtracting the effective overburden stress from the model results. At the level of -40 mPD, the effective overburden vertical stress under dry conditions is approximately 900 kPa; therefore, $\Delta\sigma_z$ is evaluated by subtracting this value from the computed $\Delta\sigma_z$ at that depth.

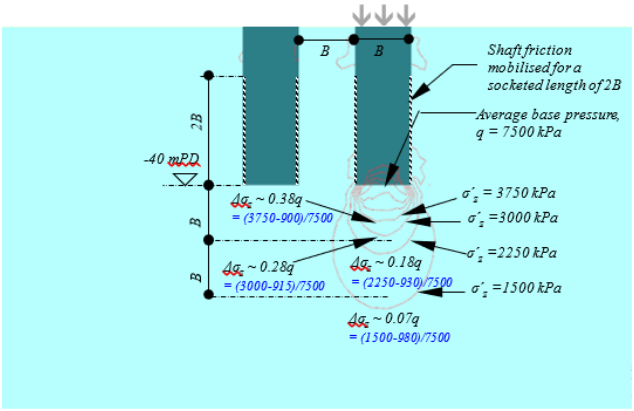

Figure 11 – Effective vertical stress contours at pile bases due to loading at single pile with shaft and end-bearing resistance

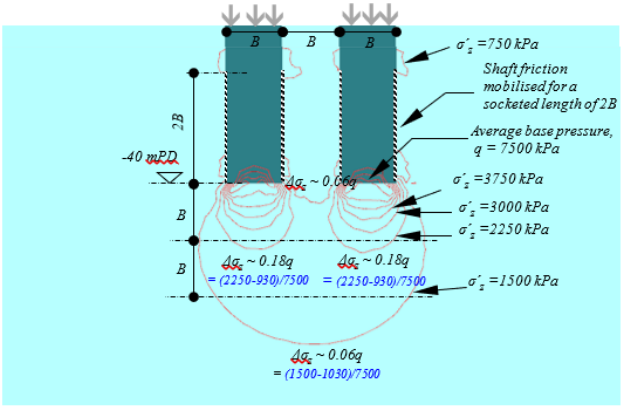

Figure 12 – Effective vertical stress contours at pile bases due to loading at both piles with shaft and end-bearing resistance

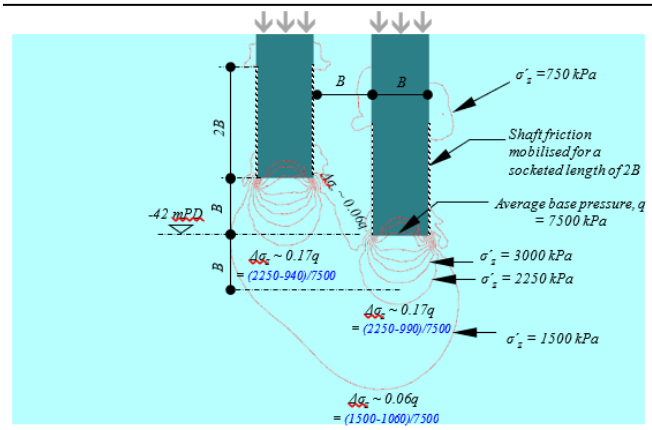

Figure 13 – Effective vertical stress contours at pile bases with 1B level difference and with shaft and end-bearing resistance

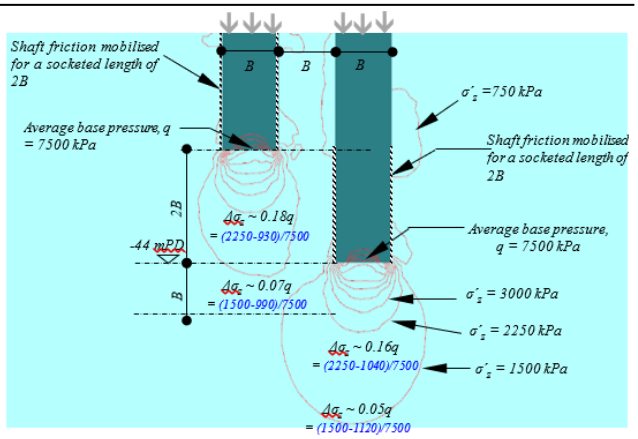

Figure 14 – Effective vertical stress contours at pile bases with 2B level difference and with shaft and end-bearing resistance

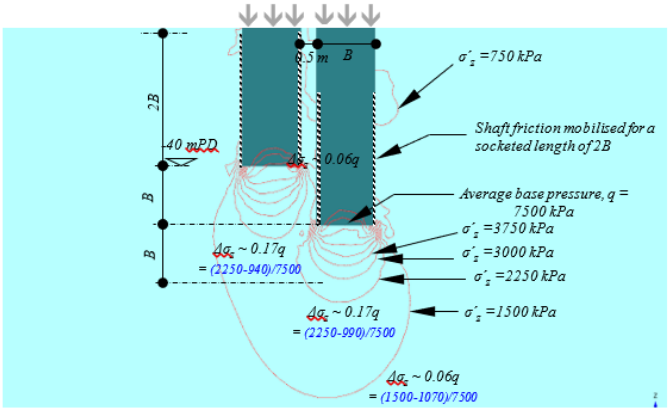

Figure 15 – Effective vertical stress contours with 1B level difference and with shaft and end-bearing resistance (0.5m pile spacing)

Figure 12 presents the effective vertical stress contours when both piles are loaded to an end-bearing pressure of 7500 kPa with shaft resistance mobilised. Only limited overlapping of vertical stress-increment contours is observed at low magnitudes (e.g. about 0.08q), and at no point beneath the pile bases does the vertical stress exceed the applied base pressure of 7500 kPa. Figures 13 and 14 show the results for piles founded with level differences of 1B and 2B, respectively. In these cases, the contours of vertical stress increment again exhibit only partial overlap at small magnitudes, and the combined vertical stress remains below the applied base pressure throughout the rock mass beneath the bases. Figure 15 illustrates the distribution of vertical stress between the two pile bases spaced at 0.5m apart. In contrast to the end-bearing-only condition, the load transferred to the base is reduced due to partial load shedding along the pile shaft. This results in a broader but attenuated stress bulb beneath each pile toe. Consequently, the overlapping stress influence between the two piles is diminished, with the interaction zone confined to approximately 0.08q to 0.18q.

The shallower extent of the vertical stress contours observed in Suite 2 analyses (Figures 11 - 15), compared to the weightless, end-bearing-only conditions of Suite 1, reflects the influence of shaft resistance and overburden pressure on load transfer mechanics. The mobilization of shaft friction along the rock socket reduces the proportion of load reaching the pile base, thereby attenuating the magnitude and vertical penetration of the resulting stress bulb. Furthermore, the presence of surcharge from soil self-weight provides an initial confining stress, which modifies the relative stress increment imposed by the pile loading. Theoretical studies (e.g., Santarelli & Brown, 1987; Hoek & Diederichs, 2006) demonstrate that stress-dependent stiffness can further localize stress distributions in rock masses. Nevertheless, the results confirm that even under simplified linear-elastic conditions, the combined effects of shaft resistance and overburden stress confine the zone of significant influence closer to the pile base. As demonstrated by Pells and Turner (1979), stress distributions in layered or confined systems can be significantly more localized than those predicted by homogeneous half-space theory. These findings reinforce that vertical stress interaction between adjacent piles remains limited, and that overlapping stresses do not exceed the applied base pressure when both shaft and base resistances are mobilized.

5.3 Piles with Shaft Resistance with Inclined Rockhead Surface

While Suites 1 and 2 models examined stress interaction between adjacent piles using vertical stress contours, Suite 3 analysis focuses on the mobilization of shaft resistance along rock sockets adjacent to inclined rockhead surfaces. For this purpose, deviatoric strain is examined rather than stress, as it provides a direct measure of shear distortion in the rock mass. It is therefore more indicative of potential yielding or plastic behaviour along the pile-rock interface, particularly where geometric irregularities such as rockhead inclination may concentrate deformation. Figure 16 shows the results for Case 5, which features a horizontal rockhead and serves as a reference model. In this case, only the deeper pile is loaded, with a base pressure of approximately 7500 kPa and shaft resistance limited to 700 kPa. The contour plots of deviatoric shear strain depict the distribution of shear deformation in the rock mass and identify regions of concentrated shear, which are indicative of potential yielding or plastic behaviour. The peak shear strain ε_{max} beneath the pile base reaches about 0.052%, representing a small to moderate level of strain in rock. Along the pile shaft, shear strain is approximately 0.02%, decaying laterally to around 0.01% at a distance of roughly 0.3B from the shaft edge.

The numerical models were subsequently rerun with the rockhead inclined at 45° and 60° (Cases 6 and 7 in Figure 4). In each case, a 0.3 m rock socket was adopted in accordance with the Code of Practice for Foundations (BD, 2024), and shaft resistance within this 0.3 m socket and the overlying portion was intentionally excluded to focus on the effect of rockhead inclination on socket deformation. The soil above the rockhead was idealised as weightless to isolate the influence of socket shear deformation from overburden stresses and to ensure that the results are not biased by assumed soil thickness.

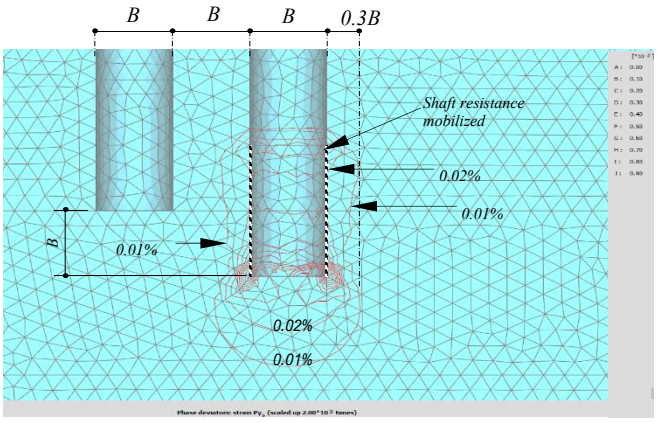

Figure 16 – Deviatoric strain distribution beneath a single pile with mobilized shaft and base resistance in horizontal rockhead

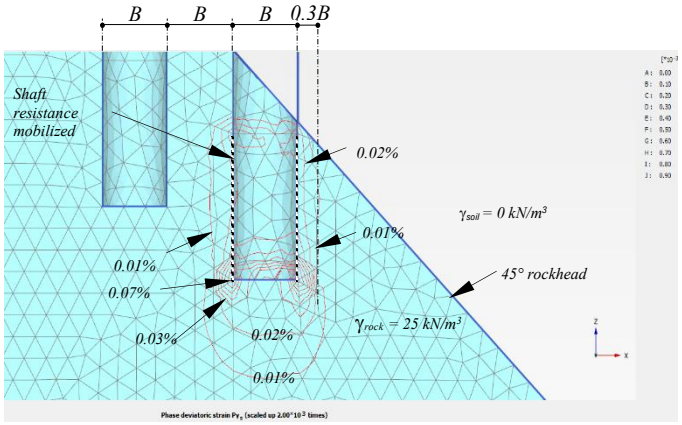

Figure 17 – Deviatoric strain distribution beneath a single pile with mobilized shaft and base resistance in 45° inclined rockhead

Figures 17 and 18 present the deviatoric shear-strain contours for Cases 6 and 7, respectively. For the 45° inclined rockhead (Case 6), the shear-strain pattern is broadly similar to that of the horizontal rockhead, but the inclined interface constrains the lateral spread of shear. Peak shear strain along the pile shaft increases modestly to about 0.02%-0.03%, again attenuating to approximately 0.01% at a lateral distance of about 0.3B from the shaft. The maximum shear strain beneath the pile base increases to around 0.10% due to the reduced overburden confinement implied by the weightless-soil assumption, which lowers the rock mass deformation modulus and allows larger strain mobilisation under the same socket loading.

For the 60° inclined rockhead (Case 7), Figure 18 shows that the deviatoric shear strain contours concentrate more sharply near the upper corner of the rock socket on the downslope side. The maximum shaft shear strain increases to approximately 0.03%, yet the lateral spread of appreciable shear deformation remains limited to about 0.3B from the pile shaft, where strain levels again fall to the negligible level of roughly 0.01%. At this strain level, the rock mass behaviour remains essentially elastic and any associated deformations are small.

The increase in shaft shear strain for the 60° inclination is expected, as the reduced overlying rock thickness diminishes the horizontal confining stress σ_3, permitting greater interface deformation. This effect also enhances shear strain at the pile base on the inclined side, where lateral confinement is lower and the rock mass is more deformable. Conversely, on the side of the shaft opposite the slope, the magnitude and distribution of mobilised shear strain remain similar across all three cases, reflecting the comparable overburden conditions on that side. Figure 19 shows the mobilised shear stress along the shaft and confirms that the maximum shaft resistance of 700 kPa is reached.

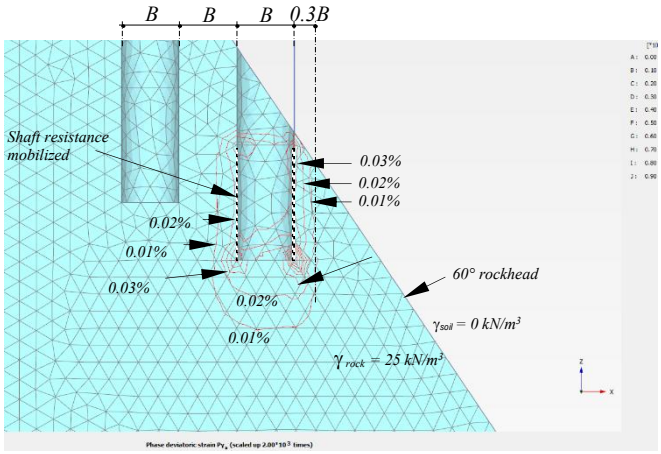

Figure 18 – Deviatoric strain distribution beneath a single pile with mobilized shaft and base resistance in 60° inclined rockhead

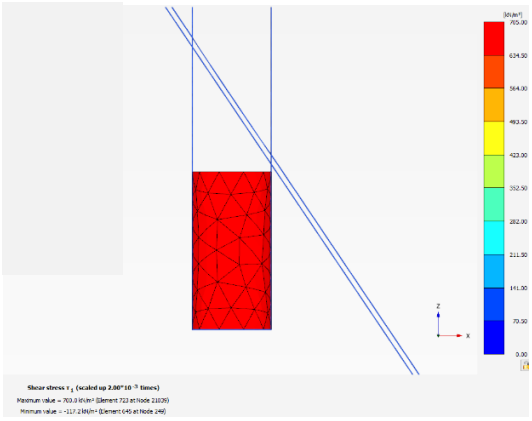

Figure 19 –Mobilized shear stress (τ) along the rock socket for a single loaded pile on a 60° inclined rockhead

In summary, these numerical models demonstrate that the presence of an inclined rockhead surface has little adverse effect on the downward mobilisation of shaft resistance in bored piles under vertical loading. No additional sacrificial penetration into the rock mass, beyond the nominal 0.3 m socket required by the Code, is needed solely because of rockhead inclination. Despite geometric changes at the soil and rock interface, the shaft resistance can still be mobilised up to the prescribed limit, indicating robust load transfer along the shaft. The inclined rockhead does, however, reduce overburden and lateral confining stress locally, primarily due to differences in unit weights of soil and rock along the sloping interface. This reduction lowers the effective confinement and local stiffness of the rock mass adjacent to the pile, which explains the observed increase in interface shear strains. The results suggest that, for shaft resistance under vertical loading, the depth of rock socket penetration and the vertical load-transfer mechanism are more critical than the inclination of the rockhead surface. The findings of this suite of models are not intended for situations where piles are subject to uplift or lateral loads, in which case the stability of adverse discontinuities and potential rock mass failure mechanisms must be assessed explicitly.

6 CONCLUSIONS AND RECOMMENDED PRACTICE

6.1 Clarifications on stress dispersion

The interaction of vertical stresses between adjacent large-diameter bored piles founded on rock has been investigated using three-dimensional numerical models and elastic half-space solutions. The following key observations are drawn:

1) The vertical stress increase beneath a pile base with a diameter of B is confined to a zone extending radially outward by a distance equal to B from the edge of the base and vertically downward to a depth of approximately 2.5B below the base.
2) The vertical stress disperses at an angle of approximately 26.5° from the vertical axis instead of the commonly assumed 45°.

6.2 Recommended practice

In light of the above findings, the following design recommendations are proposed:

1) The vertical stress beneath a pile base in rock should be considered to disperse at an angle of approximately 26.5° from the vertical axis, rather than 45°. On this basis, it is not necessary to restrict the founding levels of adjacent piles to below a 45° envelope projected upward from the deepest pile solely to prevent overlapping end-bearing stresses. The 26.5° dispersion envelope is applicable to rock masses that can be assumed to behave in a linear elastic manner under service loads, which includes the competent rock masses, ranging from fresh to moderately weathered grades, typically used as founding strata in Hong Kong.
2) Where the clear spacing between adjacent pile bases is greater than 0.5 m, no additional checks are required to verify whether overlapping vertical stresses may exceed the applied base pressure.
3) For cases where the clear spacing between adjacent pile bases is less than the larger base diameter and the difference in founding levels exceeds this clear spacing, an assessment should be undertaken to determine whether steep bedrock profiles or corestones may be present beneath the higher pile before proceeding with installation. The assessment should also confirm that axial stresses in the pile shafts are not adversely affected by adjacent piles.
4) Where steep bedrock profiles are encountered, such that the inclination of the bedrock surface exceeds the friction angle along adverse discontinuities, and the difference in founding levels between adjacent piles is greater than the clear spacing, the stability of the rock beneath the piles should be evaluated using recognised engineering methods. Where discontinuities do not daylight at the bedrock surface, or are inclined at angles less than their friction angle, explicit stability checks are not required, because no kinematically feasible sliding mechanism exists and the foundation loads provide a stabilising increase in normal stress on potential failure planes.
5) Where stability checks are necessary, targeted surveys of rock discontinuities are recommended to avoid overly conservative assumptions when assessing plausible wedge failure mechanisms affecting foundation stability. If required, founding levels may be adjusted to mitigate rock wedge failure.

These recommendations are expected to enable more economical and constructible bored pile designs in Hong Kong and similar rock conditions, while maintaining acceptable safety margins against overstressing and rock mass instability.

ACKNOWLEDGEMENTS

This paper is published with the permission of the Head of the Geotechnical Engineering Office and the Director of Civil Engineering and Development, the Government of the Hong Kong Special Administrative Region of the People's Republic of China.

REFERENCES

Building Department. (2024). *Code of Practice for Foundations* (2024 ed.). Government of the Hong Kong Special Administrative Region.

Boussinesq, J. (1885). *Application des potentiels à l'étude de l'équilibre et du mouvement des solides élastiques*. Gauthier-Villars.

Hoek, E., Carranza-Torres, C., & Corkum, B. (2002). Hoek–Brown failure criterion – 2002 edition. In *Proceedings of the 5th North American Rock Mechanics Symposium and the 17th Tunnelling Association of Canada Conference* (pp. 267–273). University of Toronto Press.

Hoek, E., & Diederichs, M. S. (2006). Empirical estimation of rock mass modulus. *International Journal of Rock Mechanics and Mining Sciences, 43*(2), 203–215.

Hoek, E., & Marinos, P. (2000). Estimating the geotechnical properties of heterogeneous rock masses such as Flysch. *Bulletin of Engineering Geology and the Environment, 60*(2), 85–92.

Kwong, A. K. L., & Wong, B. M. L. (2013). An assessment of in-situ rock stress ratio in Hong Kong. *HKIE Transactions, 20*(1), 52–61.

Pells, P. J. N., & Turner, R. M. (1979). Elastic solutions for the design and analysis of rock-socketed piles. *Canadian Geotechnical Journal, 16*(3), 481–487.

Poulos, H. G. (1968). Analysis of the settlement of pile groups. *Géotechnique, 18*(4), 449–471.

Poulos, H. G., & Davis, E. H. (1980). *Pile foundation analysis and design*. John Wiley & Sons.

Poulos, H. G., & Mattes, N. S. (1971). Settlement and load distribution analysis of pile groups. *Géotechnique, 21*(2), 101–119.

Santarelli, F. J., & Brown, E. T. (1987). Performance of deep wellbores in rock with a confining pressure-dependent elastic modulus. In *Proceedings of the 6th International Congress on Rock Mechanics* (Vol. 2, pp. 1217–1222). International Society for Rock Mechanics.

Proposed Methodology for Evaluating the Allowable Peak Particle Velocity Limit of Stabilized Rock Slopes with Rock Dowels Subject to Blasting Vibration

Ivan H.H. Chan, Stanley Y.T. Cheung & Daniel Y.P. Ho
Geotechnical Engineering Office, Civil Engineering and Development Department, The Government of the HKSAR, Hong Kong SAR, China
Guy Bridges, Genie C.Y. Nip & Matthew W.H. Fong
AECOM Asia Company Limited

ABSTRACT

Blasting-induced vibrations pose a safety concern regarding the stability of rock slopes, particularly in urban infrastructure projects where stringent peak particle velocity (PPV) limits are commonly enforced. These vibration limits, typically determined from empirical guidelines, may not reflect the actual resistance capacity of stabilized rock slopes with rock dowels. Such limitations on blasting operations, imposed through restrictions on the Maximum Instantaneous Charge (MIC) weight, can lead to increased construction time and costs. This paper presents a methodology supported by field data from a pilot project that enable the application of a higher PPV limit for stabilized rock slopes with rock dowels subject to blasting vibrations. Moreover, the site monitoring results demonstrated that stabilized rock slope could withstand blasting vibrations exceeding 25 mm/s. This work bridges the current divide between prescribed guidelines and actual field performance, enabling more cost-effective and efficient blasting operations while maintaining safety.

1 INTRODUCTION

In Hong Kong, blasting has occasionally been identified to be a contributory factor to rock slope instability, with notable cases reported by Nicolls et al. (1992). To safeguard rock slope stability - particularly in urban infrastructure projects - blasting-induced vibrations are typically controlled using stringent peak particle velocity (PPV) limits. GEO Report No. 15 provides empirical guidelines to assess the allowable vibration limits for free-sliding rock block, whereas the prescriptive criteria in Technical Guidance Note No. 28 are commonly applied in a conservative manner to stabilized rock slopes, as if it was a soil slope that meet current standards. Such conservatism may result in unnecessarily restrictive controls on the Maximum Instantaneous Charge (MIC) weight, which in turn can prolong construction durations and increased overall project costs. While existing guidelines include frameworks and methodologies to determine vibration limits for soil slopes and free-sliding rock blocks, there remains a notable gap in established methodologies for assessing the vibration resistance of stabilized rock slopes.

This paper presents a simple yet conservative pseudo-static methodology, developed and validated through a pilot project at the "Joint Cavern Development at Anderson Road Quarry Site" (JCD), with the specific aim of addressing the gap under current practice. By applying the proposed approach, a significantly higher PPV limit in the order of 150 mm/s was justified and successfully implemented. Field monitoring during cavern excavation confirmed that the stabilized rock slopes could safely withstand PPV values exceeding 100 mm/s without any signs of distress. This work bridges the current divide between prescribed guidelines and actual field performance, enabling more cost-effective and efficient blasting operations without compromising the safety standard.

2 PREVAILING APPROACH OF EVALUATING THE PPV LIMIT FOR SLOPES

2.1 PPV limit of rock slopes based on analytical methods

Section 1 of GEO Report No. 15 (Wong & Pang, 1992) introduced an analytical methodology based on energy approach for establishing the allowable vibration limits for rock slopes. This approach has since been widely adopted in Hong Kong by geotechnical practitioners. The fundamental principle of the approach is to evaluates the transmission of blasting-induced kinetic energy to a potential failure wedge, idealized as a free-sliding rock block resting along a discontinuity plane, with consideration on energy dissipation due to the displacement of rock block and frictional loss along the rock joint. Notably, this approach does not incorporate the effect of stabilizing measures such as rock dowels, thereby representing an estimate under unreinforced condition only.

Wong & Pang (1992) opined that the pseudo-static approach is not suitable for assessing the stability of rock slopes subject to blasting vibration. Compared to earthquake ground motions, blasting vibration is comprised of short duration high frequency pulses with a frequency content typically ranging from 30 to 100 Hz based on local records. Despite the large ground accelerations (with PPA up to 1g or higher from vibration monitoring records) induced by blasting, the blasting pulses often possess relatively low vibration energy. The use of a large pseudo-static inertia force derived from the measured PPA's in the analyses has been found to give dynamic factors of safety less than unity, even for slopes with reasonably high static factors of safety. These results are in contradiction to the low level of vibration energy transmitted to the potential failure wedge on the slope. Because of the unrealistic results obtained, it is generally believed that using the pseudo-static approach to analyse problems of blasting vibrations characterised by high frequency pulses is very conservative. Consequently, Wong & Pang (1992) had proposed the energy approach for assessing the stability of rock slope subject to blasting vibration.

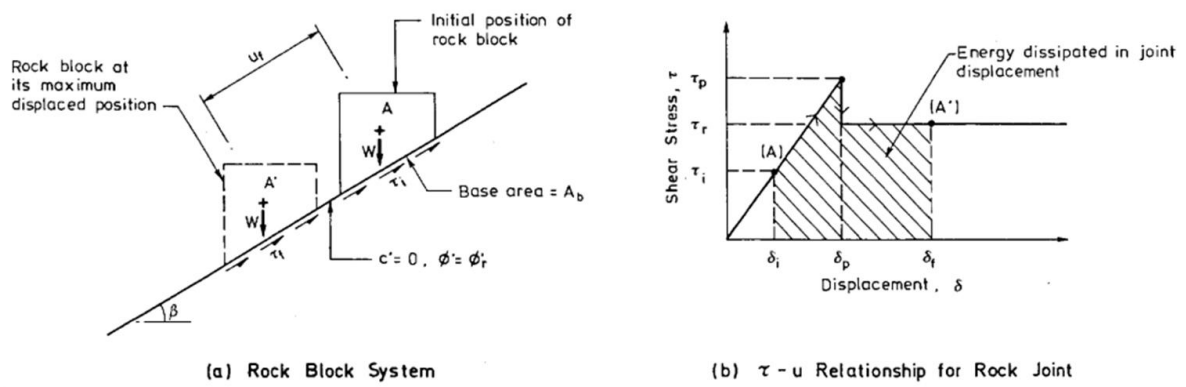

Figure 1: Energy dissipation of rock block system based on combined rock joint model (Wong & Pang, 1992)

2.2 PPV limit of soil slopes based on prescriptive guidelines

GEO Technical Guidance Note (TGN) No. 28 (GEO, 2010) established a control framework for soil slopes subjected to blasting vibration. Pursuant to this TGN, the prescriptive PPV limits of 25 mm/s could be applied to "soil slopes that pose negligible risk to life" and "consequence-to-life category 1 & 2 soil slopes that meet current standards". Under this framework, it is not necessary to carry out site-specific analysis such as the pseudo-static approach described in Wong & Pang (1992).

The prescriptive guideline is commonly adopted for cases when the soil slope is located at a moderate distance from the blast location and is not the critical sensitive receiver.

2.3 Current practice for determining the PPV limit of stabilized rock slopes

As there are no design guidelines for assessing the vibration limit of stabilized rock slopes, a prescriptive PPV limit of 25 mm/s is commonly adopted with reference to the empirical PPV limit for soil slopes as promulgated

in GEO (2010). Rock slopes in close proximity to the area of blasting works may become the critical sensitive receiver in controlling the allowable MIC weight for blasting works.

3 PROPOSED METHOD FOR DETERMINING THE PPV LIMIT FOR STABILIZED ROCK SLOPES

3.1 Assumptions and derivation of proposed method

The rock block on the rock slope is stabilized by rock dowels, and is idealized as an undamped single-degree-of-freedom (SDOF) system with the lumped mass and linear spring representing the rock block and rock dowel respectively. The idealization of the stabilized rock block system is presented in Figure 2.

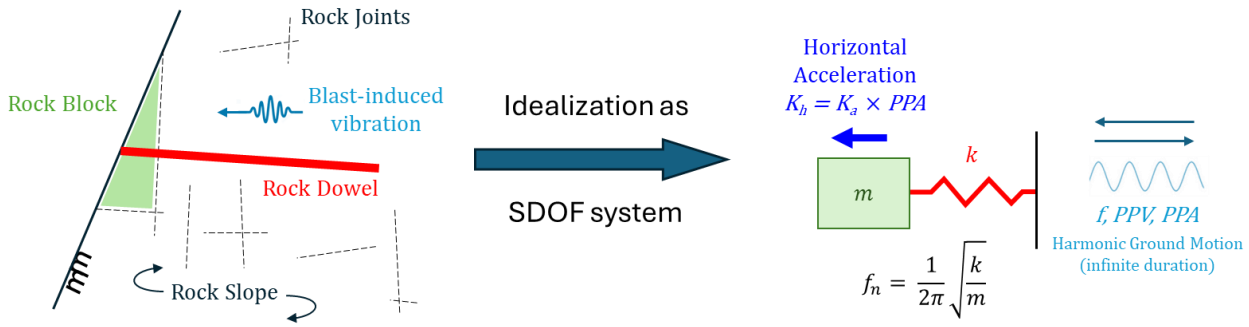

Figure 2: Idealization of the stabilized rock block as a SDOF system

The stiffness of the equivalent linear spring k and the linear natural frequency f_n of the SDOF system (in Hz) is calculated as

$$k = \frac{nEA}{L} \tag{1}$$

$$f_n = \frac{1}{2\pi}\sqrt{\frac{k}{m}} \tag{2}$$

where n = number of rock dowels stabilizing the rock block, E = Young's modulus of dowel, A = cross sectional area of dowel, L = length of dowel and m = mass of the rock block.

The blast-induced vibration is idealized as a harmonic ground motion of infinite duration. The parameters for describing the ground motion are the frequency of the blast-induced vibration f and peak particle velocity PPV which are routinely monitored during blasting operations. The peak particle acceleration PPA can be calculated as

$$PPA = 2\pi f \times PPV \tag{3}$$

For a SDOF system subjected to harmonic ground motion, the acceleration experienced by the mass (K_h) is related to the amplitude of the ground acceleration (i.e. PPA) as follows (Chopra, 2020)

$$K_a = \sqrt{\frac{1+4\zeta^2\alpha^2}{(1-\alpha^2)^2+4\zeta^2\alpha^2}} \left(= \sqrt{\frac{1}{(1-\alpha^2)^2}} \text{ for undamped systems with } \zeta=0\right) \tag{4}$$

$$K_h = K_a \times PPA \tag{5}$$

where $K_a = \frac{K_h}{PPA}$ is the magnification factor (or transmissibility), $\alpha = \frac{f}{f_n}$ is the frequency ratio and ζ is the damping ratio of the system.

Consequently, the pseudo-static force F acting on the mass can be calculated as

$$F = \text{mass} \times \text{acceleration} = m \times K_h \quad (6)$$

As the pseudo-static force is dependent on PPV and f, the pseudo-static force should be calculated based on a design PPV value for a range of f to determine the maximum response of the system. The design PPV can be estimated from the maximum instantaneous charge (MIC) weight and distance between the blast and the location of interest by the equation given by GEO (2018).

$$PPV = K(\frac{R}{\sqrt{Q}})^{-b} \quad (7)$$

where K is a rock constant, R is the distance between the blast and location of interest, Q is the MIC weight (in kg) and b is the attenuation exponent.

In the absence of site-specific constants, the local vibration attenuation constants $K = 644$ and $b = 1.22$ based on the upper 84% confidence level given by Li & Ng (1992) can be adopted for initial assessment of the design PPV.

3.3 Discussion of the proposed method

For SDOF systems with small damping ratio under harmonic ground motion of infinite duration, resonance will occur when the frequency of ground motion matches the natural frequency of the system. The acceleration experienced by the mass would be significantly amplified as shown in Figure 3, and tends to infinity for resonant systems (i.e. frequency ratio = 1).

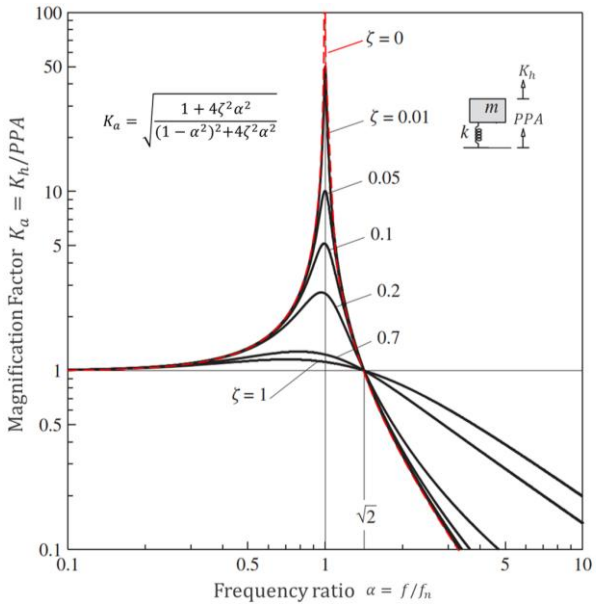

Figure 3: Plot of magnification factor against frequency ratio for various damping ratios (modified from Chopra, 2020)

The natural frequency of SDOF system with various combination of dowel configuration and block mass are generally in the range of 7 Hz to 20 Hz and tabulated in Table 1. In this case, damping ratio is assumed to be zero for conservative. As the natural frequency of these SDOF systems is generally below 30 Hz and does not

match with the excitation frequency due to blast vibration, resonance is thus not susceptible and the magnification factor is relatively small.

Table 1: Natural frequency of SDOF system with various combination of dowel configuration and block masses

Dowel diameter (mm)	32			40		
Dowel length (m)	6			6		
no. of rock dowel for each rock block	1			1		
Spring stiffness (N/m)	2.75E+07			4.29E+07		
Mass of rock block (kg)	2600	8775	20800	2600	8775	20800
Equivalent cube length (m)	1	1.5	2	1	1.5	2
Natural frequency of equivalent SDOF system (Hz)	16.36	8.91	5.78	20.45	11.13	7.23

Note: SDOF systems with natrual frequency comparable to the vibration frequency (30-100Hz) are highlighed in yellow.

Particular attention must be paid to the fact that the natural frequency of the SDOF system increases with decreasing rock block mass and increasing spring stiffness (larger and shorter dowels) of supporting system. Rock slopes composed of heavily jointed rock mass with small block sizes are theoretically prone to resonance, as its natural frequency likely fall within the range of 30 to 100 Hz. Consequently, the applicability of this proposed method for determining allowable vibration limits must be critically evaluated in such contexts, as resonance may significantly amplify dynamic responses and compromise slope stability. On the other hand, it should be also noted that a pattern rock dowel system, by itself, is generally insufficient to provide adequate stabilization for such highly fractured rock slope.

The pseudo-static force derived from the proposed method is expected to be on the conservative side. Specifically, the method assumes that the ground motion is a simple harmonic motion with infinite duration, which contrasts with the transient, short-duration nature of actual blasting vibration. Furthermore, the model neglects energy dissipation mechanisms at the rock joint interface, including frictional resistance and inelastic deformation, which would otherwise attenuate the transmitted vibrational energy. Therefore, analysis using the proposed method is expected to give conservative results.

4 CASE STUDY ON ADOPTION OF THE PROPOSED METHOD

The proposed method was adopted in the "Joint Cavern Development at Anderson Road Quarry Site" (JCD) project managed by the Geotechnical Engineering Office of the Civil Engineering and Development Department. The JCD project involves the excavation of four large span caverns of 32 to 36 m span with the cavern portals located at an existing rock slope. The caverns will be used for the Public Works Central Laboratory (PWCL) and as an archive centre (AC) for the Government Records Service. The layout of the caverns and their relative location to the existing rock slope is shown in Figure 4 and 5.

4.1 Blasting works in the JCD project

In the JCD project, blasting is adopted to excavate the competent rock at the ex-quarry site and is sequentially excavated by top heading, middle bench and bottom bench blasts. In order to minimize the nuisance to the public, the cavern portal (i.e. existing rock slope) is designated as a non-blast zone ("rock plug"). The rock plug (highlighted in red in Figure 6) encloses the blasting area and will only be removed by mechanical methods after basting works inside the cavern is completed.

Among the blasting sensitives receivers, the existing rock slope at the cavern portal is one of the critical sensitive receivers controlling the allowable charge weight of the cavern blasting operations. If the minimum non-blast zone and the closest distance between the blast and the rock slope is 10 m, and the allowable PPV limit of the rock slope is 25 mm/s, the allowable MIC weight is calculated as 0.5 kg based on the attenuation constants given by Li & Ng (1992). Such low allowable MIC weight would limit the pull length of each blast and significantly limit the excavation rate.

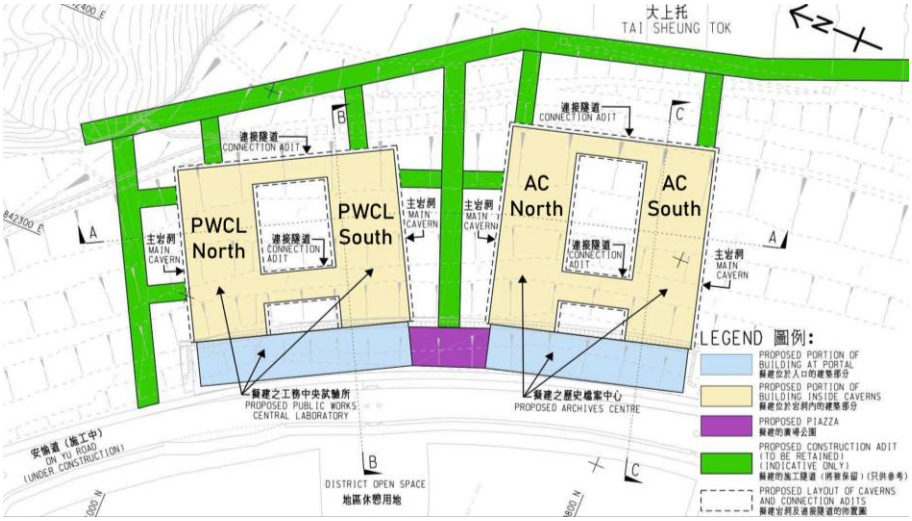

Figure 4: Layout of caverns in the JCD project

Plate 1: General view of the caverns in the JCD project and their portal located at an existing rock slope

4.2 Adoption of the proposed method in the JCD project

In view of the proximity of the rock slope and its potential constraints on blasting works, the proposed method was adopted to evaluate the allowable PPV limit and the required rock dowel layout to stabilize the rock slope for enduring the PPV limit. The PPV limit of the rock slope is set as 150 mm/s and the corresponding allowable MIC weight is approximately 9 kg at a distance of 10 m. This is a more reasonable MIC weight and enables effective blasting operations. The PPV contours based on this MIC weight was plotted in Figure 6.

The observed joint spacing is approximately 1.5 m so the rock blocks are assumed to be 1.5m cubes. The dowel diameter, length and spacing are 32 mm, 6 m and 1.5 m c/c respectively. By the proposed method, the pseudo-static force acting on the rock block is determined to be 24 kN (i.e. in the order of 0.3g). This calculated pseudo-static force was adopted to check the structural and geotechnical adequacy of the rock dowel.

In addition to the patterned rock dowels, a layer of wire mesh was also fixed to the rock face as a precautionary measure to retain any loose rock blocks.

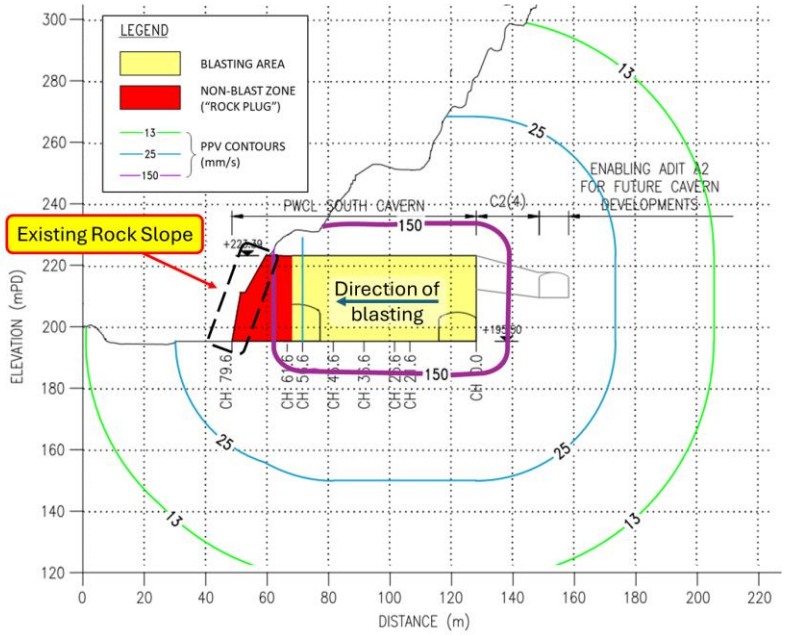

Figure 6: Longitudinal section of cavern showing the non-blast zone and the PPV contours

4.3 Performance review of blasting works in the JCD project

The blasting works for the caverns in the JCD project had been completed in November 2025. On average, 70 blasts are required for excavating one cavern in the project. Through adopting the proposed method of evaluating the PPV limit of the stabilised rock slope, the extent of the non-blast zone was minimized and the blasting works was carried out with MIC weights ranging from 2.4 to 10 kg.

The blasting monitoring records and measured PPV values at the rock slope were reviewed. The details of the blasts that generated the highest PPV values at the stabilised rock slope are summarized in Table 2.

Sensitive receiver	MIC (kg)	Distance from sensitive receiver (m)	Resultant PPV (mm/s)	
			Measured	Permissible
Stabilised Rock Slope	4.7	13.7	118	150
	4.7	15.2	95	150
	2.4	25.3	85	150
	9.5	27.6	66	150
	4.8	16.4	63	150
	9.5	24.6	58	150

Table 2: Details of the blasts which generated the highest PPV values at the stabilised rock slope

The maximum measured PPV is 118 mm/s which is within the PPV limit of 150 mm/s for the stabilised rock slope. At peak PPV values, the average measured frequency of vibration is in the order of 35 Hz which fall within the typical range of local records (30 to 100 Hz). However, some low frequency vibrations in the order of 10 to 20 Hz were also recorded at low PPV level. Nevertheless, no instability, excessive deformation, of exceedance of design dowel capacities were observed throughout the duration of the cavern blasting works. No evidence of resonance was observed, which would be attributed to two primary factors: (i) the short duration and limited energy transmission of blasting vibrations, and (ii) existence of rock joint friction and the associated energy dissipation mechanisms, as discussed in Section 3.3.

4.4 Discussion for applying the proposed method in future blasting projects

The following items could be considered when applying the proposed method in future blasting projects.

Table 3: Items to consider during different stages in the blasting project when applying the proposed method

Investigation and Design Stage	- The rock slopes within the influence zone of the proposed blasting works should be identified. Suitable inspection and mapping should be carried out to understand the nature of the rock slopes and the presence of destabilising/adverse factors (if any) - The required PPV limit should be estimated based on the anticipated range of MIC weight to be adopted in the blasting works - Typical size of the rock block and the dimension of rock dowels for computing the magnification factor and amplified pseudo-static force
Construction Stage	- Rock dowels should be properly implemented before the commencement of blasting works - Other protective or preventive measures, such as wire mesh fixed onto the slope surface should also be considered - The charge weight should be increased progressively to monitor the behaviour of the stabilised rock slope under blasting vibrations - The measured PPV values should be reviewed after each blast to ensure that the PPV limit of the stabilised rock slope is not exceeded

5 CONCLUTIONS

The analytical framework for estimating the PPV limit of stabilised rock slopes is presented herein, based on the idealisation of the rock block/dowel system to a SDOF system subjected to vibration in form of infinite harmonic ground motion. The derivation assumes an infinite-duration harmonic input, neglects energy dissipation due to joint friction and viscous damping that collectively yield a conservative estimate of allowable PPV. The proposed method was successfully applied in a local blasting project adjacent to an existing rock slope. It allowed higher MIC weights and improved the productivity of each blast. Comprehensive post-blast monitoring confirmed no evidence of displacement, cracking, or failure across the stabilised slope over the duration of the works. The method may offer a viable alternative to the prevailing prescriptive PPV for other blasting projects with similar geological setting in Hong Kong, with high potential to optimise the blasting operation while maintaining adequate safety margins.

Particular caution is warranted when applying this method to highly fracture rock slopes characterized by small rock block and stiff support (i.e. short and large diameter dowels). Under such conditions, the natural frequency of the supported rock block system may resonate with the dominant frequency of blasting vibration, potentially triggering amplified dynamic responses. Moreover, the application of this method requires appropriate adjustment when the blasting-induced excitation frequency deviates from the typical range of 30 to 100 Hz.

ACKNOWLEDGEMENTS

This paper is published with the permission of the Head of Geotechnical Engineering Office and the Director of Civil Engineering and Development, Government of the Hong Kong Special Administrative Region, China.

REFERENCES

Nicoll, K.H., Cowland, J.W. & Chan, R.K.S. 1992. Effects of blasting on the stability of adjacent rock slopes. *Proceedings of Conference "Asia Pacific – Quarrying the Rim". Hong Kong. Institute of Quarrying.*

Chopra, A.K. 2020. *Dynamics of Structures: Theory and Applications to Earthquake Engineering (5th edition in SI units).* Pearson Education Limited.

Geotechnical Engineering Office 2010. *GEO Technical Guidance Note No. 28: New Control Framework for Soil Slopes Subjected to Blasting Vibrations.* Geotechnical Engineering Office, Hong Kong SAR.

Geotechnical Engineering Office 2018. *Geoguide 4: Guide to Cavern Engineering (2nd edition).* Geotechnical Engineering Office, Hong Kong SAR.

Geotechnical Engineering Office 2020. *GEO Technical Guidance Note No. 10: Enhancement of Rock Slope Engineering Practice Based on Findings of Landslide Studies.* Geotechnical Engineering Office, Hong Kong SAR.

Li, U.K. & Ng, S.Y. 1992. Prediction of blast vibration and current practice of measurement in Hong Kong. *Proceedings of Conference "Asia Pacific – Quarrying the Rim". Hong Kong.* Institute of Quarrying.

Wong, H.N. & Pang, P.L.R. 1992 (Reprinted 2000). *GEO Report No. 15: Assessment of Stability of Slopes Subjected to Blasting Vibration (GEO Report No. 15).* Geotechnical Engineering Office, Hong Kong SAR.

Predicting Tunnel Overbreak in Drill and Blast Operations Using Random Forest Regression: A Case Study in Hong Kong Granitic Rock

Jason T.Y. Chin
Aurecon Hong Kong Limited
S. Jayawardena & George X. Coe
Aurecon Australasia Proprietary Limited

ABSTRACT

Tunnel overbreak - excavation beyond the designed profile - remains a persistent challenge in drill and blast tunnelling, driving cost escalation, schedule delays, and compromised structural integrity. Traditional estimation methods rely on empirical formulae and expert judgment, which are subjective and fail to capture complex nonlinear interactions among geological, geometric, and operational variables. This paper presents a Random Forest regression model for predicting overbreak ratios in drill and blast tunnels through Hong Kong granitic rock. The model was trained on approximately 407 samples using NGI Q-system parameters, historical overbreak ratios, drill envelope geometry, and explosive mass as inputs. Grid search hyperparameter tuning yielded an optimal configuration of seven estimators with maximum depth of ten, achieving a training R^2 of 0.858 and testing R^2 of 0.515 - outperforming linear regression, polynomial regression, and single decision tree alternatives. Feature importance analysis identified overbreak continuity from preceding sections and rock quality designation as the most influential predictors. The paper discusses practical applicability during tendering and construction phases, lessons learned, and future directions including Measurement While Drilling integration and real-time prediction frameworks. The model applies to drill and blast tunnels in granitic rock mapped using the NGI Q-system where joint water effects are negligible.

1 INTRODUCTION

1.1 Background

Underground construction is fundamental to the development of modern urban infrastructure. Tunnels serve not only as transport corridors but also as conduits for water supply, sewage conveyance, stormwater drainage, and utility distribution. Many tunnel systems incorporate geometric complexity in the form of intersections, cross-passages, ventilation shafts, and underground chambers, demanding construction methodologies that accommodate variable alignment and cross-sectional geometry (Barton et al. 1974; Palmström and Broch 2006).

While tunnel boring machines (TBMs) dominate media coverage of major infrastructure projects, the drill and blast method remains the preferred excavation technique in many geological settings, particularly in hard rock and mountainous terrain. This method involves drilling a precisely designed pattern of holes into the rock face, charging them with explosives, and detonating in a controlled sequence. The resulting blast fractures the rock, which is subsequently removed by mechanical loaders or conveyors. The tunnel advances incrementally through repeated cycles of drilling, blasting, mucking, and support installation (Jimeno et al. 1995; Jang and Topal 2013).

Drill and blast tunnelling offers considerable flexibility in excavation shape and alignment, rendering it well suited to complex geometries and heterogeneous ground conditions. However, the method introduces a persistent challenge: overbreak. Overbreak is defined as the volume of rock excavated beyond the designed tunnel profile. This excess excavation arises from geological variability, blasting inaccuracies, drill hole misalignment, and operational constraints. The consequences of overbreak are multifaceted: increased mucking volumes, extended excavation cycle times, elevated support requirements, compromised structural integrity, and heightened safety risks associated with larger unsupported spans (Jang and Topal 2013; He et al. 2023).

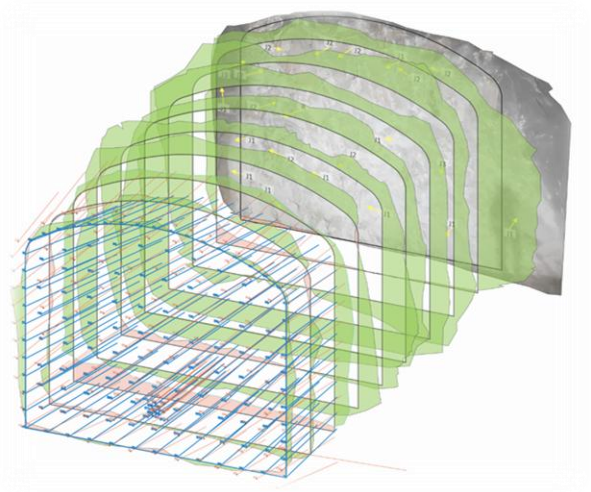

Figure 1: Example tunnel overbreak profile and blast hole orientation in 3D

1.2 Context: Hong Kong Tunnelling Practice

In Hong Kong, the prevalence of high-strength granitic rock and the increasing demand for subterranean space make drill and blast the method of choice for numerous infrastructure projects. Notable examples include Central Kowloon Bypass (Yau Ma Tei Section) and the Joint Cavern Development at Anderson Road Quarry to house public laboratories and underground archive center. These projects require precise control over tunnel geometry and rock support systems. Uncontrolled overbreak in such contexts leads to significant cost overruns, schedule disruptions, and potential invalidation of original design assumptions, necessitating redesign and rework.

1.3 Limitation of Traditional Approaches

Conventional methods for estimating overbreak rely on empirical formulae and engineering judgment. While these approaches draw upon accumulated professional experience, they are limited by subjectivity, poor reproducibility and scalability, and an inability to capture the complex, nonlinear interactions among geological parameters and excavation outcomes (Mottahedi et al. 2017; Mohammadi et al. 2018). The growing availability of digitized construction records, including geological face mapping, survey profiles, and drill logs, creates an opportunity to develop data-driven models that improve prediction reliability.

1.4 Research Objective and Scope

This paper presents a Random Forest regression model developed to predict tunnel overbreak using geological parameters derived from the NGI Q-system, historical overbreak performance data, drill envelope geometry, and explosive charge weight. The model was trained on approximately 420 samples collected from six different tunnel profiles.

The objectives of this study are threefold. First, the study seeks to demonstrate the feasibility of applying ensemble machine learning to overbreak prediction using routinely collected construction data. Second, it aims to provide contractors and engineers with a potential tool for overbreak estimation during both tendering and construction phases. Third, it identifies the relative importance of input parameters and highlights areas where additional data collection could improve predictive performance.

The model is applicable to drill and blast tunnels in granitic rock, mapped using the NGI Q-System, where joint water effects are negligible and the predominant failure mode is kinematic rather than stress-induced. The model is not applicable at tunnel junctions formed after the excavation of the first tunnel, although sections preceding junction formation are included.

It is also important to note that the development of any machine learning model is to "predict" rather than "prevent" overbreak. It is the authors' opinion that the predicted overbreak in any drill and blast tunnels during tender or construction period is to provide the contractor a tool for better risk control and pricing accordingly.

2 LITERATURE REVIEW

2.1 Overview

Overbreak prediction in drill and blast tunnels has attracted considerable research attention over the past two decades. Investigators have applied a spectrum of statistical and machine learning methods, ranging from simple regression to advanced ensemble and hybrid architecture. The common objective has been to improve prediction accuracy using geological, blasting, and geometric input parameters derived from specific tunnel projects.

2.2 Multiple Regression Models

Jang and Topal (2013) employed linear and nonlinear multiple regression analysis (LMRA and NMRA) to predict overbreak from geological parameters in the Bigye tunnel, South Korea, using a dataset of 49 blasting sections. The LMRA and NMRA models achieved R^2 values of 0.694 and 0.708, respectively. Although simple and interpretable, these models were constrained by linearity assumptions and a limited sample size.

Mohammadi et al. (2018) applied linear regression incorporating geological, blasting, and geometric parameters for overbreak prediction in sedimentary rock tunnels, achieving $R^2 = 0.93$. However, the model was affected by multicollinearity, requiring manual exclusion of correlated parameters, and was developed from only 24 samples.

2.3 Artificial Neural Networks

Artificial neural networks (ANN) have been widely applied to improve upon regression-based approaches. Jang and Topal (2013) developed an ANN with a 6-13-5-1 architecture, achieving $R^2 = 0.945$. Koopialipoor et al. (2017) combined ANN with genetic algorithms (GA-ANN) to optimise network weights and biases, reporting R^2 values of 0.903 on training data and 0.881 on testing data. Koopialipoor et al. (2019) further refined this approach using artificial bee colony optimisation (ABC-ANN), achieving $R^2 = 0.9396$ on training data, although no independent test set was reported.

While ANN models consistently demonstrated high accuracy, they suffer from poor interpretability and require specialised knowledge for implementation - characteristics that limit their adoption in routine construction practice (Koopialipoor et al. 2018).

2.4 Fuzzy Logic and Neuro-Fuzzy Systems

Mohammad et al. (2015) applied fuzzy set theory to overbreak prediction in the Alborz Tunnel, Iran, achieving $R^2 = 0.96$ and root mean square error (RMSE) of 0.55. Mottahedi et al. (2017) developed adaptive neuro-fuzzy inference system (ANFIS) models, reporting $R^2 = 0.97$ on a dataset of 267 samples. These approaches handled uncertainty effectively but required expert-defined membership functions and were difficult to calibrate, limiting industry adoption.

2.5 Support Vector Machines and Wavelet Neural Networks

Mottahedi et al. (2017) also evaluated support vector machine (SVM) models with radial basis function kernels, which performed competently but did not match ANFIS accuracy. Sun et al. (2013) combined geological statistics with wavelet neural networks (WNN), reporting 10 to 30% error between predicted and actual overbreak volumes. WNN offered fault tolerance but demanded extensive preprocessing and parameter tuning.

2.6 Ensemble Methods

Ensemble methods have demonstrated particular promise. He et al. (2023) developed Random Forest models optimised using metaheuristic algorithms, Grey Wolf Optimiser (GWO), Whale Optimisation Algorithm (WOA), and Tunicate Swarm Algorithm (TSA), on a dataset of 523 samples. The RF-TSA model achieved $R^2 >$ 0.9, identifying powder factor and total charge as dominant predictors. Hong et al. (2023) applied XGBoost with Bayesian optimisation to 250 samples, achieving R^2 = 0.934 and conducting statistical validation via Friedman and Wilcoxon tests.

Ensemble models, particularly Random Forest, balance accuracy with robustness and interpretability. They handle small datasets effectively, resist overfitting through bootstrap aggregation, and provide feature importance metrics that support engineering interpretation (Breiman 2001).

2.7 Research Gaps

Despite the diversity of published models, several gaps persist. Many studies relied on small or single-tunnel datasets, limiting generalisability. Several models excluded operationally significant factors such as blast hole orientation and charge distribution due to data unavailability. High-performing models such as ANN, ANFIS, and XGBoost are computationally intensive and lack the transparency required for routine construction decision-making. Most published models are static, offering no mechanism for real-time updating as excavation progresses. Furthermore, models trained on site-specific data require external validation before broader application can be recommended (Navarro et al. 2018; Jang et al. 2019).

The present study addresses these gaps by developing a Random Forest model that uses routinely available geological and historical data, provides interpretable feature importance, and targets practical application during both tendering and construction in the specific context of Hong Kong granitic rock tunnelling.

3 Methodology

3.1 Data Collection

The dataset comprises approximately 420 samples collected from multiple tunnel sections. Data were sourced from contractor records including jumbo drilling logs, geological face mapping reports (conducted using the NGI Q-System), and survey measurements of excavation profiles. All records were manually verified for consistency and completeness.

Each sample includes the following categories of parameters:

$$Q' = \frac{RQD}{J_n} \times \frac{J_r}{J_a} \tag{1}$$

where RQD = rock quality designation, J_n = jointset number, J_r = joint roughness number, and J_a = joint alteration number.

Geological parameters derived from Q-system face mapping: Rock Quality Designation (RQD), joint set number (J_n), joint alteration number (J_a), joint roughness number (J_r), and stress reduction factor (SRF). The modified rock mass quality index Q' was computed as Equation (1).

This formulation excludes the joint water reduction factor (J_w) and SRF from the composite index. The parameter J_w was excluded on the basis of engineering judgment: groundwater inflow through discontinuities was assessed to have negligible influence on rock fragmentation and overbreak in the studied tunnels. SRF was retained as a separate input feature to capture stress-related effects independently.

Historical overbreak data (Figure 2) included the overbreak ratio from the immediately preceding section (OB_ratio_prev1), the overbreak ratio from two sections prior (OB_ratio_prev2), and corresponding chainage differences (CH_diff1, CH_diff2). Overbreak ratio was defined as the ratio of the actual excavated cross-sectional area to the design profile area.

Drill envelope geometry (Figure 2) was derived from convex hulls of outermost perimeter drill hole positions. Parameters included start and end area ratios normalised against the design profile (de_ratio, ds_ratio), and envelope extremities (ds_max_x, ds_max_y, ds_min_y).

Design geometry (Figure 2) was represented by the maximum horizontal extent of the design tunnel profile (max_x), providing a normalisation reference.

Explosive mass (explosive_kg) was recorded as the total charge weight per blast section. This parameter did not vary along the chainage in the studied sections but was included where available to capture energy input effects.

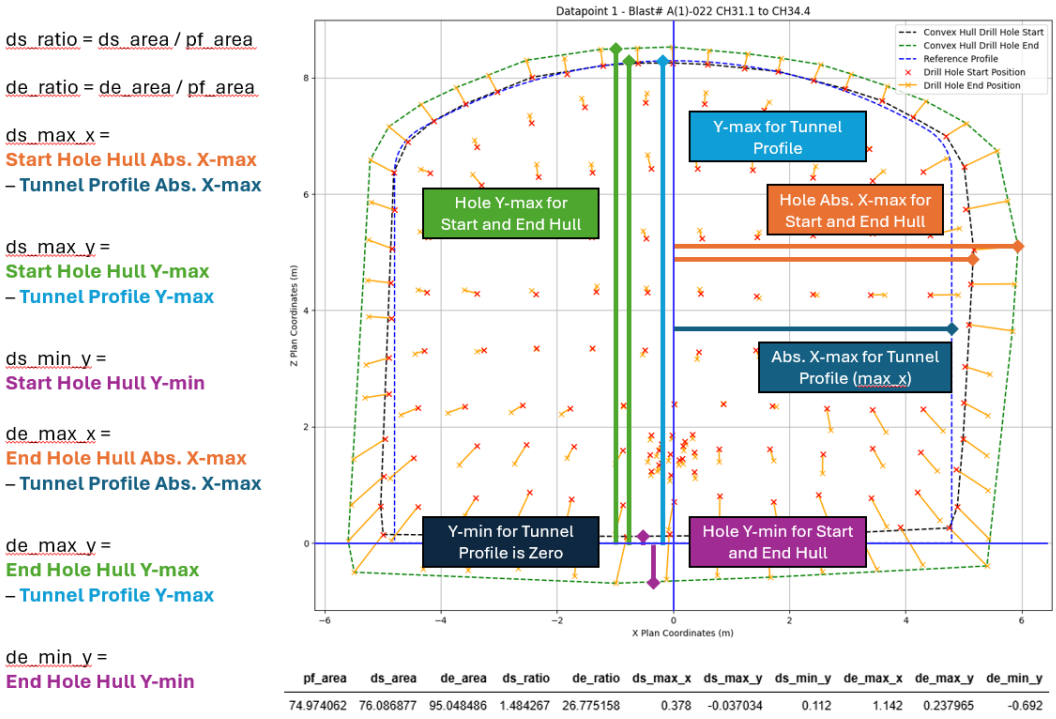

Figure 2: Illustration of the parameters used for OB profile

3.2 Data Processing

All samples were aligned by chainage to ensure correspondence between geological parameters, drill envelope data, overbreak measurements, and the correct tunnel section. Chainage alignment was performed using custom scripts that matched values across multiple data sources, with discrepancies flagged and resolved manually through cross-referencing against excavation logs and support installation records.

For sections where drill envelope data was unavailable, placeholder values of -10,000 were inserted rather than excluding incomplete rows. This is acknowledged as a pragmatic workaround which preserved dataset structure, avoided exclusion bias, and was validated empirically: model performance improved compared to the alternative of removing incomplete records. The Random Forest algorithm effectively learned to disregard these sentinel values during training.

Data types were standardised using Pandas profiling tools. Numerical inputs (*RQD*, Q-value, overbreak ratios) were typed as float64; categorical and text fields as object; and temporal data as datetime64 where applicable. Drill envelope ratios were normalised against the design profile to ensure comparability across sections of differing geometry.

3.3 Model Selection

Four modelling approaches were evaluated prior to final selection. Linear regression produced $R^2 < 0.2$ and failed to capture nonlinear geological interactions. Second-order polynomial regression yielded marginal improvement but introduced multicollinearity and overfitting sensitivity. Single decision trees achieved $R^2 \approx 0.4$ with improved nonlinear capture but exhibited instability across validation folds. Random Forest regression was selected as the final approach based on its superior accuracy, resistance to overfitting through bootstrap

aggregation, capacity to handle small datasets, and provision of feature importance metrics that support engineering interpretation (Breiman 2001).

3.4 Random Forest Configuration

The Random Forest model was implemented using Python's scikit-learn library (Pedregosa et al. 2011) and configured as follows: number of estimators (*n_estimators*) = 7; maximum tree depth (*max_depth*) = 10; bootstrap sampling enabled; feature selection per split set to the square root of total features; and the splitting criterion set to mean squared error. These hyperparameters were determined through systematic grid search. Increasing the number of trees beyond 7 did not improve testing accuracy and increased computational cost. Reducing maximum depth below 10 resulted in underfitting.

A total of 29 candidate parameters were evaluated, and 794 feature combinations were tested during model development. The final feature set of 17 parameters was selected based on a combination of correlation analysis and engineering judgment, yielding the highest predictive performance.

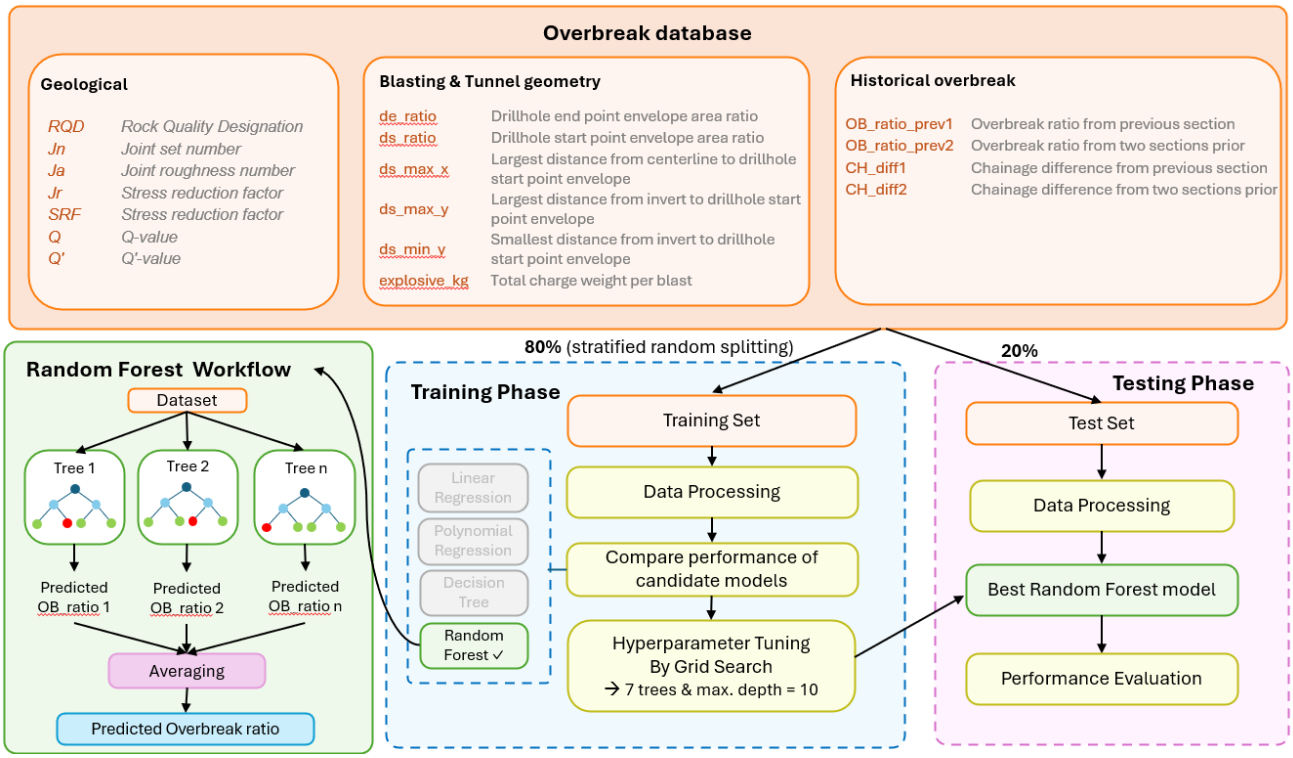

Figure 3: Workflow of Random Forest regression model

3.5 Training and Validation

The dataset was partitioned into training (80%) and testing (20%) subsets using stratified sampling to maintain proportional representation of tunnel structure types across both sets. Stratification ensured that each tunnel designation was represented in both training and testing data, reducing bias toward structure types with greater sample counts.

Model performance was assessed on the training data and independent evaluation on the held-out test set. Metrics included the coefficient of determination (R^2), mean squared error (MSE), and root mean squared error (RMSE). Training was completed on a standard workstation in under ten seconds.

4 Results

4.1 Model Performance

The trained Random Forest model achieved the performance metrics summarised in Table *1*.

Table 1 Model performance metrics

Metric	Training	Testing
R^2	0.858	0.515
MSE	6.17	16.82

The training R^2 of 0.858 indicates that the model fits the training data well. The testing R^2 of 0.515 reflects moderate generalisation capability, with the gap between training and testing performance indicative of overfitting - a common characteristic in models trained on limited datasets with high inherent variability. Figure 4 shows the comparison between the predicted and actual data for the training and the testing.

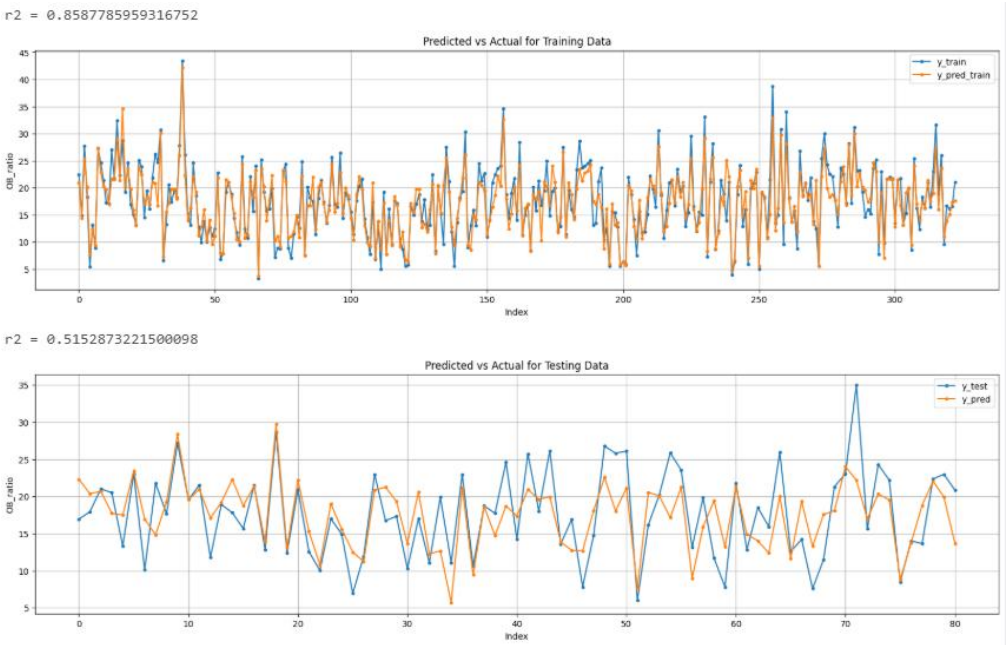

Figure 4: Comparison between predicted and actual data for training (top) and testing (bottom)

4.2 Comparative Performance

The Random Forest model outperformed all alternative approaches tested on the same dataset. Linear regression achieved $R^2 < 0.2$, polynomial regression remained below acceptable thresholds despite marginal improvement over the linear model, and single decision trees achieved $R^2 \approx 0.4$ with inconsistent performance across validation folds. The Random Forest model provided more stable predictions and better captured the nonlinear relationships inherent in the data.

While the testing R^2 of 0.515 is lower than the values reported by studies that incorporated blasting parameters - such as Mottahedi et al. (2017) at 0.97 with ANFIS, and Hong et al. (2023) at 0.935 with XGBoost - the present model was developed intentionally with a constrained input set. Blasting design parameters including charge weight distribution, hole arrangement, and detonation sequence were constant across all sampled blasts and therefore contributed no discriminative information. The moderate accuracy reflects the

inherent limitation of geology-only prediction and establishes a meaningful baseline for future enrichment with operational data.

4.3 Feature Importance

Feature importance was extracted from the trained model based on the reduction in mean squared error contributed by each input across all decision trees (Figure 5). The four most influential features were:

OB_ratio_prev1 (overbreak ratio from the immediately preceding section) ranked highest, confirming that overbreak exhibits geological continuity and that recent excavation history is a powerful predictor. RQD ranked second, with higher rock quality consistently associated with reduced overbreak. The modified Q-value (Q') ranked third, functioning as a composite geological quality index. SRF ranked fourth, reflecting the influence of in-situ stress conditions on rock stability and excavation behaviour.

Drill envelope geometry and chainage differences contributed at lower but non-negligible levels, indicating that drill hole placement and geological spatial continuity provide supplementary predictive value.

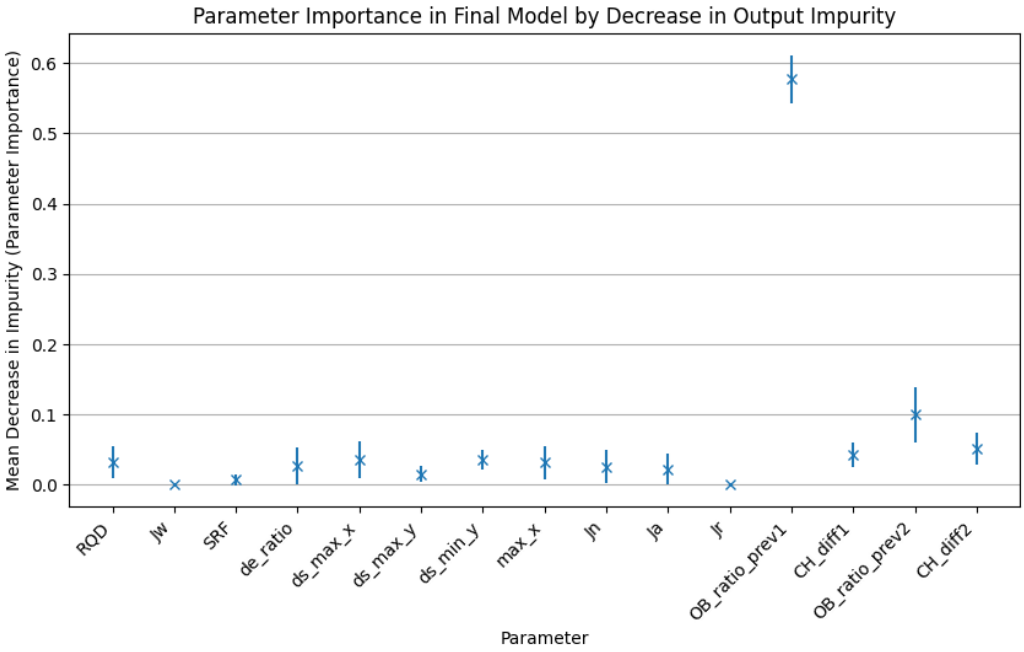

Figure 5: MSE contributed by each input across all decision trees

4.4 Correlation Analysis

A correlation matrix was computed across all input parameters and the target variable (Figure 6). Key observations include a negative correlation between *RQD* and overbreak, consistent with the expectation that superior rock quality reduces excavation excess. A positive correlation was observed between *SRF* and overbreak, reflecting stress-induced instability. OB_ratio_prev1 exhibited strong positive correlation with current overbreak, reinforcing the spatial autocorrelation of excavation outcomes. Drill envelope ratios showed moderate correlation with overbreak, indicating that hole placement contributes to but does not dominate excavation accuracy.

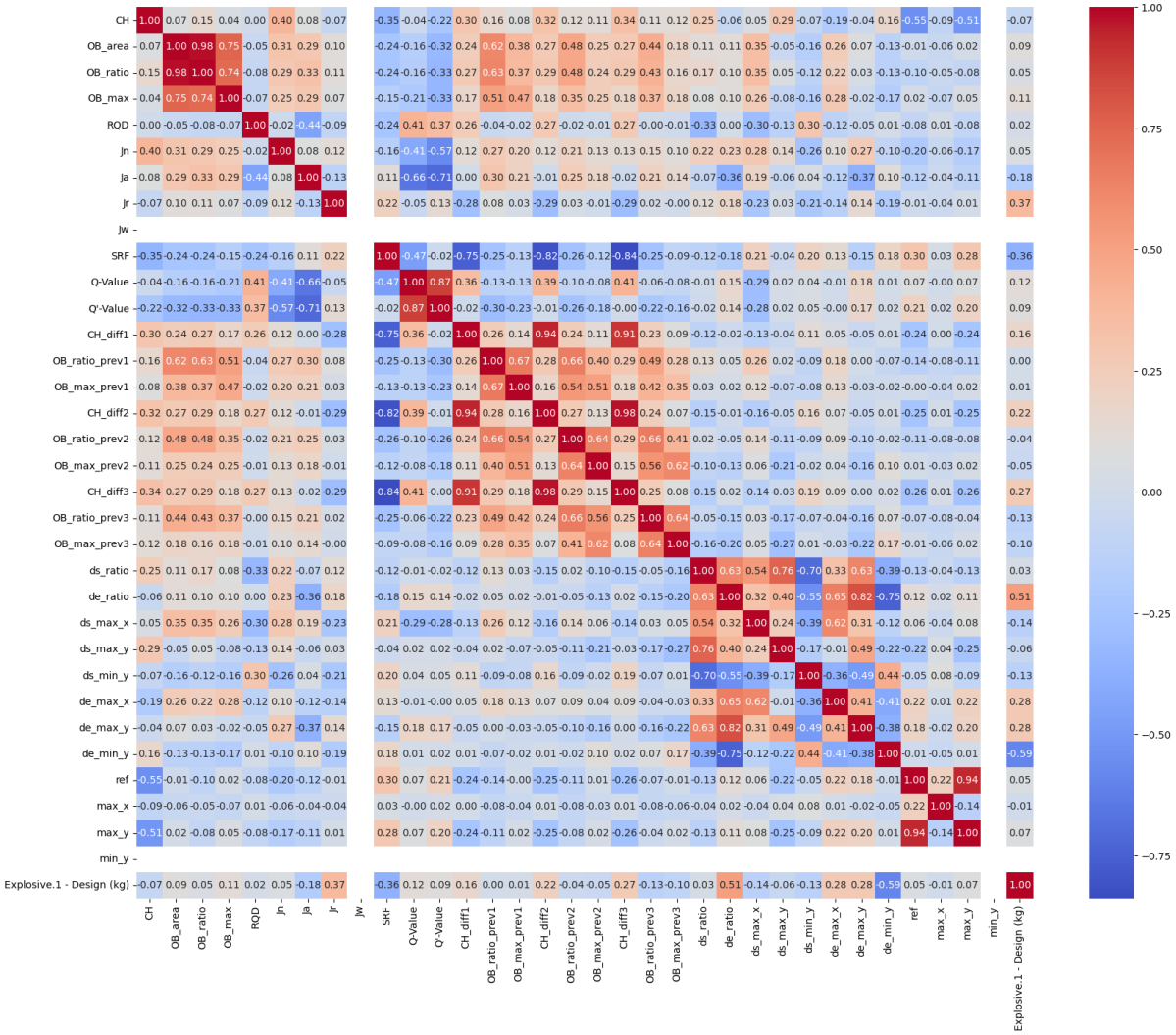

Figure 6: Correlation matrix and target values for all input parameters

4.5 Cyclic Patterns

Visual inspection of overbreak data along the tunnel alignment revealed cyclic patterns at approximately 80-metre intervals. These oscillations may correspond to structural fault zones, or systematic variations in joint set orientation. The model partially captures these patterns through the inclusion of historical overbreak ratios and chainage difference features.

5 Discussion

5.1 Practical Applications

The model developed in this study serves three primary functions within the project lifecycle of drill and blast tunnel construction.

During **tendering**, contractors can use the insight from the model to estimate overbreak for each tunnel section based on anticipated geological conditions derived from ground investigation reports. This enables more accurate calculation of mucking volumes, support quantities, and contingency provisions. Scenario analysis across optimistic and pessimistic geological assumptions could be carried out, improving bid competitiveness and risk pricing.

During **construction**, the model identifies sections at elevated risk of excessive overbreak based on face mapping data as excavation progresses. This enables proactive adjustment of support designs, blast patterns, or excavation sequencing. By comparing predicted and actual overbreak after each blast cycle, engineers can establish a feedback loop that progressively calibrates the model and refines expectations for subsequent sections.

For **design review**, the model provides early warning when predicted overbreak exceeds the assumptions underlying the rock support design. This is critical because tunnel support systems are dimensioned for assumed spans and loading conditions. If actual overbreak produces spans that exceed design limits, the support system may be inadequate, necessitating costly redesign and reinstallation. The model supports proactive design revision before such situations materialise.

The model output is expressed as a continuous overbreak ratio, which can be categorised into risk levels. For indicative purposes: ratios below 1.05 may be considered low risk, ratios between 1.05 and 1.20 moderate risk, and ratios exceeding 1.20 high risk. These thresholds are adjustable based on project-specific tolerances and contractual requirements. The output format is compatible with standard spreadsheet and dashboard environments, requiring no specialised software for deployment.

5.2 Limitations of Geology-Only Prediction

The moderate testing R^2 of 0.515 reflects a fundamental limitation: geology, while necessary, is not sufficient to fully explain overbreak. Two tunnel sections with identical Q-system parameters may produce markedly different overbreak outcomes depending on blast hole alignment, charge distribution, detonation sequencing, crew skill, and equipment condition.

Geological models are also inherently static, based on parameters recorded at the time of face mapping. They do not account for dynamic factors such as stress redistribution following excavation, progressive joint weathering at exposed faces, or transient groundwater ingress. These limitations establish a ceiling on the predictive accuracy achievable from geological inputs alone and motivate the integration of operational and real-time data in future model iterations.

5.3 Influence of Blast Design and Operation Factors

Blast hole orientation governs the spatial distribution of explosive energy across the tunnel face. Even minor deviations from the designed drilling pattern - arising from operator skill variability, jumbo calibration drift, or rock face irregularity - can direct energy beyond the intended profile boundary, particularly at the tunnel perimeter where contour holes define the excavation limit (Jimeno et al. 1995). Charge weight and its distribution across the blast pattern determine fragmentation intensity. Excessive charging generates uncontrolled fracturing beyond the design boundary, while undercharging produces poor fragmentation and irregular profiles. Detonation delay timing controls the sequential release of energy and influences the interaction between adjacent blast holes. Suboptimal timing can cause simultaneous detonation of multiple holes, concentrating energy and amplifying overbreak risk.

In the present dataset, blast design parameters (charge weight, hole arrangement, and detonation sequence) were close to constant across all sampled blasts. This constancy meant that these parameters contributed little variance and were therefore not informative as model inputs. However, on projects where blasting design varies in response to face conditions, these parameters would be expected to substantially improve predictive accuracy and should be recorded systematically for model integration.

5.4 Stakeholder Perspective

Feedback obtained from contractors, engineers, and project managers during model development affirmed the practical relevance of the tool. Contractors emphasized the value of scenario-based overbreak estimation during bid preparation and preferred deployment through spreadsheet-based interfaces that integrate with existing workflows. Engineers focused on the model's capacity to support design validation and risk identification and requested additional outputs such as confidence intervals and risk classifications. Project managers valued the

transparency of feature importance metrics and used model predictions to support progress reporting, scope change justification, and risk communication with clients.

6 Lessons Learned

The development and application of this predictive model yielded several insights that are relevant to both researchers and practitioners engaged in data-driven tunnelling.

6.1 Data Quality Gonverns Model Quality

The most significant determinant of model performance was not the choice of algorithm but the quality and alignment of input data. Geological face mapping records, survey profiles, and drill logs were generated by different teams using different instruments and reporting conventions. Ensuring spatial alignment of these records by chainage demanded substantial manual effort. Misalignment between geological parameters and the corresponding excavation profile, even by a single blast round, introduced noise that degraded model accuracy. This experience underscores the importance of integrated digital data management systems on tunnelling projects, where all records are linked to a common spatial reference from the point of collection.

6.2 Placeholder Values Outperform Row Exclusion

For samples where drill envelope data was incomplete, inserting extreme placeholder values (-10,000) and allowing the Random Forest algorithm to learn their non-informative nature proved superior to excluding incomplete rows entirely. Exclusion reduced the effective dataset size and introduced selection bias, as sections with missing drill data were not randomly distributed, they tended to correspond to earlier excavation phases or specific tunnel zones. This finding is relevant to practitioners working with real-world datasets that are invariably incomplete.

6.3 Geological Parameters Alone are Necessary but Insufficient

The feature importance analysis confirmed that geological parameters, particularly *RQD* and the composite *Q'* index , are essential inputs for overbreak prediction. However, the moderate testing R^2 demonstrates that geology alone cannot explain the full variance in overbreak outcomes. This finding aligns with engineering intuition: overbreak is a product of both rock mass behaviour and excavation execution. The practical implication is that geological mapping should continue to be performed rigorously, but predictive frameworks should aspire to incorporate operational data to achieve higher accuracy.

6.4 Spatial Autocorrelation is a Powerful Feature

The finding that the overbreak ratio from the preceding section (OB_ratio_prev1) was the single most important predictor carries significant practical implications. It implies that overbreak is not a random phenomenon but exhibits spatial persistence along the tunnel alignment, governed by geological continuity and consistent operational practices. This autocorrelation can be exploited operationally: elevated overbreak in a given section should trigger heightened vigilance and potential blast design modification for the subsequent section.

6.5 Cyclic Patterns Warrant Geological Interpretation

The observed cyclic overbreak pattern at approximately 80-metre intervals invites geological interpretation. Such periodicity may reflect alternating lithological units, regularly spaced fault or shear zones, or systematic changes in joint set dominance. Identifying and characterizing the geological drivers of these cycles would support more targeted mitigation strategies and could inform the placement of additional ground investigation points during the design phase of future projects.

6.6 Model Simplicity Supports Adoption

Feedback from industry stakeholders consistently indicated that model interpretability and ease of deployment were valued highly. The Random Forest model, with its transparent feature importance metrics and straightforward output format, was readily understood and accepted by engineers and project managers. More complex models, even if marginally more accurate, would face adoption barriers in construction environments where computational infrastructure is limited and decisions must be made rapidly by professionals whose primary expertise lies outside data science. This observation argues for prioritizing practical utility over incremental accuracy gains when developing tools for industry deployment.

6.7 Overfitting Requires Vigilance in Small Dataset Regimes

The substantial gap between training R^2 (0.858) and testing R^2 (0.515) serves as a reminder that models trained on small datasets are susceptible to learning noise rather than signal. Despite the Random Forest algorithm's inherent resistance to overfitting through bootstrap aggregation and random feature selection, a dataset of 420 samples with 17 input features operates in a regime where overfitting remains a genuine risk. Attempts to reduce model complexity (fewer trees, shallower depth) degraded performance, suggesting that the current architecture represents a pragmatic compromise. The most effective remedy for overfitting is dataset expansion.

7 Future Development Directions

7.1 Dataset Expansion and Diversification

The most impactful improvement pathway is expanding the training dataset in terms of both volume and diversity. This entails incorporating data from additional tunnel projects across different geological settings, tunnel geometries, and excavation contractors. Cross-project data aggregation would require standardized data collection protocols and collaborative data-sharing frameworks between contractors, consultants, and government agencies. The availability of larger datasets would also enable investigation of more expressive algorithms, including gradient-boosted ensembles and deep learning architectures, which require greater data volume to train effectively without overfitting (Chen and Guestrin 2016).

7.2 Integration of Measurement while Drilling Data

Measurement While Drilling (MWD) systems record real-time parameters during the drilling of blast holes, including penetration rate, rotation torque, percussion pressure, feed force, and flushing flow rate. These parameters serve as proxies for in-situ rock mass properties at a spatial resolution far exceeding that of face mapping (Navarro et al. 2018; van Eldert et al. 2020). Integration of MWD data would enable the model to capture rock mass variability within individual blast rounds and identify localised weak zones that contribute to overbreak but are not resolved by conventional geological mapping at the face scale.

7.3 Incorporation of Variable Blast Design Parameters

On projects where blast design is adapted to face conditions, parameters including per-hole charge weight, charge distribution, contour hole spacing, burden and spacing ratios, and detonation delay patterns should be systematically recorded and incorporated as model inputs. Literature consistently identifies these parameters among the strongest overbreak predictors when variation exists (He et al. 2023; Koopialipoor et al. 2019). Development of standardized digital blast logging protocols would facilitate this integration.

7.4 Dimensionality Reduction Techniques

As the number of input parameters increases with the integration of MWD, blast design, and potentially image-based data, dimensionality reduction becomes important for maintaining model tractability and avoiding the curse of dimensionality. Principal Component Analysis (PCA) offers a linear approach to extracting

uncorrelated components that maximise explained variance and are particularly suited to correlated geological indices (Jolliffe 2002). Autoencoders, a class of neural network, can learn nonlinear compressed representations of high-dimensional inputs such as MWD time series or 3D drill hole geometry. These techniques should be systematically evaluated to determine their contribution to predictive performance in the tunnelling context.

7.5 Real-Time Prediction Frameworks

The development of real-time prediction tools represents a high-value research direction. Such tools would ingest live data streams from MWD systems, blast logging databases, face mapping records, and survey systems, updating overbreak predictions as excavation advances. This requires efficient data processing pipelines, low-latency model inference, and intuitive visualisation interfaces accessible to site engineers through dashboards or mobile devices. The feedback loop between prediction and observed outcome would also enable continuous model recalibration, progressively improving accuracy over the project duration. Implementation of such systems will require interdisciplinary collaboration among tunnelling engineers, data scientists, and software developers.

7.6 Transfer Learning and Cross-Project Validation

Models developed for specific geological and operational contexts require validation before application elsewhere. A systematic programme of cross-project validation, testing Hong Kong-trained models on data from tunnels in other granitic terrains, and vice versa, would establish the degree to which learned relationships generalize. Transfer learning techniques, in which a model pre-trained on a large dataset is fine-tuned using limited data from a new project, offer a promising approach for accelerating model deployment on new sites where historical data is scarce (Pan and Yang 2010).

7.7 Image-Based and Computer Vision Approaches

Emerging work on automated face mapping using photogrammetry and deep learning-based image classification offers the prospect of objective, high-resolution geological characterization (Hong et al. 2023). Integration of image-derived features, such as joint trace maps, roughness profiles, and weathering grade classifications, could supplement or partially replace manual Q-system scoring, improving both consistency and spatial resolution of geological input data.

8 Conclusion

This study developed and validated a Random Forest regression model for predicting tunnel overbreak in drill and blast operations through granitic rock in Hong Kong. The model was trained on approximately 420 samples using NGI Q-system geological parameters, historical overbreak ratios, drill envelope geometry, and explosive mass as input features. The principal conclusions are as follows.

The Random Forest model achieved a testing R^2 of 0.515 and outperformed linear regression, polynomial regression, and single decision tree alternatives on the same dataset. This performance level, while moderate in absolute terms, represents a meaningful improvement over conventional estimation methods and establishes a credible baseline for geology-based overbreak prediction.

Feature importance analysis identified overbreak continuity from preceding sections and rock quality designation as the dominant predictors, confirming the significance of geological spatial autocorrelation and rock mass quality in determining excavation outcomes.

The model is potentially deployable during both tendering and construction phases, using data that is routinely collected on drill and blast projects. Its interpretable feature importance metrics and straightforward output format support adoption by industry practitioners without requiring specialised computational infrastructure.

The moderate predictive accuracy reflects the inherent limitation of geological-only prediction. Operational factors including blast hole alignment, charge distribution, and detonation sequencing - which were invariant in

the present dataset - are known to significantly influence overbreak and represent the primary avenue for model improvement.

Future work should prioritise dataset expansion, integration of MWD and variable blast design data, investigation of dimensionality reduction techniques, development of real-time prediction frameworks, and cross-project validation to establish model transferability.

The research contributes to the broader transition toward data-driven decision-making in geotechnical engineering and demonstrates that machine learning can be applied to practical tunnelling problems using accessible data and interpretable methods.

ACKNOWLEDGEMENTS

The authors express deep and sincere gratitude to the following colleagues: Regine Tsui for her rigorous work on data processing, model structuring, and coding; Kelly Kang for her sustained persistence and sharp focus across data collection and structuring; Christian Bordner for clear technical guidance and steady direction throughout the research.

REFERENCE

Barton, N., Lien, R. and Lunde, J. 1974. Engineering classification of rock masses for the design of tunnel support, *Rock Mechanics*, 6(4), 189-236.

Breiman, L. 2001. Random forests, *Machine Learning*, 45(1), 5-32.

Chen, T. and Guestrin, C. 2016. XGBoost: A scalable tree boosting system, in *Proceedings of the 22nd ACM SIGKDD International Conference on Knowledge Discovery and Data Mining*, 785-794.

Chin, J.T.Y. 2024. Tunnel and Caverns Design in Rock. *Proceeding, HKIE Geotechnical Division 44th Annual Seminar: Elevating Geotechnical Excellence: Novel Practice and Innovative Solutions,* 17-34.

He, B., Armaghani, D.J. and Lai, S.H. 2023. Assessment of tunnel blasting-induced overbreak: A novel metaheuristic-based random forest approach, *Tunnelling and Underground Space Technology*, 133, 104979, 1-18.

Hong, K., Feng, H. and Yue, F. 2023. Overbreak prediction in drill and blast tunnelling using XGBoost with Bayesian optimisation, *Underground Space*, 12, 186-199.

Jang, H. and Topal, E. 2013. Optimizing overbreak prediction based on geological parameters comparing multiple regression analysis and artificial neural network, *Tunnelling and Underground Space Technology*, 38, 161-169.

Jang, H., Topal, E. and Zare, M. 2019. Optimizing overbreak prediction in underground mines using ANN and overbreak risk factor, *International Journal of Rock Mechanics and Mining Sciences*, 115, 78-90.

Jimeno, C.L., Jimeno, E.L. and Carcedo, F.J.A. 1995. *Drilling and Blasting of Rocks*. Rotterdam: A.A. Balkema.

Jolliffe, I.T. 2002. *Principal Component Analysis*. 2nd edn. New York: Springer.

Koopialipoor, M., Armaghani, D.J., Haghighi, M. and Ghaleini, E.N. 2017. A neuro-genetic predictive model to approximate overbreak induced by drilling and blasting operation in tunnels, Bulletin of Engineering Geology and the Environment, 78, 981-990.

Koopialipoor, M., Fallah, A., Armaghani, D.J., Azizi, A. and Mohamad, E.T. 2018. Overbreak prediction and optimization in tunnel using neural network and bee colony techniques, Engineering with Computers, 35, 1191-1202.

Koopialipoor, M., Nikouei, S.S., Marto, A., Fahimifar, A., Armaghani, D.J. and Mohamad, E.T. 2019. Predicting tunnel boring machine performance through a new model based on the group method of data handling, Bulletin of Engineering Geology and the Environment, 78, 3455-3467.

Mohammad, M., Farouq, H.M., Bahman, M. and Nabiollah, H. 2015. Use of fuzzy set theory for minimizing overbreak in underground blasting operations - A case study of Alborz Tunnel, Iran, *International Journal of Mining Science and Technology*, 25(3), 439-445.

Mohammadi, H., Barati, B. and Chamzini, A.Y. 2018. Prediction of blast-induced overbreak based on geo-mechanical parameters, blasting factors and the area of tunnel face, *Geotechnical and Geological Engineering*, 36, pp. 425–437.

Mottahedi, A., Sereshki, F. and Ataei, M. 2017. Development of overbreak prediction models in drill and blast tunneling using soft computing methods, *Engineering with Computers*, 34, pp. 45–58.

Navarro, J., Sanchidrián, J.A., Segarra, P., Castedo, R., Paredes, C. and López, L.M. 2018. On the mutual relations of drill monitoring variables and the drill control system in tunneling operations, *Tunnelling and Underground Space Technology*, 72, 294-304.

Palmström, A. and Broch, E. 2006. Use and misuse of rock mass classification systems with particular reference to the Q-system, *Tunnelling and Underground Space Technology*, 21(6), pp. 575–593.

Pan, S.J. and Yang, Q. 2010. A survey on transfer learning, *IEEE Transactions on Knowledge and Data Engineering*, 22(10), 1345-1359.

Pedregosa, F., Varoquaux, G., Gramfort, A., Michel, V., Thirion, B., Grisel, O., Blondel, M., Prettenhofer, P., Weiss, R., Dubourg, V., Vanderplas, J., Passos, A., Cournapeau, D., Brucher, M., Perrot, M. and Duchesnay, E. 2011. Scikit-learn: Machine learning in Python, *Journal of Machine Learning Research*, 12, 2825-2830.

Sun, S., Liu, J. and Wei, J. 2013. Predictions of overbreak blocks in tunnels based on the wavelet neural network method and the geological statistics theory, *Mathematical Problems in Engineering, 2013*, 706491, 1-9.

van Eldert, J., Schunnesson, H. and Johansson, D. 2020. Application of measurement while drilling technology to predict rock mass quality and rock support for tunnelling, *Rock Mechanics and Rock Engineering*, 53, 1349-1358.

New State-of-the-art Design Guidelines for Deep Cement Mixing: Global Review and Benchmarking Study

Leo C.Y. Shu, Sunny T.C. So & Lawrence K.W. Shum

Geotechnical Engineering Office, Civil Engineering and Development Department, HKSARG, Hong Kong, China

Anthony H.K. Wong*, S.W. Lee & Z. Xu
AECOM Asia Company Limited, Hong Kong, China
**Corresponding author*

ABSTRACT

The deep cement mixing (DCM) technique has been increasingly adopted as a ground improvement method in coastal projects due to its effectiveness in enhancing soil stability. However, past design practices have varied significantly and remain inconsistent across projects. This paper presents a state-of-the-art review of global DCM design practices, examining regional variations in guidelines and methodologies. Building on substantial experience gained from recent reclamation projects in Hong Kong, new design guidelines are proposed. A benchmarking exercise was conducted to compare existing methodologies with the proposed design approach. The exercise considers a hypothetical land reclamation project comprising a 10 m thick reclamation fill and a vertical seawall. Comparative design results indicate that the proposed approach can potentially improve both robustness and cost-effectiveness while maintaining adequate safety margins. This study is expected to create a significant and lasting impact on regional design practices.

1 INTRODUCTION

Deep cement mixing (DCM) is an emerging ground improvement technique for coastal and reclamation projects, particularly in regions with soft marine deposits such as Hong Kong, Japan, and Chinese Mainland. The method involves the in-situ mixing of cementitious materials with soft soils to increase their strength and reduce compressibility, thereby improving the stability and bearing capacity of foundations for coastal structures. Over the past two decades, the use of DCM has increased rapidly, driven by the need for reliable and cost-effective solutions for large-scale reclamation and port development projects. However, the variabilities in soil conditions, construction practices, and regulatory frameworks across regions has led to different design methodologies. These differences are reflected in the selection of design parameters, safety factors, and the scope of stability checks required by various standards.

This paper aims to address these challenges by conducting a state-of-the-art review of international DCM design standards, identifying key differences and areas for improvement. Building on recent experience from major reclamation projects in Hong Kong, the study proposes new design guidelines that seek to balance safety, cost, constructability, and sustainability. A benchmarking exercise is then performed, comparing the new design guidelines with prevailing international standards using a hypothetical project scenario. The comparison of results provides a basis for evaluating the effectiveness and robustness of different design approaches, with a view to informing future practice in Hong Kong and similar coastal environments.

2 REVIEW OF INTERNATIONAL DESIGN STANDARDS

DCM has evolved into a critical ground improvement technique for coastal and reclamation projects worldwide. While there are numerous international standards documenting the design of DCM, those most relevant to coastal / reclamation applications are reviewed in this study, including the *Technical Standards and Commentaries for Port and Harbour Facilities* by the Overseas Coastal Area Development Institute (OCDI) in Japan, the *Code of Foundation Design on Port and Waterway Engineering (JTS 147-2017)* in Chinese Mainland,

and the *Federal Highway Administration Design Manual: Deep Mixing for Embankment and Foundation Support (FHWA-HRT-13-046)* in the United States.

2.1 Technical Standards and Commentaries for Port and Harbour Facilities in Japan

Since the 1960s, Japan has been a leading country in research and development associated with DCM (Kitazume & Terashi, 2013). DCM has been widely employed in both marine and land-based projects in Japan, with most applications related to coastal facilities. The latest and prevailing design reference for Japanese projects is the *Technical Standards and Commentaries for Port and Harbour Facilities*, which was issued by OCDI in 2018 and later translated to English in 2020. The OCDI Technical Standards summarise the ministerial ordinance, public notice articles, related commentaries, and technical notes in relation to Japan's Ministry of Land, Infrastructure, Transport and Tourism (MLIT) based on the provisions of the Port and Harbour Act.

2.1.1 Design strength of DCM

The OCDI Technical Standards recommend that the effective cross-sectional area (α) and the reliability index due to overlapping columns after mixing (β) be considered in the design compressive strength (f_{c_k}) of DCM.

The design shear strength of the deep mixed soil, f_{sh_k} is obtained from the design compressive strength (f_{c_k}), which in turn is evaluated from the standard design strength (q_{uc_k}) with incorporation of correction factors, as shown in equation (1) based on the recommendations under the Technical Standards.

$$f_{sh_k} = \frac{1}{2} \cdot f_{c_k} = \frac{1}{2} \alpha\beta q_{uc_k} = \frac{1}{2} \alpha\beta \left(\bar{q}_{uf} \cdot (1 - KV) \right) \quad (1)$$

where q_{uc_k} = characteristic value of unconfined compressive strength (UCS), the subscript k denotes a characteristic value, $\bar{q}_{uf}$ = average compressive strength of field stabilised soil, K = number of standard deviation from the mean value, and V = coefficient of variation.

The factor α is introduced to account for soils near the overlapped sections that remain unimproved due to the geometry of the mixing blades, which is calculated by the chord length of the overlapped sections over the effective width of a DCM wall panel. The factor β accounts for the reliability of overlapped region. The OCDI Technical Standards recommend a β value of 1.0.

2.1.2 Design methodology and safety factors

The OCDI Technical Standards adopt a partial factor approach for performance verification. Partial factors γ_R and γ_s are applied to the resistance term (R_k) and load term (S_k) respectively as shown in equation (2).

$$m \cdot \frac{S_d}{R_d} = m \cdot \frac{\gamma_s \cdot S_k}{\gamma_R \cdot R_k} \leq 1.0 \quad (2)$$

where m = adjustment factor, S_k = characteristic load actions, R_k = characteristic value of resistance, γ_R = partial factor for resistance, γ_s = partial factor for load.

To add flexibility to this design framework, an adjustment factor (m) is introduced to incorporate design methods from past experience, which adopted the global factor of safety approach. Table 1 summarises the recommended design checks and corresponding partial factors.

Table 1: Design safety factors for stability checking under OCDI (2020)

Failure mode	Partial factor, γ_R (for resistance terms, R_k)		Partial factor, γ_s (for load terms, S_k)		Adjustment factor (m)	
	Permanent State	Variable State (i.e. seismic action considered)	Permanent State	Variable State (i.e. seismic action considered)	Permanent State	Variable State (i.e. seismic action considered)
Sliding failure of the stabilised body	0.90 ~ 0.91	1.0	1.09 ~ 1.10	1.0	1.0	1.0
Overturning failure of the stabilised body	0.97	1.0	1.18	1.0	1.0	1.1
Bearing capacity failure of the layer under the DCM improved ground	0.49	1.0	1.15	1.0	1.0	1.0**
Crushing at the bottom of the stabilised body	0.72	1.0	1.33	1.0	1.0	1.5
Shearing on vertical plane immediately beneath the face lines of the superstructure	1.0	1.0	1.0	1.0	1.8	1.5
Soil extrusion failure of the untreated soil between the long walls	0.81	1.0	1.04	1.0	1.0	1.0
Slope stability failure of foundation ground in circular arc*	1.0	-	1.0	-	1.3^	-

* Applicable to gravity type breakwaters as protective facilities for harbour, and gravity-type quay wall as mooring facilities only.

** An adjustment factor with respect to bearing capacity m_B = 1.5 should be applied separately when designing for variable state of level 1 seismic ground motions.

^ An adjustment factor m (equivalent to the safety factor in this case) could be set as 1.1 or more then the reliability of the constants used in the verification is considered high.

2.2 Code of Foundation Design on Port and Waterway Engineering (JTS 147-2017) in Chinese Mainland

In Chinese Mainland, the use of DCM began in 1978 (Han et al. 2002). Earlier DCM projects in Chinese Mainland collaborated with Japanese contractors. To date, it is noted that the design and construction practices in Chinese Mainland have primarily referred to the Japanese practice. In relation to DCM works, the latest and prevailing design reference for projects in Chinese Mainland is *Code of Foundation Design on Port and Waterway Engineering (JTS 147-2017)* published by the Ministry of Transport of the People's Republic of China.

2.2.1 Design strength of DCM

Under *JTS 147-2017*, the shear strength of the deep-mixed soils is determined in a similar manner to that recommended in OCDI (2020). The characteristic shear strength (τ_{ca_k}) and the characteristic compressive strength (σ_{ca_k}) are interpreted as follows:

$$\tau_{a_k} = \frac{1}{2}\sigma_{ca_k} = \frac{1}{2}\kappa f_{cu} \quad (3)$$

where κ= a lumped factor of $\alpha \cdot \beta \cdot \gamma \cdot \lambda$, *JTS 147-2017* recommends that $\kappa = 0.6$, $\alpha \cdot \beta = 0.9$, $\gamma = 2/3$, and $\lambda = 1$, f_{cu} = UCS of laboratory prepared DCM specimens.

2.2.2 Design methodology and safety factors

The design methodology of the *JTS 147-2017* is similar to OCDI (2020) (e.g. soil extrusion failure and shearing on vertical plane of deep mixed ground), with exceptions on the choice of partial factors on action and resistance based on the Chinese experience. *JTS 147-2017* introduced a partial factor γ_0 to account for the significance of the structure. For instance, the slope stability can be calculated using equation (4), and other types of stability checks are carried out in a similar manner.

$$\gamma_0 \cdot M_{sd} \leq \frac{1}{\gamma_R} \cdot M_{Rk} \quad (4)$$

where M_{sd} = design sliding moment, M_{Rk} = characteristic restoring moment, γ_R = partial factor applied to resistance, γ_0 = partial factor to account for the significance of structure.

The determination of γ_0 depends on the designated structure significance with the highest value γ_0 = 1.1 for Class I structures, γ_0 = 1.0 for Class II structures, and γ_0 = 0.9 for Class III structures. γ_0 = 1.1 could be adopted for marine structures or reclamation edges as coastal protection.

Unlike OCDI (2020), *JTS 147-2017* applies the load factor to the action directly considering various ULS conditions. These includes a combination of different adverse loading conditions (e.g. active earth pressures, wave loading and mooring loads) in which individual partial factors should be considered. The recommended partial factors in JTS-147-2017 are presented in Table 2 and Table 3.

Table 2: Recommended partial factors of safety for sliding and overturning checking under Code for Foundation Design on Port and Waterway Engineering (*JTS 147-2017*)

Failure mode	**Partial factor of safety**		**Recommended Values**			
			Permanent action		**Variable action**	
			Sustained	**Transient**	**Sustained**	**Transient**
Sliding / Overturning	Partial factor of active earth pressure (γ_E)	Mainly applied to load action terms	1.35	1.35	1.35 (1.25)*	1.25
	Partial factor of net pore water pressure (γ_{PW})		1.05	1.05	-	-
	Partial factor of mooring load (γ_{PR})		-	-	1.40 (1.30)	1.30
	Partial factor of wave load (γ_P)		-	-	1.30 (1.20)	1.20
	Factor accounting for importance of a structure* (γ_0)		1.1			
	Partial factor of passive earth pressure (γ_{EP})	Applied to resistance terms	1.0			
	Partial factor of self-weight of DCM (γ_G)		1.0			
	Partial factor of cohesion base soil (γ_c)		1.0			
	Structural Coefficient (γ_d)		1.1#			
	Factor accounting for Combined Effect (f)		0.7	1.0	0.7	1.0

* When the highest possible and lowest possible groundwater levels are adopted considering load combinations under sustained conditions, the partial factors in the brackets shall be adopted.

Table 3: Recommended partial factors of safety for crushing, vertical shearing and soil extrusion checking under Code for Foundation Design on Port and Waterway Engineering (*JTS 147-2017*)

Failure Mode	Factor accounting for importance of structure (γ_0)	Partial factor for bearing stress (γ_σ)	Partial factor for shear stress (γ_τ)	Combined partial factor unfavourable loads (γ_S)	Partial factor for resistance (γ_R)
Crushing	1.1	1.35	-	-	2.2
Vertical shearing	1.1	-	1.35	-	2.2
Soil extrusion	-	-	-	1.0	≥1.2

The bearing capacity check recommended by *JTS 147-2017* is demonstrated by equation (5).

$$\gamma_0 \cdot \gamma_s \cdot V_k \leq \frac{1}{\gamma_R} \cdot F_k \tag{5}$$

where γ_R = partial factor applied to resistance (2.0 to 3.0 for permanent loading condition and 1.5 to 2.0 for transient loading condition, γ_0 = partial factor to account for the significance of structure, γ_s = partial factor for action, equalling to 1.0, V_k = characteristic value of vertical force, F_k = characteristic value of vertical bearing capacity.

2.3 Federal Highway Administration Design Manual: Deep Mixing for Embankment and Foundation Support (FHWA-HRT-13-046) in the US

Significant technological developments in Japan and successful examples prompted the application of DCM in the US in the late 1980s (Bruce et al. 1998). Since then, US practitioners have used deep mixing (DM) for dam rehabilitation and have also gained a leading role in developing technologies related to environmental and transportation applications. In 2013, the *Federal Highway Administration Design Manual: Deep Mixing for Embankment and Foundation Support (FHWA-HRT-13-046)* was published. It has since been the prevailing design reference for the DCM projects in the US. In addition, *FHWA-HRT-13-046* has also been serving as the primary reference for design of deep mixing in recent reclamation projects in Hong Kong.

2.3.1 Design strength of DCM

Under *FHWA-HRT-13-046*, the design shear strength of the deep mixed ground (s_{dm}) is estimated from the specified unconfined compressive strength (UCS) ($q_{dm,spec}$) as shown in equation (6).

$$s_{dm} = \frac{1}{2} \cdot f_r \cdot f_c \cdot q_{dm,spec} \tag{6}$$

where f_r = factor accounts for differences between unconfined peak and confined large-strain strengths (i.e. the residual strength factor), f_c = the curing factor increasing with curing time, $q_{dm,spec}$ = the specified UCS.

The strength of deep mixed soil increases with time for cement and cement-slag improvement. Based on a review of the available data, *FHWA-HRT-13-046* recommends equation (7) for an estimate of the time effect except for some highly organic clay.

$$f_c = 0.187 \cdot \ln(t) + 0.375 \tag{7}$$

where f_c = curing factor corresponding to the ratio of UCS at time *t* to the UCS at 28-day, t = curing time (days).

As for the residual strength factor (f_r), the design value is recommended as 0.8 for the application to transportation embankments for accounting post-peak strain softening effect.

As the deep mixed ground may possess high variability in strength depending on the in-situ soil conditions and operational environment, a strength variability factor (f_v) based on statistical analyses from previous research findings has also been introduced to adjust the specified strength of deep-mixed ground to obtain a design value that accounts for the variability (see Table 4).

Table 4: Values of f_v recommended by *FHWA-HRT-13-046*

Design Factor of Safety	Coefficient of Variation of Deep Mixed Strength	f_v		
		$p_{dm} = 0.7$	$p_{dm} = 0.8$	$p_{dm} = 0.9$
1.2	0.4	0.93	1.05	1.25
	0.5	0.88	1.02	1.26
	0.6	0.83	0.99	1.27
1.3	0.4	0.89	1.01	1.19
	0.5	0.82	0.95	1.17
	0.6	0.75	0.90	1.15
1.4	0.4	0.85	0.97	1.14
	0.5	0.76	0.89	1.09
	0.6	0.69	0.82	1.05
1.5	0.4	0.82	0.93	1.10
	0.5	0.72	0.83	1.03
	0.6	0.63	0.75	0.96
1.6	0.4	0.79	0.90	1.06
	0.5	0.68	0.79	0.97
	0.6	0.58	0.69	0.89

2.3.2 Design methodology and safety factors

Under *FHWA-HRT-13-046*, slope stability checking for deep mixed shear walls is carried out using a global factor of safety approach. For stability checking of other failure modes, a strength reduction method is adopted, i.e. the soil shear strength and DCM shear strength are factored down by the same strength reduction factor to achieve a safety margin in the DCM design. Table 5 summarises the recommended design checks and corresponding factors of safety.

Table 5: Design safety factors for stability checking under *FHWA-HRT-13-046*

Failure mode	Typical minimum FoS for design
Crushing of the centre isolated deep mixed columns (F_{cc})	1.3
Slope stability failure, including global stability and shearing through the deep mixed zone (F_s)	1.5
Combined overturning and bearing capacity failure of the deep mixed shear walls (F_o)	1.3
Crushing of the deep mixed ground at the toe of deep mixed zone (F_c)	1.3
Shearing on vertical plane through the deep mixed zone (F_v)	1.3
Soil extrusion through deep mixed shear walls (F_e)	1.3

3 NEW DESIGN GUIDELINES TO DEEP CEMENT MIXING FOR RECLAMATION WORKS

Based on this study's review and accumulated experience in large-scale DCM implementation in Hong Kong, the authors proposed several targeted improvements over established international guidelines. Key aspects addressed include scheming on improvement pattern, the adopted design strength of DCM by optimising factors on curing, variability and residual strength of DCM, and the required design checks.

In July 2025, the Geotechnical Engineering Office of the Government of the Hong Kong SAR promulgated the *Interim Design Guide to Deep Cement Mixing for Reclamation Works*, introducing new design guidelines to deep cement mixing for reclamation works. While the key provisions are briefly discussed below, designers are advised to consult the original publication for full details on any particular subject.

3.1 Improvement pattern

It is recommended that wall-type or grid-type DCM improvement patterns be adopted for coastal edge structures such as seawalls and breakwaters. Wall-type improvements consist of shear wall panels formed by overlapping DCM elements, providing effective lateral support and enhanced flexural rigidity. Grid-type improvements incorporate cross walls linking up wall panels. They are particularly beneficial for preventing soil extrusion and racking failures, and are recommended where multidirectional stresses or seismic considerations are present.

Drawing on recent experience and performance data, it is further recommended that a minimum area replacement ratio of 35% should be adopted for DCM supporting seawalls or breakwaters. This recommendation is made to ensure adequate lateral and vertical load transfer, to limit deformation, and to safeguard the stability of the improved ground.

In regions where reduced fill cover or elevated stress concentrations are anticipated, such as directly beneath the toe of a vertical seawall, the provision of a continuous DCM slab is recommended. This DCM slab is a specific block-type DCM improvement formed by short, conjoined DCM elements that bridge between DCM wall panels or grids. It acts as a transfer layer that distributes loads, increases rigidity, and mitigates the risk of localised crushing, shearing, or differential settlement. Recent projects have also selectively increased the DCM area replacement ratio in these critical regions to further accommodate stress concentrations.

3.2 Optimised design strength

The design strength of DCM is determined through a holistic approach that integrates curing effects, statistical variability, and the consideration of residual strength, which is expressed by equation (8).

$$S_{dm} = \frac{1}{2} q_{t,day} \tag{8}$$

where S_{dm} = design shear strength of DCM (in kPa), $q_{t,day}$ = design unconfined compressive strength (UCS) of DCM (in kPa), incorporating curing effects of DCM up to the tth day, which is the design date.

3.2.1 Consideration for curing effect (f_c)

In equation 8, the design UCS of DCM ($q_{t,day}$) incorporates the effects of curing. It is recommended that the design UCS ($q_{t,day}$) be verified through UCS testing on core samples, typically at 28 days but not exceeding 90 days post-installation. This ensures that the adopted strength reflects the actual, in-situ performance at the time of loading, while providing adequate time for rectifying any non-compliant work.

3.2.2 Consideration for progressive failure (f_r)

DCM can exhibit strain softening after peak strength, leading to concerns about progressive failure. However, provided that the design UCS is set well below the actual mean UCS achieved on site (as is common in recent practice), and that wall/grid-type patterns with high flexural rigidity are used, no further reduction for post-peak strain softening behaviour is considered necessary.

On the other hand, for column-type DCM under significant lateral loading, it is recommended that the design shear strength should be reduced accordingly to account for bending-induced tensile failure. This is because the bending stiffness of individual DCM columns is relatively low. When coupled with the relatively low tensile strength of cement-stabilised soils, the columns are susceptible to bending-induced tensile failure.

3.2.3 Consideration for strength variability (f_v)

With reference to the performance of DCM works in recent projects, it is recommended that one of the acceptance criteria for DCM works be specified such that 90% of all UCS test results from field-cored DCM specimens exceed the contract-required value. On this basis, no further reduction in the design shear strength is required to account for the variability in UCS test results.

3.3 Comprehensive assessment of failure modes

The proposed design approach incorporates all relevant failure mechanisms recognised in international design guides, together with insights gained from recent project experiences. Figure 1 illustrates the recommended design against ultimate limit states, including the evaluation of both external and internal stability of the DCM-improved ground. In the evaluation of external stability, the improved ground together with the overlying seawall or reclamation fill are considered integrally as a rigid unit. In the evaluation of internal stability, the induced stresses in DCM due to external forces are calculated and compared against the allowable values.

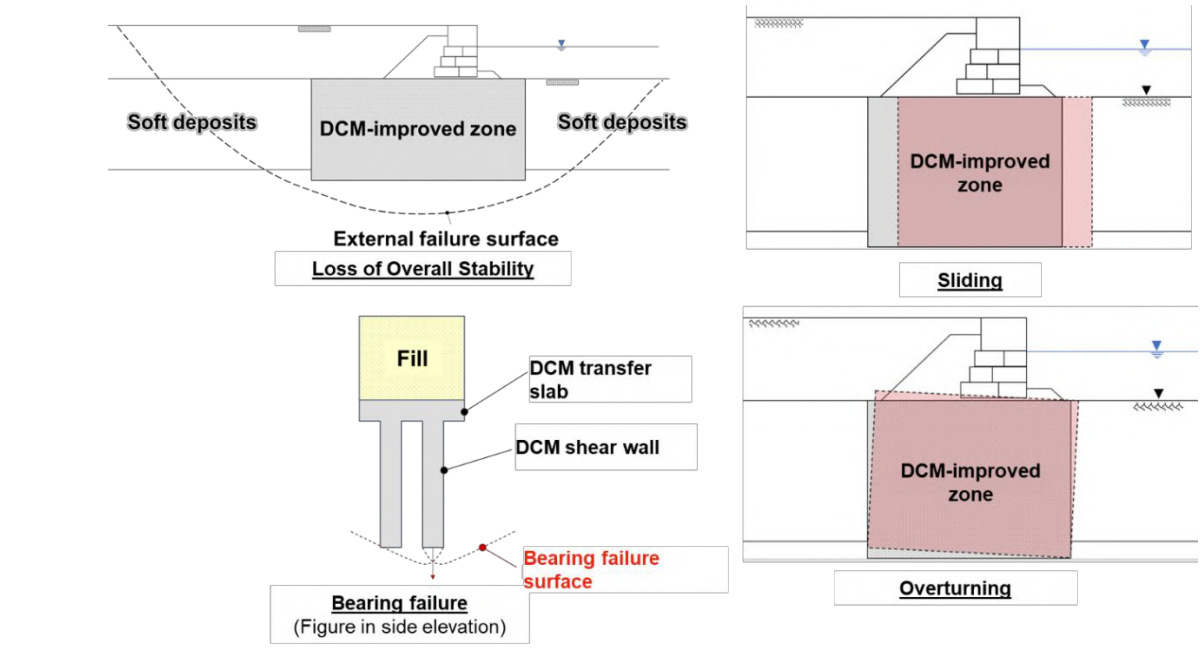

(a)

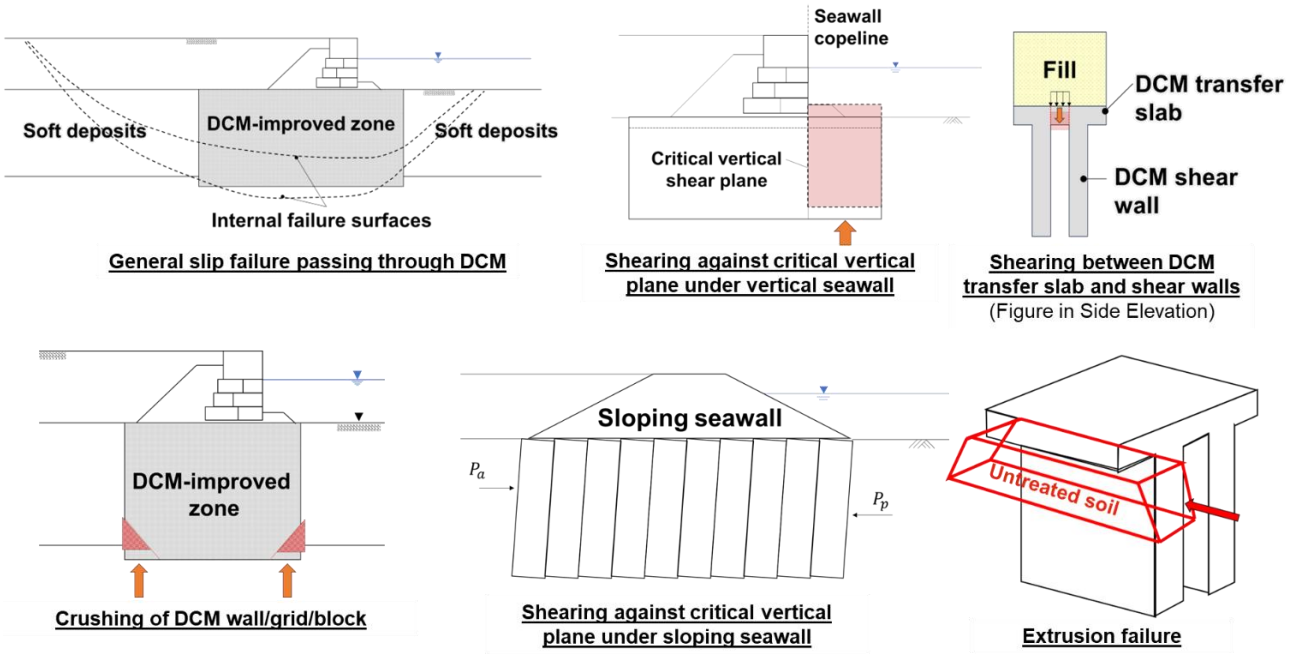

(b)

Figure 1: Recommended design checks against ultimate limit states:
(a) external instabilities; and (b) internal instabilities

The failure modes covered in the design checks and their recommended minimum factors of safety are presented in Table 6. Safety factors against limit states are applied either by the "Global Factor Method" or the "Strength Reduction Method". The Global Factor Method is adopted for checks against overall stability, under external stability; and general slip failure passing through DCM-improved ground, under internal stability. The Strength Reduction Method is adopted for all other stability checks.

Table 6: Recommended minimum factors of safety for assessing DCM stability

Type of Stability Check		Global Factor (F_s)		Strength Reduction Factor			
				Factor on Soil Strength (γ_s)		Factor on DCM Strength (γ_m)	
		Normal / Temporary(1)	Extreme / Accident(2)	Normal / Temporary(1)	Extreme / Accident(2)	Normal / Temporary(1)	Extreme / Accident(2)
External Stability	Overall Stability	1.3	1.2	–	–	–	–
	Sliding	–		1.3	1.2	–	–
	Overturning						
	Bearing						
Internal Stability	General slip failure passing through DCM-improved ground	1.3	1.2	–	–	–	–
	Crushing of Individual Elements	–		–	–	1.3	1.2
	Crushing of Panel/Grid/Block at Bottom Edges			1.3	1.2		
	Shearing along Vertical Planes in Sloping Seawall						
	Shearing along Vertical Planes in Vertical Seawall						
	Shearing between DCM Transfer Slab and DCM Shear Wall Panels						
	Soil Extrusion						

(1) A minimum factor of safety of 1.3 should be applied to specific temporary loading conditions during construction that involve surcharge behind seawalls and in main reclamation areas supported by DCM improvement works.
(2) When extreme environmental loads or accidental loads are involved, a reduced minimum factor of safety of 1.2 could be considered.
(3) The factors of safety provided are the recommended minimum values for design. Larger values may be considered when greater uncertainties exist. For example, higher strength reduction factors may be specifically adopted for undrained shear strengths given their higher variability compared to drained shear strengths.

4 BENCHMARKING EXERCISE

To benchmark the proposed design approach against international practices, the new design guidelines, together with the three previously described design standards, are applied to assess a hypothetical project scenario. The project setting comprises DCM-supported vertical seawalls, and preloading with vertical drains implemented in the inland reclamation area behind the seawall. This example considers only the short-term condition in which surcharge is applied behind the DCM-supported seawall, representing the most critical design scenario.

The seawall geometry, loadings, geology and design soil parameters used in this example are shown in Figure 2. The vertical seawalls are founded on a 13 m thick soft marine deposits, overlying stiff alluvial clays. The design water level is assumed to be +1.0 mPD on the landside and +0.3 mPD on the seaside, i.e., a tidal lag of 0.7 m. Wall-type DCM with a 4 m-thick DCM transfer slab as shown in Figure 2 is provided to enhance the overall rigidity of the improved ground. The DCM layout pattern and the geometry of DCM elements are shown in Figure 3.

A surcharge of 36 kPa (equivalent to 2 m of surcharge fill) is applied within the inland reclamation area behind the seawall. The surcharge increases to 108 kPa (equivalent to 6 m of surcharge fill) further inland. Adequate separation is maintained to prevent the highest surcharge from adversely affecting seawall stability or influencing the evaluation of earth pressures on the DCM-improved zone. Additionally, a 10 kPa live load on top of all fill platforms, representing live construction load. A standard wave load is also considered.

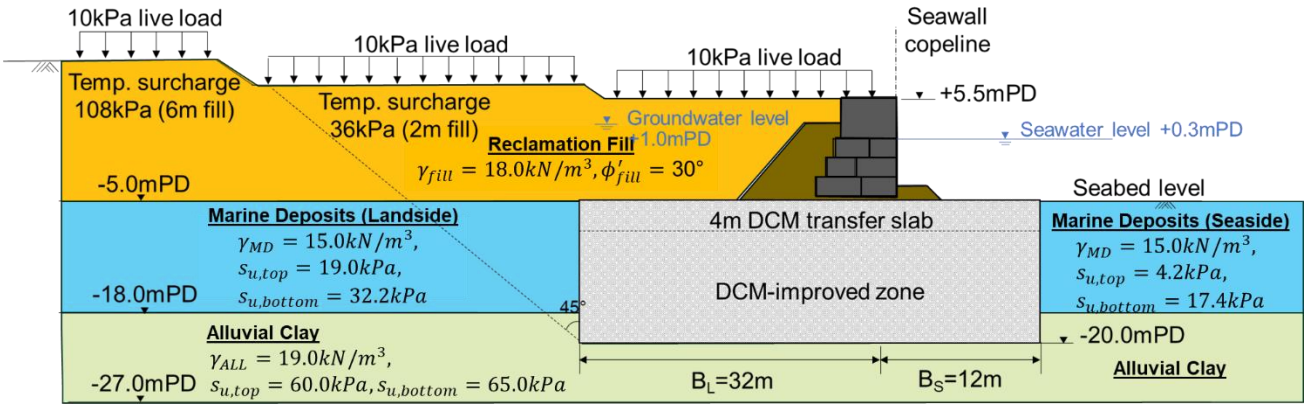

Figure 2: Seawall geometry, geological condition and soil parameters

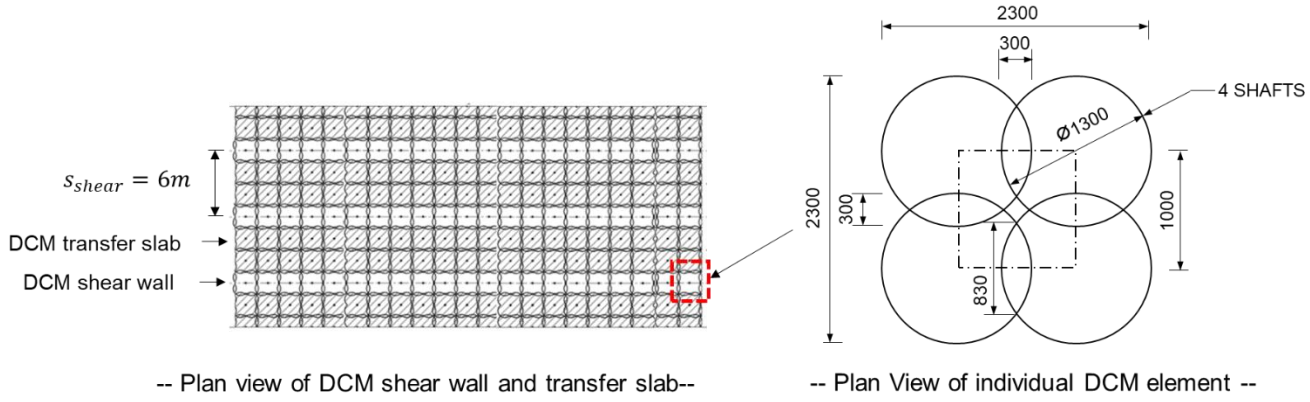

Figure 3: Plan views of DCM layout pattern and individual DCM element under vertical seawall

To enable a quantitative comparison across various design standards, a "utilisation" value is defined as the ratio of the factored disturbing term (e.g. moment or force) to the allowable resistance term. A utilisation value of less than 100% indicates that the design is safe, while a value exceeding 100% means that the design check has failed to satisfy the required safety margin.

5 RESULTS OF BENCHMARKING EXERCISE AND DISCUSSION

Table 7 summarises the results of the benchmarking exercise. Despite adopting the same DCM dimensions and field strength requirements, considerably different utilisation values are observed across various design standards. Utilisation values marked in red indicate exceedance, which is observed in the design checks following the OCDI Technical Standards and *JTS-147-2017*. The reasons for such exceedance under the two guides are briefly described below.

The exceedance observed in the sliding checks is primarily attributed to the assumption of partial mobilisation of passive earth pressures, rather than full mobilisation. Moreover, the partial factors of safety adopted in the OCDI Technical Standards and *JTS-147-2017* result in a slightly higher safety margin. Collectively, these assumptions lead to increased conservatism compared with established practice in recent reclamation projects.

Regarding the exceedance observed in the bearing capacity checks, it is primarily attributable to differing assumptions adopted in deriving the bearing pressure beneath the DCM elements as recommended by the OCDI Technical Standards and *JTS-147-2017*. A separate study was undertaken using a series of three-dimensional finite element models to compare the analytical solutions with numerical results under various site settings and DCM improvement geometries. It was concluded that the analytical solutions recommended by *FHWA-HRT-13-046* and this study provided better match with the computed results, while the OCDI Technical Standards and *JTS-147-2017* substantially overestimated the bearing pressures. In addition, higher partial factors of safety are specified for bearing capacity checks in both the OCDI Technical Standards and *JTS-147-2017*. It is worth

noting that projects designed in accordance with these two standards typically involve DCM elements embedded in sandy strata, where the allowable bearing capacity is significantly greater than that of clayey strata. Consequently, past overseas projects adopting these two standards were generally found to be feasible as DCM was embedded in sandy strata. Nonetheless, the bearing pressure formulations recommended in the OCDI Technical Standards and *JTS-147-2017* appear overly conservative and are likely not applicable to regions where DCM is embedded in clayey strata (e.g. Hong Kong).

As for the exceedance observed in the internal crushing check under *JTS-147-2017*, it is primarily caused by a high material partial factor of 2.2, together with the omission of the beneficial contribution from lateral earth pressure in the design calculations. It is considered that the more stringent material partial factor may have originated from an older edition (2002) of the Japanese technical standards. In the current edition of the OCDI Technical Standards, this partial factor has since been reduced.

Table 7: Summary of benchmarking exercise

		This study	**OCDI Technical Standards**	**JTS-147-2017**	**FHWA-HRT-13-046**
DCM area replacement ratio (%)		35	35	35	35
Width of DCM-improved zone (m)		44	44	44	44
DCM design compressive strength (kPa)		$q_{t,day}$ $= 1200$	f_{ck} $= \alpha\beta q_{uck}$ $= 0.81 \times 1.0 \times 1200$ $= 972$	σ_{cak} $= 1200$	$f_c f_r f_v q_{dm,spec}$ $= 1.2 \times 0.8 \times 1.15$ $\times 1000$ $= 1{,}104$
Utilisation of external stability checks (%)	Slip circle	Comparable across all four guides given the same DCM dimensions and site conditions			
	Overturning	55	14	17	Not required
	Sliding	96	127	155	Not required
	Bearing	69	246	209	Automatically satisfied*
Utilisation of internal stability checks (%)	Crushing at DCM toe	14	83	175	Automatically satisfied*
	Racking failure	Not required	Not required	Not required	Automatically satisfied*
	Shearing on vertical plane	38	35	71	Not required
	Soil extrusion	21	15	12	21

* *FHWA-HRT-13-046* recommends that no further checks would be required if the location of the resultant normal force at the base of the DCM-improved zone is located within the landside half of the improvement width

For design checks conducted in accordance with *FHWA-HRT-13-046*, the position of the resultant normal force at the base of the DCM-improved zone was found to be located within the landside half of the improvement width. According to the FHWA standard, "the design is safe against overturning and bearing capacity failure, no further analysis of this failure mode needs to be done". The same simplification also applies to those internal stability checks.

The new design approach proposed in this paper can be regarded as more cost-effective compared to the OCDI Technical Standards and *JTS-147-2017*, while maintaining a reasonable margin of safety. Furthermore, the new design approach also demonstrates greater rigour than *FHWA-HRT-13-046* by incorporating design checks that are otherwise omitted in the US manual.

While international standards provide valuable guidance, their direct application in other overseas regions may not always be appropriate. The results demonstrate that overly conservative approaches, such as the application of high partial factors and the amplification of bearing pressures, can lead to designs that are unnecessarily costly and complex. Conversely, approaches that omit critical design checks may potentially compromise safety, particularly in challenging or high-risk environments.

6 CONCLUSIONS

This paper has presented a comprehensive review of international DCM design standards, identifying key aspects for improvement in the proposed new design guidelines. A benchmarking exercise, applying the main international standards and the proposed design guidelines to a hypothetical project scenario, has demonstrated the potential benefits of the new approach. The proposed methodology achieves a robust and cost-effective design, maintaining safety while optimising constructability and sustainability. The findings provide valuable guidance for the future development of DCM design practices in coastal environments.

ACKNOWLEDGEMENTS

This paper is published with the permission of the Head of Geotechnical Engineering Office and the Director of Civil Engineering and Development, Government of the Hong Kong Special Administrative Region, China.

REFERENCES

Bruce, D.A., Bruce, M.E.C. & DiMillio, A. F. 1998. Deep mixing method: a global perspective, *Geotechnical Special Publication*, 1-26.

Bruce, M.E.C., Berg, R.R., Collin, J.G., Filz, G.M., Terashi, M. & Yang, D.S. 2013. *Federal Highway Administration Design Manual: Deep Mixing for Embankment and Foundation Support (No. FHWA-HRT-13-046)*, Federal Highway Administration. Offices of Research & Development, United States, 228 p.

Han, J., Zhou, H.T. & Ye, F. 2002. State-of-practice review of deep soil mixing techniques in China, *Transportation Research Record*, 1806: 49-57.

Kitazume, M. & Terashi, M. 2013. *The Deep Mixing Method*, CRC Press, London, 405p.

Overseas Coastal Area Development Institute (OCDI) of Japan. 2020. Technical Standards and Commentaries for Port and Harbour Facilities in Japan, OCDI, Tokyo, Japan, 2182p.

Ministry of Transport of the People's Republic of China. 2017. *Code for Foundation Design on Port and Waterway Engineering*, China Communications Press, (in Chinese).

Recent Advancement in the Estimation of Design Debris Volume for Natural Terrain Hazard Mitigation Measures

R.W.M. Cheung, I. Li, C. Lam, A.C.Y. Fu & E.Y.C. Zeng
Geotechnical Engineering Office, Civil Engineering and Development Department, Hong Kong SAR, China

ABSTRACT

Design Event Approach (DEA) is one of the approaches as specified in GEO Report No. 138 (2nd Edition) that is commonly adopted for the design of natural terrain hazard mitigation measures, with design source volume being one of the most important design parameters. Current practice in estimating design source volume relies heavily on site-specific historical landslide records, aerial photo interpretation and field mapping. Although this approach is appropriate for natural hillsides with abundant and reliable historical data, challenges arise for natural hillsides with limited or even no such information. To address this, the GEO initiated a study in 2025 and proposed an enhanced methodology by integrating territory-wide data with site-specific data. Statistical analyses of over 22,000 recent landslides from the Enhanced Natural Terrain Landslide Inventory were conducted to examine the return period of territory-wide landslides. The enhancement provides useful supplementary information that can be readily integrated with site-specific landslide data for a more realistic estimation of design source volume. A case study is presented to demonstrate the application of the new methodology, which offers greater flexibility for designers to exercise engineering judgement in determining the design source volume while remaining aligned with the current principles and framework of DEA.

1 INTRODUCTION

1.1 Design Event Approach in Natural Terrain Hazard Study

Under the current strategy for the mitigation of natural terrain hazards in Hong Kong, a Natural Terrain Hazard Study (NTHS) is required to assess the potential hazards arising from natural hillsides for the design of necessary mitigation measures. Guidance on undertaking an NTHS and on the design of mitigation measures is given in GEO Report No. 138 (2nd Edition) (Ho & Roberts 2016). There are three approaches as suggested in Ho & Roberts (2016), namely Factor of Safety, Quantitative Risk Assessment, and the Design Event Approach (DEA). Among these approaches, DEA is the most commonly adopted given its simplicity of application.

Under the DEA, a design event refers to the magnitude of the hazard type selected for mitigation. The requirement of a design event is such that the likelihood of occurrence of a more severe event is sufficiently low and the notional return period is taken to be in the order of 1,000 years.

The determination of a design event that fulfils the design requirement involves the consideration of both the failure volume and debris mobility. Firstly, given that debris mobility has been assessed based on historical landslide data and the use of back-analysed rheological parameters for mobile failures, it offers at least a factor of ten in terms of likelihood of occurrence. Probabilistically speaking, this corresponds to a probability of occurrence of 0.1. Secondly, when combined with the use of the recommended rheological parameters in debris runout modelling, it suffices for the failure volume to be adopted in design so as to align with a notional return period of 100 years, which would then correspond to a notional 1,000-year design event. In other words, the failure volume, or more commonly referred to as the source volume at initiation of failure, should have a return period of 100 years to satisfy the design requirement of a design event.

1.2 Current Practice and Potential Limitations

Among the different types of mitigation measures mentioned in Ho & Roberts (2016), flexible and rigid debris-resisting barriers are more commonly adopted in recent years. In the design process, a debris mobility assessment is required to estimate various runout parameters such as velocity, runout distance, impact load and final volume, which are essential parameters for designing these measures. Some commonly used computer programs for debris mobility assessment include DAN-W (Hungr 1995), 2d-DMM (Kwan & Sun 2006) and 3d-DMM (Kwan & Sun 2007; Law et al. 2017). When using these programs, two of the most important input parameters are the design source volume and the rheological parameters.

Although sufficient and detailed guidance on the recommended values of rheological parameters for different failure types has been published by the Geotechnical Engineering Office (GEO) (GEO 2023a; 2023b; 2023c), the determination of design source volume with an occurrence return period of 100 years is less straightforward as it relies heavily on professional judgement in conjunction with site-specific historical landslide records (e.g. recent landslides or relict landslides with high degree of certainty), aerial photo interpretation (API) and field mapping. The current design practice is well recognised by practitioners and would produce mitigation measures of reasonable scale. However, this approach to estimating design source volume is only best suited for natural hillsides with abundant and reliable historical data, such as those affected by recent landslides. Since the implementation of the Landslip Prevention and Mitigation Programme (LPMitP) in 2010, high-ranking Historical Hillside Catchments (HLCs) consisting of many recent landslides have been gradually dealt with. In this regard, challenges in estimating design source volume emerge when natural hillsides with limited or even no landslide histories are selected for NTHS. Consequently, this could lead to the design source volume being estimated with less certainty, hence potentially producing mitigation measures with a scale that is disproportionate to the design event as originally required.

2 TERRITORY-WIDE LANDSLIDE DATA

2.1 Enhanced Natural Terrain Landslide Inventory

In light of the situation discussed above, the GEO initiated an in-house study in 2025 and proposed an enhanced methodology for estimating design source volume by considering territory-wide data. Taking cognizance of the Enhanced Natural Terrain Landslide Inventory (ENTLI) compiled since 2005 (Dias et al. 2009) and updated to the latest set in 2022, there is a wealth of territory-wide data for Hong Kong consisting of over 22,000 records of recent landslides since 1963. Therefore, there is a good potential in using the ENTLI database to provide supplementary information for estimating design source volume using territory-wide data.

2.2 Statistical Analyses

The study methodology is to carry out statistical analyses on the 22,000 recent landslides occurred in the past 60 years between 1963 and 2022. From the analyses, a source volume corresponding to a return period of 100 years can be determined statistically. Since the landslides in ENTLI are recorded as plan area in m^2, an assumption is needed to correlate landslide area to landslide volume. Based on an in-house review undertaken by the GEO on 218 nos. of recent landslide records complied from Landslide Study Reports as shown in Figure 1, it is found that for most landslides, this ratio is approximately 1:1, implying the landslide area can be assumed equal to the landslide volume, and is considered sufficient for the purpose of this study.

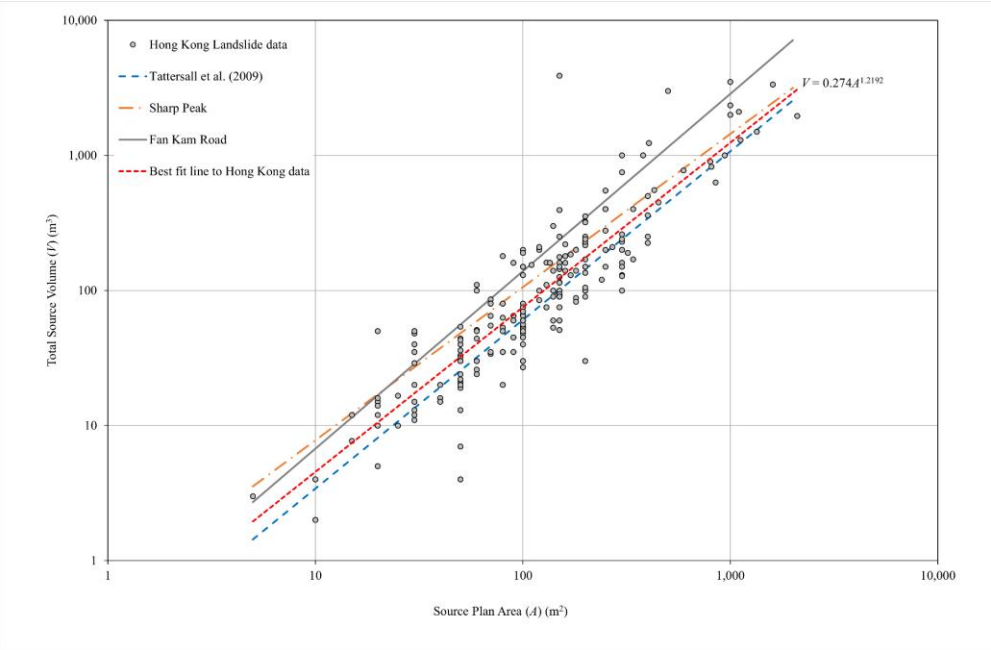

Figure 1: Correlation between source volume and source area

Two methods were attempted. The first method (Method 1) involves fitting a Probability Density Function (PDF) using log-normal distribution to all the 22,000 landslide data ranked according to the landslide volume. The volume corresponding to a probability exceedance (p) of 1% (i.e. 0.01) of the entire data set could provide an indication of a 100-year return period source volume as shown in Figure 2, which is estimated to be around 400 m^3.

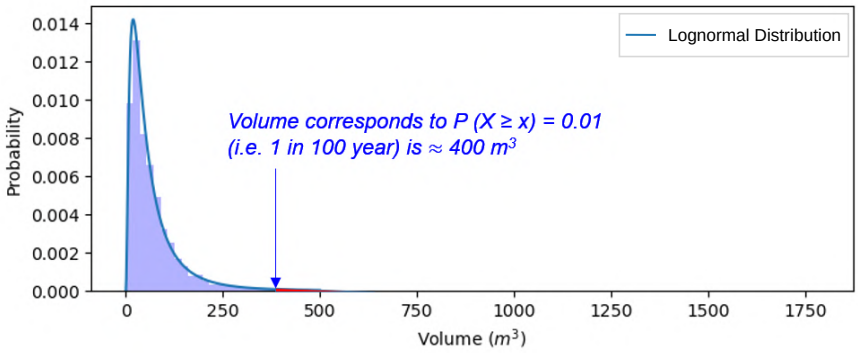

Figure 2: Source volume from 22,000 territory-wide data (Method 1)

This assumes the probability of exceedance of 1% equals to the reciprocal of the return period (T) of 100 years. However, since the dataset does not represent annual data as the 22,000 landslides are the total number of landslides occurred in 60 years, this method only gives an approximation of a 100-year return period source volume.

To address the limitation of Method 1, the second method (Method 2) involves extracting annual volume statistics from the entire database for statistical analysis. Similar concept has been widely adopted in frequency analysis of extreme rainfall values (Tang & Cheung, 2011). Instead of annual maxima, a representative landslide volume is selected for each year. For the purpose of the study, three different annual statistics were selected as representative volumes, namely, the annual mean, the annual median and annual 90th percentile. As a result, three sets of annual landslide volume data with each set containing 60 annual volume statistics are used for fitting PDF. As the dataset contains annual data, the volume with probability of exceedance of 1% will be theoretically equal to a volume with a return period of 100 years, hence the source volume.

However, it is expected that the distribution characteristics depend on the choice of annual statistics. Therefore, goodness-of-fit tests using the Chi-square tests method on different distribution models were performed to select the appropriate distribution model for each set of annual statistic such that all tests would pass at 2.5% significant level. The distribution models used for the respective annual statistics and the resulting source volumes are shown in Figures 3 to 5. A summary table showing the source volumes obtained from Methods 1 and 2 is given in Table 1.

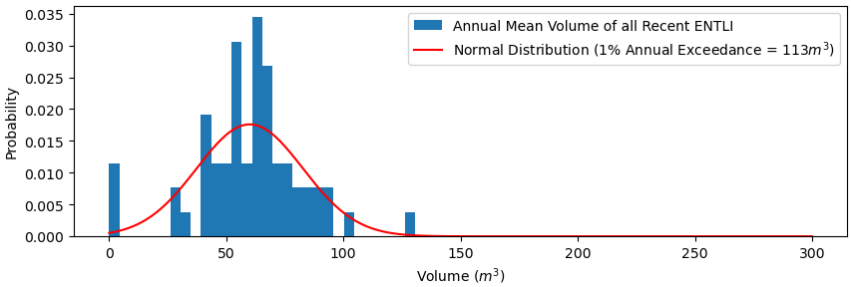

Figure 3: Source volume from 60 annual data (Method 2 – annual mean)

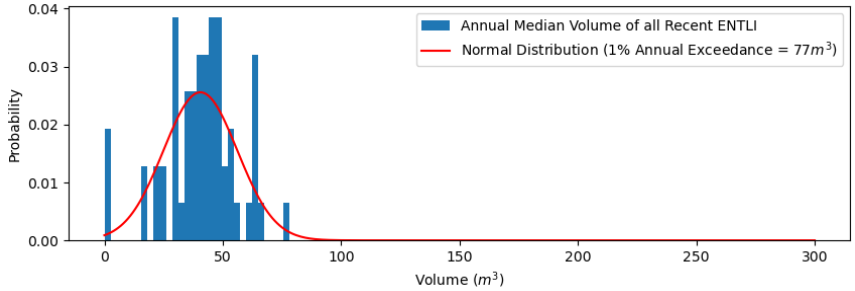

Figure 4: Source volume from 60 annual data (Method 2 – annual median)

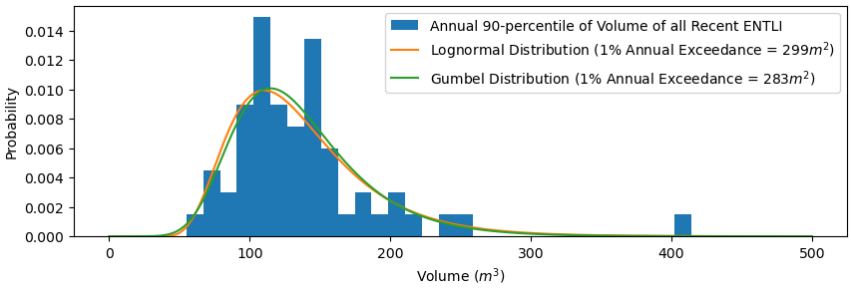

Figure 5: Source volume from 60 annual data (Method 2 – annual 90th percentile)

Table 1: Summary of source volume corresponding to a return period of 100 years (Method 1 and Method 2)

Method	Annual Statistics	Sample Mean (for Method 1)/Annual Sample Mean (for Method 2) (m^3)	Sample Standard Deviation (for Method 1)/Annual Sample Standard Deviation (for Method 2) (m^3)	Distribution Model	Source Volume (m^3)
1	N/A	71	86	Log-normal	400
2	Annual Mean	60	23	Normal	110
	Annual Median	41	16		80
	Annual 90th Percentile	137	55	Log-normal	300
				Gumbel	280

2.3 Discussions

From Table 1, it can be seen that in Method 2, using the mean or median as annual statistics provides a similar order of magnitude of source volume with a return period of 100 years, which is about 100 m^3. When the 90th percentile is adopted as the annual statistic, the source volume increases to about 300 m^3 regardless of the distribution models used. The results provide valuable information on the territory-wide behavior over 60 years, indicating that the source volume with a return period of 100 years is in the order of hundreds m^3 and is unlikely to exceed 400 m^3.

The territory-wide study on ENTLI, in addition to the site-specific data, provides useful supplementary information to designers to refer to when undertaking an NTHS. This is particularly useful when there is uncertainty in the site-specific data. Nevertheless, it should be borne in mind that the study involves some key assumptions, such as the source area-to-volume conversion ratio and the distribution models adopted. In this regard, potential enhancements to the statistical analyses may be explored in future, such as refining the area-to-volume correlation by categorising it according to volume class and trialling other distribution models. Additionally, as the territory-wide data are derived from ENTLI, it is anticipated that the analysis results would need to be updated regularly, subject to the progress of ENTLI updates.

Most importantly, the volume derived from territory-wide data should be regarded as a basis for formulating the design source volume only. Engineering judgement and site-specific considerations remain crucial in determining the design event when undertaking an NTHS.

3 CASE STUDY

3.1 Site Background

A case study is presented herein to demonstrate the application of an enhanced methodology that considers both territory-wide and site-specific landslide data for determining the design source volume, which is essential information for the design of natural terrain hazard mitigation measures. This methodology offers greater flexibility for designers to exercise engineering judgement in determining the design source volume while still remaining aligned with the DEA framework set out in Ho & Roberts (2016).

The site considered in the case study is located above Tregunter Path, Mid-Levels of Hong Kong. This site is situated on a northeast-facing hillside between the Peak Tramway (including the Barker Road Peak Tram Station) and Old Peak Road at the crest, and Tregunter Path at the toe. The study area is approximately 240 m long and 340 m wide and has a plan area of approximately 59,000 m^2. The study area is about 160 m high, starting from approximately 200 mPD at the slope toe up to 360 mPD at the crest. There are three open hillslope (OH) catchments, one topographic depression (TD) catchment and two channelised (CD) catchments within the study area. Figure 6 shows the catchments on a location plan.

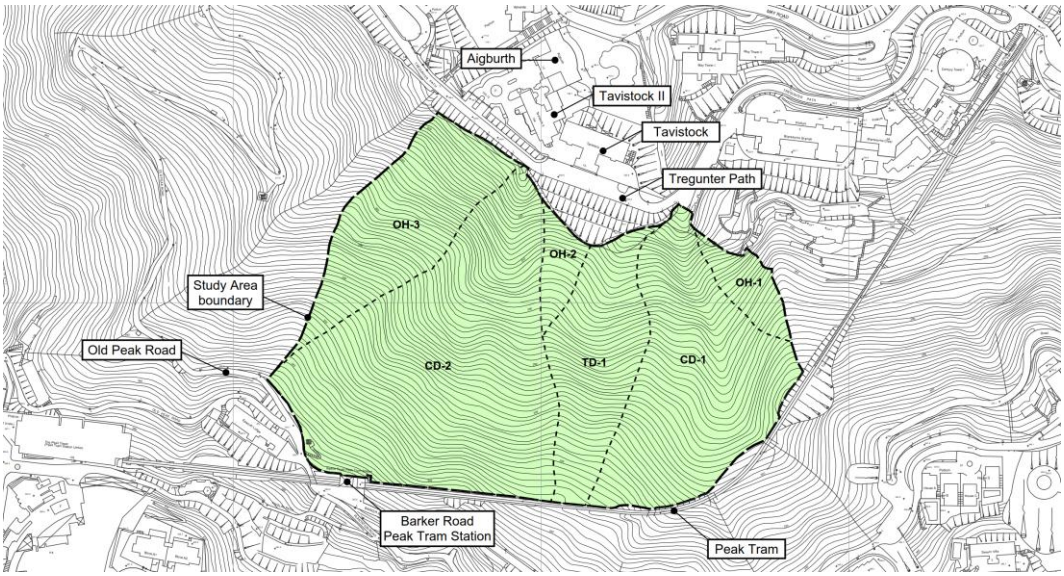

Figure 6: Location Plan of the Study Area

3.2 Landslide Information Considered

The following information is considered for estimating the design source volume with a 100-year return period:

(i) Results of statistical analyses of territory-wide recent landslide records from ENTLI collected across Hong Kong over a period of about 60 years (see Section 2)

(ii) Site-specific recent and relict landslide data (with a high degree of certainty) within the study area, verified by API and field mapping

3.2.1 Territory-wide Landslide Data

The statistical analyses of over 22,000 recent natural terrain landslides from ENTLI have been discussed in Section 2. The estimated source volumes corresponding to a return period of 100 years are summarised in Table 1. This information may be considered as prior knowledge before conducting a site-specific assessment. The annual median, which has a value of 80 m^3, is adopted for estimating the design source volume for the hazard assessment and the design of natural terrain mitigation measures in this case study.

It is worth noting that, when compared with territory-wide recent landslides observed over a period of about 60 years, the ages of territory-wide relict landslides are unknown but are expected to be much longer. Considering that their return periods cannot be estimated and given the uncertainty in the size of the landslide corresponding to a single event, relatively large uncertainty would be introduced into the design event if information on territory-wide relict landslides were used. Therefore, territory-wide relict landslides are not used for determining the design source volume.

3.2.2 Site-specific Landslide Data

Site-specific landslide records have been evaluated to assess the scale of landslides with a 100-year return period that may be encountered within the study area. In fact, these 100-year return events were determined on the basis of engineering judgement, not by statistical analysis. A summary of the recent and relict natural terrain landslides in the six catchments within the study area is shown in Table 2.

Table 2: Summary of Recent and Relict Natural Terrain Landslides in the Six Catchments within the Study Area

Catchment	No. of recent landslides	Largest recent landslide volume (m^3)	No. of relict landslides	Largest relict landslide (with a high degree of certainty) volume (m^3)	Largest relict landslide (with a low degree of certainty) volume (m^3)
CD-1	1	13.2	4	89.0	-
CD-2	1	1.7	5	214.0	15
TD-1	-	-	5	83.8	-
OH-1	1	13.1	3	50.3	220
OH-2	No landslide records				
OH-3	1	2.1	-	-	-

The largest recent and relict landslides with a high degree of certainty within the study area have volumes of 13 m^3 and 214 m^3, respectively. This information may be considered as new evidence when determining the design event source volume for the study area. Relict landslides with a low degree of certainty are not considered. Figure 7 shows a geomorphological map and the locations of the site-specific recent (RC) and relict (RL) landslides within the study area.

It should be borne in mind that the site-specific recent landslides were observed over a period of about 60 years starting in 1963, and there is no information about the time of the site-specific relict landslides.

Nevertheless, these landslide records still indicate the condition of the natural hillside under consideration and are used to estimate the design source volume corresponding to a return period of 100 years.

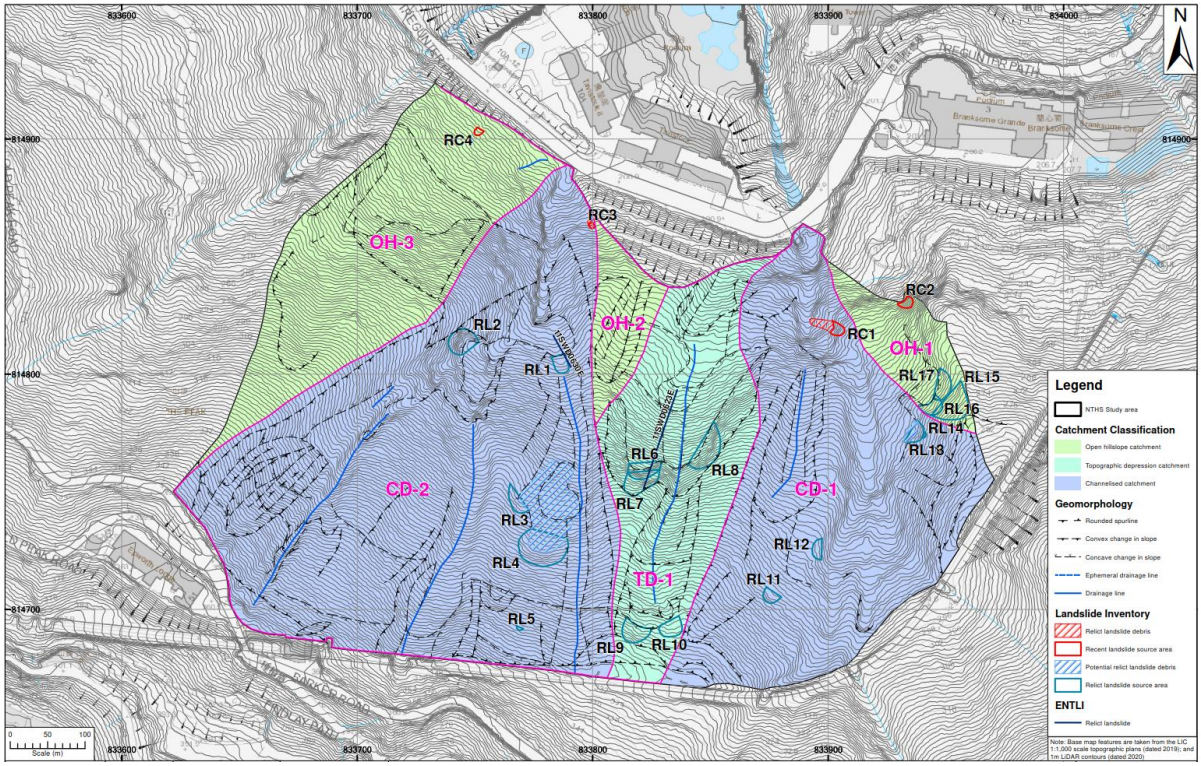

Figure 7: Geomorphological Map Showing the Locations of Site-specific Recent and Relict Landslides

3.3 Integration of Territory-wide and Site-specific Landslide Data by Weighting

The design source volume with a return period of 100 years is determined by considering both the territory-wide recent landslide volume (prior knowledge) and site-specific recent and relict landslide data (new evidence). Engineering judgement that reflects the relevance of the information, as represented by weighting factors applied to each landslide volume, is also duly exercised in the process. Equation (1) is used to calculate the weighted source volume:

$$\begin{aligned}\text{Weighted source volume} = {} & A \times \text{notional territory-wide recent landslide volume} + \\ & B \times \text{largest site-specific recent landslide volume} + \\ & C \times \text{largest site-specific relict landslide volume}\end{aligned} \quad (1)$$

where A, B and C are weighting factors determined according to their relative level of relevance to the design source volume with a 100-year return period.

The weighting factors in Equation (1) are used to reflect the level of relevance of various landslide information to the design landslide source volume, with engineering judgement exercised by the designer. As mentioned, the territory-wide notional recent landslide volume is derived from an analysis of more than 20,000 recent natural terrain landslide records across Hong Kong over the past 60 years. This information is important as the notional landslide volume corresponding to 100 years return period is estimated through formal statistical analysis. In addition, this piece of information is particularly useful whenever little or no instability data are available within a study area. However, it should be borne in mind that this value, by its nature, represents an average that smooths out site-specific characteristics such as geological and geomorphological features. Having said that, depending on the availability and relevance of other landslide data (e.g. site-specific data), a medium weighting factor of 25% (A = 0.25) is considered appropriate for the notional territory-wide landslide volume.

As the largest recent site-specific landslide volume is a good indicator of the recent past and the current stability conditions of the hillslopes within the study area, this piece of information is regarded as the most relevant to the assessment. Hence, a high weighting factor of 50% (B = 0.5) is considered appropriate for the site-specific recent landslide volume.

The largest site-specific relict landslide volume with a high degree of certainty is also considered useful for the assessment. However, since its age is unknown, it is inevitably less reliable than the recent landslide data. Sewell & Campbell (2005) reported that large relict natural terrain landslides with scars wider than 20 m can generally be thousands to tens of thousands of years old, whereas smaller ones may still be hundreds of years old. The direct use of the largest relict landslide volume without adjustment to approximate a 100-year return period event may therefore lead to an overly conservative estimate, which could in turn unnecessarily increase the scale and cost of mitigation works. Consequently, a medium weighting factor of 25% (C = 0.25) is considered appropriate.

To summarise, the order of relevance of various landslide data to the estimation of a 1-in-100-year return period landslide can be ranked as follows: *site-specific recent landslide volume > territory-wide notional landslide volume = site-specific relict landslide volume.*

3.4 Sensitivity Analysis of Different Combinations of Weighting Factors

A sensitivity study has been carried out to assess the effect of the selected values of the different weighting factors (A, B and C), which are applied to the landslide volumes mentioned in Sections 3.2.1 and 3.2.2. Four cases have been considered. Case 1 represents the situation where the designer adopts the weighting factors suggested in Section 3.3, whereas in Cases 2–4 a higher weighting factor B is adopted for the site-specific recent landslide volume. In each case, the factors A and C equally share the remaining weighting, as they are considered equally relevant to the estimation of a 1-in-100-year return period landslide, as mentioned in Section 3.3. The results of the sensitivity study are summarised in Table 3.

Table 3: Sensitivity Analysis on the Effect of Different Weighting Factors

Case	Weighting factor combinations (A : B : C)	Weighted source volume (m^3)
1	25% : 50% : 25%	80
2	20% : 60% : 20%	67
3	15% : 70% : 15%	53
4	10% : 80% : 10%	40

As expected, the weighted source volume is sensitive to the selected weighting factors, but the difference is not significant in the context of the design of natural terrain hazard mitigation measures. In view of this, it is considered rational and scientific to fix the weighting factors as suggested in Section 3, that is, A = 0.25, B = 0.5 and C = 0.25. If sound arguments are available, the calculated (weighted) source volume can be adjusted (increased or decreased) to give the design source volume for the NTHS. Finally, it should be borne in mind that given the inherent uncertainties in the assessment, the design source volume should be regarded as an estimate based on the available information and the designer's professional judgement, rather than as a precise calculation.

4 CONCLUSIONS

The design event is one of the most important parameters in NTHS using the DEA and for the subsequent design of any mitigation measures. The estimation of design event, particularly on the design source volume, relies primarily on site-specific information such as recent landslides. However, for sites with insufficient landslide data or even without any past landslides, the estimation of the design source volume may become difficult. To address these potential challenges, statistical analyses using territory-wide ENTLI data were undertaken to estimate a design source volume aligning with the current design requirement (i.e. a 100-year return period). A case example is used to demonstrate the enhanced flexibility in NTHS by making reference to the territory-wide study to better estimate a design source volume by means of weighting factors. Further

development and refinement on the territory-wide study are envisaged, including the area-to-volume conversion ratio, the use of different statistical models, and the regular updating of the ENTLI database. Regardless of the methods used, engineering judgement shall always be exercised, with due considerations given to the site-specific conditions in the determination of the design volume.

ACKNOWLEDGEMENTS

This paper is published with the permission of the Head of the Geotechnical Engineering Office and the Director of Civil Engineering and Development, the Government of the Hong Kong Special Administrative Region.

REFERENCES

Dias, A., Hart., J & Fung, E.K.S. 2009. The Enhanced Natural Terrain Landslide Inventory. *Proceedings of the HKIE Geotechnical Division Annual Seminar 2009.* Hong Kong Institution of Engineers, Hong Kong, 71-78.

GEO. 2023a. *Guidelines on the Assessment of Debris Mobility for Channelised Debris Flows (GEO Technical Guidance Note No. 29 (TGN 29))*. Geotechnical Engineering Office, Civil Engineering and Development Department, HKSAR Government, 6.

GEO. 2023b. *Guidelines on Assessment of Debris Mobility for Open Hillslope Failures (GEO Technical Guidance Note No. 29 (TGN 34))*. Geotechnical Engineering Office, Civil Engineering and Development Department, HKSAR Government, 16.

GEO. 2023c. *Guidelines on the Assessment of Debris Mobility for Failures within Topographic Depression Catchments (GEO Technical Guidance Note No. 29 (TGN 38))*. Geotechnical Engineering Office, Civil Engineering and Development Department, HKSAR Government, 16.

Ho, H.Y., and Roberts, K.J. 2016. *Guidelines for Natural Terrain Hazard Studies (GEO Report No. 138, 2nd Edition).* Geotechnical Engineering Office, Civil Engineering and Development Department, HKSAR Government.

Hungr, O.A. 1995. A model for the runout analysis of rapid flow slides, debris flows, and avalanches. *Canadian Geotechnical Journal*, 32(4):610-623.

Kwan, J.S.H. & Sun, H.W. 2006. An improved landslide mobility model. *Canadian Geotechnical Journal*, 43(5):531-539.

Kwan, J.S.H. & Sun, H.W. 2007. Benchmarking exercise on landslide mobility modelling – runout analyses using 3dDMM. *Proceedings of the International Forum on Landslide Disaster Management, Hong Kong*. Geotechnical Division, Hong Kong Institution of Engineers, Hong Kong. Vol II, 945-966.

Law, R.P.H., Kwan, J.S.H., Ko, F.W.Y. & Sun, H.W. 2017. Three-dimensional debris mobility modelling coupling smoothed particle hydrodynamics and ArcGIS. *Proceedings of the 19th International Conference on Soil Mechanics and Geotechnical Engineering (Seoul), South Korea*, 945-966.

Sewell, R.J. & Campbell, S.D.G. 2005. *Report on the Dating of Natural Terrain Landslides in Hong Kong (GEO Report No. 170)*. Geotechnical Engineering Office, Civil Engineering and Development Department, HKSAR Government, 151.

Tang, C.S.C. & Cheung, S.P.Y. 2011. *Frequency Analysis of Extreme Rainfall Values (GEO Report No. 261)*. Geotechnical Engineering Office, Civil Engineering and Development Department, HKSAR Government, 209.

Tattersall, J.W., Devonald, D.M., Hung, R.K.C. & Kwong, R.T.S. (2009). Estimation of 'Design Event' Landslide Sources for the North Lantau Expressway and Yu Tung Road Natural Terrain Hazard Mitigation Works Study. *Proceedings of the HKIE Geotechnical Division 29th Annual Seminar*, 7 p.

Application of the Circucore Pro Method in the Boardwalk underneath Island Eastern Corridor Project

C.K. Tse, KENNETH
Oriental Boring & Engineering Ltd.

S H Chung
Leighton Contractors (Asia) Limited

Vincent L T Chan
Leighton Contractors (Asia) Limited

Philip Daynes
Sum Kee Construction Limited

ABSTRACT

Marine foundation works in Hong Kong are often carried out under stringent environmental and site constraints, particularly in waterfront developments where control of ground disturbance and environmental impact is critical. Conventional down-the-hole (DTH) drilling methods utilise high-pressure air flushing, which may induce outward pressure transmission into the surrounding ground and contribute to disturbance of the soil stress regime. These effects may lead to increased turbidity, dust, and noise, which require careful management, in sensitive environments. In the Boardwalk underneath Island Eastern Corridor (IEC) project, an alternative drilling approach, namely the Circucore Pro (CP) Method, was adopted to mitigate these potential effects. The method is developed with reference to fundamental geotechnical principles governing effective stress, pore pressure response, and soil–fluid interaction. By directing flushing air within the drill rod, the method limits the release of excess pressure into the surrounding ground and reduces disturbance during drilling.

1 INTRODUCTION

Marine foundation works in Hong Kong are frequently undertaken in densely developed urban environments, where construction activities are carried out in close proximity to existing infrastructure and environmentally sensitive waterfronts. In recent years, there has been increasing emphasis on minimising environmental impact during construction, particularly with respect to the control of turbidity, noise and dust in marine and near-shore projects. These requirements are reinforced through project-specific environmental management measures and regulatory frameworks, including those arising from environmental impact assessment processes and harbour protection considerations, which necessitate careful selection of construction methods.

The behaviour of the ground during construction is closely related to subsurface conditions and groundwater response, both of which are recognised as key considerations in geotechnical practice in Hong Kong (GEO, 2017). In saturated granular soils, such as alluvium and completely decomposed granite, increased pore pressure conditions to the surroundings may cause over cutting beyond the piling shaft. On the other hand, saturated clayey soil, such as marine deposit are sensitive to unbalanced uplift pressures due to its low shear strength nature under liquid state in-situ marine deposit in Hong Kong (Liu, A. S., Li, W., & Kwok, C. Y., 2025). With excessive soil material being flushed out of containment by pile casing, the release of suspended solids into the surrounding water must be strictly controlled.

Conventional down-the-hole (DTH) drilling methods are widely used in foundation construction due to their effectiveness in penetrating hard materials. However, high-pressure air flushing may introduce outward pressure transmission into the surrounding ground, potentially affecting pore pressure conditions and contributing to environmental impacts.

In view of these considerations, there is a need to adopt construction methods that are more closely aligned with fundamental geotechnical principles governing soil behaviour. By improving control over pressure

transmission and soil–fluid interaction during drilling, it is possible to reduce unintended disturbance while maintaining construction efficiency.

This paper presents the application of an alternative drilling approach, namely the Circucore Pro (CP) Method, in the Boardwalk underneath Island Eastern Corridor (IEC) project. The study examines the engineering principles underlying the method, its implementation under site constraints, and the observed performance in terms of environmental control and operational behaviour.

2 PROJECT BACKGROUND

The Boardwalk underneath Island Eastern Corridor (IEC) project forms part of the enhancement works along the northern shoreline of Hong Kong Island, aiming to improve public accessibility and connectivity along the harbourfront. The works are located beneath the existing IEC structure, a critical elevated transport corridor, and are carried out at the marine environment. The project therefore presents significant engineering and environmental constraints.

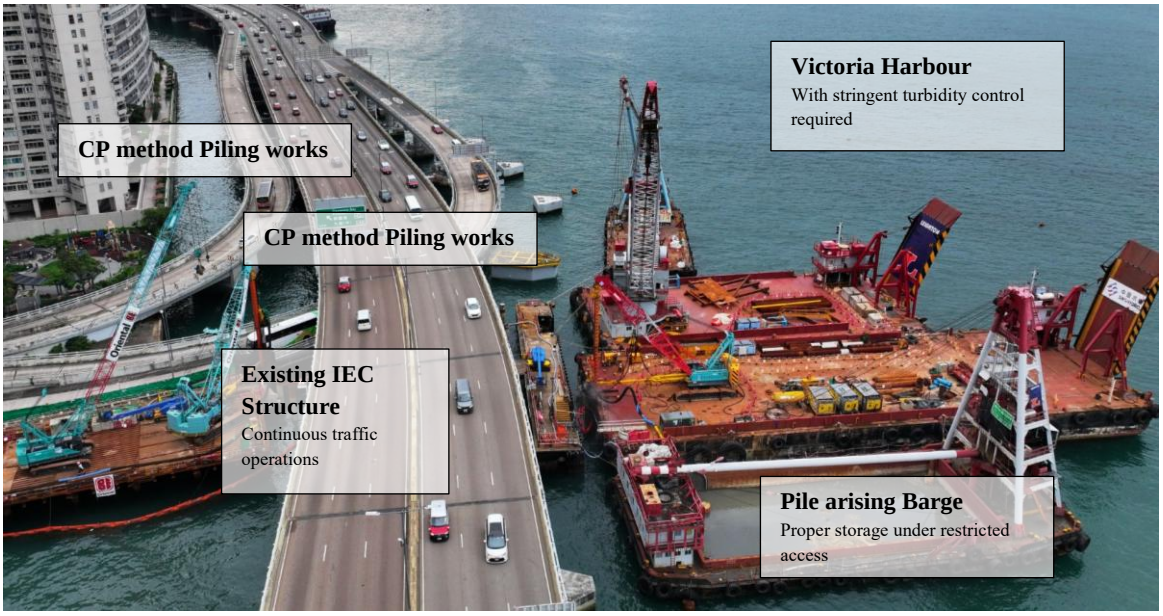

Figure 1. Marine piling works beneath the Island Eastern Corridor (IEC) for the Boardwalk Project

Foundation works for the boardwalk structures are required to be executed within a confined working corridor beneath the existing viaduct, where headroom is limited with restricted access. The proximity to the seawall and exposed open water environment further imposes stringent environmental controls, particularly with respect to turbidity, noise, and dust emissions. In addition, the presence of existing structures and utilities necessitates careful control of ground disturbance to avoid adverse effects on adjacent facilities.

The subsurface conditions in the project area generally comprise marine deposits overlying alluvial materials and decomposed rock, with underlying bedrock encountered at depth. Drilling works are required to penetrate these strata to form foundation elements, and the selection of drilling method is therefore critical to both construction performance and environmental control.

Given the site constraints and environmental sensitivity, particular attention was given to the potential geotechnical and environmental impact of conventional drilling practices. The project provided an opportunity to adopt and assess an alternative drilling approach with the objective of improving control of ground response and minimizing environmental impact during piling works. The assessment of subsurface conditions and groundwater regime forms an essential component in the planning of foundation works in Hong Kong (GEO, 2017).

3 CONVENTIONAL DRILLING PRACTICE AND LIMITATIONS

Down-the-hole (DTH) drilling methods are commonly adopted in foundation construction works in Hong Kong, particularly where penetration through hard ground or rock strata is required. The method typically employs

compressed air to drive a down-the-hole hammer while simultaneously flushing drill cuttings from the borehole. The flushing process generally involves releasing high-pressure air at the drill bit, which transports cuttings upward through the annulus between the drill string and the borehole wall.

While the DTH method is effective in achieving drilling efficiency and penetration in competent materials, the release of compressed air at the base of the borehole during drilling and flushing procedure can result in outward pressure transmission into the adjacent soil and groundwater. From a geotechnical perspective, this may influence the in-situ stress state and pore pressure conditions in the vicinity of the borehole, particularly in loose or saturated soils. Previous studies have indicated that air-powered drilling processes may lead to increases in pore pressure and associated ground disturbance under certain conditions (Ahlund, 2016).

In marine or near-shore environments, such effects may disturb the surrounding materials and generate suspended solids. The upward movement of air and cuttings through the borehole may also result in the release of fine particles into the surrounding environment, giving rise to turbidity concerns. In addition, the use of high-pressure air systems may cause increased noise levels and airborne emissions during operation.

Under constrained site conditions, such as those encountered in the IEC Boardwalk project, these potential effects require careful consideration. The interaction between drilling operations and the surrounding ground becomes a key factor in determining the suitability of the construction method, particularly where environmental control is of primary importance.

4 ENGINEERING PRINCIPLES GOVERNING GROUND DISTURBANCE

The response of soil to drilling activities is fundamentally governed by the principles of effective stress, pore pressure behaviour, and soil–fluid interaction. In saturated or partially saturated ground, the effective stress, defined as the difference between total stress and pore pressure, controls the strength and deformation characteristics of the soil (Terzaghi, 1925). The importance of understanding subsurface conditions and groundwater behaviour in assessing soil response is well recognised in local practice, particularly in Hong Kong where marine deposits and reclamation soils are commonly encountered (GEO, 2017).

During drilling operations, the introduction of compressed air and the removal of materials from the borehole may result in localised changes in pore pressure. In conventional air-flushed drilling systems, high-pressure air is discharged at the base of the borehole, creating a pressure gradient between the borehole and the surrounding ground. This pressure differential may drive air into the adjacent soil mass, particularly where permeable pathways or discontinuities exist.

In practice, compressed air pressure imposed can drastically change the porewater pressure of in-situ soil. Under normal piling depth (50m below sea level) and hydrostatic pore water pressure condition, the in-situ pore water pressure may be estimated to be around 500kPa. On the other hand, flushing pressure of common DTH hammer drill can be around or over 10 bars (1000kPa). Thus, applied pressurized flushing during DTH drilling, which may potentially be amplified by dynamic movement during drilling, can result in significant increase in pore water pressure of soil.

From a geotechnical perspective, the increase in pore water pressure can lead to a temporary reduction in effective stress, as expressed by:

$$\sigma' = \sigma - u \qquad (1)$$

where σ' is the effective stress, σ is the total stress, and u is the pore pressure.

An increase in pore pressure reduces the effective stress, which moves the soil towards its failure criterion. In loose or sensitive soils, this reduction may lead to disturbance of the soil structure, increased compressibility, and mobilisation of fine particles (Zhang, 2013).

The behaviour of pore pressure during drilling is influenced by several factors, including soil permeability, and the drainage length. In the case of piling, the closest drainage path at pile shaft / soil interface is in confining state due to the higher water pressure. On the contrary, soil layers above the drilling position lengthened the dissipation of excess pore water pressure. It is important to consider both the magnitude and dissipation characteristics of pore pressure in assessing ground response (Yin et al., 2022).

In addition to pressure effects, the movement of drilling fluids and cuttings introduces a coupled soil–fluid interaction mechanism. The upward transport of cuttings, particularly through the annular space in conventional drilling systems, generates a continuous flow regime that may entrain fine particles from the borehole boundary.

This process can contribute to the migration of fines and the generation of suspended solids, especially in marine or saturated environments. Similar mechanisms have been discussed in relation to drilling-induced disturbance and pore pressure response (Ahlund, 2016).

The extent of ground disturbance is therefore not solely dependent on the mechanical action of drilling, but also on the hydraulic and pneumatic processes associated with the flushing mechanism. The interaction between airflow, pore pressure, and soil structure forms a coupled system in which small changes in pressure conditions may lead to disproportionate changes in soil response.

From an engineering standpoint, effective control of drilling-induced disturbance requires management of both pressure transmission and flow path characteristics. By limiting the magnitude of pressure introduced into the ground and controlling the direction of fluid movement, it is possible to maintain more stable pore pressure conditions and reduce the potential for soil disturbance.

These considerations underline the importance of aligning drilling methods with fundamental geotechnical principles. In particular, controlling the interaction between airflow and the surrounding soil mass is critical in achieving both ground stability and environmental protection, especially in constrained marine construction environments such as the IEC Boardwalk project.

5 CP METHOD AND OPERATIONAL MECHANISM

In response to the need for improved control of ground disturbance during drilling, an alternative method, namely the Circucore Pro (CP) Drilling Method, was adopted in the IEC Boardwalk project. The method is developed with consideration of the engineering principles described in the preceding section, with particular emphasis on controlling pressure transmission and maintaining stable pore pressure conditions in the surrounding ground.

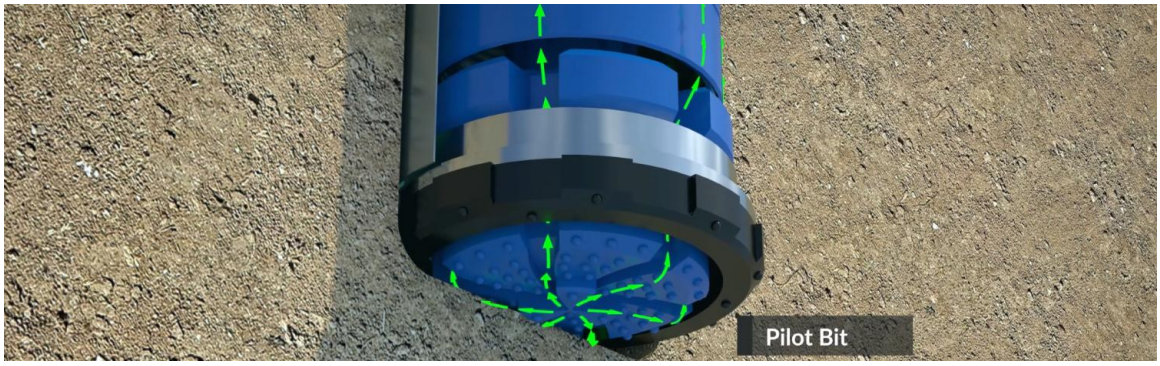

Figure 2. CP drilling head at soil interface showing internal airflow circulation and cuttings intake mechanism

The CP method utilises a modified drilling system in which the flow path of flushing air is reconfigured. Unlike conventional down-the-hole (DTH) systems, where compressed air is discharged outward at the drill bit and subsequently travels through the annular space between the drill string and the borehole wall, the CP system directs the flushing air laterally and upward within the drill rod. This configuration enables drill cuttings to be conveyed through an internal passage, reducing reliance on outward air flow into the surrounding ground.

From an engineering perspective, this modification alters the interaction between the drilling process and the soil–fluid system. By limiting the release of compressed air into the borehole interface, the potential for outward pressure transmission into the adjacent soil is reduced. This in return helps to minimise the generation of excess pore air pressure and reduces the likelihood of disturbing in-situ stress regime, as discussed in Section 4.

In conventional DTH drilling, drill cuttings are transported through the annulus, which has a relatively large cross-sectional area. To achieve effective lifting of cuttings, a relatively high airflow rate and uphole velocity are required. Based on fundamental flow considerations, the relationship between the required uphole velocity and the flow path diameter may be expressed as:

$$UHV \propto Q/D^2 \qquad (2)$$

where UHV= uphole velocity of return air and drill cuttings, Q=uphole discharge of pile arisings and D= equivalent diameter of the flow path.

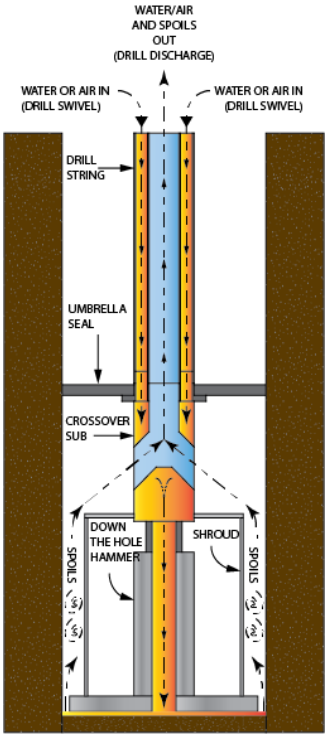

Figure 3. Airflow mechanism in the Circucore Pro (CP) drilling method
(Source: Berminghammer Foundation Equipment)

This relationship is consistent with general principles of fluid transport in conduits, where flow behaviour is governed by the interaction between flow velocity, cross-sectional area and volumetric discharge (White, 2011). Similar considerations are also recognised in drilling engineering practice, where cuttings transport efficiency is influenced by flow geometry and circulation conditions (Bourgoyne et al., 1986).

A smaller equivalent flow path diameter in traditional DTH method, where pile arising travel through solely between the gap of pile casing and drilling rod, requires a higher airflow rate and greater uphole velocity to maintain effective transport of drill cuttings. This results in increased air volume consumption and greater energy input into the surrounding ground, which may contribute to pressure transmission and ground disturbance.

In contrast, the CP method conveys drill cuttings through the internal passage of the drill rod, where cross-sectional area of pile arising transportation was concentrated for achieving a larger diameter of flow. The required uphole velocity and airflow rate can be reduced while still maintaining effective transport of drill cuttings. This results in lower air volume demand and reduced pressure transmission into the surrounding soil.

The confinement of airflow and return path within the drill rod limits interaction between the drilling process and the surrounding ground. As a result, pore pressure conditions remain relatively stable during drilling. This contributes to a more controlled drilling environment and reduces the risk of unintended ground response.

The controlled internal conveyance of drill cuttings also contributes to improved management of drilling by-products. As cuttings are transported through the drill rod to a cuttings collection system on the barge, the risk of uncontrolled discharge into the surrounding environment is reduced. This is particularly relevant in marine conditions, where containment of fine materials is essential to limit turbidity.

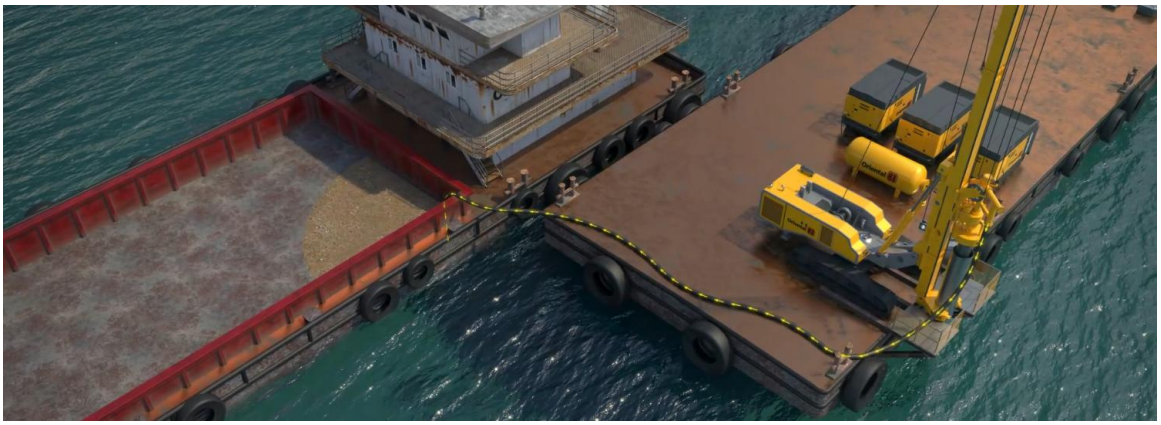

Figure 4. Internal conveyance of drill cuttings to a cuttings collection system on the barge for controlled handling under marine conditions

In addition, the reconfigured airflow path allows for more consistent and controlled drilling conditions. The reduction in outward air release may contribute to lower levels of airborne emissions and noise during operation, while also improving site housekeeping by concentrating debris handling within a defined system.

Overall, the CP method represents an adjustment to conventional drilling practice that is grounded in fundamental geotechnical and fluid interaction principles. By controlling the direction and magnitude of pressure transmission during drilling, the method aims to reduce ground disturbance and improve environmental performance under constrained site conditions.

6 IMPLEMENTATION IN IEC BOARDWALK PROJECT

The Circucore Pro (CP) Drilling Method was implemented for foundation works in the IEC Boardwalk project, taking into account the constrained site conditions and environmental requirements described in Section 2. The working area was located beneath the existing IEC viaduct where headroom limitations, restricted access, and proximity to the marine environment imposed practical constraints on plant arrangement and construction sequence.

Drilling works were carried out using CP-equipped rigs configured to suit the available working space. The arrangement of equipment was planned to maintain safe access and efficient workflow within the confined corridor, while ensuring that drilling operations could be conducted without interference to adjacent structures and ongoing activities. Particular attention was given to the positioning of auxiliary systems for air supply and cuttings collection, so that the internal conveyance mechanism of the CP system could be effectively utilised.

The construction sequence generally followed conventional drilling procedures, including positioning of the rig, installation of temporary casing where required, and advancement of the drill string to the target depth. The key difference in operation was associated with the flushing mechanism, whereby drill cuttings were conveyed internally through the drill rod rather than being expelled into the borehole annulus. The collected materials were directed to designated containment facilities for handling and disposal, thereby reducing the potential for releasing pile arisings into the surrounding marine environment.

During implementation, monitoring and site supervision were carried out to ensure that drilling operations remained within acceptable environmental and operational limits. Measures were adopted to coordinate drilling activities with other site operations, and to maintain compliance with project-specific environmental control requirements. The performance of the CP method was observed continuously, with particular focus on its interaction with the surrounding ground and its effectiveness in managing drilling by-products.

The implementation of the CP method under these conditions provided an opportunity to assess its practicality and performance in a constrained marine construction environment. The experience gained from site application forms the basis for the observations presented in the following section.

7 PERFORMANCE AND OBSERVATIONS

The performance of the Circucore Pro (CP) Drilling Method was assessed based on site observations during foundation works in the IEC Boardwalk project, with particular attention to environmental control and operational behaviour under the constrained site conditions.

During drilling operations, it was observed that the CP method provided improved control of suspended materials within the working area. The internal conveyance of drill cuttings through the drill rod enabled materials to be directed to designated collection points, reducing the extent of dispersion into the surrounding marine environment. Compared with conventional drilling practice, the occurrence of visible turbidity in the adjacent water was observed to be reduced, particularly during continuous drilling activities.

In terms of water quality performance, there is no observable impact to the surrounding waters. To measure any soil disturbance at sea, suspended solids measured by Environmental Protection Department, as one of the specified Water Quality Objectives, is presented in the following table.

Table 1. Table of Suspended Solid at Victoria Harbour near IEC Boardwalk from 2022 to 2024

Year	Suspended solid (mg/L)	
	VM2	VM4
2022	5.8 (2.8-10.3)	6.1 (3.5-10.3)
2023	5.5 (2.3-8.7)	5.4 (3.0-9.5)
2024	5.1 (1.3-9.3)	4.7 (1.2-10.7)

Note: 1. Data presented are depth averaged; 2. Data in brackets indicate the ranges
Source: EPD (2023, 2024, 2025)

Monitoring point VM2 and VM4 near the IEC Boardwalk project, which are water monitoring point at Victoria Harbour (East) and Victoria Harbour (Central) respectively, are taken. With most of the piling works of the project were conducted from 2023 and 2024, data in 2022 before piling work can serve as a baseline suspension solid level. Throughout the piling period, the total suspended solid near the site remains stable. This serves as solid evidence towards no observable disturbance of soil due to the works.

In terms of airborne emissions, the CP method was associated with lower levels of dust generation during operation. The reduced outward release of air and fine particles from the borehole contributed to improved local air quality within the confined working corridor beneath the IEC structure. Similarly, site observations indicated that noise levels during drilling were more controlled, which may be attributed to the modified airflow mechanism and reduced external discharge.

Indicative measurements from site operations further illustrate the environmental benefits of the CP method. During conventional drilling, airborne dust levels increased from a background level of approximately 38 $\mu g/m^3$ to around 135 $\mu g/m^3$ during active operations. In contrast, under comparable conditions, the CP method maintained dust levels at approximately 40 $\mu g/m^3$, close to the measured background level. Similarly, noise measurements within 3m of the piling rig indicated a reduction from approximately 91 dB(A) under conventional drilling to around 78 dB(A) during CP operation.

From an operational perspective, the controlled handling of drill cuttings facilitated improved site housekeeping and reduced the need for supplementary cleaning measures. The concentration of drilling by-products within a defined collection system enabled more efficient management of waste materials and reduced the reliance on water-based cleaning processes.

Overall, the observations from the IEC project indicate that the CP method provides improved environmental control under pile drilling operations, including turbidity, dust, and noise. While quantitative measurements were not the primary focus of this study, the consistent performance observed during site implementation suggests that the method offers practical advantages under conditions where environmental control is of particular importance.

8 DISCUSSION

Observations presented in Section 7 may be interpreted with reference to the engineering principles outlined in Section 4. The improved environmental performance associated with the CP method can be understood primarily in terms of its influence on pressure transmission, pore pressure response, and the interaction between drilling-induced fluid flow and the surrounding ground.

In conventional down-the-hole (DTH) drilling, high-pressure air release at the base of the borehole creates a direct pathway for pressure to be transmitted outward into the surrounding soil and groundwater. This may lead to localised increases in pore water pressure and disturbance of the in-situ stress regime, particularly in permeable or weakly bonded materials. Such disturbance can contribute to the generation of suspended solids in water, as well as the release of dust and noise associated with uncontrolled air discharge. These mechanisms are consistent with observations reported in previous studies on drilling-induced pore pressure effects (Ahlund, 2016).

By contrast, the CP method modifies the direction and containment of airflow during drilling. The redirection of flushing air within the drill rod reduces the magnitude of outward pressure transfer at the borehole interface. From a geotechnical perspective, this limits the development of excess pore water pressure in the surrounding soil and helps maintain more stable effective stress conditions (Terzaghi, 1925; Zhang, 2013). As a result, the potential for soil disturbance and particle migration is reduced, which is consistent with the observed improvements in turbidity control.

In a more precise manner, drilling of marine piles in Hong Kong, can be elaborated in 2 approaches. Clayey marine deposit at the top layer, and granular soil layer below, which includes alluvium and completely decomposed granite.

For marine deposit layer, disturbance of soil can be caused by direct failure and uplifting of soil. Saturated clay layer in liquid states has low shear strength. Top layer of marine deposit also lacks weight to compensate uplift from pressurized flushing. However, due to cohesiveness property of clayey material, substantial reduction in flushing pressure or penetration rate may lead to blockage of pile annulus. It is therefore necessary to adopt CP method to reduce the impact of pressurized flushing, while maintaining normal flushing pressure and penetration rate during excavation.

For granular soil, excess pore water pressure can be developed to the soil in the surroundings, while flushing should be maintained to ensure soil in front of drill bit to be fluidized. Einar John Lande et al. (2021), using physical modeling of flushing drill in sand, measured a development of excess pore water pressure in surrounding soils upon flushing. From the physical model, 7% of excess drill cutting could be resulted optimized conventional flush drilling under laboratory setting. For stringent water quality control in the Victoria Harbour, CP method is preferred to reduce induction of excess pore water pressure and subsequent over cutting from source.

For further application of the CP system, it may also help to confront adverse sediment layers with abnormal pore pressure. Pore water pressure profile may be in excess of hydrostatic pressure, which may due to rapid deposition of sediments in certain geomorphology (Zhang, J., 2013). In this case, the CP system with constrained pressure application to the surrounding soil may be critical. It may help to limit pore water pressure increase where in-situ soil stress state is already closer to its failure criterion. Although such geomorphology is not likely to be encountered in Hong Kong, where Quaternary deposition of sediments has been under stable intertidal, estuarine or marine environment (J.A. Fyfe, R. Shaw, S.D.G. Campbell, K.W. Lai & P.A. Kirk, 2000), design of the CP system allows wider application in challenging sedimentary layers.

For Hong Kong's marine geomorphology regarding layered sediments of marine deposit, alluvium, and completely decomposed granite above bedrock. The setting results in various soil strength and hydraulic conductivity over depth. Based on site standard penetration test (SPT) result, deeper layer of completely decomposed granite is in general stronger than marine deposit in the surface. However, localized reduction in soil strength with depth (as in Figure 5 below) can also occur due to heterogeneity in the degree of compaction of deposits.

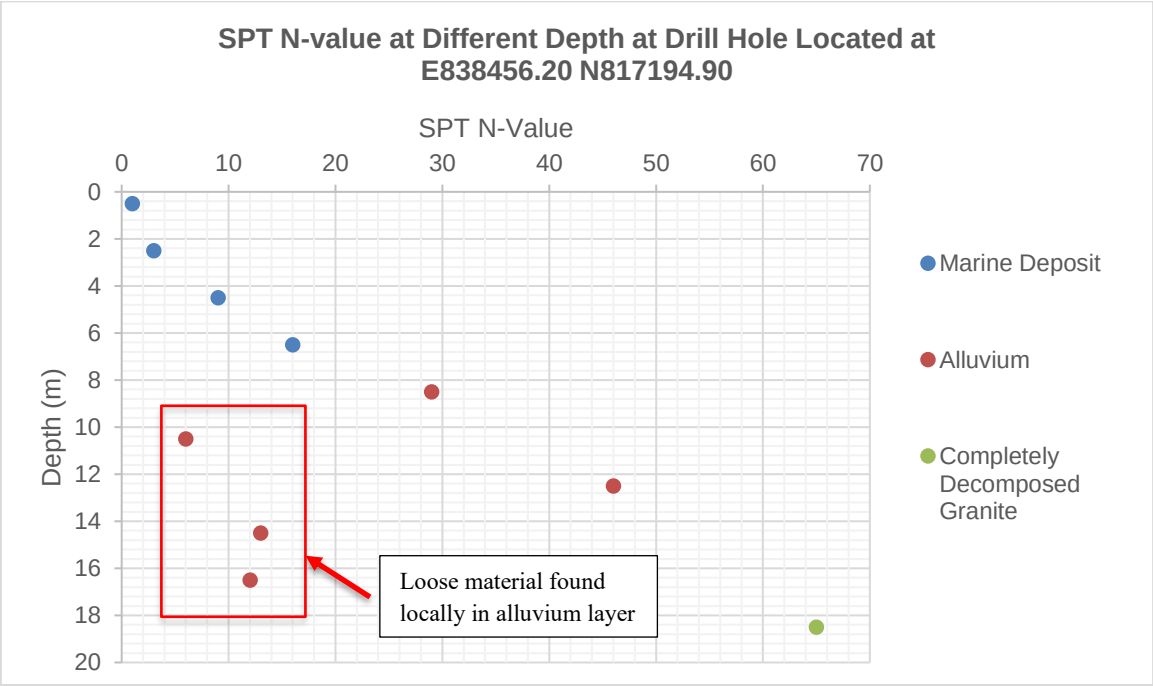

Figure 5. Example of site profile of SPT N-value with depth

In addition, alluvium layer, which usually comprise of the largest proportion of soil depth within the Site, is made of mixed silty, clayey, and sandy material. This may result in reduced hydraulic conductivity, when compared to pure granular soil, to dissipate excess pore water pressure at the region. Retention of excess pore water pressure, with reduced effective stress state, in the region may result in prolonged overcutting of soil when the drill progresses downwards. On the potential variability of soil in seabed, the CP method which minimize impact to the surrounding soil can help to ensure minimized disturbance to surrounding soil and drilling stability in different soil layer.

From the perspective of spillage containment during construction, controlled internal conveyance of drill cuttings further reduces interaction between drilling by-products and the surroundings. By minimising the exposure of fine materials to external flow paths, the likelihood of dispersion into the marine environment is reduced. This mechanism also contributes to improved dust control, as the release of fine particles into the air is limited.

The findings from the IEC project therefore illustrate how adjustments to the configuration of drilling systems, when guided by first principles and supported by an understanding of pore pressure control (Yin et al., 2022), can lead to meaningful improvements in both environmental and operational performance.

9 CONCLUSIONS

The observations from the IEC Boardwalk project demonstrate that the adoption of the CP drilling method provides a better controlled interaction between drilling operations and the surrounding ground, particularly under constrained marine conditions. Compared with conventional DTH drilling, the CP system exhibited reduced disturbance effects, which can be interpreted in light of the engineering principles described in Section 5.

As established in Equation (2), the required uphole velocity for transporting drill cuttings inversely proportional to the square of diameter of the flow area. In conventional DTH systems, the annular return path presents a relatively small effective diameter in between casing and the drill rod, necessitating higher airflow rates and uphole velocities to achieve sufficient lifting capacity. This results in increased energy transfer into the borehole environment and greater potential for pressure transmission into the surrounding soil mass.

In contrast, the CP method utilises an internal return path within the drill rod, where the effective flow diameter is significantly concentrated and increased. In accordance with Equation (2), the larger flow area allows the required uphole velocity and airflow volume to be reduced while maintaining effective cuttings

transportation. This reduction in airflow demand directly limits the magnitude of pressure introduced into the surrounding ground during drilling.

From a geotechnical perspective, the reduced airflow and confined return path contribute to more stable pore pressure conditions. The CP method is less likely to induce excess pore water pressure or disrupt the in-situ stress regime, which are key factors associated with ground disturbance. Furthermore, marine deposits, with low shear strength, are also sensitive to direct uplift shearing from escaped pressurised airflow during drilling. This is particularly important for piling works in marine and reclamation environments.

In addition to ground response, the internal conveyance mechanism of the CP system also improves environmental control. By directing drill cuttings through the drill rod to a designated collection system, the risk of uncontrolled discharge into the surrounding water body is reduced. This aligns with environmental management requirements for marine works, where control of turbidity and suspended solids is critical.

From an operational standpoint, the CP method was found to be compatible with the spatial constraints of the IEC site. The arrangement of equipment and supporting systems allowed drilling activities to be carried out efficiently within the limited headroom and restricted access conditions beneath the viaduct. The controlled nature of the airflow system also contributed to improved working conditions, including reduced noise and better site housekeeping.

Overall, the performance of the CP method observed in this project supports the underlying premise that controlling airflow path geometry, which plays a key role in managing ground disturbance during drilling. The results suggest that the method provides a practical and effective alternative to conventional DTH drilling in situations where environmental sensitivity and site constraints are significant considerations.

REFERENCES

Ahlund, R. (2016). Pore pressures and settlements generated from different drilling methods.

Berminghammer Foundation Equipment (n.d.). Drilling Methods. Available at: https://www.berminghammer.com/Drilling.html (Accessed: 19 March 2026).

Bourgoyne, A.T., Millheim, K.K., Chenevert, M.E. and Young, F.S. (1986). *Applied Drilling Engineering*.

Richardson, TX: Society of Petroleum Engineers.

Einar John Lande, Stefan Ritter, Henning Tyvold, and Steinar Nordal (2021) Physical modelling of pile drilling

in sand. Canadian Geotechnical Journal. 58(10): 1437-1451.

EPD(2025). *Marine Water Quality in Hong Kong 2024.* Environmental Protection Department, HKSAR Government.
https://www.epd.gov.hk/epd/sites/default/files/epd/english/environmentinhk/water/hkwqrc/files/waterquality/annual-report/marinereport2024.pdf

EPD (2024). *Marine Water Quality in Hong Kong 2023*. Environmental Protection Department, HKSAR Government.
https://www.epd.gov.hk/epd/sites/default/files/epd/english/environmentinhk/water/hkwqrc/files/waterquality/annual-report/marinereport2023.pdf

EPD (2023). *Marine Water Quality in Hong Kong 2022*. Environmental Protection Department, HKSAR Government.
https://www.epd.gov.hk/epd/sites/default/files/epd/english/environmentinhk/water/hkwqrc/files/waterquality/annual-report/marinereport2022.pdf

Geotechnical Engineering Office (GEO) (2017). Guide to Site Investigation (GEOGUIDE 2). Civil Engineering and Development Department, Hong Kong SAR Government.

J.A. Fyfe, R. Shaw, S.D.G. Campbell, K.W. Lai & P.A. Kirk (2000) The Quaternary Geology of Hong Kong. Geotechnical Engineering Office, HKSAR Government

Liu, A. S., Li, W., & Kwok, C. Y. (2025). Seawater effects on ground granulated blast furnace slag (GGBS)-stabilized marine deposits in land reclamation. *Acta Geotechnica*.

Terzaghi, K. (1925). *Principles of Soil Mechanics*.

White, F.M. (2011). *Fluid Mechanics (7th ed.).* New York: McGraw-Hill Education

Yin, H., et al. (2022). Research on pore pressure detection while drilling. Zhang, J. (2013). Effective stress, porosity, velocity and abnormal pore pressure prediction. *Journal of Petroleum Science and Engineering*.

From Heterogeneous Borehole Data to City-Scale 3D Geological Modelling Supporting Seismic Response Studies for Northern Metropolis in Hong Kong

K.I.M Ismail & G. Wang

State Key Laboratory of Climate Resilience for Coastal Cities, Civil and Environmental Engineering Department, School of Engineering, Hong Kong University of Science and Technology, Hong Kong SAR

ABSTRACT

Complex geologic conditions in Hong Kong necessitate high-fidelity geological models to ensure safe infrastructure development and effective risk mitigation. While the region possesses a vast repository of geotechnical data, managing mix of many different data creates a significant challenge for data utilization. This study introduces a comprehensive workflow to address these challenges through the development of two Python-based automation tools: AGSGEOHKpy and PDFGEOHKpy. These tools facilitate rapid, uniform extraction of critical geotechnical parameters including stratigraphy, *SPT-N* values, undrained shear strength (S_u), and groundwater level from heterogeneous datasets. To synthesize this extracted data into a coherent spatial model, a Python-based hybrid geo-interpolation framework was employed. This approach utilizes the Kriging Interpolation Method (KIM) to generate continuous surfaces for primary soil and weathered rock layers, while Inverse Distance Weighting (IDW) is applied to determine specific lithologies at unknown interpolated coordinates between these main geological boundaries. Leveraging this automated framework, a high-resolution 3D geological model was constructed based on a dataset of thousands of collected boreholes in Hong Kong island. The model has been rigorously validated against existing geological maps and cross-sections. Then, the proposed methodology has been applied for Northern Metropolis Hong Kong (NMHK). Beyond stratigraphic visualization, this paper demonstrates the model's capacity to support advanced engineering and hazard assessment applications. A 3D Shear Wave Velocity (V_s) model was derived to calculate fundamental site periods based on rockhead depth, providing essential data for seismic site-specific response analysis in Northern Metropolis. Furthermore, the enhanced precision of this geological modelling framework significantly improves design confidence for complex infrastructure projects.

1 INTRODUCTION

Rapid urbanization and increasing infrastructure demand in metropolitan regions necessitate reliable characterization of subsurface geological conditions to ensure safe, resilient, and sustainable development. In densely populated cities such as Hong Kong, highly heterogeneous stratigraphy and complex geological formations have a great effect on the performance of foundations, underground excavations, and transportation infrastructure. More recently, the integration of large geotechnical datasets and geostatistical techniques has enabled higher-resolution subsurface reconstructions and improved representation of spatial variability (Agrawal & McCloskey 2024; Wang 2021). Nevertheless, these approaches often remain computationally intensive and require substantial manual preprocessing, limiting their scalability for city-scale applications.

Beyond geological characterization, 3D subsurface models are increasingly recognized as essential inputs for seismic hazard assessment and site response analysis. Recent studies have shown that integrating multi-source datasets into 3D geological models can significantly enhance the accuracy of seismic response predictions and microzonation analyses (Antonielli et al. 2023; Ji et al. 2024). Furthermore, advances in numerical simulation and high-performance computing have enabled regional and city-scale seismic analyses that incorporate complex geological structures (Adhikari & Molnar 2024).

A critical but often under-addressed challenge lies in the efficient utilization of large and heterogeneous geotechnical datasets. Although extensive ground investigation data are available in many urban regions, these datasets are typically stored in diverse formats, including structured databases, reports, and legacy documents.

The extraction, standardization, and integration of key geotechnical parameters such as stratigraphy, Standard Penetration Test (*SPT-N*) values, undrained shear strength, and groundwater levels remain labor-intensive processes that delay the development of consistent and high-resolution 3D models. Moreover, uncertainties arising from incomplete data coverage and interpretative assumptions continue to affect model reliability (Bowden 2004; Lee 2016; Wang 2021). Existing workflows often lack automation and reproducibility, which limits their applicability to large-scale urban modelling.

While recent studies have advanced digital geological modelling in Hong Kong through the development of 3D subsurface platforms (Liu et al. 2022), machine learning-based modelling approaches (Shi & Wang 2022), and city-scale marine geological models (Lai et al. 2023), the integration of heterogeneous datasets into automated and scalable modelling workflows remains limited. In particular, the lack of efficient data-processing frameworks constrains the ability to fully exploit available geotechnical information.

In response to these challenges, this study develops an integrated and automated framework for constructing high-resolution 3D geological models from heterogeneous geotechnical datasets and demonstrates its application to regional seismic site response analysis in Hong Kong. The main contributions of this study are summarized as follows:

- Automated geotechnical data extraction: Development of Python-based tools (AGSGEOHKpy and PDFGEOHKpy) for rapid and standardized extraction of key parameters from mixed-format datasets.
- Hybrid 3D geological modelling framework: Integration of Kriging interpolation and Inverse Distance Weighting (IDW) to reconstruct geological boundaries and lithological variability at city scale.
- Application to seismic site response analysis: Generation and validation of a high-resolution 3D geological model and derived shear-wave velocity (V_s) model to support seismic analysis in the Northern Metropolis.

2 HONG KONG GEOLOGICAL CONDITIONS

Hong Kong's geology is predominantly composed of Mesozoic igneous rocks, which account for approximately 85% of the land surface and are mainly represented by granitic and volcanic formations. The remaining geological units consist primarily of sedimentary rocks located in the northeastern New Territories, with only minor occurrences of metamorphic rocks (<1%) as shown in Figure 1. In contrast, the Northern Metropolis region exhibits greater geological complexity, comprising a combination of superficial deposits, metamorphic rocks, volcanic formations, and sedimentary sequences.

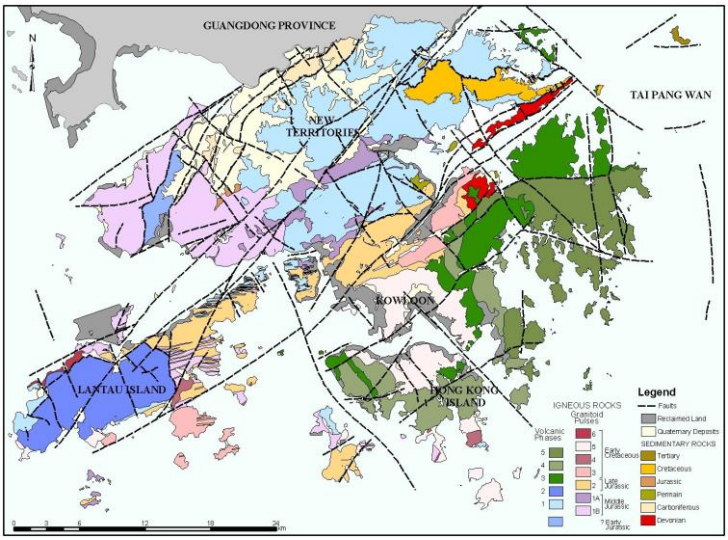

Figure 1: Simplified geological map of Hong Kong. Modified from CEDD, HKSAR (Sewell et al. 2000)

3 CONSEPTULIZATION OF THREE-DIMENSIONAL GEOLOGICAL MODEL

The framework used in this study follows four main stages: geotechnical data collection, geotechnical data processing, lithology interpolation including digital elevation model data (DEM) and finally construction three-dimensional geological and shear wave velocity models as shown in Figure 2.

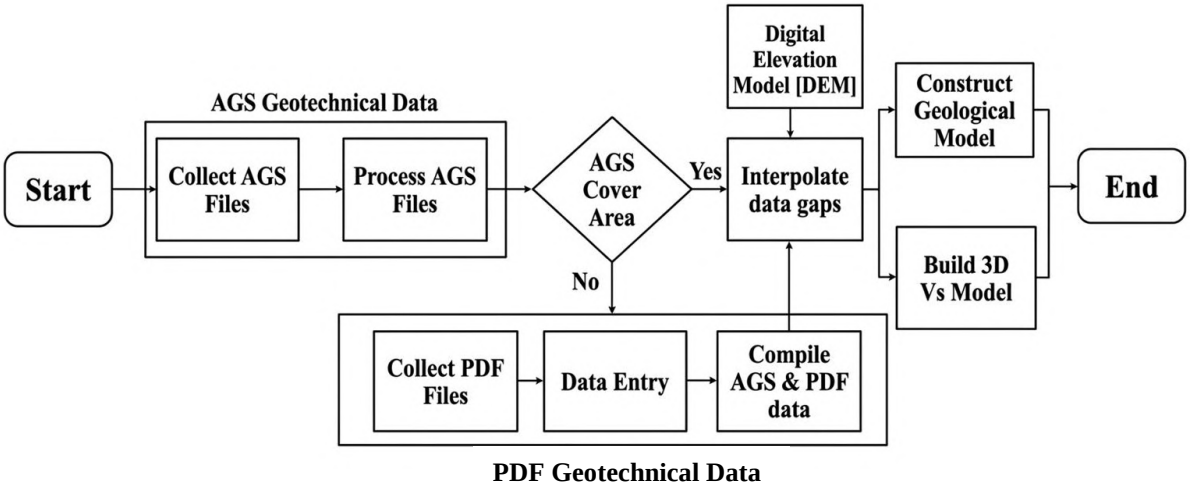

Figure 2: Framework of three-dimensional geological model construction

3.1 Geological Data Processing

To standardize the AGS data, modified AGS formats (AGS 3.1 (AGS. 2004) and AGS 4.1 (AGS. 2017)) were adopted to introduce computed field for (ROCK_HDEP) rockhead depth (top level of rock grade III) and ground water depth (HOLE_GWD). AGS files often contain formatting errors and require pre-processing. This step yields clean, strictly compliant AGS files. Next, the lithology legend (GEOL_LEG) is assigned based on the keywords following the workflow of AGSGEOHKpy in Figure 3 (a).

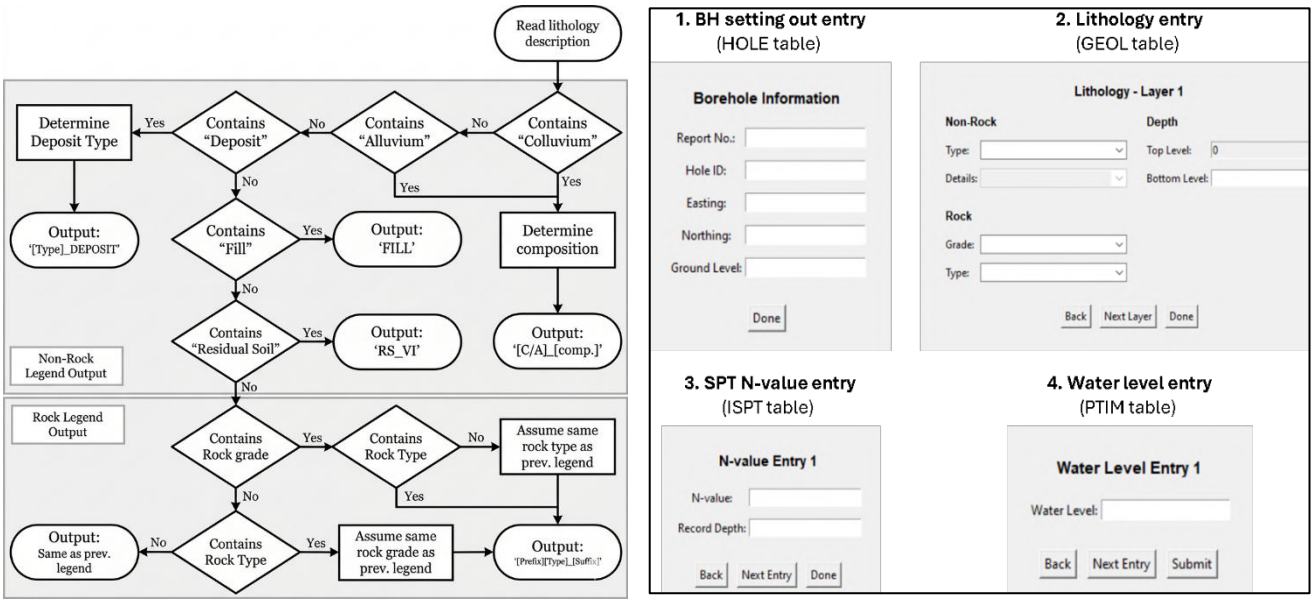

(a) AGS Processing (b) GUI PDF Extraction and Processing

Figure 3: AGS lithology processing (a) and GUI PDF geological data extraction and processing

Data gaps identified post-AGS processing are filled using PDF borehole logs. Initial extraction trials using Python-based via Computer Vision (CV) and Optical Character Recognition (OCR) libraries that succeeded for only the latest PDFs. Consequently, a custom Python Graphical User Interface (GUI) PDFGEOHKpy was developed to streamline manual data entry and conversion into the modified AGS format as shown in Figure 3 (b). This optimized workflow reduces time expenditure and decreases the error rate compared to manual Excel entry. Furthermore, embedded validation rules dramatically increase the data extraction accuracy.

The geological data types include Unique borehole code (Report_No'_'Station_ID), HK Grid System Easting, Northing, Ground level, Final depth borehole; Ground water depth; Rockhead level; Dip direction of borehole and Dip angle of borehole for the boreholes identification data. In addition, geological data includes Unique borehole Code; Depth to the top of stratum; Depth to the base of stratum; Description of lithology and Lithology legend code. For standard penetration tests' (SPT) records data include Unique borehole Code; Depth of the SPT test; SPT 'N' value. Thus, these three different data frames can be mapped together by the unique borehole code.

3.2 Geological Interpolation Strategies

3.2.1 Interpolation of Categorical Data

Traditional spatial interpolation techniques (e.g., IDW, Kriging) target discrete numerical data and cannot directly process non-numeric categorical lithology. To resolve this, categorical data was transformed into discrete probability values (Yamamoto et al., 2012). An indicator function, defined in Equation (1), assigns binary values based on the presence or absence of a specific lithological category at a given location.

$$I(x_i,k) = \begin{cases} 1, & if\ type\ k\ is\ present\ at\ location\ x_i \\ 0, & if\ type\ k\ is\ not\ present\ at\ location\ x_i \end{cases} \quad (1)$$

Where, $I(x_i, k)$ = indictor value at location x_i, k = category data type k, x_i = known data point i.

While this binary encoding effectively calculates the probability of each category at every interpolated point, it requires computing every category type universally, significantly increasing computational demand.

3.2.2 Prediction of Rockhead and Weathered Rock Depths

Predicting rockhead depth in elevated, data-sparse mountainous regions requires topological correlation. Hadlow et al. (2018) demonstrated that rockhead depth correlates strongly with digital elevation models (DEM) and topographic gradients (slope and aspect). The rockhead surface generally mimics ground elevation; however, the vertical discrepancy between the surfaces increases at low gradients and decreases on steep slopes. In our proposed lithology interpolation method, the main interpolated interfaces have been controlled by the elevation of the terrain where any geological data is missing in the mountains' zones.

3.2.3 Lithology Interpolation Mechanism

After the discretizing the boreholes geological data, lithology was interpolated via the binary encoding methodology across assigned Interpolated Boreholes (IBH) points. Post-interpolation, results were reconverted to the continuous lithology layers. Our lithology interpolation framework uses a Modified Inverse Distance Weighting (MIDW) algorithm. Standard IDW just looks at distance, however our algorithm adds a "Geological Logic" layer (Multipliers) to ensure the interpolation makes geological sense (e.g., you shouldn't find fresh rock floating inside a soil layer). The number of unique geological units and the elevation interval selection are the critical parameters not only for the results accuracy but also for the interpolation computational time. Thus, grouping the geological units that have similar properties and selecting appropriate vertical interval (1.00m used in our study) are crucial to overcome these two challenges.

The interpolation framework starts with loading the geology points and our target unknown points. Then using the KDTree library algorithm to act like a spatial search engine to instantly find the nearest neighbors to

any point without scanning the whole database. The distance weight W_{dist} calculated for every neighbor point within the search radius as in Equation (2).

$$W_{dist} = (1/Distance\ \delta) \quad (2)$$

Where δ is IDW power factor, lower values smooth the model (for regional scale), higher values prioritize proximal data to produce finer spatial details (local scale).

After getting distance weight W_{dist} and the main non-rock and rock grades' interfaces, the Multiplier M can be determined to check if the neighbor's geology matches the current layer. For example, if the target point located in Grade V layer (Completely Decomposed (CD)) and the neighbor is CD :Multiplier (M) = 1.0 (full weight), if neighbor is HD (Highly Decomposed): Multiplier = 0.7, if neighbor is MD: Multiplier = 0.50 and neighbor is SD Rock: Multiplier = 0.0 (Zero weight - it ignores this point because slightly decomposed strong rock shouldn't be in the Grade V layer).

The final weighting $W_{final\ can}$ be determined by multiplying the distance weight W_{dist} and Multiplier M as shown in Equation 3. Then the final weighting for each geological unit summed up and the material that has the highest voting picked for this target point.

$$W_{final} = W_{dist} * M \quad (3)$$

This workflow, implemented via developing new python-based software as illustrated in Figure 4.

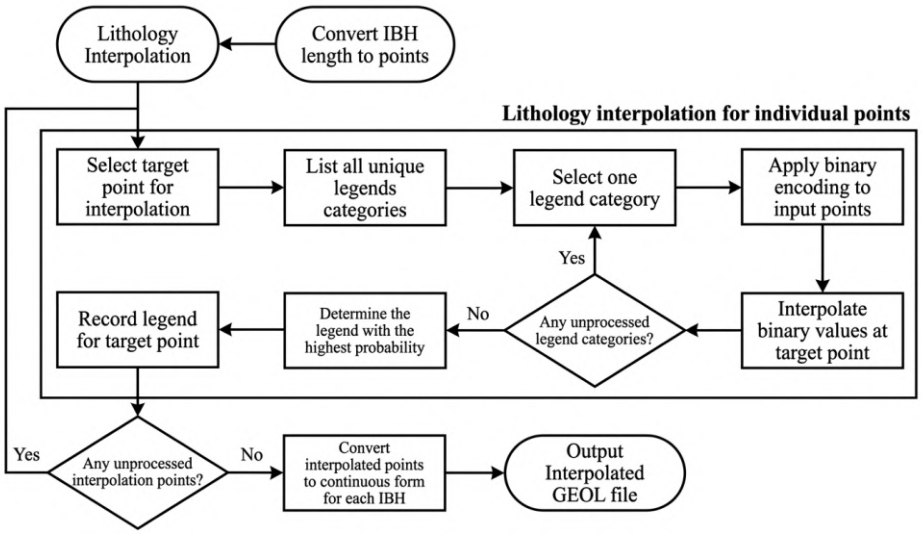

Figure 4: Lithology interpolation framework flowchart

4 VALIDATION OF GEOLOGICAL MODEL (HONG KONG ISLAND CASE)

To validate the proposed geological interpolation framework, the center of Hong Kong Island considered as a case study that will be investigated using 2000 available AGS and PDF boreholes as shown in Figure 5.

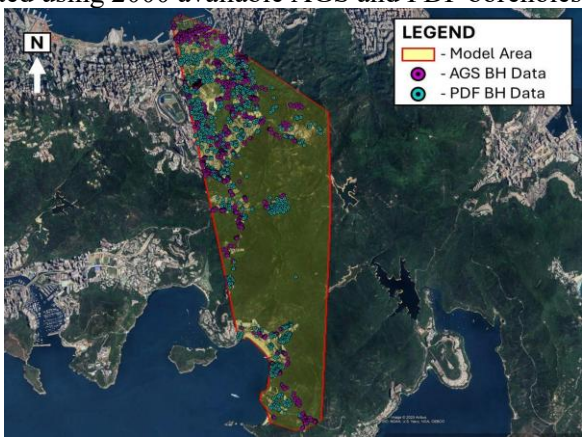

Figure 5: AGS and PDF boreholes data at the center of Hong Kong Island

4.1 Construction of Three-dimensional Geological Model

Based on the proposed geological interpolation framework, the interpolated points (target points), with resolution of 50*50m in horizontal plane and vertical interval 1.00m till -100 mPD in deep, have been chosen for the geological interpolation process. The results of the interpolated boreholes for the simplified geological units shown in Figure 6 (a). By creating surfaces of each soil/rock type, the three-dimensional geological model has been developed for simplified lithology as shown in Figure 6 (b).

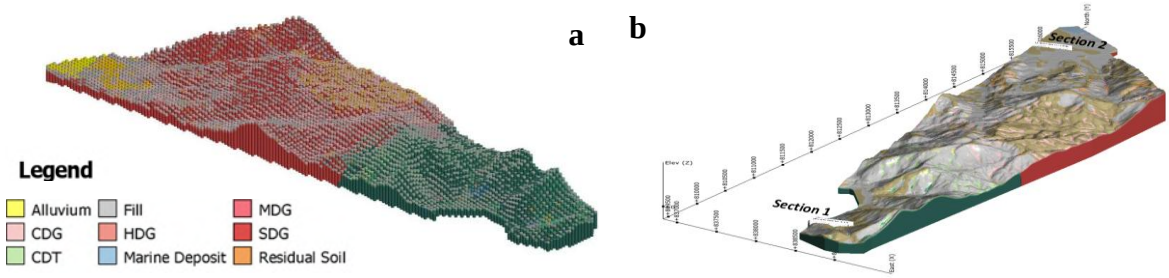

Figure 6: (a) Interpolated Boreholes of Simplified Lithology, (b) Three-dimensional geological model Hong Kong Island

4.2 Validation of Geological Interpolation Results

To evaluate the accuracy and reliability of the geological interpolation method, two cross sections have been presented to show the accuracy of the proposed lithology interpolation framework. Figure 6 (b) illustrates two cross-sections' locations: Section 1 is in the southern volcanic tuff and Section 2 is in the northern granitic zone. In Section 1 shown in Figure 7 (a), the interpolated lithology closely matches actual borehole records, exhibiting only minor surface-level discrepancies. Similarly, Section 2 is shown in Figure 7 (b) accurately captures real borehole profiles, despite slight inaccuracies in estimating residual soil thickness. Despite these minor deviations in predicting exact soil and weathered rock thicknesses, the proposed interpolation approach demonstrates strong viability for regional-scale geological modeling.

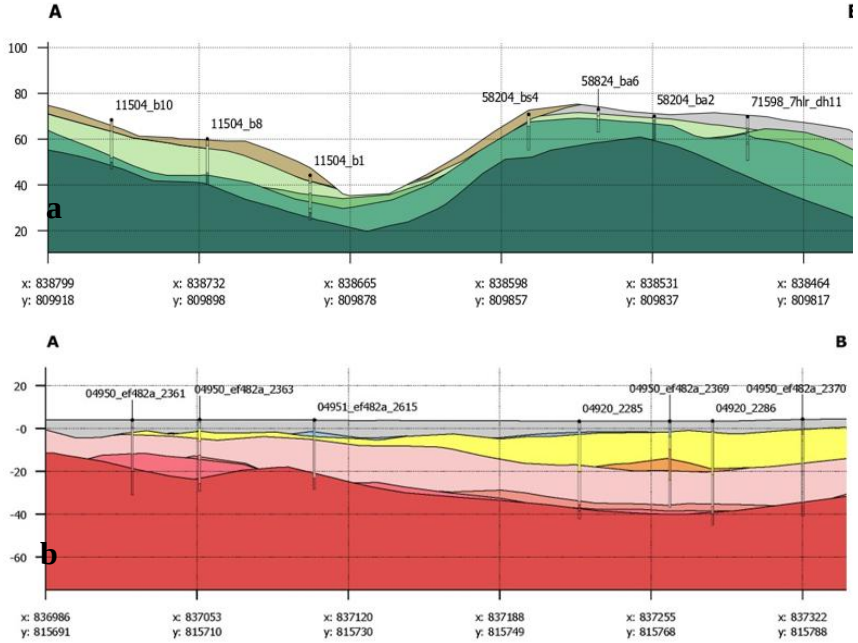

Figure 7: Cross sections validation, (a) Section 1 and (b) Section 2

5 GEOLOGICAL MODEL OF NORTHERN METROPOLIS IN HONG KONG

5.1 Study Area (Topographical and Geotechnical Data Collection)

The "Northern Metropolis" covers 30,000 hectares, about one-quarter of the total land in Hong Kong, including Yuen Long, Tin Shui Wai, and Fanling/Sheung Shui (Legislative Council 2022). The development plan includes four zones: High-end Professional services and Logistics (Zone01), Innovation and Technology Zone (Zone02), Boundary Commerce and Industry zone (Zone03) that will be focused on our study and Blue and Green Recreation, Tourism and Conservation Circle (Zone04) as shown Figure 8.

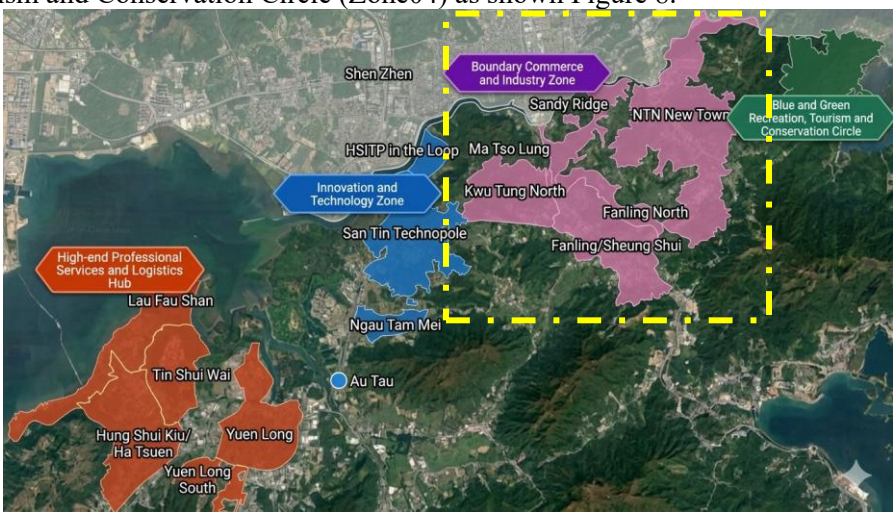

Figure 8: Layout of North Metropolis of Hong Kong (NMHK) Zones. (Zone03: dashed yellow boundary),

Based on our geological data framework and the database developed by Hong Kong Geotechnical Engineering Office, 5400 AGS and PDF boreholes' data have been collected and 190 virtual boreholes created for 10*10 km of NMHK (Zone03) and a part of Shenzhen respectively as shown in Figure 9.

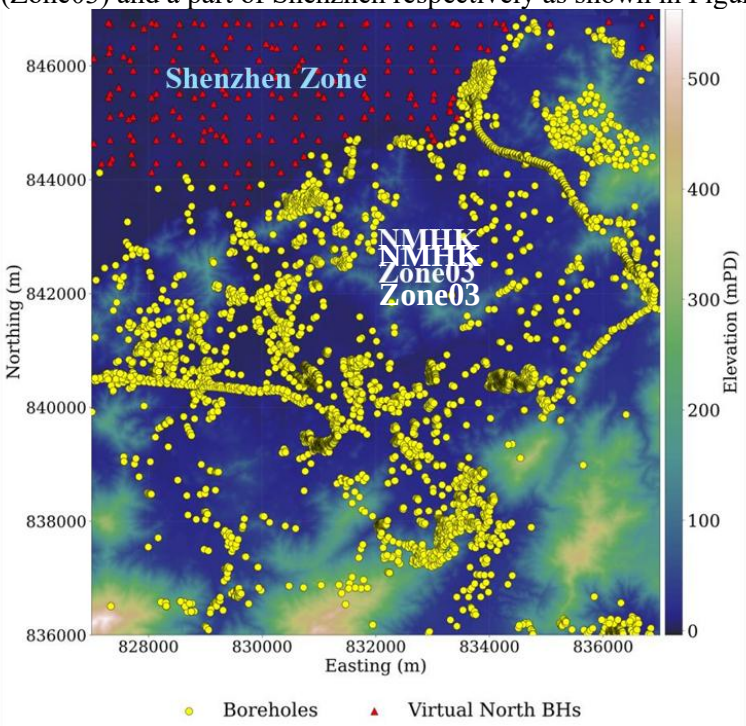

Figure 9: NMHK boreholes distributions (Zone03) and virtual boreholes at Shenzhen zone

5.2 Geological Characteristics in Northern Metropolis Hong Kong

NMHK is characterized by complex geology and a densely populated urban environment. Many buildings and infrastructures (highway and metro/railway systems) will be built in valleys and alluvial plain filled with loose sediments. Extensive weathering of rocks results in highly variable profiles of rock head underlying these sediments within a short distance.

After collecting the geological data at Zone03, the geological data processing has been performed to extract the required main tables (HOLE, GEOL and ISPT) that will be used to construct the three-dimensional geological model and shear waver velocity structure. The main geological features are Fill, Alluvium, Marine, Estuarine and Pond deposits. For rock types, there are two types of rock Igneous Rock (IGR) types (Tuff, Volcanic) and meta-Sedimentary Rock (MSR) types (Sandstone and Siltstone).

The target geological legends were subsequently standardized to reflect these optimized groupings. This systematic categorical dimensionality reduction is critical for mitigating spatial data sparsity, significantly reducing computational overhead while ensuring a robust, continuous regional lithological model.

5.3 Construction of three-dimensional Geological Model of NMHK-Zone03

Rockhead elevation and depth maps have been created to be a reference for a bed rock not only for seismic analysis, but also for deep foundation design. As shown in Figure 10 (a) and (b) respectively, the deep level and depth of rockhead is -70 mPD and 80m at the basin areas with the highest level of 400 mPD and the shallow depth of 0.0 m at the mountain area in the western-south and eastern-north zones respectively.

Applying the lithology interpolation framework as discussed in Section 3 with resolution 50*50m in horizontal plan and vertical interval with 2.0m, 43500 interpolated boreholes have been generated to create the three-dimensional precise geological model at NMHK-Zone03 as shown in Figure 11. The three-dimensional geological model has been generated as shown in Figure 12 (a) and the volumes of Fill, Alluvium, Grade V, Grade IV, Grade III and Grade II of rock types are presented in Figure 12 (b, c, d, e and f).

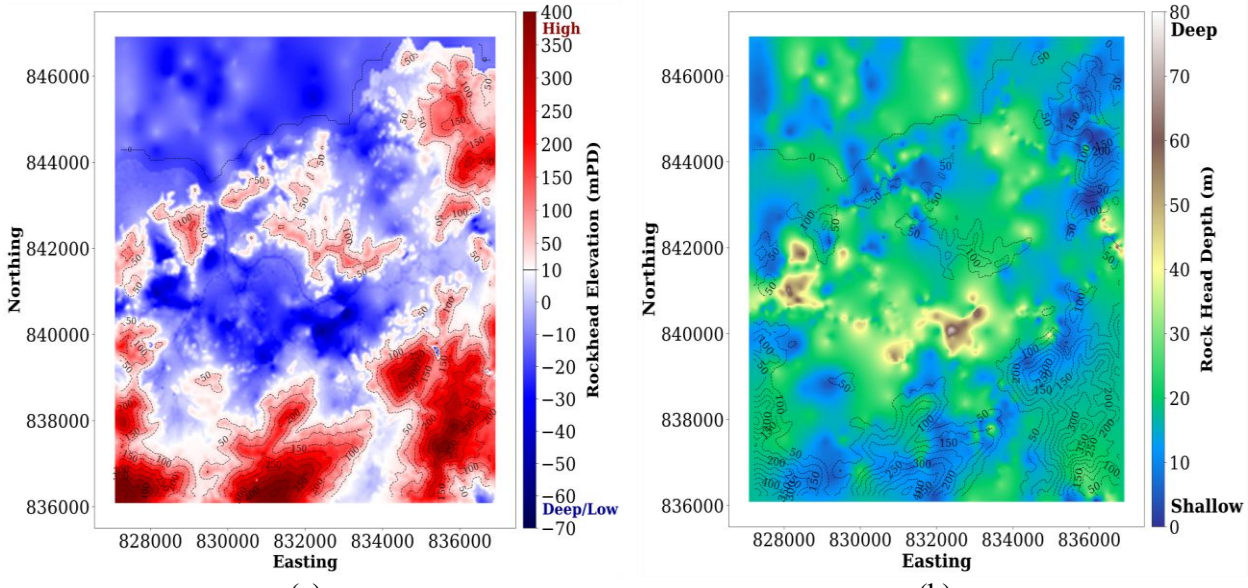

Figure 10: The rockhead maps of NMHK Zone03, a: Rockhead elevation (mPD), b: Rockhead Depth (m)

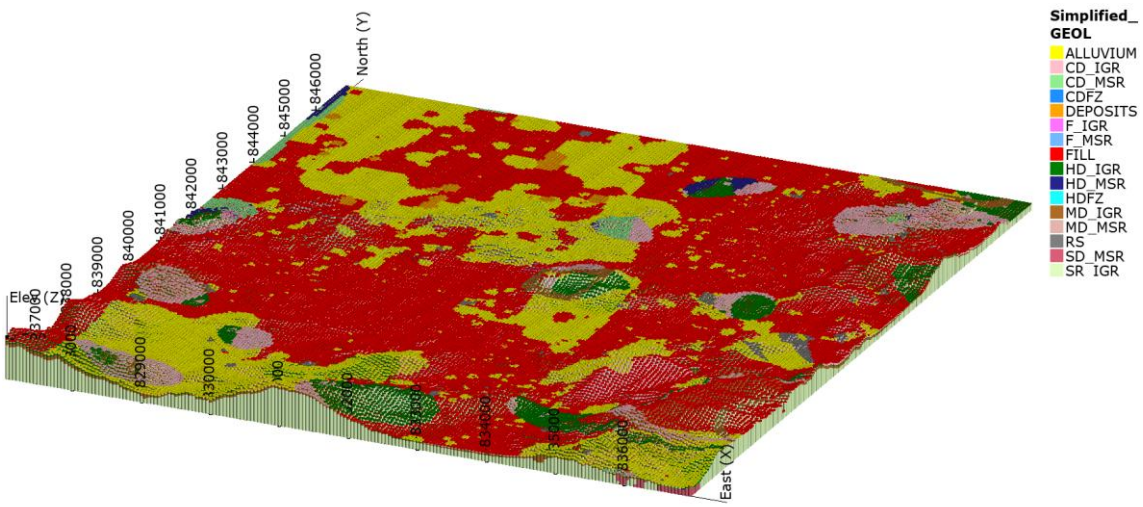

Figure 11: The interpolated boreholes at NMHK-Zone03

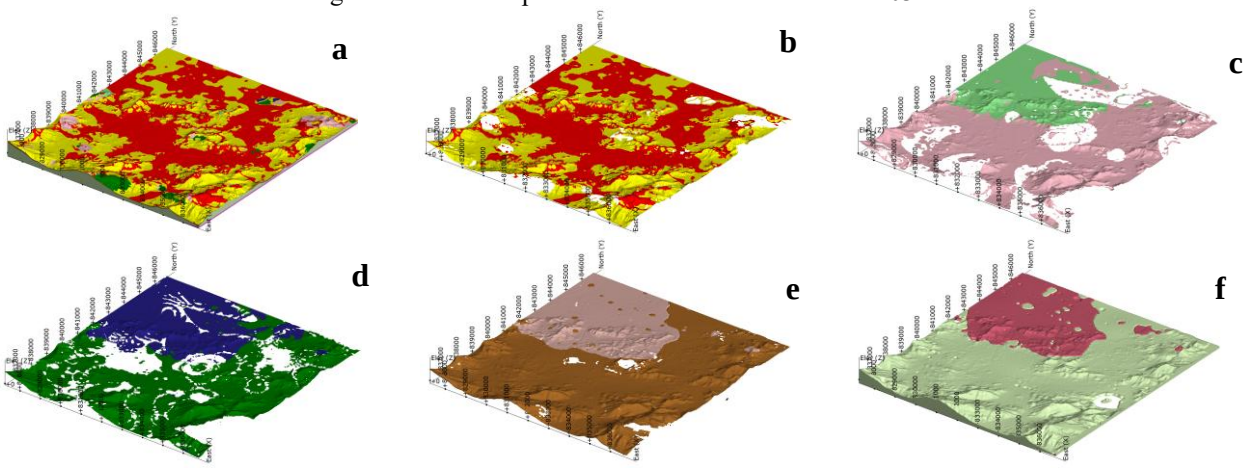

Figure 12: The three-dimensional geological model and volumes of geological units at NMHK (a: 3D geological model, b: Fill + Alluvium, c: CDIGR + CDMSR, d: HDIGR + HDMSR, e: MDIGR + MDMSR, f: SDIGR + SDMSR)

5.5 Construction of three-dimensional shear wave velocity model

The shear wave velocity (V_s) of the underlying geology is essential for estimating the very small shear strain maximum shear modulus ($G_{max} = \rho * Vs^2$), which plays a critical role in seismic site response analysis.

5.5.1 Relation between SPT_N versus depth of different soil/weathered rock types

The *SPT N*-value data (40000) were collected from in-situ tests categorized based on soil and rock types. These grouped data sets plotted against depth to observe its trends. Non constant variance linear regression analysis was subsequently performed on each group, and the resulting plots for Fill and CD_IGR as an example shown in Figure 13 (a and b). The figures show the data of *SPT_N* scattered at the same depth confirming the heterogeneity of the soil/weathered rock types. In our study, the mean linear regression equation was used. Furthermore, the equations of upper and lower boundaries based on mean +/- standard deviation (std) can be considered to evaluate the uncertainty in the *SPT_N* dataset.

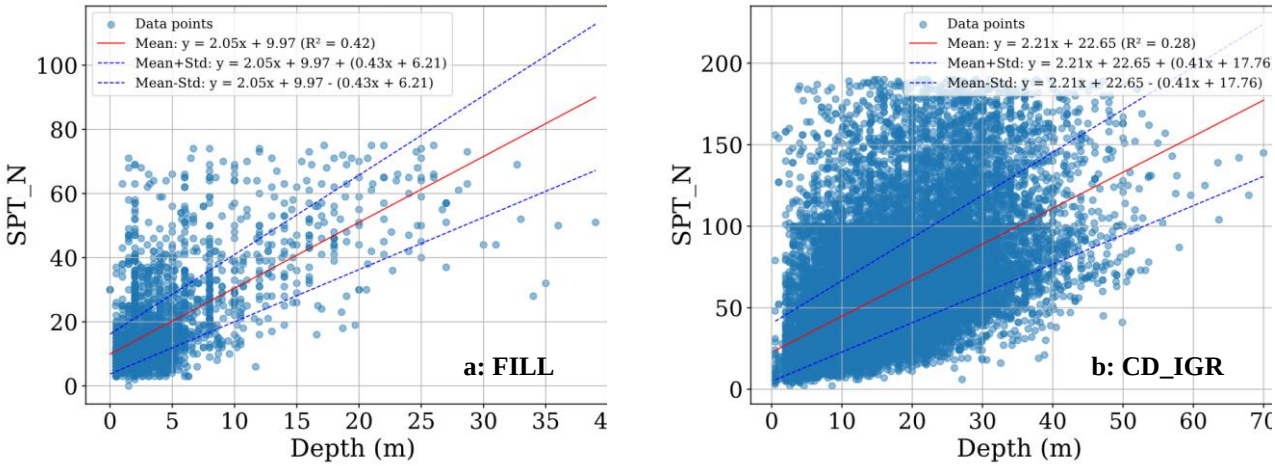

Figure 13: Non constant variance linear regression analysis of *SPT_N* versus Depth (a: FILL, b: CD_IGR)

5.5.2 Relation between shear wave velocity V_S versus SPT_N in Hong Kong

The shear wave velocity and *SPT_N* correlations have been determined based on V_s field measurements carried out in North-west New Territories in Hong Kong by Pappin et al. (2012) as shown in Figure 14. The combination between the relation between *SPT_N* with depth for each geological unit and the correlation equations of V_s with *SPT_N* in Hong Kong, the estimation of V_s at the known *SPT_N* locations and at the unknown locations can be determined to create the three-dimensional shear wave velocity model.

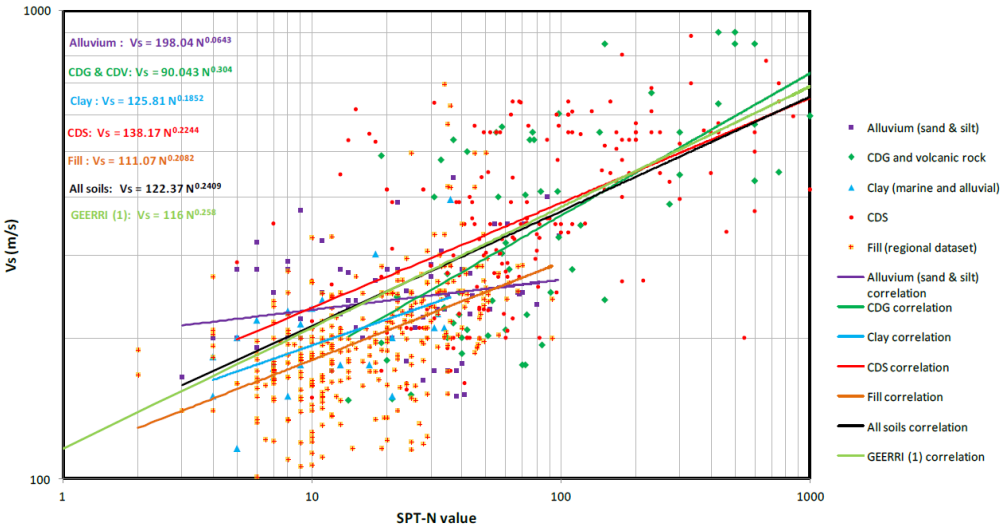

Figure 14: Correlations between V_s and *SPT-N* values proposed by Pappin et al. (2012)

5.5.3 Three-dimensional shear wave velocity V_s model at NMHK-Zone03

Based on the combination between the relations between *SPT_N* with depth for each geological unit and the correlations of V_s with *SPT_N* in Hong Kong, the three-dimensional shear wave velocity V_s model has been created at the studied area as shown in Figure 15 (a). To see the spatial variation of V_s, six slices in easting and northing directions cut the basin zone as shown in Figure 15 (b), where the mean values of V_s for soil types range from 180 to 240 m/sec. The maximum value of V_s is fixed to the top of the moderately decomposed weathered rock Grade III (Rockhead reference) 1000 m/s. This V_s digital model is very crucial for precise regional city-scale seismic response analysis at the Northern Metropolis in Hong Kong.

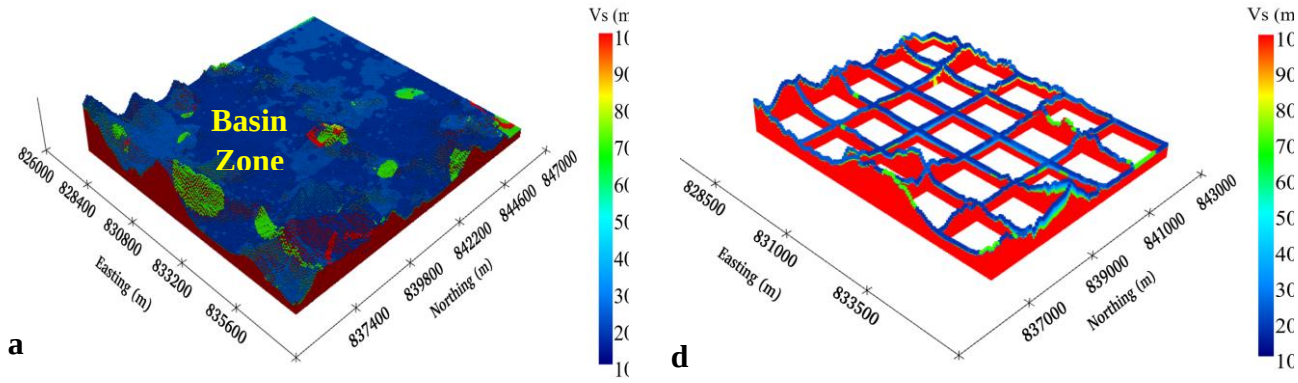

Figure 15: (a)Three-dimensional shear wave V_s model, (b) Easting and Northing slices of V_s at the basin zone

6 CONCLUSIONS

Constructing a city-scale geological model is vital for applications such as regional seismic site response numerical simulations. However, the geotechnical industry currently lacks efficient tools to extrapolate lithological and geological data to address large data gaps. This paper aimed to address this gap by processing existing geotechnical data, developing a hybrid lithology interpolation method, and constructing a geological and shear wave velocity models in Northern Metropolis in Hong Kong (NMHK) as a case study.

Two python-based tools, AGSGEOHKpy and PDFGEOHKpy, have been developed to extract and process precise big geological data that will be the backbone of building high resolution three-dimensional geological models. The lithological interpolation framework developed in this study is based on a Modified Inverse Distance Weighting (MIDW) algorithm. While conventional IDW relies solely on spatial proximity, the proposed approach incorporates an additional geological constraint layer through the application of weighting multipliers, ensuring that interpolated results remain geologically consistent. The number of distinct geological units and the selection of vertical discretization intervals are identified as critical parameters influencing both interpolation's accuracy and computational efficiency. Accordingly, grouping lithologies with similar characteristics and adopting an appropriate vertical resolution are essential for optimizing performance.

The accuracy and reliability of the proposed geological interpolation framework were evaluated through cross-sectional comparison in both volcanic and granitic terrains demonstrate close consistency between interpolated lithology and borehole records with some minor differences. Overall, the results confirm the robustness and applicability of the proposed method for regional-scale geological modelling.

As the application of the proposed geological modeling framework, the three-dimensional geological model at the North Metropolis (Zone03) in Hong Kong has been created. Rockhead elevation and depth maps were developed to provide essential inputs for both seismic analysis and deep foundation design. The results indicate significant spatial variability, with maximum rockhead elevations reaching approximately 400 mPD and shallow depths near surface levels in mountainous regions, while basin areas exhibit deeper rockhead conditions of up to 80 m depth and elevations as low as −70 mPD. In addition, the shear wave velocity Vs structure was developed based on the SPT_N records. The mean of Vs values of each soil/weathered rock types estimated. Thus, the small-strain shear modulus Gmax can be determined. As a result, the digital high resolution three-dimensional model of Vs has been generated to be used for regional scale seismic numerical simulations to assess seismic site effects at Northern Metropolis in Hong Kong.

ACKNOWLEDGEMENTS

The authors acknowledge financial support from Hong Kong Research Grants Council (RGC) General Research Fund No. 16219424, Theme-based Research Scheme T22-606/23-R, and State Key Laboratory of Climate Resilience for Coastal Cities at HKUST (ITC-SKLCRCC26EG01). The first author also acknowledges financial support of Hong Kong PhD Fellowship Scheme from RGC.

REFERENCES

Adhikari, B. & Molnar, P. 2024. Three-dimensional seismic response analysis incorporating detailed subsurface geological models in urban basins. Soil Dynamics and Earthquake Engineering, 175: 108268.

Agrawal, S. & McCloskey, J. 2024. Multi-scale three-dimensional geological modelling for regional seismic hazard simulations. Computers & Geosciences, 183: 105421.

AGS (Association of Geotechnical and Geoenvironmental Specialists) 2004. Electronic transfer of geotechnical and geoenvironmental data (Edition 3.1). Association of Geotechnical and Geoenvironmental Specialists, UK.

AGS (Association of Geotechnical and Geoenvironmental Specialists) 2017. Electronic transfer of geotechnical and geoenvironmental data (Edition 4.1). Association of Geotechnical and Geoenvironmental Specialists, UK.

Antonielli, B., Aucelli, P.P.C., Cesarano, M., Pappone, G. & Rosskopf, C.M. 2023. Engineering–geological modelling for supporting local seismic response analysis: The Rieti intermountain basin (Central Italy). Engineering Geology, 321: 107103.

Bowden, A.J. 2004. The uncertainty concept in geological modelling. In R. Chessell & A.B. Editor (eds), *Geological Prior Information: Informing Science and Engineering*: 45–60. Geological Society, London.

Borcherdt, R. D. (1994). Estimates of site-dependent response spectra for design (methodology and justification). Earthquake Spectra, 10(4), 617-653. DOI: 10.1193/1.158579.

Building Seismic Safety Council (BSSC). (2020). NEHRP Recommended Seismic Provisions for New Buildings and Other Structures. FEMA P-2082, Washington, D.C.

CEN 2004. Eurocode 7: Geotechnical design—Part 1: General rules. European Committee for Standardization, Brussels.

Civil Engineering and Development Department (CEDD) 2020. *Hong Kong Geological Survey Memoirs and Maps*. Civil Engineering and Development Department, Hong Kong SAR Government.

Civil Engineering and Development Department (CEDD). Ground Investigation (GI) data in AGS format. Available at: https://www.ginfo.cedd.gov.hk/geoopendata/eng/GI.aspx.

Civil Engineering and Development Department (CEDD). GeoInfo database for ground investigation reports. Available at: https://www.ginfo.cedd.gov.hk/GInfoInt/Default.aspx.

Civil Engineering and Development Department (CEDD). Spatial Data Portal: LiDAR Digital Terrain Model (DTM) data. Available at: https://sdportal.cedd.gov.hk/#/en/lidar.

Geotechnical Engineering Office (GEO) 2012. *Seismic hazard assessment in Hong Kong*. Civil Engineering and Development Department, Hong Kong SAR Government.

Geotechnical Engineering Office (GEO) 2022. *Updated seismic hazard analysis for Hong Kong*. Civil Engineering and Development Department, Hong Kong SAR Government.

Geotechnical Control Office (GCO) 1990a. *Geotechnical manual for slopes*. Geotechnical Control Office, Hong Kong Government.

Hadlow, P., Mortimore, R. N., & Hopkirk, A. (2018). Predicting the depth of weathering in the Chalk of southern England and northern France. *Quarterly Journal of Engineering Geology and Hydrogeology*, *51*(3), 291–305.

Isaaks, E. H., & Srivastava, R. M. (1989). An Introduction to Applied Geostatistics. Oxford University Press.

Ji, Z., Chen, H., Li, Y. & Zhang, J. 2024. Integrated three-dimensional geological modelling and seismic site response analysis for urban seismic hazard assessment. Engineering Geology, 330: 107512.

Kramer, S. L. (1996). Geotechnical Earthquake Engineering. Prentice Hall, Upper Saddle River, NJ. Chapter 7: Site Response Analysis, pp. 266-268.

Langford, R.L. 1996. *Geology of Hong Kong*. Geological Society, London.

Lai, K.W., Campbell, S.D.G. & Shaw, R. 1996. *Geology of the Northeastern New Territories*. Hong Kong Geological Survey Memoir No. 5. Geotechnical Engineering Office, Hong Kong Government.

Lai, K.W., Ng, C.W.W., Wang, J. & Liu, X. 2023. Three-dimensional city-scale marine geological model for Hong Kong. Engineering Geology, 318: 107019.

Lee, J.R. 2016. Geological uncertainty and risk in ground models. In A.B. Editor (ed.), *Advances in Engineering Geology*: 85–102. Geological Society, London.

Legislative Council (2022), Fact Sheet, Northern Metropolis. https://www.legco.gov.hk/research-publications/english/2022fs03-northern-metropolis- 20221007-e.pdf

Liu, X., Shi, X., Wang, J. & Ng, C.W.W. 2022. Three-dimensional geological modelling and management system for the shallow subsurface in Hong Kong. *Computers & Geosciences*, 164: 105119.

Lu, C. T., Chen, D., & Kou, Y. (2003). Algorithms for spatial outlier detection. Proceedings of the Third IEEE International Conference on Data Mining, 597-600.

Parry, S., Baynes, F., Culshaw, M.G. & Royse, K.R. 2014. Engineering geological models: An introduction. *Quarterly Journal of Engineering Geology and Hydrogeology*, 47(4): 375–385.

Pappin, J.W., Jirouskova, N.K., Arup, M.M.L.S., Kong, H., Jiang, H., Yu, Y.B., Ho, K.K.S., Koo, R.C.H., Kwan, J.S.H. & Shum, L.K.W. 2012. Seismic microzonation assessment in Hong Kong. In A.B. Editor & C.D. Editor (eds), Proceedings of the 15th World Conference on Earthquake Engineering. Lisbon, Portugal, 24–28 September 2012.

Shi, X. & Wang, J. 2022. Machine learning of three-dimensional subsurface geological models for a reclamation site in Hong Kong. Engineering Geology, 305: 106736.

Strange, P.J., Shaw, R. & Addison, R. 1990. *Geology of Sai Kung and Clear Water Bay*. Hong Kong Geological Survey Memoir No. 4. Geotechnical Engineering Office, Hong Kong Government.

Terzaghi, K. 1946. Rock defects and loads on tunnel supports. In R.V. Proctor & T.L. White (eds), *Rock Tunneling with Steel Supports*: 15–99. Commercial Shearing and Stamping Company, Youngstown.

Tobler, W. R. (1970). A computer movie simulating urban growth in the Detroit region. Economic Geography, 46(sup1), 234-240.

Wang, G. 2021. Data-driven three-dimensional geological modelling and uncertainty analysis. Computers & Geosciences, 150: 104716.

Yamamoto, J. K., Kikuda, A. L., & Ribeiro, D. T. (2012). Interpolation of categorical variables: A methodology based on indicator kriging. *Computers & Geosciences*, *43*, 116–128.

Assessment of Foundation and Excavation and Lateral Support (ELS) Works for a Footbridge near MTR Structure in Admiralty, Hong Kong

Y.T. Shang, L.M. Wei
Ove Arup & Partners Hong Kong Ltd., Hong Kong
Y. Chen
China State Construction International Holdings Ltd., Hong Kong

ABSTRACT

Pile installation along the perimeter of, or within, the excavation area for Excavation and Lateral Support (ELS) works are common construction practice. Both foundation and ELS works that employ piling techniques are widely accepted, but they invariably induce vibration, requiring careful measures to minimize impacts on the surroundings. This technical paper presents the impacts of piling and ELS works for a newly completed footbridge adjacent to underground structures. Special attention is given to pile drilling in soil near an existing MTR station and the vibration generated. Moreover, the sensitivity of a heavily trafficked main road and the dense urban environment and the presence of nearby buildings, structures, and utilities increase the complexity of the works. To mitigate vibration across various soil types, adjustments regarding bit size, pile wall size as well as founding level were adopted. The paper draws upon precautionary measures to mitigate adverse impacts.

1 INTRODUCTION

Figure 1: Two Queensway Bridge in Hong Kong

Queensway is one of the busiest trunk roads in Hong Kong. This new bridge connects Pacific Place with Harcourt Garden, integrating seamlessly into the existing pedestrian network and extending its reach to Harcourt Road and Tim Mei Avenue (Figure 1). Notably, it enhances accessibility to key locations like the Admiralty MTR interchange hub, government facilities and commercial buildings, significantly benefiting the neighborhood. The footbridge rests on 3 supports, namely Support "A", "C" and "D". Support "A" was at Pacific Place Mall. The ELS design for the pile caps for Support "C" and Support "D" was carried out. Mini-piles and shear H-piles were adopted as the foundation at these two supports.

2 PROJECT BACKGROUND AND SITE CONSTRAINTS

2.1 Site description

The existing ground level of the Queensway is approximately +5.8 mPD, while Harcourt Garden is slightly above the Queensway. An existing ramp running down from Rodney Street to +2.8 mPD serves the Harcourt Garden basement carpark. As illustrated in Figure 2, the proposed footbridge is situated above a congested subsurface corridor with multiple existing underground assets in close proximity to the alignment. These include the Harcourt Garden basement carpark, a three-level underground facility founded on a combined raft and mini-pile system; an existing pedestrian subway linking Pacific Place One to Admiralty MTR Station; the MTR Finger Platform located at north of the proposed alignment; a further pedestrian subway connection to Three Pacific Place running along Queensway; and the Admiralty MTR Station Cavern underlying the site, with the shallowest crown level at approximately -21 mPD.

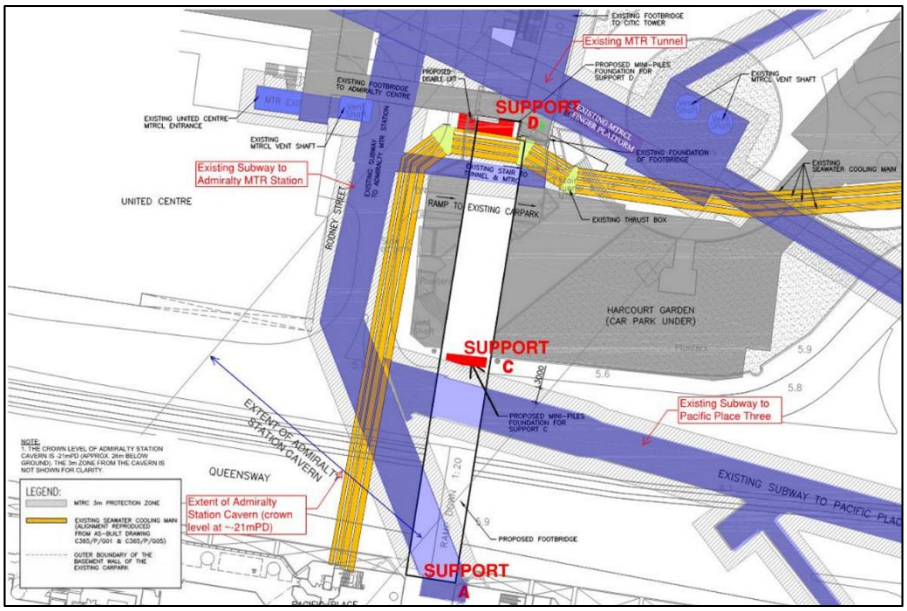

Figure 2: Existing underground structure

The proposed footbridge was constructed within a highly constrained corridor defined by existing transport and pedestrian infrastructure, which significantly increased design and construction complexity. Although the site was on reclaimed land with no registered man-made slopes or retaining walls along the alignment and the nearest recorded geotechnical feature was located more than 50 m away, the works interface directly with the existing Admiralty MTR station and entrances. The Admiralty MTR station occupied the footprint approximately bounded by the MTR Tsuen Wan and Island lines to the west of the existing CITIC Tower footbridge. In the vicinity of the connection between the proposed footbridge and the existing CITIC Tower footbridge, two MTR entrances were present. One entrance was along the Rodney Street, opposite to the Admiralty Centre and the other one located at the northeast corner of the United Centre. This imposed constraints and stringent requirements for safeguarding operational assets and passenger access. In addition, the new structure shall tie into multiple existing footbridges (CITIC Tower footbridge HF152 and the Admiralty Centre footbridges HF79 and HF164) that were founded on rock (grade III or better) via different systems (mini-

piles and caissons, respectively). The locations of raking piles at HF152 were confirmed by prior trial pit investigations. These existing substructures and foundations restrict options for new support locations, constrain construction methodology, and necessitated careful coordination and detailed verification to avoid conflicts and ensure structural compatibility at the interfaces. The proposed footbridge was also near existing utilities. Drainage Services Department assets included a stormwater main and a foul sewer. Water Supplies Department infrastructure included a fresh water main and cooling seawater mains (2×Ø700 mm and 2×Ø1200 mm). A town gas pipe was present along the Queensway. Telecommunications services were extensive, with telephone cables, TV ducts, and plant/cables from PCCW-HKT Telephone Limited, Cable TV, Hutchison Global Crossing Limited, etc.

2.2 Ground condition

The site geology was established through a review of (i) existing geological map showing regional geological information, (ii) existing ground investigation (GI) records, and (iii) as-built MTR project data for the Admiralty area. In accordance with Geological Map sheet 11 of the Hong Kong Geological Survey, the site is underlain by medium-grained granite. Relevant GI records were obtained from the Geotechnical Information Unit (GIU) of the Geotechnical Engineering Office (GEO). Because of the proximity of multiple structures near Supports "C" and "D" (Figure 2), only one borehole was drilled to characterize the underground stratum, supplemented by seven trial pits to confirm the locations of existing structures and utilities. The borehole was terminated after drilling at least 5 m into bedrock, comprising moderately decomposed rock of weathering grade III or better and a Total Core Recovery (TCR) no less than 85%. Laboratory testing was performed on rock samples to evaluate rock strength. The ground investigation, together with the existing borehole information, indicated that the site was covered by Fill material (0 to 4 m thickness) overlying completely decomposed granite of various weathering grade (4 to 7 m thickness).

3 ELS DESIGN

3.1 Design assumptions

For temporary excavation support during pile-cap construction, LSP-3B light-type sheet piles and FSPII-type sheet piles with steel grade S355 to BS EN 10025 (yield stress = 355 MPa, elastic modulus = 205 kN/mm²) were proposed as steel planking to support the excavation. Temporary shoring elements for ELS, including walers and struts, were Grade S355 to BS EN 10025. Ground investigation indicated that the site was typically overlain by approximately 2 m to 4 m of Fill, and the pile caps were proposed at about 3 m to 4 m below existing ground level. ELS installation and excavation works were anticipated to be undertaken predominantly within the Fill and partially within the Completely Decomposed Granite (CDG) layers. Upon obtaining no-objection from MTR, relevant ground investigation information from the nearby Admiralty MTR Station Cavern project was extracted and used herein for the interpretation of the soil design parameters. The interpreted soil parameters for Fill and Completely / Highly decomposed granite used for design and analysis are summarized in Table 1.

Table 1: Design soil parameters

Soil Stratum	Bulk Unit Weight, γ (kN/m^3)	Cohesion, c (kPa)	Friction Angle, φ (degrees)	Elastic Modulus, E (kPa)
Fill	18.5	0	35	6000
CDG/HDG	19	4	38	37500

No groundwater monitoring was carried out during the ground investigation. With reference to MTR's project data in Admiralty area, the groundwater level fluctuated between +3.0 mPD and -1.0 mPD in general with some spikes up to +4.0 mPD. A design groundwater level of +4.0 mPD was therefore assumed to conduct the structural design of the temporary sheet pile wall and shoring system. For settlement assessment, +3.0 mPD was considered representative, although +4.0 mPD was also applied in the settlement estimates to be conservative.

3.2 ELS support design

The ELS design was developed for construction of pile caps at Footbridge Supports "C" and "D", where existing ground levels are approximately +5.8 mPD and +6.0 mPD respectively. For support "C", the required excavation level for construction of pile caps supporting the footbridge is +2.125 mPD. A temporary light steel sheet pile wall with one level of strutting was proposed to provide stable support for the maximum 3.7 m deep excavation. Key site constraints were addressed in the design, notably the presence of numerous underground utilities identified from trial trench records, particularly along Queensway. Utility diversion within the pile cap footprint was to be completed prior to piling and excavation, except for an existing HKT concrete cable trough at Support "C". Relocating the HKT cables would require extensive diversion works, including breaking up of the concrete trough and provision of a large and deep manhole to accommodate more than 40 cable joints. Due to these constraints, the HKT cable trough was retained with necessary protection works during the excavation and foundation construction of Support "C".

3.2.1 Construction sequence of support "C"

The section plot of Section 2 for Support "C" is shown in Figure 3. The construction at Support "C" was executed following a staged sequence developed to manage utility constraints and to maintain stability of the retained ground and the in situ HKT cable trough:

(1) Existing utilities within the excavation footprint were diverted as required, and the prescribed monitoring instrumentation was installed prior to commencement of earthworks.

(2) A temporary steel sheet pile wall was installed.

(3) Excavation was carried out in stages to approximately +5.1 mPD to expose the HKT cable trough.

(4) Foundation piles were then constructed within the retained excavation.

(5) A level of steel shoring/strutting was installed at approximately +5.6 mPD to control wall deformation during subsequent excavation.

(6) Excavation proceeded to about +4.2 mPD. Local trimming was undertaken to around +4.0 mPD near the support frame, and the HKT cable trough was temporarily supported/protected by a purpose-installed supporting frame.

(7) Excavation was continued to the final excavation level (FEL).

(8) The pile cap was constructed and the pier was erected to the extent permitted within the excavation. In other words, part of the pier at Support "C" was installed.

(9) Mass concrete backfill was placed up to the soffit level of the HKT cable trough, after which the temporary supporting frame was removed.

(10) Backfill was continued to approximately +5.3 mPD, followed by removal of the steel shoring/strutting.

(11) The remaining portion of the pier was constructed, and the excavation was subsequently backfilled to the existing ground level to complete reinstatement.

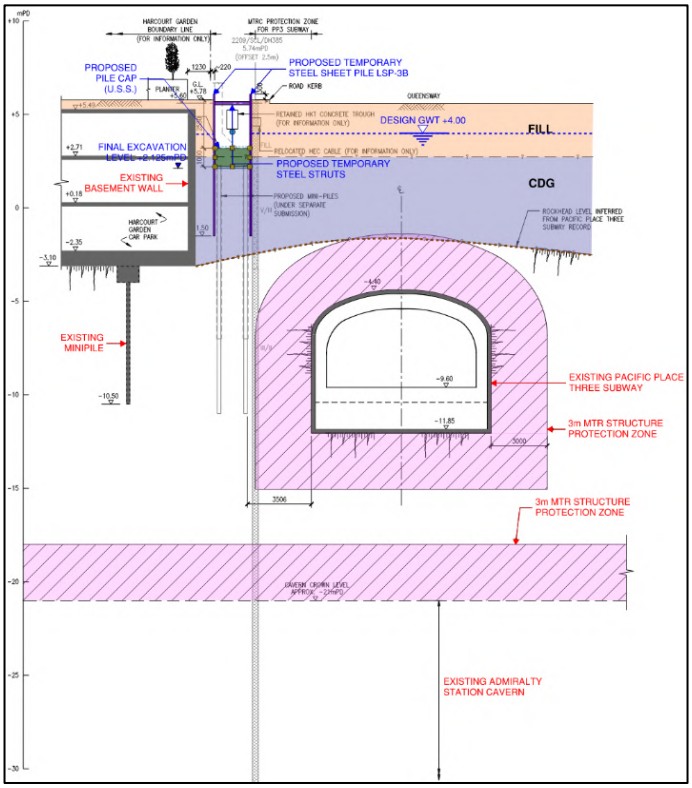

Figure 3: Section 2 of Support "C" (Section 2)

3.2.2 ELS design process

Design surcharges applied on the retained side in the analysis included footpath loading (5 kPa), traffic loading (20 kPa), and construction loading (10 kPa), all treated as strip loads. Numerical analyses using PLAXIS 2D were performed to evaluate ground movements and wall and struts force. Regarding ground settlement estimation, the total ground settlement was due to sheet pile wall installation, groundwater drawdown and bulk excavation. The settlement due to sheet pile wall installation will be highly influenced by the construction method and workmanship on site. As the maximum driven length of sheet pile is 7.3 m in this project, it was assumed that the ground settlement due to sheet pile wall installation would be 3 mm, provided that good workmanship and installation control are maintained. For ground movement due to groundwater drawdown, with reference to MTR project data in the Admiralty area, the lowest measured groundwater level at Support "C" was below +0 mPD, which is below the proposed final excavation level of +2.125 mPD. Hence no ground settlement was anticipated as no dewatering work will be carried out below the lowest measured ground level. Finally, settlement induced by bulk excavation was significantly influenced by the depth of excavation, the stiffness of the wall, the arrangement and stiffness of the ELS structural systems, the magnitude of the surcharge, the stiffness of the soil both outside and inside the site, etc.

3.2.3 Discussion on the effect of the proposed ELS system to the existing structures

The existing structures near the proposed ELS works at Support "C" include: (i) Harcourt Garden Basement Carpark, (ii) Pacific Place Three Subway, (iii) Admiralty MTR Station Cavern, and (iv) existing underground utilities. The potential impacts of the proposed excavation on these structures were evaluated through numerical analyses using PLAXIS 2D. The calculation results for deformation and stress change are presented in Figures 4 and 5.

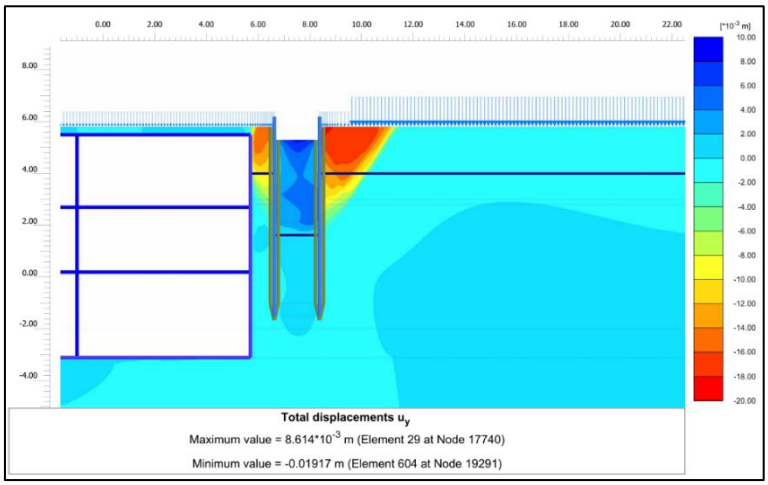

Figure 4: Contours of Total Displacement uy of Plaxis 2D Model for Support "C"(Section 2)

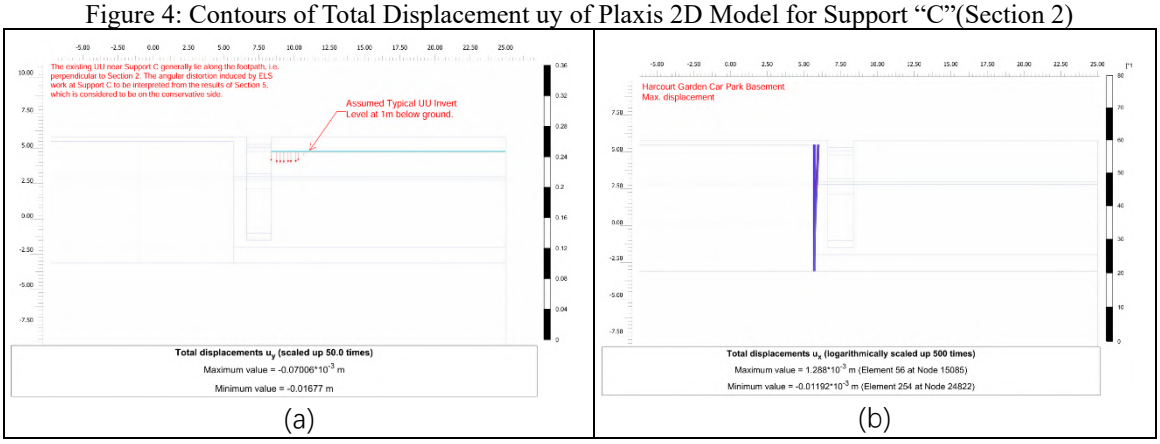

Figure 5a: Plaxis 2D Model Calculation Results of Support "C" (Section 2): (a) Predicted Total Displacement uy; (b) Predicted Total Displacement ux;

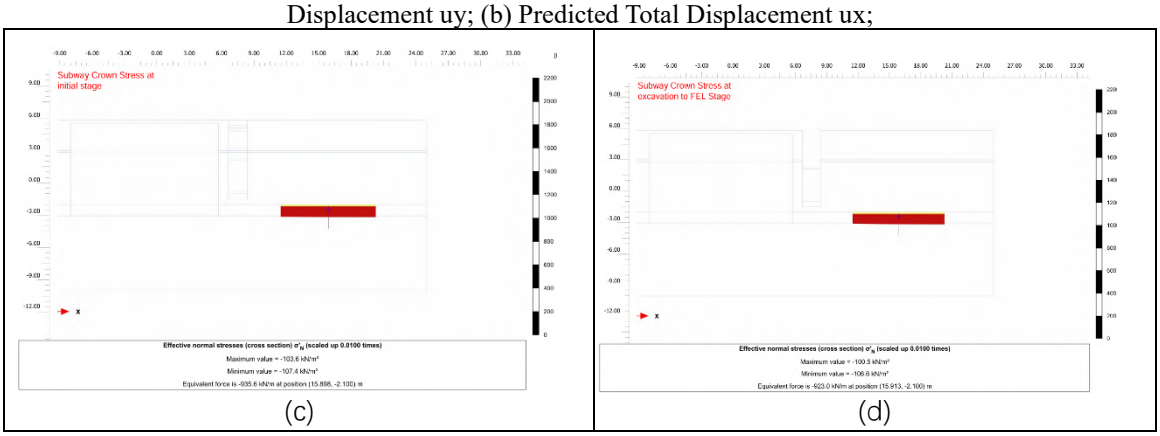

Figure 5b: Plaxis 2D Model Calculation Results of Support "C" (Section 2): (con't) (c) Predicted Subway Crown Stress at Initial Stage; (d) Predicted Subway Crown Stress at Excavation to FEL

(a) Harcourt Garden Basement Carpark: The existing Harcourt Garden Basement Carpark was located adjacent to the proposed excavation area at Support "C". Numerical results from Section 2 of the PLAXIS 2D analysis indicated that the predicted lateral displacement at the existing basement wall induced by the proposed excavation was negligible. Furthermore, the carpark was supported by deep foundations bearing at depth. Given the relatively shallow excavation depth of 3.7 m and the separation between the excavation and the deep founding levels, excavation-induced settlement at foundation level was considered unlikely. Accordingly, adverse structural effects on the basement carpark were not anticipated.

(b) Pacific Place Three Subway: The Pacific Place Three Subway was founded at levels between approximately –8.3 mPD and –17.45 mPD, with a structural height ranging from 5.85 m to 11.3 m. As-built

drawings indicated that the subway structure is socketed into bedrock. The proposed ELS works will be undertaken entirely within soil and outside the 3 m protection zone (Figure 3) of the subway structure. Numerical modelling results demonstrated that the stress changes and deformation induced in the subway structure due to the proposed excavation were negligible. Therefore, the excavation works were not expected to impose any significant structural or serviceability impacts on the existing subway.

(c) Admiralty MTR Station Cavern: The Admiralty MTR Station Cavern beneath Support "C" is constructed within rock, with an estimated rock cover of approximately 19 m (rockhead level at –2.0 mPD and cavern crown level at –21 mPD). Considering the substantial rock cover and the fact that the proposed 3.7 m deep excavation and associated ELS system were confined to overlying soil strata, the influence of the excavation on the cavern was assessed to be insignificant. The numerical analyses confirmed that excavation-induced stress redistribution within the rock mass at cavern level was negligible.

(d) Existing Utilities: Trial trench investigations indicated the presence of multiple existing utilities within the footpath along Queensway, where Support "C" was proposed. Utilities that conflict directly with the excavation works will be diverted in advance. For utilities located adjacent to the trench, the predicted maximum ground settlement induced by the ELS works were less than the allowable serviceability settlement criterion of 25 mm, and the computed angular distortion was less than 1:300. These values were within commonly accepted serviceability limits for buried utilities. Accordingly, no adverse impact on adjacent utilities was anticipated. For the HKT cable trough to be retained across the trench during excavation, appropriate protective measures (e.g., installation of a temporary supporting frame) will be implemented to prevent undue disturbance and to maintain service continuity.

4 ASSESSMENT OF VIBRATION INDUCED FROM PILING WORKS

This section focuses on the assessment of vibration monitoring due to piling works using Peak Particle Velocity (PPV). The proposed footbridge over Queensway was designed to be founded on mini-piles and shear H-piles, which were to be installed using driven or pre-boring methods. According to Code of Practice for Foundation 2017, the ground-borne vibration due to the piling works can be estimated using the following empirical formula:

$$V_{res} = k_p \left[\frac{\sqrt{W_e}}{r^{1.3}} \right] \quad (1)$$

where V_{res} = resultant PPV (mm/sec), k_p = ground bore vibration coefficient, W_e = nominal hammer energy (J), x = distance of recipient from pile measured along ground surface (m), y = depth of pile toe at the time of assessing V_{res} (m), r = slope distance of recipient from pile toe (m). More detailed discussion of the equation and the recommendation of fitting parameters were presented by Shang & Chen (2024).

4.1 Vibration resulting from H-pile installation by hammer method

The shear H-piles at Support "C" were driven using hammer / driven methods due to site constraints. As the driven length of the proposed shear H-piles is only up to 7 m, it was anticipated that the piles would pass through the fill and CDG layers. With reference to past project experience, k_p was assumed to be less than 0.5 for driving through the top soil layer with an SPT value generally lower than 20. Assuming a drop hammer weight W = 13 tons, a drop height H = 100 mm, and a hammer efficiency of 0.7, the estimated maximum vibration induced by the installation of the proposed shear H-piles is presented in Table 2.

Table 2: Vibration due to Hammer Method

Critical Pile	Critical MTR Structures	Minimum Clearance, r (m)	k_p	Hammer Energy, W_e (J)	Hammer Efficiency	PPV (mm/s)
CH4	Existing Subway to Pacific Place Three	4.547	0.5	12740	70%	6.6
CH1 to CH7	Admiralty MTR Station Cavern	19.700	0.5	12740	70%	1.0

4.2 Vibration resulting from pre-boring method

For shear H-piles at Support "D" and mini-piles, the concentric drilling method was adopted. Compared with the shear H-piles, the mini-piles were to be drilled to bedrock, which may be more critical in terms of vibration. Hence, the assessment of vibration resulting from pre-boring methods may need to be based on the kinetic energy of the DTH hammer used to form the rock socket of mini-piles. It should be noted that the vibration equation is empirical, and its application to pre-bored rock socketing is an engineering approximation. The kinematic energy of the DTH hammer piston and the applicability of equation (1) to pre-boring/DTH works were subject to preliminary assessment. The equivalence between piston kinematic energy and input energy required verification through site monitoring data. In other words, predictions for the pre-boring method were less reliable than for driven pilling, and attention shall be paid in engineering practice. In this study, for pile drilled to bedrock, the value of k_p was assumed to be 3.0 based on a first approximation according to Code of Practice for Foundation 2017. Assuming a hammer piston weight m = 68 kg, a piston movement frequency of 11.7 s^{-1}, and a stroke distance of 0.127 m, the estimated maximum vibration induced by the installation of the proposed mini-piles is presented in Table 3.

Table 3: Vibration due to Pre-boring Method

Critical Pile	Critical MTR Structures	Minimum Clearance, r (m)	k_p	Kinematic Energy of DTH Hammer, $We=(1/2)mv^2$ (J) *	PPV (mm/s)
C9	Existing Subway to Pacific Place Three	3.064	3	74.6	6.0
C1 to C12	Admiralty MTR Station Cavern	10.000	3	74.6	1.1

* The average velocity of the piston movement v = Frequency of the piston movement x Stroke distance

4.3 Precautionary measures for underground obstruction

Prior to the piling works, shallow obstruction shall be removed by the trial pit method. For underground obstruction beyond 3 m from the ground, it shall be removed by pre-boring method, such as coring or stitching coring using diamond drill bit with a slow advancing rate. For the H-piles at Support C, which were to be driven using the hammer method, precautionary measures were to be carried out to identify underground obstructions and prevent sudden increases in resistance due to their presence during piling works. At least one pre-drilled hole was to be made within the footprint of the pile cap prior to the piling works to check for any underground obstruction. Furthermore, the sheet pile wall was to be installed using a vibratory hammer or silent piler to support the excavation for pile cap construction. At Support "C", the sheet pile wall was to be installed before driving the H-piles, and the toe level of the sheet pile (-1.5 mPD) was slightly lower than that of the H-piles (-1.3 mPD). Hence the installation of the sheet pile would also help investigate the presence of underground obstruction for the following piling works of H-piles. The layout of sheet pile wall at Support "C" was presented in Figure 6:

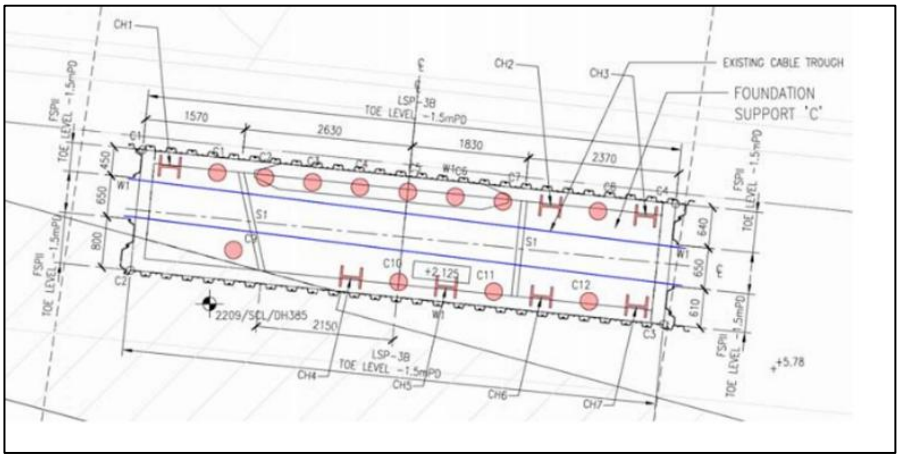

Figure 6: The layout of sheet pile wall at support "C"

In accordance with PNAP APP-24, the PPV induced in any railway structures resulting from driving or withdrawing of piles shall not exceed 15 mm/s. The estimated maximum vibration induced from the proposed piling works are less than the allowable limit, and it was therefore anticipated that there would be no adverse impact on adjacent railway structures.

4.4 Investigation report for vibration marker V8 during construction monitoring

Vibration monitoring equipment (continuous monitoring with daily review) was used to monitor the vibration induced during construction. The monitoring points are presented in Figure 7.

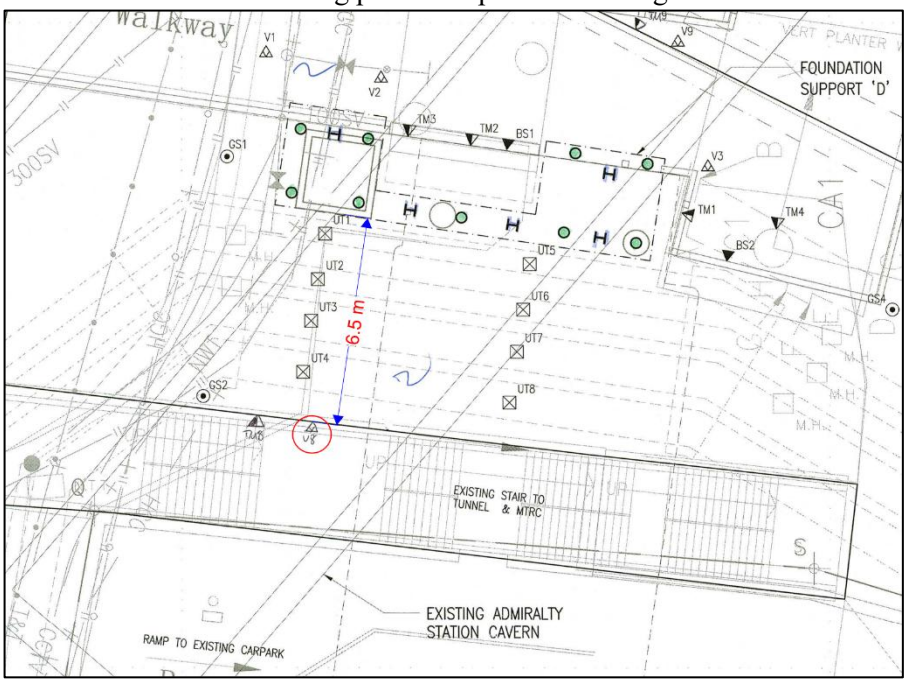

Figure 7: Approved monitoring plans

Up to 17 August 2023, no vibration reading had exceeded the Alert level except the vibration marker V8. The maximum PPV of 5.715 mm/s was measured at V8 on 26 July 2023. The measurement records are presented in Figure 8 and Table 4.

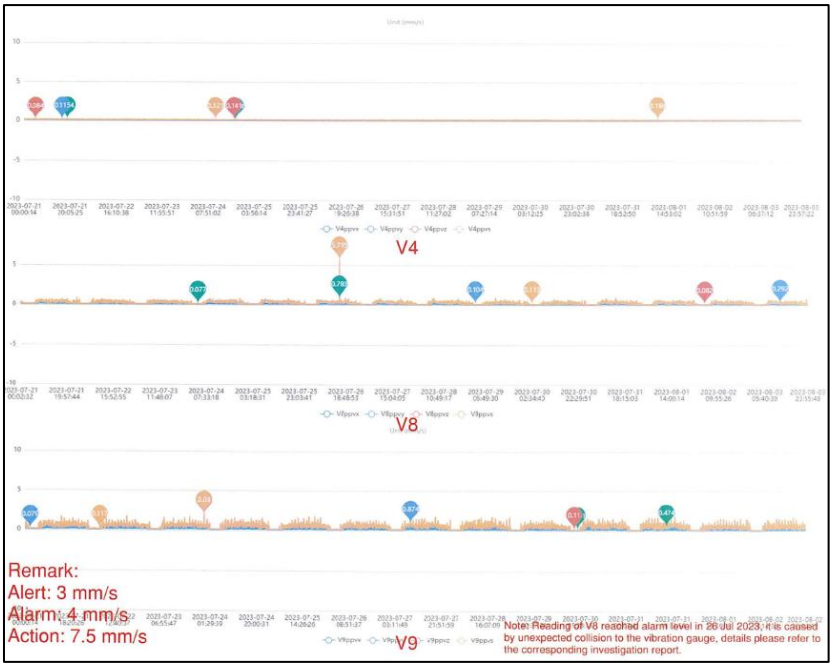

Figure 8: Excessive vibration recorded on 26 July 2023

Table 4: Summary of Vibration Monitoring (at MTR Structures) (from 21 July 2023-17 August 2023)

Check Point	Maximum Peak Velocity (mm/s)	Alert Level (mm/s)	Alarm Level (mm/s)	Action Level (mm/s)
V4	0.188	3	4	7.5
V8	5.715			
V9	2.401			

The contractor was requested to submit an investigation report. According to the report, the contractor suspected that the abnormal reading at V8 was caused by an unexpected collision with the vibration logger by passersby, as it was originally located next to a vending machine that was subsequently removed. For subsequent monitoring works, warning signage was placed on the cover of vibration logger V8 to avoid similar incidents. The site record was presented in Figure 9.

Photo 3 | Photo 4

Figure 9: Site condition photo record of vibration marker V8

Thus, it was concluded that the abnormal reading from vibration marker V8 was caused by unexpected collision of passersby for the following reasons: (1) No major site works that would induce high vibration occurred. The steady readings at V1 and V2 proved that the setup of the pile load test platform at Support "D" (18–21 July) did not generate significant vibration; (2) The vibration reading at V8 remained steady within the Alert/Alarm/Action level during the rest of the period. The preventive measures such as placing warning signage were done to prevent similar incidents occurring.

5 CONCLUSION

This paper presents a case study of ELS works for a footbridge constructed adjacent to Admiralty MTR Station and its associated underground structures in Hong Kong. Despite the highly constrained urban setting and the proximity of sensitive railway infrastructure, the combined use of numerical analysis, empirical vibration prediction, and site monitoring demonstrated that the works were carried out safely and within acceptable limits. The temporary sheet pile wall with single-level strutting provided adequate support for the excavation, while predicted and measured ground movements remained small and localized. Numerical analysis also indicated that the shallow excavation had negligible impact on the underlying MTR Cavern due to the presence of sufficient competent rock cover. For piling works, predicted and monitored vibration levels remained well below the relevant allowable limits, confirming the suitability of the adopted construction methods.

The deformation magnitudes and vibration levels documented in this study may serve as a practical reference for the design and construction of similar works in comparable ground conditions in Hong Kong. However, it is crucial to emphasize that the findings are specific to the geological context, excavation geometry, construction sequence, structural elements in the ELS system, and protective measures employed in the project. Direct extrapolation to other sites or conditions without independent judgement is not recommended.

ACKNOWLEDGEMENT

The authors are grateful to Swire Properties Limited for approval of reference to project record in this paper. Great gratitude is given to Kylie Lam and Sandy Hee for liaison during the preparation of publication. Sincere thanks to other Arup colleagues for sharing project data to gain further insights.

REFERENCES

BD 2017. *Code of Practice for Foundations 2017*. Buildings Department, Hong Kong.

GEO 2020. *Geoguide 1 – Guide to Retaining Wall Design (2020 Version)*. Geotechnical Engineering Office, Civil Engineering and Development Department, The Government of the Hong Kong Special Administrative Region, Hong Kong.

GEO 2003, *Review of Design Methods for Excavations (1990)*. Geotechnical Engineering Office, Civil Engineering and Development Department, The Government of the Hong Kong Special Administrative Region, Hong Kong.

BD 2022, *PNAP APP-24*, Buildings Department, Hong Kong.

Shang Y. T. & Chen, Y. (2024). Effects of Vibration and Mitigation Measures for Temporary Retaining Wall Installation of Excavation and Lateral Support Works. *Proceedings of The HKIE Geotechnical Division 44th Annual Seminar - Elevating Geotechnical Excellence: Novel Practices & Innovative Solutions*.

SmartLog: Transforming Ground Investigation Records and Applications

Caleb Sang & Stuart W. Millis
Ove Arup & Partners Hong Kong Limited

Regis L.G. Chee, Rachel W.Y. Lau, Eric H.Y. Sze
Geotechnical Engineering Office, Civil Engineering and Development Department of the Hong Kong Special Administrative Region, Hong Kong SAR, China

Anthony C.T. So
Development Bureau, Government of the Hong Kong Special Administrative Region, Hong Kong SAR, China

ABSTRACT

Hong Kong's geotechnical community has long benefited from the Geotechnical Information Infrastructure System (GInfo), a comprehensive web portal providing access to an extensive data repository as developed and maintained by the Geotechnical Engineering Office (GEO) of the Government of the HKSAR. Yet, project-specific investigations remain indispensable for building precise ground models that underpin diverse engineering works. Against this backdrop, the development of a native mobile application — SmartLog — conceptualised and commissioned by the GEO and developed by Arup — emerges as a pivotal innovation in geotechnical data management, signalling local readiness for digital transformation and resilience in the face of technological change.

SmartLog is closely aligned with Hong Kong's vision of a territory-wide unified 3D geological model and readily accessible ground investigation (GI) data for design, analysis and modelling. Achieving this vision requires two critical foundations: first, fine-scale data modelling to ensure consistency across geotechnical parameters and lithological units; second, the growth of a system tailored to the unique needs of Hong Kong's GI workforce and regulatory framework.

Cloud-hosted for scalability, SmartLog integrates mobile-based data input and future navigation with web-based data review. Its design adheres to established Association of Geotechnical and Geoenvironmental (AGS) and Geoguide standards, providing drillers, certified logging geologists and field technicians with an intuitive, streamlined workflow. This ensures that all levels of the GI workforce are involved, despite some inherent barriers in adoption.

Traditional geotechnical data management has often been constrained by proprietary systems, making migration and integration difficult. SmartLog breaks this mould by harnessing open-source compatible components within a government-recognised platform. This approach not only reduces barriers to adoption but also opens the door to future applications that can evolve alongside industry needs, benefiting many parties.

The introduction of SmartLog represents more than a technical upgrade—it is a strategic step toward a digitally unified geotechnical landscape. By embedding flexibility, scalability and compliance into its architecture, Smartlog positions Hong Kong’s geotechnical sector to embrace innovation while safeguarding continuity. In doing so, it lays the groundwork for a new era of data-driven engineering practice.

Keywords: Ground Investigation, Geotechnical Data Management, Open-Source Compatible, Innovation

1 INTRODUCTION

Information about the ground is the primary driver for cost effective and prudent design of the built structures underpinning our civilization. Hong Kong has one of the most densely distributed development in the world, partly due to the city being land scarce. In hindsight, it also has a very well catalogued database of existing ground investigation records within the Geotechnical Information Unit (GIU). As Geographical Information System (GIS) became increasingly prevalent in the spatial data management sphere, the Geotechnical Information Infrastructure System (GInfo) was created by the Geotechnical Engineering Office (GEO) to serve as the authoritative data hub. A full set of data is available to those involved in government-related projects via a web-based application powered by Esri ArcGIS technology, retrieved from the Digital Geotechnical

Information Unit (DGIU). A partial set of open data is also freely available, released via the Geo Data Portal. This opens the door to efficient data retrieval and a sense of collaboration among peers in the construction industry that is the dominating user base of this ground information database [6]. This paper presents the process of implementing a geotechnical data ecosystem with a focus on the aspects of digital borehole logging while incorporating locally unique workflows.

1.1. Ground Investigation Data

Ground engineering works involving excavation, piling, stabilising and other earthworks require prior knowledge of the ground, whether in the shallow or in the depths. In Hong Kong, private GI contractors and other organisations with specialised GI teams or laboratories conduct the fieldwork in a variety of environments, as shown in **Figure 1** (drilling, logging, in-situ testing and monitoring) and subsequent laboratory testing of the ground samples (groundwater, soil & rock alike). Regardless of how the data was recorded by the field workers (**Figure 2**), the dataset shall be submitted in PDF/hardcopy reports and digital data in the AGS format for both fieldwork and laboratory tests [2, 3]. In the process of producing a typical GI fieldwork report, a minimum of five (5) people is involved in the data input, namely the project engineer/geologist, the driller, the geotechnical field technician (GFT), the logging geologist and the surveyor. The number of participants may double where laboratory testing and/or instrumentation and monitoring is involved. The consolidation, verification, and publishing of the data in its most accurate form can be understandably arduous, if not time consuming.

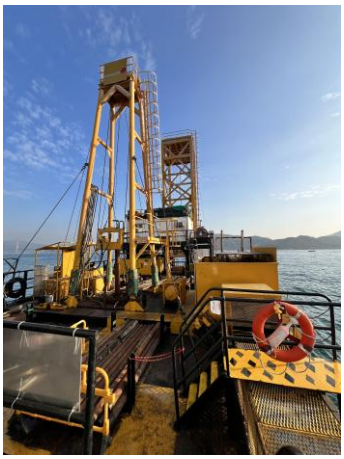

Figure 1: Ongoing ground investigation works on land and sea in Hong Kong

Figure 2: Recording data (monitoring instruments, core logging) with a classic notebook

Moreover, even as the ubiquitous AGS formats are available, industry standards vary between each practice, with versions such as 3.0, 3.1, 4.0.x and 4.1.x being the most prevalent in the recent few decades. While the AGS is primarily an American Standard Code for Information Interchange (ASCII) formatted file serving as a file database for each GI project, they can only be purposefully decoded via proprietary data management software, such as gINT or interpreted within Notepad by regular users. In some cases, tools have arisen among

geotechnical consultancies that transforms the AGS file into formats that are more legible in Excel formats, or into database that are Structured Query Language (SQL) compatible as shown in **Figure 3**. Such complex tools serve to ease the effort of extracting, transforming and loading the data into ground modelling software, where the engineering rockhead, among other resultants are generated for downstream applications, such as cross-section generation and geological interpretation.

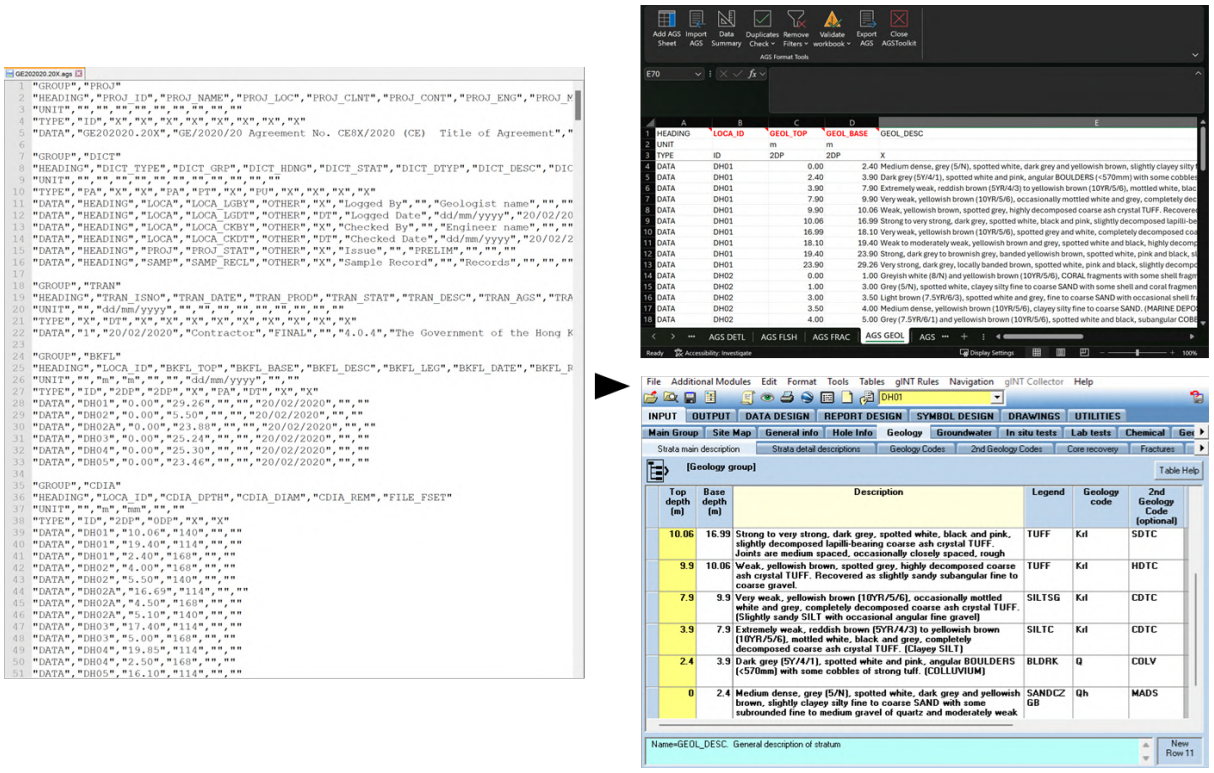

Figure 3: A sample AGS file in its raw text format (left) is transformed to Excel spreadsheets (top right) and into a gINT database

Geotechnical engineers and engineering geologists take GI data, in any form, to be valuable in expanding the geological model of the site and informing the intricacies of the ground model. Where structured forms of GI data (AGS) is unavailable, unstructured data such as borehole logs in PDF and images as shown in **Figure 4**, prevails. One can appreciate the reduction in time spent digitising and/or transforming the unstructured data into more legible formats such as in excel sheets, where digital borehole data (including its core recovery, fracture index, geological description, etc.) is presented in fine detail. Moreover, the potential for discrepancies caused by human errors during data transfer and digitising can often hinder the efficacy of a manual approach.

DRILLHOLE RECORD | HOLE No. DH03 | CONTRACT No.: | SHEET: 3 of 3

PROJECT:

METHOD: Rotary Drilling | CO-ORDINATES: E N | TASK ORDER No.:

MACHINE & No.: | DATE from: to

FLUSHING MEDIUM: Water | ORIENTATION: Vertical | SEABED LEVEL: mPD

Drilling Progress	Casing size (mm)	Water Depth at Shift Start / End	Water Return %	TCR %	SCR %	RQD %	FI	Tests	Samples No. Type Depth	Reduced Level	Depth (m)	Legend	Grade	Description
21		7.60m at 18:00 / 8.30m at 08:00	80	100	94	56	6.9			-26.25	20.00		III	18.05 - 18.20m : Moderately weak, moderately decomposed.
										-26.47	20.22		II	18.46 - 18.65m : Quartz vein (<22mm), dipping at 60°-70°.
			80	100	74	64	3.8			-27.16	20.91		III	Strong, dark grey, locally banded greyish brown, spotted yellow, white and black, slightly decomposed lapilli-bearing coarse ash crystal TUFF.
							15.4			-27.50	21.25		II	Joints are closely to medium spaced, occasionally very closely spaced, rough planar, smooth planar and smooth undulating, extremely narrow, iron oxide and manganese oxide stained, occasionally kaolin (<1mm) coated, dipping at 0°-10°, 30°-40°, 50°-60°, 70°-80° and subvertical.
22			80	100	100	95	4.2							
							7.5							20.91 - 21.25m : Moderately strong, moderately decomposed.
23			80	99	95	85	2.0							
							7.1							
24							18.2							
			80	100	90	52	8.9			-31.49	25.24			End of investigation hole at 25.24m.
25		7.70m at 18:00												

Figure 4: Sample corebox photo fresh from the field (top left) and official record taken in a warehouse (bottom left). Sample drillhole record of the corresponding drillhole on the right

1.2. Ground Modelling

Ground models synthesise lithology, geomorphology, geohydrology and structural geology to reduce construction risk, drawing heavily on invasive GI data such as drilling records, in-situ tests and laboratory results. Once consolidated and cleaned, these datasets allow geologists to interpret stratigraphy using principles like superposition and original horizontality [12]. Yet real ground conditions rarely behave as simple layered systems; expert judgement is required to delineate compressible alluvial pockets, identify corestone zones affecting foundation feasibility, or recognise fault-related structures. Increasing data density progressively reduces geotechnical uncertainty to acceptable levels for design and construction [10]. In the process of building the geological model, the 440,000 GI data points recorded in GInfo [4] forms the basis in the preliminary phase. Project-specific ground investigation data recorded via SmartLog improves the upstream data foundation and bridges the gap between field data collection and ground modelling.

2 SYSTEM DEVELOPMENT

2.1. User Requirements & Solution Overview

In the year 2023, a feasibility study was conducted for the 'Smart Logging' approach which aims to improve the efficiency of transfer of ground information between site and office teams [9]. The mobile application was built within the Microsoft ecosystem, with PowerApps as the interface on the two most common mobile operating systems i.e., iOS and Android. After a few rounds of testing with selected local GI contractors and consultants, the mobile application has proven its ability to record weathering grades and parts of the full geological description in accordance with Geoguide 3. It was concluded that the Smart Logging approach should be implemented in pilot GI contracts, thus allowing users who are specialists in their field to provide feedback and for the system developers to gain experience. The feasibility study was fruitful in a sense that the foresight of digitalising the ground information transfer process has taken its first leap.

While consolidating the user requirements, it was identified that several functionalities are readily available in a few commercial software. Subsequently, tests were performed on the available commercial off-the-shelf (COTS) software to explore their user interface and gain insights on the various design philosophies. The experience and insights gained from the tests aided in the system analysis and design process. Now, the task in hand is to develop a geotechnical data management platform, fronted by a mobile-native application, hereon referred to as SmartLog (**Figure 5**).

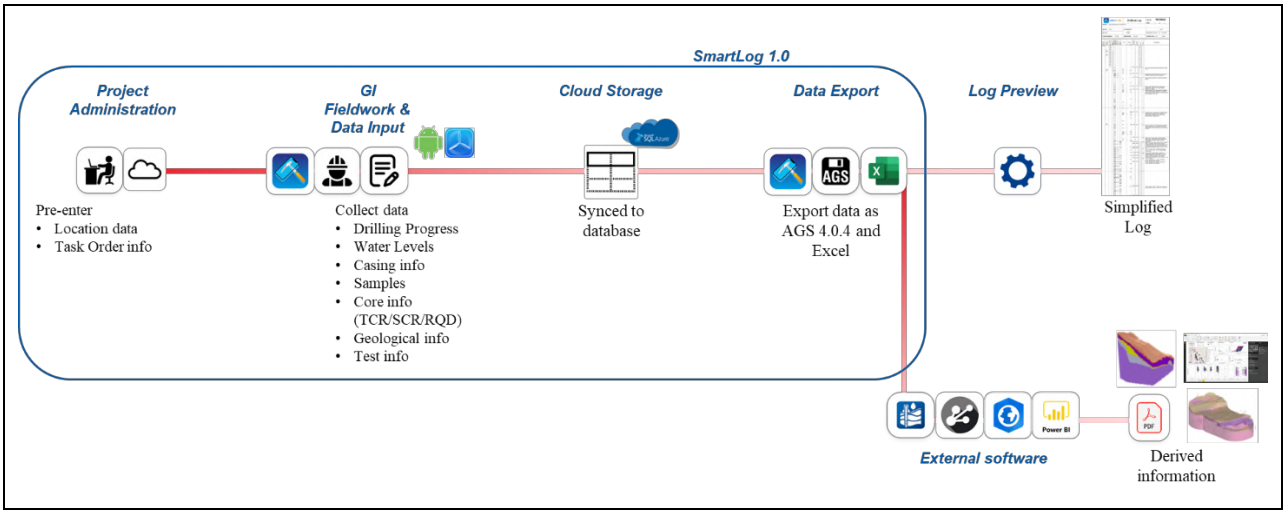

Figure 5: An overview of the SmartLog system as a solution

The requirements of SmartLog can be broken down to three parts: input, storage and output. Within the scope of the 'input' component, the relevant users in the field shall be able to record all ground investigation information that is pertinent to generating a complete AGS dataset plus photo records and digital sketches. Subsequent production of borehole/trial pit/slope stripping log can take place in external software. Furthermore, role-based access control will be enabled for project administration and user-verification purposes.

Storage of the input data shall have local and cloud upload functionalities. While Hong Kong's cellular network coverage is excellent, the application needs to be able to store GI field work data locally, within the device while disconnected. When connection to the internet is reestablished, all the cached data shall be uploaded securely to the system's server. From a version control perspective, the data with the most recent timestamp shall prevail, and is recorded along with some digital fingerprints to track edits.

As for the output component, the mobile application shall be capable of exporting corresponding borehole/trial pit/slope stripping (GI) data for each project in the AGS 4 format. This core functionality will enable a smooth workflow downstream. The potential applications include generating PDF logs as an add-on functionality or via proprietary software with client-specific libraries, informing the assessment of ground conditions and generating predictive ground models.

2.2. System Architecture

The proposed system architecture delivers a modern, cloud-native platform designed to transform ground investigation workflows into a secure, efficient, and fully digital process. The solution is engineered for mobility, resilience, and long-term maintainability, ensuring that field personnel can reliably capture and synchronise GI data across diverse site conditions.

As seen in **Figure 6**, at the application tier, the mobile client is built using React Native and utilizes native UI components and maps them to the corresponding native controls, providing better performance and user experience. This ensures a consistent interface across iOS and Android while reducing lifecycle maintenance overhead. To support field operations in remote environments, the application incorporates a local SQLite datastore, enabling uninterrupted data capture. Data will be synced back to SQL Database once the device has internet access, ensuring seamless alignment between offline and cloud datasets.

The cloud platform is deployed on Microsoft Azure using a fully serverless model. Azure Function Apps serve as the integration layer and act as a web API between cloud database and the application. These functions orchestrate authentication, project management, data synchronisation, and AGS export workflows. Structured business data resides in Azure SQL Database, while photos, videos, and generated files are stored in Azure Storage Account. All system data will be stored in the database or saved as files, with core project records retained permanently and backups maintained for 30 days.

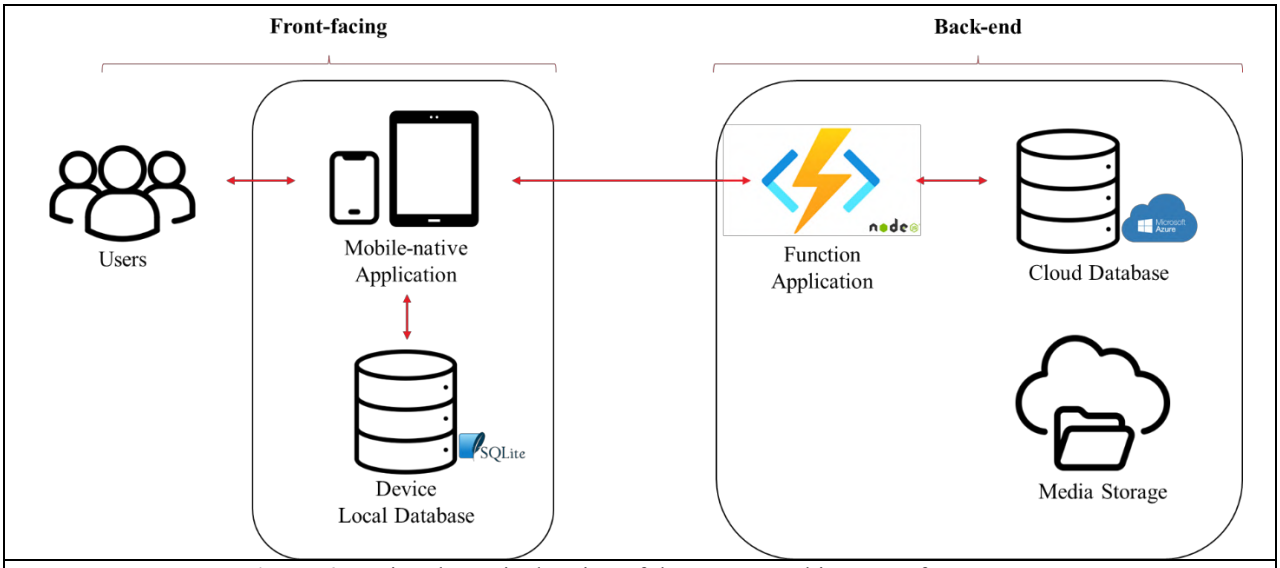

Figure 6: Basic schematic drawing of the system architecture of SmartLog

The sizing model defines a scalable and cost-efficient baseline: Function Apps provisioned with 1024MB memory and SQL Database tiers ranging from 1 to 4 vCores with up to 8GB of memory. This ensures the platform maintains predictable operational expenditure and remains performant during peak field activity of up to 160 concurrent users.

2.3. Data Model

The SmartLog data model is designed as a modern, cloud-native evolution of the data structures used in conventional ground investigation workflows. Historically, gINT's underlying Microsoft Access database management system has served as the production-level software to store and produce deliverables such as AGS files and borehole logs. While effective in its time, this legacy approach is constrained by scalability limits, prevention of multilateral data editing, and limited readiness of data extraction. SmartLog addresses some of these limitations by re-engineering the AGS schema into a fully normalised relational schema hosted in Azure SQL database as seen in **Figure 7**.

At the core of the model is AGS 4, transformed into a RDBMS in Azure SQL Server. AGS 4 provides more flexible input line lengths, stronger metadata structures for QA/QC, and better support for modern data management. Furthermore, choosing AGS 4 positions the industry for long-term interoperability, reduces ambiguity in data exchange, and allows extract, transform and load tools to be standardized across platforms. As the industry is currently using AGS 4 as the standard transmittal version, the development of SmartLog is primed to be founded on it.

The data model organises SmartLog's operational workflow into modular entities: Project, User, Drillhole, Trial Pit, Slope Stripping, GFT input, Geologist input and Media Files. Each entity reflects a distinct stage of GI activity, with discipline-specific child tables capturing driller inputs, in-situ tests, lithological descriptions, sampling records, and monitoring installations. This structure mirrors the real-world process where a borehole log contains information that is consolidated from the Daily Site Record (DSR) that is the responsibility of the driller, the in-situ test and sampling information, which is part of the GFT's duty, and geological description, which is under the geologist's purview.

SmartLog's offline-first architecture is supported by a mirrored SQLite schema on the mobile device, enabling uninterrupted field logging. Data will be synced back to the Azure SQL database once the device is connected to the internet, requiring timestamps, versioning, and conflict-resolution logic. Unstructured data such as photos, sketches, and AGS exports is stored in Azure Storage, consistent with the requirement that all system data will be stored in database or saved as files.

Data governance is embedded directly into the model. Role-based access control ensures that only authorised personnel can modify specific data categories, while audit trails and timestamping preserve the integrity of field records. Controlled vocabularies – such as GEOL legend codes and AGS 4-compliant lookup tables ensure

consistency across projects. Cloud-based retention policies preserve core project records permanently, while backups follow a defined lifecycle to balance durability and cost efficiency.

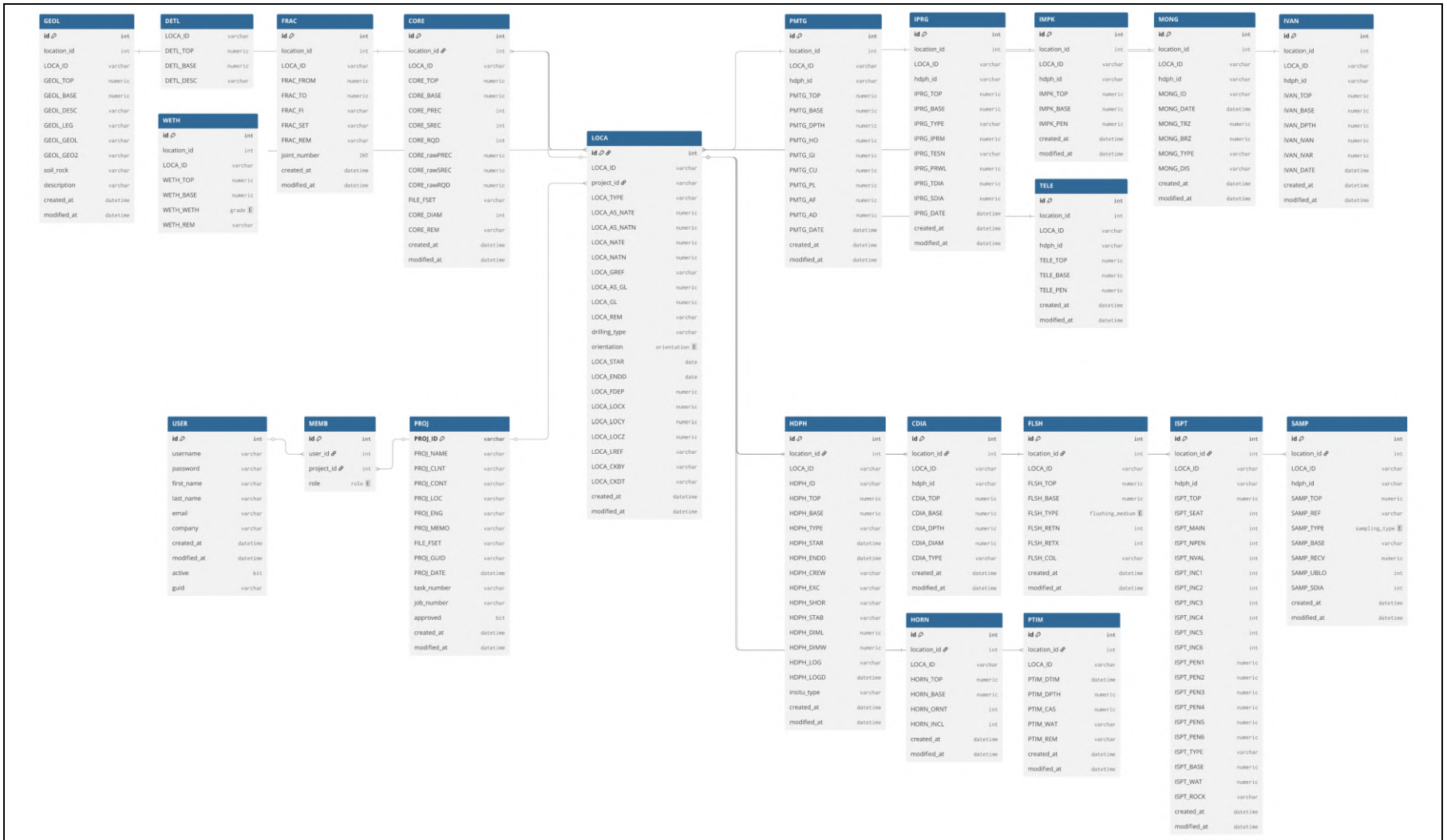

Figure 7: SmartLog database's Entity-Relationship Diagram

2.4. Development Operations

Amid developing the mobile application, periodic releases of test versions allow the product to evolve with increasing functionality and bug fixes. During this time, 7 major contractors from the Development Bureau's specialist contractor's list have been invited to participate in the Early Adopters Program (EAP). The involvement of working members within the EAP (**Figure 8**) was a true blessing for many reasons. Their valued feedback shaped the design principles adopted by the developer team in fine tuning the user interface and experience, improving the workflow and logics, and most importantly, gathering user sentiment. Furthermore, pilot contracts mandating practicing of the application encouraged the field workers to perform data input exercises in the mobile application. This allowed the product to be tested to its limits to ensure the software issues are discovered and dealt with.

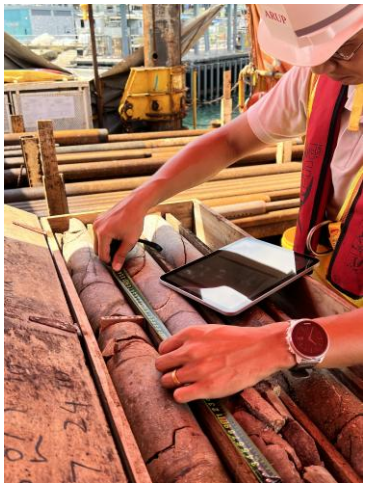
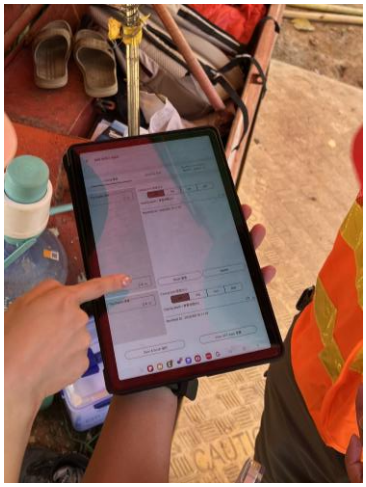

Figure 8: Using the mobile application to collect data on site

Various methods have been used to gather feedback from the EAP, the GEO, and testers within the development team. These comprised of fixed response-to-comment tables (4 to date) involving various sections of the GEO and members of the Site Investigation Committee (SIC) of the Hong Kong Construction Association (HKCA), email responses and dialogue with working members of the EAP. A sample is shown in **Table 1**, illustrating the preferred way of describing an issue with the system, and describing the expected behaviour as an instruction to the developers.

A backlog was created to ensure that the numerous feedback were correctly understood, interpreted and triaged, thus ensuring no voice is left unheard and accountability is upheld. An analysis of the interpreted feedback shows that most of the feedback (numbered at ~200 at the time of analysis) can be attributed to the datamodel, user interface and experience (UIX), among others in **Figure 9**. In due time, the issues and suggestions were prioritised for solving in the staged development process, or kept in a database, such that the suggestions can be considered for future development. Periodic releases in the form of Android Packages (APK) and TestFlight versions are used to keep track of development milestones and bug fixes. Additional user interface and experience enhancements, along with the refinement of security measures were applied to the front end of SmartLog with the assistance of Animae Technologies Limited.

Table 1: Examples of good descriptions of issues relating to the SmartLog system

Comment / Problematic Behaviour	Category	Expected Behavior
Project selection in the main menu would be better off using project no. which is assigned by individual company admin, so it will be easier to search for the job rather than the generic contract no. or name (eg. It will be troublesome if you search for a site in Tuen Mun when it returns hundreds of results)	datamodel, search	Enable text search in ID/primary key tables. Enable gallery UI of cards and include more info in each card, such as the job number, district, etc. Enable a map/location search feature?

Currently during start up, the project page can appear as empty even when there are projects that have been input prior. Allow offline mode to enter data and save in cache, and sync back when online.	datastore, cloudsync	Ensure that the project data is available upon start up even in offline environments, and the cache saves all data input by user and also imports cloud-synced data if there is data input by other users in other devices while referring to the same project/borehole. (conflict resolve) Allow 'refresh' capability in projects page when the page is 'pulled down' to show new boreholes/updates.

User_Rep	Comment/Problematic Behavior	Tags*1	Tags*2	Instructions for Developer/Expected Behavior	Urgency	Status
Contractor A	In the same run, have to move the screen up and down to enter the data, not convenient	UI		for all the pages, for driller/GFT/geologist - reduce the frame size so that everything can be fit in one, if i enter the bottom depth, i should be able to input data in the following data point without scrolling again - resize the daily water level to a smaller row, - for the daily water level, remove the delete and add button, enable swipe left to delete and an '+' button to add water level records	1	Resolved
ARUP_CS	AGS4.1.1 deprecates IPRG for permeability and replaces with FGRG (geohydraulic)	datamodel		Keep IPRG for the time being and although 4.0 to 4.1 seems like a major update, ARUP is unsure if other contractors are kept up. Maintain with 4.0.4	2	Resolved
Contractor B	not sure how to input the disturbed sample in mazier sampling	datamodel	UI	A small disturbed sample (SDS) is collected for every U76/U100/Mazier (undisturbed samples) and SPT (disturbed sample). - even disturbed samples should have their own row of data, as is usually recorded in the DSR/log with a 10cm length. - these applies to all the sampling methods above	2	Resolved
GEO	Elevation recorded is not mPD (principal datum) as it is not verified by surveyor, only based on mobile GPS	datamodel		change it to 'as-built' instead of as-build. Make it an editable field and include hint to make sure the data is based on mobile GPS. Only update manually after verified by surveyor.	1	Resolved
Contractor D	details within a lithology cannot be input	datamodel	lithology	Within geological information, for the Saprolite option, add '/Detailed Description' - sometimes there is a very short section of Grade V or completely decomposed rock say at 14.12-14.21m (usually less than 0.1m) within a Grade III or Grade IV rock section (say between 12.60m - 15.75m. We don't want to break up one description section and have to repeat it. So we insert a *detailed description* for this small section, as it is still important in our modelling.	2	Resolved
Contractor E	App starts very slowly when more data are input in the 'Fracture Index' section	UX	cloudsync	display of the depth section takes a while, we might need a major UIX revamp	2	Resolved
Contractor F	Apparently there is no centralized server to: - export the input log data from office - unable to track usage of app as per input time and ID - only local sharing via whatsapp or email linked to the phone or tablet, and on a project/task order basis, not per hole (via the pin icon)	UX	workflow	solved in web interface	1	Resolved

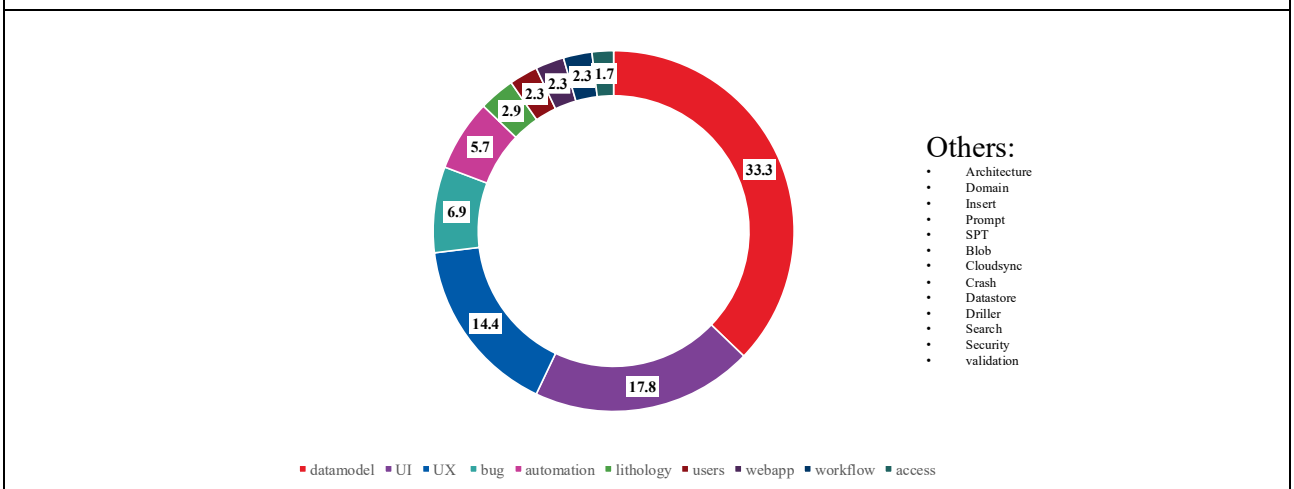

Figure 9: A snippet of the development backlog (top) and the types of issues registered from comments (bottom)

2.5. Maintenance

The long-term viability of SmartLog hinges on a maintenance strategy that is deliberate and leverages on the preceding development effort. While the initial scope focused on building the mobile application, cloud platform, and AGS-compliant data workflows, the system's transition into operational use across multiple GI contracts introduces a new set of demands. Maintenance is not an afterthought but a continuation of the system's lifecycle – ensuring that SmartLog remains stable, secure and responsive as adoption grows and the technical requirements evolve.

A key part of this strategy involved early engagement with the government through a non-technical questionnaire, designed to clarify expectations, operational priorities, and constraints. This ensured that the maintenance approach was aligned with government IT policy, the requirements of the stakeholders, and potential future applications/functionalities. As SmartLog scales to support more users and potentially migrates to government-owned infrastructure, continuity becomes a central concern. The system must remain performant under increased load, resilient to device and OS variability, and adaptable to changes in cloud hosting arrangements. To support this, a guidance note – derived from the updated System Design Document – serves as a user-facing manual that documents system behaviour, data flows, and operational procedures. This ensures that knowledge is not locked within the development team but is transferred to administrators, contractors, and future maintainers. Information relating to system setup, configuration, and operational boundaries has already been delivered to facilitate the handover.

Maintenance also extends beyond technical fixes. Promotion and engagement with the SIC have been essential in building industry confidence and encouraging adoption. As SmartLog becomes embedded in GI practice, the ability to provide technical support that resolves both known and emerging issues directly influences user trust and the system's reputation. This is paramount for field personnel, whose work depends on the reliability of the application under real-world conditions.

3 DISCUSSION

3.1. Limitations

SmartLog's development has been a rewarding climb, but as the saying goes, there's always a bigger hill to come. Building a system entirely from scratch means some ambitions naturally take longer to arrive at. Some features – most notably the ability to generate a fully formatted borehole log with a complete geological legend and unique iconography – remain on the horizon. These elements demands both technical finesse and harmonized standardisation, especially on the unification of geological codes and abbreviations. While it remains on the roadmap, the team has focused first on ensuring that the core data capture and synchronisation workflows are robust and dependable.

The journey has also been shaped by the people who log boreholes every day. Their experience revealed nuances and micro-workflows that only emerge through years of field practice – details that early system designs simply could not have anticipated. These lessons highlighted where the initial approach did not fully capture the end-to-end process, but they also opened the door to meaningful refinement. By embracing the principles of total design, SmartLog is now incorporating previously overlooked steps and stitching together a more inclusive and intuitive workflow. The limitations that remain serve as reminders that digital transformation is a journey – one that improves as more voices, insights and real-world experience shape the path forward.

3.2. Strengths

The process of developing SmartLog has revealed its greatest strength, in how it has brought the industry together around a shared language and workflow. By aligning terminology and structure, SmartLog helps ensure that everyone is working within a single, coherent framework. This alignment has also encouraged industry players to look beyond their traditional siloes and recognise the value of collaboration within the ecosystem. Instead of isolated steps handled by separate teams, SmartLog is the foundation that serves to link entire chain of GI activities, making data more accessible, more consistent and far easier to reuse. The platform's modern data management approach breaks down barriers that once limited visibility and replaced them with a system designed for clarity, interoperability and shared understanding.

3.3. Potential Applications

The interim use of OCR for Daily Site Records in tandem with the development of SmartLog assists in the capture of key data points from the current local GI workflow. Further work is needed to attentively learn the challenges and requirements of drillers and the local industry as we support the gradual shift from handwritten routines to digital-first practices. Once adopted, this unified data stream strengthens the entire GI workflow by ensuring that field observations, test results, and daily records flow consistently into downstream interpretation,

modelling, and reporting activities. With consistent terminology and structured inputs, SmartLog becomes a reliable foundation for ground model generation, geotechnical analyses, and the eventual production of drilling, pit and stripping logs that complete the GI cycle.

Furthermore, the system's dynamic data flow also creates opportunities for more responsive project oversight. Real-time dashboards can support progress monitoring, highlight anomalies, and provide early signals of delays or unexpected ground conditions. As the dataset grows, SmartLog can support a new generation of data-driven storytelling – summaries of lithologies, engineering rockhead trends, or potential corestone distributions presented in groundbreaking ways. One of the principal uncertainties in geotechnical engineering is the risk of encountering unexpected geological conditions, and this is where a dedicated GI planning tool becomes valuable. By drawing on existing information and updating continuously as new data is collected, such a tool can help close gaps in geological understanding, guide designers in anticipating likely subsurface scenarios, and ensure that the investigation captures the parameters required for design. This alignment between planning and real-world conditions ultimately supports more efficient, value-engineered outcomes. These applications remain grounded in practicality, but they hint at a future where GI data is not only captured efficiently but also communicated with greater clarity and insight.

4 CONCLUSION

By putting people first and process second, the digital design behind SmartLog has been able to adapt to the intricate and user-centric requirements of ground investigation workflows. This initiative stems from a government-driven digitalisation of processes while embracing and supporting the culture embedded within the local industry. At present, the SmartLog ecosystem lowers the adoption barrier for new ground investigation contracts and contractors. In the future, more data will become available on a platform that is faster to access and use, and people can find better insights and drive better decisions to reduce geotechnical risk.

ACKNOWLEDGEMENT

This paper is published with the permission of the GEO, CEDD and the Development Bureau of the Government of HKSAR. All interpretations, conclusions and final editorial decisions remain solely those of the authors.

REFERENCES

Arup Hong Kong Limited (2023) System Analysis & Design Report for the Development of Mobile App. Final 1, 16 November 2023. Prepared for the Geotechnical Engineering Office under Agreement No. CE 87/2022 (GE). Report reference: REP/294697/ST03/SADR002. Hong Kong: Arup. (Unpublished internal report).

Association of Geotechnical and Geoenvironmental Specialists (AGS) (2017) Electronic Transfer of Geotechnical Data, 4th Edition: Addendum 4. UK: AGS.

Civil Engineering and Development Department (CEDD) (n.d.) Guidance Notes on Submission of GI and LT Reports in Digital Format.

Civil Engineering and Development Department (CEDD) (2025) GI Location [GIS dataset]. Hong Kong SAR Government. Available at: https://ginfo.cedd.gov.hk/server/rest/services/Overlay/QuickView/ MapServer/2 (Accessed: 3 January 2026).

Hong Kong Lands Department (2023) Digital Topographic Map 1:5000 [GIS dataset]. Hong Kong SAR Government. Available at: https://www.landsd.gov.hk (Accessed: 18 March 2026).

Geotechnical Engineering Office (GEO) (2017) Geoguide 2: Guide to Site Investigation. Hong Kong SAR: Civil Engineering and Development Department.

Geotechnical Engineering Office (GEO) (2017) Geoguide 3: Guide to Rock and Soil Descriptions. Hong Kong SAR: Civil Engineering and Development Department.

Lai, A.C.S., So, A.C.T. & Mok, S.C. (2019) AGS Data – Subsurface Data in Digital Format in Hong Kong. Proceedings of the HKIE Geotechnical Division 39th Annual Seminar: Transformation in Geotechnical Engineering – Technology, Digital and Innovation, pp. 78–83.

So, A.C.T., Wong, L.N.Y. & Ho, T.Y.K. (2023) Smart Logging – An Innovative Approach for Generation of Digital Subsurface Data. Proceedings of the HKIE Geotechnical Division Annual Seminar 2023, pp. 62–69.

Wong, D., Chan, K., Ma, T., Lui, D. and Lun, S. (2023). *A BIM-Integrated Ground Modelling Approach for Fast-Paced Infrastructure Projects: A Case Study from Siu Ho Wan Depot Property Development*. The CIE-HKIE-IEM Tripartite Seminar, Taipei, Taiwan.

Wong, H.N. (2009) Rising to the Challenges of Natural Terrain Landslides. Geotechnical Engineering Office, Civil Engineering and Development Department, HKSAR.

Wong, Y. (2026) Fundamentals of 3D Ground Modelling – Geological Case Study of HSITP. Ove Arup & Partners Hong Kong Ltd. (Unpublished)

Yuen, D. (2009) General Practice of Ground Investigation Works in Hong Kong Special Administrative Region. Geological Society of Hong Kong Bulletin No. 8.

Exploring a Cost-Effective and Sustainable Design Solution for Rock Tunnels in Hong Kong – the Rock Reinforcement Approach (RRA) and Norwegian Method of Tunnelling (NMT)

Franklin K. L. To & Clayton Y. K. Chan
AECOM Asia Company Ltd., Hong Kong, China

Nick R. Barton
Nick Barton & Associates, Oslo, Norway

ABSTRACT

High construction costs for rock tunnels remain a major concern in Hong Kong, highlighting the urgent need for more cost-effective and sustainable design solutions for major public infrastructure, including underground highways and railway systems. Conventionally, the New Austrian Tunnelling Method (NATM) has been widely adopted in Hong Kong and is often preferred by project clients. NATM typically employs a double-shell support system comprising temporary sprayed concrete and rock dowels as first support, followed by a secondary cast-in-situ plain or heavily reinforced concrete lining. Under the favourable hard rock conditions often encountered in Hong Kong, the NATM approach is inefficient to fully utilize the inherent strength of the rock mass and imposes in increased construction costs and extended programme durations.

In contrast, the Norwegian Method of Tunnelling (NMT), commonly referred to the Rock Reinforcement Approach (RRA) in Hong Kong, adopts a reinforced rock mass philosophy through the use of permanent systematic rock bolts and single-shell sprayed concrete linings. In recent years, the NMT/RRA has been successfully implemented in pilot government cavern projects, notably the Relocation of Sha Tin Sewage Treatment Works to Caverns and the Joint Cavern Development at Anderson Road Quarry Site. Building upon these successful applications, NMT/RRA presents a viable alternative design methodology for achieving improved economy while maintaining structural safety and durability. In addition to cost and programme benefits, the approach offers opportunities to address long-term performance considerations including durability, waterproofing strategy, fire resistance, monitoring, and maintenance.

This paper explores the wider application of NMT/RRA as a cost-effective and sustainable design solution for future road and railway tunnels in Hong Kong. The discussion is also supported by the successful examples in China and overseas.

1 INTRODUCTION

1.1 Rock Tunnel Development in Hong Kong

Hong Kong is characterised by steep natural terrain, extensive rural areas, and large statutory protected zones including country parks and restricted areas. These geographical and regulatory constraints have significantly limited available land for development. As a result, urbanisation has historically expanded from foothills towards reclaimed shorelines, forming a linear and highly constrained development pattern. To connect these built-up areas, transport infrastructure has been developed in the form of at-grade roads, viaducts, and underground tunnels. While at-grade road construction is traditionally perceived as simpler and less expensive, it often requires extensive site formation works, land acquisition, and the installation of large-scale noise mitigation structures. In contrast, underground tunnels can provide shorter and direct alignments, reduced disruption to surface lands, lower visual and noise impact to the surrounding neighbors.

Geologically, more than 80% of Hong Kong's rock mass consists of hard and massive igneous formations, including granite and volcanic rocks. These competent rock conditions provide favourable circumstances for underground space development, including transportation tunnels and large-span caverns. Conventionally, rock tunnels in Hong Kong are temporarily supported by a thin layer of shotcrete with rock dowels immediately after excavation. Permanent support is subsequently provided by cast-in-situ plain or reinforced concrete lining. This double-shell support philosophy is generally referred to as the New Austrian Tunnelling Method (NATM).

In recent years, HKSAR government departments have led rock cavern development in Hong Kong and explored an alternative single-shell support philosophy. Successful projects, including the Drainage Services Department (DSD)'s Relocation of Sha Tin Sewage Treatment Works to Caverns and the Civil Engineering and Development Department (CEDD)'s Joint Cavern Development at Anderson Road Quarry Site, have adopted the Rock Reinforcement Approach (RRA), which integrates permanent rock bolts and permanent shotcrete to form a reinforced rock arch as the final structural support system. Internationally, this philosophy aligns with the Norwegian Method of Tunnelling (NMT). These successful local cases demonstrate the feasibility of utilising the inherent strength of competent rock masses, rather than the heavy secondary concrete linings.

1.2 Conventional Practice in Hong Kong – the New Austrian Tunnelling Method (NATM)

For overseas projects, NATM is most appropriate for soft/mixed-ground and shallow rock cover tunnels. It is based on descriptive classification of weaker rock masses, the application of additional temporary load-bearing structures (e.g. canopy roofs, steel ribs/lattice girders), and deformation monitoring under the observational approach to satisfy ground reaction principles.

Under conventional and conservative NATM practice in Hong Kong for hard-rock tunnels, two structurally independent (i.e. double-shell) support systems are installed during construction. Temporary support typically consists of rock dowels and a thin layer of sprayed concrete applied immediately after excavation. Permanent support is subsequently installed in the form of cast-in-situ plain or reinforced concrete lining. A waterproofing membrane system, commonly comprising geotextile and sheet membrane, is installed between the temporary shotcrete and the permanent lining. Although this approach provides a conservative and robust solution, it does not fully utilise the inherent load-bearing capacity of competent rock masses, particularly under favourable geological conditions.

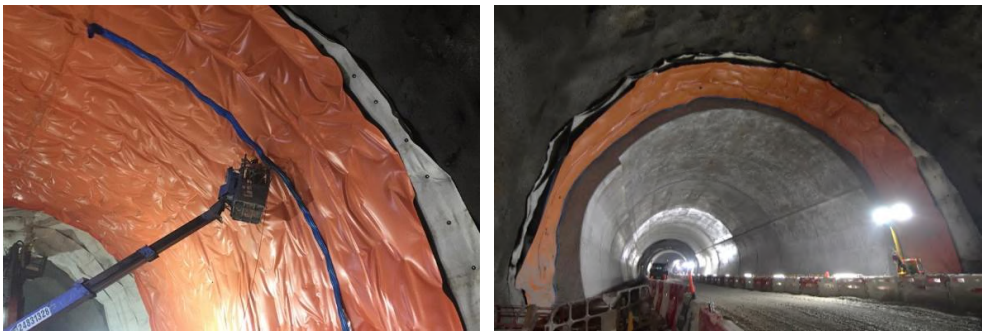

Figure 1: Conventional NATM Cast-in-situ Concrete Lining with Sheet Waterproofing Membrane

1.3 Norwegian Method of Tunnelling (NMT) and the Rock Reinforcement Approach (RRA)

The Norwegian Method of Tunnelling (NMT) adopts a fundamentally different philosophy compared with NATM. Instead of separating temporary and permanent supports, NMT integrates rock reinforcement elements (i.e. rock bolts and shotcrete lining) into a single-shell system. The surrounding rock mass, when properly reinforced, forms a load-bearing rock arch that carries the majority of applied loads.

In Hong Kong, this philosophy is referred to as the Rock Reinforcement Approach (RRA). Under RRA, permanent systematic rock bolts provide confinement and enhance the thrust capacity of the rock mass, while sprayed concrete lining stabilises local wedges between bolts and provides surface protection. The combined system functions as both temporary and permanent support. The applicability of RRA depends strongly on rock mass quality, structural discontinuities, groundwater conditions, and long-term durability considerations. Recent cavern projects in Hong Kong have successfully demonstrated its feasibility, providing a basis for broader application to road and railway tunnels.

Figure 2: Installation of Permanent Systematic Rock Bolts as Primary Support System

2 DESIGN CONSIDERATIONS IN HONG KONG

2.1 Overall Design Philosophy based on Recent Cavern Projects in Hong Kong

Conventional cast-in-situ concrete lining in NATM is inefficient for hard rock tunnels, as it does not utilise the inherent strength of the rock mass. It also involves redundant temporary support, bulky formwork systems, and extensive reinforcement works. Therefore, a rock reinforcement design approach is considered more suitable and sustainable in terms of cost and material efficiency.

Permanent rock reinforcement in hard rock caverns comprises rock bolts and sprayed concrete. Rock bolts act as primary supports to form the reinforced rock arch, while sprayed concrete stabilises wedges between bolts. The inherent strength of the rock mass is mobilised through confinement provided by the bolts, thereby increasing thrust capacity and forming a stable rock arch. Spot bolts are installed as required to stabilise identified wedges. Permanent rock bolts serve both immediate construction support and long-term structural functions.

The following three-stage design procedure for Rock Reinforcement Approach (RRA) has been established for pilot government cavern projects in Hong Kong and reviewed by relevant government authorities:

(i) Derivation of initial support using the empirical Q-system
(ii) Checking using the reinforced rock arch theory to consider the thrust capacity of the rock arch reinforced by permanent systematic rock bolts; and
(iii) Verification using numerical analyses (e.g. Discrete Element and Finite Element Modelling) to refine the permanent support requirements

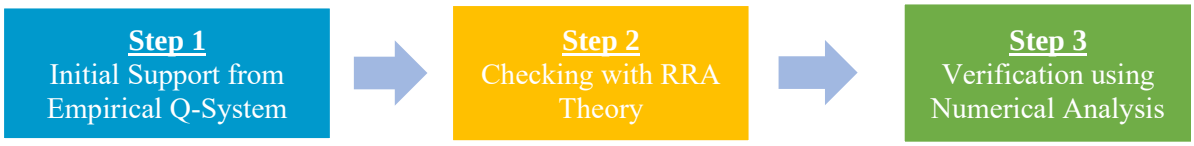

Figure 3: Three-stage Design Procedures for RRA established in Hong Kong

2.2 Initial Support from Empirical Q-system

The empirical Q-system for rock mass classification and its relationship to tunnel support was first developed by Barton et al. (1974) and later updated by Grimstad & Barton (1993) at the Norwegian Geotechnical Institute (NGI), Norway. It has since been refined using more than 2,000 case histories from underground openings, incorporating advancements in construction technology. The Q-system is widely adopted in Hong Kong to assess rock mass quality, estimate rock support pressure, and determine support requirements for hard rock excavations. The Q-value is defined as the product of six rock mass parameters, as shown in Equation 1:

$$Q = \frac{RQD}{J_n} \times \frac{J_r}{J_a} \times \frac{J_w}{SRF} \quad (1)$$

(i) Rock Quality Designation RQD
(ii) Joint Set Number J_n
(iii) Joint Roughness Number J_r
(iv) Joint Alteration Number J_a
(v) Joint Water Reduction Factor J_w
(vi) Stress Reduction Factor SRF

The first component (RQD / J_n) describes the relative block size or degree of fracturing of the rock mass. The second component (J_r / J_a) describes the inter-block shear strength of discontinuities. The third component (J_w / SRF) reflects in-situ stress conditions and the influence of groundwater within joints surrounding the excavation.

The Q-value provides an indication of the stability of an underground opening in jointed rock masses. High Q-values indicate good stability, whereas low values indicate poor conditions. The Q-system, together with the Excavation Support Ratio (ESR) and excavation size, is used to determine required support measures such as rock bolt spacing and shotcrete thickness.

The factor of safety depends on the intended use of the tunnel. For example, a highway or railway tunnel carrying heavy traffic requires more stringent safety criteria than a sewage tunnel with limited maintenance access. This is accounted for through the ESR and excavation dimensions (span and height). In general, larger excavations require more support. For a given Q-value and Equivalent Dimension, the required support class, including bolt spacing and shotcrete thickness, can be obtained.

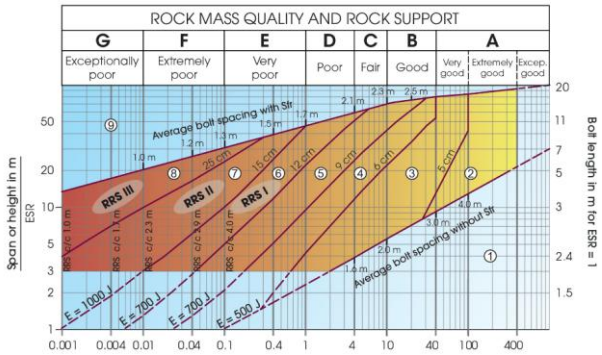

Figure 4: The latest Q-system rock support chart (NGI, 2022)

The empirical formula proposed by Barton et al. (1977), as cited in Geoguide 4 (2018), can be used to determine the initial systematic rock bolt length as presented in Equation 2. This is appropriate for systematic support, but may not be sufficient bolt length for potential rock wedges, which need to be assessed separately.

$$L = 2 + \frac{0.15\,B}{ESR} \qquad (2)$$

where L = bolt length (in m)
B = tunnel span for roof support (tunnel height H for wall support) (in m)
ESR = excavation support ratio (safety requirement)

For local practices in Hong Kong, additional checking are required for large-span excavation and to study the influence of multiple parallel excavations.

2.2 Checking of Support with Reinforced Rock Arch Theory

From structural mechanics, an arch is a structural member that transmits loads primarily through axial compressive thrust to its supports at two ends. This concept is widely applied in bridges and dams. According to Bischoff and Smart (1977), the thrust capacity of the rock arch is determined by the ratio of unconfined compressive strength to tensile strength with the confinement pressure by rock bolts.

The systematic rock bolt force F_b provides confining pressure to contribute the thrust capacity ΔT_A (half span of opening) as given by Equation 3. The inherent rock mass strength is utilised to form the reinforced rock arch.

$$\Delta T_A = \frac{\sigma_c}{\sigma_t} \times \frac{F_b}{S^2} \times (L - S) = tan^2\left(45^o + \frac{\emptyset}{2}\right)\frac{F_b}{S^2}(L - S) \qquad (3)$$

where σ_c = unconfined compressive strength of rock σ_t = tensile strength of rock
ϕ = the rock mass friction angle

The empirical relationship of Q-system to rock loadings were first developed by Barton et al. (1974) and further updated by Grimstad & Barton (1993). The tunnel support pressure at crown (P_{roof}) can be estimated using Equation 4. In Hong Kong, it is a standard practice the check the thrust capacity of the reinforced rock arch ΔT_A against the rock pressure at crown (P_{roof}) at the springline as illustrated in Figure 5.

$$P_{roof} = \frac{0.2\ J_n^{1/2}\ Q^{-1/3}}{3\ J_r} \quad \text{(MPa)} \qquad (4)$$

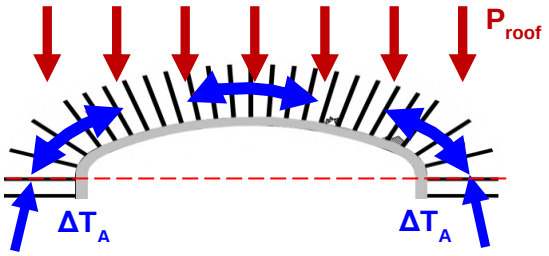

Figure 5: Checking of thrust capacity against rock pressure at crown

The permanent shotcrete lining is treated as a thin shell and checked against potential failure modes, including adhesive, flexural, shear, punching, compressive, and tensile failures (Barrett & McCreath, 1995) as illustrated in Figure 6. The required thickness is also governed by the stability of potential wedges between adjacent bolts.

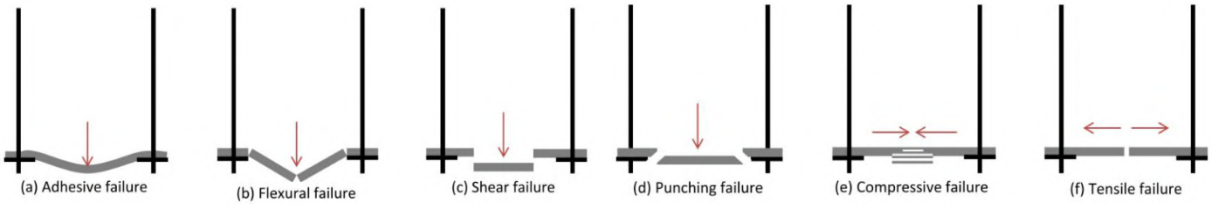

Figure 6: Six failure modes of shotcrete lining between bolts (modified from Barrett and McCreath 1995)

2.3 Verification using Numerical Analysis

The empirical and analytical designs can be further verified using numerical modelling. Both Discrete Element Modelling (DEM) and Finite Element Modelling (FEM) can be adopted to simulate rock mass behaviour and rock bolt performance.

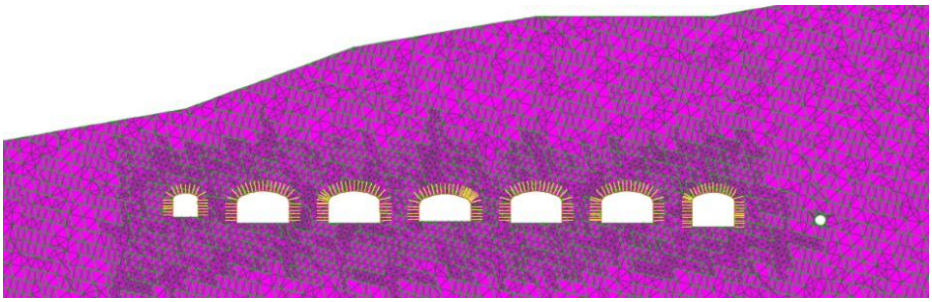

Figure 7: An example of DEM analysis for a cavern project in Hong Kong

The proposed rock supports, derived from the empirical Q-system and RRA theory, are then incorporated into the numerical models to evaluate stress redistribution, rock mass deformation, axial forces in rock bolts, and shotcrete performance. Permanent rock bolts and shotcrete are checked against their design capacities and refined as necessary. Numerical analyses are particularly important for assessing large-span caverns, interaction between parallel excavations, and stress redistribution under staged excavation.

2.4 Reference from National Standard in China

The Specifications for Design of Highway Tunnels — Volume 1: Civil Engineering (JTG 3370.1-2018), issued by the Ministry of Transport of the People's Republic of China, govern the planning, design, and structural requirements of highway tunnels within the national road network.

According to Table P.0.3, permanent rock bolts and shotcrete lining are proposed for rock with weathering Grades I to III. The support requirements are classified by tunnel functional category, including pedestrian and vehicular cross passages and dual two-lane vehicular tunnels. The parameters primarily cover shotcrete thickness, rock bolt diameter and length, bolt spacing, and, where required, steel mesh reinforcement.

P. 0. 3 采用喷锚支护作久支护时设计参数可按表 P. 0. 3 取值。

表 P. 0. 3 喷锚永久支护设计参数表

围岩级别	Ⅰ	Ⅱ	Ⅲ
人行通道	喷混凝土 5cm	喷混凝土 5cm	①喷混凝土 6～8cm ②锚杆 Φ22，长 1. 0～2. 0m
汽车横通道	喷混凝土 5cm	①喷混凝土 5cm ②锚杆 Φ22，长 1. 5～2. 0m ③间距 1. 0×1. 0m	①喷混凝土 8～10cm ②锚杆 Φ22，长 2. 0～2. 5m ③锚杆间距@1. 0×1. 0m
两车道隧道	喷混凝土 5cm	①喷混凝土 5～8cm ②锚杆 Φ22，长 2. 0～2. 5m ③锚杆间距 1. 2×1. 2m	①混凝土 8～15cm ②锚杆 Φ22，长 2. 0～3. 5m ③锚杆间距@1. 0×1. 0m ④钢筋网 Φ6. 5，@25×25cm

注：Ⅳ～Ⅵ级围岩，地质软弱、破碎，一般多地下水，宜采用复合式衬砌。

Figure 8: Extract of Table P.0.3 from China's National Standard (JTG 3370.1-2018)

For rock with weathering Grades IV to VI (i.e. saprolite and residual soil in Hong Kong), composite tunnel lining is recommended due to the weaker strength, higher degree of fracturing of the ground, and the presence of significant groundwater inflow.

4 CONSTRUCTION CONSIDERATIONS IN HONG KONG

4.1 Construction Time

For conventional NATM tunnelling, cast-in-situ plain/reinforced concrete lining with a sheet waterproofing membrane is commonly used as permanent support. This involves lengthy works and significant allocation of resources for waterproofing, concreting at the kicker, erection of rebar gantries, rebar fixing, installation of lining shutter formwork, and erection of stop-end formworks. Based on local site experience, each of these preparatory activities can add an additional working period on the order of 2 weeks to 2 months. Approximately 3 months are typically required to set up these works before achieving the first concrete lining pour after commencement of lining works.

Alternatively, the RRA/NMT method integrates temporary and permanent rock bolts, thereby simplifying the drill-and-blast cycle. Compared with the use of frictional dowels in NATM, the use of fully grouted permanent rock bolts in RRA/NMT has minimal impact (approximately 0–0.5 day) on the daily blasting cycle. Shotcreting can commence before the completion of blasting works and has minimal impact on site traffic logistics compared with rebar fixing and shuttering works. Shotcrete spraying machines significantly reduce the need for formwork and reinforcement activities, while also lowering safety risks associated with working at height.

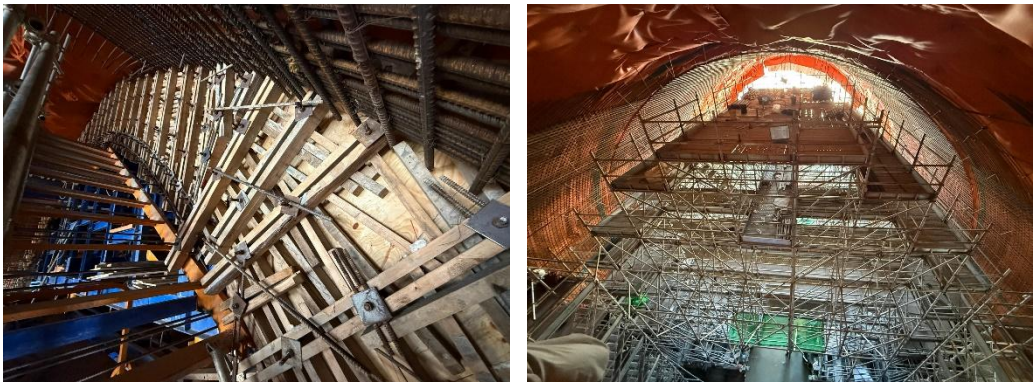

Figure 9: Massive Stop-end Formworks and Rebar Fixing Platforms for NATM Cast-in-situ Lining Works

4.2 Construction Cost and Carbon Footprint

When comparing the construction cost of RRA/NMT with conventional NATM in competent rock conditions, the principal cost savings arise from the elimination of the secondary lining and the associated reduction in material usage. There are significant reductions in concrete volume required for overbreak backfilling, as well as reductions in steel reinforcement and temporary works. This can significantly reduce both construction cost and programme duration.

Nevertheless, the use of RRA/NMT also involves a higher demand for workmanship, including the employment of certified nozzlemen. Shotcrete rebound must also be considered (approximately 20-30% based on local experience and less than 10% in Scandinavia). The use of specialised sprayed concrete mixes may be more expensive than conventional cast-in-situ concrete on a per m^3 basis.

The installation of permanent lining in NATM requires heavy steel shutters and formwork systems, extensive reinforcement fixing, and staged concrete pouring. This process is labour-intensive and time-consuming, and introduces additional safety risks associated with working at height. Based on international experience, the construction cost associated with NATM can be an order of 4 to 5 times higher than NMT. Overbreak further contributes significantly to cost due to concrete backfilling and associated risks in volume control.

4.3 Quality Supervision and Site Safety

For conventional NATM, the extent of complex and high-risk construction activities associated with cast-in-situ lining is obviously much greater than that for RRA/NMT (with possible cast-concrete sections only through major fault zones), thereby increasing the need for site supervision. For waterproofing works, supervision includes heat welding and extensive air-tightness testing. For rebar fixing, it includes installation of rebar anchors through the waterproofing membrane, rebar fixing, review of bar bending schedules, and checking of concrete cover. The assembly of shutter systems involves lifting heavy steel and formwork components, while concreting in such complex environments requires extensive steel working platforms.

In addition, cast-in-situ lining works involve significantly more working at height and heavy lifting within confined space environments. These are among the most critical safety concerns contributing to construction-related accidents in recent years in Hong Kong. Eliminating these redundant works, and hence the associated risks, aligns with the principle of “design for safety”.

4.4 Internal Structures

Where NMT/RRA is adopted, with the omission of a tunnel lining and associated corbel structures, the use of overhead ventilation ducts (OHVD) slab becomes more challenging. Additional concrete footings and columns may be required to support the OHVD and internal concrete slab structures. Precast structures could be a possible solution to this issue. Alternatively, the use of jet fans and permanent anchorage systems into the rock mass may be explored, which could also reduce the need for extensive ventilation buildings.

5 DURABILITY CONSIDERATIONS IN HONG KONG

5.1 Design Life and Durability of Permanent Rock Support System

For civil infrastructure, including highway and railway tunnels in Hong Kong, a design life of 120 years is typically adopted. For conventional NATM cast-in-situ lining, durability is achieved by providing sufficient concrete cover to the steel reinforcement. This introduces additional requirements for crack width control and serviceability, and results in increased quantities of steel reinforcement.

For NMT/RRA, the long-term durability of permanent rock bolts is achieved through the use of proprietary rock bolts with specific corrosion protection measures, such as special coatings (e.g. hot-dip galvanised or epoxy-coated) and plastic sheathing, together with full grouting to ensure bond strength and durability. For shotcrete, according to ITA WG12 and ITAtech (2014), Section 7.3.4 "Durability of reinforcement", the design philosophy for permanent sprayed concrete aims to avoid steel reinforcing bars wherever possible. This minimises corrosion risk, as steel fibres do not corrode when embedded in concrete, and macrosynthetic fibres are resistant to corrosion under most exposure conditions.

Figure 10: Workmanship control for permanent shotcrete (left) and proprietary rock bolts with corrosion protection (right)

5.2 Waterproofing Performance

For hard rock conditions, tunnel structures are typically designed as drained systems, incorporating groundwater pressure relief measures to prevent long-term build-up of hydrostatic pressure. For tunnelling in hard rock without causing significant impact to sensitive receivers or existing structures, the allowable groundwater inflow criterion in Hong Kong during construction is generally relaxed to 50 L/min/100 m.

Undoubtedly, the use of continuous sheet waterproofing membranes in NATM provides effective waterproofing performance. However, the drainage fleece and membrane installed behind the final cast-in-situ concrete lining result in a costly tunnelling solution. For permanent rock reinforcement systems, waterproofing can be achieved through probing and pre-excavation grouting, installation of localised drainage strips to divert groundwater, or the application of sprayed waterproofing membranes in conjunction with successful pre-injection that provides controlled groundwater inflow. In general, post-grouting after excavation is difficult and relatively ineffective in controlling groundwater inflow.

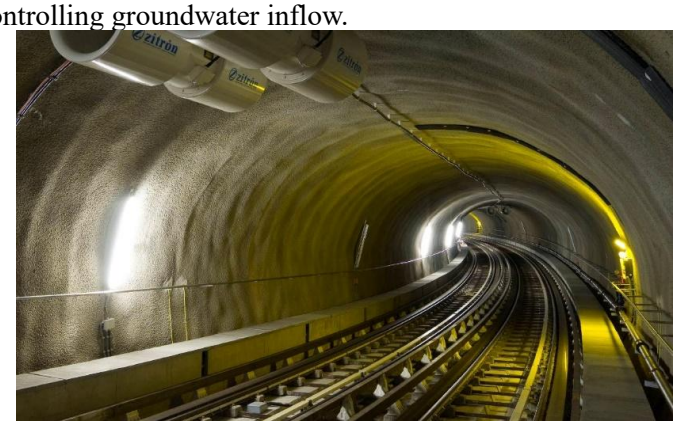

Figure 11: Photo of dry single-shell tunnel example – Lausanne Metro, Switzerland

Experience from Norway provides an alternative approach through systematic pre-grouting in cases where groundwater inflow is critical. Instead of 50 L/min/100 m as commonly adopted in Hong Kong, inflow can be reduced to approximately 5 L/min/100 m, or even 1–2 L/min/100 m. The typical range of grout consumption in pre-injected tunnels in Norway is about 1 to 5 litres/m³, assuming an average 5 m thick cylindrical zone of surrounding rock is treated according to Barton and Roald, 2023. Effective pre-injection requires appropriate grout materials and additives, suitable injection pressures, and proper control procedures to prevent hydraulic fracturing while allowing controlled joint opening where necessary.

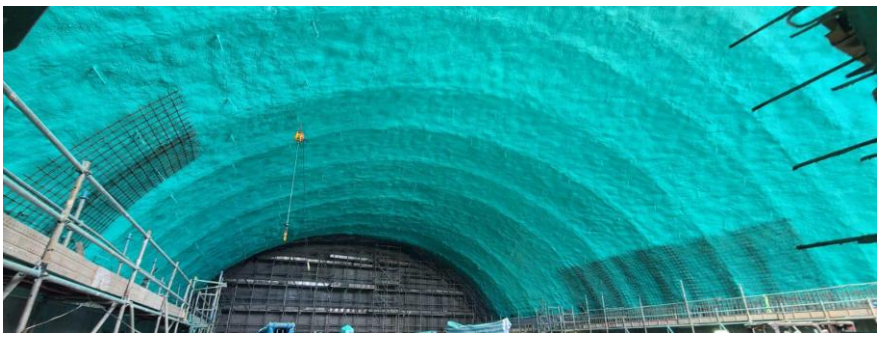

Figure 12: Application of Sprayed Waterproofing Membrane for a highway tunnel project in Hong Kong

In addition, pre-grouting can significantly improve the quality of the surrounding rock mass by enhancing several parameters in the Q-system classification. Based on overseas tunnelling experience, a rock mass with initial parameters of RQD = 30, Jn = 9, Jr = 1, Ja = 2, Jw = 0.5, and SRF = 2.5 (i.e. Q = 0.3) may improve after pre-grouting to RQD = 50, Jn = 6, Jr = 2, Ja = 1, and Jw = 0.66. The corresponding Q-value may increase to approximately 4.4. This conservative demonstration that pre-grouting can enhance the Q-value by more than an order of magnitude (Note that the most permeable joint set with Jr/Ja = ½ has been preinjected and set No. 2 (with Jr/Ja 2/1) is now the least favourable for Q-value estimation), thereby improving the self-supporting capacity of the rock mass and reducing the demand for permanent rock support.

5.3 Fire Safety Requirements to Permanent Rock Supports

Permanent rock reinforcement systems must satisfy fire resistance requirements. A prescriptive approach has been adopted in recent cavern projects, rather than directly applying fire loading in structural analysis. Under RRA, systematic rock bolts serve as the primary support, while the shotcrete lining acts as secondary support. Similar to reinforcement in conventional reinforced concrete, the temporary shotcrete (minimum 50 mm thick) and permanent shotcrete lining (typically 150–300 mm thick) also provide protective cover to the rock bolts, reducing the risk of damage under fire exposure. To further reduce the risk of concrete spalling under fire, monofilament polypropylene fibres (approximately 1–1.5 kg/m³) are incorporated into the shotcrete mix, with reference to HyD BS/GN/046 for tunnel structures with a 120-year design life and a 4-hour fire resistance rating.

An example of fire resistance test results in accordance with BS 476: Part 20: 1987 + Amd. 6487 + Corr.1:2014 to assess integrity and insulation performance was presented. The furnace temperature was monitored by six thermocouples, while the unexposed surface temperature was measured using five thermocouples. The specimen satisfied the integrity requirements after 241 minutes of heating, as shown in Figure 13.

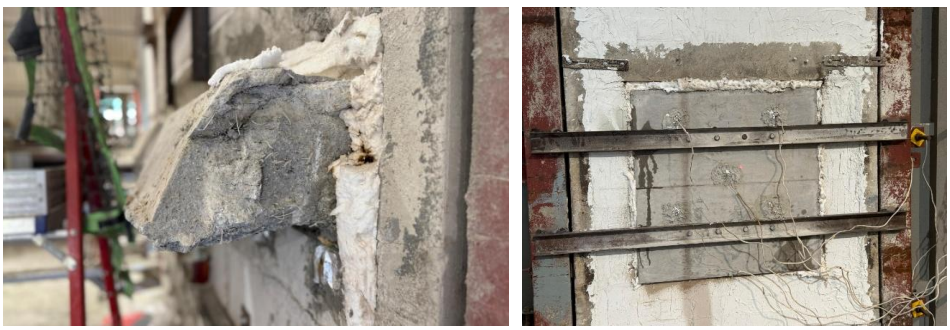

Figure 13: Shotcrete samples (after the fire test) for a recent cavern project in Hong Kong

5.4 Instrumentation & Monitoring

The long-term performance of RRA systems can be ensured through the use of monitoring arrays as illustrated in Figure 14 for deformation, bolt load, and groundwater conditions. Instruments can be embedded within the shotcrete layer, allowing for efficient data collection through wireless monitoring systems.

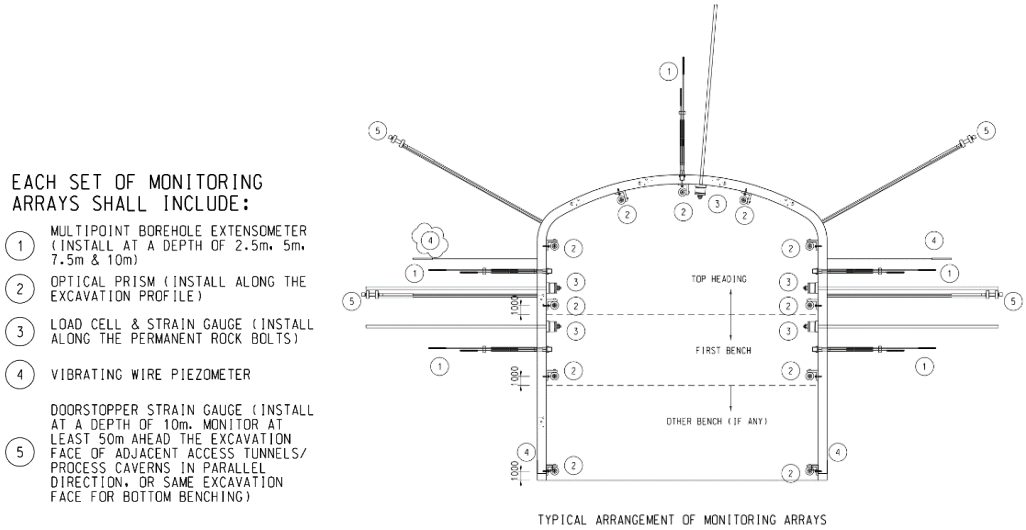

Figure 14: Monitoring Arrays for RRA

6 PROJECT REFERENCES FOR RRA/NMT IN HIGHWAY & RAILYWAY TUNNELS

6.1 Xizhen Station on Qingdao Metro Line, Mainland China

Recent metro projects in Qingdao have adopted single-layer lining concepts based on rock reinforcement principles similar to NMT. In hard rock sections of Qingdao Metro Line 3, the design adopted a sprayed concrete lining reinforced with rock bolts to stabilise the surrounding rock mass. Waterproofing was achieved through a combination of pre-grouting, drainage measures, and sprayed waterproofing membranes. The successful application of this approach demonstrates that single-layer rock reinforcement systems can provide adequate structural performance and waterproofing in Mainland China.

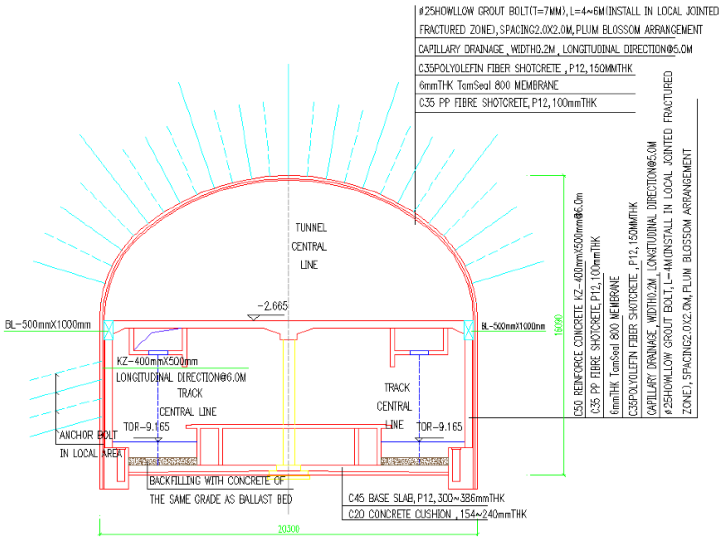

Figure 15: Typical Single-Layer Lining Support for Xizhen Station of Qingdao Metro (Qing Du et al 2019)

According to Shi et al. (2019), compared with conventional composite lining systems, the single-layer lining reduced construction complexity and achieved an estimated cost reduction of approximately 34.5%, while maintaining equivalent structural safety and waterproofing performance.

6.2 Vallavik Tunnel, Norway

The Vallavik Tunnel in Norway provides a notable example of NMT applied to road tunnel construction. The tunnel includes complex underground geometries, including a roundabout cavern, constructed using systematic rock bolting and fibre-reinforced shotcrete as permanent support. Permanent rock bolts stabilise the rock mass, while fibre-reinforced shotcrete provides surface support and controls local block instability.

Figure 16: Vallavik Tunnel with an underground Roundabout (Photo Source: Wikipedia)

6.3 WestConnex M5 Tunnel, Austrlia

Recent tunnel projects in Sydney have applied similar design and construction principles. In hard sandstone formations, primary support systems consisting of permanent rock bolts and fibre-reinforced shotcrete are used as permanent structural support. Double corrosion-protected rock bolts are adopted to ensure long-term durability, and additional sprayed concrete layers are applied (if necessary) to meet durability requirements. Mechanical and electrical installations, including jet ventilation fans, are anchored directly into the rock mass.

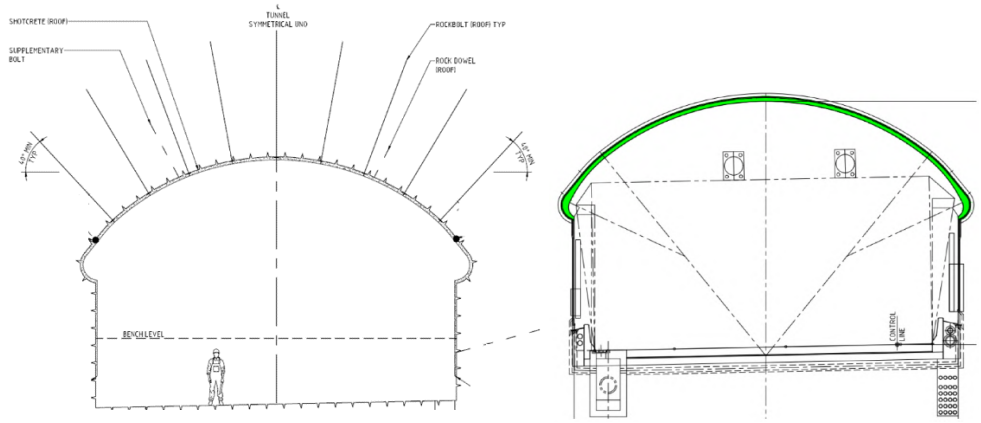

Figure 17: Primary support (rock bolts and shotcrete) and Final shotcrete lining in Hawkesbury Sandstone for a typical 3-lane drained road tunnel (Kost et al., 2021 and Bodner and Hesterman, 2017)

Figure 18: WestConnex M5 Tunnel, Austrlia (Photo Source: Westconnex)

7 CONCLUSION AND RECOMMENDATIONS

Based on recent local and long-term overseas experience, the adoption of a single-shell tunnel support system using RRA/NMT represents a rational and technically viable alternative to conventional NATM double-shell systems, particularly in competent rock masses in Hong Kong. By mobilising the inherent strength of the rock mass through systematic rock bolting and fibre-reinforced shotcrete, significant reductions in construction cost and programme duration can obviously be achieved.

With appropriate design verification and construction quality control, NMT/RRA can provide adequate long-term structural integrity, durability, waterproofing, and fire resistance. It offers a promising and cost-effective solution for future tunnel development in Hong Kong.

REFERENCES

Barton N., Lien R. and Lunde J. 1974. Engineering Classification of Rock Masses for the Design of Tunnel Support. Rock Mechanics, vol. 6, pp 189-236.

Bischoff J.A. & Smart J.D. 1977. A method of computing a rock reinforcement system which is structurally equivalent to an internal support system. In Proceedings of the 16th US Symposium on Rock Mechanics, Minneapolis, MN, USA (Fairhurst C and Crouch SL (eds)). ASCE, New York, NY, USA, pp. 279–284

Grimstad E., and Barton N. 1993. Updating of the Q-system for NMT. Proceedings of the International Symposium on Sprayed Concrete, Fagernes, Oslo. pp46-66.

International Tunnelling and Underground Space Association (ITA) Working Group No. 12 and ITAtech. 2014. Permanent Sprayed Concrete Linings. ITA Report, International Tunnelling and Underground Space Association.

NGI. 2015. Using the Q-system: Rock Mass Classifications and Support Design (handbook). Norwegian Geotechnical Institute, Oslo.

Bodner, Christian and Hesterman, Uwe. 2017. “Bigger, Better, More” 16th Australian Tunnelling Conference 2017

GEO. 2018. Geoguide 4: Guide to Cavern Engineering, Second Edition (2018). Geotechnical Engineering Office, Hong Kong SAR.

Shi Y., Yang L., Yan J., Zhou G., Li D., Cheng X., Wen S. and Xu Z. 2019. Application of Single-Layer Lining Based on Geological Sketch-Map in Qingdao Metro. Journal of Engineering Geology, vol. 27 (Suppl.), pp. 23–30.

Du Q., Sun S., Wen S., Zhan G. and Li Y. 2019. Application of Composite Shell Lining for Qingdao Metro Xizhen Station. IOP Conference Series: Earth and Environmental Science, vol. 267, 042066.

Kost S., Ching I. and Gomes A.R.A. 2021. Tunnel design – recent experiences from design and certification of major tunnel projects in Sydney. Australasian Tunnelling Conference (ATS 2020+1), Melbourne, Victoria, Australia, 10–13 May 2021.

Barton, N. and S. Roald, 2023. Pre-grouting of transport tunnels in jointed rock for successful control of water. Bergmekanikkdag, Oslo, 34.1 – 34.17.

Deng Y., Li J., Li X., Zhao Q. and Wen S. 2023. Application of Waterproof Single-layer Lining in Qingdao Metro Hard-rock Tunnel. Urban Mass Transit (城市轨道交通研究), vol. 26, no. 6, pp. xx–xx. doi:10.16037/j.1007-869x.2023.06.022.

AI-Enabled Slope Upgrading Works: From Static Archives to Operational Intelligence

I.H.H. Chan & K.S.T. Kwong
Landslip Preventive Measures Division 1
Geotechnical Engineering Office, Civil Engineering and Development Department, Hong Kong
B.J. Jiang, T.M. Ma, C.S. Sun & I.W. Wong
BuildWave Innovation Ltd, Hong Kong
C.T.L. Lee & H.H.L. Cheng
C.M. Wong & Associates Ltd, Hong Kong

ABSTRACT

The planning of slope upgrading works under Hong Kong's Landslip Prevention and Mitigation Programme requires reliable early-stage cost and schedule forecasting, together with efficient review of historical district archive records. In practice, this process suffers from limited structured expenditure data and the fragmented nature of scanned archival documents. This paper presents an AI-enabled workflow using a novel AI system that integrates explainable estimator based on structured slope attributes with a vision-based information retrieval pipeline for district archive PDFs. The estimator combines Random Forest and XGBoost models to generate bounded cost and schedule predictions with explicit confidence indicators. The information retrieval pipeline employs cascaded CLIP and VLM-based page classification, grid-label extraction, and robust spatial reconstruction to identify map pages relevant to a target slope location. The effectiveness of the proposed approach is validated using 360 historical slope upgrading works records and 799 archival image samples. Overall, this AI system, combining both estimator and information retrieval pipeline, transforms static archival resources into operational intelligence, improving planning consistency, reducing manual document review, and supporting more transparent early-stage decision-making.

1 INTRODUCTION

Hong Kong manages landslide risks through a comprehensive, territory-wide slope safety programme administered by the Geotechnical Engineering Office (GEO) of the Civil Engineering and Development Department (CEDD). Under the Landslip Prevention and Mitigation Programme (LPMitP), man-made slope features are selected for investigation based on a risk-based priority ranking system. These features are subsequently packaged into consultancy agreements for investigation and design (GEO 2011; 2013).

In practice, slope selection typically precedes the commencement of upgrading works by more than three years. To ensure meeting annual targets and budgetary constraints, preliminary cost and schedule estimate of upgrading works must be conducted during slope selection process before detailed ground investigation results or final designs are available. Consequently, a predictive workflow is essential during the initial slope selection stage to support informed decision-making and ensure the long-term feasibility of the programme.

The necessity for precise estimation is further amplified when more complex and critical man-made slope features—such as those overlooking sole access roads followed by the landslide incidents along Shek O Road (GEO, 2025a)—are included in consultancy agreements. This requirement is especially critical given the government's commitment in the 2025 Policy Address to progressively increase annual upgrading targets by approximately 30% over three years, starting from 2025 (HKSAR Government, 2025). In this demanding environment, more rigorous forecasting is indispensable to prevent budget overruns and ensure project delivery in the future.

Effective slope selection also necessitates a thorough review of archival documentation to identify features that have already been upgraded to current safety standards. Failure to filter these out leads to redundant studies, administrative waste, and increased uncertainty in cost and schedule estimation. However, these archival records

are often dispersed across heterogeneous sources and are typically consulted in a fragmented, sequential manner, hindering the efficiency of the planning process.

To address these challenges, an AI system is developed to support a new workflow designed to enhance the LPMitP slope selection process. This workflow enables early estimation of costs and schedules for slope upgrading works using easily accessible geometric data. Furthermore, it facilitates the automated retrieval of relevant historical documentation, streamlining the preliminary assessment of man-made features and ensuring a more robust planning foundation.

2 CURRENT PRACTICE AND CHALLENGES

Accurate cost and schedule estimation and information retrieval process during the slope selection stage faces several significant challenges in current practice.

2.1 Costs and schedule estimation of slope upgrading works

Cost and schedule estimation for slope upgrading work faces two major challenges: existing digital databases lack records of final expenditures for each man-made slope feature, leaving only paper-based documentation available. Furthermore, crucial factors affecting costs and construction duration, such as site accessibility, seasonal weather conditions, and site-specific geological conditions, are abstract and not easily quantified with the existing databases, such as the Slope Information System (SIS) (GEO, 2025b) and the Catalogue of Slopes maintained by GEO available from the Common Spatial Data Infrastructure (CSDI) website (2026).

Table 1: Example categories of structured slope attributes available in the Slope Information System (SIS).

Attributes	Example Fields
Identification	Slope No., District, Maintenance party
Geometry	Height, Length, Angle, Shape area
Spatial Location	Coordinates, Crest distance, Toe distance
Surrounding Features	Crest facility, Toe facility
Structural Components	Retaining walls
Administrative	Control category, Lot reference

2.2 Retrieval of supporting information from district archives

To investigate site conditions and verify assumptions, engineers consult district archival records. These archives consist of scanned project files accumulated over long time periods and covering a wide range of engineering activities. Figure 1 illustrates typical archive pages.

Relevant information may appear in maps, sketches, annotations, investigation reports, or internal memoranda embedded within large collections of unrelated material. Unlike structured databases, these documents preserve engineering context but are not indexed by slope identifier or feature type.

Manual review of district files presents several practical difficulties:

- Documents are scanned from legacy records and may contain degraded text or drawings.
- Coordinate references and scales are inconsistent across drawings.
- Hundreds of pages may require inspection before useful evidence is located.

As a result, locating supporting information is time-consuming and relies on iterative searching and interpretation.

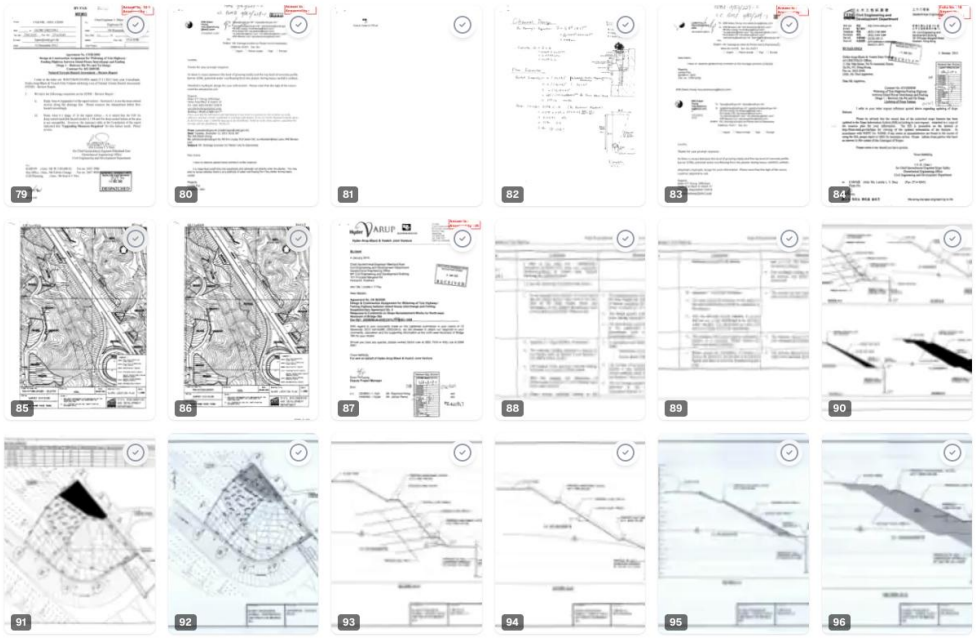

Figure 1: Example pages from district archive records containing mixed document types, including correspondence, sketches, tabulated records, and engineering drawings. Relevant slope information is embedded within heterogeneous and non-indexed materials.

3 METHODOLOGY

To resolve these current challenges, a novel AI system is developed. This AI system consists of two parts: explainable estimator and vision-based information retrieval.

3.1 Explainable estimator

To provide preliminary predictions of construction duration and financial cost, this AI system employs an explainable estimator that relies exclusively on structured attributes available prior to detailed ground investigation.

3.1.1 Feature engineering with expert knowledge

Translating raw slope parameters into accurate predictive variables requires embedding geotechnical engineering expertise directly into the feature space. Instead of relying only on raw inputs such as geometry, access distance, and slope type, this AI system derives a set of engineered features based on statistical analysis to better capture the factors associated with construction difficulty in Hong Kong.

This expert knowledge is primarily captured through interaction terms, derived metrics, and non-linear transformations. For example, geometric scale is represented not only by raw height and length, but also by derived quantities such as $FaceArea(H \times L/\sin\alpha)$, where H, L, and α are height, length and gradient of the slope, respectively. This metric more directly reflects the physical working surface requiring mitigation. Because construction cost is highly sensitive to absolute physical scale, logarithmic transformations are further applied to area- and size-related variables to reduce skewness and improve model stability.

Material composition is captured via categorical indicators such as $RockLikely$, a binary term distinguishing slopes with rock components (e.g., Cut-in-Rock, Fill-over-Rock) from pure soil fill. To account for distinct geotechnical challenges, excavation volume is mathematically interacted with this $RockLikely$ term. This explicitly teaches the model that excavating a large volume of rock demands fundamentally different plant machinery and time profiles compared to handling soil. Similarly, logistical constraints are modelled by multiplying geometric scale parameters by the logarithmic slant distance to vehicular access, effectively penalising large-scale works situated in remote or inaccessible terrain.

Table 2 summarises the main categories of these engineered features. It should be noted that this table presents illustrative examples rather than the full feature set, which comprises 22 features for the duration model and 40 features for the cost model. In addition to the interaction terms highlighted in the table, these features include continuous geometric variables, binary indicators for seasonal constraints such as winter start dates, and one-hot encoded administrative classifications, including consequence-to-life categories and slope types.

Table 2: Summary of engineered feature categories used in the explainable estimator, illustrating the integration of domain knowledge.

Category	Engineering Rationale	Example Derived Features
Geometry	Normalises absolute physical scale, as construction costs scale non-linearly with size.	$\log(1 + Volume)$ $\log(1 + FaceArea)$
Logistics & Access	Penalises large-scale operations situated far from vehicular access points.	$FaceArea \times \log(1 + d_{access})$
Material Interaction	Differentiates resource and plant requirements for rock excavation versus soil placement.	$\log(1 + Volume) \times RockLikely$
Seasonality	Models productivity impacts from wet-season mobility constraints and start-date delays.	$\sin(2\pi \cdot m/12)$ $WinterStart\ (binary)$
Administrative	Captures project constraints tied to consequence-to-life (Cons) categories and government land portions.	$\log(1 + GovtArea) \times 1[Cons = 1]$

3.1.2 Model selection and model training

The inherent non-linearities in geotechnical project data are addressed through a cascaded modelling approach. Random Forest (Breiman, 2001) serves as the primary point estimator due to its robustness against outliers in historical cost data. A classification variant then discretises predictions into standard time and cost buckets (e.g., 90–180 days; 1M–2M HKD), yielding a probability distribution for the most likely categorical outcomes.

To reliably define the lower and upper bounds of the predictions, separate eXtreme Gradient Boosting (XGBoost) models (Chen & Guestrin, 2016) are trained using quantile regression. Rather than predicting a single mean value, these models are optimised using the pinball loss function to target specific percentiles, such as the 10th and 90th percentiles. For a target quantile τ, actual value y, and predicted value $\hat{y}$, the pinball loss, L_τ is defined as:

$$L_\tau(y, \hat{y}) = \max\big(\tau(y - \hat{y}), (\tau - 1)(y - \hat{y})\big) \quad (1)$$

By minimising this loss function for $\tau = 0.1$ and $\tau = 0.9$, the AI system estimates the lower and upper prediction bounds in a mathematically rigorous manner. These bounds provide conservative and aggressive baselines for the preliminary estimate before any manual review takes place.

3.1.3 Quantifying prediction confidence

Rather than relying on a deterministic single-point forecast, the AI system provides a confidence score that immediately indicates how much trust the engineers should place in the baseline prediction.

This confidence score is formulated by triangulating three primary signals: the per-tree variance within the Random Forest, the relative width of the prediction boundaries, and the cross-model interval overlap. The interval overlap evaluates the consensus between the Random Forest prediction bounds $[L_{RF}, U_{RF}]$ and the XGBoost quantile bounds $[L_{XGB}, U_{XGB}]$ using a 1-Dimensional Intersection over Union (IoU) formulation:

$$IoU = \frac{\min(U_{RF}, U_{XGB}) - \max(L_{RF}, L_{XGB})}{\max(U_{RF}, U_{XGB}) - \min(L_{RF}, L_{XGB})} \quad (2)$$

A high IoU value (approaching 1) indicates strong agreement across models and supports a "High Confidence" classification. Conversely, if the variance is large or the interval overlap is poor, the AI system flags a "Low Confidence" warning to the slope. In practice, this explicit quantification of confidence acts as a crucial trigger in the workflow, directing the engineers to move beyond the baseline estimate and immediately initiate the AI-guided retrieval of historical archive files to resolve the flagged uncertainty.

3.1.4 Training results and operational performance

The production models were trained on 360 historical slope records, with 288 used for training and 72 reserved for held-out testing, and 5-fold cross-validation applied within the training set. Evaluation on the held-out test set reveals a clear difference in performance between cost and schedule forecasting.

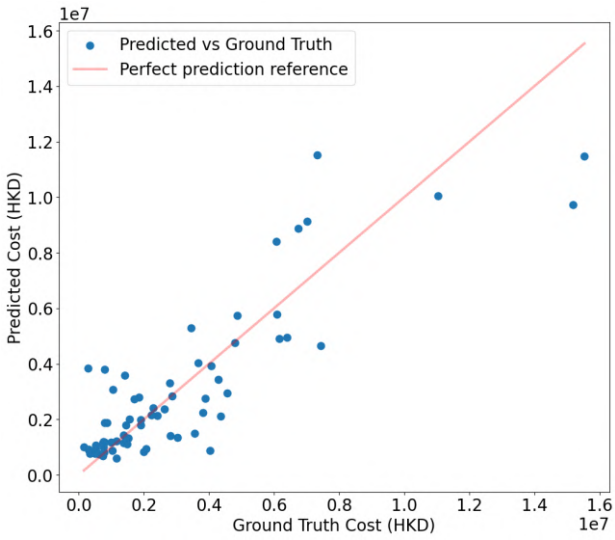

Figure 2: Predicted vs. Ground Truth Cost (HKD). The ensemble demonstrates a strong linear correlation along the perfect prediction reference, indicating robust generalization for cost estimation.

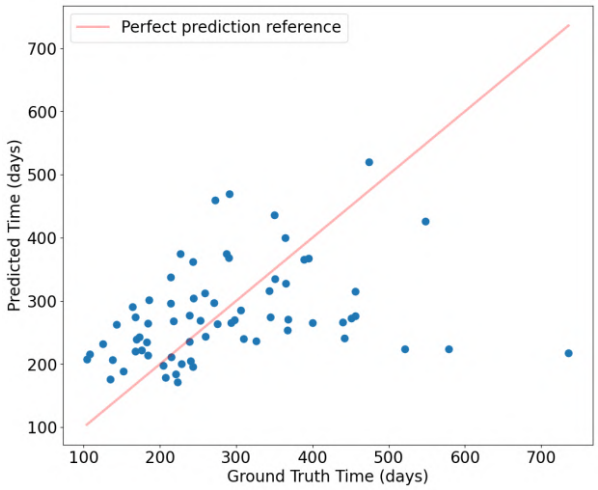

Figure 3: Predicted vs. Ground Truth Time (days). The high variance and scatter highlight the inherent difficulty of providing deterministic point estimates for construction schedules based solely on upstream structured attributes.

As illustrated in Figure 2 and Figure 3, the cost model demonstrates substantially stronger predictive performance, achieving an R^2 of 0.762 on the test set; while the point-estimate regression for construction time yielded poor generalisation, with a test set R^2 of 0.11. This disparity reflects the inherent complexities and typical performance variances in geotechnical engineering data: construction cost correlates directly with measurable physical attributes (e.g., slope geometry, face area, rock presence), while construction duration is heavily influenced by external constraints such as weather events, administrative re-scheduling, and contractor-specific resource allocation. As a result, deterministic to-the-day-level predictions are rarely necessary during early works package planning.

To provide greater practical value for schedule estimation, we reframed it as a classification problem, allowing the AI system to predict schedule intervals rather than exact day-level values.

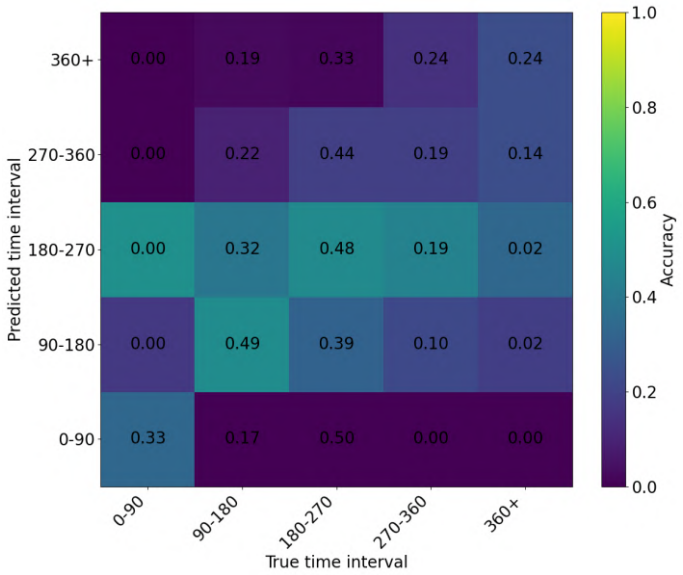

Figure 4: Confusion matrix for construction time interval classification. While exact day predictions are highly volatile, the classifier effectively groups projects into broader, actionable schedule buckets.

By discretising the timeline into standard planning intervals, the Random Forest classifier achieves approximately 40% test accuracy across five time buckets, significantly outperforming a 20% random baseline. When the adjacent intervals (± 1 bucket) are also considered, the accuracy rises to 80.6%. This indicates that even when the model misses the exact class, its prediction usually remains close to the true schedule, making it a useful tool for defining a preliminary planning range.

Furthermore, the XGBoost quantile model successfully captures 76.4% of actual durations within a bounded 226-day interval. Combined, these classification and quantile bounds transition the time estimator from an unreliable definitive forecast into a mathematically bounded, objective planning range that effectively guides early engineering assumptions.

3.2 Information retrieval pipeline

The retrieval pipeline processes uploaded district archive PDFs to identify pages containing drawings that spatially cover a given slope location. To avoid brute-force manual searching, the pipeline isolates relevant pages through a three-stage automated process: page classification, grid label detection, and spatial reconstruction.

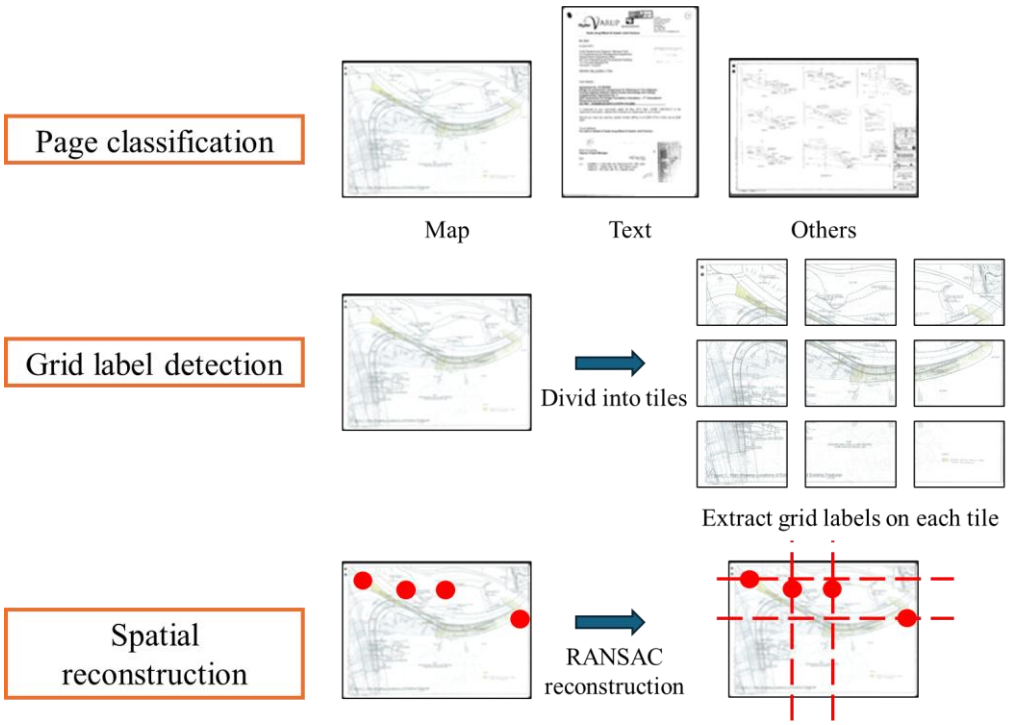

Figure 5: The automated information retrieval pipeline. Pages are first classified by visual type, maps are tiled for coordinate extraction, and robust spatial reconstruction generates a real-world geographic bounding box.

3.2.1 Page classification with cascaded vision models

A cascaded, two-stage vision architecture is used to classify scanned document pages into three categories—text, map, and others. This cascaded approach balances computational efficiency with high precision.

The first stage utilises a zero-shot image classification approach based on CLIP (Contrastive Language-Image Pre-training; Radford et al., 2021). CLIP is highly computationally efficient and excels at macro-level visual distinctions, making it ideal for rapidly separating dense text documents from graphical drawings. As shown in the confusion matrix in Table 3, the CLIP-based classifier achieves a strong baseline performance.

Table 3: Confusion matrix for the Stage 1 CLIP-based page classifier. The model demonstrates high overall accuracy (90.86%) and excellent recall for map identification, though it exhibits some confusion between general engineering drawings and text documents

		Prediction		
		Text	Map	Others
Ground Truth	Text	283	4	31
	Map	0	351	13
	Others	3	22	92

While CLIP effectively isolates non-text pages, distinguishing between plan-view maps (which contain border coordinates) and detailed cross-sectional engineering drawings requires deeper contextual understanding of visual layout cues. To address this, the pipeline introduces an optional Vision Language Model (VLM) review stage. This secondary VLM agent processes ambiguous graphical pages and specifically searches for coordinate grids and other plan-view characteristics. Integrating this refinement step substantially improves the distinction between maps and general drawings, pushing the overall classification accuracy to over 96.5% while maintaining high throughput.

3.2.2 Grid label detection

Pages successfully classified as maps proceed to the coordinate extraction stage, where the AI system identifies Hong Kong 1980 Grid (HK1980, EPSG:2326) labels printed along the map borders. This process relies on a VLM agent operating on localised image patches:

Tiling: To preserve the high resolution required to read small text, map images (rendered at 300 DPI) are divided into overlapping tiles of 1120×1120 pixels using a sliding window. Because grid reference labels conventionally appear at map margins, only tiles covering the outer 25% band of each edge are processed.

Grid label extraction: For each tile, four orientations (0°, 90°, 180°, 270°) are sent to the VLM to handle rotated text. The model is prompted to search along grid lines for standard 6-digit HK1980 grid references (e.g., numbers starting with 8 and ending with 0) and report their bounding boxes and direction indicators.

VLM post-validation (Hallucination filtering): A second VLM call strictly validates each detection. The reported bounding box is cropped from the original image and sent back to the agent with a verification prompt. In this call, any detections deemed hallucinated or unreadable are discarded. Surviving detections are then spatially clustered and filtered for outliers using known HK1980 coordinate bounds.

3.2.3 Spatial reconstruction

The final technical step translates the isolated grid labels, each defined by a numeric value, an axis direction, and a 2D pixel position, into a mathematical mapping from image space to real-world HK1980 coordinates.

Because scanned documents frequently suffer from skew, stretching, and missing labels, the AI system relies on the RANdom SAmple Consensus (RANSAC; Fischler & Bolles, 1981) algorithm to obtain a robust 2D similarity fit. When at least four valid control points are detected, the transformation is defined as:

$$\begin{aligned} E &= a \cdot x + b \cdot y + E_0 \\ N &= -b \cdot x + a \cdot y + N_0 \end{aligned} \tag{3}$$

Where (x, y) denote pixel coordinates, and (E, N) denote the geographic Easting and Northing coordinates. RANSAC iteratively samples subsets of the control points to estimate the transformation parameters (rotation, scale, and translation offsets (E_0, N_0), and then evaluates the remaining points to identify the model with the highest number of geometrically consistent inliers. This iterative approach effectively rejects misread labels or misaligned grid marks that may have survived the earlier VLM filtering.

The ultimate output of this reconstruction is a definitive coordinate frame consisting of four corner points that define the geographic extent of the page. This spatial bounding box is saved to the AI system database, enabling downstream matching algorithms to instantly determine if the map covers the geographic coordinates of a targeted slope.

4 CASE STUDY

To demonstrate the practical application of the proposed workflow, this section steps through a complete project preparation workflow.

4.1 Step 1: Contract-level preliminary estimation

In a typical scenario, engineers begin by preparing a proposed works contract covering multiple man-made slopes. The engineer needs to enter the required structured attributes (such as geometry, access distance, and feature type) derived from the SIS for the target batch of slopes.

Figure 6: The contract-level dashboard. The AI system instantly generates predicted point estimates, bounds the predictions within 10th–90th percentile intervals, and assigns a composite confidence score to each slope

As shown in Figure 6, the AI system instantly returns preliminary time and cost predictions for the entire contract. Crucially, the interface explicitly presents the uncertainty analysis, allowing engineers to view the 10th–90th percentile prediction bounds and the composite confidence level (High, Medium, Low) derived from cross-model agreement. This dashboard acts as a triage tool, allowing engineers to identify which slopes have reliable baseline estimates and which require immediate, more detailed investigation.

4.2 Step 2: Individual slope investigation

When a slope is flagged with a "Low" confidence score, or when its estimated cost represents a disproportionate risk to the contract budget, the engineer can drill down into a detailed slope-specific analysis interface.

At this stage, the AI system performs a K-Nearest Neighbours (KNN) search to retrieve historically comparable past works. As illustrated in Figure 7, the engineer can review the target slope alongside similar historical projects on a scatter plot. By presenting these specific reference cases, the platform adds interpretability to the algorithmic prediction, allowing the engineer to assess whether the estimated outcome is reasonably aligned with past engineering realities.

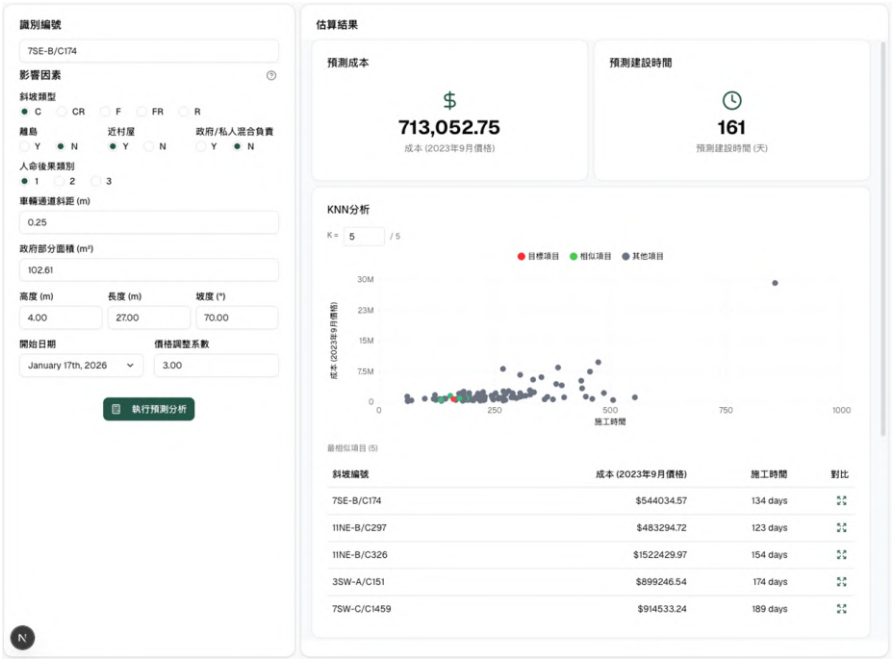

Figure 7: Individual slope analysis interface featuring K-Nearest Neighbours (KNN) retrieval. The scatter plot provides visual context by situating the model's prediction among historically similar projects.

4.3 Step 3: Targeted archive retrieval

If the historical comparison cannot fully explain the specific complexities of the site, the engineer proceeds to qualitative evidence gathering by uploading relevant district archive PDFs. Rather than requiring manual review of hundreds of pages, the automated vision pipeline immediately processes the uploaded documents.

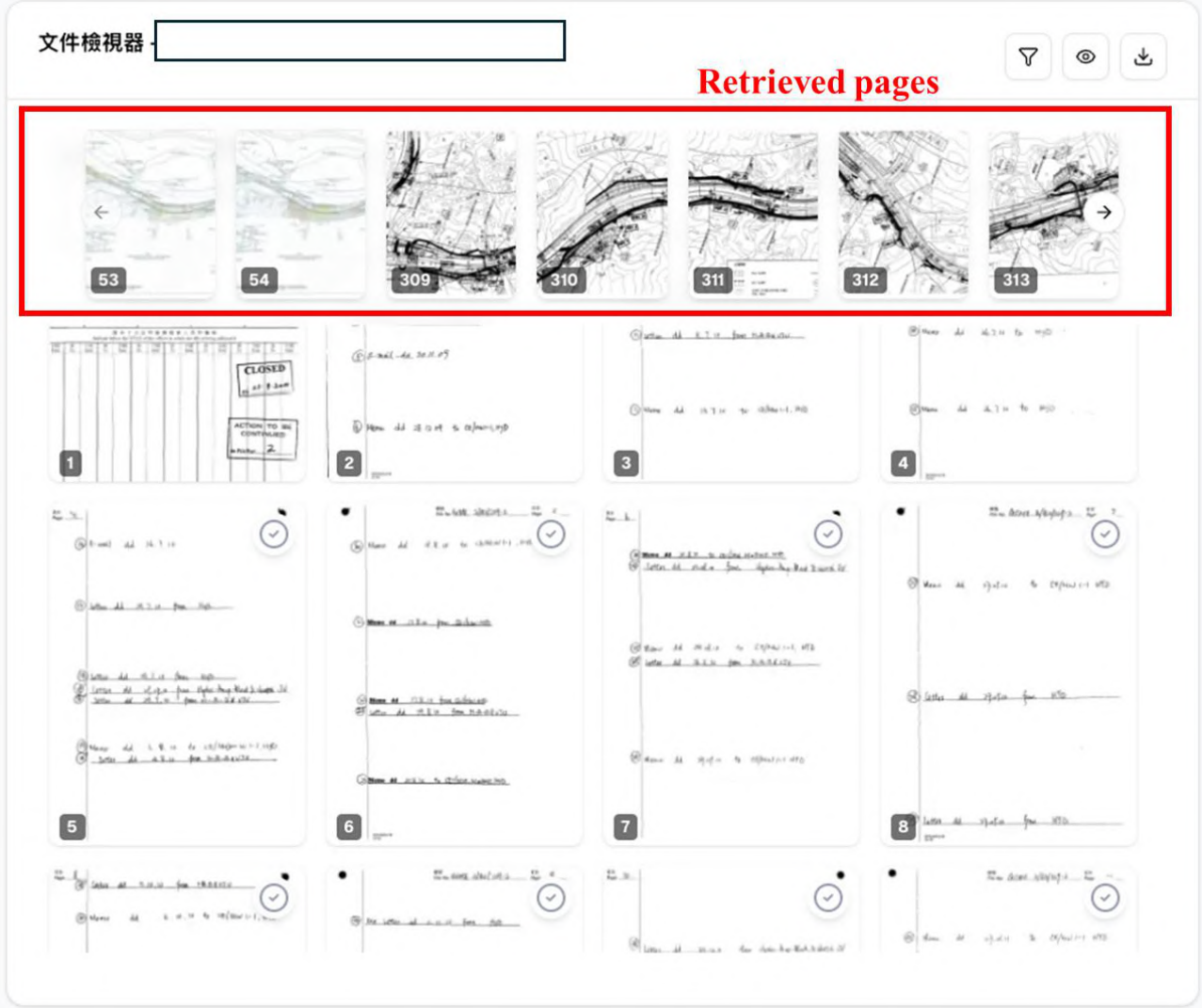

Figure 8: Document overview post-processing. The AI system filters the multi-page PDF to highlight the specific map pages that spatially cover the targeted slope.

The AI system classifies the document pages, extracts spatial references, and cross-references the reconstructed coordinates against the known HK1980 location of the target slope. As shown in Figure 8, the user interface prominently isolates the spatially relevant maps, allowing the engineer to navigate directly to the pertinent pages.

Figure 9: High-resolution map inspection. The interface displays the reconstructed coordinate frame, the extracted grid labels (red dots), and the VLM parsing details, allowing the engineers to verify the automated spatial match.

Engineers can click into any retrieved page to view the high-resolution scan, as well as the underlying AI-extracted coordinate data (Figure 9). By isolating these specific map pages, the engineers are also strategically positioned to review the immediately surrounding pages in the original document, which frequently contain crucial context such as site access constraints, geological records, or previous treatment histories.

4.4 Step 4: Evidence-based refinement

Equipped with concrete evidence from the targeted archive retrieval, the engineers can make informed adjustments to the initial assumptions. For example, if the retrieved maps reveal severe, undocumented site access constraints, the engineers can manually refine the preliminary estimate, with the AI system updating the overall contract total in real time.

Ultimately, the initial algorithmic prediction acts as a stable reference point. The manual investigation is subsequently focused entirely on confirming or adjusting specific assumptions, effectively reducing redundant document review and significantly improving standardisation across the early planning stages.

5 OPERATIONAL IMPACT

The proposed application is designed to streamline the practical planning stage of the LPMitP by integrating predictive analytics with automated data retrieval.

5.1 Early planning support

When packaging man-made slope features into a consultancy agreement, engineers can input a list of slope identifiers to obtain preliminary cost estimates derived from machine learning models. This enables early-stage projection of the total expenditure associated with the proposed works. Consequently, engineers can dynamically adjust slope selections to ensure that the scope is financially viable and that annual budgetary requirements remain stable.

This capability shifts the role of cost estimation from a passive, static reference to an interactive planning tool. Instead of manually updating spreadsheets after each investigation, users can establish a robust baseline

and refine it progressively as new information becomes available. In this way, the estimate serves as a consistent framework for organizing subsequent investigation and verification activities.

5.2 Guided investigation of historical records

Following the initial estimation, the AI system facilitates seamless access to slope records through search functions integrated with the structured SIS. Relevant district archive files can be uploaded and processed by the platform, which automatically identifies map pages, reconstructs spatial references, and verifies whether a specific slope feature falls within the drawing's extent.

This functionality transforms document review from an exhaustive manual search into a targeted investigation. Engineers can immediately pinpoint relevant drawings and focus on the immediate context rather than scanning entire archival volumes. By minimizing the administrative effort required to locate records, the AI system allows practitioners to dedicate more time to high-level engineering interpretation and risk assessment.

6 LIMITATIONS AND FUTURE WORKS

While the current implementation demonstrates practical usefulness, several limitations remain that motivate future development.

6.1 Document understanding scope

The present system focuses primarily on map pages for spatial verification. However, district files contain substantial textual information, including descriptions of previous works, geological observations, and site constraints. These records often provide important context that cannot be captured solely through geometric interpretation.

Future work will extend analysis beyond maps to full document understanding using visual language models. This includes identifying references to slope numbers, construction types, and geological descriptions within textual pages.

6.2 Document segmentation and metadata structure

District archive files typically contain multiple unrelated documents combined within a single scanned file. The absence of structural organisation limits efficient indexing and retrieval.

A planned extension is automated document segmentation to separate correspondence, investigation reports, drawings, and tabulated records into individual logical units. A metadata structure will then be constructed to support indexing by features such as road names, construction methods, and engineering topics. This will allow users to perform more advanced queries beyond spatial association.

6.3 Estimation model refinement

Current estimation models rely primarily on structured slope attributes. Although effective for preliminary expectation, prediction accuracy is influenced by variables not explicitly represented in the database.

Future work will incorporate additional features derived from parsed documents and engineering descriptions to improve predictive capability and reduce uncertainty. The objective is not to produce an exact cost prediction but to improve the reliability of early-stage planning references.

7 CONCLUSIONS

This paper presents an AI-enabled workflow to support the early planning of slope upgrading works under the LPMitP. By combining explainable cost and schedule estimators trained on structured slope attributes with an automated archive retrieval pipeline for scanned district records, a novel AI system provides a more efficient and accurate forecasting of cost and time for upgrading man-made slopes to avoid budget overruns and ensure project delivery in the future. The results show that the framework provides practical value at the planning stage: cost estimation demonstrates strong predictive capability, while schedule estimation is more meaningfully

expressed as bounded planning intervals rather than deterministic to-the-day forecasts. In addition, the vision-based retrieval pipeline leverages an advanced VLM-driven framework together with robust inference algorithms, enabling engineers to identify spatially relevant archive drawings more effectively while substantially reducing the need for exhaustive manual review.

Overall, the major contribution of the platform is procedural rather than purely algorithmic. It establishes a stable and transparent baseline for preliminary decision-making, directs engineering attention to the uncertainties that matter most, and improves the consistency and traceability of slope selection and project preparation. The study demonstrates that integrating predictive analytics with targeted information retrieval can transform static archival resources into operational intelligence for geotechnical planning.

ACKNOWLEDGEMENTS

This paper is published with the permission of the Head of the Geotechnical Engineering Office and the Director of Civil Engineering and Development, the Government of the Hong Kong Special Administrative Region.

REFERENCES

Common Spatial Data Infrastructure (CSDI), 2026. Catalogue of Slopes maintained by Geotechnical Engineering Office of Civil Engineering and Development Department [WWW Document]. CSDI. URL https://portal.csdi.gov.hk/geoportal/#metadataInfoPanel

GEO, 2011. GEO Publication No. 1/2011.

GEO, 2013. The New Priority Ranking Systems for Man-made Slopes and Retaining Walls (GEO Report No. 284).

GEO, 2025a. Past Notable Landslides [WWW Document]. Hong Kong Slope Safety (HKSS) Website. URL https://hkss.cedd.gov.hk/hkss/en/facts-and-figures/past-notable-landslides/index.html

GEO, 2025b. Slope Information System [WWW Document]. Hong Kong Slope Safety (HKSS) Website. URL https://hkss.cedd.gov.hk/hkss/en/facts-and-figures/slope-information-system/sis/index.html

Hong Kong Special Administrative Region (HKSAR) Government, 2025. The Chief Executive's 2025 Policy Address Supplement.

Stevenson, W.J., 2015. Operations management, Twelfth edition. ed, The McGraw-Hill Series in operations and decision sciences. McGraw-Hill Education, New York.

Wu, K., 2014. A Unified View on Planning, Scheduling and Dispatching in Production Systems.

Breiman, L., 2001. Random forests. Machine learning, 45(1), pp.5-32.

Chen, T. and Guestrin, C., 2016. XGBoost: A scalable tree boosting system. In Proceedings of the 22nd acm sigkdd international conference on knowledge discovery and data mining (pp. 785-794).

Fischler, M.A. and Bolles, R.C., 1981. Random sample consensus: a paradigm for model fitting with applications to image analysis and automated cartography. Communications of the ACM, 24(6), pp.381-395.

Radford, A., Kim, J.W., Hallacy, C., Ramesh, A., Goh, G., Agarwal, S., Sastry, G., Askell, A., Mishkin, P., Clark, J. and Krueger, G., 2021. Learning transferable visual models from natural language supervision. In International conference on machine learning (pp. 8748-8763). PMLR.

Rainfall-Induced Loose Fill Slope Failure: New Insights from MPM Analysis

Z.Q. Zhan & C. Zhou*
The Hong Kong Polytechnic University, Hong Kong

ABSTRACT

Loose fill slopes are widespread globally, and their failures during rainstorms are frequently reported. While previous research has primarily concentrated on the initiation of such failures, the post-failure movement has received limited attention. This study presents an advanced Material Point Method (MPM) framework to analyze both initiation and post-failure behaviour of loose fill landslides. The model achieves hydro-mechanical coupling by incorporating non-linear strain-softening during undrained shearing through soil contractive behaviour, and accounting for soil density effects on hydraulic properties. The proposed MPM model was used to back-analyze the 1976 Sau Mau Ping landslide in Hong Kong and conduct parametric studies. Results show that contractive behaviour in loose coarse-grained soils generates positive excess pore water pressure, reducing Bishop's stress and soil strength, which is critical to landslide initiation. The model's predictions closely align with field observations. The failure process is divided into three phases: local slide, global slide, and flow-like slide, each with distinct stress paths. Parametric studies reveal that lower dilation angles decrease landslide extent and runout, while assuming a constant soil-water retention curve (SWRC) can overestimate these factors. These findings highlight the importance of considering soil contraction and its effects on hydro-mechanical behaviour in landslide analysis.

1 INTRODUCTION

Urbanization has resulted in the creation of numerous fill slopes. In some cases, the fill materials are inadequately compacted, leading to the formation of loose fill slopes. Hong Kong serves as a prime example, with widespread occurrences of such slopes. The mechanism of rain-induced loose fill slope failure involves significant excess pore water pressure and Bishop's stress reduction, as well as noticeable strain softening during monotonic shearing, all caused by soil contraction tendencies (Knill et al., 1976; Take et al., 2004).

Various mesh-based numerical methods have been utilized in literature. However, these studies primarily focused on the pre-failure stages and were unable to simulate the post-failure motion of landslides due to mesh distortion. Therefore, several mesh-free methods have been developed, with the Material Point Method (MPM) being one such method suitable for large deformation geotechnical problems involving hydro-mechanical coupling. MPM has been utilized to simulate landslides involving strain softening, a key characteristic of loose fill slope failure. Yerro et al. (2019) utilized MPM to simulate the Oso landslide, simplifying the strain-softening of the debris at the slope's base by reducing shear strength parameters in the Mohr-Coulomb model without considering the liquid phase in their simulation. Cuomo et al. (2019) conducted a simulation of a retrogressive slope failure involving loose coarse-grained materials, simplifying the soils above water level to be a dry material without considering unsaturated behaviour. Di Carluccio et al. (2022) examined liquefaction-induced flow-like landslides in Valarties, considering both saturated and partially saturated loose soils. These studies primarily focused on the post-failure movement of liquefaction-induced landslides, which differ from the mechanism of rainfall-induced failure of initially unsaturated loose-fill slopes.

This study aims to enhance the understanding of the initiation and motion of rainfall-induced loose fill slope failure. To achieve this goal, a hydro-mechanical coupled MPM approach within the two-phase, two-point framework (Zhan et al., 2023) was utilized to back-analyze the 1976 Sau Mau Ping landslide in Hong Kong. The Sau Mau Ping landslide is a catastrophic loose-fill slope failure in Hong Kong. On the morning of 25 August 1976, at approximately 10 am, the fill slope located behind Block 9 of the Sau Mau Ping Estate in Hong Kong abruptly failed (Figure 1). This incident occurred during a heavy rainstorm brought on by severe Tropical Storm Elleen. The maximum hourly rainfall intensity reached close to 70 mm/h before the landslide occurred. The resulting landslide buried the ground floor of Block 9, resulting in 18 deaths and 24 injuries (Vail, 1984). The Geotechnical Engineering Office (GEO) Reports No. 86 and 96 of the Hong Kong government (Sun, 1999) provide detailed investigation results. According to the site investigations, the face of the slope at Sau Mau Ping

was formed by the end-tipping of fill without any compaction. The soil was in a loose condition with 75% of standard compaction. In GEO Report No. 96, an investigation into the initiation mechanism of the landslide was carried out using an FDM simulation. This investigation incorporated a strain-softening model similar to the one employed by Gu (1992).

The above literature provides a reasonable analysis of the initiation mechanism of the landslide, but the post-failure motion characteristics remain unclear. In the current study, the MPM simulations analyze the triggering and motion of this landslide. The simulation results were validated with actual field observation, thereby enhancing the reliability of the findings. This process not only uncovers the triggering and failure mechanisms of the landslide but also reveals the post-failure stage, which involves a transition from sliding to flowing. This whole failure process has been newly classified into three distinct phases based on the stress path of the points on the sliding surface and the evaluation of the sliding volume.

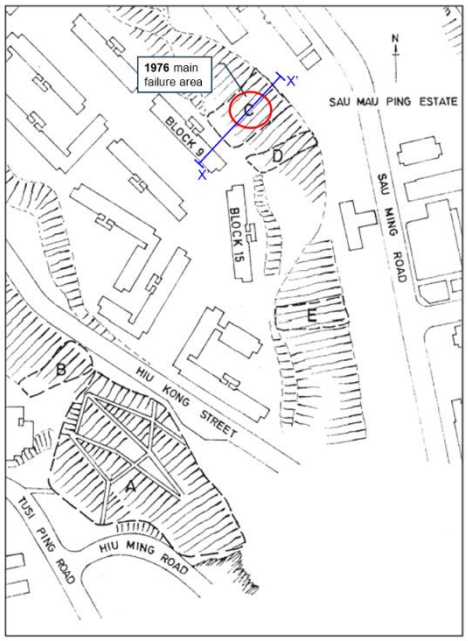

Figure 1: The 1976 Sau Mau Ping landslide area (modified from Vail, 1984)

2 MPM FORMULATIONS FOR MODELLING THE HYDRO-MECHANICAL BEHAVIOUR OF LOOSE FILL

This study used the two-phase, two-point MPM formulations developed by Zhan et al. (2023) to model the hydro-mechanical behaviour of saturated and unsaturated soils. This section briefly introduces constitutive equations of the mechanical and hydraulic behaviour.

In this study, the Drucker-Prager model is employed to characterize the mechanical behaviour of both saturated and unsaturated soils, with Bishop's effective stress $\boldsymbol{\sigma}^*$ incorporated to account for the contribution of matric suction to the soils:

$$\boldsymbol{\sigma}^* = \boldsymbol{\sigma} + \chi p^l \boldsymbol{\delta} \quad (1)$$

where $\boldsymbol{\sigma}$ is the total stress, χ is the Bishop's parameter and here it is simplified as the effective degree of saturation S_{eff}, p^l is the pore water pressure, and $\boldsymbol{\delta}$ is the Kronecker delta.

The loose filled soil exhibits a contractive behaviour during the shearing process. This contraction causes the arrangement of soil particles to become denser and more compact, leading to increasing friction and dilation angles, while the cohesion decreases. The mobilized friction angle (φ'^{mob}), dilation angle (ψ'^{mob}), and cohesion (c'^{mob}) are both correlated with the plastic deviatoric strain (γ^p), following an exponential function relationship (Soga et al., 2016):

$$\varphi'^{mob} = \varphi'^{c} + (\varphi'^{y} - \varphi'^{c})\exp^{-\eta\gamma^p} \quad (2a)$$

$$\psi'^{mob} = \psi'^{y}\exp^{-\eta\gamma^{p}} \quad (2b)$$

$$c'^{mob} = c'^{c} + (c'^{y} - c'^{c})\exp^{-\eta\gamma^{p}} \quad (2c)$$

where φ'^{y}, ψ'^{y} and c'^{y} denote the mobilized friction angle, dilation angle and cohesion at the onset of yielding, φ'^{c} and c'^{c} are critical state friction angle and cohesion, respectively. The shape factor η governs the rate at which mobilized strength parameters transition from their values at the onset of yielding to the critical-state values as plastic shear strain.

To model hydraulic behaviour of loose soil during shearing process, including the SWRC and permeability functions, the void ratio has a substantial effect that must not be ignored. This study therefore adopts the approach proposed by Chang et al. (2025), an extension of the Van Genuchten (1980) model that accounts for changes in both the air-entry value and the adsorption/desorption rates resulting from change in void ratio:

$$S_{eff} = \frac{S_r - S_{res}}{1 - S_{res}} = \left[1 + \left(\frac{a}{(p^l)_{ref}^{1-\exp[-b(e_0-e)]}}(p^l)^{2-\exp[-b(e_0-e)]}\right)^{\frac{1}{1-\lambda}}\right]^{-\lambda}, (p^l)_{ref} = 10^6 \text{ kPa} \quad (3a)$$

$$e = \frac{\mathrm{n}}{1-n} \quad (3b)$$

where S_{res} the residual saturation, e the void ratio, and n the porosity. The coefficients a and λ depend strongly on both soil type as well as soil state, whereas b quantifies the sensitivity of soil water retention ability to change in void ratio.

The influence of degree of saturation and porosity on the saturated and relative permeability is described as follows (Mualem, 1976; Carrier III, 2003; Chang et al., 2025):

$$k = k_{sat}k_r = k_{sat}\left[\frac{\int_0^{S_{eff}}(p^l)^{-1}d(S_{eff})}{\int_0^1(p^l)^{-1}d(S_{eff})}\right]^2(S_{eff})^{0.5\sqrt{1+l*\Delta e}} \quad (4a)$$

$$k_{sat} = C_H\frac{n^3}{(1-n)^2} \quad (4b)$$

where k_{sat} denotes the saturated permeability, k_r the relative permeability, and l and C_H are soil parameters related to soil type.

3 BACK ANALYSIS OF THE 1976 SAU MAU PING LANDSLIDE

3.1 Numerical model and procedures

Figure 2 shows the geometry and boundary conditions of the loose fill slope (x'-x' cross section in Figure 1), which is initially unsaturated. The slope stands at a height of 33 m, with an angle of 33°. According to the GEO Report No. 96 of the Hong Kong government (Sun, 1999), the unsaturated state is represented by assigning a suction value of 80 kPa throughout the fill slope. This suction value corresponds to a degree of saturation of around 50%, which is consistent with the findings of the post-failure site investigation.

The simulations utilize a pseudo-2D model with a spatial extent of only 0.5 m in one direction to save computational time. As the geological condition in this direction does not vary too much, analysis based on this simplification can still provide the initial mechanism and post-failure motion characteristics. The cell size is 0.5 m × 0.5 m × 0.5 m to achieve relatively high resolution and keep the computational cost within a limited and manageable range. There are initially eight material points for each phase in one cell.

Two points, A and B, located at different depths on the sliding surface, are chosen for further analysis of the soil stress path. The y-coordinate values of points A and B are equal to 18.6 m and 4.5 m. Analyzing the stress path of these points can provide a more comprehensive understanding of the landslide mechanism.

In terms of boundary conditions, the ground surface is impermeable during the initial stress generation, then it is designed to be a rainfall infiltration boundary and free moving after an equilibrium state is achieved. The side boundaries are set to be impermeable, with no allowance for horizontal displacement. The bottom boundary is also impermeable, with a restriction on displacement in all directions. The rainfall infiltration rate computed with zero suction at the ground surface is close to the actual value.

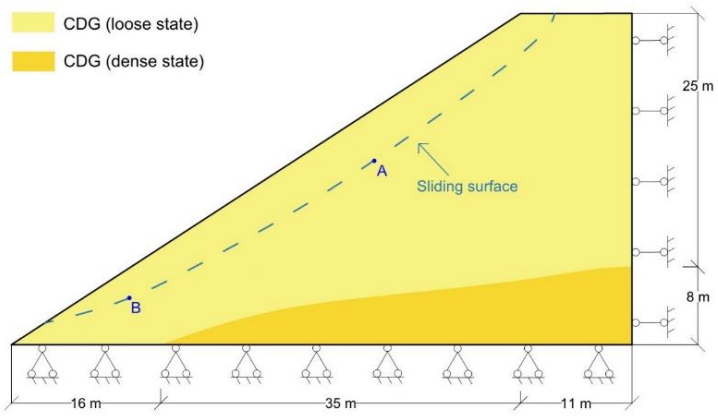

Figure 2: Geometry and boundary conditions for simulating the 1976 Sau Mau Ping landslide

The input mechanical parameters of two layers of CDG are given in Table 1. Parameters of the stiffness and critical state shear strength are deduced from the results of site investigation (Sun, 1999). It is worth noting that according to the triaxial compression test conducted by Gray (1980), the typical value of the mobilized friction angle at initial yielding (φ'^{y}) for loose CDG is 25 ° to 27°. Hence, φ'^{y} is taken as 26.8° in this study, with a dilation angle of -10°. η is set to be 6.5 in the back analysis, which is a typical value.

Table 1 also summarizes the hydraulic parameters of the two layers of CDG. The water retention parameters are typical values of CDG based on the GEO report No. 96 (Sun, 1999). As the void ratio decreases, the water retention capacity increases. Therefore, at a given degree of saturation, the matric suction of soil increases with decreasing void ratio.

Table 1: Key parameters for all soil layers in the back analysis

	CDG (Loose fill)	CDG (Dense)
Critical state friction angle	36.8°	36.8°
Mobilized friction angle at initial yielding	26.8°	36.8°
Dilation angle (ψ')	-10°	0°
Cohesion (c')	0 kPa	0 kPa
η	6.5	0
Saturated permeability (k_{sat})	1×10^{-3} m/s	1×10^{-8} m/s
a	0.98	0.98
λ	0.17	0.17
S_{res}	0	0
e_0	0.79	0.79
b	0.3	0.3
l	996	996

3.2 Computed results

3.2.1 Initiation and post-failure motion of the landslide

Figure 3 presents the computed results for mobilized soil volume. In this study, soil is considered mobilized if its displacement exceeds a threshold of 1 m. The sliding volume is then calculated by summing the volumes of all soil that surpass this displacement threshold (Liu et al., 2020).

The landslide transpires in two distinct phases: the pre-failure stage (the soil sliding volume = 0) and the subsequent post-failure stage (soil sliding volume > 0). According to the results in Figure 3, the second stage starts at about 110 s. Figure 4 presents the landslide zone and soil movement in the post-failure stage. Based on the results shown in Figs. 3 and 4, the post-failure motion can be divided into three phases. In the first phase (from 110 s to 115 s), a local slide is initiated near the slope crest. The sliding volume slightly increases over time. During this period, the soil volume reaches 10% of its maximum value. During the second phase (from 110 s to 130 s), the sliding soil flows along the slope surface. During this process, the volume of mobilized soil continues to increase over time at a rate much higher than that in the first stage. Consequently, the landslide transitions from a local slide to a global slide. At the end of this phase, the mobilized soil volume reaches 95% of its maximum value. In the third phase (from 130 s to 140 s), the landslide undergoes a transition from a global slide to a flow-like slide in this phase. The sliding soil flows along the slope and ground, and the volume of mobilized soil does not change too much.

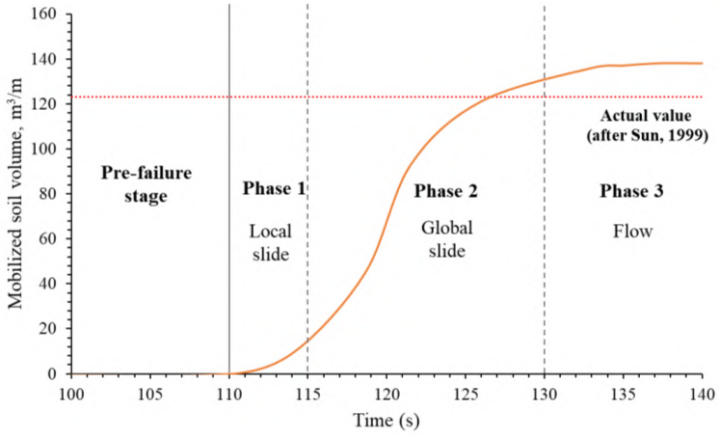

Figure 3: Evolution of mobilized soil volume with time.

It should be noted that the computed results are consistent with the field data in different aspects. The final result of mobilized soil volume (138 m³/m) is close to the field observation result (123 m³/m), showing a difference of approximately 10%. The maximum thickness of the landslide zone is approximately 3.6 m, with an average value of around 3.2 m. This depth aligns closely with the observed value of 3 m. In addition, the landslide's runout distance on the ground is 21.8 meters, indicating that it flowed into Block 9, which is less than 20 meters away from the base of the slope (Knill et al., 1976).

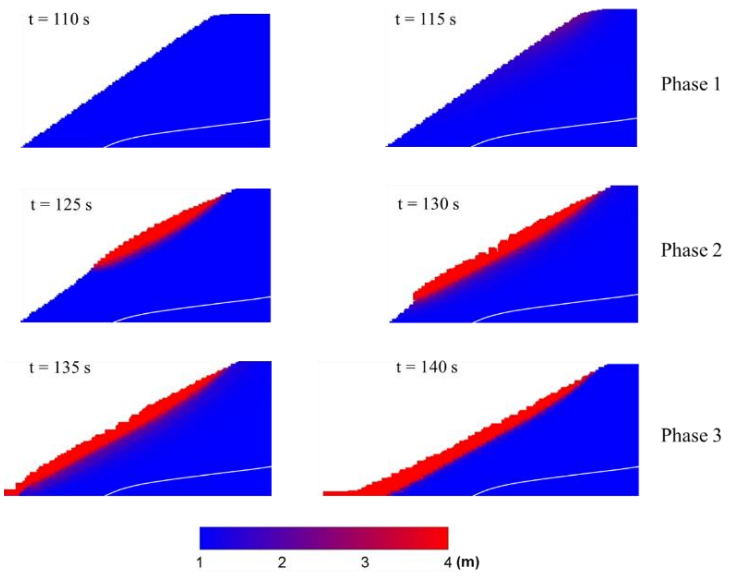

Figure 4: Displacement contour at six different times at the post-failure stage

3.2.2 Stress path of soil

The stress paths of two representative points (A and B in Figure 2) along the sliding surface are summarized in Figure 5. Points A and B are located at a depth of 3.5 m and 1.6 m, respectively. The initial yielding surface and the critical state line are included in the figure as references.

For point A, the initial mean Bishop's stress and deviatoric stress are computed to be 125.2 kPa and 45.3 kPa, respectively. This places point A on the left side of the initial yielding surface. During rainfall infiltration, the mean Bishop's stress of point A decreases, and there is no obvious change in the deviatoric stress. The mobilized friction angle increases during this process, and the soil at point A reaches the yielding surface at t = 116 s. When the stress path reaches the initial yielding surface, the loose fill slope tends to collapse. There is a trend of soil contraction, which results in the build-up of positive excess pore water pressure. Concurrently, the deviatoric stress also exhibits a decreasing trend. As the stress path moves to the left lower side, the mobilized friction angle of the soil increases and eventually reaches the critical state line. At t = 131 s, point A reaches the critical state, leading to the flow-like landslide in Figure 5 (Take et al., 2004).

The stress path of point B is qualitatively similar to that of point A. The initial mean Bishop's stress and deviatoric stress are equal to 106 kPa and 45.3 kPa. It is also located on the left side of the initial yielding surface. As rainfall infiltrates, the mean Bishop's stress decreases and reaches the initial yielding surface at t = 111 s. Afterwards, the stress path of point B reaches the critical state line at t = 129 s. Point B reaches the initial yielding surface and critical state than point B, mainly because the former is located closer to the yield surface.

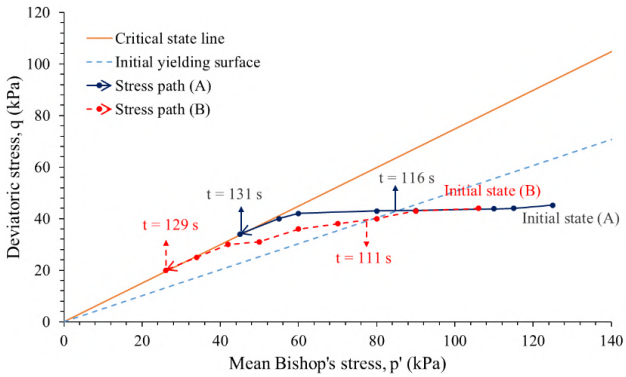

Figure 5. Stress paths of points A and B in the $p' - q$ space.

4 PARAMETRIC STUDIES

4.1 Effects of dilation angle

Two additional values of the dilation angle (-15° and 0°) are chosen for the parametric studies. Among these, a dilation angle of -15° has also been chosen for the numerical study of the 1976 Sau Mau Ping landslide by previous researchers. A dilation angle of 0° implies that soil contraction-induced strain softening is not taken into account. The friction angle in the yielding state is 21.8° with a dilation angle of -15°, while it is 36.8° with a dilation angle of 0°. The remaining conditions are identical to those given in the Section 3.

By comparing the final profile under three different dilation angles with the field observed result (Figure 6(a)), it is found that the condition with a dilation angle of -10° is the most consistent with the field observed result. It is noted that there is no collapse occurring at the slope crest (Sau Po Street) in the field, mainly because Sau Po Street is a paved road surface, but it is not considered in the numerical simulation.

Figure 6(b) compares the mobilized soil volume between numerical simulations with the field observed result. When the dilation angle is -15 °, the final value of mobilized soil volume is up to 234 m³/m, about 80% higher than the actual value (123 m³/m) in the field. When the dilation angle is -10°, the maximum mobilized volume decreases to 138 m³/m. With a dilation angle of 0°, the maximum mobilized volume is only 4.2 m³/m.

Based on the above comparisons, it is evident that a dilation angle of -10° can provide results closest to the field observations from various aspects, including the mobilized soil volume, sliding surface, thickness of the landslide zone, and runout distance. Furthermore, the slope can almost maintain a stable condition under the rainstorm if the dilation angle is zero, suggesting that the contractive behaviour of loose CDG is a major factor contributing to the catastrophic Sau Mau Ping landslide. In the future management of loose slopes, it is important to give proper consideration to soil contraction.

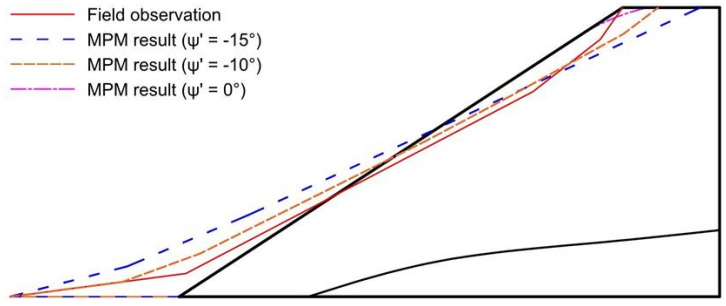

(a)

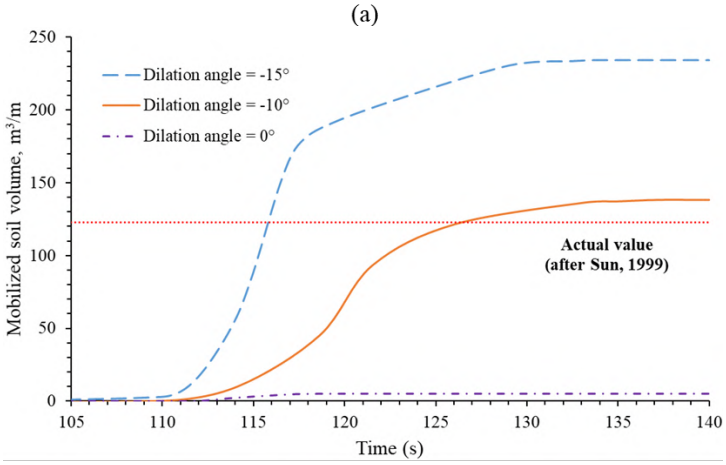

(b)

Figure 6. Comparisons between the field observed and the MPM simulated results with three different dilation angles: (a) Final profile; and (b) Mobilized soil volume of sliding mass in the post-failure stage.

Figure 7 illustrates the stress path of point A under three different dilation angles, with an explanation for the observed differences. All three stress paths show a decrease in Bishop's stress caused by rainfall infiltration. The stress path with a dilation angle of -15° first reaches the initial yielding surface, leading to the generation of excess pore water pressure due to the contractive behaviour, and then it reaches the critical state line. The mean Bishop's stress decreases to 30 kPa with a dilation angle of -15°, which is lower than the condition with a -10° dilation angle (45 kPa). Therefore, the sliding mass significantly increases with a lower value of the dilation angle. The mean Bishop's stress decreases to 83 kPa when the dilation angle is equal to 0°, with no significant change in deviatoric stress. Furthermore, the stress path never reaches the collapse line, ensuring the stability of the slope.

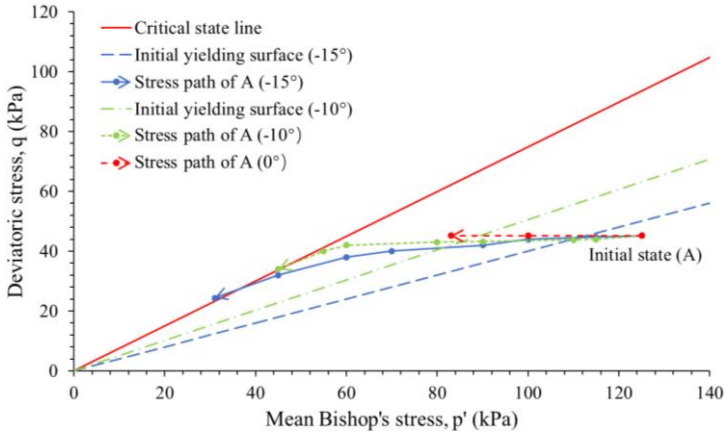

Figure 7. Simulation results with different dilation angles: Stress paths of point A in the $p' - q$ space.

4.2 Effects of void ratio-dependent SWRC

Changes in porosity can impact the water retention ability of soil, which is why the void ratio-dependency of SWRC is utilized in the back analysis in Section 3. To assess the significance of this aspect in the slope analysis, a simulation with a constant SWRC is also conducted for comparison. The remaining conditions for these two simulations are identical to those outlined in Section 3.

Figure 8(a) compares the final profile under two SWRCs with the field-observed result. When using a void ratio-dependent SWRC, the measured and computed results are more consistent with the field observation. Conversely, a constant SWRC leads to an overestimation of the sliding mass when the soil exhibits contraction behaviour. A similar conclusion is also drawn in Figure 8(b), where the maximum mobilized volume of the slope mass is 165 m³/m when using a constant SWRC, which is 33% higher than the field-observed value.

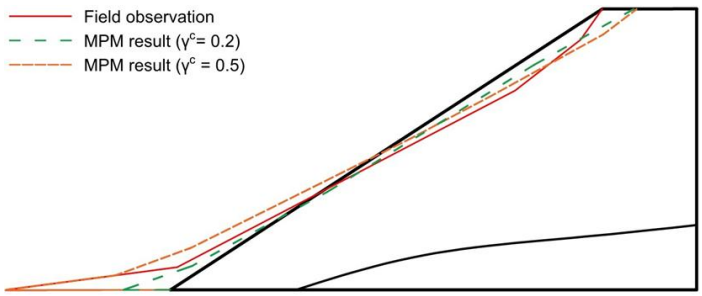

(a)

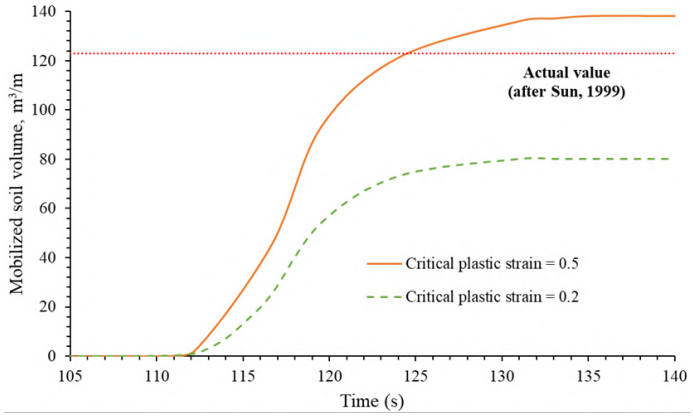

(b)

Figure 8. Comparisons between the field observed final profile and the MPM simulated results with two different strain softening rates: (a) Final profile and (b) Mobilized soil volume of sliding mass in the post-failure stage.

Figure 9 illustrates the stress path of point A using two different modelling approaches for SWRCs. The trends of these two stress paths are similar to those previously discussed, so a detailed description is not repeated here. Ultimately, with a constant SWRC, the mean Bishop's stress decreases to 38 kPa, which is lower than the condition using a void ratio-dependent SWRC (45 kPa). This is attributed to the contractive behaviour exhibited by the test soil during the slope deformation process. When the effects of porosity on SWRC are considered through Eq. (3), the soil demonstrates a higher water retention ability, resulting in a higher predicted equilibrium suction at a given degree of saturation, leading to increased strength.

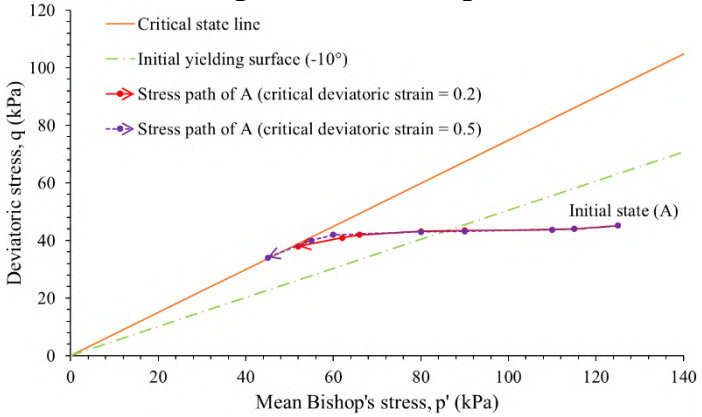

Figure 9. Simulation results with different strain softening rates: Stress paths in the $p' - q$ space.

5 CONCLUSIONS

This study aims to enhance the understanding of the initiation and motion of rainfall-induced loose fill slope failure. To achieve this goal, an MPM model was utilized to back-analyze the 1976 Sau Mau Ping landslide in Hong Kong. The advanced MPM model considers the hydro-mechanical coupled behaviour of both saturated and unsaturated soils. To model the hydraulic behaviour with changes in soil volume, the MPM formulations consider the impact of changes in the void ratio on the SWRC and permeability function. A non-linear strain hardening/softening law is also adopted to simulate the mechanical behaviour of both saturated and unsaturated soils.

The entire process of the Sau Mau Ping landslide, from the pre-failure stage to the post-failure stage, is simulated and verified by comparing the results with field observations. The computed results closely match the field measurements on various aspects, including the landslide zone, mobilized volume, and runout distance.

The entire process of the Sau Mau Ping landslide can be classified into three phases with different failure modes: local slide, global slide, and flow-like slide. In the first stage, rainfall infiltration leads to a decrease in the mean Bishop's stress on the sliding surface, initiating the landslide near the slope surface. In the second stage, as the stress path moves from the initial yielding surface to the critical state line, excess pore water

pressure is generated due to the tendency of soil contraction. Finally, the stress path of soils ultimately reaches a critical state. In the future management of loose slopes, it is important to give proper consideration to soil contraction and its influence on hydro-mechanical behaviour.

A series of parametric studies were also conducted to examine the influence of two parameters closely associated with strain softening: the dilation angle, and the void ratio-dependent SWRC. For landslides with a lower value of dilation angle, the landslide zone, mobilized soil volume, and final runout distance tend to be underestimated. Conversely, for landslides with a constant SWRC, there tends to be an overestimation of these parameters. In particular, the slope can almost maintain a stable condition under the rainstorm if the dilation angle is zero, suggesting that the contractive behaviour of loose CDG is a major factor contributing to the catastrophic Sau Mau Ping landslide. In the future management of loose slopes, it is important to give proper consideration to soil contraction and its influence on hydro-mechanical behaviour.

The high-fidelity runout simulations provided by the MPM framework offer significant advantages for the practical design of landslide debris-resisting barriers. By accurately capturing the spatio-temporal evolution of flow thickness and velocity, the model provides quantifiable metrics for the geometrical optimization and spatial placement of mitigation structures. Specifically, the simulated impact force and flow height at various locations allow engineers to determine the optimal distance of barriers from the source area—balancing energy dissipation against impact intensity. Furthermore, the ability to predict the final deposition morphology assists in sizing the storage capacity of catch-basins. Integrating these numerical insights into the design phase bridges the gap between theoretical multi-physics modeling and risk-informed engineering interventions, ensuring that barriers are both structurally robust and strategically positioned to minimize landslide hazards.

REFERENCES

Carrier Iii, W. D. 2003. Goodbye, hazen; hello, kozeny-carman. *Journal of Geotechnical and Geoenvironmental Engineering* 129(11):1054-1056.

Chang, Z. & Zhou, C. 2025. A new model for water retention and hydraulic conductivity curves of deformable unsaturated soils. *Water resources research* 61(5):e2024WR037826.

Cuomo, S., Ghasemi, P., Martinelli, M. & Calvello, M. 2019. Simulation of liquefaction and retrogressive slope failure in loose coarse-grained material. *International Journal of Geomechanics* 19(10):04019116.

Di Carluccio, G., Pinyol, N. M., Alonso, E. E. & Hürlimann, M. 2022. Liquefaction-induced flow-like landslides: The case of Valarties (Spain). *Géotechnique* 74(4):307-324.

Gray, M. 1980. The behaviour of a granitic soil in shear. *Material Division Report* 14.

Gu, W.-H. 1992. Liquefaction and post-earthquake deformation analysis.

Knill, J., Lumb, P., Mackey, S., Mello, V., Morgenstern, N. & Richards, B. 1976. Report of the independent review panel on fill slopes. *Government of Hong Kong*.

Liu, X., Wang, Y. & Li, D.-Q. 2020. Numerical simulation of the 1995 rainfall-induced Fei Tsui Road landslide in Hong Kong: new insights from hydro-mechanically coupled material point method. *Landslides* 17:2755-2775.

Mualem, Y. 1976. A new model for predicting the hydraulic conductivity of unsaturated porous media. *Water resources research* 12(3):513-522.

Soga, K., Alonso, E., Yerro, A., Kumar, K. & Bandara, S. 2016. Trends in large-deformation analysis of landslide mass movements with particular emphasis on the material point method. *Géotechnique* 66(3):248-273.

Sun, H. 1999. *Review of fill slope failures in Hong Kong.* Geotechnical Engineering Office, Civil Engineering Department.

Take, W., Bolton, M., Wong, P. & Yeung, F. 2004. Evaluation of landslide triggering mechanisms in model fill slopes. *Landslides* 1:173-184.

Vail, A. 1984. Two landslides in Hong Kong In *Proceedings of Proceedings of 4th international symposium on landslides, Toronto*, vol. 1, pp. 717-722.

Van Genuchten, M. T. 1980. A closed-form equation for predicting the hydraulic conductivity of unsaturated soils. *Soil science society of America journal* 44(5):892-898.

Yerro, A., Soga, K. & Bray, J. 2019. Runout evaluation of Oso landslide with the material point method. *Canadian geotechnical journal* 56(9):1304-1317.

Zhan, Z., Zhou, C., Liu, C. & Ng, C. 2023. Modelling hydro-mechanical coupled behaviour of unsaturated soil with two-phase two-point material point method. *Computers and Geotechnics* 155:105224.

An Unprecedented Incident of Concrete Contamination by Marine Deposits in Bored Pile Construction Leading to Abandonment of the Piles in a Hong Kong Building Project

Thomas S.K. Lam
Wilson & Associates Limited, Hong Kong

ABSTRACT

In a building project constructed on Hong Kong Island near the seashore, bored piles of 1.5 m and 2.0 m in diameter founded on Grade III or better rock were used as foundation for the building. The site is underlain by fill, marine deposits, alluvium, completely decomposed granite and moderately to slightly decomposed granite. In the concreting of two bored piles, a sudden drop of some 4.7 m and 6.5 m in the concrete level in the temporary casing was noted, as the casing was lifted. In both piles, it was suspected that a hardened concrete layer was formed in the piles during concreting. These two piles were abandoned in the end. An investigation was carried out. Taking into account of the new information obtained, it was established that there was concrete contamination by marine deposits at the casing toe level upon lifting of the casing, leading to early setting of concrete and formation of a hardened concrete layer in the piles.
In this paper, the concreting problem encountered in the two piles and the new information obtained are presented. The mechanism of concrete contamination by marine deposits, leading to early setting of concrete and formation of a hardened concrete layer in the piles, is given.

1 INTRODUCTION

In a building project constructed on Hong Kong Island near the seashore, bored piles of 1.5 m and 2.0 m in diameter founded on Grade III or better rock are used as foundation for the building. The site is underlain by fill, marine deposits, alluvium, completely decomposed granite and moderately to slightly decomposed granite.

In the construction of the bored piles, a temporary casing was first oscillated into the ground at the pile location. After the casing was installed, the materials inside the casing were excavated using a hammer grab. Throughout the excavation, water level inside the casing was checked to ensure that it was above the groundwater level in the vicinity. The installation of casing and excavation were carried out in sequence with the excavation carried out in at least 2 m above the casing toe. When the bedrock was reached, reverse circulation drilling was used to form the rock socket. A minimum socket of 500 mm in rock was provided for the casing. The concrete used for the piles (a grade 45D/20PFA concrete was used) was placed under water by a tremie pipe. An immersion of at least 2 m of the tremie pipe in the concrete was maintained during concreting.

In the concreting of two bored piles (BP30 and BP9), which are 59.23 m and 63.50 m long respectively, a sudden and significant drop of concrete level in the casing was noted, as the casing was lifted. In BP30, the concrete dropped by 4.7 m from 14.9 m to 19.6 m depth, which failed to rise even after adding a further five loads of concrete of 37.5 m^3, followed by lifting of the casing. In BP9, the concrete dropped by 6.5 m from 19.1 m to 25.6 m depth. There was difficulty to re-insert the tremie pipe back into the concrete at 28.0 m depth after it was lifted. In both piles, it was suspected that a hardened concrete layer was formed in the piles during concreting. These two piles were abandoned in the end.

An investigation was carried out, which included completion of four additional drillholes, installation of vibrating wire (VW) piezometers in the drillholes to continuously monitor the groundwater level fluctuation, determination of the composition and contents of the affected concrete in the piles by Particle Size Distribution (PSD), X-ray Diffraction (XRD) and X-ray Fluorescence (XRF) tests, testing of groundwater for dissolved carbon dioxide (CO_2) and marine deposits for organic matter, etc. Taking into account of the new information obtained, it was established that there was concrete contamination by marine deposits at the casing toe level upon lifting of the casing, leading to early setting of concrete and formation of a hardened concrete layer in the piles.

In this paper, the concreting problem encountered in the two piles during construction and the new information obtained from the investigation are presented. A detailed description of the mechanism of concrete

contamination by marine deposits, leading to early setting of concrete and formation of a hardened concrete layer in the piles, is given.

2 TENDER GI WORKS

2.1 Ground Conditions

A total of 9 drillholes (DH1, DH2, DH3, DH4, DH6, DH7, DH8, DH9 and DH10) were completed. Location of the drillholes is shown in Figure 1. Location of BP30 and BP90 is also included. The geological profile of the site based on the tender GI information along Section C-C' is shown in Figure 2.

The site is underlain by fill, marine deposits, alluvium, completely decomposed granite (CDG) and moderately to slightly decomposed granite (MDG/SDG).

Fill is about 22 m thick. It was described as a medium dense, greyish brown and grey, silty fine to coarse SAND with some subangular fine gravel sized rock fragments.

As indicated in the Hong Kong Geological Survey Memoir No. 2 (GCO, 1986) , the site is underlain by two formations of the offshore Marine Deposits: Chek Lap Kok Formation and Hang Hau Formation which are respectively equivalent to the terms Alluvium and Marine Deposits commonly used in the site investigation practice.

Marine Deposits were found in DH2, DH3, DH7, DH8, DH9 and DH10, as shown in Figure 1. Marine Deposits were described as a firm to very stiff, greenish grey, sandy silty CLAY with some shell fragments. Alluvium is thick, in the range of 10 m to 27 m, in the site. It is interbedded with very stiff, greyish brown, slightly sandy SILT, very stiff, dark grey sandy silty CLAY, and very dense, yellowish brown, silty fine to coarse SAND with some subangular fine gravel sized rock fragments

Underlain the alluvium is the residual soil/CDG zone, which is 6 m to 52 m thick in the site. Bedrock of MDG/SDG is found at about 50 m below ground.

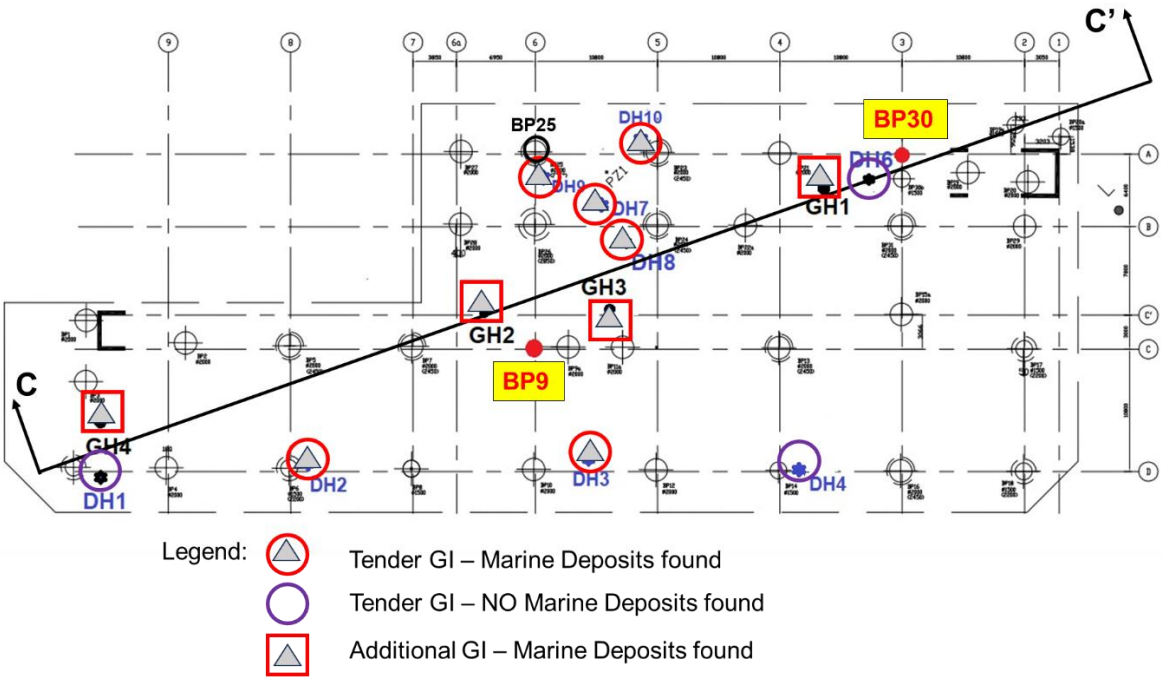

Figure 1: Location of Tender and Additional GI Drillholes

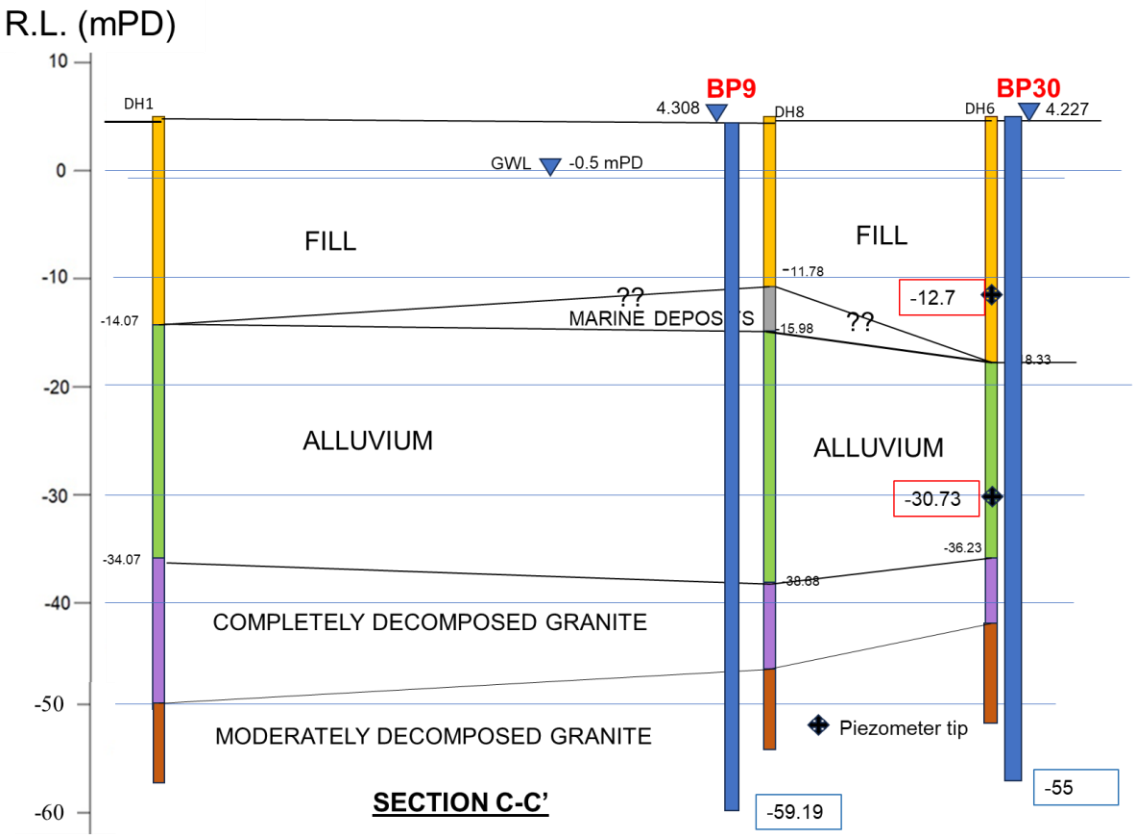

Figure 2: Geological Profile of the Site based on Tender GI information

2.2 Groundwater Conditions

Piezometers/standpipes were installed in DH6 and DH7. The tips of the piezometers/standpipes were located in fill and alluvium. The levels at which the tips were installed in DH6 are included in Figure 2.

The GWL recorded was steady with no marked fluctuation. At DH6, GWL was at -1.0 mPD to -1.2 mPD, at about 5.3 m below ground. At DH7, GWL was at -1.3 mPD to -0.3 mPD, at about 5.0 m below ground.

3 CONCRETING PROBLEM

3.1 Concreting Problem in BP30

BP30 is a 2 m diameter pile founded at -55 mPD with a 2 m rock socket. It has no bell-out. At this pile location, the ground level is at 4.227 mPD. In all, a total of 8 lengths of casing up to 59.14 m long were installed, and the final casing toe level was at -52.91 mPD.

After the 29th truck concrete pour of 217.4 m^3, the casing toe level was lifted by 600 mm from -25.123 mPD to -24.523 mPD. The concrete level in the casing dropped suddenly by 4.7 m from -10.673 mPD to -15.373 mPD, as shown in Figure 3.

Another 5 loads of concrete of 37.5 m^3 (30th to 34th truck) were added, followed by lifting of the casing. The concrete level failed to rise. A further length of the casing was extracted, lifting the casing toe level to -21.663 mPD. The concrete level became -12.773 mPD.

The concrete overflew when the tremie pipe was cut after the 34th truck concrete pour. It was not possible to re-insert the tremie pipe through the hardened concrete layer at -12.773 mPD. It was suspected that there was a hardened concrete layer from -12.773 mPD down to the casing toe level of -24.523 mPD where the casing toe level was lifted.

As compared with the theoretical volume of concrete, there was a huge increase in the actual concrete volume used at the casing toe level between -41.033 mPD and -25.123 mPD. On completion of the 34th concrete pour,

254.9 m^3 of concrete was used giving an overbreak of 92.14%, and a 28.36 m long casing with the casing toe at -21.633 mPD was left in. The pile was abandoned.

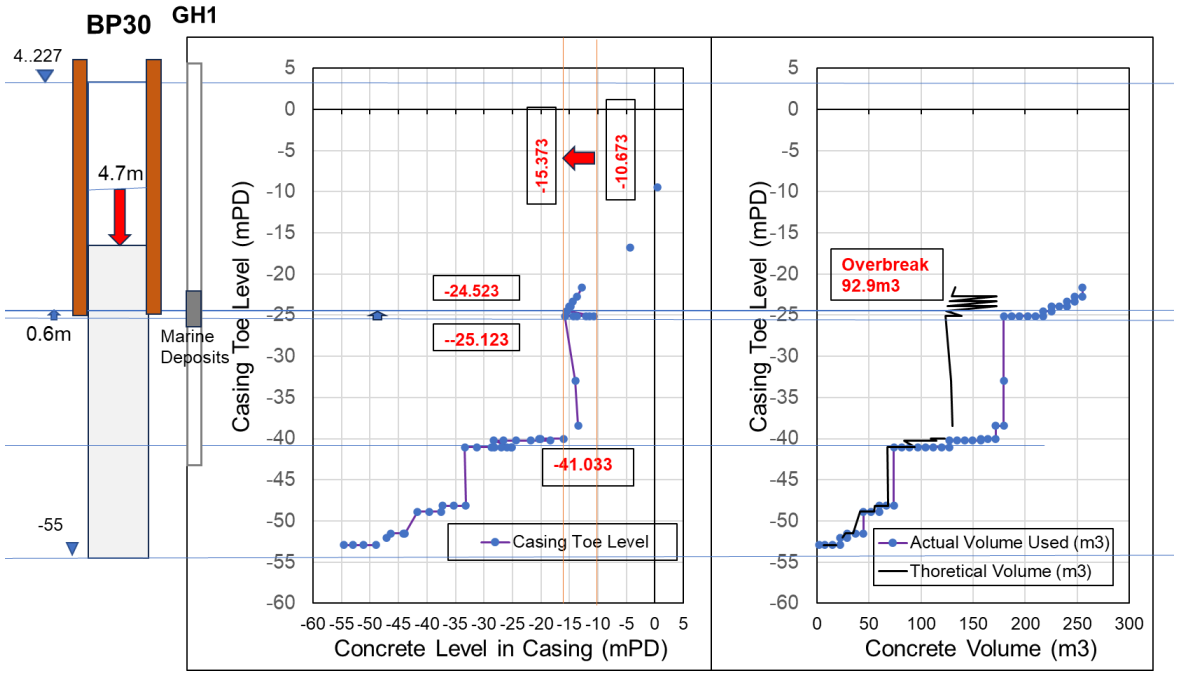

Figure 3: Concreting Records of BP30

3.2 Concreting Problem in BP9

BP9 is a 2 m diameter pile founded at -59.19 mPD with a 2 m rock socket. It has a bell-out of 2.85 m. At this pile location, the ground level is at 4.308 mPD. In all, a total of 8 lengths of casing up to 56.03 m long were installed, and the final casing toe level was at -47.122 mPD.

After the 22nd truck concrete pour of 154 m^3, the casing toe level was lifted by 13.75 m from -37.472 mPD to -23.722 mPD. The concrete level in the casing dropped by 6.5 m from -14.792 mPD to -21.292 mPD, as shown in Figure 4.

There was difficulty to re-insert the tremie pipe into the concrete at -23.722 mPD to continue the concreting. It was suspected that there was a hardened concrete layer at -23.722 mPD.

Another 4 loads of concrete of 28 m^3 (23rd to 26th truck) were added, followed by lifting of the casing toe to -23.122 mPD. The concrete level did not rise. Another 2 loads of concrete of 14 m^3 (27th to 28th truck) were added, followed by lifting of the casing toe to -21.922 mPD. The concrete level rose by 300 mm only to -20.992 mPD. Another 11 loads of concrete of 77 m^3 (29th to 39th truck) were added. The concrete level rose by 20.10 m to 2.308 mPD.

As compared with the theoretical volume of concrete, there was a huge increase in the concrete volume used at the casing toe level between -37.472 mPD and -23.722 mPD. On completion of the concrete pour, 273.0 m^3 of concrete was used giving an overbreak of 44.15%, and a 30.83 m long casing with the casing toe at -21.922 mPD was left in. The pile was subsequently abandoned after widespread concrete defects were found between -21 mPD and -23 mPD (where the Marine Deposits were found (see Figure 5)) by sonic logging and in the samples retrieved from the investigation coring,

4 ADDITIONAL GI WORKS

The objective of the additional GI works was to establish if there was any significant variation in the ground and groundwater conditions at the BP30 and BP9 locations which could give rise to the concreting problem in the piles.

A total of 4 additional drillholes (GH1, GH2, GH3 and GH4) were completed. Two VW piezometers with one each in fill and alluvium were installed in GH2, GH3 and GH4. The data from the piezometers were collected by wireless dataloggers and transmitted by long range radio to a data server embedded in the gateway

(see Figure 7) . Location of these drillholes is included in Figure 1. The geological profile of the site based on the additional GI information along Section C-C' is shown in Figure 5. The levels at which the VW piezometers were installed are also included.

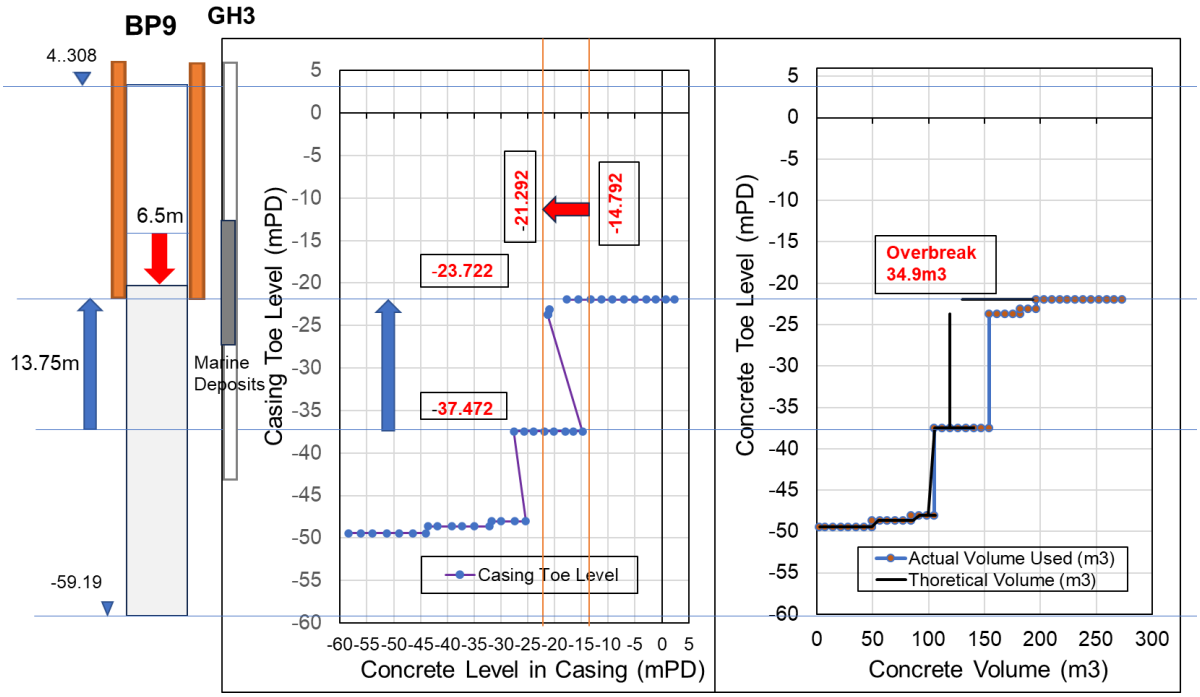

Figure 4: Concreting Records of BP9

5 FINDINGS OF ADDITIONAL GI WORKS

5.1 Greater Extent and Thickness of Marine Deposits at BP30 and BP9 Locations

Marine Deposits were found in all additional drillholes (GH1 to GH4). The extent and thickness of the Marine Deposits at the BP30 and BP9 locations were more substantial than those indicated in the tender GI information.

GH1 was close to BP30, and GH3 to BP9. The tender GI drillholes close to GH1 and GH3 were DH6 and DH8 respectively. At GH1, there was a 3 m thick Marine Deposits, but no Marine Deposits were found at DH6. Marine Deposits were 14 m thick at GH3, but 4.5 m thick at DH8.

There were Marine Deposits at the casing toe level of -24.523 mPD and -23.722 mPD in BP30 and BP9 respectively at which the concreting problem occurred.

Marine Deposits were also found in GH4 and GH2: 6.2 m thick at GH4 and 2.5 m thick at GH2. In between GH2 and GH3, the thickness of the Marine Deposits increased from 2.5 m to 14 m.

It is noted in GCO (1986) that Marine Deposits of the Hang Hau Formation could go up to 20 m thick.

5.2 Weaker and More Compressible Marine Deposits at BP30 and BP9 Locations

A comparison of the SPT N values of Marine Deposits between those indicated in the tender and additional GI works is given in Figure 6.

The SPT N values of Marine Deposits taken in the tender GI works were significantly higher than those taken in the additional GI works. An average SPT N value of 23.3 and 8 was obtained from the tender and additional GI works respectively. At -20 mPD, the SPT N value was found to be 23 from the tender GI works and 8 from the additional GI works. The Marine Deposits encountered were weaker and more compressible, as compared with those shown in the tender GI works.

5.3 Strong Tidal Fluctuation of Groundwater Level

There was a strong tidal fluctuation of groundwater level at the site. Typical plots of the groundwater levels recorded by the VW piezometers PZ2b in fill and PZ2a in alluvium in GH2 are shown in Figure 7. There was a tidal fluctuation of over 1.5 m/day and 2 m/day for the groundwater in fill and alluvium.

This tidal fluctuation of groundwater could lead to a significant loss in soil strength from its initial value (Ke & Takahashi, 2012), in particular for the weaker Marine Deposits at BP30 and BP9.

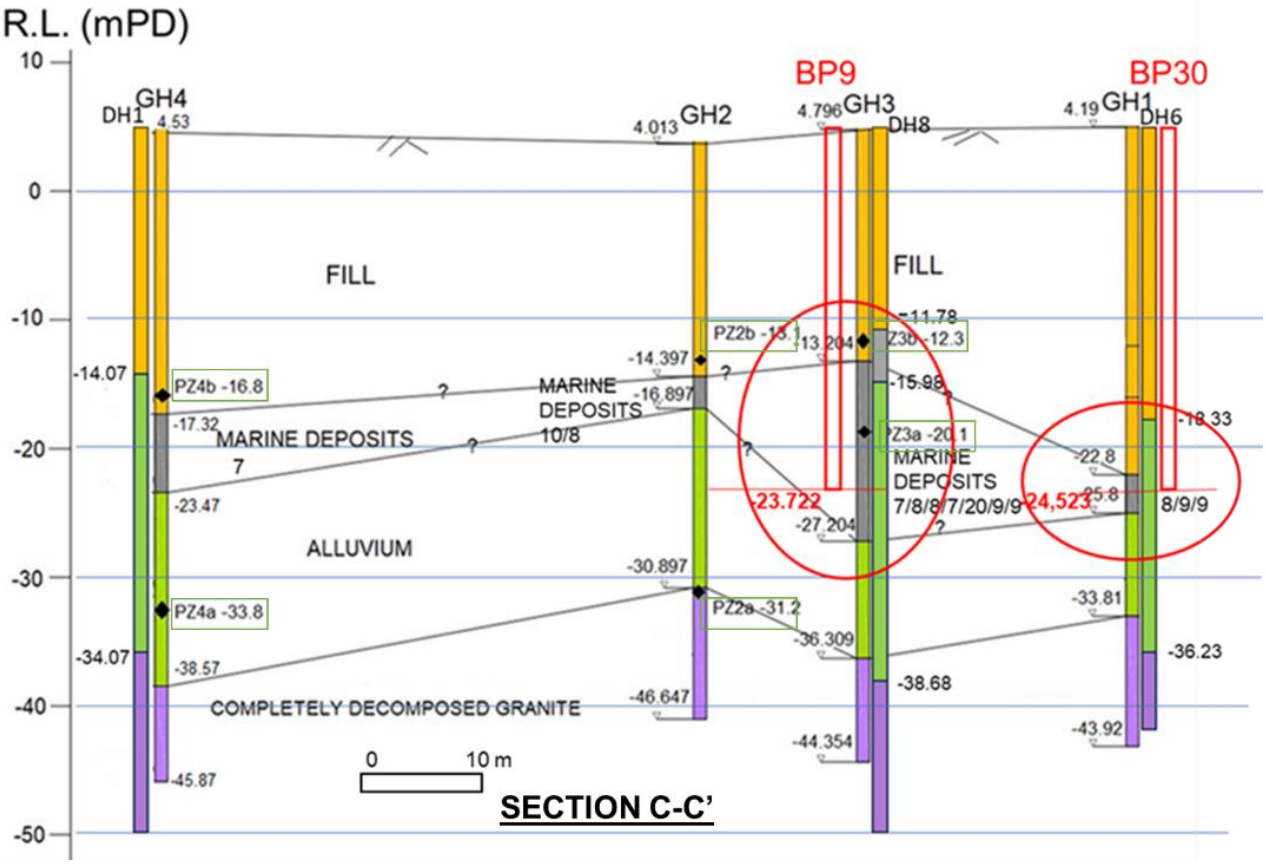

Figure 5: Geological Profile of the Site based on Additional GI information

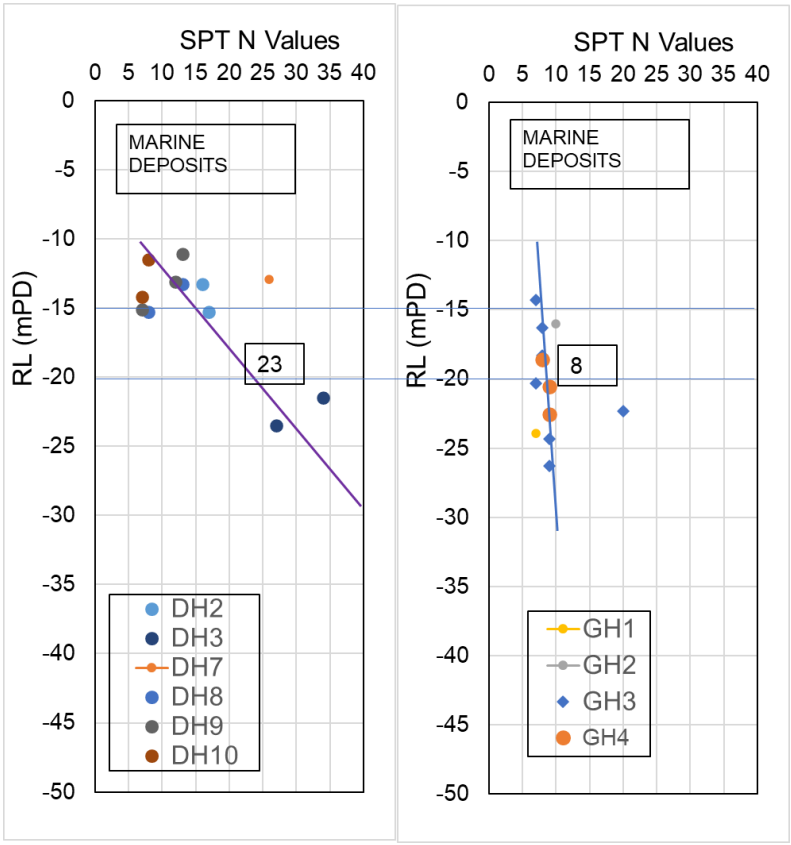

Figure 6: Plot of SPT N Values Between Tender and Additional GI Works

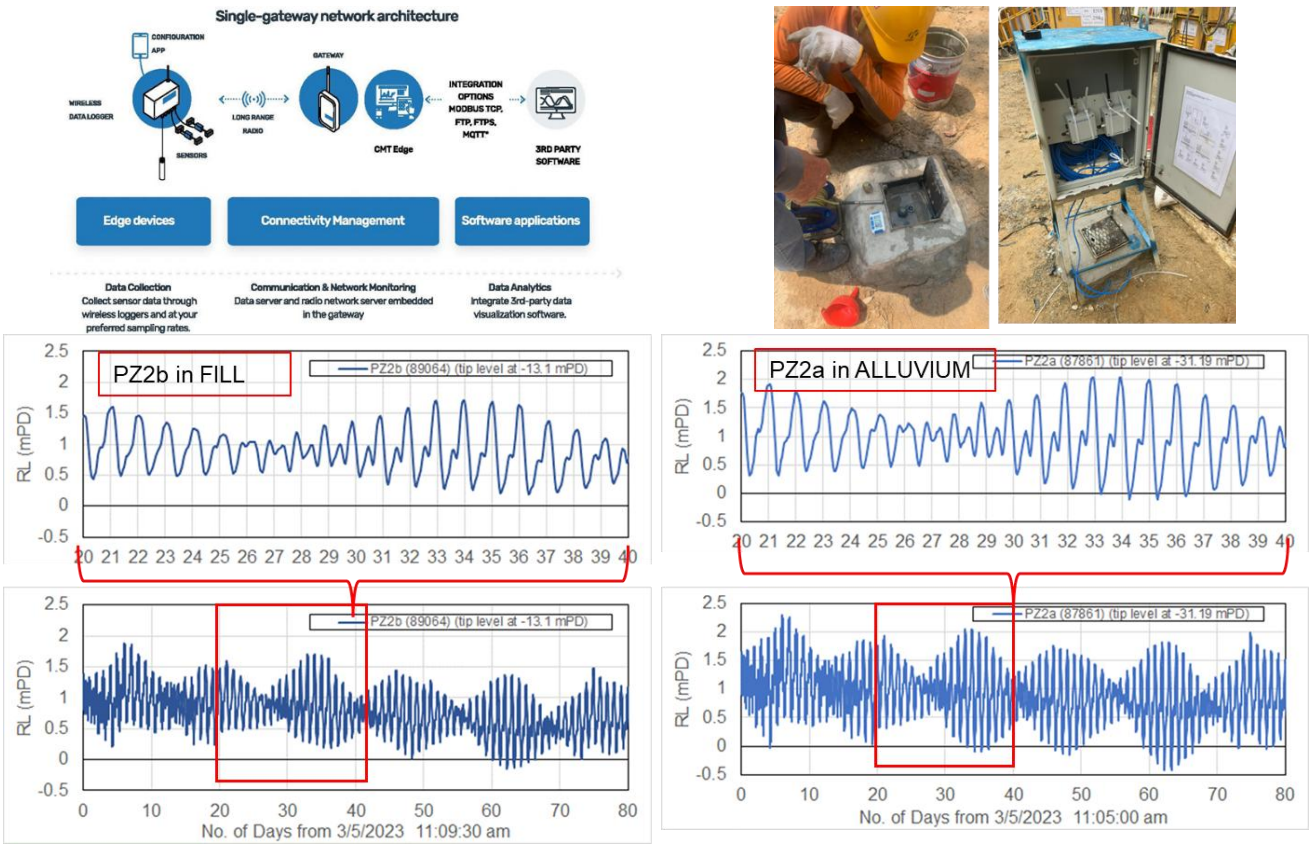

Figure 7: Typical Plot of Groundwater Levels at PZb and PZa at GH2

6 INVESTIGATION

The objective of the investigation was to gather evidence to support the mechanism postulated for the early setting of concrete, and hence the formation of a hardened concrete layer. This was achieved by examination of (i) the composition and contents of the contaminated concrete in the piles; (ii) the effect of Marine Deposits on the early setting of concrete, and (iii) other ambient factors, such as presence of dissolved CO_2 in groundwater and organic matter in Marine Deposits that could favour the process of early setting of concrete.

An investigation drillhole (C3) had been taken at the centre of BP30 upon completion of the concreting. The cement grout/concrete samples retrieved from C3 at -5.891 mPD and -7.94 mPD were sent for PSD, XRD and XRF tests. The tests were carried out by the Hong Kong Polytechnic University.

Water samples from a nearby pile (BP25) (see Figure 1) were taken at -24 mPD and -28 mPD and sent for testing of dissolved CO_2 content. The tests were carried out by Fugro Technical Services Ltd. and SGS Hong Kong Ltd. Soil samples of Marine Deposits retrieved from GH4 were tested for organic matter content. The tests were carried out by ETS-Testconsult Limited.

7 FINDINGS OF THE INVESTIGATION

7.1 Presence of Clay Minerals in Contaminated Concrete

A summary of the PSD, XRD and XRF test results is given in Tables 1 and 2. Typical plot of the XRD test results is given in Figure 8.

There was some 3% clay in the samples from the PSD tests, and 0.53% to 2.88% from the XRD tests, which confirmed the ingress of Marine Deposits into BP30. The clay minerals are represented by illite and kaolinite.

The presence of clay in the wet concrete has a detrimental effect on the concrete. The clay absorbed water from the wet concrete to form a paste, resulting in loss in workability and early setting of concrete.

The effects of clay on the concrete properties had been investigated by Elahi & Ali (2017). The results of the studies showed that there was a drastic loss in the slump values of concrete as the clay content in the concrete increased. A loss in the slump values from 14% to 64% up to a clay content of 6% was measured. Similar studies were carried out by Choudhary et. al. (2019). In this case, the slump value decreased from 140 mm to 125 mm, as the clay content was increased to 2%.

7.2 Presence of Calcium Carbonate in Contaminated Concrete

In the hydration (setting) of concrete, the main components of cement (alite (C_3S) and belite (C_2S)) react with water to form new compounds, including calcium silicate hydroxide (C-S-H) and calcium hydroxide ($Ca(OH)_2$), as shown in Table 3.

As seen in Table 2, there is some 68.26% to 69.77% of calcium carbonate ($CaCO_3$) in the samples as revealed by the XRD tests, and 26.15% to 51.14% by the XRF tests. A slight difference in the percentage of $CaCO_3$ was found between the XRD and XRF tests because different samples were involved. $CaCO_3$ is represented by calcite and vaterite (which is a polymorph of $CaCO_3$).

Apophyllite, which is a potassium-calcium-fluoride silicate mineral, was also found in the XFD/XRF tests, which represented the C-S-H.

The formation of C-S-H and $CaCO_3$ led to the early setting of concrete, and hence the formation of a hardened concrete layer in BP30.

7.3 Presence of Dissolved CO_2 in Groundwater and Organic Matter in Marine Deposits

It was found that there was some 5 to 8% mg/L dissolved CO_2 in groundwater and some 0.1% organic matter in Marine Deposits. CO_2 enhances early setting of concrete. With CO_2, further carbonation reactions of C_3S and C_2S (the cement components of the wet concrete) took place forming $CaCO_3$ and C-S-H, as follows:

$$C_3S + CO_2 + H_2O \rightarrow \text{C-S-H} + H_2O + CaCO_3 \quad (1)$$

$$C_2S + CO_2 + H_2O \rightarrow \text{C-S-H} + H_2O + CaCO_3 \quad (2)$$

Presence of CO_2 can produce a rapid strength gain in concrete (Khan et. al., 2018). Monkman et. al. (2016) in their tests using CO_2 as an accelerating admixture to concrete found that the reaction between CO_2 and the hydrating cement created finely distributed $CaCO_3$ that influenced the subsequent hydration. It was found that for the concrete batch with the CO_2 injection, the time to initial set and final set was reduced by an average 25% and 23% respectively with respect to the batch without the CO_2 injection.

The organic matter in Marine Deposits produced CO_2 which helps facilitate the process of early setting of concrete.

Table 1: Summary of PSD Test Results for Samples from Drillhole C3 in BP30

PSD by weight				
Sample	Clay	Silt	Sand	Gravel
at -5.891 mPD	3%	50%	47%	0%
at -7.94 mPD	0%	10%	90%	0%

Table 2: Summary of XRD and XRF Test Results for Samples from Drillhole C3 in BP30

		Samples at	
Mineral	Description	-5.891 mPD	-7.94 mPD
		% by weight	
Apophyllite	a potassium-calcium fluoride-silicate mineral	1.26%	7.69%
Illite	a clay mineral	1.99%	0.53%
Kaolinite	a clay mineral	0.89%	0.00%
Albite	a plagioclase feldspar mineral	12.33%	4.15%
Calcite	calcium carbonate ($CaCO_3$)	48.20%	62.60%
Vaterite	a polymorph of calcium carbonate ($CaCO_3$)	21.57%	5.36%
Quartz	an essential mineral in granites, granodiorites & rhyolites	13.76%	19.67%
		100.00%	100.00%

XRD

		Samples at	
Mineral	Description	-5.891 mPD	-7.94 mPD
		% by weight	
Apophyllite	a potassium-calcium fluoride-silicate mineral	1.70%	1.68%
Amorphous		21.24%	18.03%
Microcline	an igneous rock-forming tectosilicate mineral	3.53%	0.00%
Albite	a plagioclase feldspar mineral	13.31%	37.23%
Calcite	calcium carbonate ($CaCO_3$)	44.47%	24.48%
Vaterite	a polymorph of calcium carbonate ($CaCO_3$)	6.67%	1.67%
Quartz	an essential mineral in granites, granodiorites & rhyolites	9.07%	16.91%
		100.00%	100.00%

XRF

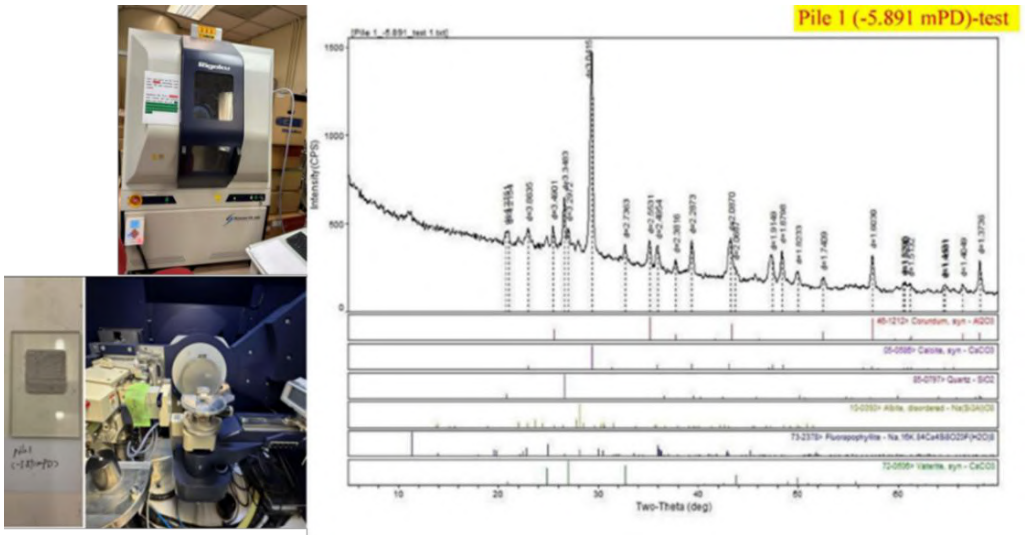

(a) Equipment Used (b) X-ray Diffraction Plot

Figure 8: Typical X-ray Diffraction Test Result

Table 3: Hydration of Cement

Ordinary Portland Cement (OPC)					Concrete		
Chemical Compounds			% (by weight)		Chemical Compounds		% (by weight)
	Chemical Formula				Calcium Silicate Hydrate	C-S-H	48%
Alite	$3CaO.SiO_2$	C_3S	70%	Hydration →	Calcium Hydroxide	$Ca(OH)_2$	14%
Belite	$2CaO.SiO_2$	C_2S	15%		Ettringite	Aft (ett)	4%
Aluminate	$3CaO.Al_2O_3$	C_3A	8%		Hydrated Calcium Aluminate	Afm	11%
Ferrite	$4CaO.Al_2O_3.Fe_2O_3$	C_4AF	7%			Anhyd	3%
						Pores	16%
						Other	4%

8 MECHANISM OF CONCRETE CONTAMINATION BY MARINE DEPOSITS IN BP30 AND BP9

The mechanism that took place in BP30 and BP9 leading to the concreting problem is postulated, as follows:

8.1 Turbulent flow of Wet Concrete Down the Casing Upon Lifting of the Casing

The downward flow of wet concrete in the casing is like a flow through a sudden expansion in a pipe, as shown in Figure 9(a), except that the flow is vertically downwards.

Reynolds number (Re) was used to assess the nature of flow. Re is a dimensionless number given by the ratio of inertia force to viscous force, as follows:

$$R_e = \frac{\rho v D}{\mu} \tag{3}$$

where ρ is the density of the fluid (kg/m^3); v is the flow speed (m/s); D is a characteristic linear dimension (m) and μ is the dynamic viscosity of the fluid (Pa·s, N·s/m^2 or kg/(m·s)).

When Re is less than 2000, the flow is laminar. If Re is greater than 3500, the flow is turbulent. When Re lies between 2000 and 3500, the flow is a transitional flow. In laminar flow, viscous forces are dominant, and fluids move along smooth streamlines. In turbulent flow, inertial forces dominate and tend to produce chaotic eddies, vortices and other flow instabilities. A comparison of the flow pattern of laminar flow and turbulent flow is shown in Figure 9(b). In the figure, the straight, parallel black lines are streamlines which are parallel to the mean flow (streamlines). In laminar flow, the fluid particles follow the streamlines. In turbulent flow, eddies of different sizes are superimposed onto the mean flow, and in the turbulent region, the flow follows both the mean flow and the eddies. Larger eddies cause lateral flow across streamlines, and small eddies create smaller scale stirring that causes the flow to spread (diffuse).

There was a rapid change in head as the wet concrete flowed downwards. The change in head of the wet concrete before and after lifting of the casing can be represented by the Bernoulli's equation, assuming that the wet concrete is an incompressible, frictionless fluid, as follows:

$$P + \frac{1}{2}\rho v^2 + \rho g h = constant \tag{4}$$

$$\frac{P}{\rho g} + \frac{v^2}{2g} + h = constant \tag{5}$$

where P = Pressure head = pressure energy per unit volume; V = Velocity head = $\frac{1}{2}\rho v^2$ = kinetic energy per unit volume and Z = Elevation head = ρgh = potential energy per unit volume

Applying Equation (5) to the flow conditions before and after lifting of the casing toe level from -25.123 mPD to -24.523 mPD for BP30, and from -37.472 mPD to -23.722 mPD for BP9 (see Figures 3 and 4), the Re for the downward flow of the wet concrete was calculated. The typical parameters used in the evaluation of the Re for BP9 are given in Figure 10. In the evaluation, a density of 2600 kg/m^3 and a dynamic viscosity of 25 Pa.s were used for the wet concrete (see Ferraris (1999)).

The Re for the downward flow of the wet concrete was found to be 5365 for BP30 and 2121 for BP9, which indicates that the flow of the wet concrete in BP30 was fully turbulent, whereas the flow in BP9 was transitional. The diameter of the bulged diameter of BP30 developed was calculated to be 5.9 m, as compared with 2.4 m in BP9. The downward velocity of the flow of the wet concrete was calculated to be about 8.5 m/s in both cases.

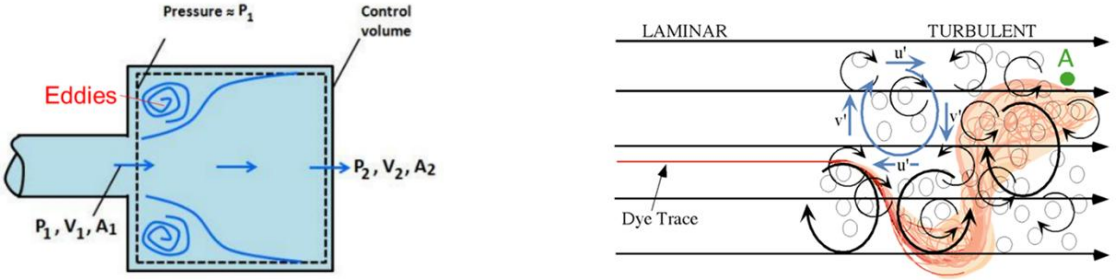

(a) Flow through a Sudden Expansion in a Pipe (b) Flow Pattern of Laminar and Turbulent Flow

Figure 9: Characteristics of Laminar and Turbulent Flow

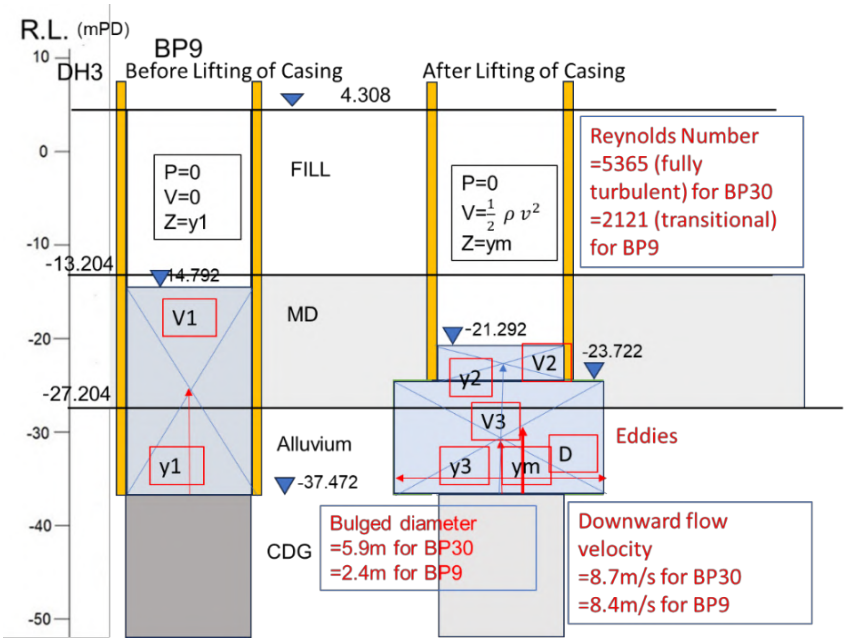

Figure 10: Parameters Used in the Evaluation of Reynolds Number

8.2 Base Heave Failure and Squeezing Out of Marine Deposits by Wet Concrete at the Casing Toe Level

There was base heave failure during shaft excavation in BP30 and BP9. The factor of safety (FS) for base heave for BP30 and BP9 at 27.3 m depth (=25.8m-2m+4.3m, where the 2 m is the height of the soil above the casing toe) and 29.507 m depth (=27.204m-2m+4.3m) respectively (which correspond closely to the depths at which the concreting problem occurred in the piles) was used and computed using Equation (6) (the method by Bjerrum and Eide (1956)).

$$FS = \frac{C_u N_c}{\gamma H} \tag{6}$$

where Cu = undrained shear strength (kPa); Nc = bearing capacity factor; γ = unit weight of soil (kN/m^3) and H = depth to excavation (m).

In the evaluation, a SPT N value of 8, as that obtained from the additional GI works at -20 mPD, was used. This gives an unconfined compressive strength (qu) of 50 kPa to 100 kPa or a Cu of 75/2 = 37.5 kPa, corresponding to a medium stiff CLAY (see Das (2007)).

The FS for base heave was found to be less than 1 in both cases.

For BP30, given H = 27.3 m, L/B = 1 and H/B > 4, Nc becomes 9 (see Bjerrum and Eide (1956)). Using an average γ of 18 kN/m^3, the FS for base heave was 0.687, as shown below:

$$FS = \frac{C_u N_c}{\gamma H} = \frac{37.5x9}{18x27.3} = 0.687 \lll 1 \ (failure) \quad (7)$$

For BP9, H is 29.507 m. The FS for base heave was 0.635, as shown below:

$$FS = \frac{C_u N_c}{\gamma H} = \frac{37.5x9}{18x29.507} = 0.635 \lll 1 \ (failure) \quad (8)$$

With the base heave failure occurring, Marine Deposits outside the casing flew into the casing creating cavities outside the casing, as the Marine Deposits inside the casing were excavated.

Upon lifting of the casing toe level from -25.123 mPD to -24.523 mPD for BP30, and from -37.472 mPD to -23.722 mPD for BP9, the wet concrete flew down the casing, pushed the Marine Deposits outwards and squeezed into the cavities inside the Marine Deposits. Based on the concrete placement records, the overbreak for this portion of the pile was 74.63% for BP30 and 29.35% for BP9, with the diameter increasing from 2 m to 5.9 m for BP30 and to 2.4 m for BP9 respectively (see Section 8.1).

It should be noted that if a SPT N value of 23 was used, as that obtained from the tender GI works at -20 mPD, a qu of 200 kPa to 400 kPa or a Cu of 300/2=150 kPa, corresponding to a very stiff CLAY, would be obtained. This would give a FS for base heave of 2.747 and 2.542 for BP30 and BP9 respectively, implying that base heave in the piles would not occur.

8.3 Turbulent Mixing and Contamination of Wet Concrete by Marine Deposits in particular at the Casing Toe Area

The flow of the wet concrete down the casing in BP30 was fully turbulent. The flow produced eddies and vortices which caused ingress of the Marine Deposits and turbulent mixing and contamination with the wet concrete, in particular near the casing toe area. The flow in BP9 was a transitional flow. Some eddies and vortices were developed causing minor ingress of Marine Deposits and mixing with the wet concrete. Hence, the ingress of Marine Deposits into the wet concrete, and the concreting problem, was less serious in BP9 than in BP30.

8.4 Early Setting of Concrete Forming a Hardened Concrete Layer

The Marine Deposits, which contained clay and dissolved CO_2, contaminated the wet concrete and triggered the early setting of the concrete forming a hardened concrete layer. The dissolved CO_2 in groundwater and organic matter in Marine Deposits provide a good environment for the early setting of concrete. The tidal fluctuation of groundwater helped recharge CO_2 in groundwater and organic matter in Marine Deposits and further facilitate the process of early setting of concrete.

9 CONCLUSIONS

The following conclusions can be made from the study:

(a) The concreting problem that had occurred in BP30 and BP9 was not the result of a single event, but a combination of different latent conditions that had stacked up to produce the major defect (like a Swiss Cheese Model incident). The latent conditions are defined as hidden, unexpected physical or systemic issues (like subsurface rock, contaminated soil, or design flaws) that are not reasonably discoverable during initial site inspections or tendering but emerge during the works, causing extra costs or delays. They represent pre-existing weaknesses that lie dormant until triggered, leading to failures or adverse outcomes, especially in construction, engineering, and safety. In this case, the latent conditions included the presence of an unexpected layer of thicker and weaker Marine Deposits at the pile locations, strong tidal fluctuation of groundwater (which weakened the soils), and presence of dissolved CO_2 in groundwater and organic matter in Marine Deposits (which provided a favourable condition for the occurrence of the problem).

(b) The mechanism for the concreting problem in BP30 and BP9 was complicated involving (i) turbulent flow of wet concrete down the casing upon lifting of the casing; (ii) base heave failure and squeezing out of Marine Deposits by wet concrete at the casing toe level; (iii) turbulent mixing and contamination of wet concrete by Marine Deposits in particular at the casing toe area; and eventually (iv) early setting of concrete forming a hardened concrete layer. The new information obtained by the additional GI works and the investigation provided good support for the mechanism postulated.

ACKNOWLEDGEMENTS

The author would like to thank Wilson & Associates Limited for the support and permission to publish the paper. Thanks are also due to Professor J.H. Yin of the Hong Kong Polytechnic University for reviewing the investigation report and supervising the PSD, XRD and XRF tests for the study.

REFERENCES

Bjerrum, L. & Eide, O. (1956). Stability of Strutted Excavations in Clay. Geotechnique, Vol. 6, No. 1. pp. 32-47.

Choudhary, H. Siddiqui, M.A. & Saha, D. (2019). Effect of Clay Fines on Strength and Workability of Concrete. J. of Civil Engineering and Environmental Technology, Vol. 6, Issue 5, July-September, pp 311-315.

Das, B.M. (2007). Principles of Foundation Engineering.

Elahi, A. & Ali, A. (2017). Effects of Clay on properties of Concrete. Resilient Structures and Sustainable Construction.

Ferraris, C. F. (1999). Measurement of the Rheological Properties of High Performance Concrete: State of the Art Report. Vol. 104, No. 5, September–October 1999 Journal of Research of the National Institute of Standards and Technology.

GCO (1986). Hong Kong Geological Survey Memoir No. 2. Geology of Hong Kong Island and Kowloon.

Ke, L. & Takahashi, A. (2012). Strength Reduction of Cohesionless Soil due to Internal Erosion Induced by One-dimensional Upward Seepage Flow. Soils and Foundations 2012:52(4):698-711, The Japanese Geotechnical Society.

Khan, M.T., Saud, K.R., Irfan, K.A. & Ibrahim, S. (2018). Curing of Concrete by Carbon Dioxide. International Research Journal of Engineering and Technology, Volume: 05 Issue: 04.

Monkman, S., MacDonald, M., Doug Hooton, R. & Sandberg, P. (2016). Properties and Durability of Concrete Produced Using CO2 as an Accelerating Admixture. CarbonCure Technologies, 60 Trider Crescent, Dartmouth, NS B3B 1R6, Canada.

Implementing the 5A Control Framework: Case Studies Demonstrating Economic and Safety Benefits in Deep Excavation Design

Terence L Y Yau
&
Rachel Y K Chan
C M Wong & Associates Ltd

ABSTRACT

The design of excavation and lateral support (ELS) systems has traditionally been constrained by the conservative 3A empirical rule, often resulting in over-conservative and heavy strut systems. The Geotechnical Engineering Office (GEO) has initiated a paradigm shift with its Technical Guidance Note No. 54 (TGN 54) and Publication No. 1/2023, advocating for an enhanced 5A Approach. This new methodology introduces a five-tier performance-based control framework (Alert, Alarm, Action Levels 1-3), linking rational and often relaxed deformation limits (e.g., 0.5%H_e for Action Level 3) to explicit monitoring and response protocols.

This paper presents two detailed case studies demonstrating the successful application of the codified 5A framework. Our findings indicate that designing to the 5A deformation limit, in accordance with the TGN 54 control mechanism, resulted in a 15% reduction in the weight of steel struts and a decrease of 30% to 50% in preload force compared to conventional 3A designs. A key outcome was a notable enhancement in construction safety: lighter struts facilitated reduced crane lift weights, simplified handling, and smaller preload forces, thereby lowering the risk of damaging existing underground utilities and accelerating installation processes. Additionally, material cost savings of approximately 15% were achieved.

This paper serves as a blueprint for implementing this advanced methodology in urban excavation projects.

Keywords: Deep Excavation, 5A Approach, TGN 54, Performance-Based Design, Strut Optimization, Construction Safety, Monitoring and Control

1 INTRODUCTION

In 2023, the Geotechnical Engineering Office (GEO) of the Hong Kong Special Administrative Region issued GEO Publication No. 1/2023 (GEO, 2023) and Technical Guidance Note (TGN) No. 54 (GEO, 2024a) these two landmark documents to guide the control of ground deformation in major geotechnical works. Traditionally, the industry relies on three-tier triggered control mechanism (3A), i.e. Alert-Alarm-Action (AAA) Levels, to provide a clear protocol for monitoring and responding to ground movements. The traditional 3A levels in Hong Kong used rational empirical limit (BD,2018) to forewarn before damage, prompt inspections and mitigation.

Table 1 Recommended Empirical Limits for 3A Approach (BD,2018)

Instrument	Criterion	Alert	Alarm	Action
Ground monitoring marker	Total settlement	12mm	18mm	25mm
Tilting monitoring marker	Angular distortion	1:1000	1:750	1:500

The 3A control mechanism has been successfully applied for many simple excavation projects. However, for those deeper and more complicated excavation, adoption of 3A empirical values has resulted in some distorted solution in ELS design such as excessive preloading and highly congested shoring systems.

Recognizing the need for greater flexibility and projects grew in complexity, GEO introduced enhanced empirical approach by expanding 3-tier system (3A) into a 5-tier system (5A) by sub-dividing the third response actions into 3 levels, i.e. Alert-Alarm-Action Levels 1-3.

Table 2 Recommended Empirical Limits for 5A Approach (GEO,2023)

Instrument	Criterion	Alert	Alarm	Action		
				Level 1	Level 2	Level 3
Ground monitoring marker	Total settlement	10mm	15mm	20mm	0.3% He*	0.5%He*
Tilting monitoring marker	Angular distortion	1:600	1:500	1:400	1:350	1:300

*He is the maximum excavation depth of the ELS works and subject to a maximum empirical value of 100mm

Under the 5A approach, cumulative settlement triggers specific response actions:

- Action Level 1 addresses serviceability concerns related to road pavements.
- Action Level 2 triggers a review of ELS works performance and further investigation, e.g. GPR surveys, CCTV or open trench inspection of underground services and probing tests should be carried out to investigate any underlying problems.
- Action Level 3 indicates under-performing ELS works, necessitating work suspension and additional precautionary measures to minimize further ground settlement.

Action Level 2 and 3 make the control mechanism more meaningful and practical by reporting to relevant authorities and stakeholders, e.g. BD/ GEO/Utilities Undertakers, ELS design reviews, utilities exposures/ repairs and suspension of works for ineffective response actions.

The essence of 5A approach is to emphasize regular performance verification via instrumentation monitoring data, design review at key stages, i.e. after reaching Action Level 2/3 and the execute mitigation measures to minimize the construction impact to acceptable level. This dynamic loop ensures the serviceability and safety counting on proper execution of adaptive control of design assumptions.

2 CASE STUDY

Two deep excavation sites for residential development, named site A with approximately 22m excavation depth and site B with approximately 17m excavation depth, 6 to 8 nos. of shoring layers adjacent to each other are located at Kowloon.

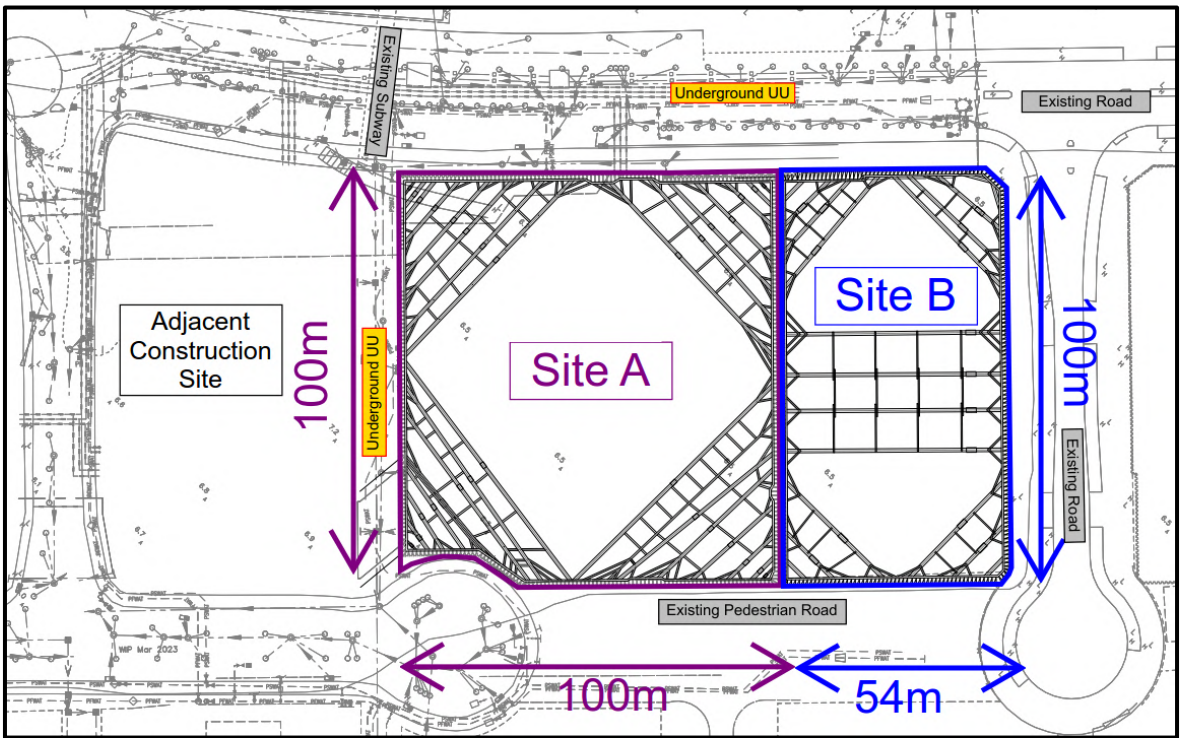

Figure 1 – Site A and B Layout Plan

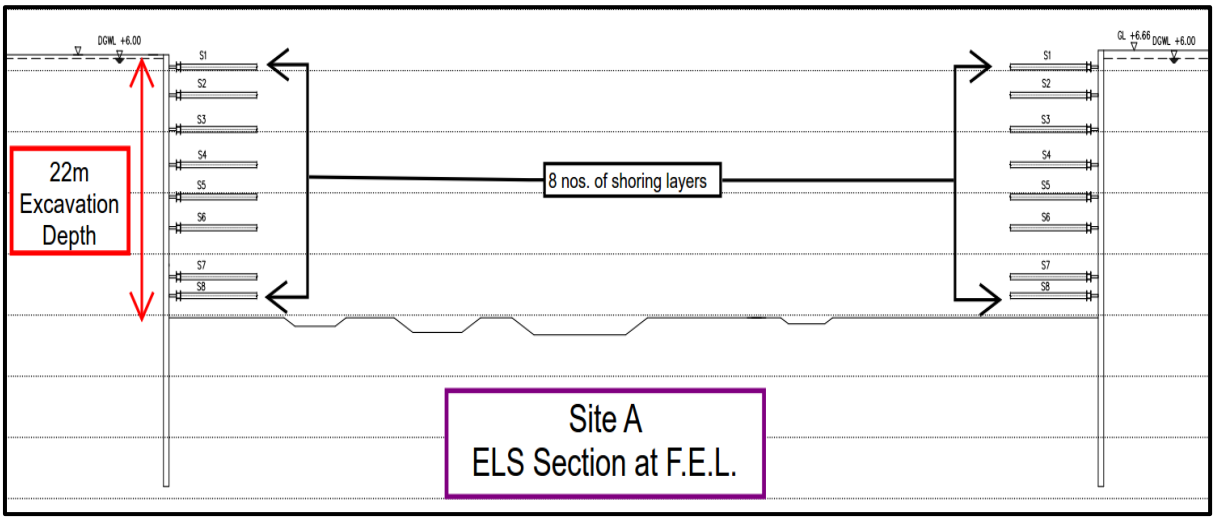

Figure 2 – Site A ELS Section

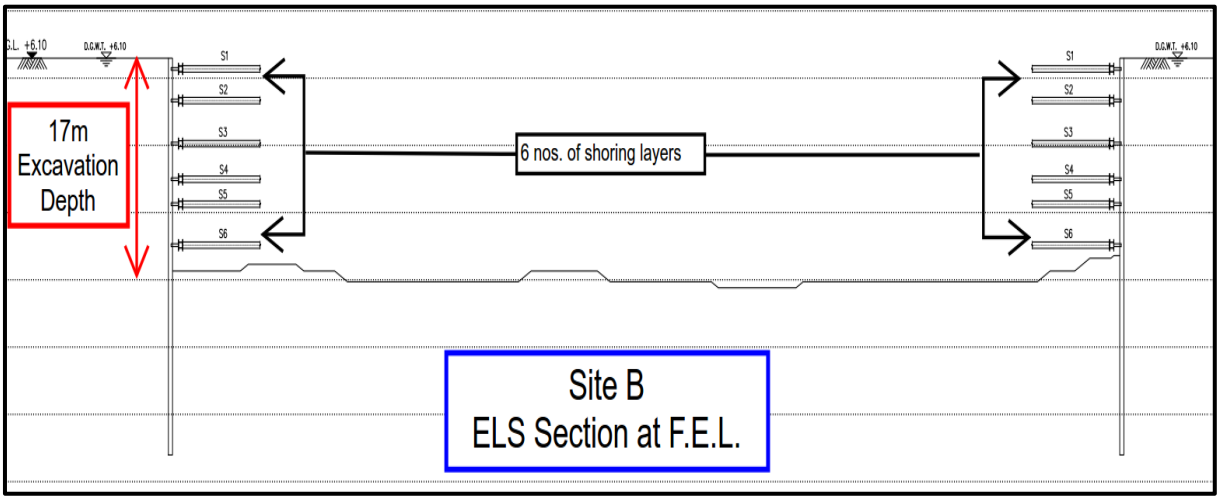

Figure 3 – Site B ELS Section

2.1 Site Description and Topography

Site A: The topography is generally flat, with an average ground level of approximately +6.5 mPD. The proposed development includes several tower blocks with basements, leading to a general final excavation level of -15.2 mPD. A short underground tunnel is designed to connect to an adjacent development. Existing roads and utilities (drainage, water, electric, and district cooling systems) are present nearby, along with registered retaining structures for abandoned subways and footpaths.

Site B: Similarly flat, with an average ground level of +6.5 mPD. The proposed development includes tower blocks with basements, with a final excavation level of -10.5 mPD. An existing underground box culvert and tunnel are located nearby, along with two adjacent residential developments under construction. Utilities in the vicinity include fiber optic cables and DCS pipes.

2.2 Site Geology

With reference to the findings from the site specific ground investigation (GI), the geology of the sites are summarized as follows:

Site A generally comprises of 6m to 13m fill overlaying 2m to 24m alluvium. Completely to highly decomposed granite are encountered underneath these layers of soil. Below the weathered granite, Grade III or better rock is encountered. The highest and lowest measured groundwater level at site A are at +4.8mPD and -0.5mPD. The ELS design is split into ULS and SLS cases and the adopted groundwater levels are +6.0mPD and

+4.0mPD respectively.

Site B generally comprises of 6m to 9m fill overlaying 3m to 8m alluvium. Completely to highly decomposed granite are encountered underneath these layers of soil. Below the weathered granite, Grade III or better rock is encountered. The highest and lowest measured groundwater level at site B are at +3.0mPD and -1.0mPD. The ELS design is split into ULS and SLS cases and the adopted groundwater levels are +6.5mPD and +4.0mPD respectively.

2.3 ELS Design for Site A and B

The first approval of the ELS design for both sites were approved by the Buildings Department (BD) before the authors involved in these two projects based on the 3A approach.

In order to comply with 3A tiers system specified in section 7.2.4 (Monitoring of Ground Movement) from Code of Practice for Foundation (2017) issued by BD in 2017, i.e. 25mm Action limit, and relative high design groundwater level, i.e. +6.0mPD for both site A (22m excavation depth) and site B (17m excavation depth), total 8 nos. of shoring layers were designed for site A while total 6 nos. of shoring layers were designed for site B respectively. Also, to control the settlement at final excavation stage, heavy preload forces were applied at different excavation level, i.e. max. 950kN/m preload force was adopted for site A while max. 900kN/m preload force was adopted for site B.

Following the release of GEO Publication No. 1/2023 (Dec 2023) and the subsequent introduction of the 5-tier system in PNAP-137 (Nov 2024), the authors opted to adopt the 5A deformation limit to redesign the lateral support system to optimize the design.

Given the proximity of utilities (gas, water, sewage, electrical), extensive collaboration with stakeholders (Towngas, CPL, DSD, EMSD, WSD, CEDD) was undertaken prior to submission. Impact assessments were conducted and agreements were reached regarding trigger levels and response actions. Approval for the 5A design approach was granted after all engineering assessments were deemed satisfactory.

2.4 Engineering Comparison

The engineering enhancements achieved under the 5A approach compared to the original 3A designs are summarized below:

Table 3: Site A and B Engineering Enhancement under 3A and 5A Approaches

Engineering Design	Enhancement under 5A approach compared to 3A approach	
	Site A	Site B
Preload force	32% to 50% reduction	32% to 48% reduction
Shoring steel tonnage	14% reduction (880 tons)	14% reduction (310 tons)

Adopting the 5A monitoring limit resulted in a 30–50% reduction in preload force, mitigating the risk of damaging underground utilities. The 14% reduction in steel shoring mass lowered costs, reduced installation risks, and improved site constructability by providing larger headroom. However, the above savings do not reflect the most optimized design, because material orders were partially placed before the revised design was approved under the 5A approach, and some elements had already been installed on site. Therefore, full optimization could not be achieved.

The traditional 3A approach in deformation limit served as the standard for ground deformation control in ELS works by establishing clear trigger level and predefined responses to manage risks to nearby buildings and infrastructure. However, the use of generic limits also leads to over-conversative in ELS strut design and late identification of exceedance of 3A trigger thresholds.

In 2024, GEO issued TGN 49 (GEO, 2024b) to provide a review on incidents of excessive ground loss occurred between 2007 and 2019 with supplementary guidelines recommended based on the outcome of the review. Two incident records are extracted to show the ineffective identification of excessive settlement and ineffective stipulation of 3A trigger level.

Case No. 1 – Yip Kan Street, Aberdeen

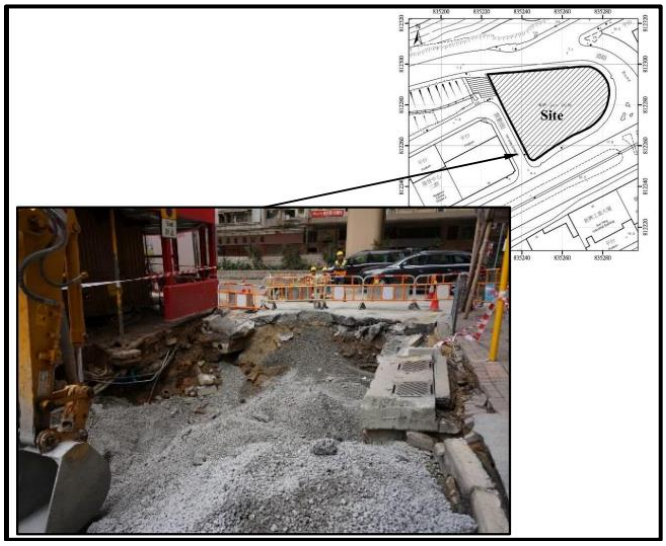

Figure 4 – 4m x 4m x 6m deep in Yip Kan Street, Aberdeen

A 4 m x 4 m x 6 m deep sinkhole was discovered, leading to the temporary full closure of Yip Kan Street.

Case No. 2 – Hok Yuen Street, Hung Hom

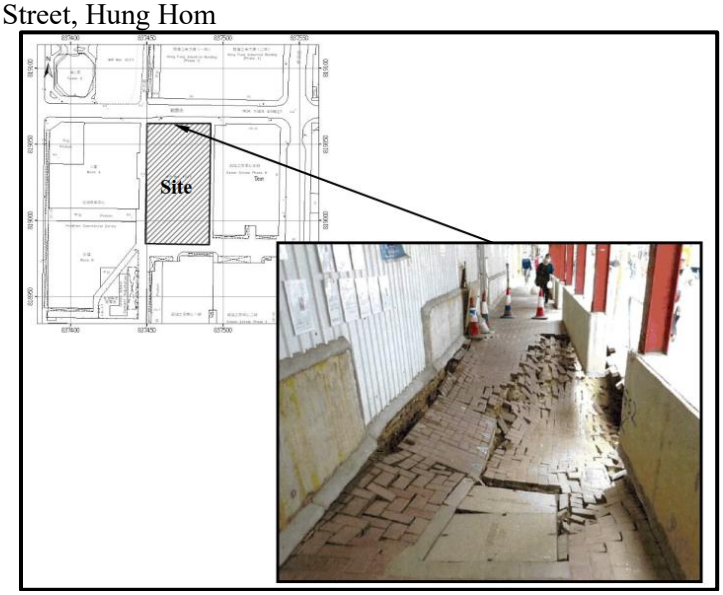

Figure 5 – 6m x 3.8m x 1.8m Sinkhole in Hok Yuen Street, Hung Hom

A 6 m x 3.8 m x 1.8 m deep sinkhole was found, resulting in the temporary closure of the adjacent footpath, undermining of the carriageway, and damage to underground utilities.

These incidents reveal two common patterns under the 3A approach:

1. Effectiveness depends heavily on instrument coverage, monitoring frequency, and rapid data review. Reaching the Action Level often mandates an immediate work stoppage.
2. Excessive ground loss frequently occurred before mitigation measures could be effectively implemented.

In contrast, the 5A approach offers a proactive control mechanism for managing ground settlements:

1. Early Warning: Action Levels 1 and 2 act as buffers, allowing formal design reviews and mitigation before reaching the critical threshold, preventing unnecessary work suspensions if the Building Authority is satisfied with interim assessments.
2. Risk Management: It provides a clear communication framework between contractors, Utilities Undertakers, the Registered Structural Engineer, and the government authorities.
3. Real-time Alignment: It formalizes the process of continuous review based on the lates monitoring data, enforcing documented reassessments of soil-structure interaction.

3 CONCLUSION

Adopting the 5A deformation limit under the TGN 54 control mechanism reduced steel strut weight and preload forces compared to conventional 3A designs. Continuous monitoring, predefined responses (e.g., Action Level 2 design review), and stakeholder-verified limits enhanced construction safety: lighter struts enabled reduced crane lift weights, simplified handling, smaller preload forces, lower risk of utility damage, and faster installation. Material cost savings of approximately 15% were achieved.

The 5A deformation limit represents a rational method for managing ground movement—proactively rather than reactively. While settlements during ELS works in Hong Kong are inevitable, the 5A framework provides a professional response that maintains safety without paralyzing construction activity.

REFERENCES

Building Department. 2017 "*Code of Practice for Foundation 2017*", Building Department, Hong Kong

Building Department. 2024 "*Ground-borne Vibration and Ground Settlement arising from Pile Foundation and Excavation and Lateral Support Works*", APP-137, , Building Department, Hong Kong

Geotechnical Engineering Office. 2023. *"Deep Excavation Design and Construction"*, GEO Publication No. 1/2023, Geotechnical Engineering Office, Civil Engineering and Development Department, Hong Kong.

Geotechnical Engineering Office. 2024a. *"Guidelines on Ground Deformation Control Mechanism for Geotechnical Works"*, GEO Technical Guidance Note No. 54, Geotechnical Engineering Office, Civil Engineering and Development Department, Hong Kong.

Geotechnical Engineering Office. 2024b. *"Supplementary Guidelines on Precautionary Measures for Mitigating the Risks of Excessive Ground Loss and Sinkhole Formation Associated with Deep Excavations"*, GEO Technical Guidance Note No. 49, Geotechnical Engineering Office, Civil Engineering and Development Department, Hong Kong.

Integrating Design Theory to Practical Construction of Reinforced Fill Slope

Clifford W.C. Phung & K.F. Yeung
Tapbo Civil Engineering Co. Ltd.
Penny K.C. Choy & Ben M.H. Wong
WSP (Asia) Limited

ABSTRACT

Reinforced fill slopes have become increasingly popular in modern geotechnical engineering for their ability to accommodate complex site constraints while enabling steeper geometries, optimized land use, and streamlined construction. Supported by mature design methodologies and established standards, these systems now offer reliable approaches that ensure structural integrity and safety across diverse geological conditions. Despite these advancements, practical implementation remains challenging. Many design assumptions require verification through laboratory or field testing, which depends on specialized facilities and resource availability. Construction issues also extend beyond material supply and equipment efficiency to include strict sampling and quality assurance requirements, often causing delays, especially on fast-track or remote projects. This paper highlights the critical factors that influence successful reinforced fill slope delivery. An integrated approach that connects theoretical design with construction practice is essential. Key considerations include early planning, robust material specifications, timely testing, and proactive risk management. By embracing innovative methods, even in areas lacking formal guidelines, engineers can improve cost efficiency and programme certainty without compromising safety. Ultimately, fostering a deeper understanding of both technical and practical aspects will support better performance, reliability, and sustainability in slope engineering.

1 INTRODUCTION

1.1 Purpose of adopting reinforced fill slope

The use of reinforced fill slopes has been widely adopted in site formation works due to their geometric flexibility, ability to optimize land use, ease of construction, and, most importantly, their relatively competitive cost for accommodating high retaining heights.

In a local site formation project, a reinforced fill slope is selected to expand the proposed golf course's usable area from 32 hectares to 45 hectares. This is achieved by constructing a peripheral reinforced fill slope along the existing sloping ground, thereby extending the platform and creating additional usable land.

However, the project is located in a uniquely constrained area: the site was previously used as a landfill. Beneath the existing fill layer (soil blanket) lies waste material. As a result, neither conventional piled foundations nor shear keys for a 10-metre-high retaining structure are permitted to penetrate through the soil blanket into the underlying waste.

1.2 Selection of reinforced fill system

The selection criteria are generally referenced from GEOGUIDE 6 (GEO, 2022), with the primary factors being the size of the reinforced fill structure and the construction time. A polymeric grid system (TENSAR RE500 Geogrid) is selected due to its durability and flexibility in accommodating potential future differential settlement. The total length of reinforced fill slope is approximately 1800m and six types of reinforced fill slopes (Type A~F) are proposed to cope with the geometric conditions. A total of about 244,000m^3 of selected fill material will be used, reinforced with 40,000 m^2 of geogrid.

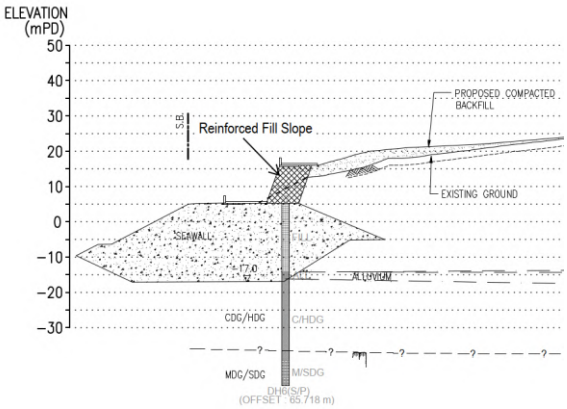

Plate 1: Indicative Section of Reinforced Fill Slope

1.3 Objectives

There are many technical papers and guidelines that provide a hands-on design criteria for reinforced fill slope in Hong Kong (DeepSeek, 2026). However the challenges encountered during the course of the project have only been addressed to a limited extent. This paper aims to (1) illustrate material testing procedures and associated lead time (2) discuss the current availability of testing in the private market (3) demonstrate good construction practices incorporating design for safety principles (4) raise industry awareness that these difficulties can be overcome with strong engineering support from design stage through to the construction stage.

2 DESIGN RATIONALE

2.1 Regulatory requirements

One of the constraints imposed by the Environmental Protection Department (EPD) is the prohibition of any encroachment into the existing waste within the landfill. Therefore, a reinforced fill structure using a polymeric grid system is selected.

Although geogrids have been used in many projects in Hong Kong, detailed design information is rarely published in the literature (S T G Ng, 2022). Furthermore, the assessment of reinforced fill products has been ceased since March 2022 (CEDD, 2026). As a result, newly proprietary product geogrid may require undergoing assessment by the BD Technical Support Section for the inclusion in Central Data Bank (CDB) building materials.

2.2 Testing requirements

According to the GEOGUIDE 6 (GEO, 2022), model specification is recommended. In this project, apart from the regular earthworks, two major elements will be tested, namely the selected fill material and the polymeric reinforcing element.

The selected fill material shall be subjected to the tests including, but not limited to, compaction tests, particle size distribution, liquid limit and plasticity index, coefficient of uniformity and direct sliding resistance.

The reinforcing element shall be subjected to tests including tensile test (BS EN ISO 10319:2015), carbon black content test (BS2782:Part 4 Method 452(1993)), dispersal of carbon black test (ASTM D5596) and direct shear test (large shear box apparatus) (Section 16.2 of GEOSPEC 3).

2.3 Testing agency accreditation

Having specified the required material tests, the implementation of these tests shall also be standardized and recognized. According to Practice Notes No. PNAP APP-118 (BD, 2012), the Building Authority will recognize testing agency accredited by the Hong Kong Laboratory Accreditation Scheme (HOKLAS) or by other laboratory accreditation bodies which have reached mutual recognition arrangements (MRA) with HOKLAS. Therefore, the project specification shall impose this requirement on the registered building contractor to ensure that all tests conducted by an accredited testing agency are within its accredited scope of testing.

3 DESIGN APPROVAL PROCESS

3.1 Programme

In recent years, the construction industry has increasingly shifted toward fast-track project delivery, resulting in significantly compressed design timelines. A fast-track project programme is often expected, leaving only a minimal design period. Typically, a 30-day design coordination period among the Client, Authorized Person (AP), Registered Structural Engineer (RSE), and Registered Geotechnical Engineer (RGE) will be arranged to review, comment, and consolidate all design inputs. This is then followed by a 60-day statutory approval period for the Buildings Department (BD) to assess the submission.

To secure the earliest possible approval from the authority, the key strategy is to streamline the BD submission process. Therefore, the project programme will consider shifting certain necessary material testing and in-situ testing to the construction stage, where appropriate.

3.2 Robust design parameters and assumptions

Given these tight timeframes, the design team is naturally compelled to adopt a conservative and robust design approach from the outset in order to obtain authority approval in one go without the need for re-submission. By adopting the existing certification of building product which has been accepted by individual organization referenced from CDB (BD, 2026) for certified product TENSAR RE500 Geogrid (Product No. RF 5/2025) and allowing the design to follow the technical data provided by the proprietor based on the previously approved design parameters, including design tensile strength, creep behaviour, and durability test data, the reinforced fill slope design would be considered sufficiently robust for vetting and approval.

3.3 Curtailed check system

The approval authority will rely on these design parameters and assumptions to check the submission under the curtailed check system specified in Practice Notes No. PNAP ADM-19 (BD, 2025) covering the fundamental issues of the building proposal. Therefore the AP, RSE and RGE may not be required to further resolve the design principles, allowing the design to proceed through the approval process with confidence and without the risk of abortive work.

3.4 Conditions and requirements imposed under the Buildings Ordinance

Upon obtaining design approval, the adopted the design parameters and assumptions, however, shall be still under verification prior to construction stage. The material should only be used after all testing requirements pertinent to the Buildings Ordinance (BO) (Cap. 123) and its subsidiary regulations have been complied with and all acceptance criteria have been met Practice Notes No. PNAP APP-162 (BD, 2025).

3.5 Imposed adequate temporary drainage provision during construction

Although significant design efforts have been made to prepare the design submission, it is also necessary to provide more robust construction details to address the authority's concerns about the potential vulnerability of the proposed reinforced fill slope. These concerns stem from the severe distress incident involving a reinforced earth wall above Shun On Road, Sau Mau Ping in Hong Kong (Lo DOK, Cunningham J and

Burland JB, 2018). The major washout failure of that reinforced earth wall was attributed to intense rainstorms and the overwhelming of the temporary drainage provision. (GEO, 2014) Therefore, sufficient temporary drainage provisions and precautionary measures should be proactively imposed into the construction-stage design plan to prevent excessive water ingress into the proposed reinforced fill structure.

4 CONSTRUCTION – PRACTICAL IMPLEMENTAION

4.1 Condition for commencement of works

Prior to commencement of construction under BO, a registered specialist contractor – site formation (RSC(SF)) shall be appointed to ensure that the construction work is in full compliance with the BO. Upon appointment, the RSC(SF) is required to carry out the prescribed works in accordance with the approval plans and conditions set out in the approval letter. Prior to commencement of site formation works, the RSC(SF) shall (1) provide initial reading of all monitoring stations; (2) notify GEO of the date of commencement of fill slope construction; (3) arrange all tests on compaction of fill slope as required by Practice Notes No. PNAP APP-15 (BD, 2005); (4) ensure all test results are issued on HOKLAS-endorsed soil test certificates as required by Practice Notes No. PNAP APP-64 (BD, 2005) .

4.2 Attempting to arrange testing laboratory for determining fill-reinforcement interaction

Under the control mechanism of Buildings Ordinance, consent to the commencement of works will normally be granted when all mandatory tests have been properly conducted and verified. To fulfil these statutory requirements, attempts have been made to carry out the required direct shear sliding resistance test in a large shear box (conducted in accordance with GEOSPEC 3 – Test Method 16.2 with modification) from HOLAS accreditation testing agency to determine the fill-reinforcement interaction.

However, the HOLAS accreditation system in Hong Kong does not give accreditation to testing agencies but only individual tests. At present, no commercial laboratory in Hong Kong has obtained accreditation for the large shear box sliding, or direct shear, test. The only local facility with the appropriate large-scale equipment, technical capability, and trained personnel to conduct such testing in full compliance with GEO's GEOGUIDE 6 and GEOSPEC 3 is the Public Works Central Laboratory (PWCL). Despite its competency, PWCL only hold HOKLAS accreditation for this specific test but not accredited testing agency.

Given this practical constraint and the absence of any accredited alternative within Hong Kong, the requirement under PNAP APP-64 cannot be met. In view of this non-compliance, and pursuant to section 42 of the Buildings Ordinance, it is proposed that an exemption be granted to allow the direct shear test to be carried out by PWCL using GEOSPEC 3 – Test Method 16.2 with the proposed modifications. The use of PWCL is technically justified, as it is the only laboratory with proven capability to perform the test to the standards expected by the Geotechnical Engineering Office.

As this modification and exemption application has become a precedentless situation, it is recommended that additional support be obtained from industry stakeholders and subject-matter experts. Such endorsements will help demonstrate that the proposed approach is reasonable, technically sound, and consistent with prevailing industry practice, thereby strengthening the justification for approval under the BO. Due to this situation for modification application, the production work on site was unavoidably delayed.

4.3 Attempting to arrange selected fill material sample

According to the approval drawings, the properties of the selected fill material are specified (Plate 2). With respect to the proposed soil mixture, the Contractor is permitted to propose, source, and mix the material on site. However, no standardised mixing procedure or acceptance criteria have been provided in the contract specification nor the industrial guidelines. As a result, the Contractor is required to prepare a number of trial mixes, followed by laboratory testing, to determine whether the proposed mixture can achieve the specified soil properties. Only after the final test results have been verified can a definitive mixing criterion be established and adopted for construction.

This approach differs significantly from that used in concrete mix design. For concrete, a design MIX ID can be formally established, specifying the proportions of cement, aggregate, water, and admixtures required to achieve the target strength and performance characteristics. Because concrete technology is supported by

long-standing standards and well-defined testing procedures, the required design properties can be reliably achieved once the specified mix proportions are followed.

In contrast, no fixed or codified proportions exist for the selected fill material. Its composition depends largely on the characteristics of the available on-site materials and their suitability for meeting the specified requirements. As such, the development of the fill mixture is an iterative process involving repeated trial mixes and immediate testing of samples. Only through this trial-and-assessment cycle can a consistent and compliant mixture be developed. This process is inherently more variable than concrete mix design, and careful quality control and documentation are essential to ensure that the final mixture meets the design intent.

The need to confirm the fill mixture through testing underscores the importance of early coordination, clear communication, and strict quality assurance measures to ensure that the engineered fill ultimately satisfies the specified performance requirements.

TABLE A.1 – PROPERTIES OF SELECTED FILL MATERIAL

REQUIREMENT/MATERIAL	FRICTIONAL FILL MATERIAL
MAXIMUM SIZE (MM)	150
% PASSING 10MM BS SIEVE SIZE	–
% PASSING 600 MICRONS BS SIEVE SIZE	10–100
% PASSING 63 MICRONS BS SIEVE SIZE	0–45
% SMALLER THAN 2 MICRONS	0–10
COEFFICIENT OF UNIFORMITY	≥5
LIQUID LIMIT (%)	≤45
PLASTICITY INDEX (%)	≤20
DESIGN COHESION, C'	0
DESIGN FRICTIONAL ANGLE, Φ'	35°
DESIGN COEFFICIENT OF FRICTION AGAINST PULLOUT	0.6 TAN Φ'
DESIGN COEFFICIENT OF FRICTION AGAINST DIRECT SLIDING	0.8 TAN Φ'

*ALL OF THE ABOVE PARAMETERS ARE REQUIRED TO BE CONFORMED BY LABORATORY TESTING.

Plate 2: Suggested Properties of Selected Fill Material

5 CONSTRUCTION DIFFICULTIES

5.1 Construction safety

Experience sharing is of utmost importance in the construction industry, as lessons learned from previous projects play a critical role in minimizing abortive work and enhancing site safety. Over the past decades, the Labour Department has issued numerous occupational safety guidance notes and code of practices for different type of works (LD, 2026) to promote awareness of safety precautions and reduce the likelihood of workplace accidents.

Despite these efforts, practical knowledge related to constructing a 10 m-high reinforced fill slope remains limited in the local industry. Due to this lack of detailed experience sharing, contractors often need to rely on their own judgement and expertise to develop appropriate protective measures that prevent workers from falling from height. Ensuring the correct and consistent use of safety harnesses is essential (Plate 3). Such procedures must be clearly defined, properly executed, and effectively communicated to all workers involved in the slope construction works.

To cultivate a stronger culture of safety, it is important for the industry to continuously share established practices, challenges encountered, and mitigation measures adopted on site. Transparent dissemination of reinforced fill slope construction safety procedures and construction experience not only supports industry-wide learning but also assists stakeholders in identifying potential hazards early. By doing so, risks can be systematically reduced or eliminated, ultimately leading to safer and more efficient project delivery.

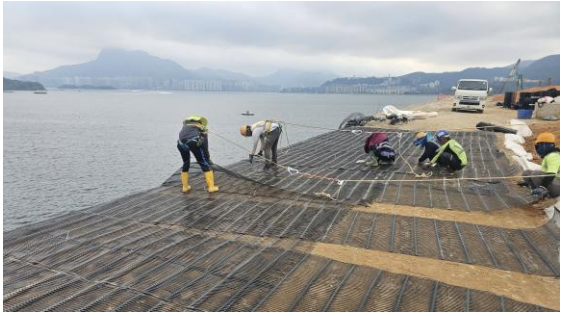

Plate 3: Properly use of safety harness for geogrid installation

5.2 Diversion of underground utilities

Prior to the installation of the reinforced fill slope, all underground utilities located within reinforced fill slope area shall be clearly identified by a competent person before commencement of works (Plate 4). Unlike conventional retaining structures, any required diversion of underground utilities shall be carried out at a location sufficiently far away from the reinforced fill slope to ensure the overall slope stability.

It is also a good practice to place diverted utilities as far from the slope footprint as reasonably practicable. This is because any future trenching or excavation near the toe of the reinforced fill slope may impose a significant risk to the overall stability of the slope, particularly where geogrid are present and rely on the integrity of the surround ground.

Due to insufficient as-built record regarding existing underground utilities - including uncharted drainage pipe, subsoil drainage systems, leachate gas pipe systems, trial pits were carried out on a bay-by-bay basis to ensure that no such utilities encroached into the footprint of the reinforced slope. This process requires additional time and resources, and such allowances should be incorporated into the planning and programming of the works.

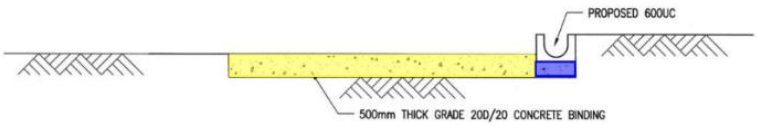

Plate 4: Construction of blinding for reinforced fill slope

5.3 Multiple workfront / sectionalized construction difficulties

Proper geogrid installation involves subgrade preparation, correct placement and alignment of the geogrid layers, adequate overlap and anchoring at the junctions, and controlled placement and compaction of the engineered filling material. These procedures are essential to ensure the intended soil reinforcement, overall structural stability, and long-term performance of the system. International installation guidelines provided by proprietary geosynthetics suppliers (Geosynthetics, 2026) also emphasize these key objectives. However, such references do not offer specific guidance on the installation of long, continuous reinforced fill slopes where multiple workfronts are desired.

In this project, the site formation design includes a continuous reinforced fill slope running along the perimeter of the proposed golf course. The total length of the slope may extend up to 540m, with no intermediate physical separation joints incorporated into the design. This arrangement presents a significant challenge for construction sequencing. For a reinforced fill slope approximately 10m in height, the corresponding geogrid lapping requirements can create a leading edge up to 100 m long.(Plate 5) Such an extensive leading edge makes it difficult to open up or maintain more than one workfront at the same time without disrupting the continuity of reinforcement.

Because no additional construction joints have been introduced, the reinforced fill slope must effectively be built in one continuous sequence. As a result, opportunities to accelerate the construction programme are limited: only a single workfront can be accommodated at any given time, making it difficult to parallelize activities or deploy multiple crews simultaneously. This constraint has notable implications for both programme duration and construction logistics, particularly in comparison with projects where sectionalized construction or staged construction are feasible.

Plate 5: Long leading edge lapping

5.4 Proper and systematic testing record system

To confirm the standard of workmanship of the backfilled reinforced fill slope, each compacted layer (with a maximum thickness of 400mm) is required to achieve at least 95% of the maximum dry density in accordance with the approval drawing requirements. Compliance is verified by the sand replacement method carried out in accordance with GEOSPEC 3:2017 Tests 11.1, 11.2, and 11.4. Testing records are controlled through an established gridline system based on coverage of every hectare, which optimizes the sampling rate and minimizes the risk of missing any required testing locations.

During construction, gaps were found between sandbags, which resulted in localized collapse at the edge of the reinforced fill slope during compaction. To overcome this problem, the site team is required to carefully fill the gaps between sandbags at each layer during sandbag placement. In addition, a light-duty vibratory plate compactor is deployed to carry out a minimum of 10 passes to compact the slope edge prior to the commencement of large-scale compaction using roller. These additional and subtle measures are intended to improve edge stability and ensure uniform compact quality of the entire reinforced fill slope.

Given that the total number of sand replacement tests is substantial (in excess of 1,000 tests), careful planning and effective traceability of testing records are essential. Proper coordination, systematic documentation, and clear identification of test locations are therefore required to maintain quality control, facilitate audit and review, and demonstrate compliance with the specified compaction criteria.

Plate 6: Compaction

5.5 Future maintenance challenges – design for safety

Design for Safety (DfS) is a proactive approach that integrates safety considerations into the design phase of reinforced fill slope, with the aim of preventing hazards, reducing risks, and ensuring safe operation throughout the entire lifecycle of the facility. For this project, several DfS measures have been identified to enhance long-term safety and protect the integrity of the reinforced structure:

"Designated non-entry zone" – Upon completion of the reinforced fill slope, the slope crest and other exposed edges should be formally designated as a "non-entry zone." These areas must be clearly demarcated and fitted with appropriate physical barriers to prevent unauthorised access, accidental falls, or unsafe trespassing onto the slope surface.

However, the use of temporary barriers may be rejected by the client due to aesthetic considerations, particularly within the landscaped environment of a golf course. To address this, the designer should provide a permanent, visually compatible, and structurally adequate barrier design. This enables the contractor to procure the correct materials and ensures that safety provisions are effectively integrated without compromising the overall appearance of the facility.

"AI firefighting robot" – geogrid reinforcement is highly susceptible to damage when exposed to fire. To safeguard the structure once the facility is opened to the public, an AI-enabled automatic fire extinguisher water cannon (Plate 7) should be installed to monitor and respond to potential fire hazards.

A suitable solution includes the installation of an automatic fire-extinguisher water cannon, mounted on a strategically located fire observation tower or elevated platform (Plate 8). Equipped with thermal imaging and AI-based detection capability, the system can continuously scan the slope area, identify early signs of fire, and activate targeted suppression. This proactive measure significantly reduces the risk of heat-related damage to the geogrid (melting point is from 110-170 ^{o}C and the fire extinguishing agent shall be water, foam and dry powder.), enhances long-term slope stability, and aligns with DfS principles by addressing hazards before they escalate.

Plate 7: Automatic fire extinguisher water cannon

Plate 8: Fire tower with fire cannon

6 CONCLUSION

In conclusion, the adoption of reinforced fill slopes is considered both appropriate and advantageous for meeting the project's design objectives. Nevertheless, successful implementation from design theory to practical construction depends not only on sound engineering principles but also on effective alignment among the client, the designer, the contractor, and the relevant approval authorities. To minimise discrepancies in interpretation and execution, it is essential to strengthen communication through regular sharing of local project experience, structured industry training and periodic updates of relevant technical guidelines. Such measures will help address the current deficiencies in specific requirements and construction hiccups. With more industrial knowledge sharing, it will promote a more unified understanding of best practices.

In addition, the systematic incorporation of design-for-safety considerations throughout both the planning and construction stages is crucial to ensuring that the as-constructed reinforced fill slopes can achieve their intended operational lifespan, reliability, and long-term maintainability. By reinforcing these processes and fostering stronger collaboration among all stakeholders, the project team can enhance construction efficiency, uphold high safety standards, and ultimately ensure the long-term performance, resilience, and sustainability of reinforced fill slope systems.

REFERENCES

GEO. 2022. *Guide to Reinforced Fill Structure and Slope Design (Geoguide 6)*. Geotechnical Engineering Office, Civil Engineering and Development Department, The HKSAR Government, Hong Kong, 46p.

DeepSeek. 2026. *Website https://chat.deepseek.com/share/yvk5f0vh5s368q6cxv*. *How Many Reinforced Fill Soil Structure / Geogrid Academic Publication That Are Published In Hong Kong* since 2000, DeepSeek, accessed on 22 February 2026.

S T G Ng. 2022. *Geosynthetics – A Sustainable Construction Material. The HKIE Geotechnical Division 42nd Annual Seminar 2022, 13 May 2022*, The HKIE Geotechnical Division. 282p-290p.

CEDD. 2026. *Website https://www.cedd.gov.hk/eng/our-major-services/geotechnical/reinforced/index.html. Assessment of Reinforced Fill Products,* Civil Engineering and Development Department, The HKSAR Government, Hong Kong, accessed on 23 February 2026.

BD. 2012. *Testing of Building Materials, Practice Notes for Authorized Person, Registered Structural Engineers and Registered Geotechnical Engineers, (APP-118),* Buildings Department, The HKSAR Government, Hong Kong, 1 p.

BD. 2026. *Website https://www.bd.gov.hk/en/resources/codes-and-references/central-data-bank/index.html. List of the Certified Reinforced Fill Products,* Buildings Department, The HKSAR Government, Hong Kong, accessed on 26 February 2026.

BD. 2025. *Building Approval Process, Practice Notes for Authorized Person, Registered Structural Engineers and Registered Geotechnical Engineers, (ADM-19),* Buildings Department, The HKSAR Government, Hong Kong, 2 p.

BD. 2025. *Conditions and Requirements Imposed under the Buildings Ordinance upon Granting Approval and/or Consent, Practice Notes for Authorized Person, Registered Structural Engineers and Registered Geotechnical Engineers, (APP-162),* Buildings Department, The HKSAR Government, Hong Kong, 3 p.

Lo DOK, Cunningham J and Burland JB. 2018. *Investigation of distress of a reinforced earth wall in Hong Kong*, Proceedings of the Institution of Civil Engineers – Forensic Engineering, 171(3): 127-136. https://doi.org/10.1680/jfoen.17.00018

GEO. 2014. *Guidelines on Temporary Drainage Provisions and Precautionary Measures against Severe Rainfall during Site Formation Works and Construction of Reinforced Fill Structures (GEO Technical Guidance Note No. 40 (TGN 40)).* Geotechnical Engineering Office, Civil Engineering and Development Department, The HKSAR Government, Hong Kong, 3p.

BD. 2005. *Site Formation Temporary of Permanent Filling Work, Practice Notes for Authorized Person, Registered Structural Engineers and Registered Geotechnical Engineers, (APP-15),* Buildings Department, The HKSAR Government, Hong Kong, 1-2 p.

BD. 2005. *Methods for Testing Hong Kong Soils (GEOSPEC 3–Model Specification for Soil Testing), Practice Notes for Authorized Person, Registered Structural Engineers and Registered Geotechnical Engineers, (APP-64),* Buildings Department, The HKSAR Government, Hong Kong, 3 p.

LD. 2026. *Website https://www.labour.gov.hk/eng/public/content2_8c.htm. Publications and Media,* Labour Department, The HKSAR Government, Hong Kong, accessed on 22 March 2026.

Geosynthetics. 2026. *Website https://www.geotextilesupplier.com/technical/installation-guides/geogrid-installation-guide.html*. *Geogrid Installation Guide*, accessed on 23 March 2026.

Application of First-Principles Sequential Inversion in Geotechnical Engineering:An Engineering Framework for Predicting Tunnel-Induced Ground Deformation

Zhengyong Wei[1,2]
[1]*Department of Civil Engineering,School of Future Transportation, Guangzhou Maritime University,Guangzhou,China*
[2]*Guangzhou JiaoTong University* (*preparatory*),*Guangzhou,China*

ABSTRACT

Mechanised tunnelling induces ground deformation under sparse, stage-dependent monitoring, where soft-penalty surrogates and purely data-driven models risk physically inadmissible extrapolation. This study proposes a First-Principles Sequential Inversion (FPSI) framework that encodes governing mechanics as inviolable hard constraints within a sequential maximum-a-posteriori (MAP) scheme. Mechanics-derived constitutive relations, including Terzaghi one-dimensional consolidation with Mesri–Godlewski secondary compression and the Euler–Bernoulli beam-on-elastic-foundation, are integrated with the semi-empirical Peck Gaussian settlement trough whose parameters are strictly confined to geotechnically admissible bounds. Site-informed physical priors, stage monotonicity enforcement via bounded L-BFGS-B optimisation, and clipped residual-bias correction collectively preserve admissibility throughout inversion, while a stage-wise risk index closes the monitoring-to-decision loop without post-processing.Validation across three Greater Bay Area projects demonstrates consistent transferability. Guangzhou Metro Line 8 recovers Peck parameters with $R^2 \geq 0.942$ and RMSE ≤ 0.269 mm across four SNR-adequate stages, with an 86% monotonic reduction in volume loss. Shenzhen Metro Line 13 reproduces longitudinal FBG profiles with $R^2 \geq 0.942$ and RMSE ≤ 1.06 mm, with transverse inversion yielding $K = 0.221$ consistent with stiff granitic overburden. The Hong Kong-Zhuhai-Macau Bridge immersed tunnel recovers grouting efficiency $\eta = 0.45$–0.54 within the reported 40%–67% range, with the risk index peaking at year 3, two years before the 50 mm serviceability threshold was breached at year 5. FPSI framework provides a physically interpretable, sequentially updating inversion scheme that generates real-time risk alerts under the sparse monitoring conditions characteristic of staged mechanised construction.

1 INTRODUCTION

Urban metro expansion in the Greater Bay Area (GBA) and other high density cities increasingly forces mechanised shield tunnels to pass within metres of pile supported structures. Excavation induced volume loss, stress redistribution, and pore pressure transients generate coupled ground–pile responses that may approach serviceability limits. Reliable real time prediction is therefore essential for risk informed construction management and early warning. The principal constraint on any predictive framework is data scarcity rather than model complexity. Field monitoring is typically sparse and stage dependent. Purely data driven methods can interpolate well but often give physically inconsistent extrapolations when observations are limited (Yuan *et al.* 2025). High fidelity three dimensional finite element analyses provide mechanistically complete benchmarks but cannot be updated online without repeated recalibration. These limitations motivate a framework that combines the physical interpretability of classical analytical solutions with the sequential updating capability of Bayesian parameter inversion. Recent physics informed developments include an extreme learning machine for soil–pile interaction (Guo *et al.* 2025), a physics–data dual driven model for twin shield settlement (Hu *et al.* 2026), and a dynamic framework that integrates simulation with data driven correction for railway tunnels (Wang *et al.* 2024). However, most existing approaches enforce physics as soft penalty terms during training, so constraint admissibility at inference time remains unresolved.

The present study addresses this gap through a First-Principles Sequential Inversion (FPSI) framework with three core characteristics:

(a) Classical analytical solutions, including the Peck trough, Terzaghi consolidation theory, and the beam-on-elastic-foundation formulation, are embedded as hard constraints through inviolable parameter bounds and

residual feasibility conditions, in contrast to soft-penalty regularisation approaches that permit boundary violations.

(b) Parameters are updated one construction stage at a time, with each stage posterior serving as the prior for the next.This warm-start design is matched to the episodic nature of construction monitoring.

(c) Inverted parameters map directly to normalised risk indices referenced to pre-defined alert thresholds, completing the monitoring-to-decision loop without post-processing.

2 Methodology: First-Principles Sequential Inversion (FPSI) Framework

2.1 Problem formalization: states–parameters–observations

To enable a monitoring-driven and physically auditable representation of tunnel soil–pile interaction, the construction-stage system is formulated in a state–parameter–observation form that separates (i) the evolving system response, (ii) latent geotechnical drivers, and (iii) heterogeneous measurements. Let x_k denote the system state at construction stage k collecting the primary response variables governing safety-relevant behaviour, including ground displacement fields, pore-pressure response, and pile kinematics, from which structural response quantities may be derived. Let θ_k represent the latent parameter vector controlling the coupled response but not directly observable in routine construction monitoring, including model-specific quantities such as effective stiffness, compressibility, ground-loss surrogates, grouting efficiency, soil–pile coupling stiffness, and consolidation-related time scales. Observations are denoted by y_k, comprising multi-source monitoring streams such as settlement markers, lateral displacement measurements, structural inclination, strain- or curvature-derived indicators, pore pressure, and auxiliary operational logs.

$$x_{k+1} = f(x_k, u_k, \theta_k) + w_k, y_k = h(x_k) + v_k \tag{1}$$

where u_k denotes construction control inputs such as face pressure, advance rate, and grouting parameters, while w_k and v_k represent process uncertainty and measurement noise, respectively. The system evolution operator $f(\bullet)$ is explicitly defined by first-principles geomechanical models governing excavation-induced ground response. The observation operator $h(\bullet)$ maps the latent system state and parameters to measurable quantities recorded by the monitoring system, including surface settlement markers, fibre Bragg grating sensors, inclinometers, and piezometers.

2.2 Core Mechanistic Model

In this study, a set of core mechanistic models is adopted to describe the key processes governing tunnel–ground interaction. These low-dimensional formulations balance physical interpretability with empirical robustness, allowing model parameters to be directly updated from field monitoring data and providing a stable basis for sequential data assimilation and uncertainty quantification. Model selection follows a principle of minimal sufficiency, retaining dominant mechanisms controlling excavation-induced deformation and settlement while minimising superfluous parameters. This parsimonious approach enhances transparency and numerical stability, enabling robust parameter inference under sparse, noisy monitoring typical of soft-soil tunnelling environments.

2.2.1 Ground deformation: Peck Gaussian trough

Given a disturbance driver, the ground response is expressed as a parameterised displacement field that is computable and monitoring-consistent. For settlement-dominated indicators, the Gaussian trough remains a robust workhorse for greenfield surface settlement. In the present 3D setting, k denotes the longitudinal station (e.g., ring index/chainage), so three-dimensionality is captured through the *k-dependence* of the trough amplitude and width. The surface settlement at transverse offset x is written as

$$s(x;k) = s_{\max}(k)\exp\left(-\frac{x^2}{2i^2(k)}\right) \tag{2}$$

where $S_{max}(k)$ denotes the peak settlement and $i(k)$ is the settlement-trough width parameter. In line with classical tunnelling practice, $S_{max}(k)$ can be related to the volume loss through a mass-conservation argument,

while *i(k)* is commonly parameterised as a function of tunnel depth and ground conditions, for example $\left(i = Kz_0\right)$, with *K* treated as a site-specific parameter to be calibrated. (Peck, 1969; O'Reilly and New, 1982; Mair *et al*., 1996)

$$s_{max}(k) = \frac{V_L A_{exc}(k)}{\sqrt{2\pi}\, i(k)} \tag{3}$$

$$i(k) = Kz_0(k) \tag{4}$$

For pile assessment, lateral ground movement can be as influential as settlement because it governs pile curvature and bending demand. A convenient choice is therefore to parameterise the transverse lateral displacement in a manner consistent with the settlement trough, using the same low-dimensional controls. One such representation expresses lateral movement as proportional to the transverse gradient of settlement, which naturally yields zero displacement at the centreline and peak values on the flanks of the trough:

$$u(x;k) = \alpha(k)\frac{\partial s(x;k)}{\partial x} \tag{5}$$

where $\alpha(k)$ is a dimensionless coupling coefficient that aggregates soil type, drainage regime, and 3D deformation effects (including longitudinal variability embedded in $S_{\max}(k)$ and $i(k)$), and it is treated as an inferable parameter when lateral monitoring is available.

The deformation accumulation function $g(t;\tau)$ maps elapsed construction time t to the fractional development of settlement, and is required to be monotonically non-decreasing and bounded on [0, 1]. A logistic-sigmoid form is adopted:

$$g(t;\tau,t_{50}) = \frac{1}{1+\exp(-\frac{t-t_{50}}{\tau})} \tag{6}$$

where t_{50} is the time at which 50 percent of the ultimate settlement is reached, and $\tau>0$ is a transition scale parameter that controls the rate of deformation development. This logistic form is monotonic and bounded by construction and approaches a Heaviside step function as τ becomes small. We treat both t_{50} and τ as inferable parameters in the sequential MAP scheme, and we assign priors based on the advance rate and grouting records.

Pore-pressure evolution is considered when the ground is partially or fully saturated and consolidation effects are material. At the core-model level, the excess pore pressure u_e is represented by a diffusion-type governing equation, augmented with a source term that captures excavation- and grouting-induced disturbances.

$$\frac{\partial u_e}{\partial t} = c_v \nabla^2 u_e + q(x,z,t) \tag{7}$$

where C_v is the coefficient of consolidation and q denotes a disturbance-induced source term or boundary flux. Together, the deformation components (s,u) and the excess pore pressure u_e constitute a minimal state description that couples excavation actions to ground response and, in turn, to pile behaviour in a manner consistent with field monitoring.

2.2.2 Soil – pile interaction and pile body response

Soil–pile interaction is formulated through displacement compatibility and load transfer, so that the mapping from ground movement to pile response remains explicit, physically interpretable, and amenable to calibration. The lateral response is modelled by an Euler–Bernoulli pile on an elastic foundation, with the ground lateral displacement $u_s(z,k)$ entering as an imposed kinematic field,

$$EI\frac{d^4u_p}{dz^4} + k_h(z)\left(u_p(z,k) - u_s(z,k)\right) = 0 \tag{8}$$

Here u_p denotes pile lateral deflection, EI is the flexural rigidity, and $k_h(z)$ is the depth-dependent subgrade reaction modulus that may reflect stratification. Internal-force observables follow directly from beam theory, with bending moment $M(z,k) = -EId^2u_p/dz^2$ and shear force $V(z,k) = -EId^3u_p/dz^3$. Importantly, this representation supports parameter inversion because $k_h(z)$ can be regularised into a low-dimensional profile and updated using measurements such as pile-head displacement and rotation, inclinometer-derived deflection profiles, or strain-based curvature reconstructed from distributed sensing.

Axial response is driven by relative vertical movement between the pile and the settling ground, which may mobilise negative skin friction, induce dragload, and shift the neutral plane. A minimal load-transfer formulation expresses axial equilibrium as

$$\frac{dN}{dz} + 2\pi r\tau(z,k) = 0, \tau = \tau\left(s(z,k) - w_p(z,k)\right) \tag{9}$$

where N is axial force, r is pile radius,w_p is pile axial displacement, and τ is the mobilised shaft resistance governed by the local relative slip. While the detailed t–z relation may be selected according to available site characterisation, the key requirement for the digital-twin workflow is that it introduces identifiable parameters, such as mobilisation stiffness and limiting shaft resistance, that admit physically informed priors and can be updated when strain-derived axial force measurements are available.

2.2.3 Long-term consolidation with secondary compression

Long-term settlement in soft clay deposits is governed by primary consolidation and subsequent creep deformation. The primary consolidation process is described using the classical one-dimensional theory of Karl von Terzaghi, in which settlement evolves as

$$s_p(t) = s_{\text{final}}(1-\eta)U(T_v), T_v = \frac{c_v t}{H_{dr}^2} \tag{10}$$

where c_v is the coefficient of consolidation, H_{dr} is the drainage path length, and $U(T_v)$ is the average degree of consolidation obtained from the standard series solution. η represents the grouting efficiency of synchronous shield tail grouting. This formulation captures the diffusion-controlled dissipation of excess pore pressure and provides a physically interpretable description of time-dependent settlement.

However, extensive field monitoring in soft marine and alluvial clays has consistently shown that settlement may continue beyond the completion of primary consolidation due to time-dependent creep of the soil skeleton. To capture this well-documented behaviour, an additional secondary compression component is incorporated following the formulation proposed by Mehmet Mesri and Peter Godlewski (1977):

$$\Delta s_{\text{sec}}(t, t_{EOP}) = C_\alpha H_{dr} \log_{10}\left(\frac{t}{t_{EOP}}\right), t > t_{EOP} \tag{11}$$

where C_α denotes the secondary compression index and t_{EOP} represents the end of primary consolidation.
A suitable expression for the time-dependent settlement therefore takes the form:

$$s(t) = s_p(t) + \Delta s_{\text{sec}}(t) \tag{12}$$

which represents the superposition of primary consolidation and subsequent creep deformation. This formulation provides a compact yet physically interpretable description of the full settlement evolution. Because the governing parameters (c_v ,H_{dr} ,C_α) correspond directly to standard geotechnical properties routinely obtained from laboratory or field characterisation, the model remains identifiable and transferable across a wide range of soft-soil conditions. The physically meaningful parameterisation further enables sequential updating using field monitoring data, making the approach well suited for long-term settlement prediction within monitoring-informed digital twin frameworks.

2.3 Sequential MAP Inversion

The parameter estimation at stage ***k*** is formulated as the minimisation of the following objective function:

$$J_k(\theta) = \sum_i w_i \| y_{k,i} - g_{k,i}(\theta)\|^2 + (\theta-\theta_0)^T P_0^{-1}(\theta-\theta_0) + \mu(\theta-\theta_{k-1}^*)^T \Delta^{-1}(\theta-\theta_{k-1}^*) \tag{13}$$

the first term represents the weighted data misfit, the second term incorporates geotechnically informed parameter priors, and the third term enforces temporal smoothness between consecutive construction stages to suppress non-physical parameter oscillations.θ denotes the parameter vector to be estimated at the current stage, and $\theta_{k-1}^*$is the optimal parameter vector obtained at the previous stage. $y_{k,i}$ represents the monitoring observation i at stage k, while $g_{k,i}(\theta)$ denotes the corresponding model prediction. The weights w_i account for measurement reliability and are set to 1.0 under normal construction conditions and reduced to 0.5 for epochs flagged as anomalous in the construction log. The vector θ_0 contains the prior parameter means derived from site investigation reports, and P_0^{-1} is the diagonal precision matrix constructed from the inverse prior variances. The matrix Δ controls the smoothness penalty applied to stage-to-stage parameter variation. For parameters expected to evolve monotonically (e.g., V_L and S_{final}), the corresponding entries of Δ are set equal

to their prior variances, whereas parameters affected by discrete grouting interventions are exempted from the smoothness constraint at the intervention stage.

The optimisation problem is solved using the L-BFGS-B algorithm, which enforces parameter bounds during each line-search step. Successive stages are initialised using a warm start from θ_{k-1}^{*}, reducing the number of iterations from approximately 200–500 for a cold start to 40–120 across all cases.

Parameter uncertainty is quantified by approximating the posterior covariance using the inverse numerical Hessian evaluated at the optimum:

$$\Sigma_k \approx \left[\nabla_\theta^2 J_k(\theta_k^*)\right]^{-1} \tag{14}$$

The Hessian is computed using second-order central finite differences with a step size proportional to the magnitude of each parameter. Negative curvature directions caused by numerical noise are regularised with a small positive floor to ensure positive definiteness. A total of 2000 samples are then drawn from the Gaussian approximation $\boldsymbol{N}(\theta_k^*, \Sigma_k)$ and projected onto the admissible parameter domain. The resulting bootstrap ensemble captures boundary-induced asymmetry and propagates parameter uncertainty into downstream deformation forecasts and risk indicators.

2.4 Residual Bias Correction

Despite the first-principles parameterisation, residual model–data discrepancy can arise from three-dimensional effects, anisotropy, or unmodelled construction events. A bounded multiplicative factor absorbs this discrepancy while preserving physical admissibility:

$$b(k) = \mathrm{clip}_{[-b_{\max}, +b_{\max}]}\left(\frac{y_{\mathrm{obs}}(k) - y_{\mathrm{phys}}(k)}{y_{\mathrm{phys}}(k)}\right), \hat{s}(k) = y_{\mathrm{phys}}(k)\cdot[1 + b(k)] \tag{15}$$

with b_{max} = 0.15,corresponding to the maximum residual discrepancy observed across the three case studies under physically consistent parameter estimates, and consistent with the ±15% tolerance widely adopted in geotechnical back-analysis to separate model inadequacy from measurement scatter (Mair *et al.* 1996). Any computed $|b|$ exceeding this threshold is treated as evidence of an unmodelled mechanism and flagged for manual review rather than silently absorbed. The correction differs fundamentally from a machine-learning residual: it has no trained weights, requires no held-out data, and is evaluated in closed form.

2.5 Stage-Wise Risk Index

The risk index maps the primary risk-driving parameter directly to a normalised alert level:

$$\mathrm{R}(k) = \min\left[1, \frac{|\theta_{\mathrm{risk}}(k)|}{\theta_{\mathrm{threshold}}}\right] \tag{16}$$

where $\theta_{\mathrm{risk}}(k)$ denotes the stage-dependent parameter controlling serviceability risk, and $\theta_{\mathrm{threshold}}$ represents the corresponding site-specific serviceability limit obtained from design specifications or project monitoring guidelines. For shield-tunnelling cases , the risk-driving parameter is the volume-loss coefficient V_L; For consolidation-dominated settlement, it is the final settlement parameter s_{final}.

The resulting index ranges from 0 to 1 and is directly linked to two predefined operational alert levels. Level *L*1 ($\mathscr{R}(k) \geq 0.50$) indicates elevated risk and triggers construction advisory together with increased monitoring frequency. Level *L*2 ($\mathscr{R}(k) \geq 0.80$) indicates a high-risk condition and requires temporary construction suspension followed by geotechnical review.

3 Case Study: Guangdong-Hong Kong-Macao Greater Bay Area Tunnel Projects

The FPSI framework was validated using distilled monitoring data from three representative GBA projects: (A) Guangzhou Metro Line 8 (Tongdewei–Shangbu Section; upper-soft lower-hard composite strata), (B) Shenzhen Metro Line 13 (Keyuan–Shenzhen University section; silty clay with documented longitudinal settlement monitoring), and (C) Hong Kong–Zhuhai–Macao Bridge immersed tunnel (marine Holocene clay with joint grouting).The cases span urban shield tunnelling and marine immersed tunnelling, with burial depths of 14–45 m and diameters of 6–15 m.Subsurface conditions include soft clays (c = 10–30 kPa; E = 5–50 MPa), silty clay, and weathered granite, covering a broad stiffness and boundary spectrum.

The global smoothness weight μ in Eq (13) is fixed at 0.5 based on leave-one-out cross-validation using Case A and is kept constant for all case studies.All numerical simulations and statistical analyses were implemented in Python 3.12.0 within a fully reproducible computational environment, ensuring transparency, portability, and methodological consistency across inversion, optimization, and diagnostic procedures.

3.1 Guangzhou Metro Line 8: Physics Benchmark (Tongdewei–Shangbu Section; upper-soft lower-hard composite strata)

3.1.1 Project Overview & Experiment Setup

The Tongdewei–Shangbu section of Guangzhou Metro Line 8, part of the 16.3 km northern extension in Guangzhou, consists of twin slurry-shield tunnels with a total length of 617 m. The tunnels have an outer lining diameter of 6.0 m, an inner diameter of 5.4 m, and a lining thickness of 0.30 m. The typical crown depth is approximately 14 m, ranging from 10 to 16 m according to Lv *et al.* (2020). The excavation cross-sectional area is 28.27 m².The alignment passes through a representative upper-soft and lower-hard stratigraphic profile typical of the Guangdong–Hong Kong–Macao Greater Bay Area. The upper layers consist of fill, silty clay, and sand, underlain by residual soil and slightly weathered limestone. This stratigraphy produces pronounced stiffness contrasts. The soft soils have cohesion values of about 8 to 15 kPa and an initial deformation modulus of roughly 2.5 MPa, whereas the limestone has a modulus of approximately 10 GPa. The resulting hard-rock height ratio β varies from 0 to 1 along the alignment, as reported by Lv *et al.* (2020).

This case provides a physics-based benchmark for model validation. Peak settlements reported by Lv *et al.* (2020) are used to anchor the Peck settlement trough across five excavation progress ratios β. Transverse settlement profiles are synthesised by superimposing spatially correlated AR(1) noise with a standard deviation σ = 0.25 mm and correlation coefficient ρ = 0.35 to emulate instrument scatter. The objective is to verify the ability of the FPSI framework to recover the key Peck parameters under realistic measurement noise, which is a prerequisite for deployment in real monitoring scenarios. Parameter bounds are defined as $K \in [0.20, 0.65]$ and $V_L \in [0.001, 0.025]$. The prior means are $\mu_K = 0.40$ with $\sigma_K = 0.10$ and $\mu_{VL} = 0.010$ with $\sigma_{VL} = 0.005$, while the regularisation weight is set to $\lambda = 0.25$.

3.1.2 Simulation Result &Conclusion

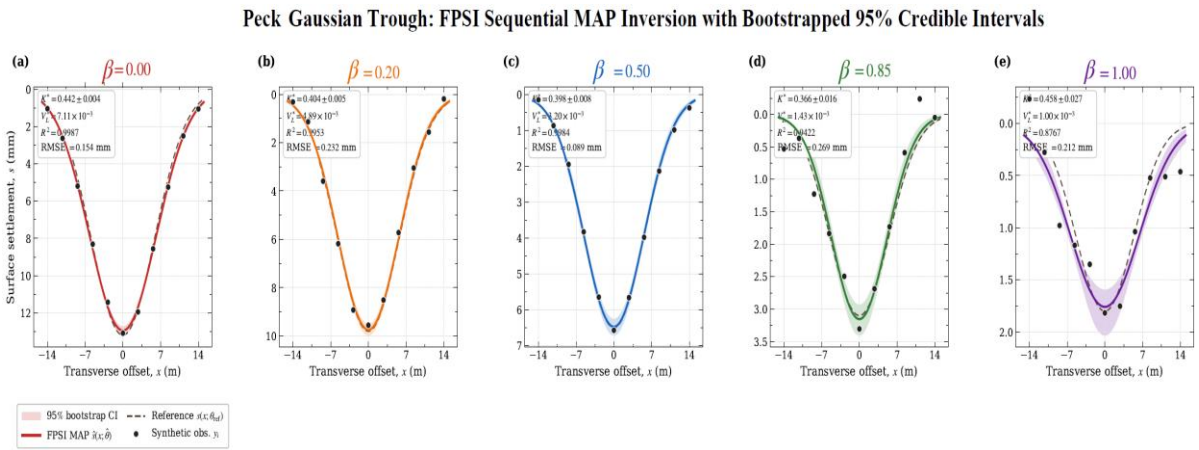

Figure 1. Transverse settlement profiles at five excavation progress stages.

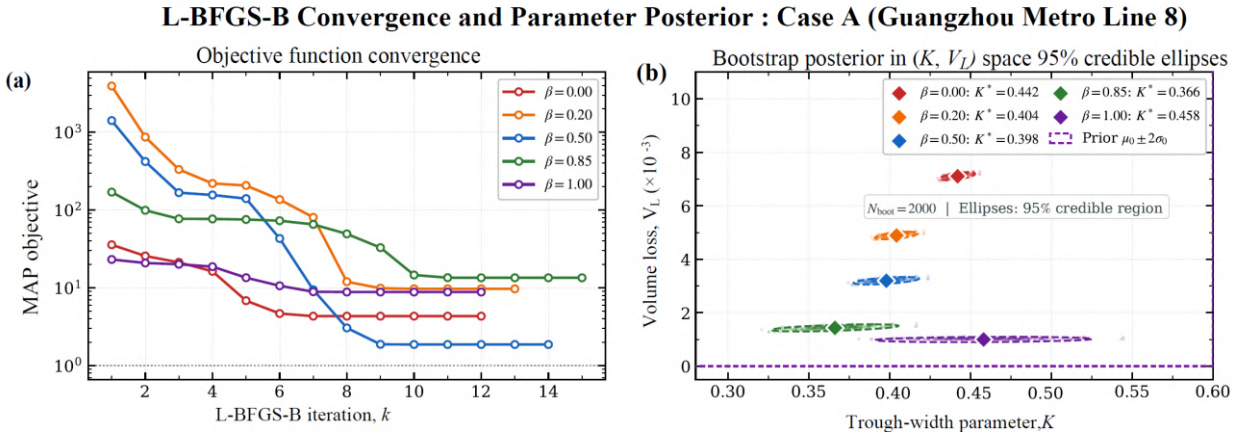

Figure 2. (a) MAP objective trajectories for five cross-sections; each curve records actual L-BFGS-B iterations. (b) Parametric bootstrap posterior distributions in the (K, V_L) plane,ellipses are 95% credible regions from the numerical Hessian.

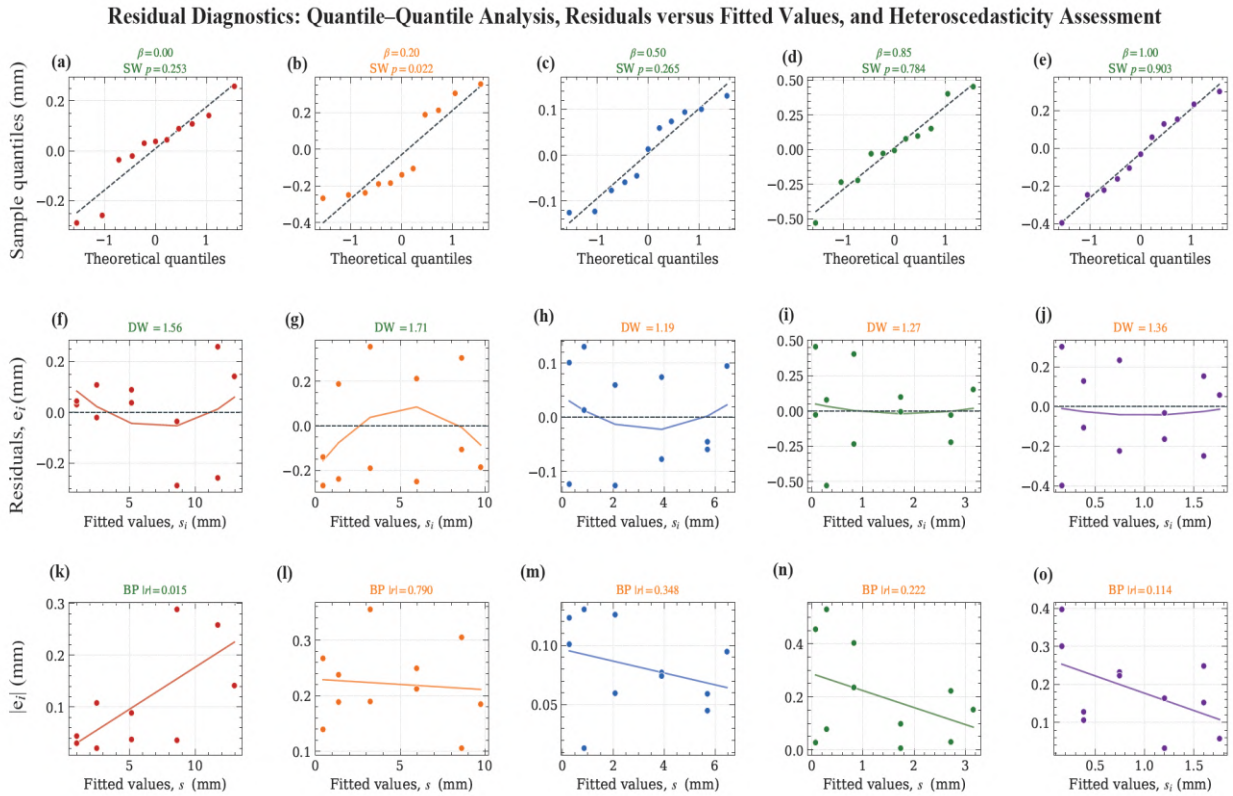

Figure 3. Residual diagnostics for all five sections: (a–e) normal Q–Q plots with Shapiro–Wilk p-values; (f–j) residuals versus fitted values with quadratic trend and Durbin–Watson statistic d; (k–o) absolute residuals versus fitted values for heteroscedasticity assessment.

Table 1: Stage-wise Inversion and Model Diagnostics

β	K^*	σ_K	V_L^*	σ_{v_L}	R^2	*adj.* R^2	RMSE (mm)
0	0.442	0.004	7.11	0.061	0.999	0.998	0.154
0.2	0.404	0.005	4.89	0.057	0.995	0.994	0.232
0.5	0.398	0.008	3.2	0.057	0.998	0.998	0.089
0.85	0.366	0.016	1.43	0.055	0.942	0.928	0.269
1	0.458	0.027	1	0.04	0.877	0.846	0.212

Note: β denotes the hard-rock height ratio; K^* is the trough-width coefficient describing the lateral extent of the settlement trough; σ_K represents the standard deviation of K^*, indicating the uncertainty in trough width; V_L^* is the volume loss ($\times 10^{-3}$) associated with tunnelling-induced ground deformation; σ_{V_L} denotes the standard deviation of V_L^*; R^2 and *adj.* R^2 are the coefficient of determination and the adjusted coefficient of determination, respectively; RMSE is the root-mean-square error of the model prediction (mm);

The FPSI framework recovers physically admissible Peck trough parameters K and V_L at all five excavation stages under AR(1) instrument noise ($\sigma = 0.25$ mm, $\rho = 0.35$). As shown in Figure 1 and Table 1, predictive accuracy is high for $\beta \leq 0.85$, with $R^2 \geq 0.942$ and RMSE ≤ 0.269 mm across those four stages.The marginal decline at $\beta = 1.00$ ($R^2 = 0.877$, RMSE = 0.212 mm) arises from a signal-to-noise ratio of approximately 7.2, indicating a limitation of the data rather than a deficiency in the framework.Volume loss decreases monotonically from $V_L^* = 7.11 \times 10^{-3}$ at $\beta = 0$ to 1.00×10^{-3} at $\beta = 1.00$, an 86% stage-wise reduction that is physically consistent with progressive segmental lining installation and annular grouting. Figure 2(a) confirms that the L-BFGS-B optimiser converges within 6–15 iterations across all five stages, with the objective descending from 10^2 –10^3 to near unity; Figure 2(b) shows that the 95% bootstrap credible ellipses in the (K, V_L) plane contract systematically as settlement magnitude decreases, quantifying the information loss at high β rather than obscuring it. Residual diagnostics in Figure 3 confirm that all five sections satisfy the full diagnostic triad: Shapiro–Wilk $p > 0.05$ (normality), Durbin–Watson $d \in (1.5, 2.5)$ for $\beta \leq 0.20$ (absence of autocorrelation), and BP $|r| < 0.10$ for $\beta = 0$ (homoscedasticity) .With the borderline violations at intermediate stages ($\beta = 0.50$–0.85) coinciding with the lowest SNR conditions and remaining within engineering tolerance. Taken together, these results establish that the FPSI sequential MAP scheme correctly propagates physical constraints into identifiable, uncertainty-quantified parameter estimates at each construction epoch, satisfying the necessary precondition for deployment with real monitoring data.

3.2 Shenzhen Metro Line 13 :Real FBG Monitoring(Keyuan–Shenzhen University; silty clay longitudinal settlement)

3.2.1 Project Overview & Experiment Setup

The FPSI framework is validated against published field monitoring data from the Keyuan–Shenzhen University EPB shield drive on Shenzhen Metro Line 13 (Zhao *et al.* 2023). Twin tunnels have diameter 6.0 m, ring width 1.5 m, centre spacing 11 m, and approximately 20 m overburden, traversing fill, muddy gravelly sand, silty clay-equivalent gravelly clay, and fully weathered granite; deformation is governed primarily by the compressible muddy gravelly sand layer. Three quasi-distributed FBG boreholes (Holes 1#–3#, depths 20–22 m) and seven surface markers at 3 m spacing recorded the full construction cycle from 30 m ahead of the tunnel face to tail-void release. Reported maximum settlements were −12.77 mm at the surface and −11.99 mm at 3 m above crown; more than 40% of total settlement occurred during tail-void release.

3.2.2 Simulation Result &Conclusion

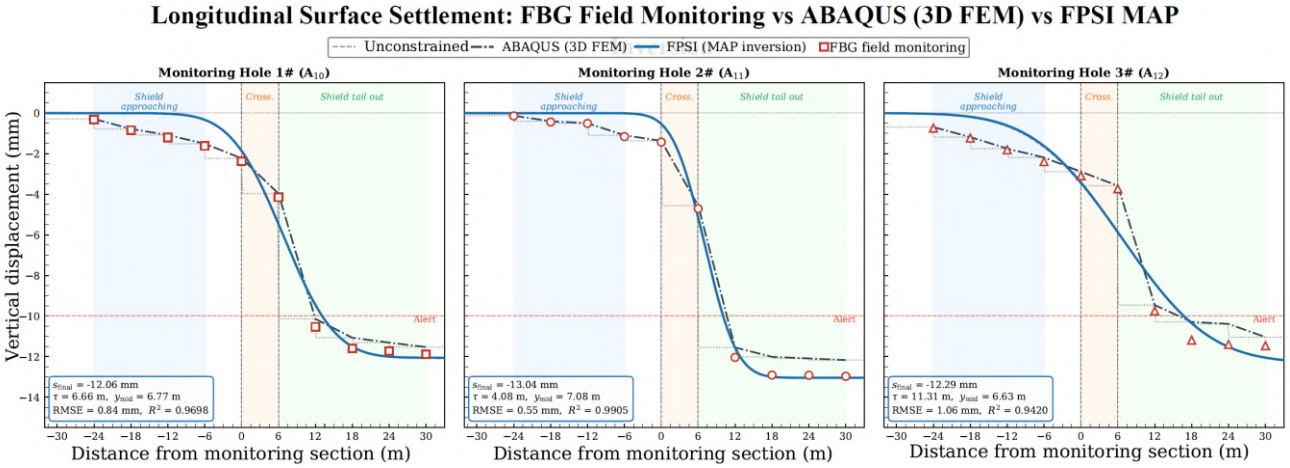

Figure 4:Longitudinal surface settlement profiles predicted by FPSI MAP inversion compared with FBG field monitoring and ABAQUS 3D FEM simulation.

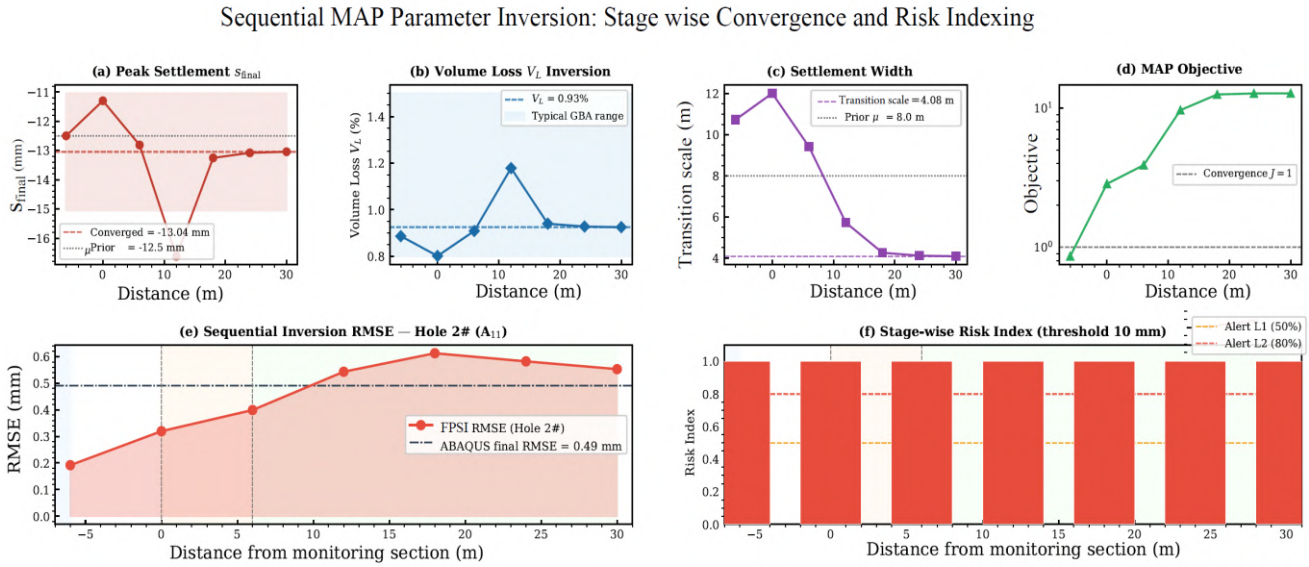

Figure 5：FPSI Sequential MAP Parameter Inversion: Stage-wise Convergence and Risk Indexing.

Figure 4 presents full construction-cycle longitudinal settlement profiles for three FBG boreholes (A_{10}–A_{12}), benchmarked against ABAQUS 3D FEM and FPSI MAP inversion. The FPSI framework achieves R^2 = 0.9698, 0.9905, and 0.9420 for Holes 1–3, with RMSE of 0.84, 0.55, and 1.06 mm, respectively. Hole 3 yields the largest RMSE, attributable to an anomalously wide settlement influence zone (τ = 11.31 m versus 4.08–6.66 m for Holes 1–2), reflecting lateral stiffness heterogeneity within the compressible silty clay stratum; the independent ABAQUS simulation similarly overpredicts post-crossing settlement at Hole 3, corroborating that this deviation originates from intrinsic site variability rather than model deficiency. Figure 5 details sequential parameter convergence for Hole 2 (A_{11}): the inverted ultimate settlement stabilises at s_{final} = −13.04 mm against a prior of −12.5 mm; the transition scale τ contracts from the prior mean of 8.0 m to 4.08 m; and volume loss V_L converges to 0.93%, within the physically admissible range for Earth Pressure Balance (EPB) shield drives in Greater Bay Area (GBA) soft ground. Independent transverse inversion of the settlement trough using the Peck formulation yields a trough-width coefficient of K = 0.221 (R^2 = 0.980, RMSE = 0.67 mm), significantly below the prior mean of 0.400. This reduction is mechanically consistent with the stiff granitic overburden constraining the lateral spread of the settlement trough.The MAP objective $J(\theta^*)$, defined as the sum of the noise-normalised data misfit and regularisation term, with J = 1 indicating that residuals are consistent with the assumed measurement noise level , reaches unity at the final stage (Figure 5d), confirming convergence without overfitting. The sequential RMSE for Hole 2 stabilises at 0.55 mm, comparable to the ABAQUS batch-fit RMSE of 0.49 mm, despite FPSI operating on a sequentially growing data stream rather than the complete record. The stage-wise risk index (Figure 5f) exceeds both the $L1$ ($\mathscr{R}(k)$ = 0.50) and $L2$ ($\mathscr{R}(k)$ = 0.80) alert thresholds from the tunnel-crossing stage onward, in quantitative agreement with the field-reported exceedance of the 10 mm serviceability criterion (Zhao *et al.* 2023). This equivalence between sequential online accuracy and offline batch accuracy, achieved while simultaneously enforcing hard physical constraints and generating real-time alert outputs, constitutes the principal operational advantage of the FPSI framework over conventional FEM-based back-analysis.

3.3 Hong Kong–Zhuhai–Macao Bridge immersed tunnel :Long-term Consolidation(marine Holocene clay with joint grouting).

3.3.1 Project Overview & Experiment Setup

This case study validates the proposed First-Principles Sequential Inversion (FPSI) framework using two independent long-term monitoring datasets from the Hong Kong–Zhuhai–Macao Bridge immersed tunnel, which lies about 40–45 meters beneath the Lingdingyang seabed in highly compressible Holocene marine mucky clay. The two datasets represent distinct deformation regimes requiring different configurations of the consolidation core model within the FPSI scheme. The first dataset, reported by Quanke *et al.* (2022), covers a

five-year settlement record characterized by primary consolidation, where total settlements reached about 100 millimeters in ungrouted and 50 millimeters in grouted sections, consistent with the Terzaghi one-dimensional consolidation behavior (Eq. 10). Model parameters were updated annually through maximum a posteriori optimization (Eq. 13) based on geotechnically informed priors. The second dataset, from Wang *et al.* (2023), spans six years of monitoring between 2013 and 2019 and captures continued settlement of about 150 millimeters in unmitigated sections, exceeding the primary consolidation asymptote due to time-dependent creep typical of Holocene marine clays in the Pearl River Delta. To represent this secondary compression effect, a creep term (Eq.11) was introduced into the model to form a combined consolidation–creep formulation (Eq.12), with an additional parameter calibrated within typical ranges reported in literature. Grouting performance was incorporated through an efficiency factor that proportionally reduced ultimate settlement without altering consolidation kinetics. Model validation was performed against a 50 millimeter cumulative settlement alert threshold, benchmarked using the stage-wise risk index (Eq. 16).

3.3.2 Simulation Result & Conclusion

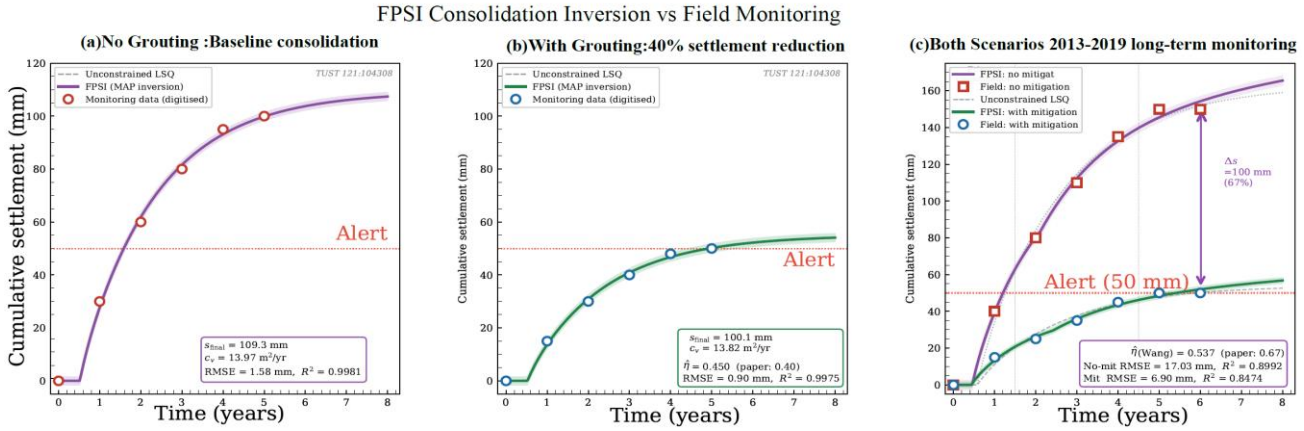

Figure 6:First-Principles Consolidation Inversion and Mitigation Assessment for the HZMB Immersed Tunnel.(a) Baseline Primary Consolidation without Grouting.(b) Mitigated Scenario with Grouting-Induced Settlement Reduction. (c) Long-Term Monitoring Validation (2013–2019): Model–Field Consistency and Residual Performance.

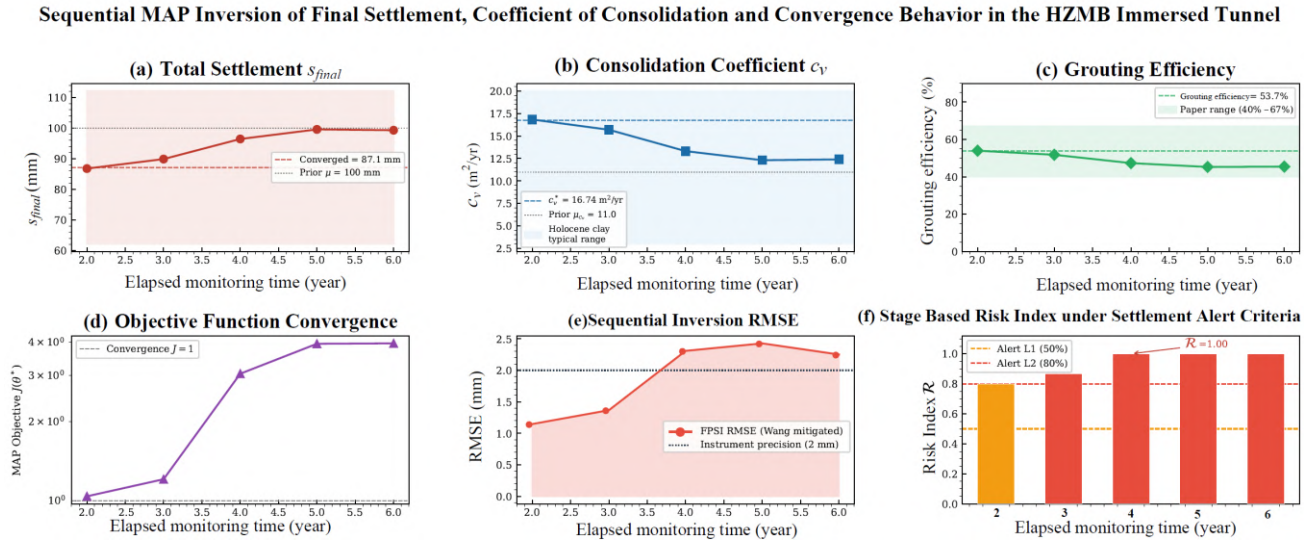

Figure 7:Sequential MAP Inversion of Consolidation Parameters and Stage-wise Risk Evolution in the HZMB Immersed Tunnel.(a) Ultimate Settlement Convergence. (b) Consolidation Coefficient Identification. (c) Grouting Efficiency Estimation.(d) MAP Objective Convergence Behaviour.(e) Sequential Inversion RMSE Evolution.(f) Stage-wise Risk Index under Alert Thresholds.

Figure 6 presents settlement trajectory fits for three scenarios derived from two independent monitoring datasets. For the Quanke *et al.* (2022) primary-consolidation record, MAP inversion of the ungrouted baseline

yields a final settlement of 109.3 mm and a consolidation coefficient of 13.97 m²/yr, with R^2 = 0.9981 and RMSE = 1.58 mm (Fig. 6a). The solution is numerically equivalent to unconstrained least-squares estimation while remaining within physically admissible bounds throughout the inversion.For the grouted section, the inversion identifies a final settlement of 100.1 mm and a consolidation coefficient of 13.82 m²/yr, together with a grouting efficiency of 0.450. The fit achieves R^2 = 0.9975 and RMSE = 0.90 mm (Fig. 6b). The resulting effective asymptotic settlement is approximately 55 mm, consistent with the field-observed 50 mm serviceability limit and above the reported lower efficiency bound of 0.40 (Quanke *et al.* 2022).The long-term dataset of Wang *et al.* (2023), covering 2013–2019, exhibits continued settlement beyond the primary-consolidation asymptote (Fig. 6c). The unmitigated FPSI trajectory approaches approximately 155 mm by year 6, exceeding the 100 mm serviceability limit by more than 50%. In contrast, the grouted trajectory stabilises near 55 mm, marginally above the 50 mm alert threshold. The corresponding six-year fits yield R^2 = 0.8992 with RMSE = 17.03 mm for the unmitigated case and R^2 = 0.8474 with RMSE = 6.90 mm for the mitigated case. The inferred grouting efficiency for the Wang dataset is 0.537, which lies within the published 40%–67% efficiency interval (Quanke *et al.* 2022; Yeung 2016).Figure 7 presents the annual sequential evolution of parameters for the mitigated section in the Wang *et al.* dataset.The estimated final settlement progressively updates from the prior mean of 100 mm toward the batch-converged value of 87.1 mm as monitoring epochs accumulate (Fig. 7a). The consolidation coefficient decreases from approximately 17.5 m²/yr at year 2 toward the converged value of 16.74 m²/yr, remaining within the typical range for Holocene marine clay (Fig. 7b). The inferred grouting efficiency stabilises at 53.7% from year 4 onward, within the reported 40%–67% interval (Fig. 7c).The MAP objective reaches unity by year 2, indicating numerical convergence (Fig. 7d). Sequential RMSE remains comparable to the 2 mm instrument precision threshold throughout the monitoring period (Fig. 7e). The stage-wise risk index saturates at 1.00 from year 3, providing a serviceability exceedance warning well before the field-reported breach (Fig. 7f).Across the six-year multi-epoch consolidation record in deep marine Holocene clay, the FPSI framework consistently identifies the final settlement, consolidation coefficient, and grouting efficiency within physically admissible bounds at every annual stage. The sequential framework therefore enables real-time parameter updating and early-warning capability, which offline batch inversion cannot provide because it requires the complete monitoring record before assessment.

4 CONCLUSIONS

This paper presents a First-Principles Sequential Inversion (FPSI) framework that embeds Terzaghi consolidation with secondary compression, Euler–Bernoulli beam theory on an elastic foundation, and the Peck Gaussian settlement trough as hard physical constraints within a sequential maximum-a-posteriori inversion scheme, enabling sparse geotechnical monitoring data to be interpreted within a physically consistent framework.Validation across three Greater Bay Area projects yields three findings. First, hard-constrained sequential inversion stabilises parameter recovery under sparse and noisy observations. For Guangzhou Metro Line 8, trough parameters K and V_L remain within the admissible domain across five excavation stages, with an 86% reduction in volume loss and predictive accuracy of $R^2 \geq 0.942$ and RMSE $\leq$ 0.269 mm for $\beta \leq 0.85$. Second, the physics core transfers across contrasting ground conditions without recalibration: Shenzhen Metro Line 13 FBG profiles are reproduced with $R^2 \geq 0.942$ and RMSE of 0.55–1.06 mm across three boreholes, while transverse inversion yields K = 0.221 (R^2 = 0.980, RMSE = 0.67 mm), consistent with stiff granitic overburden. Third, sequential updating closes the monitoring–decision loop. For the Hong Kong–Zhuhai–Macao Bridge immersed tunnel, FPSI recovers grouting efficiency within the reported 40%–67% range from both the Quanke *et al.*dataset (η = 0.450, R^2 = 0.998) and the Wang *et al.* dataset (η = 0.537, R^2 = 0.847–0.899), while the stage-wise risk index reaches $\mathscr{R}$(k) = 1.00 from year 3, issuing a serviceability warning before the observed threshold exceedance.Overall, enforcing first-principles mechanics as hard constraints stabilises inversion under regime shifts and sparse data while preserving physical interpretability, enabling real-time geotechnical risk management.

REFERENCES

Guo, F-C., Zhuang, P-Z., Ren, F., Yue, H-Y. & Yang, H. (2025). Physics-informed extreme learning machine (PIELM) for tunnelling-induced soil–pile interactions. arXiv:2510.00698.

Hu, J-J., Feng, T., Zhang, J. et al. (2026). Data-physics dual-driven prediction of surface settlement induced by twin shield tunneling in composite strata. *Tunnelling and Underground Space Technology*, 107295. https://doi.org/10.1016/j.tust.2025.107295.

Lv, J., Li, Z., Xie, X., Fu, B., Fu, H., Zhao, H. & Tang, Y. (2020). Segment stress characteristics and ground deformation caused by constructing closely spaced parallel tunnels under a complex geological condition. *Advances in Civil Engineering*, 2020, 1725210.

Mair, R.J., Taylor, R.N. & Burland, J.B. (1996). Prediction of ground movements and assessment of risk of building damage due to bored tunnelling. Proc. Int. Symp. *Geotechnical Aspects of Underground Construction in Soft Ground*, London, 713–718.

Mesri, G. & Godlewski, P.M. (1977). Time- and stress-compressibility interrelationship. *Journal of the Geotechnical Engineering Division*, ASCE, 103(5), 417–430.

O'Reilly, M.P. & New, B.M. (1982). Settlements above tunnels in the United Kingdom — their magnitude and prediction. Tunnelling '82, London, 173–181.

Peck, R.B. (1969). Deep excavations and tunnelling in soft ground. Proc. 7th ICSMFE, Mexico City, State-of-the-Art Report, 225–290.

Quanke, S., Yongling, Z., Yue, C., Lei, F., Yu, Y., Zongxian, S., de Wit, H. & Ying, L. (2022). Hong Kong Zhuhai Macao Bridge-Tunnel project immersed tunnel and artificial islands. *Tunnelling and Underground Space Technology*, 121, 104308.

Wang, Y., Wang, L. & Zhao, L. (2023). Settlement characteristics of immersed tunnel of Hong Kong–Zhuhai–Macau Bridge project. Proc. ICE — *Geotechnical Engineering*, 176(6), 605–617. https://doi.org/10.1680/jgeen.22.00200.

Yeung, A. (2016). Geotechnical works of the Hong Kong–Zhuhai–Macao Bridge project. *Japanese Geotechnical Society Special Publication*, The Japanese Geotechnical Society.

Yuan, B., Choo, C.S., Yeo, L.Y., Wang, Y., Yang, Z., Guan, Q., Suryasentana, S., Choo, J., Shen, H., Megia, M., Zhang, J., Liu, Z., Song, Y., Wang, H. & Chen, X. (2025). Physics-informed machine learning in geotechnical engineering: a direction paper. *Geomechanics and Geoengineering*, 20(5), 1128–1159. https://doi.org/10.1080/17486025.2025.2502029.

Zhao, F., Lu, X., Shi, H., Liu, B., Liu, S., Dai, K. & Fan, Y. (2023). Study on stratified settlement and weak reflectivity fiber grating monitoring of shield tunnel crossing composite strata. *Applied Sciences*, 13, 1769. https://doi.org/10.3390/app13031769.

AI-Enhanced Detection of Untrained Compound Damage and Scour in Wind Turbines

De-Jie Song[1], Li Long[2], Zohreh Mousavi[1], Wei-Qiang Feng[1*]
[1]Southern University of Science and Technology, Shenzhen; [2]Offshore Oil Engineering CO., LTD., Shenzhen, China.

ABSTRACT

Monopiles are the most used foundation type in Offshore Wind Turbines (OWTs) and are constantly subjected to environmental forces. Structural Health Monitoring (SHM) of OWTs faces many challenges, such as the identification of compound damage and scouring damage. To address these issues, this study proposes an integrated AI-Enhanced Digital Twin Framework. The framework consists of two parts: (1) It employs a few-shot learning approach that combines wavelet transform and Multiple Interference Deep Convolutional Neural Network (MIDCNN). By analyzing the probability superposition of features, the model identifies multi-fault conditions without using compound samples during training. (2) a physics-informed Digital Twin (DT) is established through Finite Element Model Updating (FEMU) to generate high-fidelity synthetic datasets. Subsequently, a novel Graph Neural Network architecture, GAT_GATv2 is introduced, which is based on Proper Orthogonal Decomposition (POD) combined with dynamic sensor topology, for classifying scour depths. The validation demonstrates that the MIDCNN achieves 97% precision for compound states without training, while the GAT_GATv2 achieve an accuracy 83.3% for scour detection. This approach provides an efficient solution for OWT monitoring.

1 INTRODUCTION

SHM plays a crucial role in detecting damage in OWTs. Due to the complexity of offshore structures and their exposure to diverse loads, simultaneous compound damages across different components can occur, posing a significant challenge for damage detection. For instance, waves and currents can cause scour and damage to the foundation, reducing lateral stiffness and altering the natural frequencies (Prendergast et al., 2019). Although finite element (FE) modeling is a standard tool for analyzing these, due to the nonlinearity of soil-structure interaction (SSI) (Arany et al., 2016), the results of FE simulations differ from the actual conditions. This requires model updating to ensure physical fidelity (Friswell and Mottershead, 1995). In addition to the scouring, OWTs are also prone to compound damages, as shown in Figure 1.

There are two limitations in addressing these situations: (1) current methods treat compound damage as an independent class and require collecting a large amount of labeled data for each possible combination of faults (Niu et al., 2023). However, due to the inability to collect such a wide variety of data from OWTs, traditional supervised learning models are limited (Mousavi et al., 2024). Therefore, models trained solely based on a single damage state often fail to generalize the learned knowledge to untrained scenarios, resulting in poor recognition of new fault features. (2) traditional data-driven methods handle sensor data separately, ignoring the spatial dependence in sensor networks (Scarselli et al., 2009). Moreover, the physical complexity of SSI has not been fully addressed. This leads to the model being unable to capture the structural stiffness changes during early scouring (Jawalageri et al., 2024). The current models have limited ability to effectively integrate spatial sensor relationships and the physical phenomena of scour, and there are significant gaps in achieving data-efficient SHM.

In the realm of vibration-based monitoring, Graph Neural Networks (GNNs) have recently emerged. GNNs model sensors as nodes and the interactions between them as edges to process data from sensor networks with irregular distributions. This ability enables GNNs to capture non-Euclidean spatial dependencies and propagate information across structural topologies, which is beneficial for damage localization (Corso et al., 2024).

However, most graph-based methods rely on a fixed topology and assume that the relationships between sensors are static. This fails to capture the dynamic correlations of the structure (Kim et al., 2025). As the soil stiffness decreases, the boundary conditions change, leading to alterations in the mode shape and energy.

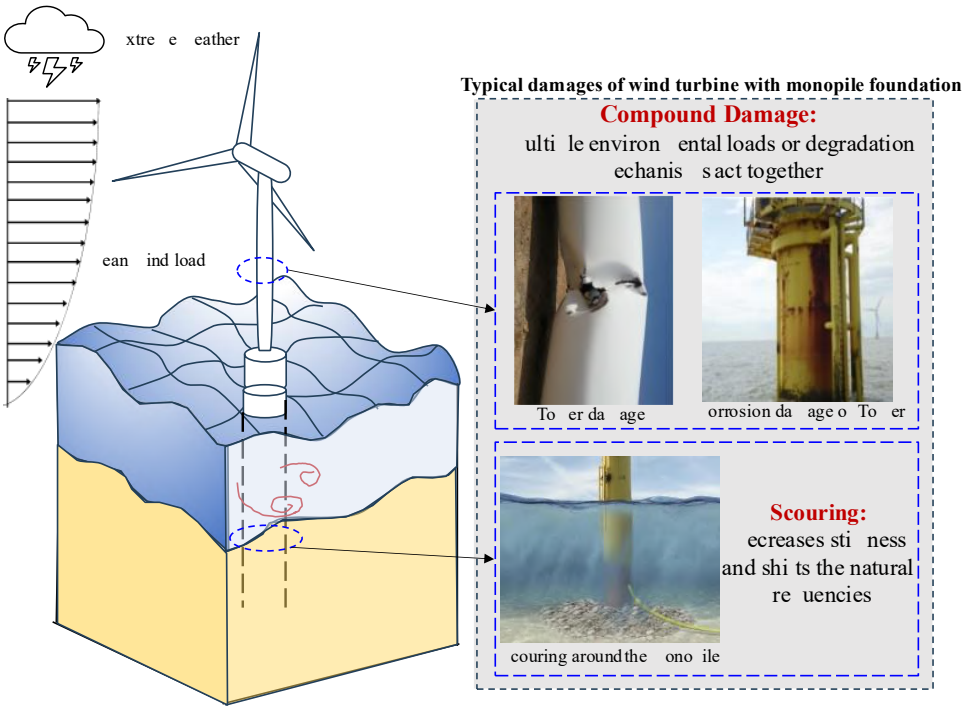

Figure 1: Some types of structural damage in offshore monopile structures

To address the challenges of data scarcity and the detection of compound damage, this study proposes an integrated AI-Enhanced Digital Twin Framework. This approach synthesizes FE modeling with deep learning to detect pile foundation scour and untrained compound damages. The contributions of this research are as follows:

1. We employ a Wavelet Transform (WT) and MIDCNN to handle temporal-frequency features. This module is trained on healthy and single-damage states. By analyzing the probabilities of decoupled features, the system can identify and classify complex compound damage scenarios that did not occur during the training, ensuring reliable detection even when the data is incomplete.

2. To address the issue of lacking comprehensive damage data, we established a DT model based on FEMU. By updating physical parameters based on experimental modal analysis, this model accurately captures the nonlinear SSI. This enables the generation of robust synthetic datasets that reflect realistic behaviors under various scour depths, compensating for the limitations of field data.

3. To utilize the topology of the sensor network, we introduce a Graph Neural Network model, GAT_GATv2. It adopts a hybrid attention mechanism that combines the static stability of GAT with the dynamic response of GATv2 to capture the complex spatial relationships between sensors, significantly improving the localization accuracy of scour damage.

2 APPROACHES AND PROCEDURES

2.1 Wavelet transform and DCNN

Standard 1D analysis, like time-domain or frequency-domain analysis, often cannot capture the true pattern of damage circumstances, particularly for compound damage recognition, which means the detection may be difficult using only time or frequency domains. The TFR emerges as a valuable tool in the analysis of vibration signals for damage detection, providing insights into the original time-domain data.

The WT is a tool for improving time precision and reducing frequency precision in the high-frequency range. The WT can reveal high-frequency features on a small scale and display low-frequency information on a large scale. Due to the various uncertainties in offshore environments, vibration signals from structures often contain extraneous and irrelevant data regarding the structure's nature. This noise data may lead to errors or diminish the accuracy of both feature learning and damage detection. When WT is employed for SHM or damage

detection, the objective is to extract meaningful representations from the raw signals that can better assess the condition of the structure. This method is more likely to capture the natural characteristics of the structure and minimize the influence of noise or other irrelevant components.

The implementation of the WT involves computing the inner product of the signal, represented as $y(t)$, and the wavelet basis function $\phi_{a,\lambda}$, which is expressed as:

$$WT_y(a,\lambda) = \int_{-\infty}^{+\infty} y(t)\,\phi_{a,\lambda}(t)\,dt = \int_{-\infty}^{+\infty} y(t)\,\phi(\frac{t-\lambda}{a})\,dt \tag{1}$$

where α represents the dilation factor, which controls the basic stretching of the wavelet, λ denotes the translation factor, determining the displacement of the wavelet function during the transformation.

Following this signal processing, Deep Convolutional Neural Networks (DCNNs) serve as the core engine for feature learning and classification. The DCNN architecture typically integrates convolutional layers for extracting feature maps, max-pooling layers for dimensionality reduction and location invariance, and fully-connected (FC) layers for final classification. To ensure robust performance and accelerate training, mechanisms such as Dropout, Batch Normalization (BN), and Leaky-ReLU activation functions are incorporated.

Typically, in multi-class classification tasks, the final FC layer employs the Softmax activation function. This function generates conditional probabilities for each class as output. Given C classes for data classification, the probability of the output relating to the K-th node or class ($O_K \in [0, 1]$) in the output layer can be calculated as follows using the Softmax function:

$$O_K = P(Y = K \,|\, X; W_K, b_K) = Soft\max(W_K X + b_K) = \frac{\exp(W_K X + b_K)}{\sum_{j=1}^{C} \exp(W_j X + b_j)} \tag{2}$$

where $P(.)$ represents the conditional probability function, X denotes the input of the output layer and $\sum_{j=1}^{C} O_j = 1$. The output node corresponding to the highest value of the conditional probability is identified as the label for the input training data.

2.2 Numerical model and model updating

The numerical model refers to the framework of Niu et al. (2023). To accurately capture the dynamic behavior of the offshore monopile under scouring conditions, a physics-based numerical framework is established. The surrounding soil is assumed to remain in a small-strain state, with its dynamic shear modulus (G_0) and elastic modulus (E_s). The SSI is modeled using the Winkler spring model, where the spring stiffness coefficient (k_{sp}^r) is calculated via Eq. (3).

$$k_{sp}^r = K * l \tag{3}$$

$$K = \frac{0.65 E_s}{(1-\mu^2)} \left[\frac{E_s D^4}{E_p I_p} \right]^{\frac{1}{12}} \tag{4}$$

where μ is the Poisson's ratio of the soil, and l represents the scour depth.

To quantitatively simulate scour, the upper soil layers are idealized as massless springs, and the scouring process is realized by unloading these specific springs. The monopile is modeled as a Bernoulli-Euler beam, discretized into elements with 8 degrees of freedom.

A critical feature of this model is the pile-soil coupling below the mudline: the element stiffness matrix is constructed by su eri osing the soil s ring sti ness onto the ile's structural sti ness. Follo ing scour, the system matrix is modified by deleting the soil stiffness coefficients associated with the scouring layers. The stiffness of the surface layer coupling element is specifically defined in Eq. (5). These local contributions are then assembled into the global stiffness and mass matrices to represent the complete system.

$$k_{e-sub} = k_e + \begin{bmatrix} k_{sp}^m & 0 & 0 & 0 & 0 & 0 & 0 & 0 \\ 0 & k_{sp}^m & 0 & 0 & 0 & 0 & 0 & 0 \\ 0 & 0 & 0 & 0 & 0 & 0 & 0 & 0 \\ 0 & 0 & 0 & 0 & 0 & 0 & 0 & 0 \\ 0 & 0 & 0 & 0 & k_{sp}^{m+1} & 0 & 0 & 0 \\ 0 & 0 & 0 & 0 & 0 & k_{sp}^{m+1} & 0 & 0 \\ 0 & 0 & 0 & 0 & 0 & 0 & 0 & 0 \\ 0 & 0 & 0 & 0 & 0 & 0 & 0 & 0 \end{bmatrix} \tag{5}$$

To bridge the discrepancies between FE predictions and experimental results, a sensitivity-based FEMU strategy is employed. This process uses perturbation analysis (Eq. (6)) to iteratively adjust model parameters. The system equations are linearized (Eq. (7)), and the sensitivity matrix is derived using numerical approximations (Eq. (8)). Finally, the model is calibrated by minimizing an objective function (Eq. (9)), which represents the weighted sum of squared residuals between the measured and predicted natural frequencies and Mode Assurance Criterion (MAC) values.

$$\varepsilon_z \approx \mathbf{r}_i - \mathbf{G}_{i|\theta=\theta_i} \Delta\theta_i \tag{6}$$

$$\begin{bmatrix} \frac{\varepsilon_1}{z_{0,1}} \\ \vdots \\ \frac{\varepsilon_q}{z_{0,q}} \end{bmatrix} = \begin{bmatrix} \frac{r_1}{z_{0,1}} \\ \vdots \\ \frac{r_q}{z_{0,q}} \end{bmatrix} - \begin{bmatrix} \frac{\partial z_1}{\partial \theta_1}\frac{\theta_{0,1}}{z_{0,1}} & \cdots & \frac{\partial z_1}{\partial \theta_p}\frac{\theta_{0,p}}{z_{0,1}} \\ \vdots & \ddots & \vdots \\ \frac{\partial z_q}{\partial \theta_1}\frac{\theta_{0,1}}{z_{0,q}} & \cdots & \frac{\partial z_q}{\partial \theta_p}\frac{\theta_{0,p}}{z_{0,q}} \end{bmatrix} \begin{bmatrix} \frac{\Delta\theta_1}{\theta_{0,1}} \\ \vdots \\ \frac{\Delta\theta_p}{\theta_{0,p}} \end{bmatrix} \tag{7}$$

$$\begin{aligned} \partial z_q &= z_{i,q}^{pert} - z_{i,q} \\ \partial \theta_p &= \theta_{i,p}^{pert} - \theta_{i,p} \end{aligned} \tag{8}$$

$$J\left(\Delta\theta_i\right)^* = \sum_{j=1}^{q} \left[\mathbf{w}_\varepsilon\right]_{j,j} \left(\frac{z_{m,j} - z_{i,j}}{z_{0,j}} \right)^2 \tag{9}$$

where $\mathbf{r}_i = \mathbf{z}_m - \mathbf{z}\left(\theta_i\right)$ represents the residual vector between the measured outputs $\mathbf{z}_m$ and the predicted outputs $\mathbf{z}(\theta_i)$ at iteration i; $\mathbf{G}_{i|\theta=\theta_i}$ denotes the sensitivity matrix; $\Delta\theta_i$ is the parameter increment vector; $z_{i,q}^{pert}$ and $\theta_{i,p}^{pert}$ represent the perturbed output and parameter values used for calculating sensitivity, $\mathbf{W}\varepsilon$ is a symmetric diagonal weighting matrix that balances contributions from natural frequencies and MAC values, and $z_{0,j}$ serves as the normalization factor for the j-th output component.

2.3 Graph neural networks and attention mechanism

To overcome the limitations of CNNs in capturing non-Euclidean spatial dependencies within sensor networks, GNNs are employed. The sensor network is modeled as a graph structure $G = (V, E)$, and the adjacency matrix is used to encode connectivity.

Although traditional graph convolutional networks (GCN) effectively aggregate information by using a fixed graph structure, they assign equal weights to neighbors. To address this issue, the graph attention network (GAT) is introduced as a superior architecture. GAT incorporates a self-attention mechanism, which can dynamically calculate attention coefficients, enabling the model to adaptively weigh the importance of neighboring nodes during the feature aggregation process. This capability allows the network to capture subtle changes in signal correlations and focus on the most relevant sensors for damage detection.

$$\mathbf{H}^{(l+1)} = \sigma\left(\overline{\mathbf{D}}^{-\frac{1}{2}}\overline{\mathbf{A}}\overline{\mathbf{D}}^{-\frac{1}{2}}\mathbf{H}^{(l)}\mathbf{W}^{(l)}\right) \tag{10}$$

$$e_{ij} = LeakyReLU\left(b^T\left[\mathbf{W}^{(l)}\mathbf{H}_i^{(l)} \square \mathbf{W}^{(l)}\mathbf{H}_j^{(l)}\right]\right) \tag{11}$$

$$\alpha_{ij} = \frac{\exp\left(e_{ij}\right)}{\sum_{k\in \mathrm{N}(i)} \exp\left(e_{ik}\right)} \tag{12}$$

$$\vec{h}_i^{'} = \sigma\left(\sum_{j\in \mathrm{N}(i)} \alpha_{ij}\mathbf{W}\vec{h}_j\right) \tag{13}$$

where G, V, and E represent the graph, nodes (sensors), and edges, respectively; $\overline{\mathbf{A}}=\mathbf{A}+\mathbf{I}_N$ is the adjacency matrix with added self-loops, and $\mathbf{D}$ is the corresponding degree matrix, $H(l)$ and $W(l)$ denote the feature matrix and learnable weight matrix at layer l, with σ representing the activation function; regarding the GAT mechanism, e_{ij} is the unnormalized attention score indicating the importance of node j to node I, $[\cdot\|\cdot]$ denotes vector concatenation; b and $\mathbf{W}$ are trainable weight vector and matrices; α_{ij} is the normalized attention coefficient computed via Softmax, and N(i) represents the neighborhood of node i used for the final weighted feature aggregation $\vec{h}_i^{'}$.

3 PROPOSED DAMAGE DETECTION APPROACH

This section provides an overview of the comprehensive framework for damage detection. Firstly, it introduces the construction of the physical experimental setup and the damage detection system. Subsequently, it describes the generation process of datasets for compound damage and for scour detection. Finally, it presents the hybrid WT-MIDCNN for compound damage and GAT_GATv2 for scouring. Figure 2 illustrates the few-shot learning pipeline for compound damage, while Figure 3 depicts the DT-based framework for foundation scour.

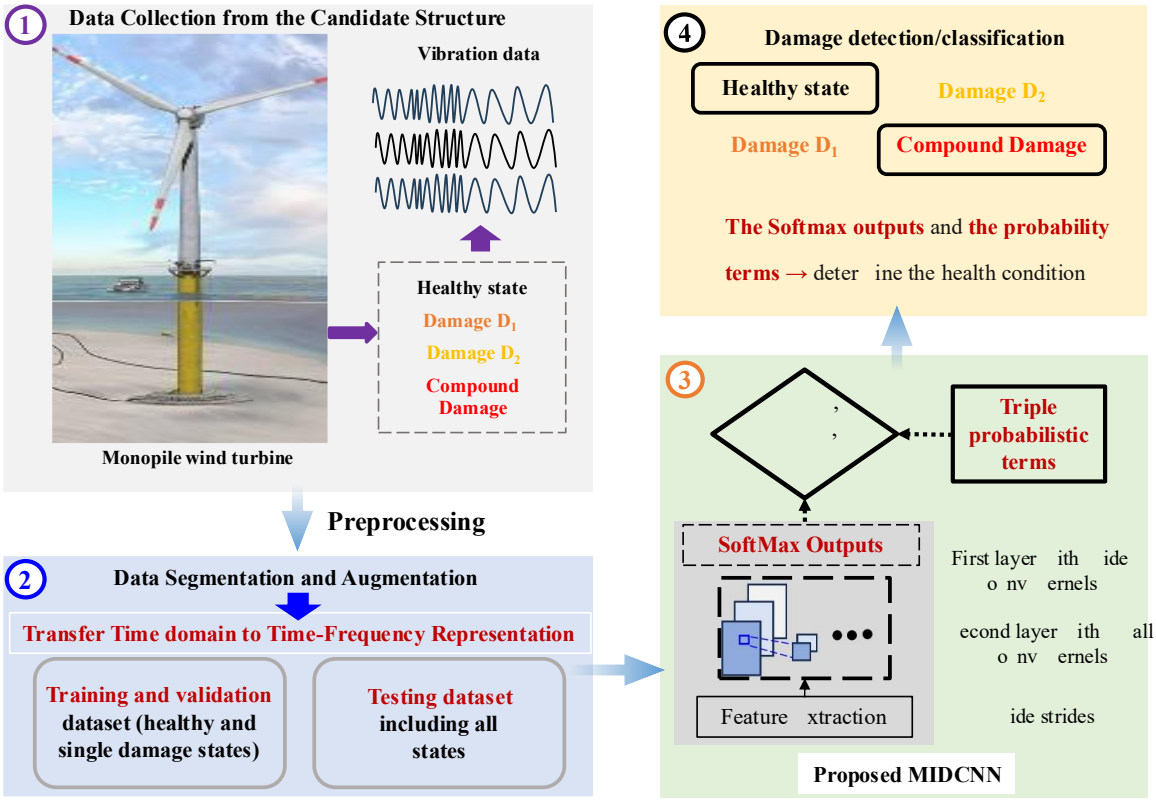

Figure 2: Flowchart of detection for compound damage

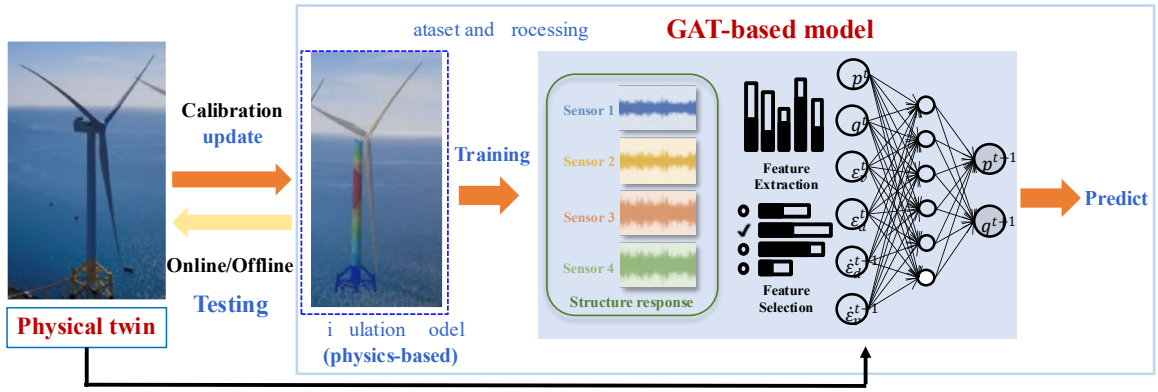

Figure 3: Flowchart of the DT-based method

3.1 Experimental setup and physical-informed digital twin construction

A laboratory-scale offshore monopile model was constructed to acquire real-world vibration data, as shown in Figure 4. The setup is designed based on Froude scaling laws with a geometric scale of 1:75 relative to a prototype 5 MW OWT. A steel pipe simulates the monopile with a length of 1100 mm, an outer diameter of 60 mm, and a wall thickness of 2 mm. It is embedded in a model container (1.2m×1.2m×0.8m) filled with sandy soil. The soil used is dry sand with a relative density of approximately 70%. Key parameters include a specific gravity Gs = 2.65, void ratios e_{max} = 0.94 and e_{min} = 0.54, and an internal friction angle ϕ=36°. The pile is embedded to a depth of 400 mm. Seven accelerometers (A1–A7) are mounted along the pile shaft. A shaker attached to the pile top applies Gaussian white noise excitation to simulate ambient environmental loads.

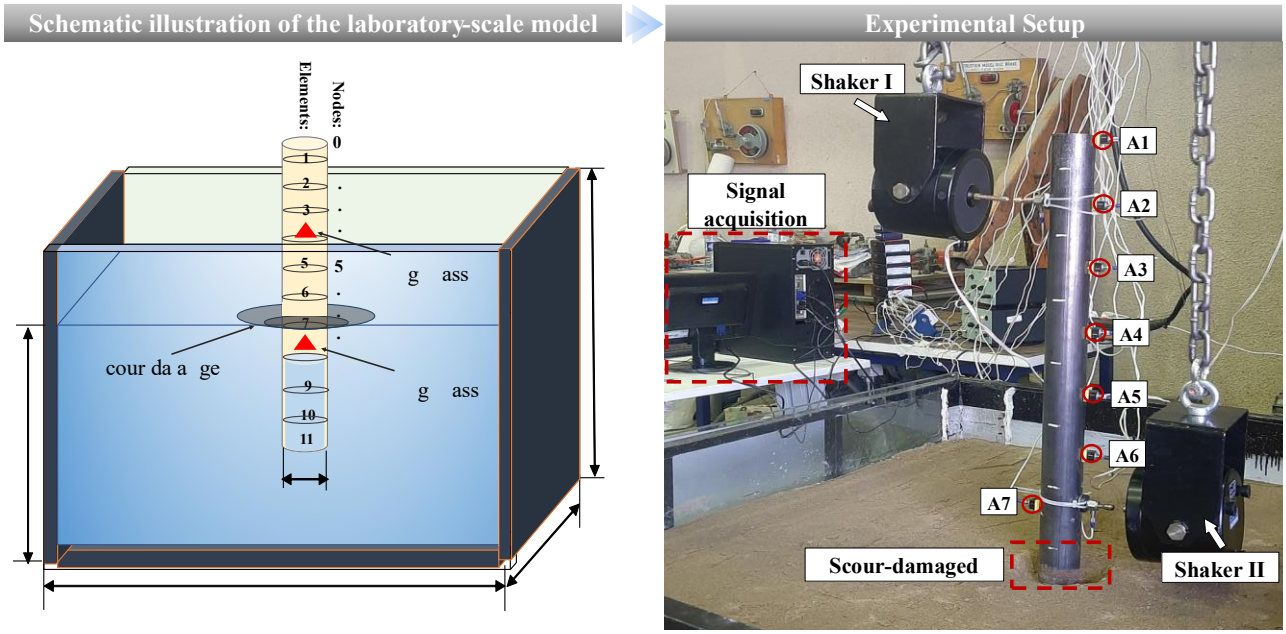

Figure 4: Schematic diagram and experimental setup of the laboratory-scale model

Corresponding to the physical setup, a numerical baseline is modeled as a Bernoulli-Euler beam with 8-DOF elements in Abaqus. The pile was discretized using S4R shell elements to capture thin-walled behavior, while the SSI was simulated via distributed Winkler springs. Scour was efficiently modeled by deactivating the spring elements at specific depths. To ensure physical consistency, a sensitivity-based FEMU strategy was employed.

A total of 34 parameters (steel density, elastic modulus, and 32 soil spring stiffness coefficients) were iteratively calibrated.

3.2 Dataset generation

To verify the proposed framework, we used two different datasets: Dataset I (experimental data) for compound damage detection, and Dataset II (synthetic data) for foundation erosion identification. We employ a standardized data processing workflow enhanced by sliding windows to handle these two datasets to ensure reliability.

Dataset I was directly obtained from the laboratory physical model to capture the real characteristics. By attaching additional mass to the pile to simulate the damage, local stiffness changes and mode shapes were caused. We created three specific damage states: single damage D1 (150g mass at Element 8, near the soil surface), single damage D2 (60g mass at Element 4, mid-span), and a compound damage state involving the simultaneous addition of two masses. The original vibration signals were recorded at a sampling rate of 2000 Hz for 90 seconds. To facilitate the adoption of the few-sample learning strategy, we implemented a strict dataset partitioning scheme: the training set was entirely composed of healthy, D1, and D2 state data, while the compound damage samples were specifically used for the test set. The continuous time series signals were segmented using the sliding window technique (window length: 5000 points, 2.5s), with overlap to generate samples for the MIDCNN.

Dataset II was generated via the calibrated DT to overcome the impracticality of creating continuous scour depths. In the Abaqus, scour scenarios were simulated by deactivating the soil spring elements layer by layer from the mudline downwards.

Specifically, we design four different scour conditions to represent different levels of scouring damage: a complete baseline state (0 cm) and three gradually increasing erosion depths of 25 cm, 50 cm, and 75 cm. For each of these four scenarios, a dynamic simulation of 100 seconds was conducted under a Gaussian white noise excitation of 2000 Hz. These simulation responses were sliced using a sliding window (window length: 1000 points, 0.5s), with a 20% overlap. This process generated a large-scale tensor dataset (dimensions: 7 sensors × 1000 points × N samples), which captures the unique spatiotemporal evolution characteristics specific to each scour depth and is crucial for training the GNN model.

3.3 Hybrid wavelet-deep learning for compound damage

Standard time-domain analysis often fails to separate the unique non-stationary transient characteristics of structural faults. To address this issue, the original 1D acceleration signals from dataset I are transformed into 2D TFRs using the continuous wavelet transform (CWT). Since the Morlet wavelet has the best balance in time and frequency localization, it is chosen as the mother wavelet to precisely capture the frequency shifts and amplitude modulations caused by damage. This step converts the time signal segments into a 64×64, effectively suppressing environmental noise while enhancing the distinguishability of damage features.

The generated TFR is used as the input for MIDCNN. MIDCNN has parallel convolutional paths with different kernel sizes to simultaneously extract hierarchical features in different receptive fields. Crucially, the training protocol is based on class division: the model is optimized only on the healthy and single damage (D1, D2) datasets. This forces the network to learn robust and independent feature representations for each basic injury type without overfitting to specific composite patterns.

During the testing, when the network encounters a compound damage sample, it does not classify it as a new unknown category. Instead, due to the superposition of fault features in the TFR, the Softmax layer outputs the distributed probability. The confidence scores of the D1 and D2 categories are significantly shared rather than dominated by a single category. By comparing this probability distribution with a pre-set threshold, the system can identify the coexistence of multiple fault features, thereby diagnosing the composite damage situation.

3.4 Dynamic graph topology and GAT_GATv2 for scour damage detection

The traditional graph methods usually define connectivity using fixed physical distances, but this approach fails to reflect the dynamic characteristics of the scouring. To address this issue, we constructed a dynamic sensor topological structure to identify the mode correlations between sensors. We processed multi-channel vibration

data using the POD method. Through singular value decomposition (SVD), the spatio-temporal response field was decomposed into a set of appropriate orthogonal modes (POM) and corresponding singular values. These POMs represent the optimal basis for structural vibration modes. The adjacency matrix is not randomly set but is derived by calculating the correlations between sensor nodes under these main POMs. Specifically, the connection between two sensors is determined by the similarity of their normalized modal coordinates and is weighted by the energy (singular value) of each mode. This mechanism ensures that the graph edges represent the dependency of physical modes. As the boundary conditions change, the mode shapes will change, which will dynamically update the topological structure of the graph.

To accurately classify scour depths from the constructed dynamic graphs, we design a hybrid Deep GNN architecture. This architecture is called GAT_GATv2, which integrates the local stability of standard GAT with the dynamic expressiveness of GATv2 to effectively aggregate spatial features from the sensor network. To capture the subtle, non-linear stiffness changes caused by scour, the second layer utilizes GATv2Conv. Standard GAT has the problem of static attention, where attention weights only depend on the query node. GATv2 overcomes this by applying a nonlinear function before the product of the attention vector, making the attention strictly dynamic:

$$e_{ij} = b^T LeakyReLU\left(\left[\mathbf{W}^{(l)}\mathbf{H}_i^{(l)} \square \mathbf{W}^{(l)}\mathbf{H}_j^{(l)}\right]\right) \tag{14}$$

To prevent the over-smoothing problem in deep GNNs, this study introduces residual connections. The input features of a layer are added directly to its output:

$$H^{(l+1)} = \sigma\left(Attention\left(H^{(l)}\right)\right) + H^{(l)} \tag{15}$$

The final node is aggregated through a global mean pooling layer, thereby forming a graph-level feature vector. Then this vector is classified by a fully connected Softmax layer for a specific scour depth class (e.g., 0 cm, 25 cm, 50 cm, 75 cm).

4 RESULTS AND DISCUSSION

4.1 Evaluation of compound structural damage detection

To verify the superiority of the proposed hybrid wavelet-MIDCNN architecture, it was compared with other methods trained under the same constraints.

As detailed in Table 1, the proposed method achieved an overall precision of 98.0%. This significantly outperforms the Siamese Neural Network (SNN) based on raw frequency data (92.7%) and the standard CNN based on VMD time-frequency images (95.8%). The performance gap was observed in the detection of the unseen compound damage class. The proposed method achieved 97.0% of precision, while the SNN and VMD-CNN achieved 88.5% and 90.5%, respectively. This indicates that the hierarchical features extracted by the interference blocks of MIDCNN are more robust and discriminative than those extracted by the standard convolutional layers, and can better generalize to complex damage patterns.

Table 1. Precision comparison of different methods for classifying each state and overall precision

Methods	Healthy (%)	D1 (%)	D2 (%)	D1 and D2 (compound state) (%)	Overall (%)
Raw frequency data-SNN (Baquerizo et al., 2022)	100	85.0	97.5	88.5	92.7
VMD-TFR-CNN (Dibaj et al., 2021)	100	92.5	100	90.5	95.8
Proposed method	100	95.0	100	97.0	98.0

The learned feature spaces were visualized and statistically analyzed. Figure 5 shows the topological structure of the learned features. In the comparative method, there is a significant overlap between the compound damage cluster and the single damage D1 cluster. This is physically reasonable because the more severe damage

D1 dominates the vibration features. The proposed MIDCNN method successfully separated these features and formed a distinct compound cluster between D1 and D2. This separation is crucial for the inference logic to function correctly. A one-way ANOVA analysis was conducted on the t-SNE features. The proposed method yielded the highest F-statistic (996.38) and the lowest p-value (1.12×10^{-160}) compared to other methods. This statistically proves that the proposed approach maximizes the inter-class variance, ensuring that even untrained states form statistically distinct clusters rather than being misclassified as noise or existing classes.

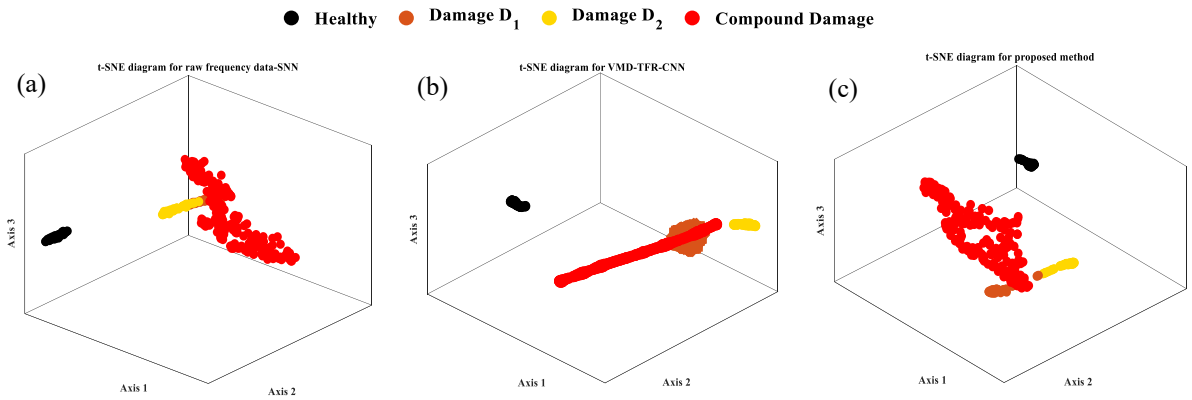

Figure 5 t-SNE for various approaches, (a) Raw frequency data-SNN (b) VMD-TFR-CNN, (c) proposed method

The system relies on a probabilistic inference mechanism, which was analyzed by the probability distributions, as shown in Figure 6. For test samples belonging to single damage D1, the model outputs a high con idence score $\approx .9$ or class D1, while for other classes, it outputs scores that are nearly zero.

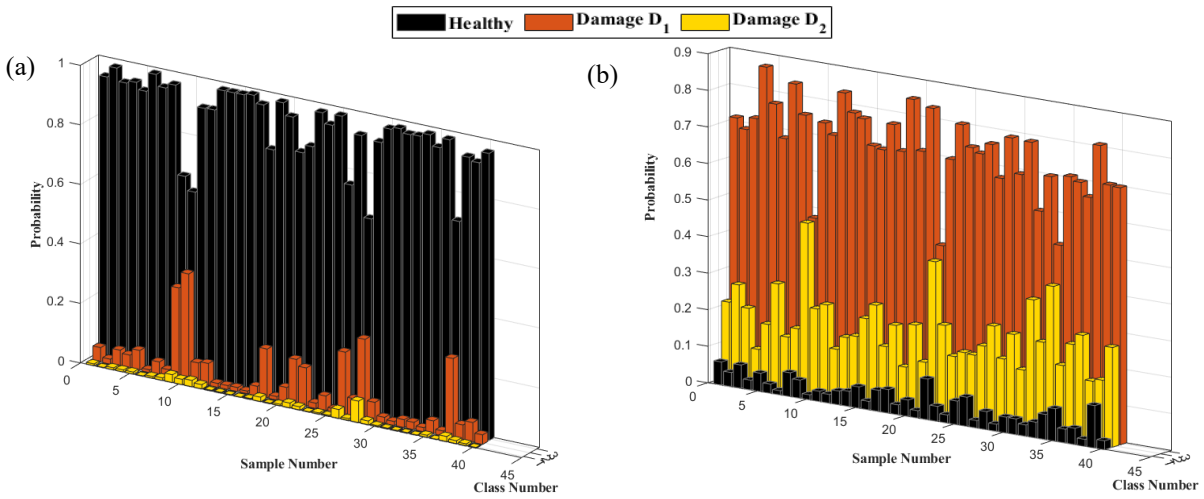

Figure 6 Displaying the computed probabilities for healthy and single damage states using MIDCNN (a) Healthy samples, (b) Compound damage samples

When training with compound damage samples, the model does not output a single dominant probability. Instead, it exhibits probability superposition. For example, a sample might yield $P(D1) \approx 0.52$ and $P(D2) \approx 0.46$. This distributed confidence validates that compound damage is the superposition of single faults. Through Eq. (16), the system correctly labels these samples as compound damage. This demonstrates that the model not only remembers labels but also learns the potential physical features of damage, thereby identifying their coexistence.

$$\begin{aligned} &Condition1: P(H) \le P(D_1) \\ &Condition2: P(H) \le P(D_2) \\ &Condition3: \left|P(D_2) - P(D_1)\right| / \left(P(D_2) + P(D_1)\right) \le Compound_{threshold} \end{aligned} \tag{16}$$

4.2 Evaluation of foundation scour detection

For scour detection, the validity of the results depends on the physical accuracy of the synthetic training data. Therefore, the discussion first addressed the calibration issue of the model, and then analyzed the classification performance.

Before generating the synthetic scouring dataset, the benchmark FE model was rigorously updated to match the actual experimental conditions. Using the sensitivity-based FEMU method, the initial difference in natural frequencies was minimized. As presented in Table 2, the error of the first natural frequency decreased from 7.37% to 0.96%, and the error of the second frequency was reduced to 0.45%. The MAC value of the first mode increased from 0.72 to 0.97, and that of the second mode increased from 0.16 to 0.86. This confirms that the updated FE model accurately captures the SSI.

Table 2 First three natural frequencies of the FE healthy model, before and after model updating

Mode	Experiment	Abaqus (before)	Abaqus (after)	$Error_1$(%)	$Error_2$(%)
Mode_1	59.5	55.114	58.931	7.37	0.96
Mode_2	334.6	319.624	333.106	4.48	0.45
Mode_3	851.6	830.028	843.114	2.53	0.99

The data generated by the calibrated DT model was then used to train the GAT_GATv2 model. The performance of the model is then verified on the experimental data. As shown in Table 3, the proposed method achieved an overall classification accuracy of 83.3%, showing better performance than baseline models such as GCN (67.8%), GAT (75.3%), and GATv2 (70.8%). This indicates that combining static and dynamic attention mechanisms effectively captures the complex spatial dependencies in the sensor network.

Table 3 Comparison of different models for classifying each state and overall precision

Model	Class_0(%)	Class_1(%)	Class_2(%)	Class_3(%)	Overall (%)
MLP (Bisong, 2019)	65.0	28.0	33.7	58.0	46.1
GCN (Kipf and Welling, 2016)	73.0	54.0	67.3	77.0	67.8
MoNet (Monti et al., 2016)	74.0	64.0	65.3	87.0	72.6
GAT Veličković et al.,	86.0	56.0	74.3	85.0	75.3
GATv2 (Brody et al., 2022)	80.0	52.0	69.3	82.0	70.8
GAT_GATv2	87.0	73.0	85.1	88.0	83.3

5 CONCLUSIONS

This study proposes a framework that combines physics-based modeling with deep learning to address the issues of single-pile scouring and composite damage monitoring. The conclusions are as follows:

1. Untrained composite damage detection: A few-shot learning strategy was implemented. By combining WT with MIDCNN, the system was able to aggregate the probabilities of diagnosing compound damage as individual faults. This model achieved an accuracy of 97.0% without training using compound damage samples, demonstrating the feasibility of inferring complex states from basic knowledge.
2. High-fidelity digital twin construction: We employed a digital twin technology based on physical principles. Through the sensitivity-based FEMU method, the numerical model achieved a high degree of physical consistency with the experimental model (frequency error < 1%, MAC > 0.9). The calibrated DT model can serve as a tool for training data in real damage scenarios.
3. Feature recognition: The proposed GAT_GATv2 model demonstrated an outstanding ability in capturing the constantly changing spatial dependencies of the sensor network. By constructing a dynamic graph topology based on modal energy correlation, this network effectively aggregated spatial

features. With only synthetic data for training, the overall accuracy on real experimental data reached 83.3%.

REFERENCES

Arany, L., Bhattacharya, S., Macdonald, J.H.G., Hogan, S.J., 2016. Closed form solution of Eigen frequency o f monopile supported offshore wind turbines in deeper waters incorporating stiffness of substructure and S SI. Soil Dynamics and Earthquake Engineering 83, 18–32. https://doi.org/10.1016/j.soildyn.2015.12.011

Baquerizo, J., Tutivén, C., Puruncajas, B., Vidal, Y., Sampietro, J., 2022. Siamese neural networks for damage detection and diagnosis of jacket-type offshore wind turbine platforms. Mathematics 10, 1131.

Bisong, E., 2019. The Multilayer Perceptron (MLP), in: Building Machine Learning and Deep Learning Mode ls on Google Cloud Platform. Apress, Berkeley, CA, pp. 401–405. https://doi.org/10.1007/978-1-4842-447 0-8_31

Brody, S., Alon, U., Yahav, E., 2022. How Attentive are Graph Attention Networks? https://doi.org/10.48550/ arXiv.2105.14491

Corso, G., Stark, H., Jegelka, S., Jaakkola, T., Barzilay, R., 2024. Graph neural networks. Nat Rev Methods Pr imers 4, 17. https://doi.org/10.1038/s43586-024-00294-7

Dibaj, A., Ettefagh, M.M., Hassannejad, R., Ehghaghi, M.B., 2021. A hybrid fine-tuned VMD and CNN sche me for untrained compound fault diagnosis of rotating machinery with unequal-severity faults. Expert Syst ems with Applications 167, 114094.

Faraonis, P., Sextos, A., Papadimitriou, C., Chatzi, E., Panetsos, P., 2019. Implications of subsoil-foundation modelling on the dynamic characteristics of a monitored bridge. Structure and Infrastructure Engineering 1 5, 180–192. https://doi.org/10.1080/15732479.2018.1503689

Friswell, M.I., Mottershead, J.E., 1995. Finite Element Model Updating in Structural Dynamics, Solid Mechan ics and its Applications. Springer Netherlands, Dordrecht. https://doi.org/10.1007/978-94-015-8508-8

Huynh, T.-C., Lee, S.-Y., Dang, N.-L., Kim, J.-T., 2019. Vibration-based structural identification of caisson-fo undation system via in situ measurement and simplified model. Struct Control Health Monit 26, e2315. http s://doi.org/10.1002/stc.2315

Jawalageri, S., Ghiasi, R., Jalilvand, S., Prendergast, L.J., Malekjafarian, A., 2024. A data-driven approach for scour detection around monopile-supported offshore wind turbines using Naive Bayes classification. Mari ne Structures 95, 103565. https://doi.org/10.1016/j.marstruc.2023.103565

Kim, M., Song, J., Kim, C.-W., 2025. Near-real-time damage identification under vehicle loads using dynamic graph neural network based on proper orthogonal decomposition. Mechanical Systems and Signal Processi ng 224, 112175. https://doi.org/10.1016/j.ymssp.2024.112175

Kipf, T.N., Welling, M., 2016. Semi-Supervised Classification with Graph Convolutional Networks. https://do i.org/10.48550/ARXIV.1609.02907

Monti, F., Boscaini, D., Masci, J., Rodolà, E., Svoboda, J., Bronstein, M.M., 2016. Geometric deep learning o n graphs and manifolds using mixture model CNNs. https://doi.org/10.48550/arXiv.1611.08402

Mousavi, Z., Varahram, S., Ettefagh, M.M., Sadeghi, M.H., Feng, W.-Q., Bayat, M., 2024. A digital twin-base d framework for damage detection of a floating wind turbine structure under various loading conditions bas ed on deep learning approach. Ocean Engineering 292, 116563. https://doi.org/10.1016/j.oceaneng.2023.11 6563

Niu, X., Lu, G., Chen, X., Wang, H., 2023. A method for structural damage detection considering scour depth under the pile-soil interaction. Mar. struct. 88, 103365. https://doi.org/10.1016/j.marstruc.2022.103365

Prendergast, L.J., Wu, W.H., Gavin, K., 2019. Experimental application of FRF-based model updating approa ch to estimate soil mass and stiffness mobilised under pile impact tests. Soil Dynamics and Earthquake Eng ineering 123, 1–15. https://doi.org/10.1016/j.soildyn.2019.04.027

Scarselli, F., Gori, M., Ah Chung Tsoi, Hagenbuchner, M., Monfardini, G., 2009. The Graph Neural Network Model. IEEE Trans. Neural Netw. 20, 61–80. https://doi.org/10.1109/TNN.2008.2005605

Veličković, ., ucurull, G., asanova, A., Ro ero, A., Liò, ., Bengio, Y., . Graph Attention Networks. https://doi.org/10.48550/arXiv.1710.10903

Sustainable Design Approaches for Large Span Rock Caverns in Hong Kong

Jacky W.H. Tsun & Jitendra Kumar Soni
AtkinsRéalis Asia Ltd., HKSAR, China

Max L.Y. Ngok
China State Construction Engineering (HK) Ltd., HKSAR, China

Genie C.Y. Nip
AECOM Asia Company., HKSAR, China

Hermann H.M. Suen
Civil Engineering and Development Department, HKSAR, China

ABSTRACT

It is essential to create new land for the sustainable development of Hong Kong, and cavern development is one of the viable options to provide valuable land for multiple functions such as accommodation of various facilities, provision for service reservoirs, etc. To ensure the constructability of such large caverns, the location of these caverns would be carefully chosen based on their geological compatibility; however, obstacles remain in their design and construction processes. This paper discusses the various design challenges to overcome unexpected issues encountered during the construction of Hong Kong's largest rock cavern under the project 'Joint Cavern Development at Anderson Road Quarry Site', which four large caverns of up to 36m span were designed with multiple adits connected, forming a complex network of underground openings. Also, the design approach that is adopted to ensure a high level of confidence for construction while maintaining cost-effectiveness of the project.

1 INTRODUCTION

To support the sustainable development of Hong Kong, the Government of the Hong Kong Special Administrative Region (HKSAR) adopts a multi-pronged approach to enhance land supply. The topography of Hong Kong, characterized by a predominance of igneous rock formations, offers a conducive environment for the formation of rock caverns. Relocating suitable government facilities into caverns offers various benefits. It can release existing surface sites for other valuable uses, while relocating facilities that are incompatible with the land uses and environment nearby, and improving the urban layout and environmental quality of the area. In addition, cavern environments have been proven ideal for housing facilities requiring secure and stable operating conditions, such as testing laboratories, archives, data centers and warehouses, etc. These facilities are protected from natural or man-made disasters by the strong cavern walls and sheltered from being affected by sunlight and weather changes, hence the temperature and humidity in caverns are relatively stable. The reduction of power consumption from cooling systems and carbon emissions during operation of the facilities does not only reduce the operational costs but also fosters Hong Kong to become a green city.

2 PROJECT BACKGROUND

The project 'Joint Cavern Development at the Anderson Road Quarry Site' aims to relocate the Public Works Central Laboratory (PWCL) of the Civil Engineering and Development Department (CEDD) and establish a new Archives Centre (AC) for the Government Records Service within caverns. This initiative addresses the growing demand for public services while leveraging the inherent advantages of cavern environments, which offer enhanced security, energy efficiency, and stable conditions ideal for laboratory and archival operations. Additionally, after relocation of the existing facilities, valuable urban land could be released for other socio-economic developments after relocation of the existing facilities.

The project comprises of construction of a cavern complex and connection adits inside the mountain body of Tai Sheung Tok at the Anderson Road Quarry Development site. Total four (4) caverns (PWCL-North, PWCL-South, AC-North and AC-South) are being constructed with maximum excavation span of 36.2m and maximum excavation height of 30.0m. The project layout plan and two of the excavated caverns are shown in Figure 1.

Figure 1. Project Layout Plan and Two of the Excavated Caverns

China State - Alchmex Joint Venture (CSAJV) is the main Contractor responsible for construction of these underground rock caverns. AtkinsRéalis is the Geotechnical Designer for under-ground excavation works. AECOM is the Project Manager for this project.

3 SITE GEOLOGY AND ROCKMASS PARAMETERS

The solid regional geology within the Project Site consists of the Early Cretaceous Lion Rock Suite, where primarily Mount Butler Granite, which is comprised of equigranular fine-grained Granite (Klb_gf), with equigranular fine to medium-grained Granite (Klb_gfm) in areas further to the west and north of the caverns is present.

All four caverns are located within the rock zone where the rockmass is predominantly Grade III or better rock with rockmass Q-value in range of 0.7 to 10.0 interpreted from boreholes. The anticipated rockmass condition is shown in Figure 2.

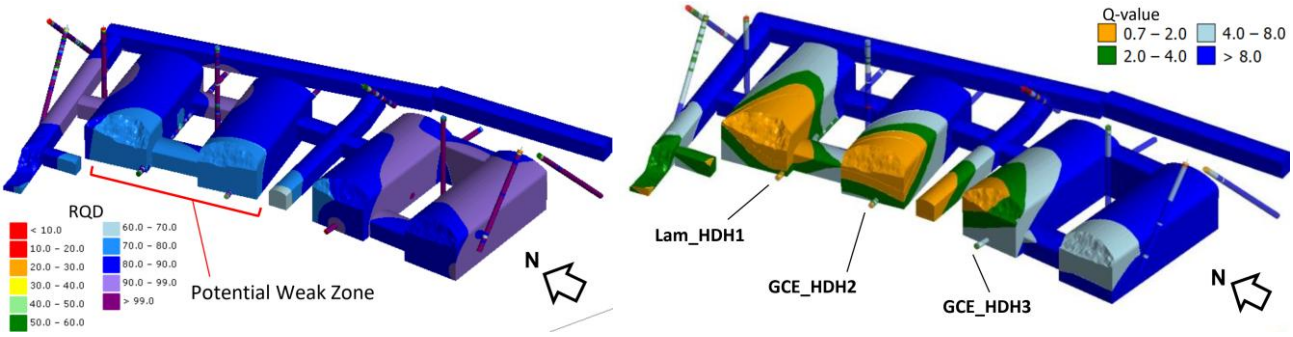

Figure 2. RQD and Q-Value Classification for Four Caverns

Rockmass parameters for geotechnical design works are derived from Ground Investigation (GI) records and laboratory tests. A total of 170 existing GI was reviewed, including their respective in-situ and laboratory testing, where available, and the findings of these data were appraised by an additional 28 GI locations, including 4 trial pits, 1 HDC, 1 inclined drillhole and 22 vertical drillholes. Project-specific field and laboratory testing included 42 lugeon and 6 televiewer tests and 188 rock and 9 soil geotechnical tests respectively. The rockmass parameters adopted for rock support design are presented in Table 1.

Table 1: Design Parameters of Rockmass

Rock Type	Bulk Unit Weight (kN/m^3)	Poisson Ratio	Intact Rock UCS (MPa)	Young's Modulus (GPa)	Tensile Strength (MPa)
Slightly Decomposed Granite (SDG)	26	0.30	140	64	13
Moderately Decomposed Granite (MDG)	26	0.30	94.6	47	12

The rockmass design parameters are derived based on the Generalized Hoek-Brown Strength Criterion:

$$\sigma_1' = \sigma_3' + \sigma_{ci}\left(m_b\frac{\sigma_3'}{\sigma_{ci}} + s\right)^a \quad (1)$$

$$GSI = 9\ln Q' + 44 \quad (2)$$

$$m_b = m_i e^{\left(\frac{GSI-100}{28-14D}\right)} \quad (3)$$

$$s = e^{\left(\frac{GSI-100}{9-3D}\right)} \quad (4)$$

$$E_m = E_i\left(0.02 + \frac{1-\frac{D}{2}}{1+e^{\left(\frac{60+15D-GSI}{11}\right)}}\right) \quad (5)$$

where σ1' and σ3' = Maximum and minimum effective principal stresses at failure (kPa), σ_{ci} = Uniaxial compressive strength of the intact rock pieces (kPa), m_b = Value of the Hoek-Brown constant of the rock mass, s and a = Constants which depend upon the rock mass characteristics, GSI = Geological Strength Index, Q' = (RQD/Jn) × (Jr/Ja), m_i = Material constant, m_b = Reduced value of material constant, s = Rock mass constant, D = Disturbance factor, E_m = Rock mass modulus (in GPa), and E_i = Intact rock modulus (in GPa).

Rock discontinuity sets are established from Borehole Televiewer Data (BHTV) and their shear strength parameters are derived from lab tests, as summarized in Table 2. These joint sets were adopted for initial design. During the construction stage, rock discontinuity sets were constantly mapped after each blast cycle and design verification was carried out accordingly.

Table 2: Major Joint Sets and Shear Strength Parameters of Rock Joints

Major Joint Set	Dip (°)	Dip Direction (°)	Joint Persistence (m)	Cohesion (kPa)	Peak Friction angle (°)	Residual Friction angle (°)
J1	57	328	15	0	45	40
J2	43	064	10	0	45	40
J3	88	261	10	0	45	40

4 KEY CHALLENGES AND THE COST-EFFECTIVE DESIGNS

During the design development stage and construction stage, several challenges are faced by the Contractor and Designer. Some of the key challenges and the cost-effective design solutions are discussed below.

4.1 Unique Scheme of Cavern Complex with Special Excavation Sequence

To ensure adequate rock cover and access to high-quality rock mass, cavern complexes are typically situated deep within hillsides and connected to surface portals via long adits or tunnel sections. These connecting structures often traverse soft or mixed ground conditions, which can lead to increased construction complexity, and higher costs. Additionally, extended access routes reduced long-term operational efficiency and pose challenges for emergency evacuation and rescue operations, particularly in fire scenarios.

Recognising these limitations, the project site was chosen to be a quarry site during the initial site selection exercise. The existing rock slope, formed by previous quarrying activities, offers an ideal portal location with competent rockmass conditions. This enabled a cost-effective layout that eliminates the need for permanent connecting adits or tunnels. Instead, the portal excavation is carried out at the face of the rock slopes, and an integrated building design is adopted, combining the surface portal facilities with underground cavern structures (Figure 3).

Figure 3. Integrated Building at Portal and inside Caverns

All cavern portals are located within 30m to public road, necessitating robust mitigation measures to minimise risks and nuisances associated with flyrock, dust, and noise generated during blasting excavation. Given the substantial height of the caverns (>30m), excavation was anticipated to be carried out in three benches: top heading, middle bench, and lower bench. A feasible excavation sequence must be developed to initiate works at the top heading level, approximately 17 meters above ground level.

To address public safety concerns and improve constructability, a unique construction sequence was adopted. The orientation of the entrance of construction adits is designed not to directly face towards public carriageway and residential development, in order to minimise blasting impacts. The blasting works are commenced from the rear of the cavern at the top heading level, while maintaining a minimum 5-meter-thick rock plug at the portal throughout all blasting activities. This approach effectively shields the portal from direct blast impacts. To access the rear top heading level, a network of small-diameter adits (span of 9.6m) was excavated, incorporating a longitudinal gradient of 1 in 8. This innovative sequence provided a key cost-effective solution to mitigate blasting risks and enhance constructability.

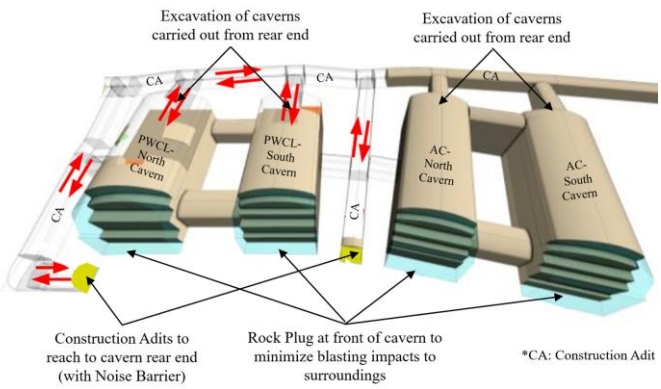

Figure 4. Cavern Excavation Sequence from Rear of Caverns, with maintaining A Rock Plug at Portal

4.2 Large Span Excavation Design

The proposed caverns are massive in size, with a maximum excavation span of 36.2m and excavation height of 30.0m. One of the key challenges was to ensure a robust design while maintaining the cost-effectiveness. In Hong Kong, conventionally two stages lining would be designed to support temporary and permanent loading. The initial stage lining comprised of rock-bolts and sprayed concrete are designed as temporary support while later stage lining using cast in-situ plain or reinforced concrete lining is designed as permanent support to take up all external loading. For such large excavations, this conventional approach requires huge number of materials for the cavern lining and a complex shutter is required to cast the permanent lining. Also, the initial stage lining installed to support the excavation is not utilized under permanent conditions. As a result, a more cost economic approach was explored to be adopted instead of the conventional design approach.

Based on the results of the ground investigation of the project site, the rock mass quality is generally good, and it is considered cost effective to adopt the rock reinforcement approach and utilize the inherent strength of the rock in the design of cavern supports. The rock reinforcement approach, which uses pattern rockbolts and shotcrete to reinforce the surrounding rock mass forming a rock arch structure to provide permanent support to the external loading instead of cast-in-situ concrete lining, thereby significantly reducing the overall lining thickness and the total volume of rock excavation. To ensure the permanent support structure fulfils the durability requirements and for 100-year design life, Double Corrosion Protection (DCP) rockbolts are adopted in the design. Spray applied waterproofing membrane is also used to achieve the watertightness requirements. In general, a three-stage design approach (Figure 5) is adopted to ensure the robustness, effectiveness and appropriateness of the designed supporting systems. The three-stage design approach is as follows:

Stage 1: Deriving initial support system from NGI Q-system Support Chart (2015);
Stage 2: Checking the suitability of the initial support system by Reinforced Rock Arch (RRA) theory, considering the thrust capacity of the reinforced rock arch against the thrust load induced by external loading. Increase the permanent support as necessary; and
Stage 3: Verifying the design by numerical analyses using Finite Element Modelling (continuum and discontinuum modelling). Increase the permanent support as necessary and confirm the permanent support requirements.

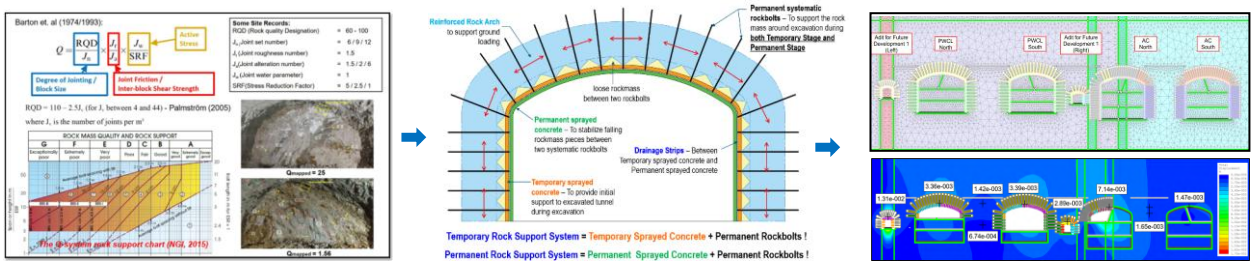

Stage 1 Stage 2 Stage 3

Figure 5. Three-stage Design Approach of Rock Reinforcement Design

Four rock support classes, as summarized in Table 3, are developed based on different Q-value ranges, representing different rockmass quality, for the above-mentioned three-stage design.

Table 3: Permanent and Temporary Rock Support for Caverns

Support Class	Rockmass As-mapped Q Value	Unsupported Length, m	Stand-up Time, Hours	Rockbolts [1]	Temporary Sprayed Concrete (mm)[2] Roof/Wall	Permanent Sprayed Concrete (mm)[3] Roof/Wall
SC-I	Q≥8.0	6m	72	5.8m Long PB1* at 1.9m C/C spacing	80(E500)/ 55(E500)	135(E700)
SC-II	8.0>Q≥4.0	6m	72	5.8m Long PB1* at 1.7m C/C spacing	95(E700)/ 60(E500)	135(E1000)
SC-III	4.0>Q ≥2.0	6m	55	5.8m Long PB1* at 1.5m C/C spacing	110(E700)/ 75(E500)	150(E1000)
SC-IV	2.0>Q ≥0.7	3m	50	5.8m Long PB1* at 1.3m C/C spacing	140(E700)/ 110(E700)	250(E1000)

[1] PB1: Permanent Rockbolts of Tensile Capacity of 204kN (with Safety Factor of 2.0)
[2] Fiber Reinforced Temporary sprayed concrete of grade C35/45 is applied within standup time.
[3] Fiber Reinforced Permanent sprayed concrete of grade C35/45, which is applied after installing the drainage strips, at least 20m behind the excavation face.

4.3 Complex Junction Network with Multiples Junction Openings

The four caverns are connected by several adits to facilitate construction logistics. With these adits all around the caverns, a complex junction network is formed with several junction openings around the cavern. The design of those openings with more precise ground stress distribution was deemed necessary. The conventional 2D design with Jnx3 to consider for junction effect might lead to a conservative design with higher density of rockbolts and thicker sprayed concrete lining, and thus adversely affect the construction cast and time. The rock pillar stability around these multiple openings is also uncertain with conventional 2D analysis which cannot consider the ground stresses distribution realistically for such complex cavern network under planned excavation sequence.

To alleviate the concerns, a 3D model is adopted to design the rock support system around the junction openings. A multistage 3D model (Figure 6) is set up with multiple staged construction according to the actual sequence adopted on site, such as multiple heading and benching sequence, to assess the ground stresses distribution around junction openings. With the help of 3D analysis, change in ground stresses and rockbolt forces are effectively evaluated for excavation stages before and after junction openings. Also, with the help of the 3D model, rock pillar stability has been checked for all critical locations, which otherwise is difficult to check with the conventional 2D model.

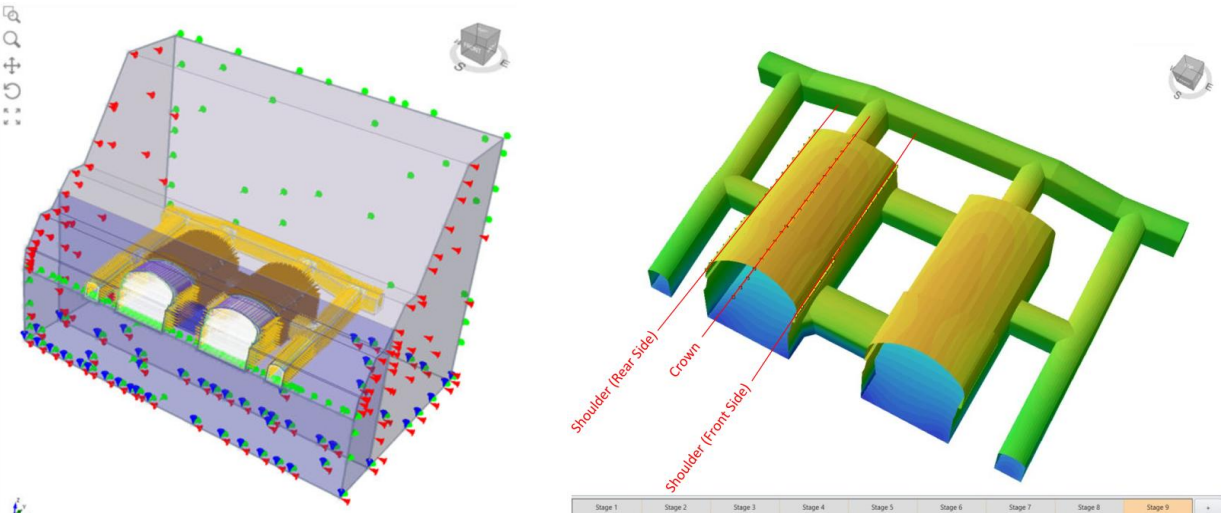

Figure 6. Staged 3D Finite Element Method (FEM) Analysis for Multiple Junction Openings

4.4 Shallow Rock Cover at Portal Area

At the cavern portals located at the face of the rock slopes, the rock cover above the cavern crown is comparatively shallow. The rock cover above the cavern crown is only 5 to 6m (less than 0.5 cavern span) imposing design concerns for instability during large cavern excavation. Also, the rockbolts of effective length cannot be installed at cavern roof due to such shallow cover, adding another challenge for cavern support design.

Multi-drift excavation is designed for this shallow rock cover location so that excavation can be carried out safely with less ground deformation and the rock conditions can be mapped in advance. To mitigate risk of instability during excavation, pre-support (pipe umbrella) is provided along the cavern crown to maintain the crown stability for interim stage between excavation and installation of support. For the cavern crown, composite lining comprised 900mm thick fiber reinforced sprayed concrete and galvanized lattice girders is adopted. Whereas for the sidewalls, permanent rockbolts and fiber reinforced sprayed concrete are designed. The rock supports for caverns at shallow rock cover are summarized in Table 4.

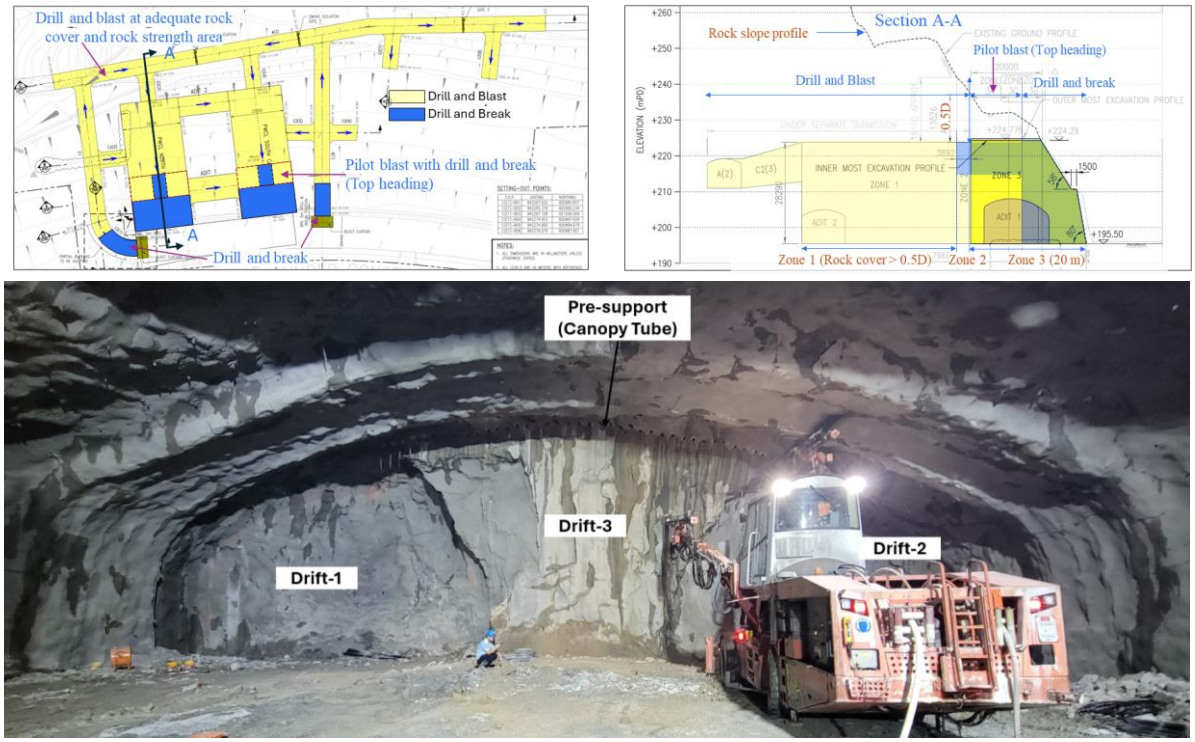

Figure 7. Multi-drift Excavation with Canopy Tubes (Pre-support) for Shallow Rock Cover Location

Table 4: Permanent and Temporary Rock Support for Caverns at Shallow Rock Cover Location

Support class	Mapped Q Value	Unsupported Length	Stand-up Time	Rock Support-Roof	Rock Support-Shoulder	Rock Support-Sidewall
Portal Area (Z3SC-IV)	Q≥0.7	3m	50 Hrs	Primary Lining [2]: 500mm FRSC with Lattice Girder at 1.0m C/C Spacing; + Secondary Lining [3]: 400mm FRSC	Primary Lining [2]: 500mm FRSC with Lattice Girder at 1.0m C/C Spacing + 5.8m Long PB1[1] at 1.5m C/C spacing; + Secondary Lining [3]: 400mm FRSC	Primary Lining [2]: 250mm FRSC + 5.8m Long PB1[1] at 1.5m C/C spacing; + Secondary Lining [3]: 400mm FRSC

[1] PB1: Permanent Rockbolts of Tensile Capacity of 204kN (with Safety Factor of 2.0)
[2] Primary lining is installed during cavern excavation, which is applied within standup time.
[3] Secondary lining is installed after completion of all cavern excavation.

4.5 Weak Zone at AC-South Cavern

During the construction stage, additional ground investigation was carried out to further verify the anticipated ground conditions. 28 additional drill holes were carried out. Among 4 caverns, one of the caverns (AC-North Cavern) encountered hints of weak seams in those additional GI. A combination of highly to completely weathered granite, core loss and highly fractured rock mass are recorded between 35m and 50m depth for drill holes no. E1, F1 and G1 as shown in Figure 8.

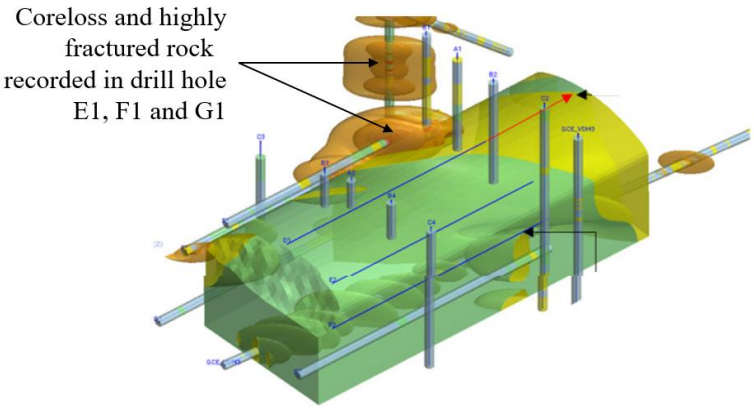

Figure 8. Project-specific Additional GI and Inferred Weak Zone for AC-North Cavern

The weak zone consists of a family of weak seams of various width. In total, the maximum width is ~8m to 10m, intermittent with competent Grade III granite. The inferred weak zone is attributed a design Q-value in range of 0.1 to 0.5. As a result, two additional rock support classes (SC-V and SC-VI), comprising shotcrete with galvanised wire meshes, are designed to cover the temporary and permanent rock support system for this weak zone. 3D modelling is adopted to simulate the 3D stresses distribution from the weak zone to the surrounding better rockmass. Prior to excavation, pre-excavation grouting was carried out for this localized weak zone to prevent the water ingress and ground lost inside the cavern. Spile bars are designed to provide as pre-support to prevent over caving during excavation in the weak zone area. Also, denser permanent bolts and thicker shotcrete lining with reinforcement bars are designed to provide sufficient strong support to the excavation.

4.6 Advanced Geotechnical Monitoring

An integrated automated monitoring system is utilized to verify the design assumptions and geological/geotechnical design parameters adopted in the three-stage design approach of rock reinforcement design. The groundwater monitoring through piezometers checks that the drop in water levels from excavation stays within safe limits, protecting nearby structures. Conventional convergence monitoring arrays and extensometers are also deployed. Advanced instrumentation such as optic fibers are installed to monitor the ground deformation during cavern excavation. The cavern convergence was monitored throughout the construction period and compared with the convergence estimated from the design analysis. This helps validate numerical models and keeps displacements below acceptable levels. Furthermore, load cells on rock bolts monitor the performance of the support system, confirming effectiveness and identifying when reinforcement is needed. The GNSS (Global Navigation Satellite System) platform enables real-time, continuous monitoring of settlement and displacement. Using a network of receivers, it delivers accurate, all-weather data collection, removing the safety risks of manual surveys in dangerous areas. In addition, the Monitoring Array Platform combines real-time data from various co-located instruments, including multipoint borehole extensometers, load cells, strain gauges on rock bolts, and piezometers. This enables a correlated analysis of deformation, structural loads, and pore pressure. Figure 9 shows the location plan within PWCL and AC caverns for instrumentation and monitoring, and the typical arrangement of monitoring array is shown in Figure 10. The instrumentation within and nearby PWCL and AC caverns are summarized in Table 5, while

the estimated convergence prior to excavation and actual measured convergence during excavation are summarized in Table 6.

Figure 9. Monitoring Location Plan Within Caverns

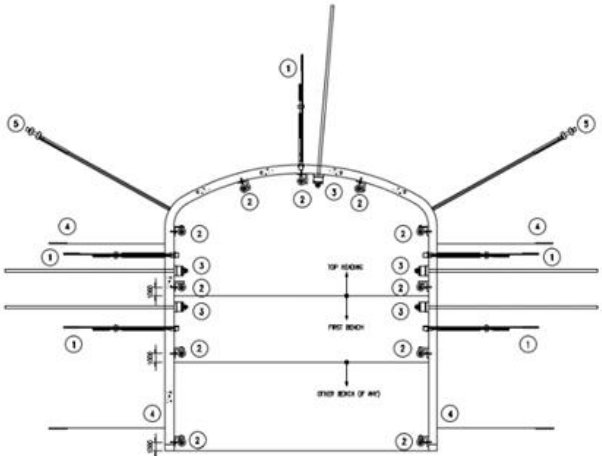

Legend:
1. Multipoint Borehole Extensometer
2. Optical Prism Along the Excavation Profile
3. Load Cell & Strain Gauge
4. Vibrating Wire Piezometer
5. Doorstopper Strain Gauge

Figure 10. Typical Arrangement of Monitoring Array

Table 5: Summary of Instrumentation

Instrument	Quantities
Ground Settlement Points	30 nos.
Standpipes and Piezometers	3 sets
Convergence Points	63 sets
Monitoring Array	3 sets plus 1 additional set

Table 6: Cavern Convergence Summary

Zone	Q-Value	Convergence estimated from FEM analysis	Convergence estimated from Empirical Methods	Actual convergence recorded on Site
Caverns with sufficient rock cover (> 0.5D cover, where D is span)	4-10	8mm	12mm	8mm
Caverns with shallow rock cover at Portal (< 0.5D cover, where D is span)	0.7-1.5	22mm	23mm	15mm

5 CONCLUSIONS

With innovative designs, cost-effectiveness can be secured without compromising the design robustness for complex underground excavation works. Design robustness can be achieved by implementing and verifying the design with multiple design approaches. This paper presents various design considerations for overcoming challenges for construction of large span caverns. Selection of appropriate geological design parameters and validation of those parameters with advanced instrumentation is crucial to ensure the design robustness. Additional ground investigation conducted during the construction stage provides better understanding of geological features with more accurate extent and width of geological features.

ACKNOWLEDGEMENTS

This paper is published with the permission of the Director of Civil Engineering and Development and the Head of the Geotechnical Engineering Office of the Government of the Hong Kong Special Administrative Region, China.

REFERENCES

Barton, Lien and Lund (1974), Engineering Classification of Rock Masses for the Design of Tunnel Support.

Barton (2002), Some new Q-value Correlations to assist in Site Characterization and Tunnel Design.

Bischoff JA and Smart JD (1977), A method of computing a rock reinforcement system which is structurally equivalent to an internal support system.

Geotechnical Engineering Office (2018), Guide to Cavern Engineering (Geoguide-4), Geotechnical Engineering Office, Civil Engineering and Development Department, Hong Kong.

Geotechnical Engineering Office (2017), Guide to Rock and Soil Description (Geoguide-3), Geotechnical Engineering Office, Civil Engineering and Development Department, Hong Kong.

Handbook - Using the Q-system, Rock mass classification and support design NGI, 2015.

Hoek, Carranza-Torres and Corkum (2002), Hoek-Brown Failure Criteria – 2002 Edition, 5th North American Rock Mechanics Symposium and the 17th Tunnelling Association of Cana-da Conference, Toronto, Ontario, Canada, 2002.

Hoek: Practical Rock Engineering, 2007.

Hoek, Carlos Carranza-Torres, Mark Diederichs & Brent Corkum (2008), The 2008 Kersten Lecture: Integration of geotechnical and structural design in tunnelling

Hoek et al. (2008), Integration of geotechnical and structural design in tunnelling.

John and Mattle (2002), Design of Tube Umbrellas.

S. V. L. Barrett and D. R. McCreath (1995), Shotcrete Support Design in Blocky Ground: To-wards A Deterministic Approach.

Yoshinao Muraki (1997), The Umbrella Method in Tunnelling.

Z.T. Bieniawski (1984), Rock Mechanics Design in Mining and Tunneling.

Case Study of Mohr–Coulomb and Hardening Soil Models in PLAXIS Using Field Monitoring Data for Excavation and Lateral Support Works

Gavin S.H. Toh, S.S. To, T.S. Ho, Y.L. Yeung & M.C. Fok
Lambeth Associates Limited, Hong Kong

ABSTRACT

This paper presents the analysis of finite element modelling using PLAXIS 2D, to evaluate the predicted performance of two modelling methods — Mohr-Coulomb model and Hardening soil model — against the monitoring data obtained in the excavation and lateral support works in project in Kwai Chung, New Territories. On-site monitoring data, including the ground movement monitoring and inclinometer readings throughout the staged excavation, were collected and reviewed in this study.

The Mohr-Coulomb model, that assumed as linearly-perfectly plastic soil behaviour, has limitations in using the linear relationship in stress and strain in soil to predict the ground movement during the excavation. The model is unlikely to illustrate the plasticity before failure, and strain hardening is not captured. In contrast, the Hardening soil model reflects the deformation behaviour under different stress, and the increase in soil stiffness at depth. It simulates a more realistic stress- strain relationship under different loading conditions.

The numerical analyses using the MC and HS models were presented and compared with the site monitoring data. The comparison showed that the HS model better reflected the actual wall deflection shape and presented closer location of maximum wall deflection with the site data. These findings highlight the significance of adopting advanced constitutive models to enhance the accuracy of estimation in designing excavation and lateral support (ELS) systems and the limitation of the modelling methods will be discussed.

1 INTRODUCTION

In Hong Kong, Mohr-Coulomb (MC) model is a commonly adopted soil model in numerical analyses in geotechnical engineering design due to its simplicity, and adoption of typical parameters with standard laboratory tests result. Nevertheless, limitations from its fundamental assumptions cannot reflect the soil nonlinearity and its stress dependent behaviour. Conversely, the Hardening soil (HS) model can be considered as a more realistic modelling method in geotechnical numerical analysis. Varying stiffness under loadings and stress dependent behaviour assumptions will be incorporated in the analysis. Parameters adopted in HS model are derived based on laboratory test interpretations and the HS model is supported by the studies of Schanz (1998) and Schanz et al. (1999). The wall deflection and soil nonlinearity of the ELS system predicted using HS model in PLAXIS can be used to compare that of using MC assumptions. Comparison of results of both models with the site monitoring records can be found in the section 7 of this paper. The findings may be presented as a case study to enrich future geotechnical modelling practices.

2 PROJECT BACKGROUND

2.1 Project location and scope of works

The project was located at Kwai Chung container terminal, and the overall site area was approximately 315m by 180m. It comprised the ELS system and foundation works. The excavation was supported by the sheet pile FSP VIL and 610 diameter clutched pipe piles. The existing ground level and general final excavation level (FEL) were +4.6mPD and -9.125mPD respectively, resulting in a retaining height of approximately 14m. Four layers of struts were installed to support the pile walls during staged excavation.

2.2 Geological and ground conditions

The site was formed by reclamation undertaken in early 1990s and it was a part of the container terminal with heavy loading on the ground level. The ground profile in this site comprised fill, overlaying alluvium clay, alluvium sand/ silt, marine deposit, completely to highly decomposed granite and slightly to moderate decomposed granite. Refer to Figure 1 for the soil profile. The fill layer was relatively thick because of the reclamation works, and the thickness was between 22m to 34.5m. Soil materials excavated for the ELS was mainly consisting of sandy, compacted fill.

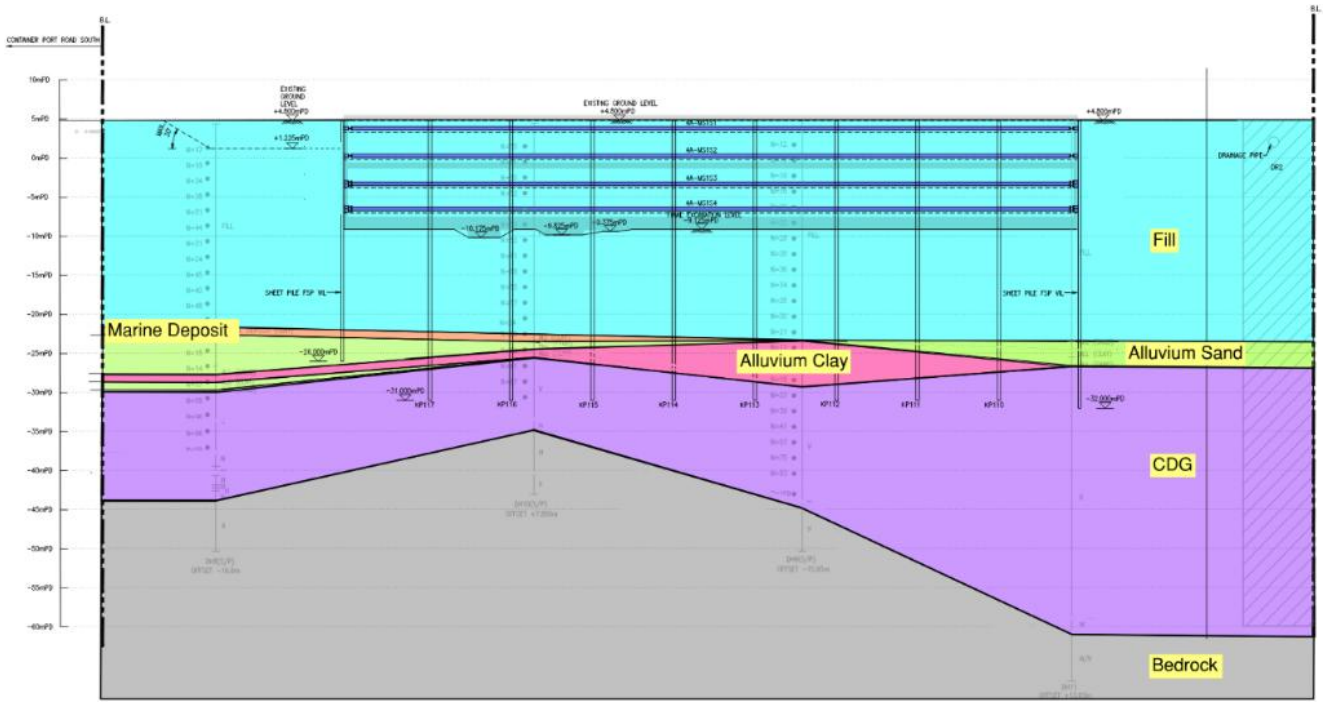

Figure 1: Section drawing of soil profile

3 ON-SITE MONITORING PROGRAMME

3.1 Inclinometer measurements

A total number of nine inclinometers were installed along the excavation to monitor the lateral movement behaviour of the pile walls throughout the construction stages. There inclinometers were used to show the deflection of the pile wall during excavation and struts installation, providing data for assessing the retaining wall behaviour and reviewing the predictions in numerical models.

Inclinometer INC A and INC B were focused on in this study, that the location of these inclinometers referred to Figure 2. They were installed behind the main strut MS1 to MS4 to monitor the bending behaviour of the sheet pile wall in this design section. A plan below was shown to illustrate the location of the inclinometers and the design section. Inclinometer INC A and INC B were installed to monitor the movement of the left-hand side (LHS) and the right-hand side (RHS) of the wall respectively.

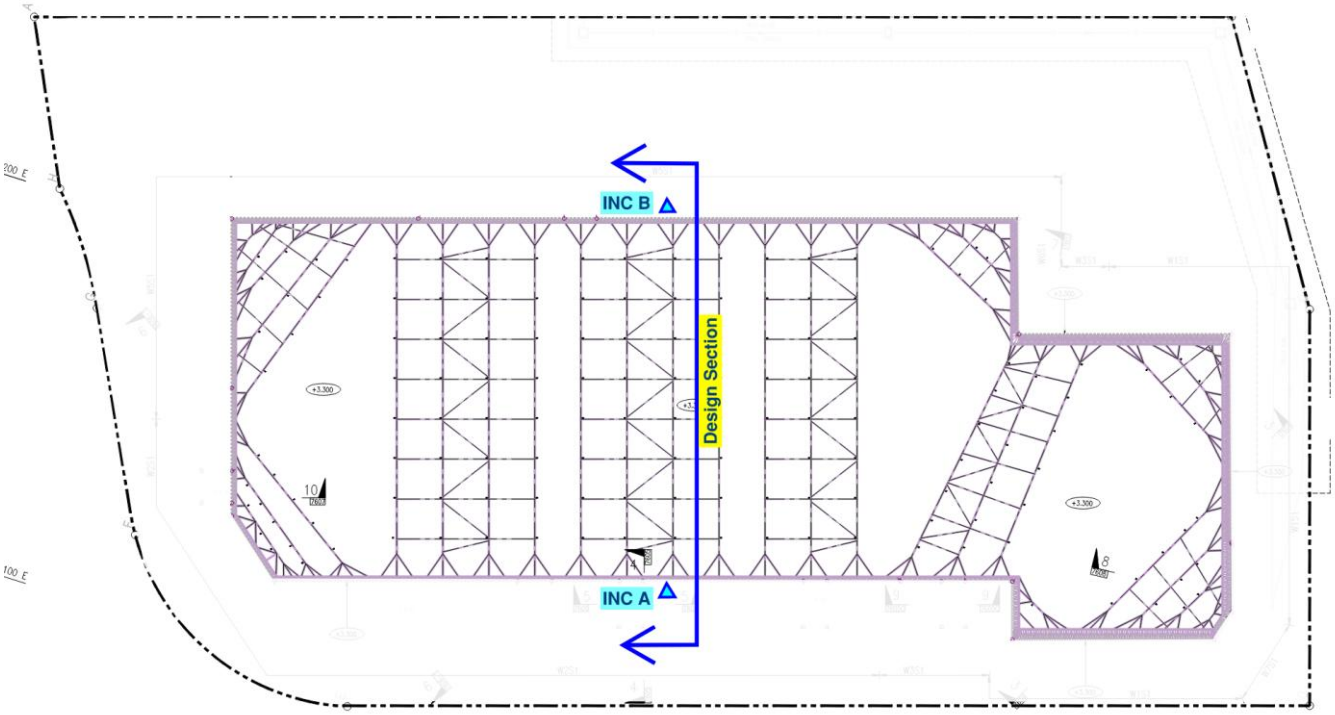

Figure 2 Location plan of the targeted inclinometers (INC A and INC B)

The PVC inclinometer access tubes were installed to the sheet pile wall toe level extending 2m below to ensure a complete reference zone, and each of the tube had a length of approximately 30m, similar to the total length of the pile walls.

Inclinometer measurements were taken in two directions, that were A-A direction which was perpendicular to the excavation, and the B-B direction which was parallel to the excavation. In this study, the interpretation focused on the A-A direction, so that the measured wall deflection could be compared with the result in numerical models. Baseline readings were recorded prior to the commencement of excavation works. Daily monitoring was carried out using portable data logger, with the readings taken at 1m depth interval. Lateral displacements were derived by comparing the measured data against the initial reading, assuming the base point of each tube as a reference point. The displacement profile was plotted and reviewed with the output of the PLAXIS model after each stage of shoring installation.

4 NUMERICAL MODELLING APPROACHES

4.1 Finite element modelling using PLAXIS

The PLAXIS finite element model is widely used for analysis of ground movement in deep excavation projects in Hong Kong. Numerical analysis is conducted using the two-dimensional finite element method, that the soil material and the structural members can be discretised into finite element meshes with deformation gradients.

The model simulated the construction sequence and the structural elements such as the shoring system. Preloading forces applied to the struts are considered as control measure for ground movement from construction aspect. Based on the modelling output, ground settlement and deformation shape of structural members are reviewed, and the potential construction impacts are assessed.

4.2 Model geometry and conditions

The sheet pile wall type FSPVIL was modelled in both the MC and HS modelling for numerical analysis. The sheet pile wall was simulated with wall toe levels at -26 and -24.5mPD for LHS and RHS respectively, with more than 80% of the sheet pile length located within the reclaimed fill materials. The design surcharge applied on the retained side was generally considered as 20kPa.

In the models, the retained height of the pile wall was approximately 14m, with wall embedded length of about 15.4m and 16.9m respectively. Four layers of lateral struts were provided to support the retaining wall, with strut preloading force applied and progressively increased from upper strut layers to the FEL.

5 MOHR-COULOMB FAILURE CRITERION ASSUMPTIONS

MC model was employed for this project in design stage due to its simplicity and feasible adoption of typical parameters since there was only limited laboratory test results available. Recommended soil parameters provided in GEOGUIDE 1 were commonly used in Hong Kong for design purpose. Owing to its conservative nature, the MC model provided a baseline for engineering design, allowed preliminary estimation of ground movements, structural member size estimation, and provided a framework for more advanced constitutive models at a later stage.

5.1 Model description and assumptions

MC failure criterion adopted isotropic, linear elastic relation for the design in excavation in Hong Kong based on Hooke's law (Chan et al. 2021). Soil failure was defined as assuming a linear failure envelope in shear stress-normal stress relationship; yielding was assumed to occur when the stress path reached this envelope. The soil behaviour was assumed to be linear elastic before yielding and perfectly plastic after yielding. In addition, the change in stiffness with unloading and reloading was not considered.

As a result, if overall stability was found satisfactory under these assumptions, the design was typically regarded as adequate for practical purposes.

5.2 Parameter selection

The parameters were applied to the MC failure equation, $\tau_f = c' + \sigma' \tan \phi'$, which c' = effective cohesion and ϕ' = effective friction angle, and adopted for long term stability assessment. Other parameters, including E and v, were adopted with a typical and standardized basis for engineering design. The parameters adopted in the MC model referred to Table 1.

Table 1 Input parameters of the soil for MC model

Soil material	Unit weight kN/m^3	Young's modulus kN/m^2	Young's modulus increment kN/m^2	c' kN/m^2	ϕ' Deg
Fill	19	35000	+1111 (from y = +2mPD)	0	35
Alluvium 1	19	23000	0	0	33
Alluvium 2	19	26090	0	0	33
CDG	19	73500	+3577 (from y = -32mPD)	0	35

5.3 Limitations

Soil parameters were assumed to be independent of stress level, with soil stiffness generally treated as a constant at certain depth in the analysis, that was, applying the same Young' modulus to the excavation stage, unloading and reloading stage, and stress redistribution stage at the same depth. MC models did not differentiate between loading and unloading stiffness.

Although the model provided conservative baseline for engineering design, it was not able to reflect the actual soil-structural deformation behaviour because the actual soil behaviour was not reflected in the linear elastic behaviour before failure (Atkinson 2000). These assumptions limited the ability of simulating the non-linear stress-dependent behaviour of soil material.

6 HARDENING SOIL MODEL

6.1 Model description and assumptions

The HS model was a nonlinear elastic-plastic constitutive model with non-linear stress-strain behaviour prior to failure. It accounted for stress-dependent stiffness (Chan et al. 2021). The soil stiffness in HS model varied with stress levels and loading history, and behaviour was governed by shear and compression hardening mechanisms which allowed a realistic stress path and a more realistic impact to the ground in staged construction.

The HS model had a same failure envelope with MC model; the difference was how the soil in the model behaved and reached failure, as the yielding progressively occurred instead of assuming perfectly plastic behaviour.

Higher unloading and reloading stiffness were adopted, and this assumption improved the prediction of soil deformation compared to MC model in staged constructions.

6.2 Parameter selection

The parameters of HS model consisted of strength and stiffness to realistically represent the soil behaviour. Strength parameters included the effective cohesion (c'), effective friction angle (ϕ'), and dilatancy angle (ψ), that the parameters shared the same fundamental concepts as those parameters adopted in the MC model and they defined the ultimate shear strength of soil.

For the stiffness parameters, the secant stiffness, E_{50}, could be derived from the triaxial compression test. According to Schanz & Vermeer,1997, the typical relationship between the oedometer stiffness, E_{oed}, and E_{50} is 1:1 for sand. Therefore, in this study, the E_{oed} was assumed to be equal to the E_{50}, which $E_{oed} \approx E_{50}$. Moreover, the ratio between unloading-reloading stiffness (E_{ur}) and E_{50} was taken from 3:1 to 6:1 for loose sand and from 2:1 to 4:1 for dense sand (Obrzud & Truty 2018). Hence, the E_{ur} was taken as three times of the secant stiffness ($E_{ur} \approx 3E_{50}$), which these parameters adoption was demonstrated by the local studies by Chan et al., 2021.

The secant stiffness was obtained by plotting the stress-strain curve using deviator stress, q, against axial strain, identifying the deviator stress at failure (qf), and determining the axial strain ε_{50} corresponding to the 50% of qf. Example of stress-strain curve, referred to Figure 3, could be referred to the figure below. When the qf was 550kPa, the 50% of qf was 275kPa, and the corresponding axial strain, ε_{50}, was 0.73%.

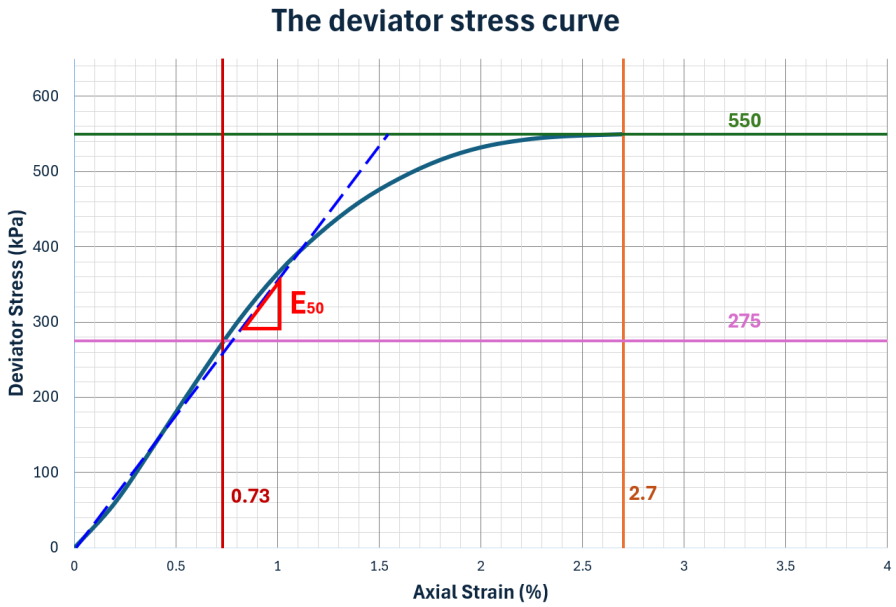

Figure 3 Example of stress-strain curve to derive the E_{50}

The stiffness E_{50} was then calculated as the ratio of 0.5 q_f to ε_{50}, and the reference stiffness E_{50}^{ref} was determined using the stress-dependent formulation.

$$E = E^{ref}\left(\frac{p'}{p_{ref}}\right)^{m} \quad (1)$$

where p' is the mean effective stress and the reference pressure p_{ref} was taken as 100 kPa.

Stress dependency of the soil stiffness was controlled by the stress dependency exponent, m. This exponent depended on the soil type to perform a non-linear behaviour with variation of level and depth. In this study, the values adopted for m were 0.5 and 0.8 for sand and silt respectively (Obrzud & Truty 2018). The parameter adopted for the HS model was presented as the Table 2 below.

Table 2 Input parameters of the soil for HS model

Soil material	Unit weight	E_{50}^{ref}	E_{oed}^{ref}	E_{ur}^{ref}	m	c'	ϕ'
	kN/m^3	kN/m^2	kN/m^2	kN/m^2	-	kN/m^2	Deg
Fill 1	19	10000	10000	30000	0.5	0	35
Fill 2	19	24000	24000	72000	0.5	0	35
Fill 3	19	38800	38800	116400	0.5	0	35
Alluvium 1	19	15500	15500	46500	0.8	0	33
Alluvium 2	19	28500	28500	85500	0.5	0	33
CDG	19	37000	37000	111000	0.5	0	35

7 COMPARISON OF MODELING RESULTS

7.1 Actual monitoring data

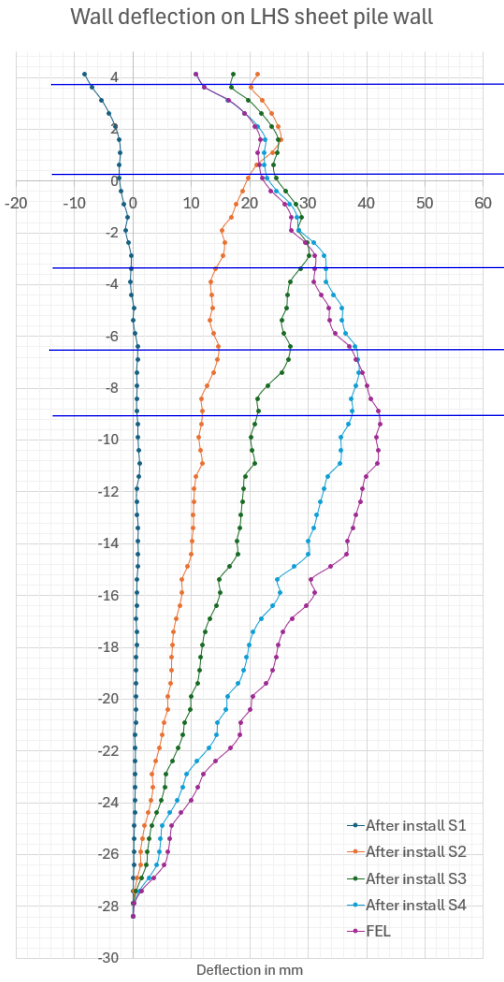

Figure 4. Sheet pile wall deflection at LHS (INC A)

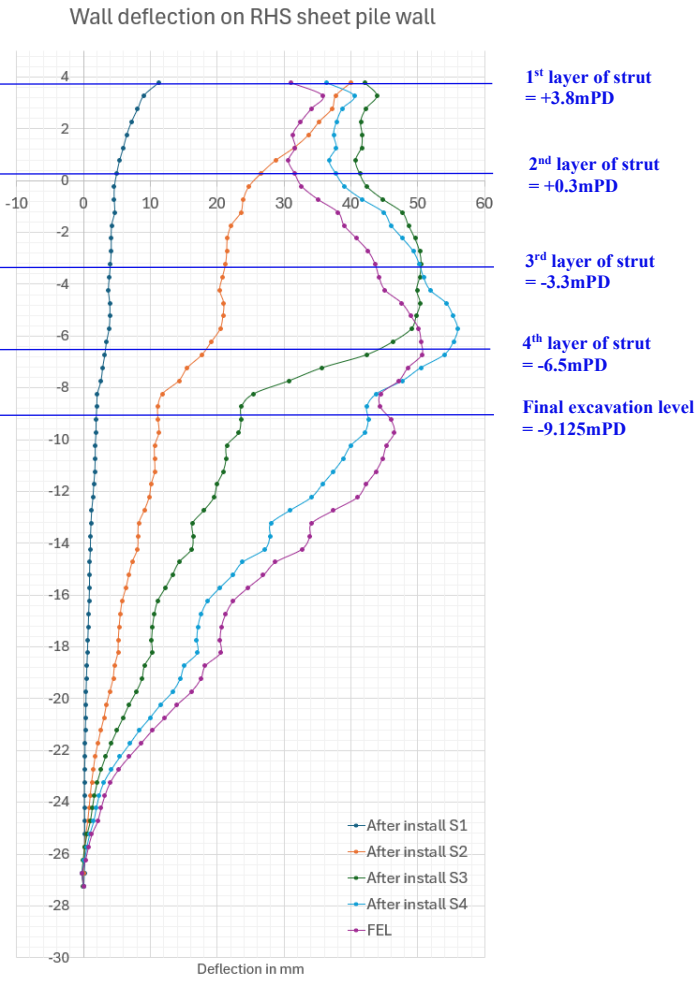

Figure 5. Sheet pile wall deflection at RHS (INC B)

The above Figure 4 and Figure 5 illustrated the measured wall deflection of the LHS and RHS sheet pile walls in the aforesaid design section. This section was supported by a main strut that was perpendicular to the pile walls, with the lateral restraint of the pile wall on both sides. The deflection curves in different colours represented the wall movement at the stages of installation of lateral supports and at the FEL.

Due to the mechanism in inclinometer, the base point of each inclinometer was taken as the reference point, and the calculated wall deflection at the base tended to be zero. The monitoring deflection profiles represented relative movements along the wall length.

The maximum wall deflection was observed approximately at the level of the fourth layer of strut and near the FEL, indicating that the critical zones of deformation was at the depth of this section. Strut preloading application did not result in a significant push back of the wall towards the retained side.

7.2 Comparison PLAXIS model outputs with actual data

In our prediction, under the same strut layout and preloading force conditions, the HS model incorporated the stress-dependent stiffness with increased with depth. The soil surrounding the lower portion of the sheet pile wall therefore exhibited higher stiffness and provided stronger confinement, leading the wall toe to remain close to its initial position. As the lateral soil support was progressively removed at the excavation side, the predicted maximum wall deflection occurred at or slightly above the FEL.

Figure 6 below showed the PLAXIS output of the MC model at the final excavation level, while the Figure 7 presented the corresponding output of the HS model.

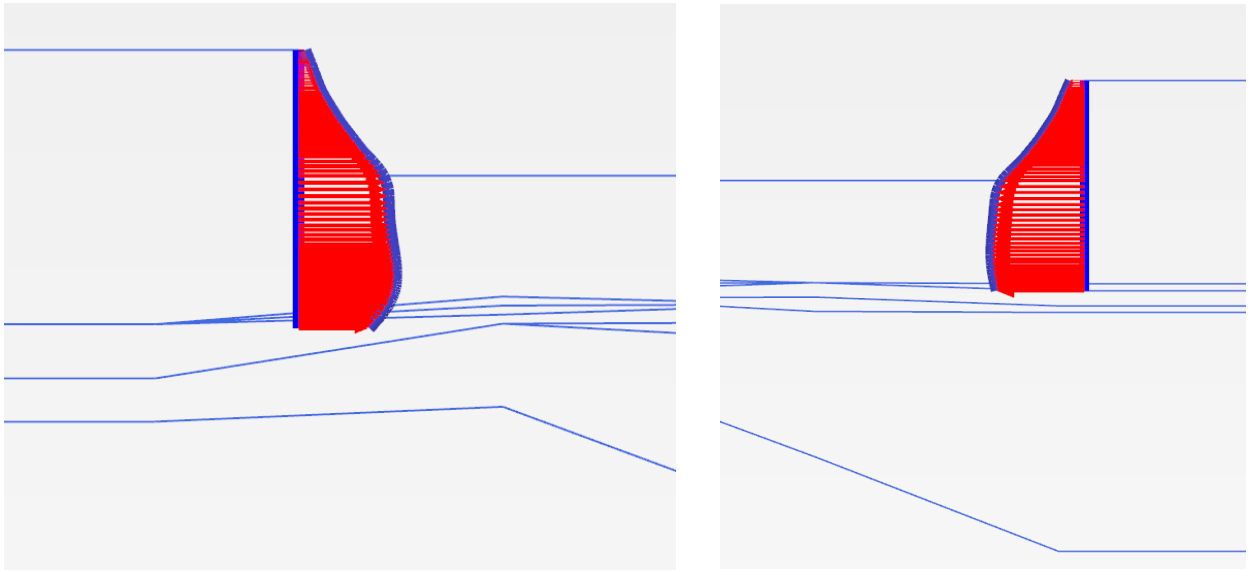

Figure 6 (Left) Mohr-Coulomb model - Sheet pile wall deflection on LHS at the FEL stage
(Right) Mohr-Coulomb model - Sheet pile wall deflection on RHS at the FEL stage

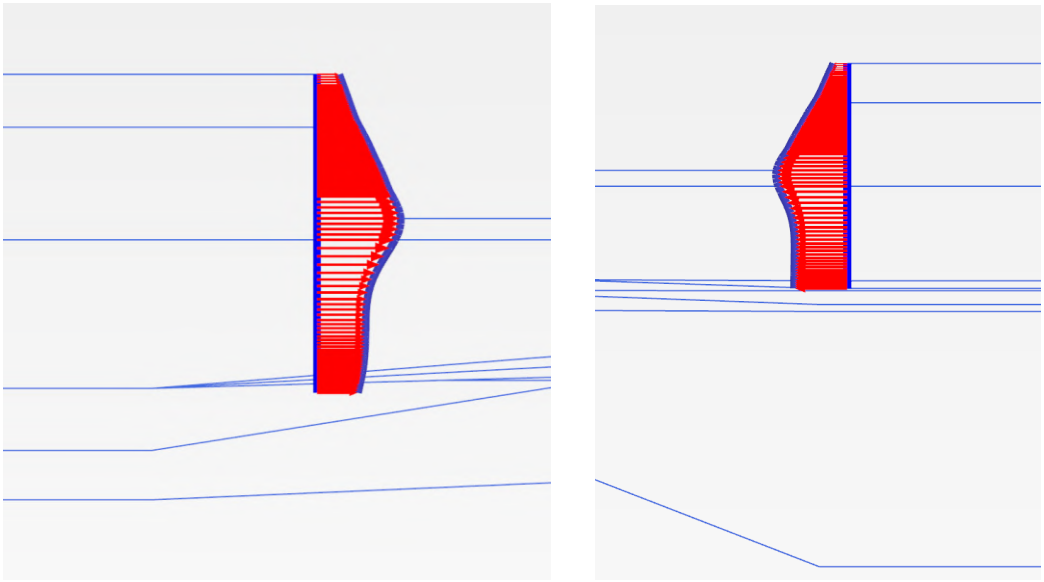

Figure 7 (Left) Hardening Soil model – Sheet pile wall deflection on LHS at the FEL stage
(Right) Hardening Soil model – Sheet pile wall deflection on RHS at FEL stage

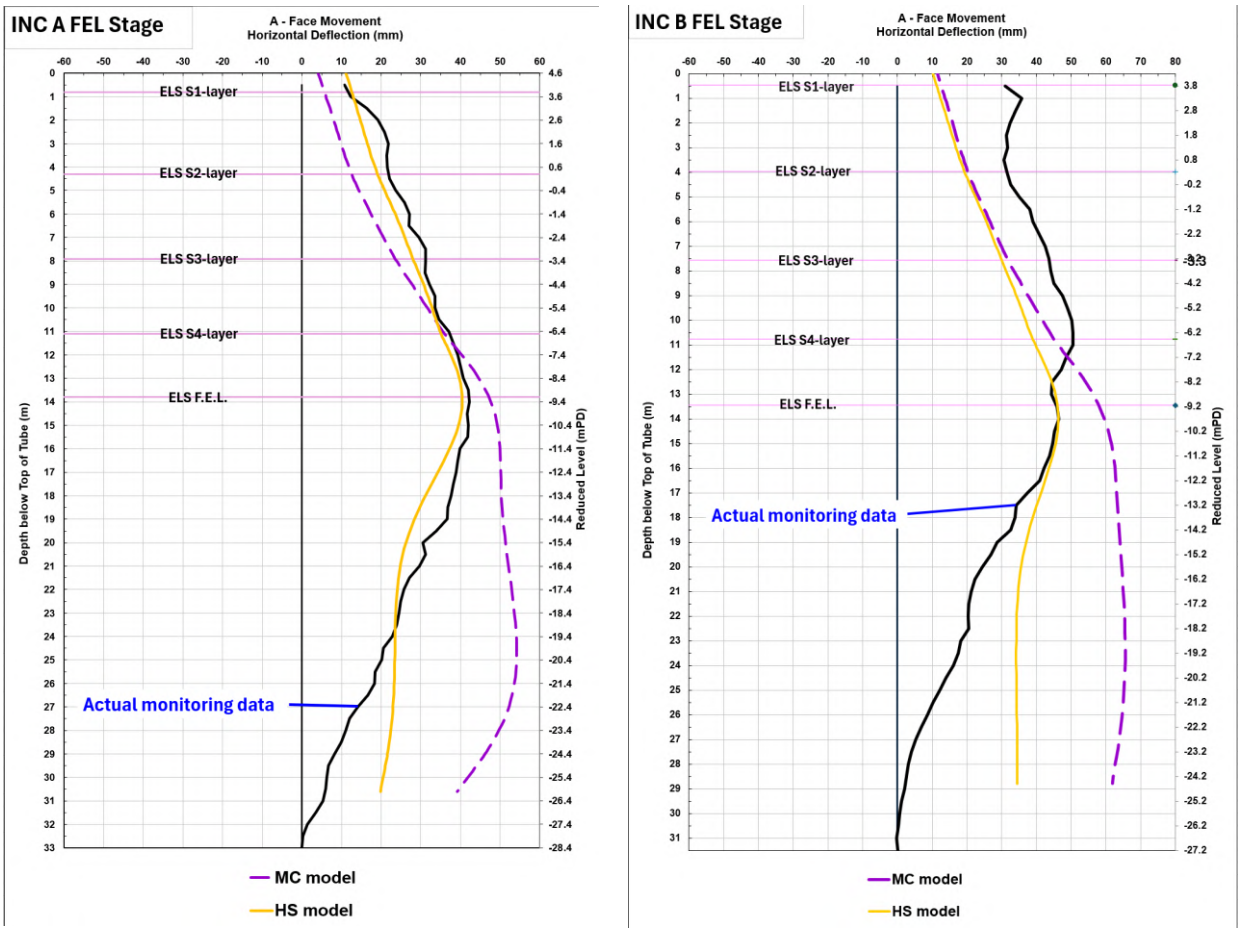

Figure 8 Wall deflection comparison with site monitoring data and result of numerical model
(Left) LHS sheet pile wall
(Right) RHS sheet pile walls

There was a trend shown in Figure 8 when comparing the measured wall deflections with the prediction in numerical models. The measured wall-top displacements were generally greater than that of the results in both models, while the measured wall-toe displacements were smaller than that of the results.

With comparing the result of MC model compared with the monitoring data, the deflection shape in MC model was found generally different from that compared to the monitoring data. The envisaged bending at the wall toe was much larger than the actual site findings. This observation indicated that the soil at shallow depth was taken relatively stiff than the reality due to the assumption of constant soil stiffness with an overestimated stiffness adopted. After the completion of the FEL, the inclinometers on both sides of walls illustrated a similar deformation pattern in the MC model, which suggested the soil beneath the final excavation level provided a greater restraint than that assumed in the MC model.

For both inclinometer INC A and INC B, the HS model provided a closer estimation particularly for the deflection shape, magnitude, and the location of the maximum bending of the wall with the measured monitoring data. Maximum wall bending took place near the FEL to exhibit the behaviour of the stress dependent stiffness with depth as restraints.

In practice, the inclinometer recorded the relative wall movement with fixed base reference at the toe; the measured maximum relative deflection occurred above the FEL rather than at the wall toe.

7.3 Observation on PLAXIS in Mohr-Coulomb model

With reference to Figure 6, the wall deflection in MC model showed that the maximum deflection was below the FEL and close to the wall toe level of the pile wall. This shape suggested that there was excessive bending at wall toe level. Although deep soil experienced stress changed during excavation, MC model assumed that the stiffness was not increased with depth. As a result, the stiffness of soil at greater depth was insufficient to resist the wall movement. This behaviour was widely discussed regarding the limitation in MC model for deep excavation.

Modified MC model with the Young's modulus value 3 times increased in the excavated area partially allowed the estimated wall deflection to be close to reality by simulating the unloading-reloading stiffness. In the plot below, referred to Figure 9, with the "MC model 3E", the wall toe deflection magnitude significantly reduced, which supported that the unloading-reloading stiffness would be a controlling actor in wall deflection control. However, this approach was an approximation only. The stiffness remained stress-independent and was not progressive hardening anyway. The soil property in exponential curve was not captured in the model. Therefore, the numerical result for this model was failed to fully reflect the actual wall deformation.

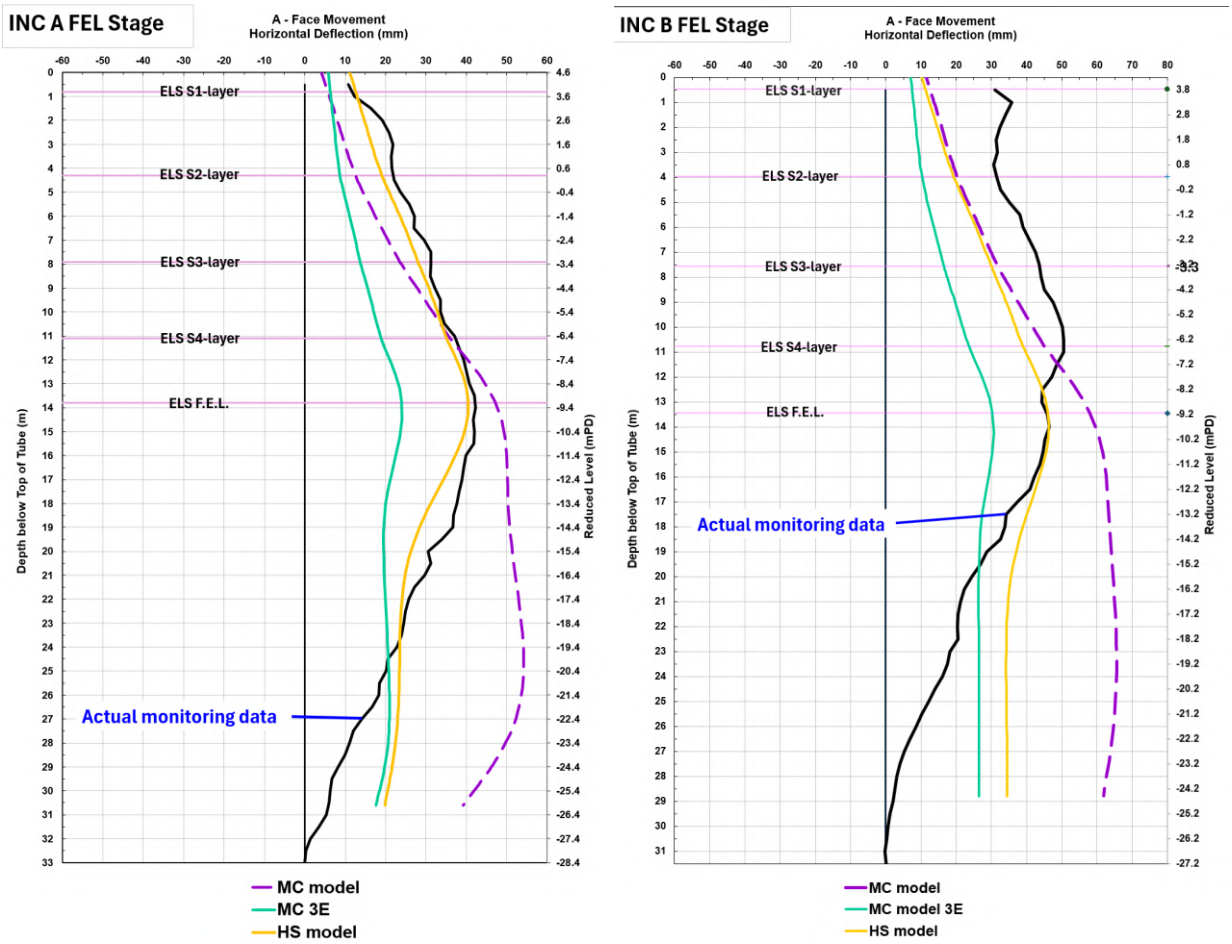

Figure 9 Wall deflection comparison with site monitoring data with the modified MC model
(Left) LHS sheet pile wall
(Right) RHS sheet pile walls

8 DISCUSSION

8.1 Interpretation of model performance

In selection of an appropriate model type in numerical analysis, the availability of sufficient laboratory test results and monitoring data should be considered. Compared with MC models, the HS model heavily required inputs derived from laboratory tests as well as the number of test results collected. All these directly affected the reliability of the parameters adopted.

HS model provided better predictions in soil behaviour by considering plastic hardening mechanism in compression and shear perspective. Therefore, the result would be more comparable with the actual wall performance including the wall-top and wall-toe deflection, and location of maximum deflection.

The findings of this study indicated that HS model was a more suitable modelling method for estimating wall deflection in staged excavation. The performance of HS model was highly influenced by the quality and quantity of input data, the application of engineering judgement, and interpretation of laboratory test results (Chan et al., 2021). The soil property significantly varied because of the heterogeneity of soil both vertically and horizontally in Hong Kong. The laboratory test results reflected the small-scale soil behaviour but were not representative of mass ground behaviour (GEO 2007; Chan et al 2021). Therefore, the selection of soil properties was suggested to be on a case-by-case basis, considering site-specific ground conditions.

8.2 Implication for design

HS model, which was a soil behaviour simulating model, demonstrated that a more realistic deflection performance and determined a more sensible preloading strut force magnitude. It helped to avoid an overly conservative assumption to have large preloading force, especially at the lower layers of strut.

It should be noted that the selection of suitable constitutive model in analysis shall be based on the availability of laboratory test results and site monitoring data. MC model remained appropriate for preliminary design or if limited laboratory data was available. The HS model required a more comprehensive data set, greater understanding of the ground history, and the reliability of the parameters which was closely tied to the quantity and quality of the test results and information available. When sufficient data was available and appropriate engineering judgements were applied in the parameters selection, the HS model offered a more rational balance between safety and deformability of the retaining wall, making it well suited for the deep excavation works.

8.3 Sensitivity of laboratory test & dependence on engineering judgment

Parameters of the HS model were highly sensitive to the quality and quantity of laboratory test data. The derived stiffness and strength parameters could be influenced by specimen quality and distribution, number of test results available, and stress paths applied during laboratory testing. Also, the limitation was especially critical for reclaimed land. The soil properties could be varied due to the heterogenous nature of fill materials and variable compaction quality.

Application of the HS model required engineering judgement as interpretation of laboratory test data on soil parameters was required. Engineers should examine the results, interpret the stress-strain behaviour with plots, and select representative stiffness values for analysis. This included the determination of an appropriate stress dependency exponent m for each soil type. Excessive reliance on the default values without calibration might reduce the confidence in predicting the deformation. Engineering judgement played a crucial role in balancing the realism and conservatism.

When the number of laboratory test results was limited, it fully depended on the engineering judgment on the parameters and stiffness value selection while this could provide over-conservative or under-conservative design value in particularly at the greater depths of soil layers. As a result, all these factors would lead to misleading deformation predictions.

8.4 History-dependent behaviour in HS models

HS model was a history-dependent model, and the soil response was affected by the stress history experienced. Correct application of the model required a good understanding of the site's reclaimed history, including the history of preceding dredging work in 1990s in this site. Misunderstanding or misinterpretation of the stress history would lead to uncertainty in the initial stress state and could adversely affect the prediction of soil deformation. This was vital to the analysis of reclaimed land as historical loading conditions were complex.

9 CONCLUSION

Mohr-coulomb model provides simple and conservative way for establishing baseline design reference in engineering modelling, particularly at the preliminary stage or when the laboratory data is limited. However, when the data is sufficient, Hardening soil model is an advanced modelling method to further analyse the ground movement. The application of Hardening soil model required parameter selection in detail, engineering judgement, and understanding of the ground history to provide valuable findings. Study on numerical predictions with site monitoring data after the construction provides beneficial feedback for evaluating the modelling assumption and design review. As a case study, this paper presents a possibility of alternative method to estimate wall deflection, and to improve deformation-based design practices for excavation projects in the future.

ACKNOWLEDGEMENTS

The authors would like to thank the whole project team for the support, contribution and participation on the project.

REFERENCES

Atkinson, J. H. 2000. Non-linear soil stiffness in routine design. *Géotechnique*, 50(5), 487–508.

Chan, C., Sun, J., & Law, C. 2021. Back analyses of two deep excavations in Hong Kong using the Mohr-Coulomb model with linear elasticity and the hardening soil model. *ISSMGE International Journal of Geoengineering Case Histories*, 6(2), 137–163.

Obrzud, R., & Truty, A. 2018. *The hardening soil model – A practical guidebook (Revised ed.).* ZACE Services Ltd, Software for Geotechnical Engineering, Lausanne, Switzerland.

Schanz, T., & Vermeer, P. A. 1997. On the stiffness of sand. In S. Shibuya, T. Mitachi, & S. Miura (Eds.), *Pre-failure Deformation Behaviour of Geomaterials* (pp. 383–387). Balkema, Rotterdam.

Schanz, T., Vermeer, P. A., & Bonnier, P. G. (1999). The hardening soil model: Formulation and verification. In R. B. J. Brinkgreve (Ed.), *Beyond 2000 in Computational Geotechnics* (pp. 281–296). Balkema, Rotterdam.

Seequent. (2025). PLAXIS 2D 2025.1: Material models manual. Bentley Systems. https://files.seequent.com/PLAXIS/Manuals/PLAXIS_2D/English/PLAXIS_2D_3_Material%20Models%20Manual.pdf

Subsurface Diagnosis Method for Undergrounds Using Distributed Acoustic Sensing with Ambient Noise Tomography

WU Ju-Yang
Guangzhou Metro Design & Research Institute Co., Ltd, Guangzhou, China
ZHANG Tian-Yu, MA Jun-Wei, Luo Bin & FENG Wei-Qiang *
Southern University of Science and Technology, Shenzhen, China
LI Yu-Xiao
School of Construction Engineering, Shenzhen Polytechnic University, Shenzhen, China

ABSTRACT

The development of urban underground space in Karst regions is significantly challenged by hidden geological hazards. Conventional borehole investigations are identified as costly, destructive, and spatially sparse, while traditional seismic arrays often lack the density required for fine-scale urban imaging. In this study, using Distributed Acoustic Sensing (DAS) for ambient noise tomography is a cost-effective and non-invasive method that can be used for detailed site characterization and dynamic engineering monitoring. To ensure high-resolution imaging of shallow stratigraphy, a comprehensive variable-aperture sub-array segmentation strategy for Common Midpoint (CMP) gathering is implemented, effectively optimizing data utilization from the DAS array. This integrated workflow was validated through a field experiment in a Karst area of Shenzhen, China, conducted before and after ground grouting improvement. The field results demonstrate that: (1) the DAS-derived velocity structure exhibits high consistency with borehole information and co-located nodal seismometers, confirming that DAS effectively bridges information gaps between discrete borehole sites as a reliable auxiliary exploration tool; (2) time-lapse monitoring quantitatively captures the ground improvement effect induced by the grouting operation, visualizing a substantial increase in shear-wave velocity from approximately 200 m/s to 300 m/s, which corresponds to grout slurry diffusion and soil solidification. These findings confirm that DAS tomography provides a rapid, economical, and quantitative solution for evaluating ground improvement, offering significant value for the lifecycle risk management of urban underground projects.

Keywords: Distributed Acoustic Sensing (DAS); Time-lapse monitoring; Ambient Noise Tomography (ANT); Urban geophysics; Karst grouting assessment

1 INTRODUCTION

The insurance of urban subsurface safety is recognized as a crucial requirement for sustainable infrastructure planning and resilient city development (Wagner & Uhlemann 2021). As urban areas expand, the utilization of underground space is diversified across subway engineering, groundwater management, and geo-energy production (Krawczyk et al. 2019; Spica et al. 2020). However, geological heterogeneities, such as unmapped sedimentary basins or hidden Karst cavities, pose significant threats including land subsidence and sinkhole collapse (Cueto et al. 2018; Viens et al. 2022). To mitigate these risks, ground grouting is widely implemented as an engineering solution to reinforce weak foundations (Niu et al. 2015). Despite its widespread existence, the evaluation of grouting quality remains a significant challenge. Traditional intrusive methods, such as drilling, are often restricted by high costs and provide only localized information, making the assessment of overall reinforcement effects difficult. Consequently, there is an imperative need for non-destructive monitoring techniques to evaluate subsurface physical properties before and after ground improvement. In this case, the shear wave velocity (V_s) is a very suitable index that can directly reflect the consolidation degree of the underground soil layer.

Passive-source surface wave methods can accurately invert the shear wave velocity (V_s) profile of underground soil layers, enabling non-destructive and efficient assessment of the consolidation degree of deep

soil strata. Specifically, Ambient Noise Tomography (ANT) have gained widespread application for imaging near-surface structures at engineering scales (Zheng et al. 2008; Abudeif et al. 2019; Li et al. 2020; Hu et al. 2022; Karslı et al. 2024; Zhang et al. 2025). By extracting dispersion information from environmental noise, high-resolution velocity imaging is achieved at shallow depths. However, the deployment of traditional seismometer arrays in densely populated urban environments is often limited by logistical constraints. Hundreds of sensors are typically required to cover a small area, leading to substantial equipment and maintenance costs. Furthermore, space occupancy permits and interference from municipal facilities often limit the installation of conventional sensors in areas with heavy traffic and dense buildings (Larose et al. 2015; Cheng et al. 2016; Wang et al. 2023).

To address the above-mentioned constraints of traditional seismometer arrays, Distributed Acoustic Sensing (DAS) has emerged as a transformative technology that converts standard telecommunication optical fibers into dense seismic arrays. The operational mechanism involves the launch of coherent laser pulses into the fiber to demodulate phase shifts of Rayleigh backscattered light in response to local strain (Hartog 2017; Parker et al. 2014). DAS offers exceptional performance with a wide frequency bandwidth and significant dynamic range. Its dense spatial sampling and continuous topology make the technology particularly suitable for imaging complex geological settings and monitoring subsurface anomalies in urban environments (Lindsey et al. 2019). By leveraging existing underground fiber infrastructure, ultra-dense spatial coverage is achieved, which parallels the capabilities of large-scale nodal arrays while reducing deployment complexity (Martin et al. 2017; Zhan 2020). Significant progress has been made in combining DAS with passive source tomography for detecting shallow structures. Researches have shifted from feasibility verification to methodological innovation, utilizing various seismic sources such as construction machinery and traffic vibrations (Tejedor et al. 2019; Tribaldos et al. 2021). To address common challenges in DAS data, including low signal-to-noise ratios (SNR) and directional sensitivity, advanced algorithms have been implemented. These include Three-station Interferometry (TSI) for noise suppression and deep learning-based denoising techniques (Curtis & Halliday 2010; Atterholt et al. 2022; Yang et al. 2023). Additionally, the Frequency-Bessel (F-J) transform method is frequently adopted to extract higher-mode surface waves, thereby improving imaging resolution in complex media (Lior et al. 2022). Beyond static profiling, the potential of DAS for time-lapse monitoring of groundwater levels and rapid microzonation has been validated in recent studies (Rodríguez Tribaldos & Ajo-Franklin 2021; Li et al. 2023).

In this study, the capability of DAS-based ambient noise tomography is investigated for both high-resolution stratigraphic imaging and the dynamic monitoring of velocity variations. The experiment was conducted in a Karst region in the Longgang District of Shenzhen, China. To ensure robust coupling, the optical fiber was deployed on the ground surface and secured with sandbags. A dense array of nodal seismometers was co-located with the fiber line for synchronous recording over a 3-hour period. A systematic preprocessing workflow was applied to the DAS data, followed by the calculation of cross-correlation functions. Common Midpoint (CMP)-based frequency-wavenumber analysis was employed to extract dispersion curves and reconstruct V_s profiles. The temporal variations in shear-wave velocity before and after grouting improvement are specifically analyzed to provide a framework for assessing ground improvement effectiveness.

2 FIELD EXPERIMENT AND DATA ACQUISITION

2.1 Site Description

The study area is situated in the Longgang District of northeastern Shenzhen, a region characterized by a complex geomorphology of low hills and alluvial plains. The subsurface stratigraphic sequence is dominated by Carboniferous carbonate rocks, primarily limestone and marble, which are unconformably overlain by Quaternary alluvial and residual deposits (Liu et al. 2022). These soluble lithologies provide the geological foundation for extensive Karst development. Investigations indicate that Karst features in Longgang are typically shallow, with an average overburden thickness of approximately 20 meters, though significant lateral variations exist (Zhang 2022). Such geological heterogeneities pose substantial engineering risks, necessitating high-resolution geophysical methods for subsurface characterization.

2.2 Distributed Acoustic Sensing (DAS) Configuration

A Silixa iDAS™ interrogator system was employed to detect dynamic strain changes along an optical fiber by analyzing the phase shifts of Rayleigh backscattered light. To prioritize engineering convenience and minimize environmental impact, a non-invasive surface-compaction coupling method was adopted. Instead of costly and time-consuming trenching or burial, the optical fiber was placed directly on the ground surface and secured with 200 sandbags to provide continuous normal loading (as shown in Figure 1(a)). This approach significantly enhanced the signal-to-noise ratio while retaining the flexibility required for rapid deployment and retrieval in active construction zones (as shown in Figure 1(b)(c)). The experiment was structured into three stages to evaluate the system's performance in both static imaging and dynamic monitoring (as shown in Figure 2). Initially, a baseline 3D volumetric image was established, followed by targeted linear monitoring conducted immediately before and after the grouting operation to track velocity variations induced by the injection process.

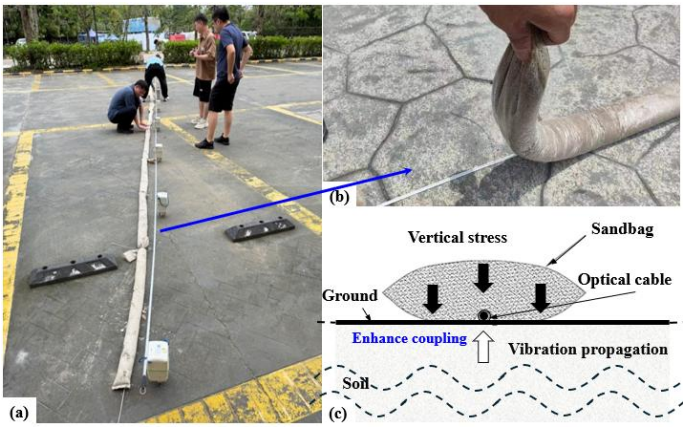

Figure 1: Schematic diagram of (a) the layout of nodal seismometers, (b) sensing fiber optic cables, sandbags, and (c) the enhanced coupling.

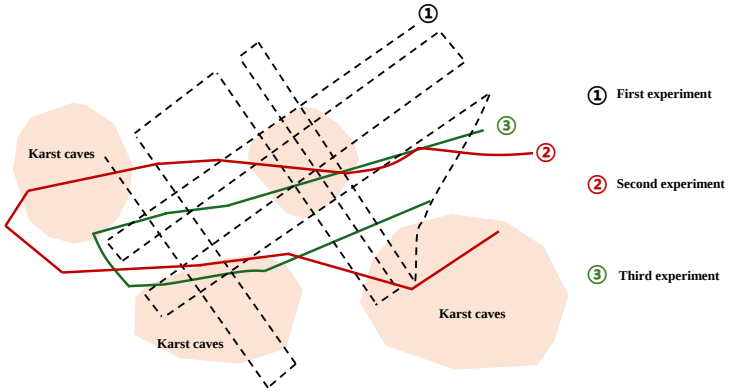

Figure 2: Three-stage layout of the fiber optic cable in the field experiment.

2.3 Nodal Seismometer Configuration

To verify the fidelity of the DAS recordings within a practical engineering context, a co-located survey was performed using SmartSolo IGU-16HR 3C nodal seismometers (as shown in Figure 1). These sensors were deployed in a linear array adjacent to the fiber trajectory, utilizing a move-and-record scheme to construct a virtual dense array with a 0.5 m spatial sampling interval. This high-density benchmark dataset was used to confirm the phase consistency of the DAS-derived signals. By comparing the results from the low-cost DAS array with those from conventional high-precision nodes, the reliability of the distributed sensing approach for routine engineering assessments was rigorously validated.

3 DATA PROCESSING AND METHODOLOGY

3.1 Data Preprocessing

A systematic preprocessing workflow was applied to the continuous DAS recordings to enhance the quality of empirical Green's functions (EGFs). Raw data were down-sampled to 100 Hz to reduce computational load while retaining the 0–5 Hz frequency band of interest. Mean and linear trends were removed to eliminate instrumental drift. To address the unique characteristics of DAS data, a spatial filter was applied to suppress common-mode noise. Subsequently, time-domain normalization and spectral whitening were performed to balance energy across the spectrum and suppress transient high-energy interference from traffic or construction (Park et al. 1999).

3.2 Ambient Noise Interferometry

In this study, ambient noise generated by traffic and human activities is recorded. Unlike traditional active-source reflection methods, Ambient Noise Tomography (ANT) relies on cross-correlating random vibrations to extract empirical Green's functions that represent the seismic response between two points. Seismic interferometry was employed to reconstruct the inter-station surface wave response. Noise Cross-Correlation Functions (NCFs) were computed for all channel pairs in the frequency domain. The cross-correlation function $C_{AB}(\omega)$ in the frequency domain for any two channels A and B is defined as:

$$C_{AB}(\omega) = U_A(\omega) \cdot U_B^*(\omega) \tag{1}$$

where, $U_A(\omega)$ and $U_B(\omega)$ are the Fourier spectra recorded by the two channels, * represents the complex conjugate operator, and ω is the angular frequency. The NCFs were segmented into 1-minute windows and linearly stacked to improve the SNR. This process effectively converts each channel into a virtual source, capturing the wave propagation characteristics between all receiver pairs.

3.3 Dispersion Analysis and Velocity Imaging

Phase velocity dispersion curves were extracted using a frequency-wavenumber (*f-k*) analysis method based on Common Midpoint (CMP) gathers. A variable-aperture sub-array strategy (VASA) was implemented to optimize the trade-off between spatial and wavenumber resolution (as shown in Figure 3). For higher frequencies, which correspond to shallow soil layers, a smaller sub-array aperture is utilized to capture fine-scale geological features. For lower frequencies, a larger aperture is employed to ensure that long-wavelength information is preserved for deeper imaging. This approach allows for a continuous V_s profile from the near-surface down to the bedrock interface. For each CMP gather, a 2D Fourier transform was applied to convert the wavefield from the time-space (*t-x*) domain to the *f-k* domain:

$$S(f,k) = \int_{-\infty}^{\infty}\int_{-\infty}^{\infty} u(x,t)\, e^{-i(2\pi f\, t - kx)}\, dt\, dx \tag{2}$$

where f is the frequency, and k is the wavenumber. The cable array is divided into overlapping segments. For each segment, the signals are transformed into the *f-k* domain. The energy maxima in the *f-k* spectra are used to identify the dispersion characteristics of surface waves. By grouping sensors into CMP sub-arrays, the local variation of velocity can be mapped more accurately than with traditional linear arrays.

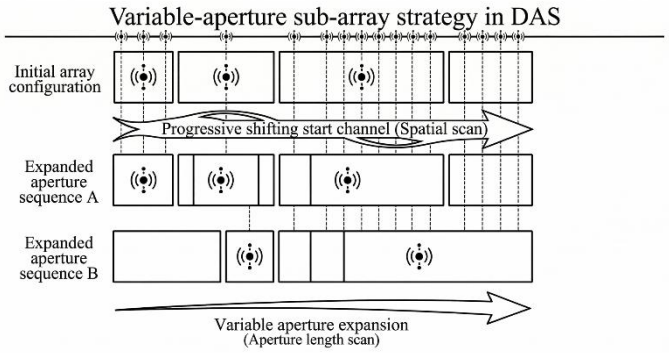

Figure 3: Schematic of variable-aperture sub-array strategy in DAS.

To mitigate directional biases from unevenly distributed noise sources, the *f-k* spectra were symmetrized and standardized. The resulting energy distribution was mapped into the frequency-velocity (*f-v*) domain using the relationship $v=2\pi f/k$. Fundamental mode dispersion curves were automatically extracted by identifying the maximum energy peaks at each frequency. These curves were subsequently inverted to reconstruct 2D shear-wave velocity (V_s) profiles, providing a high-resolution representation of both static stratigraphy and dynamic changes induced by grouting (as shown in Figure 4).

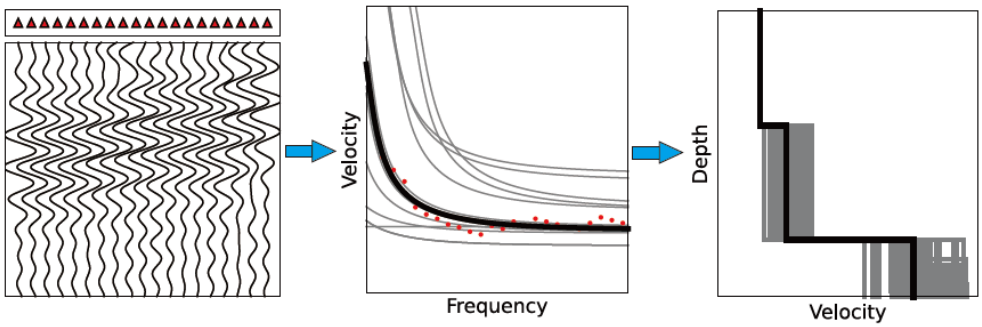

Figure 4: Dispersion curve and shear-wave velocity profiles at the CMP location.

4 RESULTS AND DISCUSSION

4.1 3D Subsurface Structural Imaging and Cost-Efficiency

Traditional geotechnical engineering investigation mainly relies on core drilling, although this method can provide high-precision geological information at specific locations, it is limited by high costs and extended project timelines. Achieving continuous subsurface coverage through high-density drilling is often impractical in complex urban environments. In this study, the feasibility of DAS technology as an efficient auxiliary exploration method is validated through three-dimensional (3D) ambient noise tomography. Borehole lithological logs are utilized to calibrate the DAS inversion results, revealing a vertical stratigraphic sequence consisting of shallow plastic silty clay, an intermediate sandstone layer, and deep limestone bedrock. By integrating the wide-coverage capability of DAS with high-precision information from a limited number of boreholes, exploration costs are effectively reduced, and a refined characterization of geological structures is achieved across a three-dimensional volume.

Multiple shear-wave velocity profiles derived from the planar DAS array prior to grouting demonstrate the system's ability to fill information gaps between sparse boreholes (as shown in Figure 5). Although the effective inversion depth is limited to approximately 40 m, the imaging results accurately reveal the stratigraphic sequence of the overburden and the undulation of the bedrock surface above Karst features. A high degree of consistency is observed between the DAS imaging and borehole data, suggesting that drilling density can be reduced in future engineering projects, thereby optimizing exploration budgets. The velocity structure within the target depth is interpreted as a reflection of lithological evolution. Low-velocity zones below 200 m/s

correspond to loose silty clay and transition into high-velocity red areas that represent competent limestone. These findings confirm that stratigraphic boundaries and lithological interfaces can be identified non-invasively, providing reliable geological evidence for underground risk assessment.

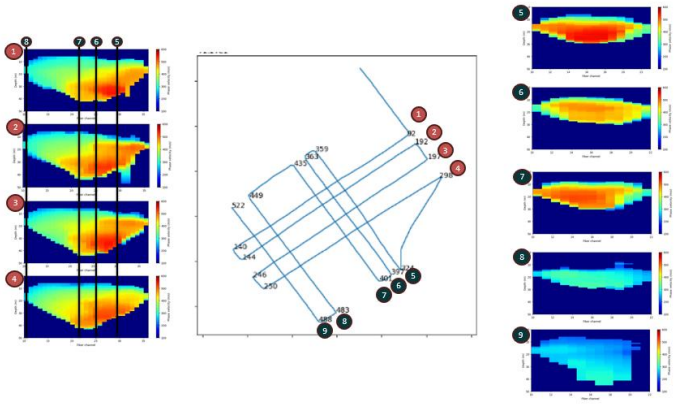

Figure 5: Pre-grouting 3D velocity imaging of the area using the 2D planar DAS array.

4.2 Time-lapse Monitoring of Grouting Reinforcements

A time-lapse comparative analysis was performed along a key survey line to quantitatively assess grouting reinforcement effectiveness, where the fiber optic cable and nodal seismometers were collocated. (as shown in Figure 6). Prior to grouting, phase velocity dispersion images show distinct low-velocity anomalies within the 5–15 Hz band. These anomalies are below 250 m/s and correspond to loose silty clay and potential karst structures with low shear stiffness. Following the grout injection, time-lapse DAS imaging successfully visualizes the transformation of the subsurface through a velocity growth map. In the 5-20 Hz frequency range, a significant increase in phase velocity of about 50% occurs, from 200 to 300 m/s at baseline. This quantitative uplift serves as a direct indicator that the injected grout effectively occupied pore spaces and cavities, thereby enhancing the shear stiffness of the ground (as shown in Figure 7).

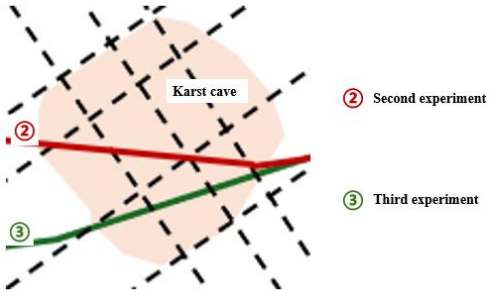

Figure 6: Schematic diagram of fiber optic cable and node seismometer lines.

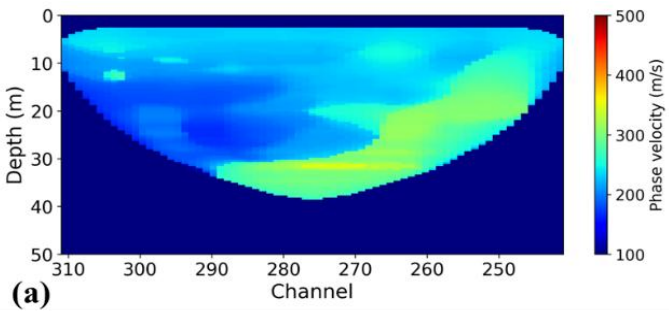

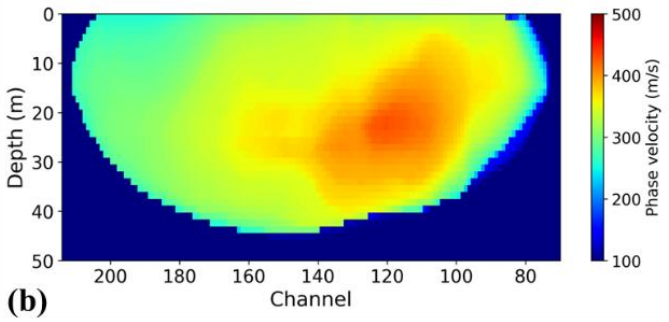

Figure 7: Subsurface wave velocity profiles by inverting DAS data along the survey line through the Karst cave: (a) before grouting; (b) after grouting.

These results were further confirmed by collocated node seismometer data, which show a high degree of consistency with the DAS findings in terms of spatial distribution and the magnitude of velocity increase (as shown in Figure 8). This cross-validation confirms that DAS provides monitoring data of comparable quality to conventional high-precision seismometers without the necessity for extensive supplementary drilling. Unlike discrete borehole data, DAS imaging offers a continuous and high-resolution spatial view, revealing the diffusion range and uniformity of the grout reinforcement. This non-invasive approach reduces the dependence on expensive and time-consuming exploration methods, providing intuitive geophysical evidence for the quality assessment of urban underground projects.

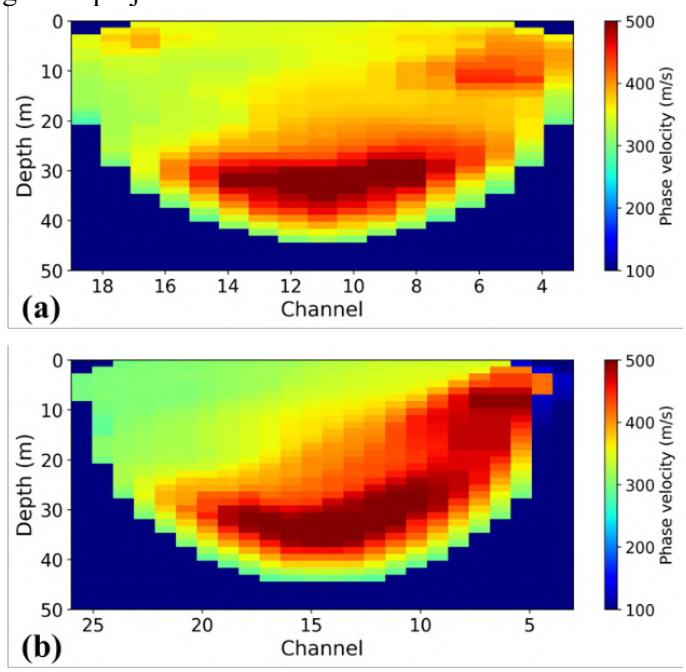

Figure 8: Subsurface wave velocity profiles obtained by inverting nodal seismic data along the survey line through the Karst caves: a) before grouting; b) after grouting.

5 CONCLUSIONS

In this study, the capability of DAS ambient noise tomography is demonstrated as a highly efficient and cost-effective framework for both stratigraphic characterization and ground improvement monitoring in urban Karst regions. Based on the experimental results obtained from the field site in Shenzhen, the following conclusions are drawn:

(a) The implementation of a comprehensive variable-aperture sub-array segmentation strategy is identified as a critical factor for high-resolution dispersion energy extraction. By optimizing the trade-off between spatial resolution and wavenumber resolution, this approach enables the precise delineation of complex stratigraphic boundaries and Karst features. The results indicate that DAS-derived velocity models can achieve a high degree of fidelity in characterizing near-surface heterogeneities within a depth of 40 meters.

(b) The utilization of DAS imaging as an auxiliary exploration tool offers a significant economic advantage over traditional intrusive methods. By reconstructing 3D shallow velocity structures that align with limited borehole data, the spatial information gaps between discrete borehole sites are effectively filled. This capability allows for a substantial reduction in drilling density during the initial stages of engineering projects, thereby optimizing both exploration budgets and project timelines without compromising the accuracy of the geological assessment.

(c) The time-lapse application of DAS provides a robust and non-destructive means to quantitatively assess the effectiveness of ground grouting. A substantial increase in shear-wave velocity from approximately 200 m/s to 300 m/s was identified and visualized through velocity growth maps. This increase in V_s serves as objective geophysical evidence of grout slurry diffusion and soil solidification, confirming that DAS technology is an invaluable tool for the safety management of urban underground infrastructure.

ACKNOWLEDGEMENTS

This study is financially supported by Guangzhou Metro Design & Research Institute Co., Ltd (KY-2022-120), a grant from Offshore Oil Engineering CO., LTD. (202518685939), Shenzhen Science and Technology Innovation Commission (JCYJ20230807093305011; JCYJ20210324105210028).

REFERENCES

Abudeif, A.M., Mohammed, M.A., Abd el-aal, A.K. & et al. 2019. Single and multi-channel passive source methods for calculating the shallow S-wave velocity structure and site effect parameters at 15th May City, Egypt. Journal of African Earth Sciences, 159: 103579.

Atterholt, J., Zhan, Z., Shen, Z. & et al. 2022. A unified wavefield-partitioning approach for distributed acoustic sensing. Geophysical Journal International, 228(2): 1410-1418.

Cheng, F., Xia, J., Luo, Y. & et al. 2016. Multichannel analysis of passive surface waves based on crosscorrelations. Geophysics, 81(5): EN57-EN66.

Cueto, M., Olona, J., Fernández-Viejo, G. & et al. 2018. Karst-induced sinkhole detection using an integrated geophysical survey: a case study along the Riyadh Metro Line 3 (Saudi Arabia). Near Surface Geophysics, 16(3): 270-281.

Curtis, A. & Halliday, D. 2010. Source-receiver wave field interferometry. Physical Review E, 81(4): 046601.

Hartog, A.H. 2017. An introduction to distributed optical fibre sensors. CRC press.

Hu, S., Zhao, Y., Ma, Z. & et al. 2022. Combined analysis of active and passive surface waves for 2D characterization of a landfill. Journal of Applied Geophysics, 206: 104832.

Karslı, H., Babacan, A.E., Akın, Ö. & et al. 2024. Subsurface characterization by active and passive source geophysical methods after the 06 February 2023 earthquakes in Turkey. Natural Hazards, 120(6): 5257-5286.

Krawczyk, C., Jousset, P. & Reinsch, T. 2019. Fibre-optic strain sensing: Game changer for (urban) seismic surveying? In Proc of 1st Conference on Geophysics for Infrastructure Planning Monitoring and BIM. European Association of Geoscientists & Engineers, 2019(1): 1-5.

Larose, E., Carrière, S., Voisin, C. & et al. 2015. Environmental seismology: What can we learn on earth surface processes with ambient noise? Journal of Applied Geophysics, 116: 62-74.

Li, X., Li, Q., Lei, Y. & et al. 2020. Active and passive source Rayleigh wave joint imaging of the shallow structure in the Caotan Camp area, southwestern Ordos Basin. Soil Dynamics and Earthquake Engineering, 130: 105986.

Li, Y., Perton, M., Gaite, B. & et al. 2023. Near-surface characterization using distributed acoustic sensing in an urban area: Granada, Spain. Geophysical Journal International, 235(2): 1849-1860.

Lindsey, N., Dawe, C.T. & Ajo-Franklin, J. 2019. Photonic seismology in Monterey Bay: Dark fiber DAS illuminates offshore faults and coastal ocean dynamics. OSF Preprints.

Lior, I., Mercerat, E.D., Rivet, D. & et al. 2022. Imaging an underwater basin and its resonance modes using optical fiber distributed acoustic sensing. Seismological Society of America, 93(3): 1573-1584.

Liu, D., Lin, P., Chen, X. & et al. 2022. Statistical analysis of karst spatial distribution in Shenzhen (in Chinese). Rock and Soil Mechanics, 43(7): 1899–1912.

Martin, E.R., Castillo, C.M., Cole, S. & et al. 2017. Seismic monitoring leveraging existing telecom infrastructure at the SDASA: Active, passive, and ambient-noise analysis. The Leading Edge, 36(12): 1025-1031.

Niu, J., Oyediran, I.A., Liu, D. & et al. 2015. Quantitative foundation stability evaluation of urban karst area: Case study of Tangshan, China. Soils and Foundations, 55(3): 493-503.

Park, C.B., Miller, R.D. & Xia, J. 1999. Multichannel analysis of surface waves. Geophysics, 64(3): 800-808.

Parker, T., Shatalin, S. & Farhadiroushan, M. 2014. Distributed Acoustic Sensing–a new tool for seismic applications. first break, 32(2).

Rodríguez Tribaldos, V.R. & Ajo-Franklin, J.B. 2021. Aquifer monitoring using ambient seismic noise recorded with distributed acoustic sensing (DAS) deployed on dark fiber. Journal of Geophysical Research: Solid Earth, 126(4): e2020JB021004.

Spica, Z.J., Nishida, K., Akuhara, T. & et al. 2020. Marine sediment characterized by ocean-bottom fiber-optic seismology. Geophysical Research Letters, 47(16): e2020GL088360.

Tejedor, J., Macias-Guarasa, J., Martins, H.F. & et al. 2019. A contextual GMM-HMM smart fiber optic surveillance system for pipeline integrity threat detection. Journal of Lightwave Technology, 37(18): 4514-4522.

Tribaldos, V.R., Ajo-Franklin, J.B., Dou, S. & et al. 2021. Surface wave imaging using distributed acoustic sensing deployed on dark fiber: Moving beyond high-frequency noise. Distributed Acoustic Sensing in Geophysics: Methods and Applications: 197-212.

Viens, L., Bonilla, L.F., Spica, Z.J. & et al. 2022. Nonlinear earthquake response of marine sediments with distributed acoustic sensing. Geophysical Research Letters, 49(21): e2022GL100122.

Wagner, F.M. & Uhlemann, S. 2021. An overview of multimethod imaging approaches in environmental geophysics. Advances in geophysics, 62: 1-72.

Wang, Y., Khorrami, M., Tran, K.T. & et al. 2023. Application of ambient noise tomography for deep void detection. Journal of Applied Geophysics, 209: 104922.

Yang, L., Fomel, S., Wang, S. & et al. 2023. Denoising of distributed acoustic sensing data using supervised deep learning. Geophysics, 88(1): WA91-WA104.

Zhan, Z. 2020. Distributed acoustic sensing turns fiber-optic cables into sensitive seismic antennas. Seismological Research Letters, 91(1): 1-15.

Zhang, Y. 2022. Study on seismic wave numerical simulation and tomography in longgang karst area (in Chinese). Southwest Jiaotong University.

Zhang, Y., Chu, J., Wu, S. & et al. 2025. New interpretation methods for rockhead determination using passive seismic surface wave data: Insights from Singapore. Journal of Rock Mechanics and Geotechnical Engineering.

Zheng, S., Sun, X., Song, X. & et al. 2008. Surface wave tomography of China from ambient seismic noise correlation. Geochemistry, Geophysics, Geosystems, 9(5).

Geotechnical Design with Rhino and Grasshopper: Reinforcing First Principles in Hong Kong Practice

E. Alnaqdy
Tony Gee & Partners (Asia) Ltd., Hong Kong

ABSTRACT

This paper demonstrates how accessible parametric tools can strengthen first-principles geotechnical design without relying on computationally intensive software. By focusing on core concepts such as stress distribution, soil consolidation, and volume assessment, the approach uses modern digital platforms to enhance visualisation, support sensitivity studies, and enable iterative, data-driven design. Rhinoceros 3D (Rhino) and its visual scripting environment, Grasshopper, are employed for efficient Excel data import, dynamic 3D surface generation, geometric manipulation, and real-time model updates, maintaining transparency to underlying calculations rather than relying on black-box software packages. Three Hong Kong–based case studies illustrate these capabilities. In Pile Design and Rockhead Projection, borehole-derived contours are converted into parametric soil and rockhead surfaces, allowing pile layouts to be projected to determine founding levels and rock-socket lengths that automatically update during predrilling. In ELS Visualisation, settlement calculations including elastic, drawdown, and creep components, are imported from Excel to generate live settlement contours for rapid sensitivity testing and serviceability assessment. In Reclamation Quantification, multiple stratigraphic surfaces are used to compute dredging volumes and ground-treatment extents, supporting efficient and environmentally informed optimisation. These examples show how parametric modelling enhances understanding, streamlines processes, and supports geotechnical decision-making.

1 INTRODUCTION

Over the past several decades, rapid advances in the availability of digital tools, computational power, and data connectivity have transformed everyday engineering practice. Modern workflows now routinely incorporate finite element analysis (FEA), extensive numerical modelling, and more recently, emerging artificial intelligence (AI) applications. While these tools provide unprecedented analytical capability, they often operate as opaque "black boxes," distancing the designer from the underlying soil mechanics principles that ultimately govern ground behaviour.

In contrast, the fundamental theories that shape geotechnical engineering; such as Terzaghi's effective stress principle (1936), Boussinesq's elastic stress distribution (1885), and the empirical frameworks used to describe soil stiffness, strength, and consolidation; have remained consistent for decades. These principles are rooted in observation, laboratory testing, and incremental scientific refinement. Despite their empirical origins and inherent uncertainties, they continue to underpin modern design codes and remain the foundation of engineering judgement. As computational tools grow more sophisticated, it is important to be aware of the disparity between the natural uncertainty of their empirical origins and today's computational precision.

This paper proposes that parametric modelling platforms—particularly Rhinoceros 3D (Rhino) and its visual programming environment Grasshopper—offer a practical means of reconnecting modern calculation workflows to core geotechnical fundamentals, without requiring specialist numerical modelling expertise or significant software investment. Rather than replacing first-principles thinking, these tools make it more visible: calculations remain transparent in Excel, while Rhino and Grasshopper handle the geometry, visualisation, and iterative updates that would otherwise consume significant manual effort. Their capacity for real-time feedback, dynamic geometry manipulation, and direct interoperability with Excel makes them well suited for procedures grounded in first-principles analysis, and their outputs can be readily converted into the standard deliverables required for formal engineering submissions.

To illustrate this, three Hong Kong–based case studies are presented. Each demonstrates how parametric tools can be integrated into geotechnical practice to enhance interpretation of subsurface conditions, improve visibility of calculations, and streamline iterative design. The examples cover:

1. Pile design and rockhead projection using contour-derived surfaces;
2. Excavation and Lateral Support (ELS) settlement visualisation directly linked to calculations; and
3. Reclamation volume estimation and ground-improvement quantification using parametric surface interactions.

These case studies highlight how parametric modelling can strengthen engineering understanding, reduce design risk, and improve design efficiency while reinforcing, rather than replacing, the fundamental concepts at the core of geotechnical design.

1 METHODOLOGY – THE USE OF RHINO3D & GRASSHOPPER FOR GEOTECHNICAL APPLICATIONS

This study employs Rhinoceros 3D (Rhino3D) together with its visual programming environment Grasshopper to develop straightforward parametric design and analyses for geotechnical engineering purposes. The methodology is structured around three core functions of the software: data import, data visualisation, and data manipulation. These functions enable the creation of dynamic, interpretable ground models and the integration of engineering calculations directly from Excel.

1.1 *Software Environment*

Rhino3D is a CAD platform built on the non-uniform rational B-spline (NURBS) modelling framework, enabling accurate representation of geometric entities such as curves, surfaces, solids, and point sets. Its lightweight architecture, affordability, and wide interoperability make it well suited to geotechnical processes, where engineers must integrate multiple data formats including contour grids, digitized borehole logs, and databases of instrumentation records.

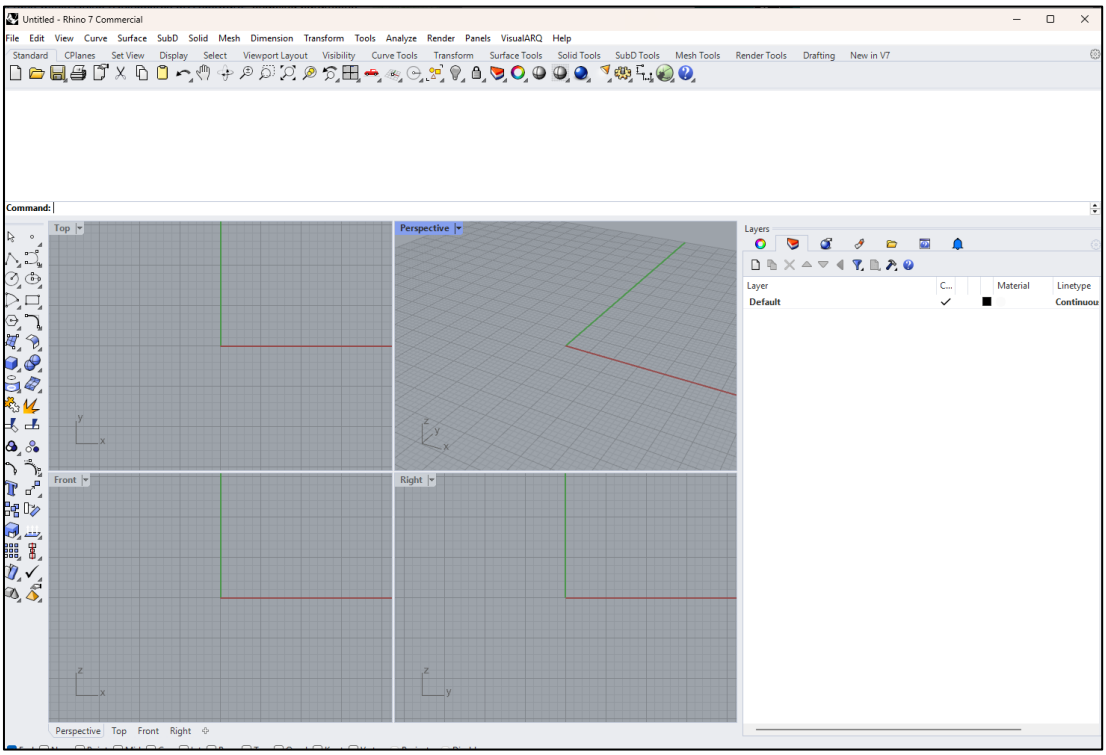

Figure 1 - The Rhino3D Interface (Rhino 7)

Grasshopper, a plugin native to Rhino, provides a visual programming interface in which users connect components representing operations, parameters, or data structures. Complex procedures can be built by linking these components into logic-based sequences. Unlike black-box numerical tools, Grasshopper exposes all intermediate steps, ensuring a clear line to the underlying calculations that inform geotechnical design.
Figures 1 and 2 depict the Rhino interface and the Grasshopper canvas respectively, providing context for the modelling environment applied throughout the methodology. The Rhino interface shows a 4-viewport setup with toolbars and layer manager open. Note that the command bar enables interoperability with traditional text based coding scripts. The grasshopper interface shows various components linked together, typically inputs and parameters on the left, execution components in the middle and output components on the right.

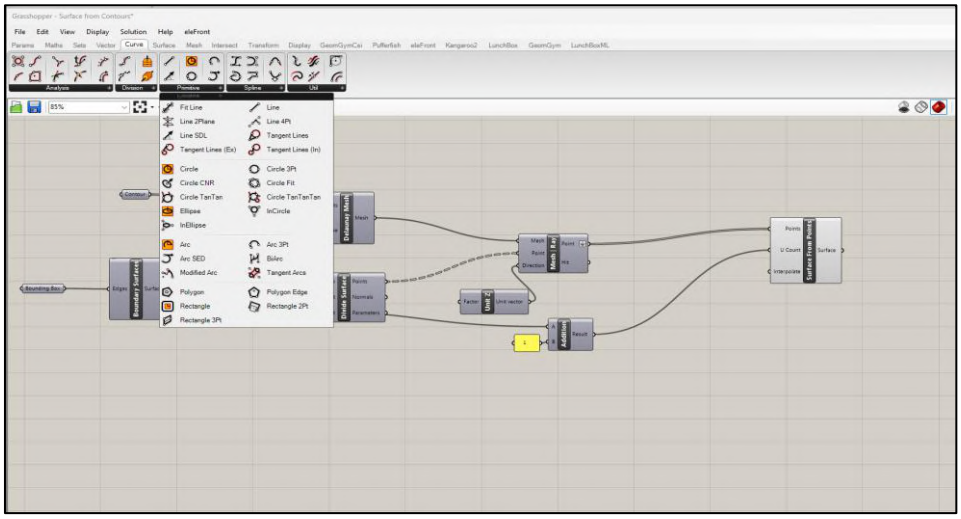

Figure 2 - Grasshopper Interface with Components on Canvas. The Component Dropdown Menu is open on the Toolbar

1.2 *Data Import and Visualisation*

Throughout its compilation and interpretation, ground investigation data in Hong Kong are usually consolidated into digital workbooks (eg. MS Excel), where borehole locations, levels, and stratigraphic boundaries are stored for design use. To import these datasets into Grasshopper, community-developed plugins such as LunchBox and TT Toolbox are used. Their Excel Reader components allow Grasshopper to link directly to workbook files with minimal setup, extracting XYZ coordinates and descriptive soil parameters, refreshing whenever the spreadsheet is updated, and structuring the data as points, lists, or hierarchical trees. The imported coordinates can then be visualised in Rhino as point clouds or used to generate curves, surfaces, or meshes, within the Grasshopper environment, based directly on the data being read. Figure 3 demonstrates this, where columns from Excel are translated into 3D points within Grasshopper. Should any of the data points be updated, the Grasshopper procedure can be set up to automatically reflect the change visually in the Rhino viewport.

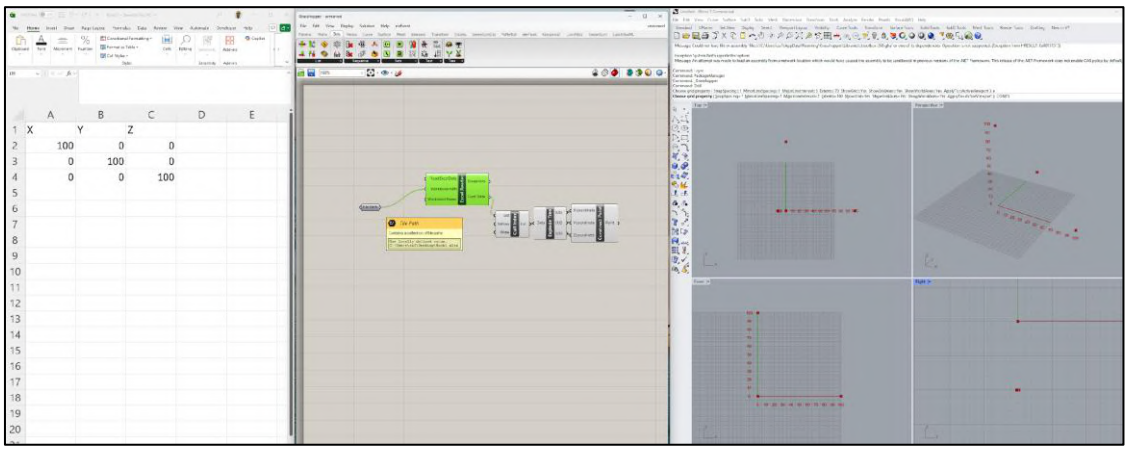

Figure 3 - Grasshopper Canvas: Live Data Import from Excel Using LunchBox Excel Reader Component

Grasshopper's data structure is based on hierarchical data trees. Each branch represents an array of items which can be organised in lists or joined together. This multi-layered system of data organisation allows the software to manage the type of complex datasets that are common in geotechnical practice (e.g. settlements data for multiple cofferdams of varying shapes, inferred levels of various strata from multiple boreholes, or in-situ test results for various soil types). This ensures that geometric and numerical data can be processed in parallel while maintaining full traceability.

1.3 *Data Processing and Geometric Transformation*

After import, the data can be manipulated using Grasshopper's broad range of geometric transformation tools. Geometry may be shifted, rotated, scaled, or reoriented, allowing ground models or structural elements to be adjusted interactively while remaining tied to underlying design parameters and calculations.

These transformations can be linked directly to parameters stored in Excel such as pile diameter, rockhead levels, or setting out points, enabling easier updates to pile toe levels, surface elevations, or excavation geometries. Grasshopper also provides tools for working with point-based data, allowing engineers to deconstruct and reconstruct points, project locations onto surfaces, and extract elevation information from terrain or geological models. These capabilities make it straightforward to interrogate and refine geotechnical geometry as design assumptions evolve. These tools are particularly useful when, for example, projecting pile footprints onto rockhead surfaces or when generating cross-sections through geological strata, both of which rely on accurate point and surface interrogation.

Once the underlying geometry is established, geotechnical contour data imported from software packages such as Surfer or from other CAD sources can be transformed into continuous 3D terrain surfaces. Instead of relying on a series of discrete contour lines, Grasshopper's meshing and surface-fitting components allow these curves to be blended into a coherent ground model. By using Grasshopper components such as Mesh From Contours, Delaunay Mesh, or NURBS Surface Fit, the contours are converted into a fully connected surface that updates automatically whenever the source data or borehole interpretations change.

Grasshopper generates geometry in a live, parametric state, but completed elements should be "baked" into Rhino to create static objects in a layer for export. These fixed outputs can then be incorporated into drawings, exported to BIM platforms, used for additional analysis, documented, or passed on to drafting teams.

2 CASE STUDIES

The following case studies illustrate how Rhino and Grasshopper can be used to visualise, interpret, and manipulate geotechnical data to address practical engineering challenges.

2.1 Pile Design and Rockhead Projection

The first case study focuses on the challenge of accurately determining pile founding levels in a Hong Kong design process setting, where a defined engineering rockhead (typically Category 1 (c) or equivalent) can vary

significantly due to fractures, weathering, topographical undulation, and the typically sparse distribution of boreholes in early design stages. Even small changes in interpreted rockhead can alter pile lengths, socket depths, and construction quantities. Traditionally, these levels are derived by reviewing boreholes, studying contour maps, and carrying out manual interpolation. This approach becomes slow, labour intensive, and prone to error when applied to large pile groups or frequently revised designs.

To streamline this process, a parametric procedure was developed using Surfer, Rhino3D, and Grasshopper. Borehole-derived rockhead levels are first interpreted and gridded in Surfer to generate a contour model of the Category I(c) rock surface. These contours are then imported into Rhino, where Grasshopper converts them into a continuous three-dimensional rockhead surface, a simple procedure for this is illustrated in Figure 4. The project's pile layout is subsequently loaded into the file as geometry and Grasshopper projects them through this surface to determine individual founding levels and socket lengths.

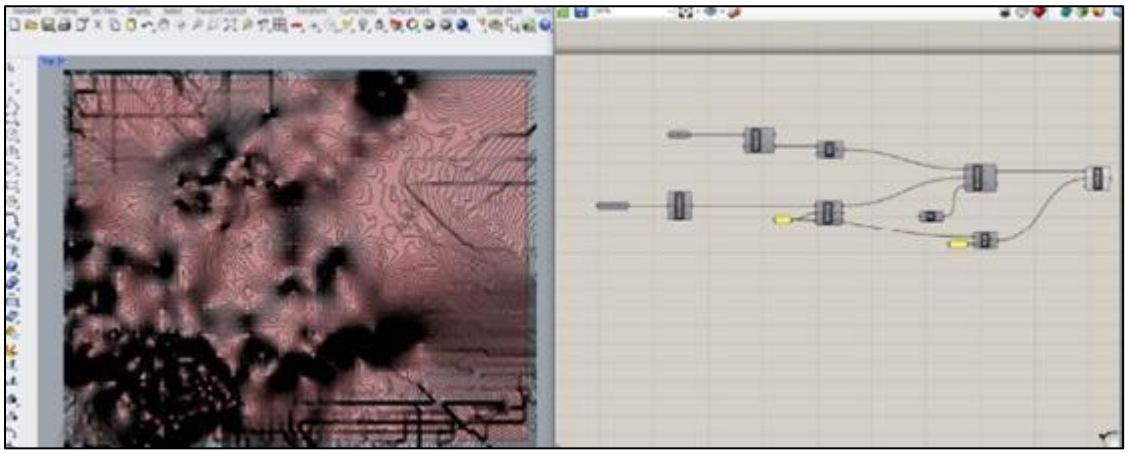

Figure 4 - Plan Rhino Viewport of Contours are Converted to a Surface by a Grasshopper Script Live

The Grasshopper protocol follows a clear sequence that links the interpreted ground model directly to the pile layout. Surfer-generated rockhead contours are first brought into Rhino and referenced in Grasshopper as curve geometry. These curves are then converted into a continuous three-dimensional surface using tools such as Mesh From Contours or Delaunay Mesh, providing a live representation of the interpreted rockhead. With the surface established, the project's pile data are imported, enabling their geometries to be modelled as curves and projected downward until they intersect the rockhead surface; these intersection points define the starting point for calculation of founding levels for each pile and form the basis of the updated pile schedule. Figure 5 shows the execution of the Grasshopper script to read from the pile schedule and project the visual image of the data onto the underlying rockhead surface, including pile lengths, rock sockets, and any bellouts.

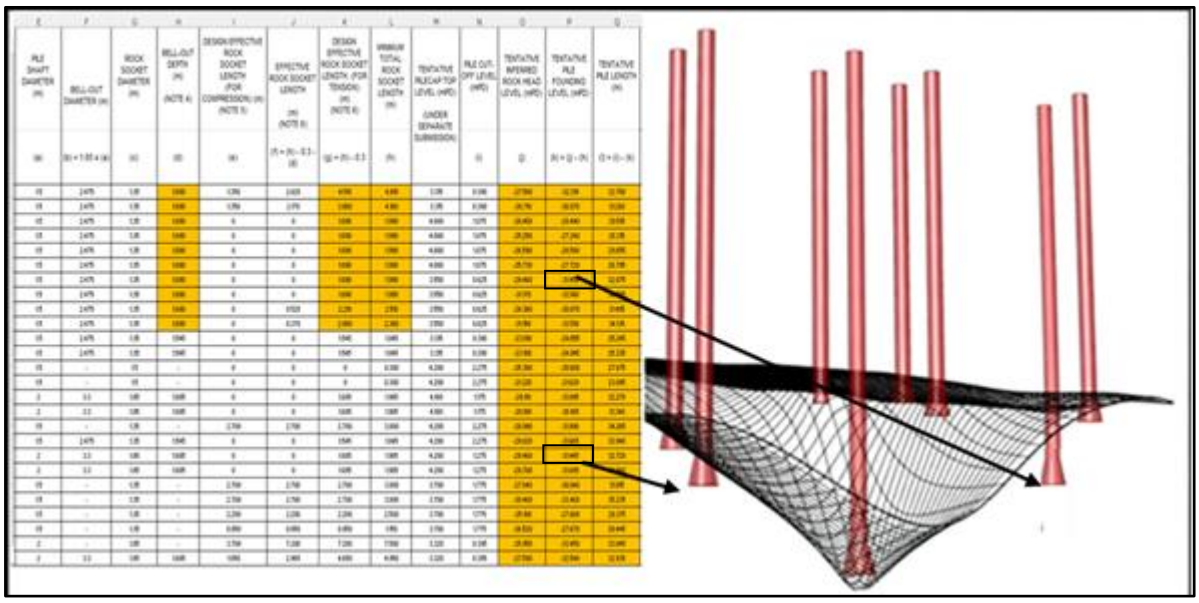

Figure 5 – Pile Schedule Updates can be Automated through Grasshopper's "Write to Excel" feature as Rockhead Surface Changes

To complete the process, calculated founding levels are written back into the relevant Excel schedule using the Write to Excel component, ensuring that any revision to the contour model or pile layout is reflected automatically across the design documentation. The pile schedule in Excel is set up to calculate the resulting final founding level accounting for minimum socket length and other relevant factors. This creates a fully parametric environment in which updates to borehole interpretation or structural layouts instantly propagate through the model.

The resulting engineering outcome is a model which provides a live, databased representation of rockhead and its interaction with the pile arrangement. Founding levels update instantaneously when boreholes are reinterpreted, when new investigation data becomes available, or when structural engineers adjust pile positions. The process also allows the designer to inspect pile-to-rock interaction visually, verify assumptions, and quickly identify anomalous or unexpected founding depths.

This approach provides several practical advantages for foundation design. By replacing manual interpolation with a fully parametric process, significant time is saved; particularly on projects involving large pile groups or frequent layout revisions. Accuracy is improved because founding levels are derived from a continuous contoured surface rather than isolated spot checks and the full pile geometry is being considered. In addition, any updates to the ground model or pile arrangement feed automatically through to the schedule. The procedure also enhances transparency, allowing engineers to visually verify how each pile interacts with the rockhead surface and to identify anomalies quickly. In addition, multiple stratigraphic surfaces can be stacked within the Rhino–Grasshopper environment, enabling the creation of geological profiles along the pile alignment and supporting more informed decisions regarding socket depths, founding criteria, and layer transitions. The direct links to Excel facilitate clearer coordination with structural teams and reduce drafting workload.

2.2 Excavation and Lateral Support (ELS) Visualisation

The second case example addresses a common challenge that arises once the engineer has completed the initial settlement calculations and must present the results clearly in drawings or design figures so that potential impacts on nearby utilities or sensitive receivers can be assessed. Evaluating ground movements around deep excavations is a critical aspect of ELS design, particularly in dense urban environments where foundations,

utilities, roads, and other assets lie close to the cofferdam. Although the settlement calculations themselves are typically grounded in first-principles soil mechanics such as elastic compression, groundwater drawdown, and long-term creep, their spatial interpretation is not as straightforward. Conventional workflows often require engineers to manually transfer the calculated settlement values into CAD or GIS platforms to generate contour plots, a process that is slow, prone to repetitive effort, and difficult to adapt when multiple cofferdam layouts, strut configurations, or pile toe levels must be compared, parameters which all have implication on the final settlement contours.

To address these limitations, a parametric Grasshopper script was created to link directly to the Excel-based settlement calculations prepared by the design team. Rather than treating calculation and visualisation as separate steps, Grasshopper reads the settlement values in real time and generates spatial contour plots within Rhino. As a result, settlement patterns update swiftly whenever input parameters change, enabling rapid sensitivity studies during ELS optimisation.

During the optimisation stage, design iterations are carried out by adjusting key stiffness and boundary-control parameters. These include strut elevation and preloading, strut and pile axial/bending stiffness, and, where relevant, excavation sequence. Then the finite-element (FE) model is run to obtain updated wall deflections and free-field ground movements. In parallel, seepage analyses are also run to quantify changes in hydraulic head during dewatering and excavation stages, and the extent of groundwater drawdown associated with the updated arrangement is exported. The FE outputs and the seepage results are brought through into Excel, where the settlement calculations are set up to convert these inputs into settlement values, with corresponding offsets to the ELS wall. On this basis, elastic compression, drawdown-induced settlement, and time-dependent consolidation are being computed at control points or along user-defined sections as desired. Grasshopper reads these computed values directly from Excel and generates the settlement contours in Rhino, providing an rapid parametric visualisation of the combined settlement response shortly after the analysis stage has been completed.

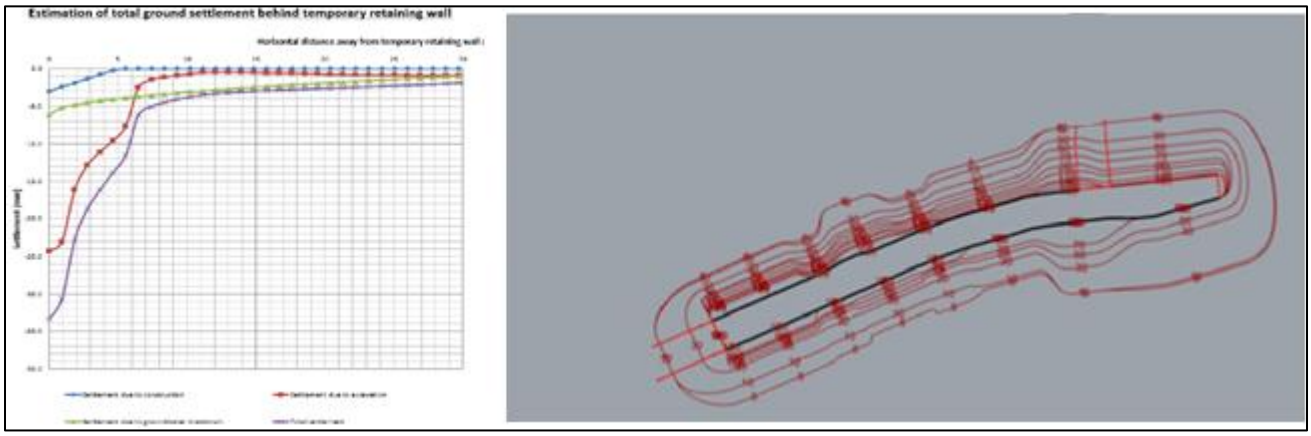

Figure 6 – Settlement Contours Generated in Rhino as Grasshopper Reads Directly from Excel

Figure 6 shows on the left an example of a set of settlement curves (including elastic settlement, drawdown, and consolidation) for a given section of a planned ELS, to the right - the Grasshopper projection of dozens of such curve sets as offset contours surrounding a proposed cofferdam. The resulting model provides a clear, intuitive view of settlement behaviour around the excavation. Since the visualisation is live-linked to the Excel-based calculations, engineers can vary key parameters such as strut levels, toe depths, or cofferdam geometry and see the impact shortly after updating the excel file, without redrawing contours by hand. This accelerates decision-making and improves transparency, as the connection between input assumptions and predicted ground movements is visible in a short space of time.

This approach delivers clear benefits for ELS design. It removes the repetitive drafting usually needed to generate settlement contours for multiple options, and its parametric setup provides rapid feedback when strut positions, pile toe depths, or other input parameters are adjusted. This makes it easier to converge on arrangements that minimise ground movements. Since the live contours sit in the same Rhino CAD environment as utility surveys and structural layouts, coordination improves and potential clashes can be identified at an

earlier stage. All outputs remain tied to calculations in Excel, strengthening auditability and engineering confidence. These advantages reduce risk by flagging potential impacts on surrounding assets early in the design process.

3.3 Reclamation and Ground Improvement Quantification

The third and final case example builds on the methods and processes introduced in Section 3.1. In the first case example, contour data was used to generate surfaces. This third case study extends that approach by demonstrating how multiple surfaces that define stratigraphic soil boundaries can be combined to tackle a common challenge encountered during the planning phases of a reclamation and seawall design project. Early-stage reclamation design requires quick yet defensible quantity take-offs to guide option selection, logistics, and pricing. For example, it is important to understand how much marine deposit must be dredged, or where ground improvement zones (ie. beneath seawalls or slopes) are required and to what extent. Contractors must also estimate fill volumes for different target platform levels and formation elevations, all at an early stage to inform their financial and logistical decisions going forward.

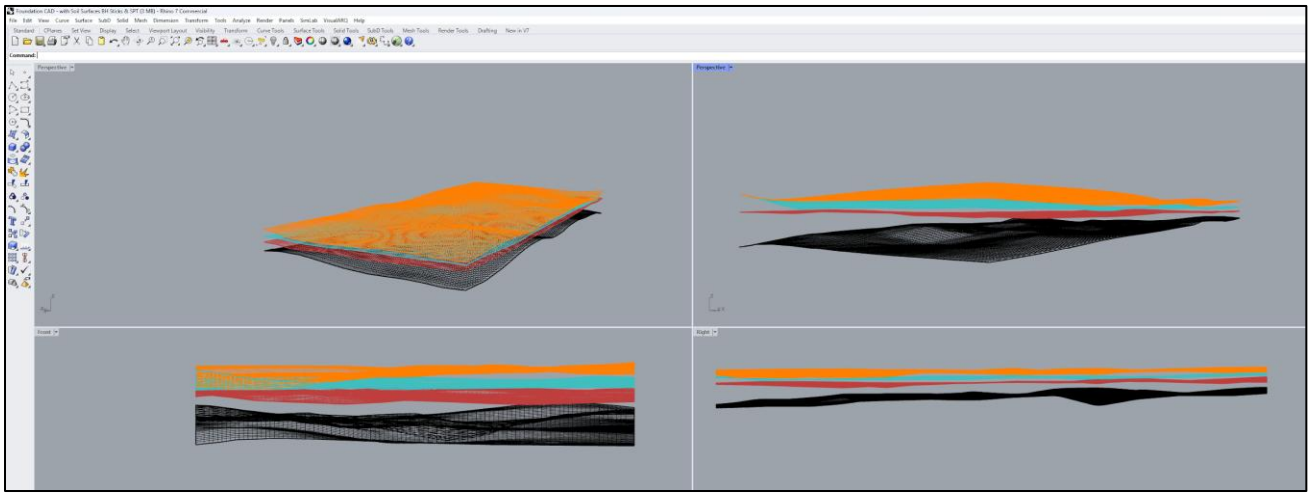

Figure 7 – Multiple Soil Surfaces Created in Grasshopper and Baked into Rhino Viewport

The solution involves developing a parametric environment in Rhino + Grasshopper that engages internal site boundaries and setting out points with stratigraphic surfaces all as initial inputs. The objective is to produce live volumes and quantity tables that will aid planning and decision making. Lines and curves representing the site boundary, seawall alignment, berthing areas, and zones designated for heavily loaded structures are imported into Rhino and used as volumetric boundaries. These boundaries are then extruded through a set of stratigraphic surfaces such as proposed ground level, existing seabed, marine deposit top and base, alluvium horizons, decomposed granite, and engineering rockhead, which have been generated using the same method described in Section 3.1.

Grasshopper then evaluates the interactions between these boundaries and the underlying surfaces to compute, by subtraction, dredging volumes, ground-treatment extents, and fill quantities at locations such as seawalls, slopes, and platform areas. Because the script is fully parametric, any adjustment to alignment, formation level, or treatment depth automatically updates the calculated volumes, allowing planning-stage design changes to be reflected in the associated logistical and financial implications.

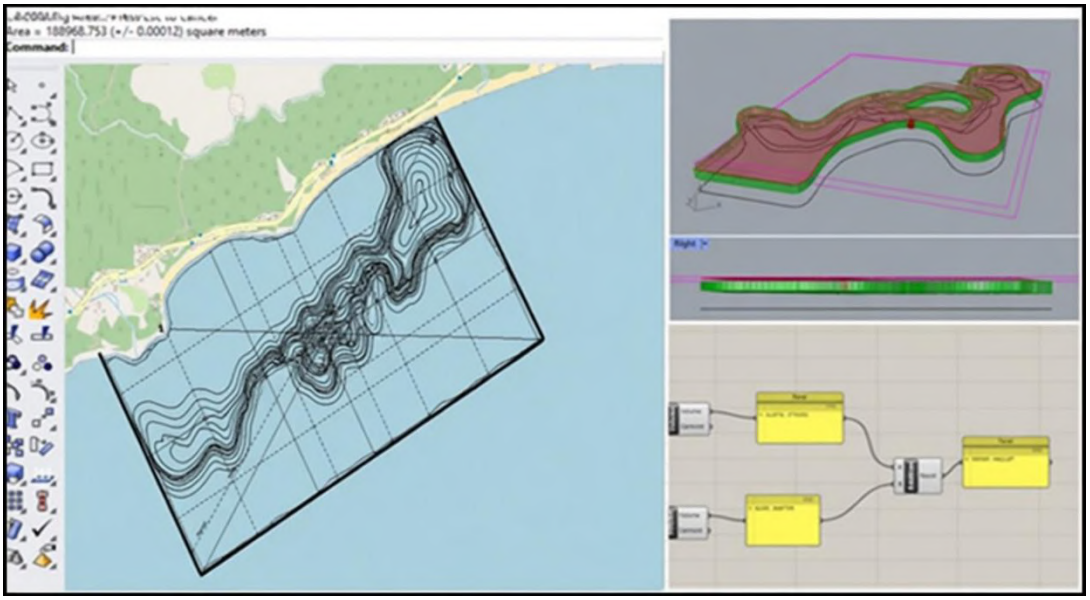

Figure 8 – Surfaces can be projected through soil layers to get volumes

The solution provides rapid updates to dredge, treatment, and fill quantities as seawall centrelines, formation levels, or treatment depths evolve during planning and tendering. Areas where soft materials thicken, such as beneath seawall corners, are quickly highlighted, allowing designers to trial minor alignment or level adjustments to reduce treatment or excavation demands. Because these volumes are computed directly from the stratigraphic model, section cuts and spot checks confirm that the results remain geologically consistent without introducing the risk of error through manual handling of CAD operations.

4 FROM PARAMETRIC MODEL TO FORMAL SUBMISSION

A practical concern for Hong Kong practitioners is how parametric model outputs translate into the standard deliverables expected by regulatory bodies such as the Geotechnical Engineering Office (GEO) and the Buildings Department (BD). The Rhino + Grasshopper workflow is designed to complement, rather than replace, conventional submission formats, and the conversion from live parametric model to formal drawing or calculation report follows a straightforward sequence.

Once a parametric geometry is finalised, Grasshopper's "Bake" function deposits static geometry into named Rhino layers. These baked objects—surfaces, curves, pile lines, settlement contours—can be exported directly as DWG or DXF files, which are then opened in AutoCAD or MicroStation for annotation, dimensioning, and title block addition in the conventional manner. The resulting drawings are indistinguishable from those produced through a traditional workflow and are fully compatible with GEO submission requirements, including the preparation of foundation layout plans, pile schedule drawings, and ELS general arrangement drawings.

On the calculation side, the Excel workbooks that drive the Grasshopper scripts already constitute the formal calculation record. Since all geotechnical assumptions, input parameters, and computed results reside in the spreadsheet, these files can be directly formatted and submitted as calculation appendices without any transcription step. This preserves auditability and satisfies the traceability requirements that checking engineers and regulatory reviewers typically expect. The parametric model therefore acts as a quality assurance layer over the conventional submission package, not a replacement for it.

5 INTEGRATION WITH NUMERICAL ANALYSIS

The geometry developed within Rhino + Grasshopper is compatible with a range of downstream analysis environments, and the ecosystem of available plugins continues to grow. For structural analysis, well-established Grasshopper plugins such as Karamba3D provide parametric finite element analysis of beam, frame, and shell elements directly within the Grasshopper canvas, while the GeometryGym suite enables direct model export to industry-standard platforms including SAP2000, ETABS, Oasys GSA, and Robot Structural Analysis.

These workflows are particularly relevant where geotechnical geometry intersects with structural design; for example, transferring pile cap layouts, retaining wall geometries, or seawall cross-sections into a structural model without rebuilding from scratch.

For geotechnical finite element software such as PLAXIS, direct interoperability with Grasshopper is achievable through the PLAXIS Python API, which allows model geometry, soil zones, and construction stages to be defined and run programmatically. Published examples of this approach include work by Arup on the Euston Station redevelopment (Major Projects Association, 2023), where Grasshopper was used to extract cross-section geometry from a BIM model, which was then passed to PLAXIS via Python scripting to automate the setup and execution of multiple FE analyses. While this level of integration goes beyond the visual, accessible workflow described in this paper, it illustrates the direction of travel for parametric geotechnical practice. In the near term, the more common workflow, and the one applied in the case studies here, is for PLAXIS outputs to be exported as CSV or pasted into Excel, from which Grasshopper reads the results for visualisation and sensitivity review.

6 CONCLUSIONS

This paper demonstrates that technological advancements in parametric modelling can be used to emphasise first-principles geotechnics rather than replace or supersede them. By keeping calculations visible in Excel and using Rhino + Grasshopper for live geometry and visualisation, engineers can interrogate assumptions, iterate parameters, and see the consequences of design changes quickly. The three Hong Kong applications—pile founding to rockhead, ELS settlement visualisation, and reclamation quantity modelling—showed similar results: faster, auditable procedures that reduce drafting effort, minimise data handling errors, and improve coordination with colleagues and stakeholders. Although the approach does not eliminate the inherent uncertainty in GI or enhance the accuracy of the analysis, it makes that uncertainty visible and easier to test through structured sensitivity studies. The workflow also sits naturally within Hong Kong's formal submission environment: parametric outputs are readily converted into the standard 2D drawings and calculation reports expected by regulatory bodies, and the same geometry can be exported to analysis platforms for further numerical investigation. In everyday practice, this turns parametric modelling into a practical advantage, with better decisions reached sooner and a clear line back to the underlying soil mechanics fundamentals.

REFERENCES

Terzaghi, K. (1936) The shearing resistance of saturated soils and the angle between planes of shear. In: Proceedings of the 1st International Conference on Soil Mechanics and Foundation Engineering, Harvard University, Cambridge, MA.

Boussinesq, J. (1885) Application of potentials to the study of the equilibrium and motion of elastic solids. Paris: Gauthier-Villars.

Buildings Department (2017). Code of Practice for Foundations 2017. Hong Kong SAR Government.

Robert McNeel & Associates (2023)

Rhinoceros User's Guide for Windows. Available at: https://docs.mcneel.com/rhino/7/training-command/en-us/usersguide/Rhino%20User's%20Guide%20for%20Windows.pdf (Accessed: 22/03/2026)

Major Projects Association (2023). *Automation of soil-structure interaction finite element modelling using Python coding and the project BIM model*. Available at: https://majorprojects.org/resources/automation-of-soil-structure-interaction-finite-element-modelling-using-python-coding-and-the-project-bim-model/ [Accessed 27/04/2026]

The Application of Multi-Temporal Unmanned Aerial Vehicle ("UAV") Imagery for Automated Landslide Identification

Leslie W. H. Tsang
Geotechnical Engineering Office, Civil Engineering and Development Department, Government of the HKSAR of the People's Republic of China, Hong Kong, China

Eugene Y. M. Tam
Survey Division, Civil Engineering and Development Department, Government of the HKSAR of the People's Republic of China, Hong Kong, China

Danny Yung
Halcrow China Limited

ABSTRACT

As extreme rainfall events driven by climate change become more frequent and severe, the window for effective disaster response narrows. Timely post-event assessments of natural hillside conditions are therefore increasingly critical for effective landslide risk management. Unmanned Aerial Vehicle ("UAV")-based surveys coupled with an automatic landslide detection algorithm offer high-resolution and accurate terrain data necessary for rapid landslide identification. However, the strict limitation of UAV operation of flight height and Visual Line of Sight ("VLOS") hinders efficient data acquisition in remote terrains or suburban areas. Under the Low-altitude Economy Regulatory Sandbox ("Sandbox"), it permits pilot trials for the unconventional UAV Beyond Visual Line of Sight ("BVLOS") operations, including extended flight height to 1000ft and automated UAV flights control by an off-site computer control platform. These break-through applications open up the opportunity for using UAVs for reliable, quick and efficient large area landslide identification.

The paper presents the findings of the study, which leverages the Sandbox application for BVLOS operation. Based on the data obtained from pre- and post-rainstorm surveys by UAV, an automated algorithm was developed by comparing the Normalised Difference Vegetation Index ("NDVI") georeferenced images and the high-density photogrammetry point clouds to identify terrain surface changes for the formulation of a fully automated landslide identification workflow.

1 INTRODUCTION

Regional landslide identification for natural hillsides commonly adopts Aerial Photo Interpretation ("API") from airborne instruments such as fixed-wing aircraft or helicopters, involving the recognition of tonal contrast, shape, texture, and contextual indicators. However, due to the congestion in the flight zones, airborne surveys can only be conducted sparingly every year. The surveys by airborne instruments might also be affected by low-level clouds and mist. All these limitations of airborne surveys lead to delayed updates following major rainstorm events. The rapid development of small Unmanned Aerial Vehicle ("UAV") with higher performance and improved miniaturisation has made it increasingly applicable for landslide mapping and characterisation (Chan et al. 2025, Rossi et al. 2018). The versatility of UAVs renders the production of landslide survey data much quicker than other remote sensing methods. Nevertheless, the limited UAV flight distance coverage under the regulations is still a major challenge. Previously, UAVs had to be maintained within Visual Line of Sight ("VLOS") with the flight height limited to 300ft (about 90m) for standard operation. It makes large area landslide identification for natural hillsides so inefficient that it is nearly impractical to carry out.

Given the above challenges, the recent development of the Low-altitude Economy ("LAE") under the Transport and Logistics Bureau has opened up the opportunity of wider application of UAVs for landslide identification. Under the LAE Regulatory Sandbox ("Sandbox"), the flight height can be considerably extended and UAVs can be flown Beyond Visual Line of Sight ("BVLOS"), subject to the approval of the Civil Aviation Department ("CAD"). This significantly increases the efficiency of UAV surveying and

renders its application to regional landslide identification practical. On the other hand, the application of BVLOS can be used together with the pre-defined flight path for the UAVs, which can be deployed from a dock station placed near the area of interest. Under this operation mode, the control of the UAVs is not by an on-site remote controller but instead by an off-site control platform manned by the pilot to perform automatic flights, without the need to have any personnel on site. This significantly reduces the mobilisation time and human resource costs, in particular for routine regular UAV flights for large area landslide identification.

While the use of UAVs with the BVLOS condition offers unparalleled advantages for landslide identification, the interpretation of data collected is still very labour-intensive. The manual cognitive recognition and interpretation of the multi-temporal imagery can be inefficient, particularly when repeated monitoring is required, which creates a practical need for automated landslide identification tools.

Against this background, the Geotechnical Engineering Office and the Survey Division of the Civil Engineering and Development Department ("CEDD") and Halcrow China Limited ("Halcrow") had jointly carried out a study using UAVs flown at an extended flight height under BVLOS to carry out surveys with multi-temporal RGB and multi-spectral images. Off-site automatic UAV flight under BLOVS controlled by a UAV flight platform was also tested for repeated flights using the same pre-defined flight paths. The collected data formed the basis to develop and calibrate an automation data processing algorithm involved in the detection of landslides using Normalised Difference Vegetation Index ("NDVI") and photogrammetry point cloud data. This paper discusses the UAVs flights and surveys conducted, methodological development of the automated process and the comparison of outputs with a view to formulating a fully automated landslide identification workflow, from UAV flights to landslide polygon outputs.

2 BVLOS WITH EXTENDED FLIGHT HEIGHT

According to regulation requirements, the maximum flight height for general small UAV operations is 300ft (about 90m) above the ground, and the remote pilot must maintain VLOS to the UAV at all times. Under the Sandbox, the CEDD obtained the approval from the CAD for an Advanced Operation Permit ("AOP") to relax the flight height to 1000ft (about 300m) and flight distance to 5km under the BVLOS condition. This significantly improves the efficiency of large-scale inspections of natural hillsides after heavy rainfall. The trial site selected was in Sai Kung (Figure 1), covering an area of about 50 km2. Restricted Flying Zones ("RFZ"), paragliding zones (Long Ke Wan, Pak Tam Au and Sai Wan) and helipads are excluded from the survey blocks.

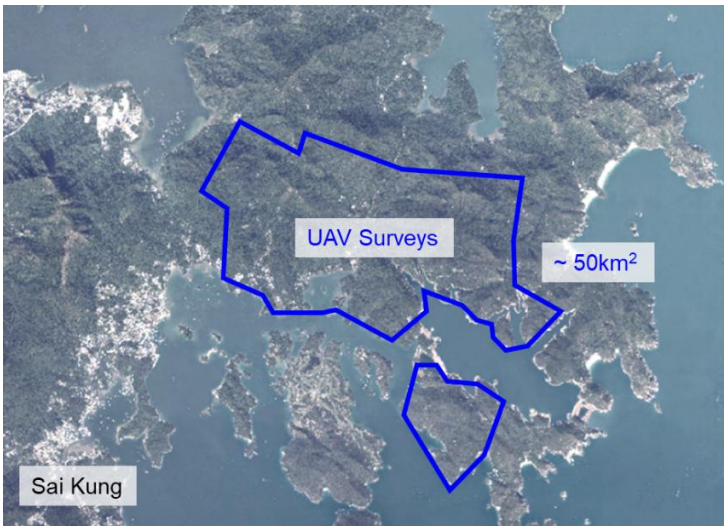

Figure 1 – UAV surveys at an altitude of 1000ft under the BVLOS condition in the Sai Kung area

Pre-rainstorm flights were carried out from May to July 2025 to collect the baseline data. The UAV models are the DJI Mavic 3M and 3E equipped with Real-Time Kinematic ("RTK"). The RGB image quality is 20 MP and the multi-spectral image quality (green, red, red-edge and near infrared) is 4 x 5MP. The forward overlapping is 75% to 80%, whereas the sideways overlapping is 70% to 75%. It must be noted that a high overlap ratio should be maintained for the formation of good quality photogrammetry models suitable

for the purpose of landslide detection. The time required to cover the 50 km2 area by UAV survey using the flight altitude of 1000ft was about 40 hours, which reduced the overall survey operation time to about one-fifth as compared to flights using the ordinary height of 300ft.

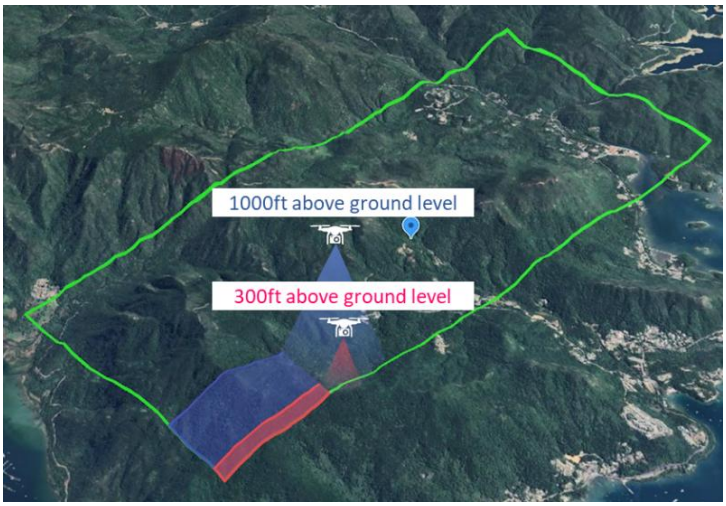

Figure 2 – Significant increase in efficiency at flight altitude of 1000ft

Heavy rainfall hit the eastern part of Hong Kong in early August 2025, and post-rainstorm UAV surveys were carried out in late August and September 2025, adopting the same flight settings to ensure consistent data quality. The collected pre- and post-rainstorm data were then used to develop and calibrate the automated landslide identification algorithm based on change detection on NDVI and photogrammetry 3D models. The software DJI Terra was used for forming photogrammetry models and point cloud generation. It must be noted that the point cloud generated using photogrammetry technology represents the Digital Surface Model ("DSM"), capturing the vegetation canopy instead of the actual ground level.

3 BVLOS WITH OFF-SITE AUTOMATED FLIGHT CONTROL

In another Sandbox pilot project under the LAE Sandbox, CEDD conducted the trial use of advanced remote UAV dock stations together with the use of a UAV control platform to conduct automated flights for repeated data collection at target facilities or areas. This system combines the two operating modes of UAVs, BVLOS and off-site automatic flight control, breaking through the technical limitations of previous UAV flight operations that required VLOS and on-site personnel. It significantly expands the application scenarios of UAVs and enables rapid and large-scale natural hazard monitoring in a short period of time. This operation mode deploys the UAV from a dock station placed in a designated location and the UAV is fully controlled by an off-site computer control platform. The pilot oversees the entire flight operation using the computer control platform, without any personnel on site. In addition to that, the flight path of the UAV can be pre-defined in the UAV control platform, and the UAV will be flown automatically to survey the hillside of interest repeatedly.

The test site selected for the automated flight is the hillside above the Yiu Hing Road landslide scar in Hong Kong East (Figure 3). The UAV dock station was placed in the Tai Tam Country Park Quarry Bay Management Centre, located about 1.5km from the area of interest. The model of the UAV is the DJI Matrice 4E, equipped with cameras with a resolution of 48MP. The flight height is set at 300ft (about 90m) with an overlapping about 70%-80%. The surveyed area is about 0.3km2. The automatic flight operation was controlled completely off-site using the UAV flight platform. By deploying the UAV directly from the dock stations, it enables very short mobilisation time and thereby provides a very reliable and quick UAV presence in the case of emergency situations. It is estimated that it could reduce the required survey time to about one-third as compared to the traditional flight mode.

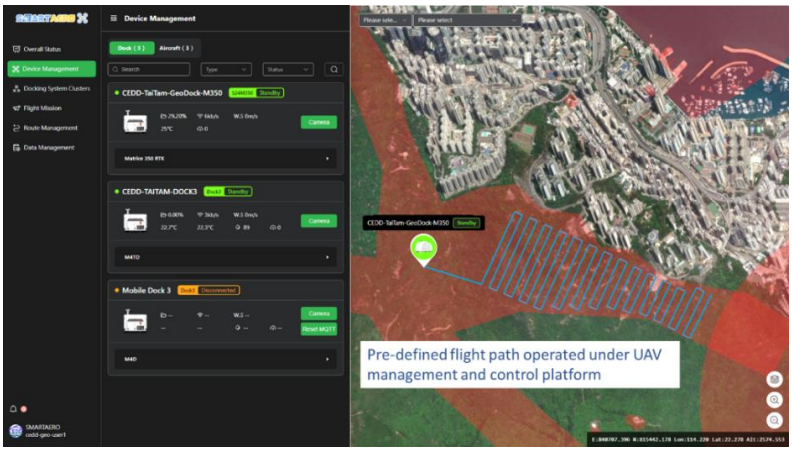

Figure 3 – Automatic flight in Hong Kong East

4 AUTOMATED LANDSLIDE IDENTIFICATION ALGORITHM

The above pioneering UAV flight modes make the survey process very efficient and thereby remarkably revolutionise the application of UAVs for landslide detection. Nevertheless, the traditional manual interpretation of collecting spectral and geometrical data, such as vegetation loss, fresh ground exposure, scarp formation, surface erosion and soil displacement, is very inefficient. This calls for a computerised landslide data processing algorithm to automate the process. The automated landslide identification algorithm developed consists of two parallel analytical branches (Figure 4), i.e. an NDVI-based spectral change-detection branch and a point cloud/DSM-based surface-change branch. Both branches operate on repeated UAV survey datasets and are designed to identify localized surface disturbance by direct inter-epoch comparison with an earlier terrain state. The numerical parameters of the algorithm developed, including threshold selection and resampling factors, are configurable to suit the need of application scenarios. The calibrated parameters used in this study correspond to 26 landslides selected in the present survey in Sai Kung, which have an average plan size of about 110m2 and a minimum area of 13m2, to discard small landslides and noise.

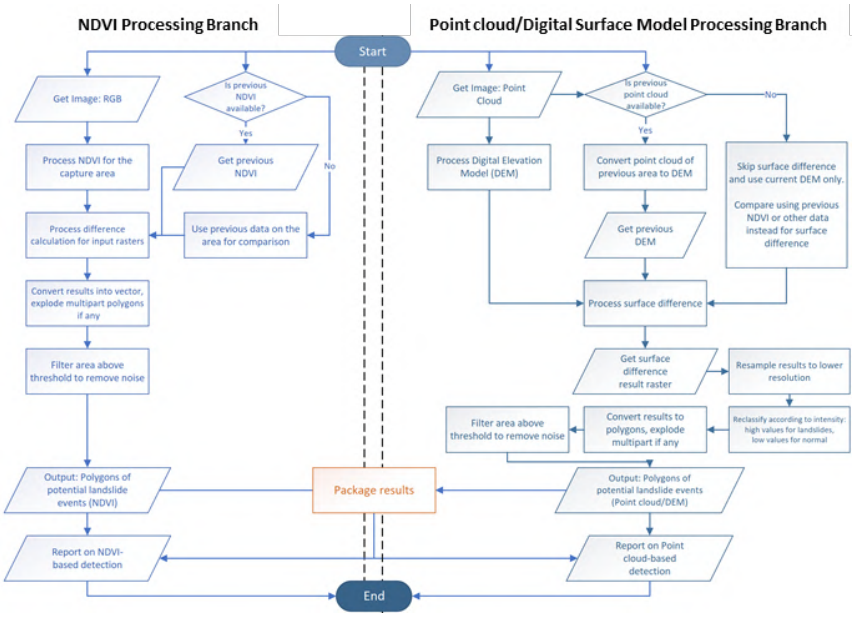

Figure 4 – Data processing workflow for automated landslide identification

Both branches share a common conceptual structure consisting of input preparation, resampling, thresholding, possible-feature extraction and output generation. This parallel structure was adopted to maintain consistency across the workflow while allowing the system to evaluate two different expressions of

terrain change. The image-based branch emphasises spectral disturbance, whereas the point cloud branch emphasises terrain geometry and surface change.

4.1 Normalised Difference Vegetation Index (NDVI) Processing

Time-series normalised difference vegetation index (NDVI), derived from remote sensing images, is widely applied in various fields, including vegetation change monitoring (Chu et al., 2019). The NDVI branch uses the red and near-infrared bands from repeated UAV raster products (Baret et al., 1989, United States Geological Survey, 2019):

$$NDVI = \frac{NIR - R}{NIR + R} \tag{1}$$

where NIR is the near-infrared channel and R is the red channel in the RGB (Red, Green, and Blue) imagery.

In the image-based branch, orthophoto products derived from consecutive UAV surveys were processed into raster layers suitable for NDVI-based change analysis. The purpose of this branch is to enhance areas exhibiting vegetation loss, fresh ground exposure, or other localised disturbance revealed by multi-temporal NDVI, which is a strong indicator of landslide activity.

The implementation preserves raster metadata from GeoTIFF inputs, including image dimensions, projection, and transform parameters, so that the output rasters remain georeferenced and could be used in the later vectorization and overlay stages of processing. After the NDVI was calculated for both survey epochs, a difference raster was generated to quantify change between the earlier and later captures. Figure 5 shows an example of this operation.

Figure 5 - Difference calculated from the NDVI rasters

The difference raster is then resampled by cubic-spline to support the automated screening of potential landslides and to suppress noise. The raster is then converted into a binary change mask using an NDVI difference threshold. The NDVI change threshold values below the threshold value of 0.175 were found to primarily represent background variability associated with illumination differences and minor seasonal vegetation change, whereas values exceeding the threshold consistently corresponded to visibly disturbed or sparsely vegetated ground, indicating evidence of landslide. Figure 6 below shows the results of conversion.

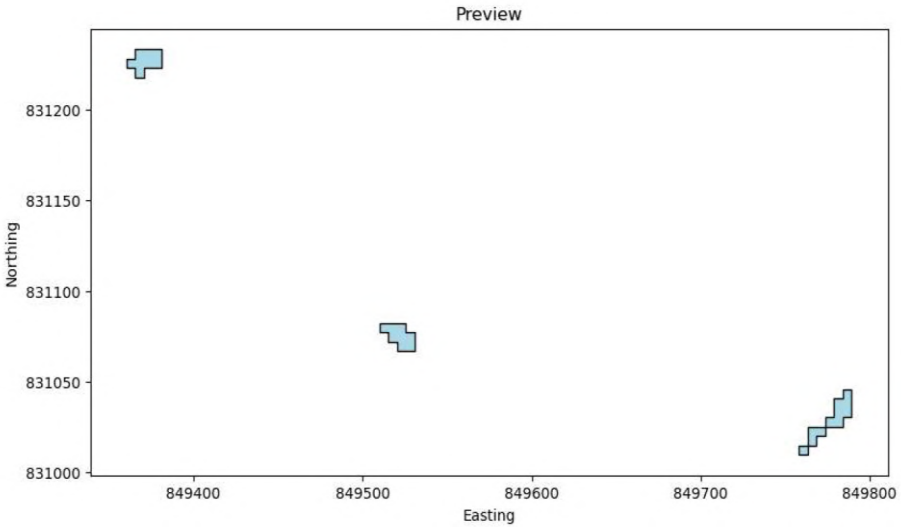

Figure 6 - Resulting polygons after the thresholding
(scaling factor of 0.015)

The thresholding stage converted a continuous change surface into a practical decision layer that could be passed into vector processing for mappable GIS outputs without requiring manual delineation. The extracted features are then overlaid on orthophotography (Figure 7) to allow direct comparison between automatically detected possible zones and visible site conditions. This branch, therefore, converts image-derived spectral change into interpretable spatial outputs suitable for engineering review.

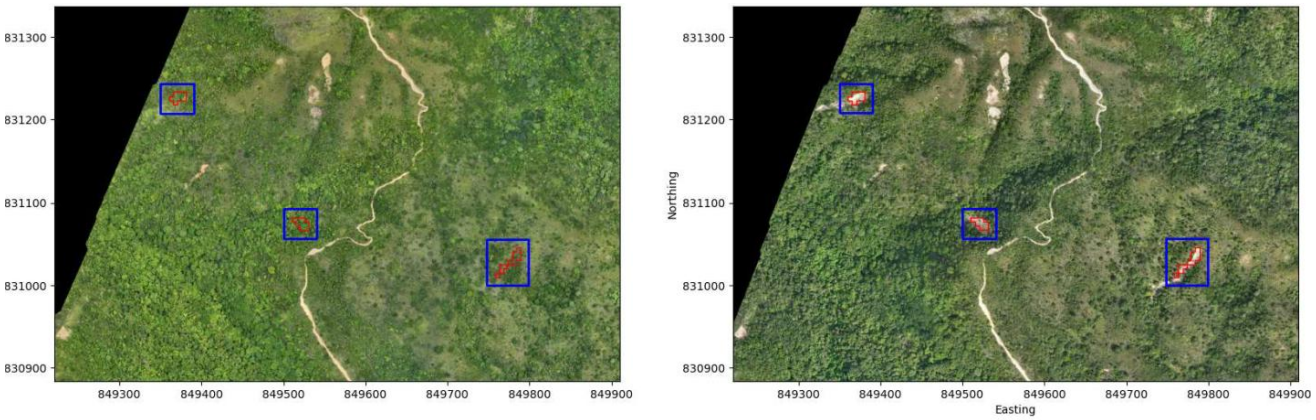

Figure 7 - Comparison of the UAV captures by NDVI branch with the automatically detected landslide events
(left - pre-rainstorm captures, right – post-rainstorm captures)

4.2 Point Cloud/Digital Surface Model (DSM) Processing

In the point cloud branch, three-dimensional survey products from consecutive UAV surveys are compared to identify topographic changes associated with landslide development, reactivation, or related surface disturbances. The workflow uses aligned point cloud data to detect geometric differences between survey epochs and to highlight areas of possible elevation change, material removal, erosion, or localized deformation. The point cloud branch is therefore particularly relevant where changes may be morphologically evident but only weakly expressed in vegetation response. Both pre- and post-rainstorm files are converted into high-resolution DSM for surface difference calculation. To automate localisation and filter noise, the surface difference raster is resampled by an upscale factor. Figure 8 shows the result of the surface difference calculation for both DSMs.

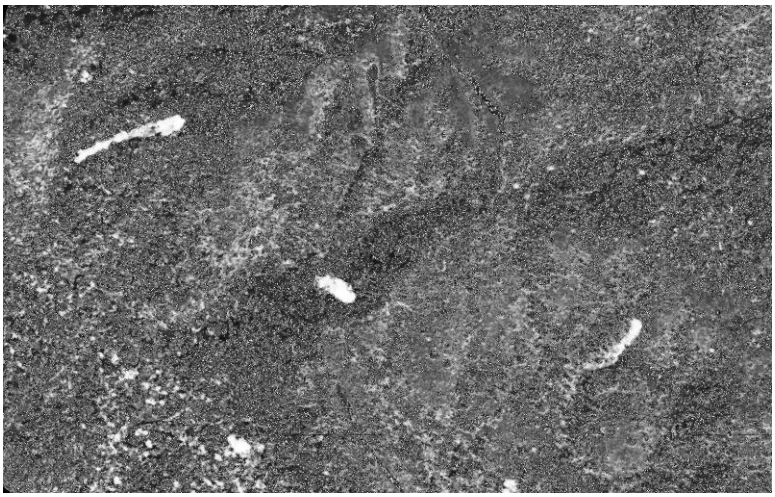

Figure 8 - Surface difference calculation between the pre- and post-rainfall DSMs.
(upscale factor of 0.03)

The resampled results are filtered by intensity, where high values (bright areas) are identified as landslide zones. The raster is then converted into a binary change mask by thresholding, which was calibrated through visual API comparison of orthophotography. These areas are converted into a vector shapefile and then overlaid on orthophotography (Figure 9) to allow direct comparison between automatically detected possible zones and visible site conditions.

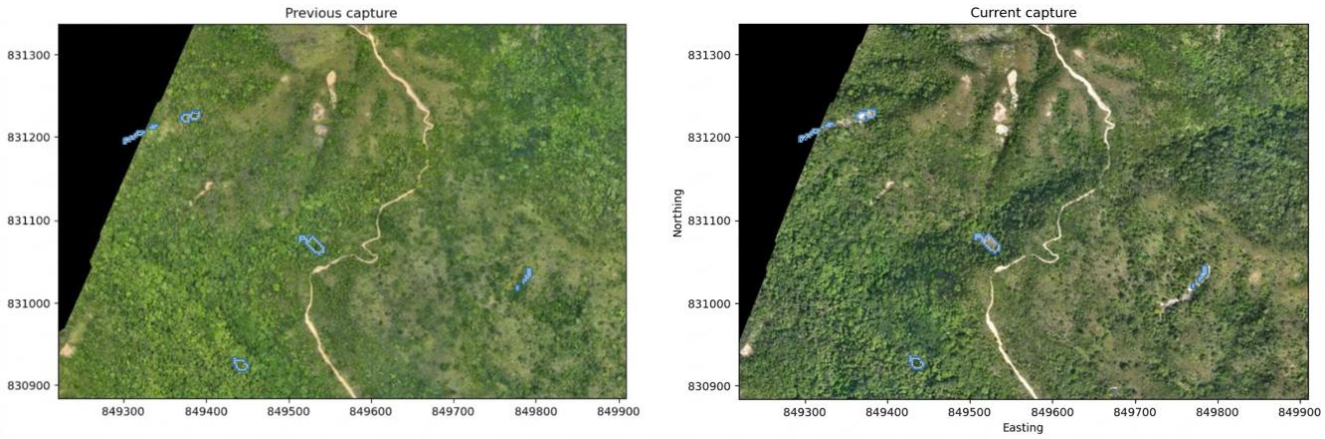

Figure 9 - Comparison of the UAV captures by point cloud branch with the automatically detected landslide events
(left - pre-rainstorm captures, right – post-rainstorm captures)

5 Discussion on the Outputs

5.1 Results comparison

The possible landslide identified from change detection of visual RGB images, multi-spectral images and point cloud model from UAV surveys are compared. In most situations, the three methods of landslide identification tally with each other. For example, in Figure 10, it shows the comparison of RGB images before and after the rainstorm, which clearly indicates that the Feature E_L2 is a newly formed landslide. When change detection is made using the multi-spectral images, the landslide is very clearly identified. The same is observed when the point cloud model is compared. In this example, the change detection using multi-spectral image and the point cloud model tally very well with the visual RGB images, which corresponds to most of the sample landslide cases in the study.

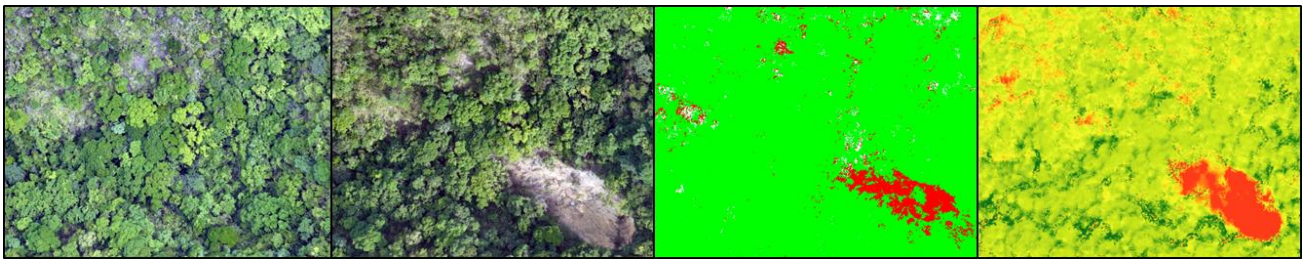

(a) (b) (c) (d)

Figure 10 – Feature E_L2 (a) Pre-rainstorm RGB image, (b) Post-rainstorm RGB image, (c) NDVI difference, (d) Photogrammetry surface difference

There are, however, some situations where the NDVI images indicate a potential landslide, but it does not show in the point cloud changes. In Figure 11, the RGB images show very slight de-vegetation at the Feature E_L3A. In the NDVI image, there is a strong indication of vegetation disturbance. However, in the point cloud height comparison, there is no landslide observed at that location. This indicates that this location is likely to have vegetation disturbance only.

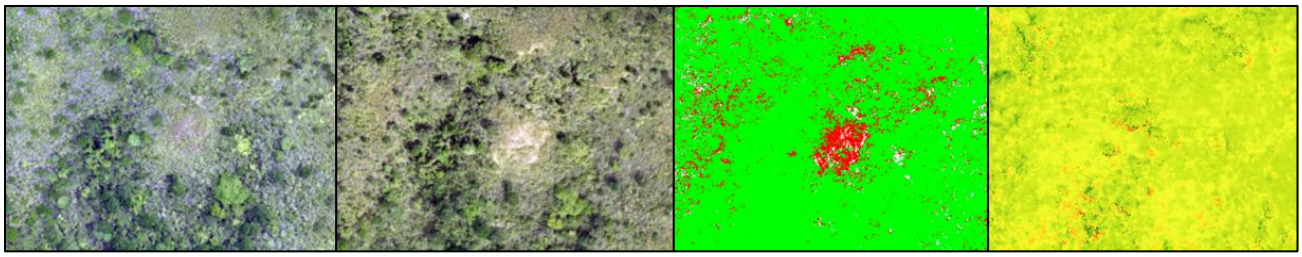

(a) (b) (c) (d)

Figure 11 – Feature E_L3A (a) Pre-rainstorm RGB image, (b) Post-rainstorm RGB image, (c) NDVI difference, (d) Photogrammetry surface difference

A comparison is also made for some existing landslide scars. In Figure 12, the scar was already captured in the pre-rainstorm images. In the post-rainstorm image, no significant enlargement is observed. The NDVI image matches with the RGB image that only the vegetation at the edge of the landslide scar is slightly worsen, while the point cloud comparison confirms that there is not much difference, save for the faint sunken areas.

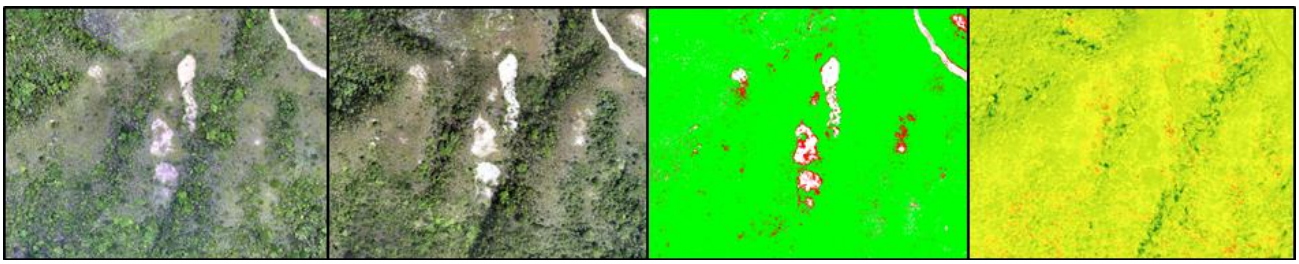

(a) (b) (c) (d)

Figure 12 – Feature E_O1 (a) Pre-rainstorm RGB image, (b) Post-rainstorm RGB image, (c) NDVI difference, (d) Photogrammetry surface difference

In some situations, a large area of depression is evident but is not captured by the NDVI-based analysis. As illustrated in Figure 13, the RGB images indicated that there could be tree falls in the area. The corresponding NDVI images, however, do not exhibit clear spectral data indicating signs of landslides, whereas the point cloud comparison reveals a substantial depression of vegetation canopy, which may be associated with localised ground failure occurring beneath the canopy cover. This example highlights the limitation of NDVI-based detection in densely vegetated terrain and demonstrates the added-value of the 3D surface change analysis for identifying potential sign of landslide that is obscured in the spectral images.

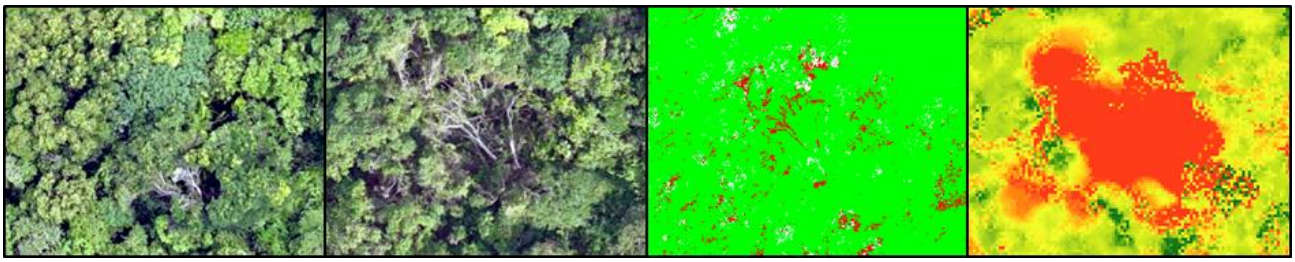

(a) (b) (c) (d)

Figure 13 – Feature E_P1 (a) Pre-rainstorm RGB image, (b) Post-rainstorm RGB image, (c) NDVI difference, (d) Photogrammetry surface difference

In this respect, the two branches provide different types of detection outputs, with the NDVI branch offering broader spectral disturbance screening and the point cloud branch offering superior spatial definition for depression mapping. The outputs of both branches offer different indicators of potential landslides, which can be followed up by further detailed surveys if needed.

6 CONCLUSION

The paper discussed the formulation of a fully automated landslide identification workflow using multi-temporal UAV surveys. The success in adopting an extended flight height of 1000ft above ground level marks an important breakthrough of using UAV surveys for practical uses in large area landslide identification. Another important milestone is the execution of off-site automated UAV flights deployed from dock stations, which makes repeated large area surveys very effective and significantly reduces the UAV mobilisation time. Based on the multi-temporal UAV surveys, a two-branch landslides identification data processing workflow was developed, calibrated by the landslides observed in the area. The combination of the above pioneering technological developments successfully enables the application of fully automated landslide identification that revolutionised the application of UAVs for landslide detection.

ACKNOWLEDGEMENTS

This paper is published with the permission of the Head of the Geotechnical Engineering Office and the Director of the Civil Engineering and Development Department of the Government of the Hong Kong Special Administrative Region.

REFERENCES

Baret F., Guyot G. and Major D.J. 1989. TSAVI: A vegetation index which minimizes soil brightness effects
on LAI and APAR estimation. *Canadian Symposium on Remote Sensing Geoscience and Remote Sensing Symposium (CSRS)*, pp. 1355–1358.
https://doi.org/10.1109/IGARSS.1989.576128.

Chen, B., Maurer, J. and Gong, W. 2025. Applications of UAV in landslide research: a review. *Landslides* 22, 3029–3048 (2025).
https://doi.org/10.1007/s10346-025-02547-2

Chu H.S., Venevsky S., Wu C. and Wang M.H. 2019. NDVI-based vegetation dynamics and its response to climate changes at Amur-Heilongjiang River Basin from 1982 to 2015. *Science of The Total Environment* 650, Part 2 pp. 2051-2062
Sci. Total Environ., 650 (2019), pp. 2051-2062

Li S., Xu L., Jing Y., Yin H., Li X. and Guan X. 2021. High-quality vegetation index product generation: A review of NDVI time series reconstruction techniques. *International Journal of Applied Earth Observations and Geoinformation* 105 (2021)

https://doi.org/10.1016/j.jag.2021.102640

Ove Arup & Partners Hong Kong Limited (2021). *Interim Study Report on Enhancing Automatic Identification of Recent Natural Terrain Landslides from Aerial Photographs.* Civil Engineering and Development Department, Government of the Hong Kong Special Administrative Region, Hong Kong, China.

Rossi G., Tanteri L., Tofani V., Vannocci P., Moretti S. and Casagli N. 2018. Multitemporal UAV surveys for landslide mapping and characterization. *Landslides* 15, 1045–1052 (2018). https://doi.org/10.1007/s10346-018-0978-0

Shi, W., Zhang, M., Ke, H., Fang, X., Zhan, Z., & Chen, S. (2020). Landslide Recognition by Deep Convolutional Neural Network and Change Detection. *IEEE Transactions on Geoscience and Remote Sensing*, 59(6), 4654- 4672.

United States Geological Survey (2019). Landsat Normalized Difference Vegetation Index. USGS Website. https://www.usgs.gov/landsat-missions/landsat-normalized-difference-vegetation-index

Back-analysis of Excavation-Induced Ground Settlement in Hong Kong Using Mohr-Coulomb and Hardening Soil Models

P.O. Tang, A.K.M. Lam, Y.X Huo
Ove Arup & Partners Hong Kong Limited, Hong Kong

W. Cheang; S. Rajbhandari
Seequent Limited

ABSTRACT

Deep basement excavations are routine in Hong Kong's dense urban environment, where excavation and lateral support (ELS) performance is often governed by serviceability criteria related to retaining wall deflection and ground settlement. Numerical assessment of excavation-induced ground movements in local practice commonly adopts the linearly elastic–perfectly plastic Mohr–Coulomb (MC) model in PLAXIS 2D as a baseline. However, the MC model employs a single elastic stiffness for both loading and unloading, which may be inconsistent with excavation stress paths and can lead to unrealistic deformation components, such as excessive unloading-induced heave.

To bridge theory and practice in the spirit of the HKIE Geotechnical Division Annual Seminar theme, this paper presents a comparative back-analysis of a deep basement excavation in Hong Kong with comprehensive monitoring records, using both the MC model and the Hardening Soil (HS) model. The HS model is adopted to represent stress-dependent, non-linear soil stiffness and to distinguish stiffness during primary loading from unloading/reloading. Model set-up, parameter selection strategy and staged construction simulation are described. Predicted ground settlement profiles are compared with field measurements to illustrate the implications of constitutive model choice on deformation assessment.

The paper concludes with practical observations for Hong Kong practitioners on when advanced constitutive modelling may be warranted for movement-sensitive ELS designs, and how monitoring-based back-analysis can be used to calibrate soil stiffness and improve confidence in deformation prediction.

Keywords: Deep excavation; ELS; Ground settlement; Back-analysis; Mohr–Coulomb; Hardening Soil; PLAXIS 2D.

1 INTRODUCTION

1.1 Background

Deep excavations for basements, stations, and underground infrastructure are a defining feature of geotechnical engineering practice in Hong Kong. In dense urban settings, excavation-induced ground movements can affect adjacent buildings, utilities, and transport assets; therefore, ELS design is frequently controlled by serviceability performance rather than ultimate limit states. Field observations and case histories remain essential to build confidence in prediction methods and to refine design conservatisms, particularly where the ground profile is heterogeneous and the in-situ stress history is difficult to quantify (e.g., residual soils and weathered rock) (Chan 2003).

In Hong Kong, numerical modelling is widely used to estimate wall deflections and ground settlements for ELS works, with the linearly elastic–perfectly plastic Mohr–Coulomb (MC) constitutive model commonly adopted as the default baseline in finite element analysis. While MC is attractive due to its simplicity and limited parameter requirements, it represents pre failure stiffness using a single linear elastic modulus, which is applied identically in loading and unloading. For excavation problems dominated by unloading and stress-path dependency, this simplification may not reliably represent deformation behaviour, and unrealistic components (e.g., exaggerated heave during unloading) can be produced in certain cases (Chan et al. 2021).

More advanced constitutive models, such as the Hardening Soil (HS) model, provide an alternative framework to represent nonlinear stress–strain response and to distinguish stiffness under primary loading from

unloading/reloading stiffness. Local and regional studies have reported that HS can improve the realism of predicted deformation profiles for excavations, particularly for ground surface settlement trough shape and for unloading dominated responses where MC may be less reliable (Chan et al. 2021).

1.2 Objectives

Against this backdrop, this paper presents a Hong Kong case study with comprehensive ground movement monitoring data and undertakes a comparative back analysis using PLAXIS 2D with both MC and HS models. The objectives are to:

(i) Compare the capability of MC and HS models in reproducing measured ground settlement associated with staged excavation;

(ii) Illustrate how constitutive model assumptions (especially stiffness under unloading) influence predicted ground movements; and

(iii) Provide practical observations that support calibration and model selection for movement sensitive ELS designs in Hong Kong, consistent with the Annual Seminar emphasis on "bridging theory and practice".

2 CONSITUTIVE SOIL MODELS

2.1 Mohr-Coulomb Model (MC)

The linearly elastic–perfectly plastic Mohr–Coulomb model is widely used in routine design of deep excavations, including Hong Kong applications. It is parameter efficient (e.g., strength and a single elastic stiffness), and its failure criterion remains practical for stability assessment when appropriate strength parameters are adopted.

For deformation prediction, the key limitation is that MC represents soil stiffness prior to yielding using a single linear elastic modulus and Poisson's ratio, without capturing nonlinear stiffness degradation with strain. Importantly for excavation, MC applies the same elastic stiffness in both loading and unloading, even though excavation-induced stress paths commonly involve significant unloading and reloading components. This can lead to unrealistic movement predictions in some scenarios, including overestimation of unloading heave and misrepresentation of settlement profiles behind retaining walls.

The MC model is a simple and widely used constitutive soil model in Hong Kong practice for predicting both stability and deformation of geotechnical structures, including deep excavations and slopes. It assumes linear elastic behaviour prior to yielding and perfectly plastic behaviour governed by the Mohr–Coulomb failure criterion, as illustrated in **Figure 1**. The model requires a limited number of input parameters, making it attractive for routine design applications.

However, soil stiffness in reality is stress-dependent, strain-dependent and stress-path dependent. In excavation problems involving significant unloading, the use of a single elastic stiffness for both loading and unloading in the MC model can lead to unrealistic deformation predictions, such as exaggerated unloading heave and misrepresentation of ground settlement profiles. While the MC model remains reliable for strength-controlled problems (e.g. overall stability), caution is required when it is used for deformation prediction in unloading-dominated problems such as deep excavations.

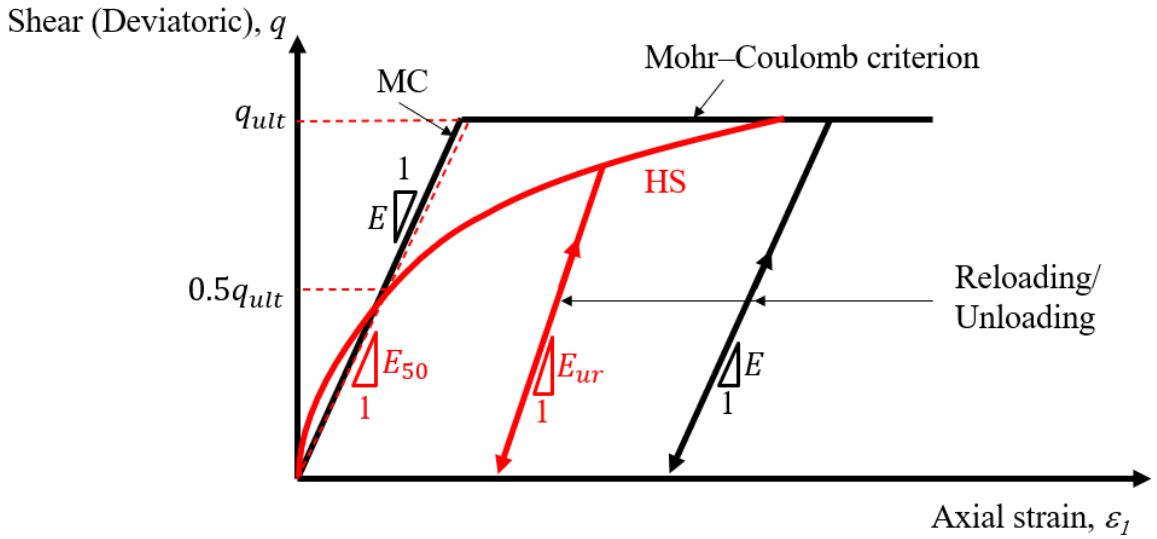

Figure 1 Stress-strain-strength behaviour of the MC and HS models in drained triaxial test

2.2 Hardening Soil Model (HS)

The Hardening Soil (HS) model is an isotropic hardening constitutive model formulated within the framework of elasto-plasticity (Schanz et al., 1999). While the ultimate failure condition is still governed by the Mohr–Coulomb criterion, the HS model provides a more realistic stress-strain relationship by incorporating:

(i) Non-linear stiffness degradation;
(ii) Stress-dependent stiffness; and
(iii) Distinct stiffness parameters for primary loading, primary compression and unloading/reloading.

Three stiffness parameters are used: the secant stiffness in drained triaxial loading E_{50}^{ref}, the tangent stiffness in oedometer loading E_{oed}^{ref}, and the elastic unloading/reloading stiffness E_{ur}^{ref}. This distinction is particularly relevant for excavation problems, where unloading and stress relief dominate soil deformation behaviour. Stress-dependent stiffness in HS model can be represented by the following equations:

$$E_{50} = E_{50}^{ref}\left(\frac{c'\cos\varphi' + \sigma_3'\sin\varphi'}{c'\cos\varphi' + p_{ref}\sin\varphi'}\right)^m$$

$$E_{oed} = E_{oed}^{ref}\left(\frac{c'\cos\varphi' + \sigma_1'\sin\varphi'}{c'\cos\varphi' + p_{ref}\sin\varphi'}\right)^m$$

$$E_{ur} = E_{ur}^{ref}\left(\frac{c'\cos\varphi' + \sigma_3'\sin\varphi'}{c'\cos\varphi' + p_{ref}\sin\varphi'}\right)^m$$

where:

E_{50}^{ref}, E_{oed}^{ref}, E_{ur}^{ref} are reference stiffness at reference confining pressure p_{ref};σ_1', σ_3' are major and minor effective principal stresses; m is the stress-dependent power.

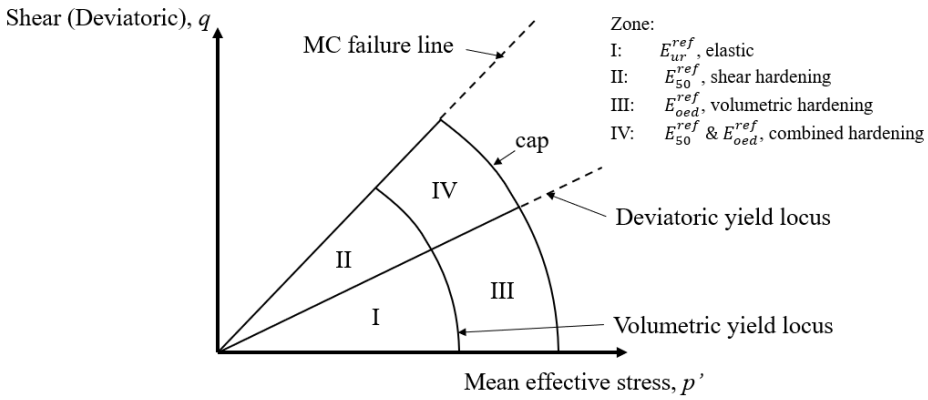

(a)

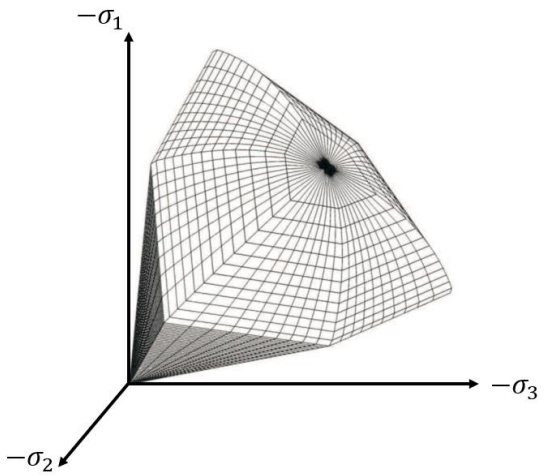

(b)

Figure 2 (a) Double yield loci of the HS model, and (b) the HS model in principal stress space

HS parameters can be derived from laboratory tests (e.g., drained triaxial and oedometer tests), but uncertainties related to sample quality and representativeness are well recognised, especially in heterogeneous Hong Kong ground. Consequently, field tests and back analysis of well documented case histories are frequently used to calibrate stiffness parameters for practical design. In Hong Kong engineering design practice, Standard Penetration Test (SPT) is commonly adopted to determine the stiffness of soils. Empirical correlations between SPT-N values and large strain soil stiffness for geotechnical engineering problem with MC model are well established, the empirical correlations are reviewed and suggested in Chan 2001, and are summarized in **Table 1**. Some local back-analysis studies from Hong Kong have been also carried out to establish the empirical correlation to soil stiffnesses for HS model. Chan et al. 2021 summarises the suggested correlations and relationships between soil stiffnesses as summarized in **Table 2**.

Table 1 Empirical correlations between SPT-N values and Young's modulus for the MC model

Soil	Modulus of Elasticity, E (MPa)
Fill	1.5 N
Alluvium	1.5 N
CDG/ HDG	2.0 N

*N means uncorrected SPT-N values.

Table 2 Suggested Relationships between HS Stiffness Parameters

HS Model Input Parameters	Relationship	Reference
E_{50}^{ref}	1.2 N (MPa), for p^{ref} = 100 kPa	Hsiung & Dao (2014)
E_{oed}^{ref}	$1.0E_{50}^{ref}$, for sand	Schanz, Vermeer and Bonnier (1999)
	$0.5E_{50}^{ref}$, for soft clays	
	0.7 to $1.0E_{50}^{ref}$ for soils in Hong Kong	Lu et al. (2018), Lee et al. (2008), and Lam (2018)
E_{ur}^{ref}	3 to $6E_{50}^{ref}$, for loose sand	Schanz, Vermeer and Bonnier (1999)
	2 to $4E_{50}^{ref}$, for dense sand	
	3 to $5E_{50}^{ref}$, for clays	
	$3E_{50}^{ref}$	Khoiri & Ou (2013)
	2 to $3E_{50}^{ref}$, for soils in Hong Kong	Lu et al. (2018), Lee et al. (2008), and Lam (2018)
m	0.5 for sands and gravels 0.75 for silts 1.0 for clays	Ohde (1951 – 1955); Janbu (1963), Janbu (1970)

3 CASE STUDY

3.1 Background

The Mass Transit Railway Corporation (MTRC) proposed to construct an airport railway from Hong Kong to Check Lap Kok. Hong Kong Station was going to form the terminus for the Airport Express Line (AEL) to the new airport at Check Lap Kok and also the Lantau Line (LAL). The Station was constructed in three phases as shown in **Figure** 3. Phase III basement excavation works are selected as the case study for back-analysis.

The case study relates to a deep basement excavation forming part of a major underground development in a dense urban area of Hong Kong. The project involved construction of a large plan-area basement supported by diaphragm walls and temporary strutting, with excavation extending to more than 25 m below ground level. Owing to the proximity of sensitive structures and transport infrastructure, excavation and lateral support (ELS) design was governed primarily by serviceability requirements related to ground settlement and wall deformation.

Phase III excavation was instrumented with a comprehensive monitoring system, including diaphragm wall inclinometers, ground settlement markers and groundwater observation points, providing high-quality field data for comparison with numerical predictions. The monitoring system is depicted in **Figure 4**.

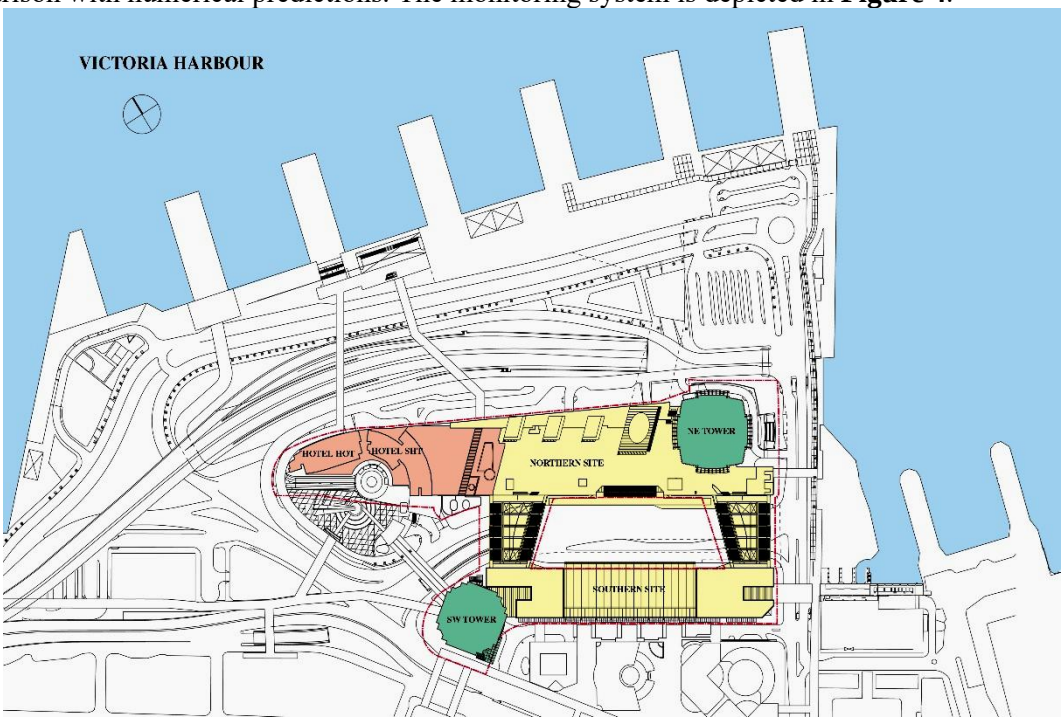

(a)

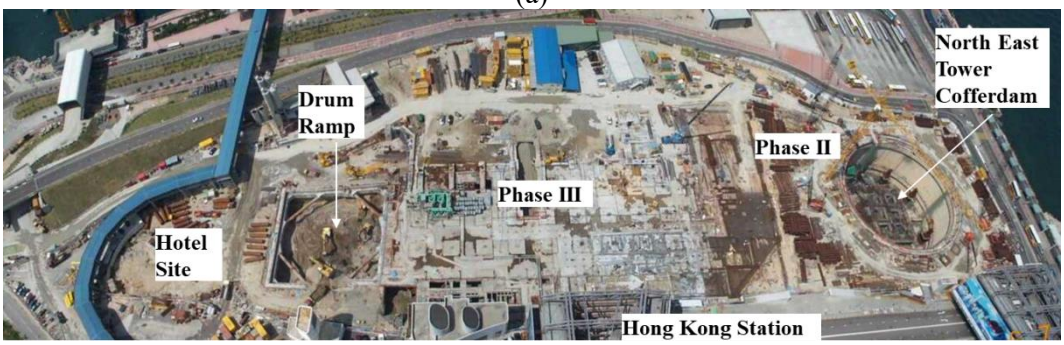

(b)

Figure 3 (a) Overall site layout plan, and (b) Phasing of construction works

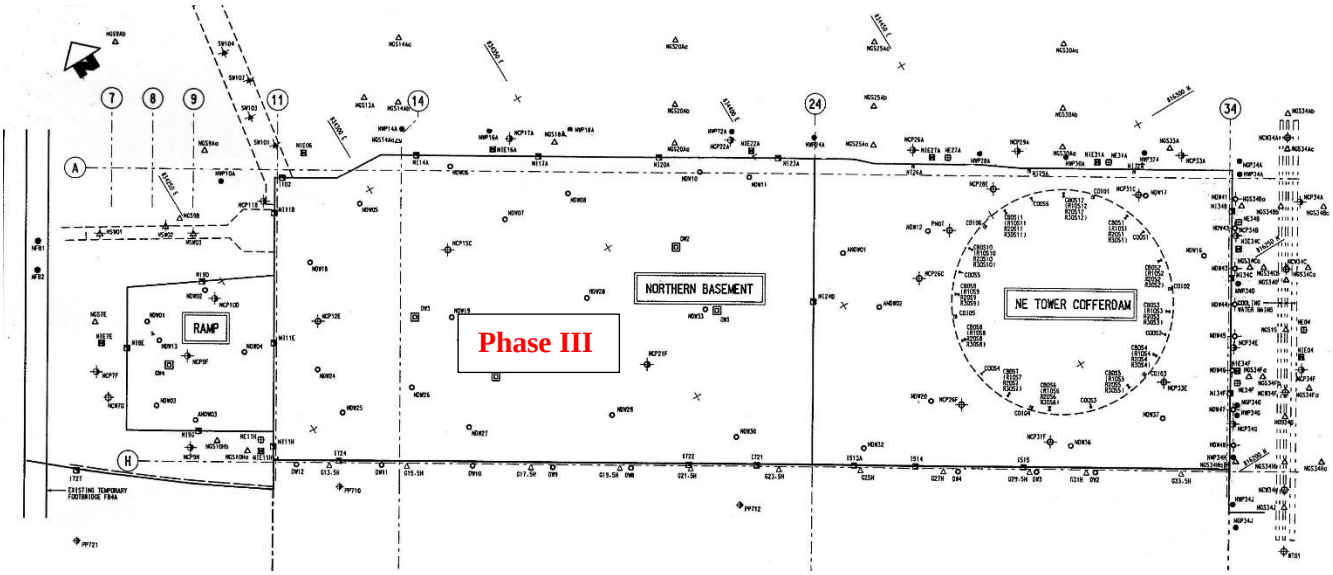

Figure 4 Monitoring and Instrumentation Plan

3.2 Ground Conditions

The site is underlain by typical Hong Kong geological materials comprising fill, marine deposits and alluvium overlying completely decomposed granite (CDG), with bedrock encountered at depth. Based on site investigation records along Gridline A as shown in **Figure 5**, the generalized ground profile consists of:

(i) Fill at ground surface, variable in thickness;
(ii) Marine deposits and/or alluvium, comprising soft to firm silty clay and sandy clay;
(iii) Completely decomposed granite (CDG), transitioning gradually to moderately decomposed granite (MDG) with depth;
(iv) Granite bedrock at greater depth.

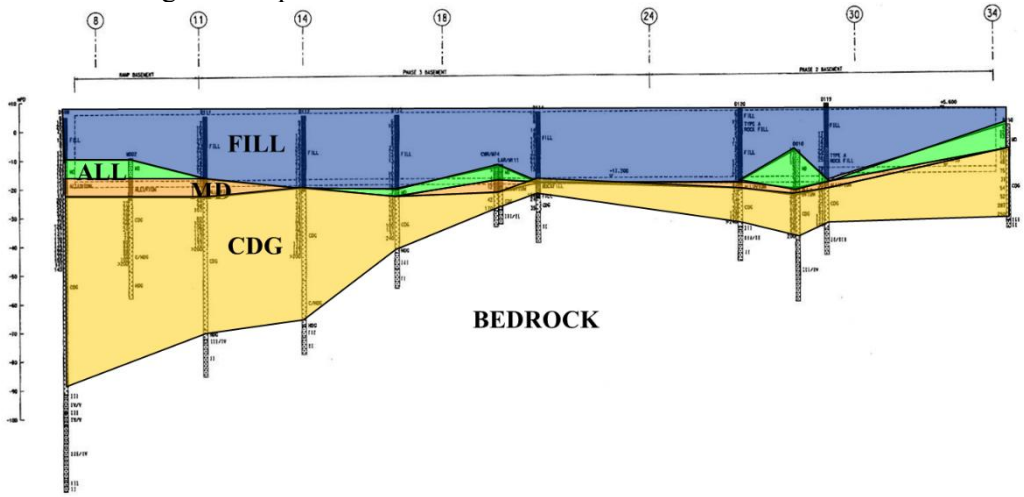

Figure 5 Geological Section along Gridline *A*

Groundwater levels were observed to be close to ground level under long-term conditions, with temporary drawdown implemented during excavation as part of the dewatering strategy. The excavation therefore involved significant unloading of both effective stress and total stress within the soil mass. Such stress paths are known to be sensitive to soil stiffness non-linearity and unloading–reloading behaviour, making this case particularly suitable for comparing the Mohr–Coulomb (MC) and Hardening Soil (HS) models.

3.3 Construction Sequences

The excavation was carried out in a staged manner with the installation of temporary supports at intermediate levels. A simplified summary of the construction sequence adopted for numerical modelling is as follows:
(i) Installation of diaphragm walls extending into the underlying decomposed granite, forming the permanent retaining system.
(ii) Initial excavation to an upper level, followed by installation of the first level of strutting.
(iii) Subsequent staged excavation and installation of additional struts at progressively lower levels.
(iv) Continued excavation to final formation level, with dewatering implemented to control groundwater inflow and pore water pressure beneath the excavation base.
(v) Completion of temporary works prior to construction of permanent basement slabs.
(vi) Backfill the unexcavated side to a higher ground level.

The staged excavation resulted in repeated cycles of unloading and partial reloading of the retained soil mass. The timing and elevation of excavation stages and strut installations were well documented and were explicitly reproduced in the numerical analyses to enable meaningful comparison with measured performance. **Figure 6** shows the design ground profiles and structural elements of the plane-strain PLAXIS models. Note that the fill layer at the excavation side was compacted before excavation commenced, hence its friction angle Φ' was set larger than uncompacted fills, as compared in **Table 3**.

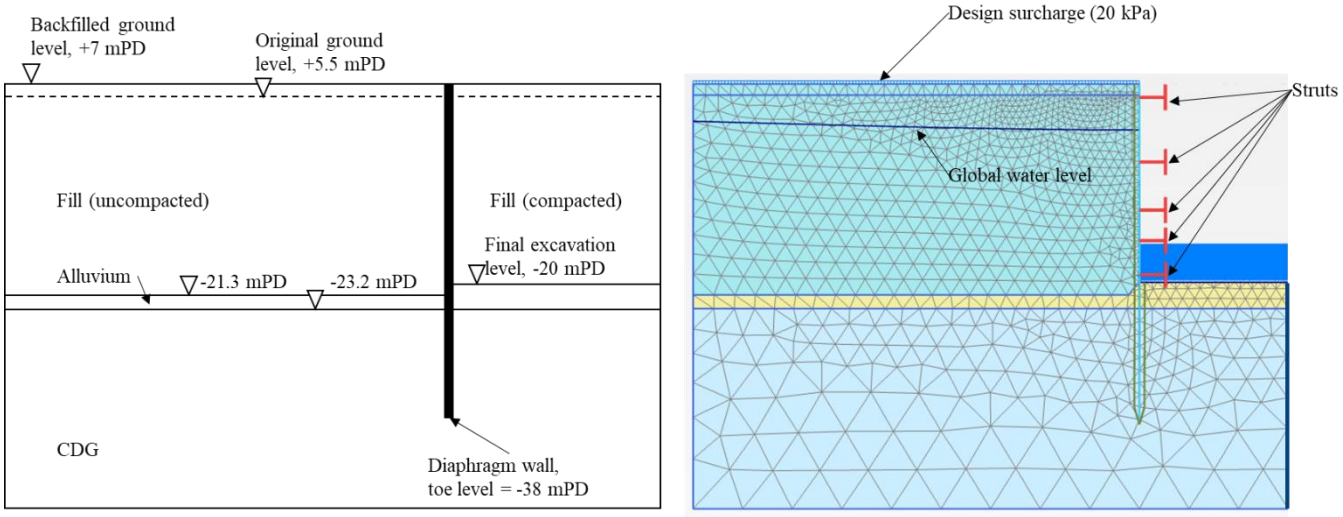

Figure 6 Illustration for Ground Profiles and Design Models

Table 3 Design Soil Densities and Strength Parameters

Soils	Fill	Compacted fill	Alluvium	CDG
Saturated unit weight γ_{sat}' [kN/m^3]	19	19	19	19.5
Friction angle ϕ' [deg]	32	38	32	37
Cohesion c' [kPa]	0	0	0	0

3.4 Instrumentation, Monitoring and Measured Performance

A comprehensive instrumentation and monitoring scheme was implemented for Phase III excavation works to track excavation-induced ground and structural movements. The monitoring system included:
(i) Diaphragm wall inclinometers, measuring lateral displacement profiles of the retaining wall at various construction stages;
(ii) Ground settlement markers, installed at multiple offsets from the diaphragm wall to record development of surface settlement troughs;
(iii) Piezometers and standpipes, monitoring groundwater levels and assessing the effectiveness of dewatering measures.

Monitoring data indicate that wall deflection and ground settlement developed progressively with excavation depth, with the maximum movements occurring during deeper excavation stages when unloading effects

dominated. The measured settlement profiles show a well-defined trough extending beyond the toe of the diaphragm wall, providing a valuable basis for assessing the ability of different constitutive models to reproduce both the magnitude and shape of ground settlement.

The completeness and consistency of monitoring records for Phase III excavation works, combined with clearly defined construction stages and boundary conditions, make this section well suited for numerical back-analysis and for evaluating the implications of constitutive soil model assumptions on deformation prediction. The measured wall deflection and the measured ground settlement profiles are used for back-analysis and will be presented in the following paragraphs.

3.5 PLAXIS Models for Prediction and Back-analysis

Three plane-strain PLAXIS models were built following the sequences introduced in Section 3.3. The first one adopted MC model, and the stiffnesses of soils were designed as in **Table 1**. This was to reproduce the prediction models in typical design submissions for acquiring approval in local industry. The second one also adopted MC model, however the stiffnesses of soils were adjusted with E = 3.0 N (in MPa) to match actual monitored deformations (the back-analysis model). The third one adopted HS model for back-analysis purposes. The densities and strengths of each soil layer are shown in **Table 3**, and the stiffness profiles are listed in **Table 4**. In the HS model, p^{ref} for fill and compacted fill was designed as the at-rest effective confining stress σ_3', at 0 mPD; p^{ref} for alluvium and CDG layers was designed as σ_3' at the top level of each layer. Correspondingly, E_{50}^{ref} of each soil layer was the reference secant modulus at the respective reference pressure. E_{oed}^{ref} was assumed to be equal to E_{50}^{ref} and E_{ur}^{ref} was assumed to be 3 times of E_{50}^{ref}, which are default PLAXIS settings.

Table 4 Summary of MC and HS Stiffness Parameters

Soils			Fill	Compacted fill	Alluvium	CDG
Model parameters	MC model (prediction), E [kPa]		10,830 + 839z, z ≤ 5 mPD	24,600 + 3417z, z ≤ 5 mPD	28,500 + 1,500z, z ≤ -19 mPD	18,000 + 14,235z, z ≤ -23 mPD
	MC model (back-analysis), E [kPa]		21,660 + 1,679z, z ≤ 5 mPD	49,200 + 6,834z, z ≤ 5 mPD	57,000 + 3,000z, z ≤ -19 mPD	27,000 + 21,350z, z ≤ -23 mPD
	HS model (back-analysis)	p^{ref} [kPa]	23.3	19.0	103.7	102.1
		E_{50}^{ref} [kPa]	25,000	80,000	60,000	100,000
		E_{oed}^{ref} [kPa]	25,000	80,000	60,000	100,000
		E_{ur}^{ref} [kPa]	75,000	240,000	180,000	300,000
		m	0.6	0.6	1.0	0.6

Figure 7 compares the modelled ground settlement and wall lateral movement against the in-situ monitored data, with both MC and HS models. The MC prediction model gave over-estimated settlement and wall movement compared to the monitored data, primarily due to the conservative assumptions in soil stiffness. This is the routine result in the local design experience, to avoid unforeseen large in-situ ground settlement. In contrast, the MC back-analysis model and the HS back-analysis model can well capture the maximum monitored ground settlement, around 41 mm at 10 - 15 m away from the wall. At further distance, all modelled settlement profiles were larger than the monitored data, probably because a strip surcharge of 20 kPa was applied in the models.

The lateral movement of walls was monitored by inclinometers at certain locations and **Figure 7**(b) presents the average monitored movements. The maximum wall movement estimated from the MC back-analysis model and HS back-analysis model was comparable to the in-situ monitored data, around 45 mm, and the elevation at which maximum movement was observed was slightly below the final excavation level (FEL). However, the monitored data showed that maximum wall movement occurred at a higher level.

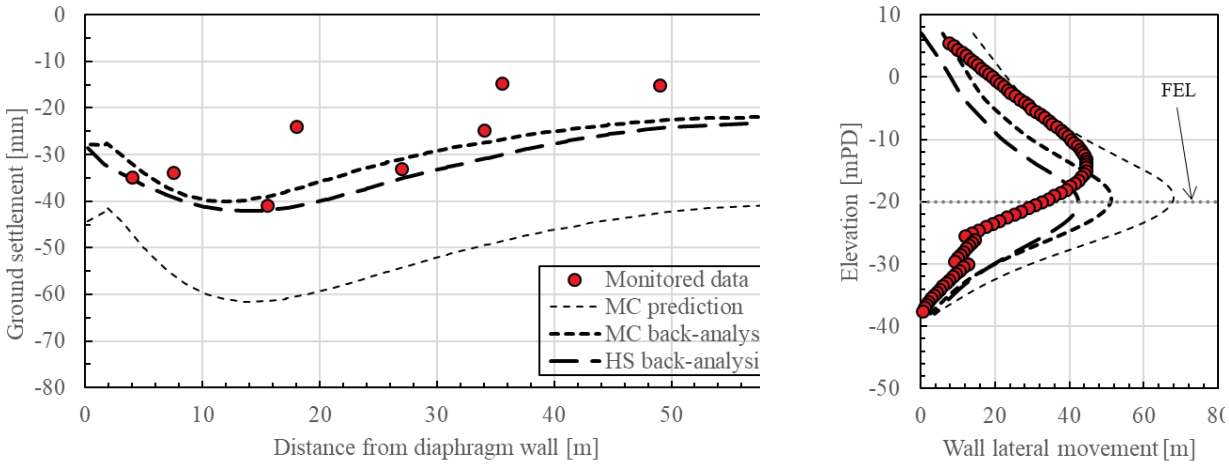

(a) (b)

Figure 7 Predicted and Back-analysed Profiles of (a) Ground Settlement and (b) Lateral Movement of Walls, by MC and HS Models

3.6 Sensitivity Study on HS Parameters

To explore the influence of the HS model stiffness parameters on the modelling responses during excavation works, a sensitivity study was also performed. The ratios of E_{oed}^{ref} / E_{50}^{ref} and E_{ur}^{ref} / E_{50}^{ref} were varied, as shown in **Table 5**, from 0.5 to 1 and from 2 to 10, respectively. These ratios are deemed to cover typical ranges adopted in previous studies, as shown in **Table 2**. Other soil and structural properties and model parameters remain the same as above.

The profile of ground settlement and wall lateral movement of each case is plotted in **Figure 8**. Case A to D investigate the influence of E_{ur}^{ref}. Maximum ground settlement is not sensitive to E_{ur}^{ref}, which varies in a narrow range between 42.1 mm to 44.1 mm. On the other hand, there is a clear tendency that maximum wall movement decreases with increasing E_{ur}^{ref}. Case A, E and F investigate the influence of E_{oed}^{ref}. With increase in E_{oed}^{ref}, ground settlement reduces significantly, while wall lateral movement increases slightly. Base heave at final excavation level at varying E_{ur}^{ref} / E_{50}^{ref} ratios is also investigated. Maximum heave reduces by about 50% when E_{ur}^{ref} / E_{50}^{ref} is increased from 2 to 10.

Table 5 Sensitivity Study on the Stiffness Ratios of HS Models

Scenarios	A (Base case)	B	C	D	E	F
E_{oed}^{ref} / E_{50}^{ref}	1	1	1	1	0.5	0.8
E_{ur}^{ref} / E_{50}^{ref}	3	2	5	10	3	3

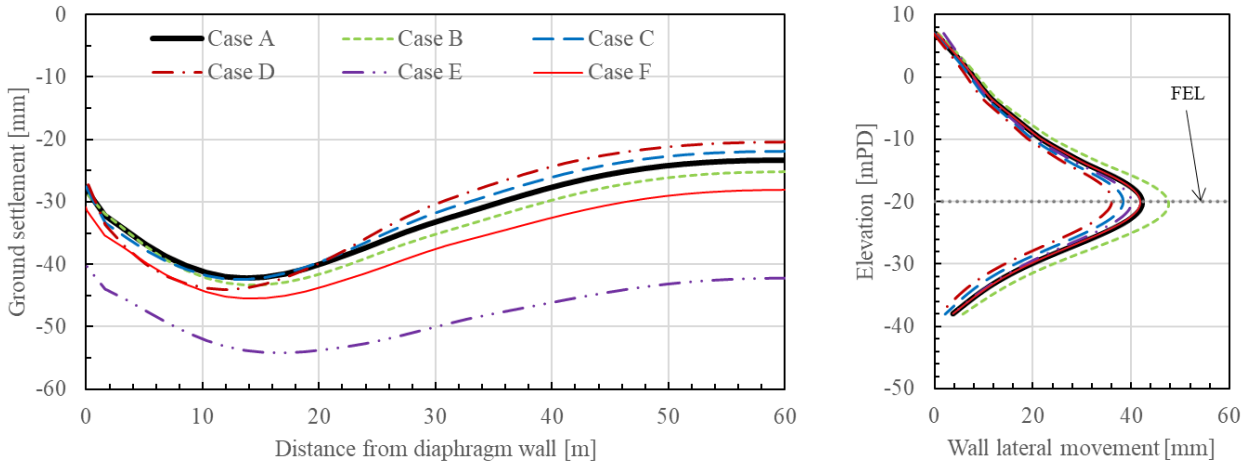

(a) (b)

Figure 8 Ground Settlements and Wall Deflections at Varying E_{oed}^{ref} / E_{50}^{ref} and E_{ur}^{ref} / E_{50}^{ref} Ratios

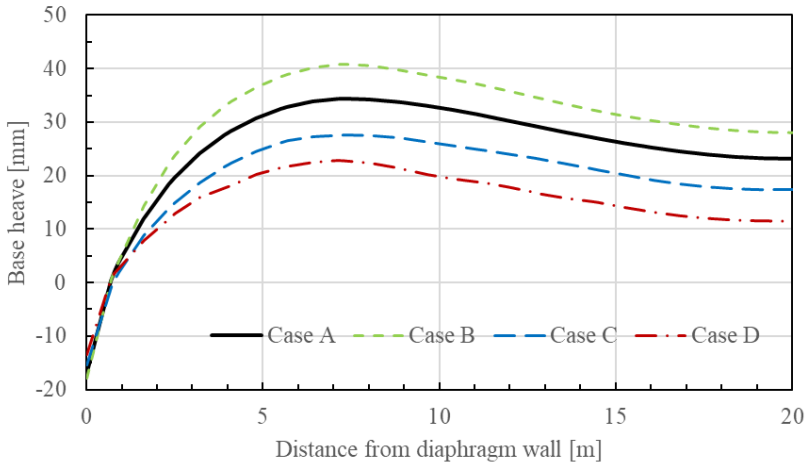

Figure 9 Variation of Base Heave with E_{ur}^{ref} / E_{50}^{ref} Ratios

4 CONCLUSIONS

This paper presents a comparative back-analysis of a deep basement excavation in Hong Kong using the Mohr–Coulomb (MC) and Hardening Soil (HS) constitutive models, with reference to comprehensive field monitoring data. Based on the case study and sensitivity analyses, the following conclusions are drawn:

The MC model, when used with stiffness parameters derived from conventional empirical correlations for design prediction, produced conservative estimates of ground settlement and wall deflection. While such conservatism is commonly adopted in Hong Kong practice to manage serviceability risk, the MC model's use of a single elastic stiffness for both loading and unloading can lead to unrealistic deformation components in unloading-dominated excavation problems, including exaggerated settlement and base heave.

Back-analysis using an adjusted MC stiffness profile and the HS model both achieved good agreement with the monitored maximum ground settlement and wall lateral movement. However, the HS model provided a more realistic representation of soil behaviour by explicitly accounting for stress-dependent stiffness and distinguishing between primary loading and unloading/reloading stiffness. This was reflected in improved reproduction of the settlement trough shape and more consistent deformation mechanisms under staged excavation.

Sensitivity studies indicate that, for the HS model, the unloading/reloading stiffness ratio (E_{ur}^{ref} / E_{50}^{ref}) has a limited influence on the magnitude of maximum settlement but affects settlement at greater distances from the wall, wall deflection profiles, and excavation-induced base heave. In contrast, the oedometer stiffness ratio (E_{oed}^{ref} / E_{50}^{ref}) exerts a more significant influence on ground settlement magnitude, highlighting the importance of appropriate stiffness selection when modelling volume change and stress redistribution during excavation. It

is suggested that sufficient triaxial compression tests and consolidation tests are carried out to determine the E_{50}^{ref}, E_{ur}^{ref} and E_{oed}^{ref} accurately, for a site-specific investigation. In absence of such test data, default settings with $E_{ur}^{ref} / E_{50}^{ref} = 3$ and $E_{oed}^{ref} / E_{50}^{ref} = 1$ may be adopted.

From a practical perspective, the study suggests that advanced constitutive modelling, such as the HS model, is particularly justified for movement-sensitive ELS designs where unloading effects are significant, monitoring data are available for calibration, and deformation performance rather than ultimate stability governs the design. For routine applications, the MC model remains suitable for strength-controlled assessments, provided its limitations in deformation prediction are recognised.

The case study also demonstrates the value of monitoring-based back-analysis in reducing uncertainty associated with soil stiffness selection. By calibrating numerical models against high-quality field data, designers can improve confidence in deformation prediction, refine constitutive model parameters, and support rational decision-making in ELS design. This approach aligns with the observational method and reinforces the importance of integrating theory, numerical modelling, and field performance in Hong Kong geotechnical practice.

5 LIMITATIONS AND SCOPE OF APPLICATION

The findings and observations presented in this paper are based on a project-specific case study involving a deep basement excavation in Hong Kong, supported by comprehensive instrumentation and monitoring data. While the back-analysis provides useful insights into the influence of constitutive soil model selection on predicted ground movements, the results should be interpreted within the context of the ground conditions, excavation geometry, construction sequence, and monitoring quality of the study site.

The numerical analyses were carried out using two-dimensional plane-strain models, which represent an idealisation of the actual three-dimensional excavation and support system. Localised three-dimensional effects, construction imperfections, and spatial variability in ground conditions may not be fully captured. In addition, the soil stiffness parameters adopted in the analyses were calibrated primarily against measured wall deflections and ground settlements for the selected section; different parameter combinations may be required for other sites with different geological profiles, stress histories, or groundwater regimes.

The empirical correlations and parameter relationships discussed in this paper reflect prevailing Hong Kong practice and published local case histories. Their applicability to projects outside Hong Kong, or to ground conditions significantly different from those considered (e.g. thick soft clay deposits, heavily structured soils, or highly anisotropic ground), should therefore be assessed with caution. Designers are advised to carry out project-specific calibration, sensitivity studies, and independent checks when applying advanced constitutive models in excavation and lateral support design.

Notwithstanding these limitations, the study demonstrates the value of monitoring-based back-analysis in improving the understanding of soil stiffness mobilisation and in supporting informed selection of constitutive models for movement-sensitive excavation problems. The approach adopted in this paper is intended to complement, rather than replace, sound engineering judgement, established empirical experience, and observational methods in geotechnical design.

ACKNOWLEDGEMENTS

The authors wish to acknowledge the project owner for granting permission to use the monitoring and project data for the purpose of this study. The contributions and support from colleagues involved in the design, construction, instrumentation, and interpretation of monitoring data are also gratefully acknowledged.

The authors would like to thank colleagues within Ove Arup & Partners Hong Kong Limited for their technical discussions and constructive feedback during the preparation of this paper. Appreciation is also extended to practitioners and researchers whose published works and case histories have contributed to the development of local excavation design practice in Hong Kong.

REFERENCES

Chan, A. K. C. (2003). Observations from excavations – A reflection. Proceedings of the HKIE Geotechnical Division Annual Seminar, Hong Kong, pp. 84–101.

Chan, C. C. L., Chiu, D. S. M., Lo, F. L. C., Kwan, J. S. H., Lee, S. W. and Leung, A. C. O. (2021). Back analyses of two deep excavations in Hong Kong using the Mohr–Coulomb model with linear elasticity and the Hardening Soil model. International Journal of Geoengineering Case Histories, Vol. 7, No. 1, pp. 137–163.

Hsiung, B. C. B. and Dao, N. T. (2014). Representing small-strain soil stiffness in excavation analyses using the Hardening Soil model. Computers and Geotechnics, Vol. 63, pp. 190–201.

Janbu, N. (1963). Soil compressibility as determined by oedometer and triaxial tests. In *Proc. European Conf. SMFE, Wiesbaden, 1963* (Vol. 1, pp. 19-25).

Janbu, N. (1970). Settlement calculations based on stress–strain relationships. ASCE Specialty Conference.

Khoiri, M. and Ou, C. Y. (2013). Evaluation of soil stiffness parameters for the Hardening Soil model based on excavation case histories. Journal of GeoEngineering, Vol. 8, No. 1, pp. 1–14.

Lam, A. K. M. (2018). An engineering solution for a hillside project in Hong Kong. Geotechnical Research, 5(3), pp. 170–181.

Lam, S. Y. (2018). Back-analysis of deep excavations in Hong Kong using advanced constitutive soil models. MPhil Thesis, The Hong Kong Polytechnic University.

Lee, D. M., Pappin, J. W. and Buckler, J. G. (2008). Prediction of ground movements arising from deep excavations. Proceedings of the 14th Southeast Asian Geotechnical Conference, Hong Kong.

Lu, Y., Ng, C. W. W. and Lei, G. H. (2018). Assessment of stiffness parameters for the Hardening Soil model in excavation analysis. Computers and Geotechnics, Vol. 100, pp. 1–14.

Lui, J. Y. H. and Yau, P. K. F. (1995). The performance of the deep basement for Dragon Centre. Proceedings of the HKIE Geotechnical Division Annual Seminar on Instrumentation in Geotechnical Engineering, Hong Kong, pp. 183–201.

Ng, C. W. W., Leung, A. K., Kwok, S. S. K. and Yip, F. H. T. (2014). Effects of stiffness nonlinearity on E' – SPT N correlations for analysing wall deflections in Hong Kong excavations. HKIE Transactions, Vol. 21, No. 1, pp. 35–49.

Ohde, K. (1951–1955). Studies on soil compressibility.

PLAXIS BV. (2019). PLAXIS Material Models Manual. Version 2019, Delft, The Netherlands.

Schanz, T., Vermeer, P. A. and Bonnier, P. G. (1999). The Hardening Soil Model: Formulation and verification. Proceedings of Beyond 2000 in Computational Geotechnics – 10 Years of PLAXIS, Balkema, Rotterdam.

Design of SFRC Segmental Tunnel Linings: A Practical Framework for Wider Implementation in Hong Kong

T.H. Lee, T.C. Choi, C.O.A. Leung, K.H. Chan & Z.Y. Li
Asia Infrastructure Solutions Limited, Hong Kong

ABSTRACT

Precast steel fibre reinforced concrete (SFRC) segmental tunnel linings offer clear benefits in fabrication efficiency, crack control, durability and lifecycle cost, yet their use in Hong Kong remains limited due to the lack of local design guidelines and uncertainty about conditions under which SFRC can replace traditional reinforcement bars. This paper reviews the existing international design practices for SFRC segments and presents results from a systematic parametric study evaluating the influence of overburden, lining stiffness and ground conditions on the structural performance of precast SFRC segments. Based on the study, a suite of practical design charts has been developed to delineate the envelopes within which precast SFRC segments satisfy ultimate and serviceability limit state criteria. Selected tunnel projects from Hong Kong and overseas are used to demonstrate the adoption of SFRC segmental linings. The study proposes a practical design framework to support wider adoption of precast SFRC segments in future Hong Kong tunnelling works.

1 INTRODUCTION

Precast segmental linings are widely used in Hong Kong's bored tunnels, yet the vast majority rely on conventional steel reinforcement. Precast steel fibre reinforced concrete (SFRC) segments offer well-documented advantages, including simplified fabrication, improved crack control, enhanced durability and reduced cost, as well as embodied carbon. Over the past two decades, SFRC segments have been adopted successfully in tunnel projects across Europe, Australasia and Southeast Asia. Despite this international track record, local adoption has been limited.

This paper presents a chart-based design framework developed through a systematic parametric study. The framework enables rapid preliminary determination of the minimum SFRC lining thickness for a given tunnel geometry and ground condition, without requiring detailed structural analysis. The design charts are validated against local and overseas case studies. The study aims to provide a practical reference to support wider adoption of SFRC segmental linings in future Hong Kong tunnelling projects.

2 DESIGN PRINCIPLES OF SFRC

The fundamental behaviour of SFRC that distinguishes it from conventional reinforced concrete is its residual flexural tensile strength after crack formation, maintained by the steel fibres at the crack. RILEM TC162-TDF "Test and Design Method for SFRC" published by the International Union of Laboratories and Experts in Construction Materials, Systems and Structures (RILEM) provides a standardised three-point bending test method using simply supported notched prisms to quantify post-cracking performance under controlled deflection or crack mouth opening displacement (CMOD). The complete load-deflection or load-CMOD curve is recorded to determine the limit of proportionality strength alongside residual flexural tensile strengths at prescribed CMOD levels, enabling classification of SFRC performance for design applications.

SFRC sections are designed by linking the residual flexural test results to sectional resistance and crack control. For the ultimate limit state (ULS) check, the cross-sectional stress-strain profile with consideration of the post-crack residual flexural tensile strength is adopted to derive the moment and axial force envelope. Other assumptions on the limiting compressive strain, maximum crack width, and height of the cracked zone are specified in the guideline.

For the serviceability limit state (SLS) check, when an uncracked section is considered, the full SFRC section is assumed to be elastic in both tension and compression. When a cracked section is considered, the SFRC is assumed to be elastic in compression to sustain a given tensile stress.

In practice, the residual tensile strength of SFRC is sometimes ignored in the ULS check to err on the safe side. Singapore's LTA pioneered the adoption of SFRC segmental lining in metro projects, often mandating that plain concrete be assumed in ULS design, with fibres credited solely for the bursting check of segment joints and SLS check. In 2025, Hong Kong granted the first Buildings Department approval for precast SFRC segments as permanent linings for railway tunnel based on RILEM methodologies.

3 CHART-BASED DESIGN FRAMEWORK FOR SFRC LINING

3.1 Overview

A chart-based design framework has been developed to provide a rational yet practical approach for the preliminary design of SFRC segmental tunnel linings. The framework is based on a comprehensive parametric study using an established closed-form solution to estimate lining response under a range of cover-to-diameter ratio (C/D), relative stiffness (Q_2), and earth pressure ratio (K). The objective is to establish design relationships between the lining thickness-to-diameter ratio (t/D) and the key influencing parameters, enabling efficient sizing during early design stages.

The developed charts are intended to serve as a supplementary tool for preliminarily identifying the adequate tunnel lining thickness without the need for design calculations or analyses. They do not supersede the standard design procedures required for the tunnel lining.

The analytical results were systematically processed and normalised to produce a series of design charts, illustrating how changes in C/D, Q_2 and K affect the required SFRC lining thickness. The charts are supported by parametric studies over the typical range of these key influencing parameters.

3.2 Establishment of Design Charts

Figure 1 illustrates the procedures for establishing design charts for determining the minimum t/D required to adopt pure SFRC tunnel segments.

The workflow begins by defining three key input parameters that govern the ground-lining interaction, which include the C/D, Q_2 and K. These parameters collectively characterise the burial depth, the stiffness of the surrounding ground relative to the lining, and the deviatoric loading of the initial stress field, respectively.

For each unique combination of C/D, Q_2 and K, the internal lining forces, comprising axial force and bending moment, are computed using the closed-form analytical solution developed by Muir-Wood (1975) and modified by Curtis (1976). The tunnel problem analysed is schematically presented in Figure 2.

A structural verification is carried out to assess whether a trial lining thickness, expressed in normalised form as t/D, satisfies the ULS and SLS criteria for an SFRC section. If the section passes all structural checks, the combination of parameters and the corresponding t/D value is recorded as acceptable; if it fails, that case is excluded from the admissible design domain. This evaluation constitutes an iterative loop across the full parametric space consisting of C/D, Q_2 and K collectively, and subsequently maps out the minimum t/D at which the SFRC section is structurally adequate.

Upon completion of the parametric analysis, the results are compiled and plotted as a design space showing t/D against C/D. From this design space, final design curves are established to relate the minimum required t/D and C/D for discrete values of Q_2 and K, enabling a practitioner to efficiently identify the minimum lining thickness needed for a given tunnel geometry and ground condition without performing a full structural analysis for every design scenario.

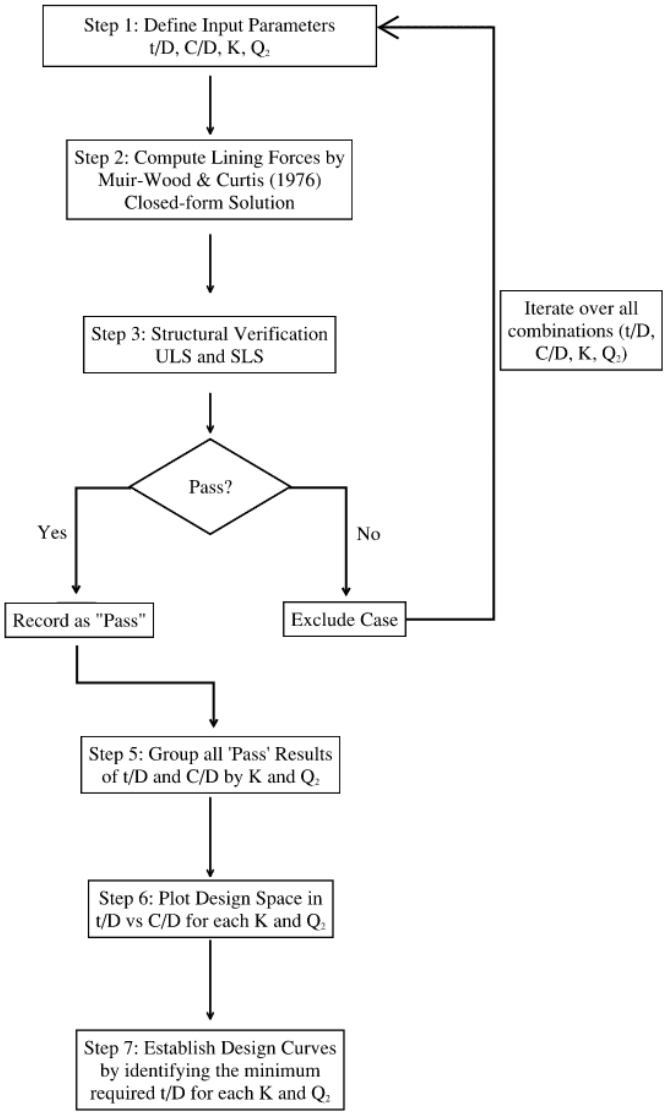

Figure 1: Workflow to Establish Design Charts for SFRC Segmental Lining

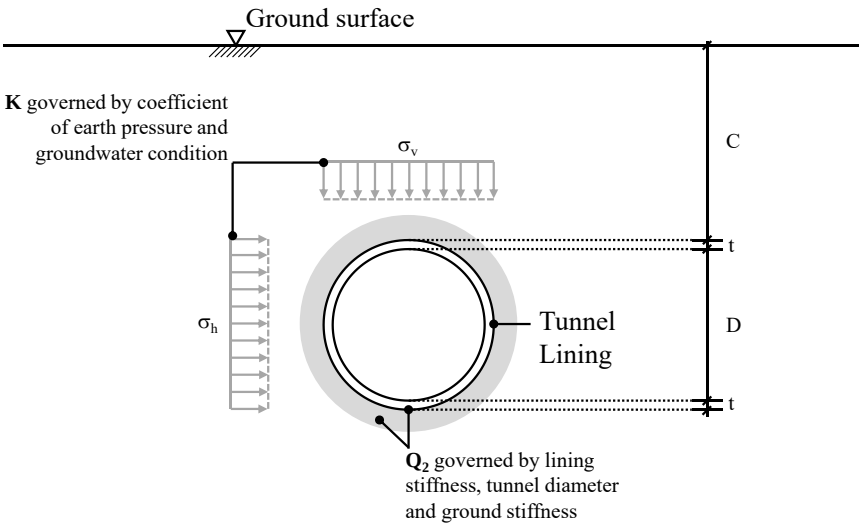

Figure 2: Schematic Illustration of Tunnel Problem Analysed

3.3 Parameter Ranges

The parametric study covers a representative range of geotechnical and tunnel geometry conditions relevant to typical segmental tunnel linings. The following parameters were systematically varied:

- Soil Overburden (C/D)
  Overburden stress represented by the ratio of ground cover (C) to tunnel diameter (D) was varied from 0.5 to 10, spanning shallow-buried to deep tunnelling conditions. This parameter controls the magnitude of overburden pressure and has a strong influence on the axial force and bending moment in the lining.
- Relative Stiffness (Q_2)
  Relative stiffness Q_2 was introduced by Muir Wood (1975) to quantify the ratio of deformability between the ground and the tunnel lining under deviatoric loading. A range of Q_2 from 1 to 200, is considered to capture the relative deformation compatibility between the ground and the lining. The parameter is expressed as:

$$Q_2 = \frac{E_g R^3}{12EI(1+\nu)} \tag{1}$$

  where E_g is the Young's modulus of the ground, R is the tunnel radius, E is the Young's modulus of the lining, I is the equivalent moment of inertia of the lining adjusted to consider segment joints according to Muir Wood (1975), and ν is the Poisson's ratio of the lining
- Earth Pressure Ratio (K)
  Earth pressure ratio K is defined as the ratio of the horizontal stress to the vertical stress (σ_h/σ_v) acting on the tunnel lining. It is governed by the coefficient of earth pressure and the groundwater conditions. A lower coefficient of earth pressure or a lower groundwater table results in higher deviatoric loading on the tunnel lining. Conversely, a coefficient of earth pressure close to unity or a higher groundwater table contributes to a more isotropic loading condition. Variations in K influence the non-uniformity of loading around the lining and, consequently, the magnitude of bending. A range of K, from 0.25 to 0.8 is considered to represent different loading conditions.

A summary of the parameter combinations (over 50 million cases computed) is presented in Table 1, which lists the full range of input variables and normalised constants used to derive the design charts.

Table 1: Summary of Parametric Study Inputs

Tunnel Diameter (m)	Lining Thickness-to-Diameter Ratio t/D	Cover-to-Diameter Ratio C/D	Relative Stiffness Q_2	Earth Pressure Ratio K
5, 10, 15	0.02 to 0.08 at intervals of 0.0005	0.5 to 10 at intervals of 0.05	1, 2, 3, 4, 5, 10, 20, 50, 100, 200	0.25, 0.33, 0.50, 0.67, 0.8

3.4 Closed-form Tunnel Analysis

The structural response of the tunnel lining is evaluated using the closed-form solution developed by Muir Wood (1975) and modified by Curtis (1976) for circular, jointed tunnel linings. The tunnel is idealised as a circular opening with diameters of 5 m, 10 m and 15 m in a homogeneous and linear-elastic continuum. Plane-strain conditions and small deformations are assumed, and both tangential slip and full bond conditions are considered at the ground-lining interface. The resulting bending moment (M) and axial force (N) around the lining vary harmonically with the circumferential angle θ as:

$$M(\theta) = M_{\max}\cos(2\theta) \tag{2}$$

$$N(\theta) = P_{av}R + N_{\mathrm{Var}}\cos(2\theta) \tag{3}$$

The amplitudes of bending moment and axial force are given by the closed-form expressions as shown in Table 2:

Table 2: Closed-form expressions based on Muir Wood (1975) and Curtis (1976)

	Full Bond	**Tangential Slip**
Normal & Shear Stress, S_n & S_t	$S_t = \frac{\frac{(1+2Q_2)P_0}{2}}{1+Q_2\left(\frac{3-2v}{3-4v}\right)}$ $S = \frac{\frac{(1-2Q_2)P_0}{2}}{1+Q_2\left(\frac{3-2v}{3-4v}\right)}$	$S_t = 0$ $S_n = \frac{\frac{3(3-4v)P_0}{2}}{5-6v+Q_2}$
Max. Bending Moment, M_{Max}	$M_{Max} = \pm\frac{(3-4v)P_0 - S_t(1-2v)}{5-6v+Q_2}R^2$	$M_{Max} = \pm\frac{1}{2}\frac{P_0(3-4v)}{5-6v+Q_2}R^2$
Hoop Thrust, N_{var}	$N_{var} = \pm\frac{\frac{(3-4v)P_0}{2}+2S_t(Q_2+1-v)}{5-6v+Q_2}R$	$N_{var} = \pm\frac{1}{2}\frac{P_0(3-4v)}{5-6v+Q_2}R$

where P_{av} is the average normal pressure on the lining, equal to $(\sigma_v + \sigma_h)/2$, and P_0 is the distortional pressure on the lining, equal to $(\sigma_v - \sigma_h)$.

3.5 Structural Verification of Lining Capacity

The resulting internal forces are verified for ULS and SLS conditions in accordance with Eurocode 2. For ULS check, the N–M design envelope is determined based on the combined effects of axial force and bending moment, conservatively assuming C50/60 plain concrete with no tensile capacity. A partial safety factor for concrete, $\gamma_c = 1.5$, is applied, together with the coefficient for long-term effects, $\alpha_{cc} = 0.8$. A factor of 1.35 is applied to the loading on the lining. For SLS check, the section is assumed to remain elastic, and the extreme fibre tensile stress is limited to the characteristic flexural tensile strength $f_{ctm,fl}$, which is 4.75 N/mm^2 for C50/60 concrete in accordance with RILEM.

3.6 Design Charts for SFRC Segmental Lining

Figures 3a to 3c present the full suite of design charts to determine the applicability of SFRC segmental linings. For a specified tunnel diameter D and a given value of K, families of curves are shown for different values of Q_2. These curves define the minimum t/D required to satisfy both ULS and SLS criteria for the SFRC segmental lining over the full range of C/D considered.

The charts can be used directly to preliminarily determine SFRC lining thickness. The required lining thickness can be determined using the figure corresponding to the tunnel's internal diameter which is illustrated as follows:

- Figure 3a: $D \leq 5$ m
- Figure 3b: 5 m < $D \leq 10$ m
- Figure 3c: 10 m < $D \leq 15$ m

If the lining thickness is already fixed, the given values of t/D and C/D can be plotted on the relevant design chart and compared with the curve corresponding to the derived value of Q_2. If the plotted point lies above this curve, the selected SFRC lining thickness is deemed acceptable upon preliminary review. If the lining thickness is not fixed, the following steps can be taken to determine the minimum t/D required to adopt SFRC lining for a given tunnel diameter and ground conditions:

- Step 1: Select the corresponding design chart and identify the minimum t/D for each Q_2 value under the given C/D;
- Step 2: Plot the minimum t/D against Q_2 ("Curve A");
- Step 3: Plot a separate curve for t/D against Q_2 derived according to $Q_2 = \frac{E_g R^3}{12EI(1+v)}$ ("Curve B");
- Step 4: Where Curve B lies above Curve A, the corresponding range of t/D satisfies the design criteria; within this range, SFRC lining is considered applicable.

An example of application is illustrated in Figure 4.

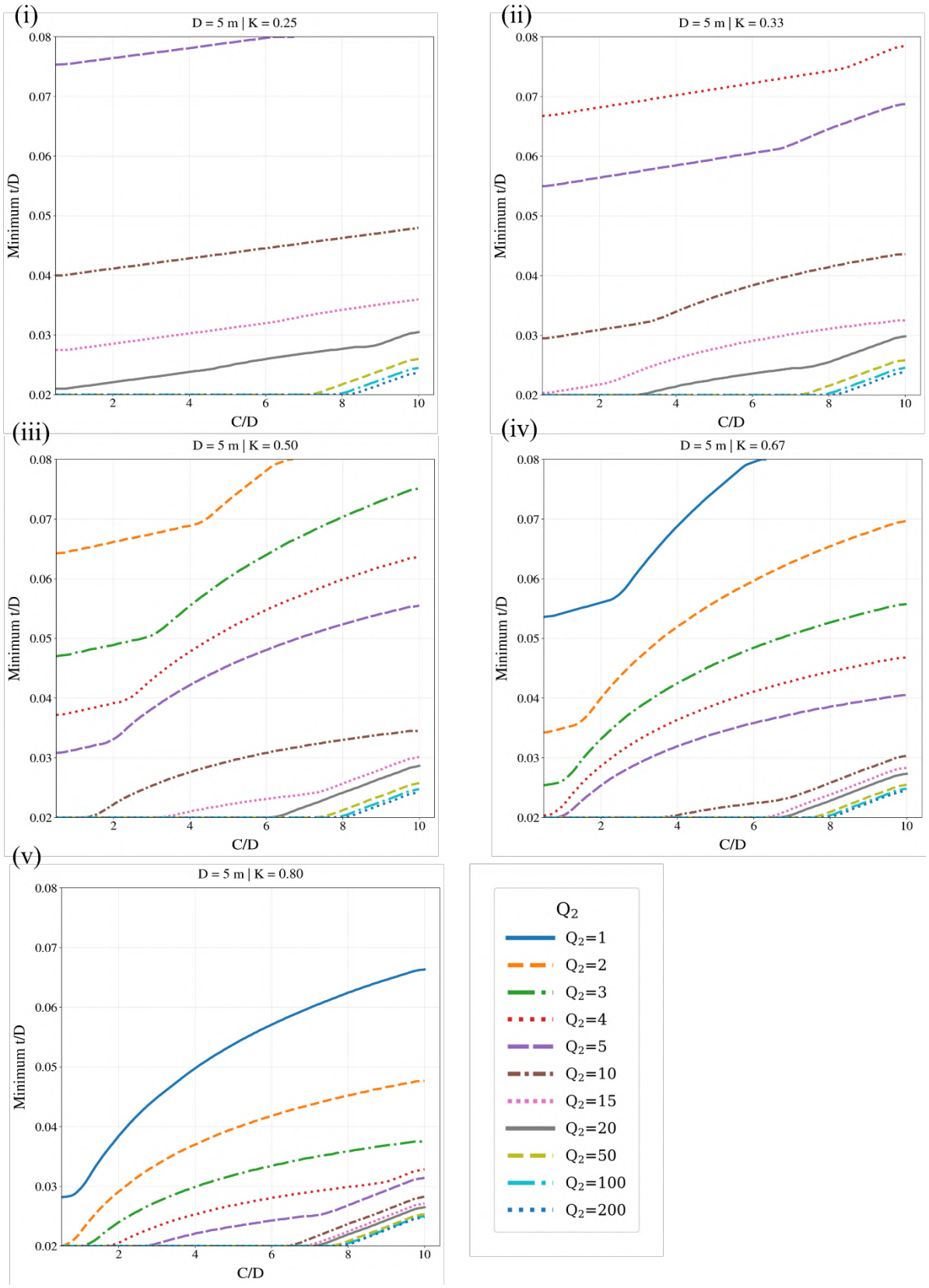

Figure 3a: Design Charts to Determine Minimum SFRC Lining Thickness for Diameter = 5 m and K = (i) 0.2, (ii) 0.33, (iii) 0.5, (iv) 0.67 and (v) 0.8

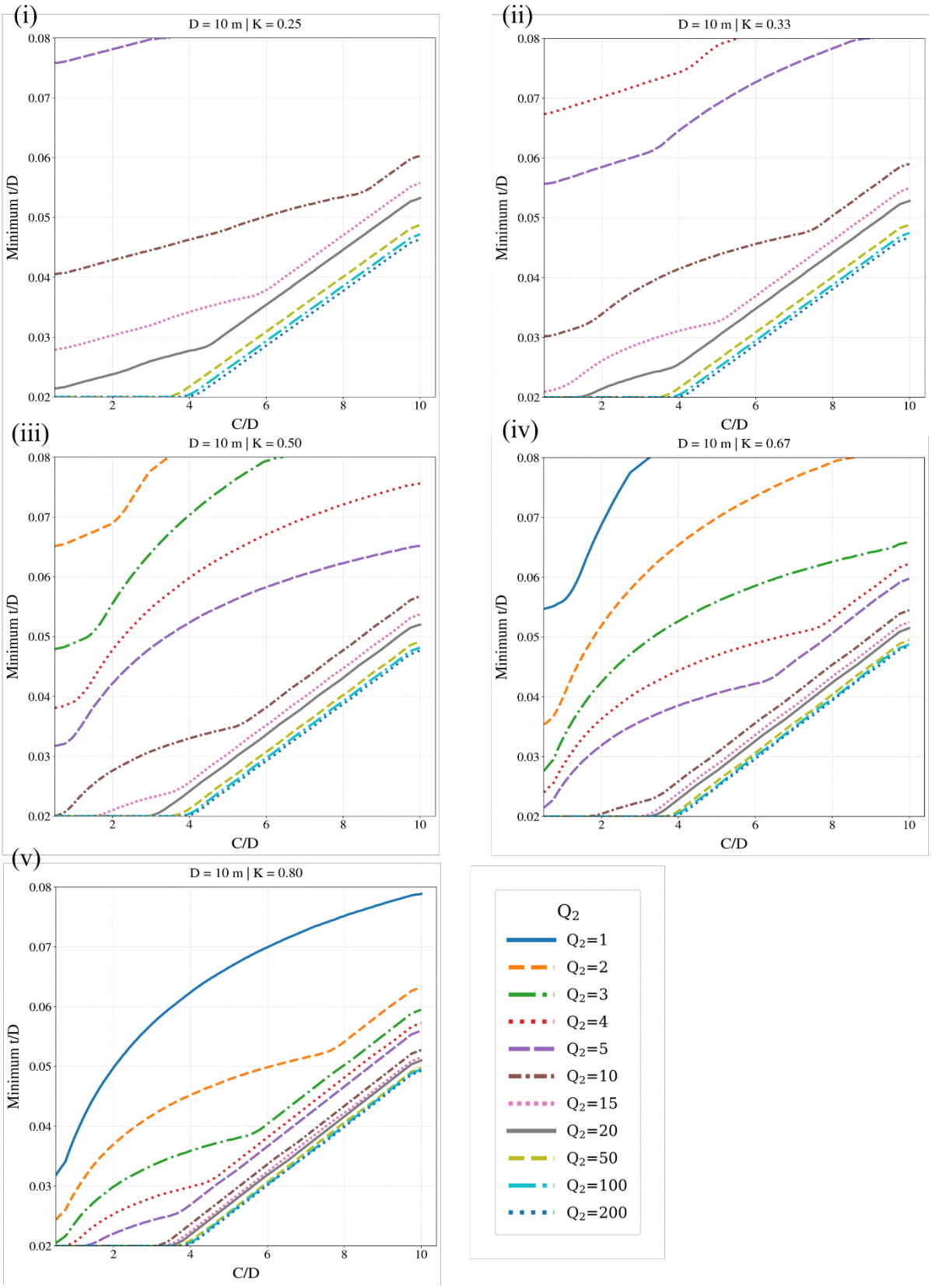

Figure 3b: Design Charts to Determine Minimum SFRC Lining Thickness for Diameter = 10 m and K = (i) 0.2, (ii) 0.33, (iii) 0.5, (iv) 0.67 and (v) 0.8

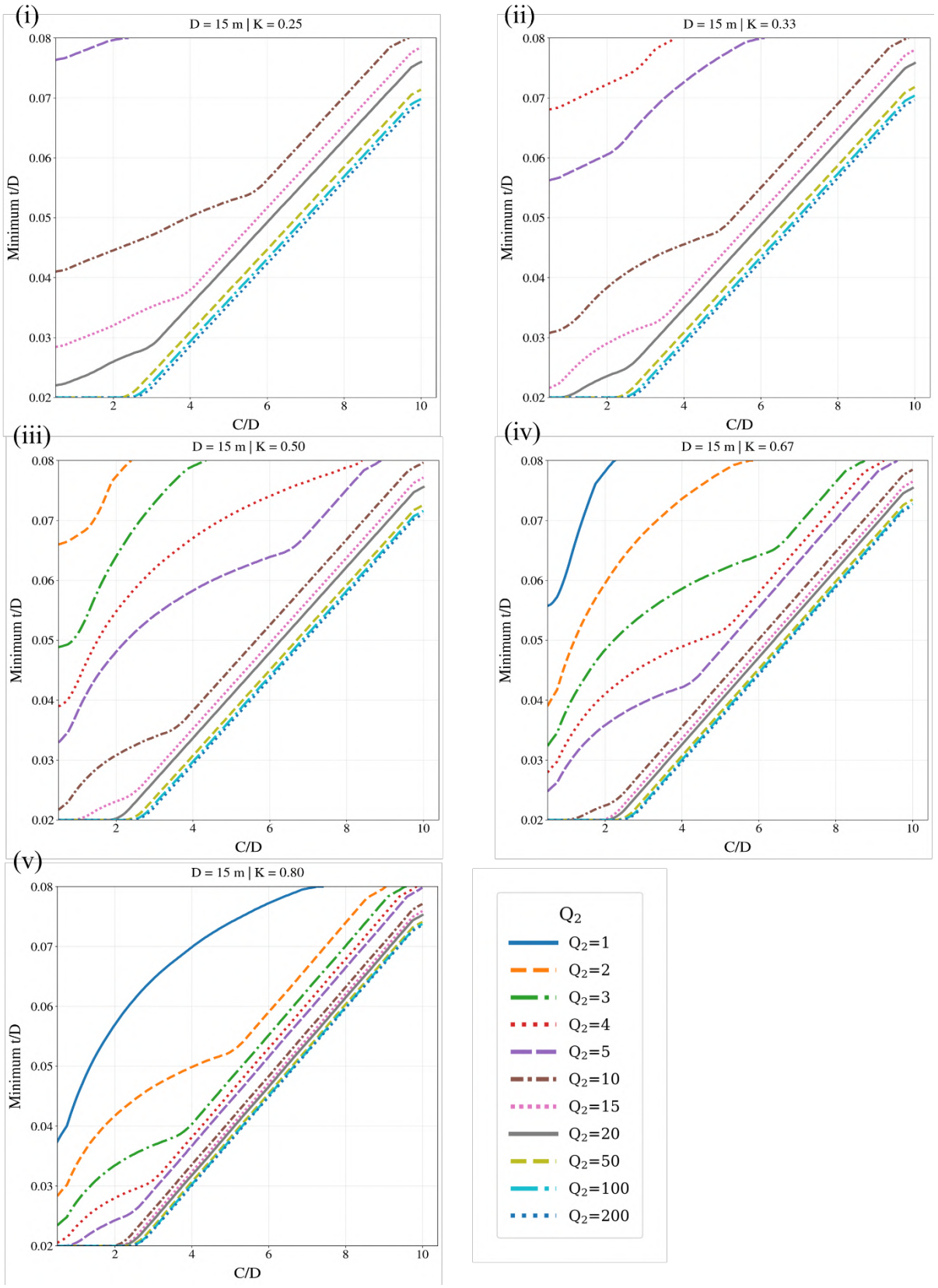

Figure 3c: Design Charts to Determine Minimum SFRC Lining Thickness for Diameter = 15 m and K = (i) 0.2, (ii) 0.33, (iii) 0.5, (iv) 0.67 and (v) 0.8

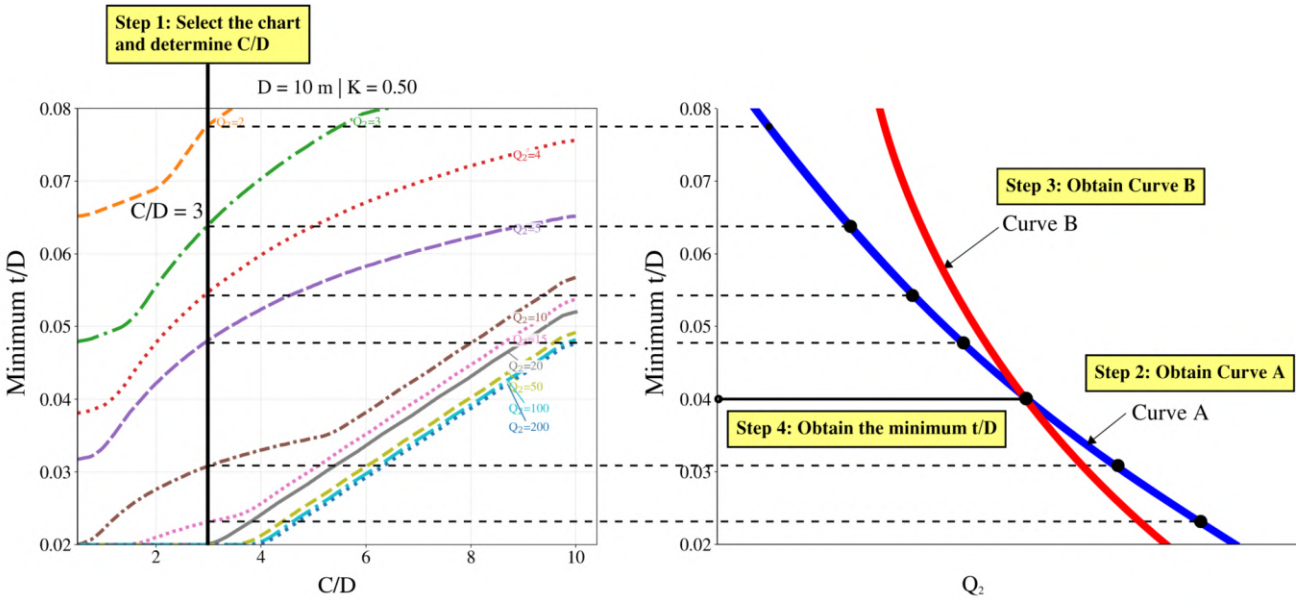

Figure 4: Example Application of SFRC Lining Design Chart for Determining Minimum Lining Thickness

For a more interactive application of the design charts, Asia Infrastructure Solutions Limited (AIS) has developed an in-house automated tool, as shown in Figure 5. This tool allows the user to input the necessary parameters (D, C/D, K, Q_2, and E_g), and any imposed design criteria. The tool automatically selects the corresponding design chart and identifies the governing design curve, to determine the minimum t/D for SFRC adoption.

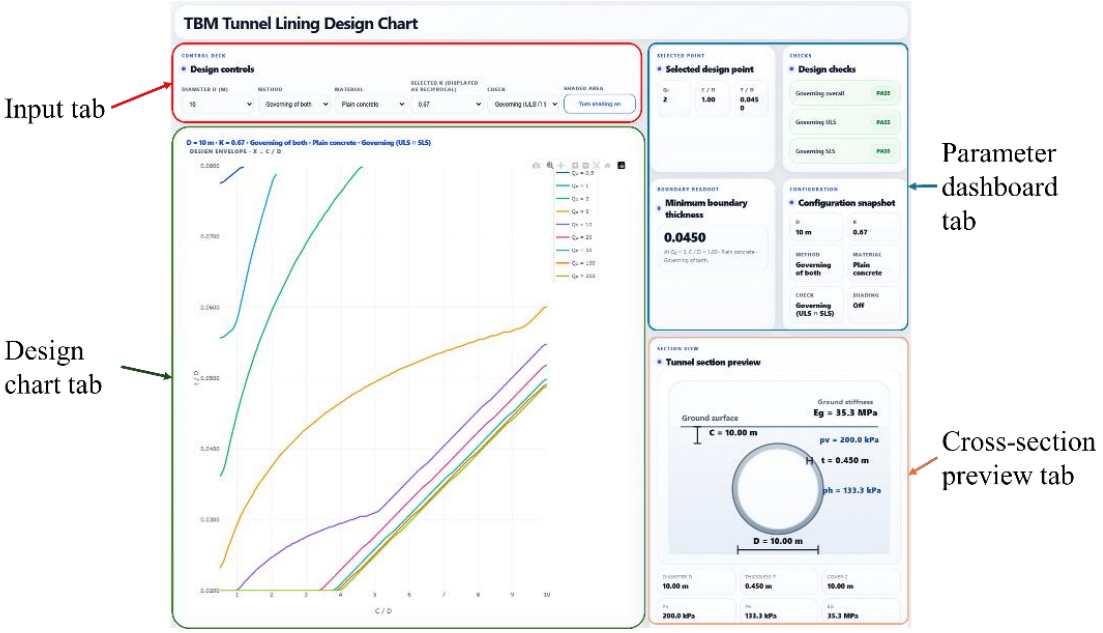

Figure 5: Automated Tool to Determine SFRC Lining Thickness

3.7 Effects of Residual Tensile Strength

Given the limited experience with SFRC adoption in Hong Kong, plain concrete has been conservatively assumed in the ULS checks to derive the charts. When SFRC is more widely adopted locally, with more local SFRC testing data and project experience, the charts can be updated to account for its beneficial effects, enabling a more reliable and optimised determination of lining thickness.

Nonetheless, the effects of residual tensile strength have been studied qualitatively. For illustrative purposes, a selected chart has been replicated with consideration of the residual tensile strength in the ULS check. As presented in Figure 6, the post-crack residual flexural tensile strength is adopted to derive the moment and axial

force envelope in accordance with RILEM. Illustrative values of 2.9 N/mm^2 and 2.6 N/mm^2 are assumed for the residual tensile strengths at CMOD 0.5 mm ($f_{R,1}$) and CMOD 3.5 mm ($f_{R,4}$), respectively.

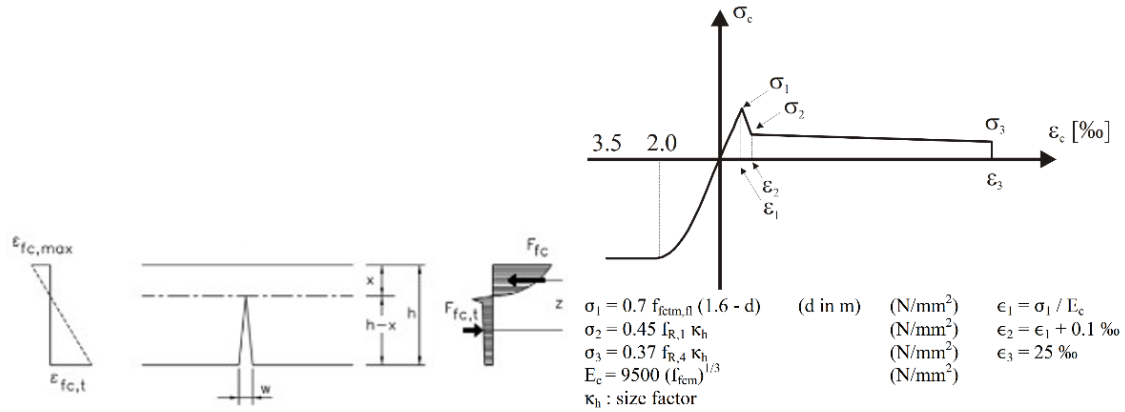

Figure 6: Stress-Strain Distribution of SFRC Section (RILEM)

Figure 7 compares the design charts for minimum t/D derived with and without consideration of residual tensile strength. The comparison highlights the observable influence of the residual tensile strength of SFRC under low overburden conditions. At shallow depths, the lining is subjected to relatively low axial forces, and the residual tensile strength contributes proportionally more to the moment capacity.

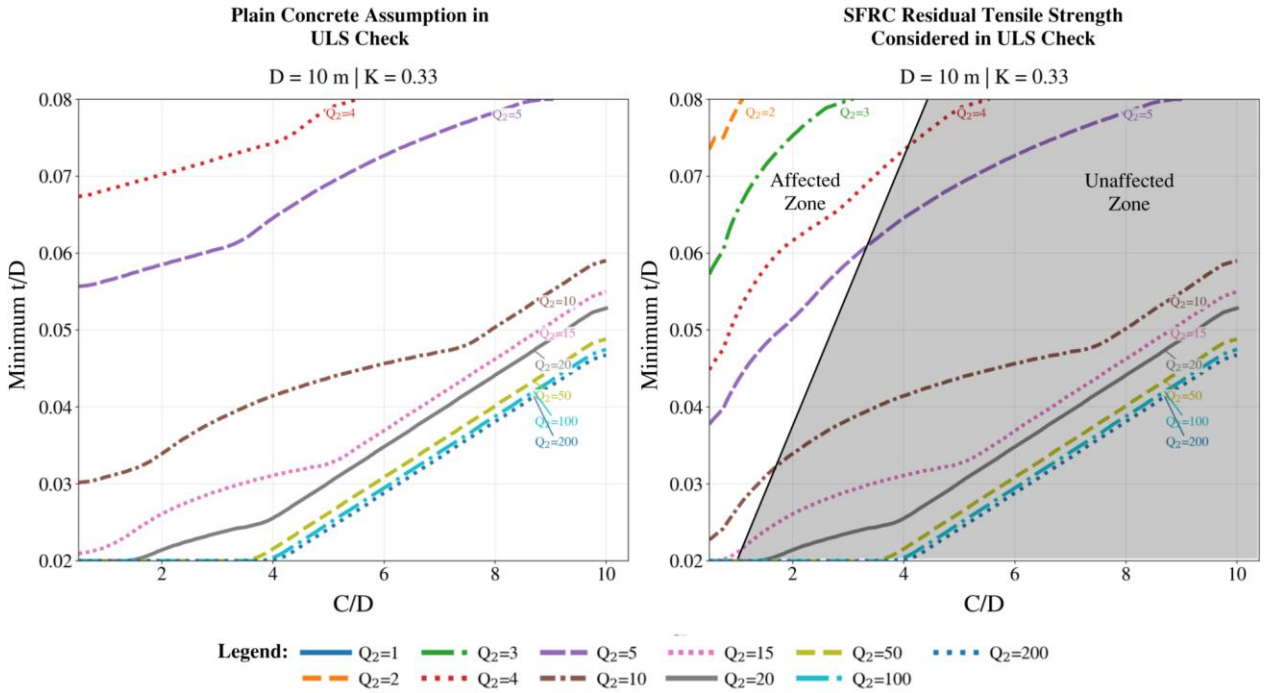

Figure 7: Comparison of Design Charts with and without Consideration of Residual Tensile Strength

4 APPLICATION FOR LOCAL AND OVERSEAS PROJECTS

4.1 Overseas Projects

To illustrate the applicability of the design charts, a total of nine overseas case studies for SFRC adoption, which are mostly documented in ITA Report N°16 (Tiberti et al. 2016), are selected for this study. The basic information on SFRC linings in these cases is summarised in Table 3. The minimum t/D for these cases is determined using the design charts for the given tunnel diameter and ground conditions. Certain project information (e.g., the earth pressure ratio and young's modulus of ground) is not made available in the publication, and assumptions have been made accordingly, as indicated in Table 3.

The actual t/D is then compared with the derived minimum t/D, as shown in Figure 8. In the figure, the position of each point relative to the parity line reflects the correspondence between observed and chart-derived lining thicknesses. Points above the parity line indicate that the actual lining thickness is deemed adequate for SFRC adoption. Most points lie close to or above the parity line, confirming that the estimates from the design charts align with observed industrial practice. Tunnels B, C, and F lie below the parity line because the high overburden becomes the governing factor, while the design charts do not account for the effects of ground arching. Overall, this convergence confirms that the design charts offer a reasonable basis for preliminary sizing.

Table 3: Summary of Case Studies

Tunnel	Information from ITA Report N°16 (Tiberti et al. 2016)				Assumptions adopted in Design Charts		
	D (m)	t/D	Max. C/D	Q_2	D (m)	E_g (MPa)	K
Tunnel A (Japan)	10.90	0.041	2.1	3.5	15	50	0.8
Tunnel B (Spain)	10.90	0.032	6.4	779.1	15	5000	0.8
Tunnel C (Australia)	11.30	0.031	6.2	868.1	15	5000	0.8
Tunnel D (Qatar)	6.17	0.049	6.0	115.3	10	2500	0.8
Tunnel E (Qatar)	3.70	0.068	3.2	43.0	5	2500	0.8
Tunnel F (Singapore)	11.30	0.040	7.6	28.6	15	350	0.8
Tunnel G (UK)	6.20	0.048	4.8	3.4	10	75	0.8
Tunnel H (Australia)	14.15	0.035	3.5	3.5	15	30	0.8
Tunnel I (Brazil)	8.40	0.042	3.6	3.7	10	50	0.8

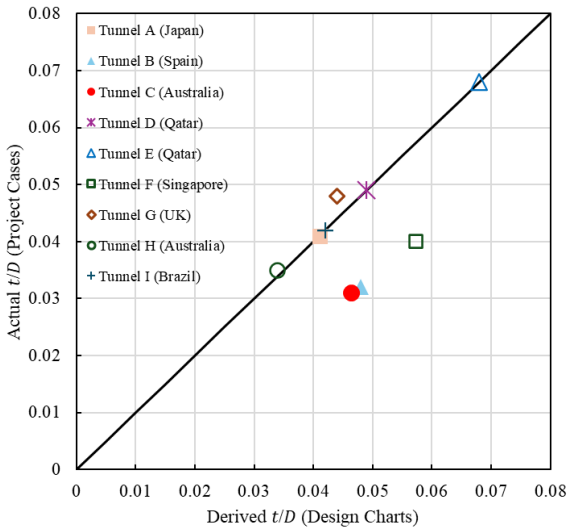

Figure 8: Comparison of Actual t/D (Project Cases) and Derived t/D (Design Charts)

4.2 A Selected Hong Kong Railway Tunnel Project

A case study was conducted to review a previous railway tunnel project in Hong Kong that adopted a conventional reinforced concrete segmental lining, with the aim of evaluating whether SFRC could be adopted by applying the design framework established in this paper. A representative section, indicating the 6.5 m diameter tunnel at 35 m depth within Completely Decomposed Granite, is presented in Figure 9.

The design charts, as shown in Figure 10, indicate that an SFRC segmental lining could be adopted in this case. Compared with a conventional reinforced concrete segmental lining, the adoption of SFRC for the tunnel reduces overall steel tonnage while maintaining the required structural performance. As a crude estimate, and excluding secondary reinforcement (e.g. bursting reinforcement, bar lapping and anchorage, wastage), the steel tonnage of the conventional reinforced concrete segmental lining is not less than 55 kg/m³. In contrast, the typical and widely adopted steel fibre dosage in SFRC tunnel segments is 40 kg/m³, which is generally sufficient to satisfy ULS and SLS requirements for similar ground and loading conditions. The adoption of SFRC could therefore reduce the total steel tonnage by approximately 27%, thereby achieving both direct construction cost savings and a corresponding 27% reduction in the embodied carbon associated with the quantity of steel usage.

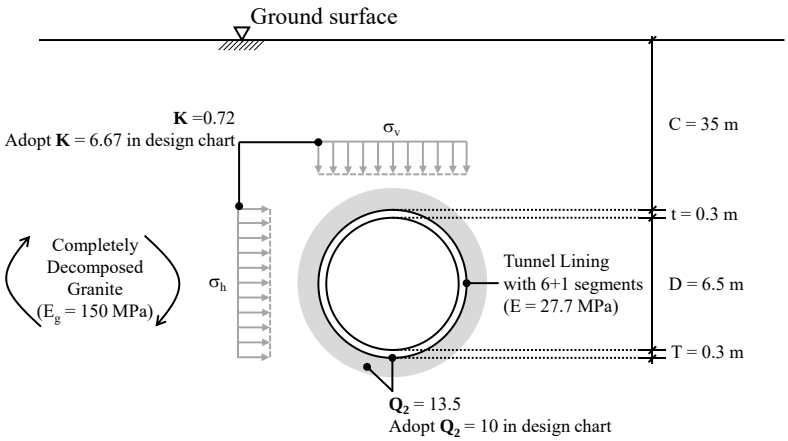

Figure 9: Ground Conditions of Hong Kong Railway Tunnel Project (Not to Scale)

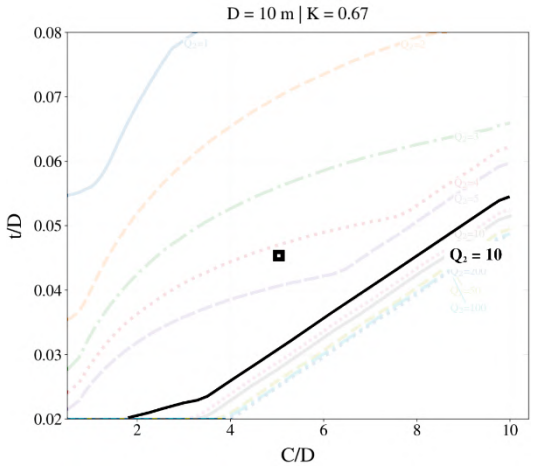

Figure 10: Application of Design Chart on the Previous Hong Kong Railway Tunnel Project for SFRC Adoption

5 CONCLUSIONS

This paper has presented a practical, chart-based framework for the preliminary sizing of SFRC segmental tunnel linings. A parametric study was systematically conducted over a range of cover-to-diameter ratio, relative ground-to-lining stiffness and earth pressure ratio, with the internal forces checked against both ultimate and serviceability limit state criteria. A full suite of design charts is established from the results for determination of the minimum lining thickness for SFRC adoption. Validation against case studies demonstrates strong consistency between the charts and adopted lining thicknesses in practice, and illustrates that SFRC linings are structurally viable in ground conditions in Hong Kong.

The framework is intended as a supplementary sizing tool. Future work should extend the study to incorporate numerical modelling validation and to refine the charts as more local SFRC testing data and project experience become available. It is hoped that this work will be a useful reference for the Hong Kong tunnelling community and support the broader adoption of SFRC technology in local practice.

REFERENCES

Curtis D.J. (1976). Discussions of "The circular tunnel in elastic ground" by Muir Wood (1975). *Géotechnique*, 26(1), 231-237.

RILEM TC162-TDF (2003): Test and design methods for steel fibre reinforced concrete.

Tiberti, G., Chiriotti, E., & Plizzari, G. (2016). Twenty years of FRC tunnel segments practice: lessons learnt and proposed design principles (ITA Report N°16). International Tunnelling and Underground Space Association (ITA).

Muir Wood, A.M. (1975). The circular tunnel in elastic ground. *Géotechnique*, 25(1), 115-127.

Design and Construction for the Largest Rock Cavern in Asia – A Case Study on the Relocation of Sha Tin Sewage Treatment Works to Caverns

Franklin K.L. To, Bridges D.C. Guy, Andrew K.W. Seto & Stephen L.C. Tam
AECOM Asia Company Ltd., Hong Kong, China

Michael W.K. Choi & Steve C.H. Leung
Drainage Services Department, the Government of the Hong Kong Special Administrative Region, Hong Kong, China

ABSTRACT

The Drainage Services Department (DSD) commenced the "Relocation of Sha Tin Sewage Treatment Works (STSTW) to Caverns" (STC) project and aims to relocate the aging STSTW in a cost-effective manner, improve the surrounding environment, and release approximately 28 hectares of land for more beneficial uses. The construction of advance works began in 2019. The successive Drill-and-blast excavation of the main caverns complex commenced in January 2022 and was completed in September 2025. The project is currently the largest rock cavern development in Asia, with about 2.3 million m³ of rock excavated.

The caverns complex comprises a grid arrangement of 4 x 7 parallel rock caverns, with individual span and height both reaching maximum of 32m. Permanent cavern support system consists of systematic rock bolts and fiber-reinforced sprayed concrete lining, designed using the Q-system empirical approach and Rock Reinforcement Approach (RRA) with advanced numerical modelling. Adoption of such three-stage rock cavern design procedure in the STC project was proven to be a successful showcase for pragmatic long-term strategic cavern development.

One of the key construction challenges was the planning of blasting sequences and logistics for concurrent top-heading and benches excavation. At peak periods, 7 daily blasts were carried out on 13 active blasting faces. To optimize flexibility and efficiency in explosives' delivery and blasting operations, a licensed temporary blasting explosives magazine (Mode A store) was established and operated on site.

This paper presents the key geological and geotechnical design considerations, construction challenges, rock handling and performance outcomes of this landmark cavern development project, providing valuable reference for future large-span cavern developments in the community.

1 INTRODUCTION

1.1 Project Background

To promote sustainable development, the Government of the HKSAR carried out a series of strategic planning and technical studies to explore the enhanced use of rock caverns in Hong Kong. Following these studies, the Drainage Services Department (DSD) commenced the "Relocation of Sha Tin Sewage Treatment Works (STSTW) to Caverns" (STC) project as shown in Figure 1. The project aims to relocate the aging STSTW in a cost-effective manner, improve the surrounding environment, and release of land for more beneficial uses.
The relocation is a pilot government project on the relocation of existing government facilities to caverns. The location at Strategic Cavern Area (SCVA) No. 20 – A Kung Kok (Nui Po Shan) near Sha Tin was selected. Upon completion of works, it is the largest rock caverns in Asia with excavated volume of about 2.3 million m^3.

The major geotechnical works include site formation works at portals, excavation works for two access tunnels, main caverns complex, ventilation adit and ventilation shaft, which is equivalent to a total length of 4.8 km. The main caverns complex is arranged in a 7 x 4 grid layout and comprises five separate process caverns, with individual span and height both reaching maximum of 32m. The stage 1 works (Contract No.: DC/2018/05) for site preparation and main access tunnel commenced in 2019 and completed in 2022. The stage 2 works (Contract No.: DC/2020/05) for main caverns complex, secondary access tunnel, ventilation adit and shaft construction commenced in July 2021, and all blasting works were completed in September 2025.

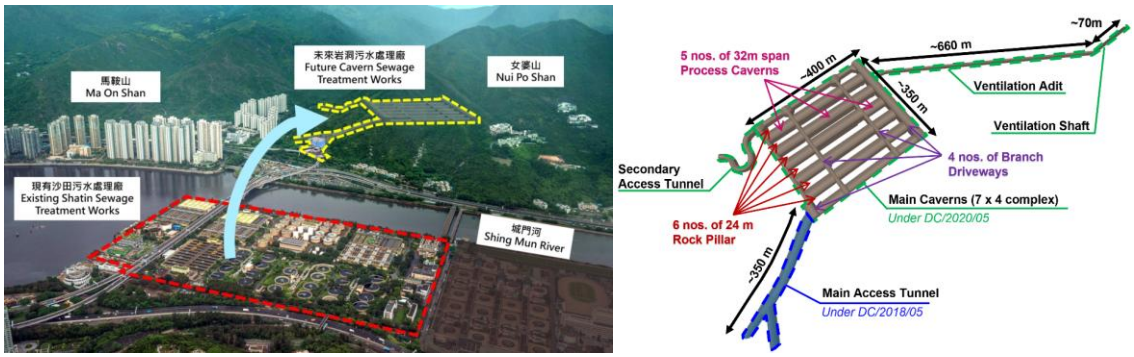

Figure 1: Relocation of Sewage Treatment Plants to Caverns – Cavern Layout and Arrangement

1.2 Conventional NATM Practice in Hong Kong and Adoption of RRA in STC Project

Under conventional and conservative New Austrian Tunnelling Method (NATM) practice in Hong Kong for hard-rock tunnels, two structurally independent (i.e. double-shell) support systems are installed. Temporary supports (typically rock dowels and sprayed concrete) are applied immediately after excavation. Permanent support is installed subsequently in the form of cast-in-situ concrete lining. Waterproofing membrane system (commonly geotextile and sheet membrane) is installed. Comparing high compressive strength of rock in Hong Kong with structural concrete grade, NATM does not fully utilise the inherent load-bearing capacity of competent rock masses. The involvement of extensive steel reinforcement and heavy steel shutters offers a labour-intensive, time-consuming, expensive and high-risk construction solution.

Figure 2: Conventional NATM involves the use of Complicated Temporary Working Platform

Alternatively, the Rock Reinforcement Approach (RRA) has been developed to consider the hard rock as a structural material to self-support itself by utilizing the hoop stress, within the reinforced rock arch above roof.

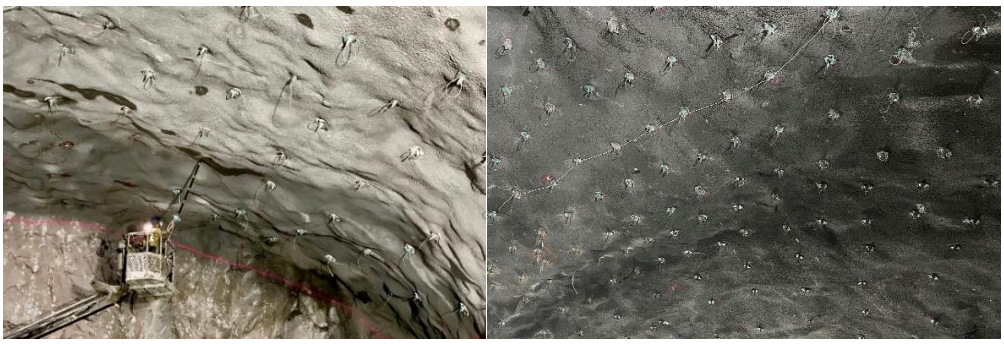

Figure 3: Installation of Permanent Systematic Rock Bolts as Primary Support System

Based on geological mapping of the excavated rock face, permanent systematic rock bolts were installed as primary supports for forming the reinforced rock arch, while permanent sprayed concrete lining is the secondary support which provides a layer of surface confinement to inhibit the kinematics of rock blocks and complement the pattern rock bolting. Permanent spot bolts were also installed to stabilize individual rock blocks/wedges.

2 GROUND INVESTIATION CONSIDERATIONS

2.1 General

The proposed cavern complex extends approximately 4.8 km. Identification of weak ground is critical under the RRA, as adverse geological conditions may affect feasibility and require costly reinforced concrete (RC) linings. Although GI costs account for less than 1% of the total project cost, they are essential for reducing geological uncertainty. A total of 133 boreholes were completed, including two Horizontal Directional Corings (HDC), supplemented by surface geophysics tests and downhole geophysical logging. It enabled identification of key geological features and improved confidence in the ground model for robust cavern planning and design.

2.2 Horizontal Directional Coring (HDC)

Two HDCs of approximately 1.9 km were completed using steerable drilling techniques. This enabled continuous rock core recovery along the planned alignments, including through sub-vertical geological features/faults, and obtained targeted core samples and field testing at specific locations of interest. This also marked the first application of optical and acoustic televiewer logging along HDC in Hong Kong.

Figure 4a & 4b: HDC drill-rig set up (left) and cable threaded through 1km long drill rod for televiewer tests (right)

2.3 In-situ Stress Measurement

In-situ stress conditions are essential for assessing cavern stability and optimising rock support design, and were assessed using overcoring and hydraulic fracturing tests. The overcoring test involved installing a triaxial cell in a pilot borehole, followed by overcoring to relieve stresses and measure strain changes. For the hydraulic fracturing tests, it was conducted by pressurising isolated borehole sections to induce fractures, from which stress magnitudes and principal stress orientations were derived. The orientation of maximum / minimum horizontal principal stress is parallel / perpendicular to the fracture plane (known by impression packer test).

Figure 5a & 5b: Overcoring Test (left) and Hydraulic Fracturing Test (right)

2.4 Ground Model and Rock Mass Quality (Q-value)

The solid geology is predominantly Shui Chuen O Granite. Based on the extensive GI data, a three-dimensional geological model was developed. The empirical Q-system first developed by Barton et al. (1974) and updated

by Grimstad & Barton (1993) was used for rock mass classification. It describes the stability of an underground opening in jointed rock masses. High Q-values indicate good stability, vice versa. The Q-value is formulated by the multiplier of six different rock mass parameters as presented in Equation 1:

$$Q = \frac{RQD}{J_n} \times \frac{J_r}{J_a} \times \frac{J_w}{SRF} \qquad (1)$$

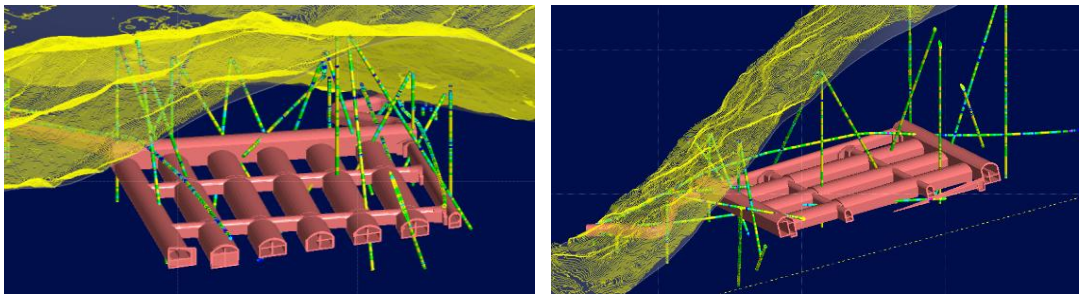

Figure 6: Three-dimensional Geological Model for the STC Project

3 DESIGN CONSIDERATIONS

3.1 Overall Design Philosophy

The main cavern complex for the STC project involves the excavation of multiple large-span caverns in a 7 × 4 grid layout, with individual spans and heights reaching up to 32 m. Each cavern is separated by 24 m wide rock pillars to suit sewage treatment facilities. According to To et al. (2021), permanent support requirements become more stringent with increasing cavern span and the presence of multiple parallel excavations.

To ensure a robust design solution, the design procedures and checks should address various possible scenarios and anticipated failure modes. The design is initially based on a preliminary assessment using a reliable global database with minimal site-specific input. It is then checked against the RRA design philosophy, in which systematic rock bolts act as primary supports to form a reinforced rock arch, while sprayed concrete stabilises wedges between adjacent bolts. Finally, the design capacities of the permanent supports are validated using site-specific geological and geotechnical parameters (joint conditions and overburden depth) and cavern configurations (span and pillar width). As the pilot cavern project, the three-stage design procedure for RRA in Figure 7 has been established for the STC project and endorsed by the relevant authorities in Hong Kong.

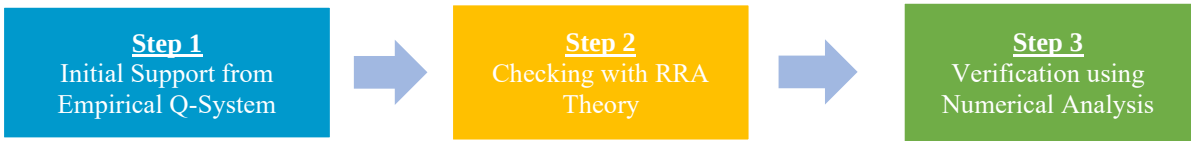

Figure 7: Three-stage Design Procedures for RRA established in Hong Kong

3.2 Initial Support from Empirical Q-system

As discussed in Section 2.4, the empirical Q-system was used for rock mass classification, and the rock support chart (Figure 8) was adopted for preliminary support assessment. For a given combination of Q-value, excavation size, and safety requirements (in terms of Excavation Support Ratio, ESR and Equivalent Dimension), the initial rock supports including the systematic rock bolt spacing and shotcrete thickness was determined for a given support class. However, empirical approaches have limitations in cavern design, particularly for large-span excavations and the influence of multiple parallel openings.

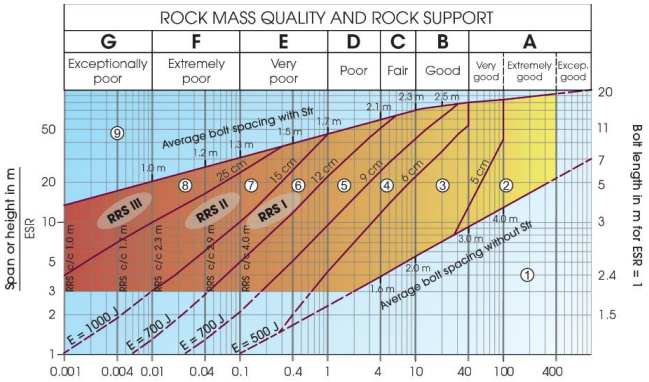

Figure 8: The latest Q-system rock support chart (NGI, 2022)

The empirical formula proposed by Barton et al. (1977), as cited in Geoguide 4 (2018), can be used to determine the initial systematic rock bolt length as presented in Equation 2. This is appropriate for systematic support, but may not be sufficient for spot bolts stabilising potential rock wedges, which need to be assessed separately.

$$L = 2 + \frac{0.15\ B}{ESR} \qquad (2)$$

where L = bolt length (in m)
B = tunnel span for roof support (tunnel height H for wall support) (in m)
ESR = excavation support ratio (safety requirement)

3.3 Checking of Support with Reinforced Rock Arch Theory

From structural mechanics, an arch is a structural member that transmits loads primarily through axial compressive thrust to its supports at two ends. This concept is widely applied in bridges and dams. According to Bischoff and Smart (1977), the thrust capacity of the rock arch is determined by the ratio of unconfined compressive strength to tensile strength with the confinement pressure by rock bolts. The systematic rock bolt force F_b provides confining pressure to contribute the thrust capacity ΔT_A (half span of opening) as given by Equation 3. The inherent rock mass strength is utilised to form the reinforced rock arch.

$$\Delta T_A = \frac{\sigma_c}{\sigma_t} \times \frac{F_b}{S^2} \times (L - S) = tan^2\left(45^o + \frac{\emptyset}{2}\right)\frac{F_b}{S^2}(L - S) \qquad (3)$$

where σ_c = unconfined compressive strength of rock σ_t = tensile strength of rock
ϕ = the rock mass friction angle

The empirical relationship of Q-system to rock loadings were first developed by Barton et al. (1974) and further updated by Grimstad & Barton (1993). The tunnel support pressure at crown (P_{roof}) was estimated using Equation 4. The thrust capacity of the reinforced rock arch ΔT_A was checked against the rock pressure at crown (P_{roof}) at the springline as illustrated in Figure 10.

$$P_{roof} = \frac{0.2\ J_n^{1/2}\ Q^{-1/3}}{3\ J_r} \quad (MPa) \qquad (4)$$

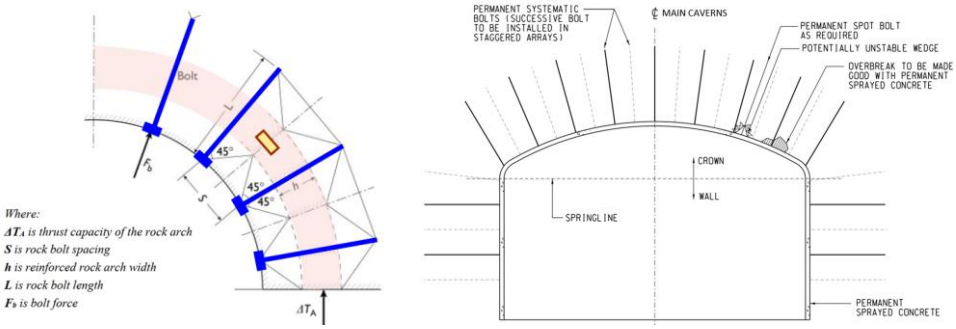

Figure 9: Permanent Cavern Support Requirements with Reinforced Rock Arch (RRA)

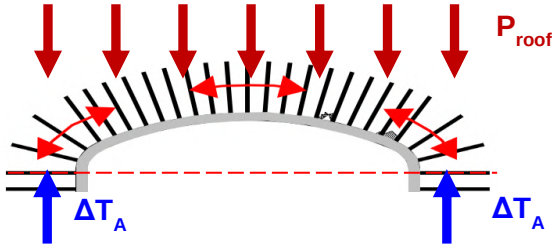

Figure 10: Checking of thrust capacity against rock pressure at crown (sketched by the author)

The permanent shotcrete lining is treated as a thin shell and checked against potential failure modes, including adhesive, flexural, shear, punching, compressive, and tensile failures (Barrett & McCreath, 1995) as illustrated in Figure 11. The required thickness is also governed by the stability of potential wedges between adjacent bolts.

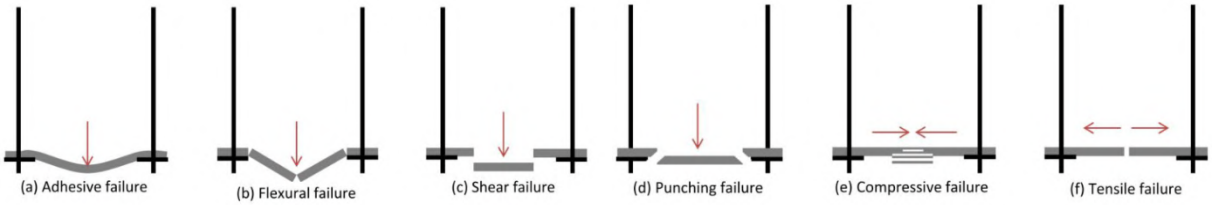

Figure 11: Six failure modes of shotcrete lining between bolts (modified from Barrett and McCreath 1995)

3.4 Verification using Numerical Analysis

The empirical and analytical designs were then verified using numerical modelling. In rock engineering, numerical models are classified as continuum modelling (e.g. finite element modelling, FEM) and discontinuum modelling (e.g. discrete element modelling, DEM), as shown in Figure 12. Scale-effect which indicates the relative size between the excavation profiles and block size shall be considered. Discontinuities of the rock mass can be considered implicitly with pseudo-discontinuities by modifying the intact rock properties to rock mass properties or explicitly by simulating the discrete discontinuity elements.

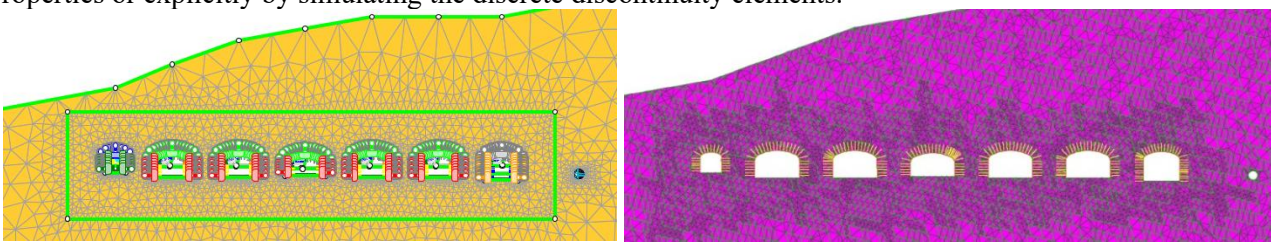

Figure 12: 2D FEM (left) and 2D DEM (right) analysis for the cavern supports

Rock at depth is subjected to stresses resulting from the weight of the overlying strata. When an underground opening is excavated, the stress field in this rock mass is locally disrupted and induces a new set of stresses surrounding the new opening. In particular at the cavern junctions, the re-distributed stresses will alter the stress fields of adjacent openings. Induced stresses (in form of loadings) from a taller cavern is transferred through the

rock arch and concentrate as an additional vertical stress above the crown of the adjacent shorter cavern. The general rock load transfer mechanism at junctions is presented in Figure 13.

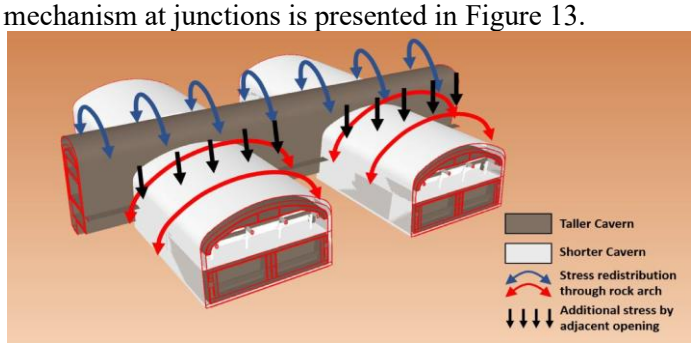

Figure 13: Rock Load Transfer Mechanism at Junctions

As recommended by Hoek E (2007), three-dimensional analyses provide a starting point for analysing a problem in which the three-dimensional geometry of the openings is important. It provides clearer results of stress concentrations due to the influence of complex geometry. Therefore, a preliminary elastic analysis with 3D FEM was used to verify the "one diameter" influence zone for cavern complex junctions as shown in Figure 14.

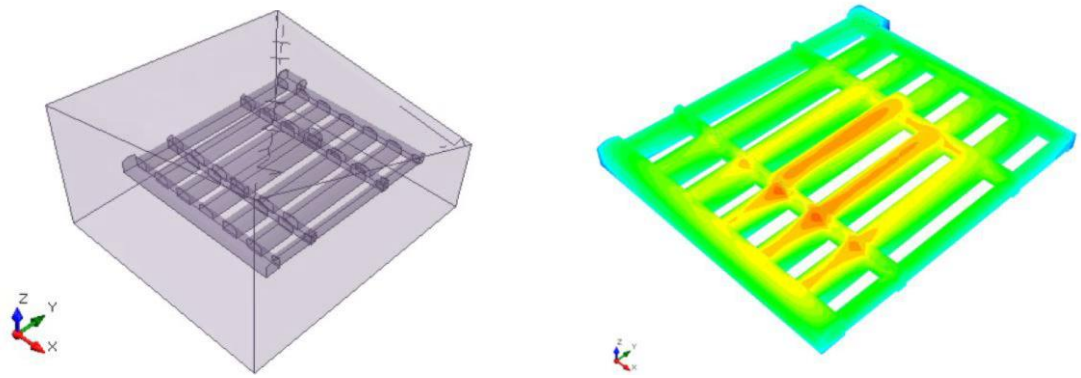

Figure 14: 3D FEM for Full Cavern Complex Model

In addition, 3D FEM analysis was conducted at each intersection of openings to check the design capacities of permanent rock bolts against concentrated loadings, as shown in Figure 15.

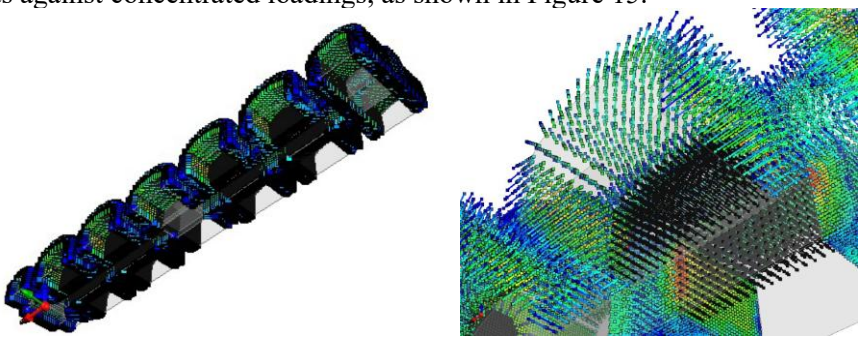

Figure 15: 3D FEM analysis at each intersection of openings for the cavern supports

3.5 Geotechnical Baseline Report

The STC project adopts the NEC4 ECC Option C (target cost contract with an activity schedule), which incorporates a risk-sharing mechanism, particularly for quantity-related risks in tunnelling works. This differs from the traditional General Conditions of Contract (GCC) for Civil Engineering Works, where the Contractor is deemed to have fully assessed the ground conditions prior to tender and is generally difficult to claim due to unforeseen ground conditions. Under NEC, a Geotechnical Baseline Report (GBR) is used to enable a fairer allocation of geotechnical risks.

Baselines are defined using parameters that can be readily identified and recorded during construction, and that can be directly linked to cost and time implications. For the STC project, the GBR includes baseline definitions of, for examples, the length range and approximate locations of defined major geotechnical features, the range of Q-values corresponding to each support class, and the length of caverns requiring pre-excavation grouting.

4 CONSTRUCTION CONSIDERATIONS

4.1 Encountered Geological Conditions

In general, Grade II granite was encountered during the excavation works for the access tunnels, main caverns, adit and shaft. From a total of 2,488 blasts, the associated geological mapping results are summarised in Table 1. Considering scale effects between the size of 32m cavern span and the width of weak zone, the rock mass quality is generally good, as further indicated in Table 2.

Table 1: Summary of Q-value (with Total Blast Nos. of 2488)

-	Q-value	RQD	Jn	Jr	Ja	Jw	SRF
Highest	11.3	90	15	-	3	1	-
Lowest	2.1	50	12	-	1	0.66	-
Average	8.4	75	~12	1.5	1.2	~1	1

Table 2: Summary of Q-value Distribution

Q-value	Distribution
$2.1 \leq Q < 4$	8%
$4 \leq Q < 8$	6%
$8 \leq Q < 11.3$	86%

The poorest ground condition encountered (Q = 2.1) comprised fractured rock mass with calcite infill, associated with moderately decomposed mafic intrusion containing numerous calcite-filled microfractures as shown in Figure 16. For groundwater control, a slightly higher groundwater inflow was observed locally during excavation, and localised pre-excavation grouting (PEG) was carried out to control inflows. No full-face PEG was required at any stage of the works. Subsequently, drainage strips were installed at an average spacing of 5 m c/c spacing across the cavern complex (locally closest at 1m c/c spacing) and to effectively collect and relieve the groundwater pressure from the drained cavern perimeter and discharge to the invert drainage layer.

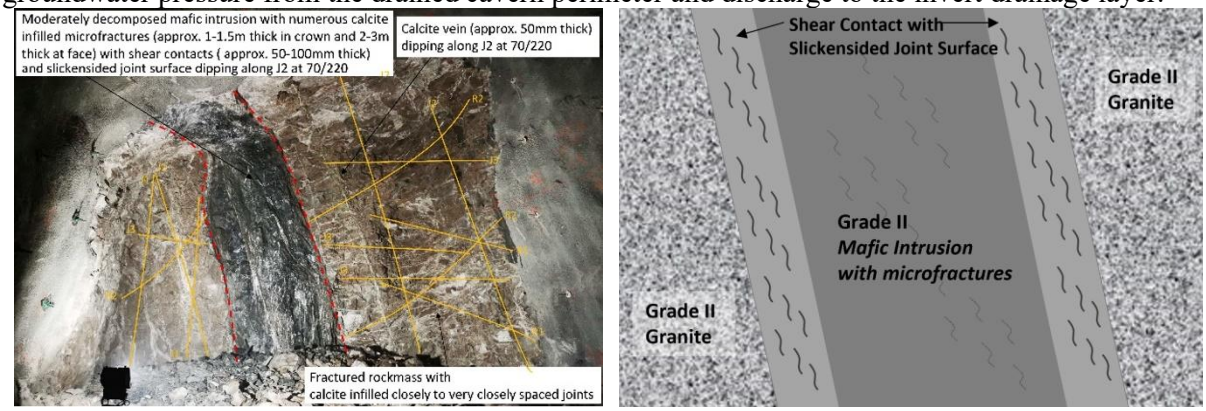

Figure 16: Encoutnered weak zone across the caverns (with lowest Q-value of 2.1)

4.2 Permanent Rock Bolts

Permanent rock bolts, together with temporary shotcrete, were installed immediately after excavation to stabilise the rock mass and maintain excavation safety during ongoing blasting activities. Proprietary rock bolts were adopted to achieve a 100-year design life (Figure 17a), incorporating enhanced corrosion protection measures, including protective coatings and plastic sheathing. An expansion shell was provided at the end of each bolt to

ensure immediate mechanical anchorage upon installation. The bolts were subsequently fully grouted to develop adequate bond strength and ensure long-term durability prior to the next blasting cycle.

Proper site supervision of grout mix and strength requirements was implemented, together with initial pull-out tests and continuous proof load tests (at a frequency of 2.5%), to verify the installation quality of rock bolts. Advanced surveying technologies were also used to validate the as-built spacing between adjacent bolts. A total of approximately 62,000 rock bolts were installed for the main cavern works.

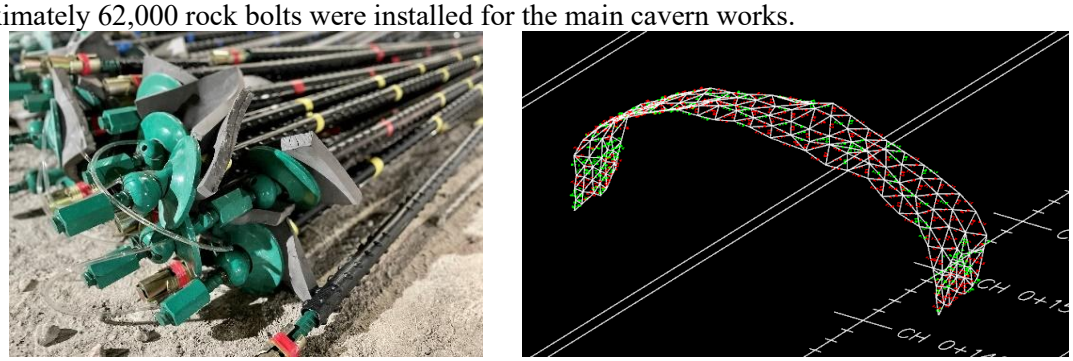

Figure 17a & 17b: Permanent rock bolts (left) and Surveying checking of as-built rock bolt head (right)

4.3 Permanent Shotcrete Lining

Temporary shotcrete is generally regarded as a sacrificial layer due to potential blast-induced damage. Accordingly, an additional layer of permanent sprayed concrete was designed and constructed to meet specified performance criteria, including thickness and strength requirements (compressive, flexural, bond, and energy absorption), with fibre dosage specified by the supplier. Macro synthetic fibres were added on site to enhance flexural strength, while micro synthetic fibres were added at the batching plant to improve resistance to fire-induced spalling. Strict workmanship control was enforced, with spraying carried out only by trained and certified nozzlemen (e.g. EFNARC-qualified or equivalent), each having successfully completed site trials. A total volume of approximately 40,000 m^3 of permanent shotcrete is consumed, including the rebound (wastage) of permanent shotcrete of typically around 30%.

Unlike conventional cast-in-situ concrete lining, acceptance of the permanent shotcrete lining was based on achieving adequate thickness over the blasted profile, without the need for additional backfilling to the theoretical internal profile. The use of 3D laser scanning using LiDAR technology was employed to generate point cloud data for accurate verification of shotcrete thickness or identification of underbreak.

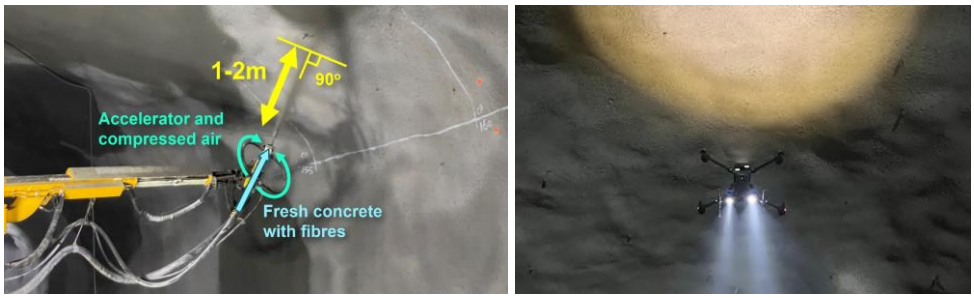

Figure 18: Workmanship control and site conditions inspection for permanent shotcrete

Figure 19: 3D laser scanning using LiDAR technology for permanent shotcrete thickness verification

4.4 Blasting Sequence and Logistics

Due to the height limitation of drilling jumbo (approximately 14 m), the cavern excavation was divided into top-heading, middle (only for tall caverns), and bottom benches, as shown in Figure 20. The overall excavation sequence comprised a combination of multiple workfronts and blast face excavation with concurrent operations. Blasting operations and logistic flow were the key challenges. In general, a 2-3 day blast cycle was achieved for the 32 m span top-heading and bench excavations. The key parameters for the typical blast design are summarised in Table 3.

Figure 20: Top-heading and Bench Excavations for the Caverns

Table 3: Summary of Blasting Parameters at Top-heading and Benches (with Total Blast Nos. of 2488)

Face	Face Area (m^2)	Rock Volume (m^3)	Charged Hole (pc)	Hole Diameter (mm)	Spacing (m)	Drill Hole Depth (m)	Charge Length (m)	Explosive per Round (kg)	Powder Factor (kg/m^3)
Top-heading	280	1540	258	51	1	5.5	4	1820	1.27
Bench	380	2100	244	51	1.2	5.5	4	1910	0.96

Concurrently, a maximum of 13 active faces was achieved, with up to seven blasts carried out per day. Critical aspects of the blasting sequence occurred at cavern intersections, where differing crown levels, access constraints between invert levels of top-heading and bench blast faces, resource utilisation (particularly shotfirers, drilling jumbos and cherry pickers), and the timely installation of permanent fully grouted rock bolts and temporary shotcrete had to be carefully managed. A holistic review and planning process was undertaken using BIM analysis to evaluate various construction programme scenarios as shown in Figure 21 and Figure 22.

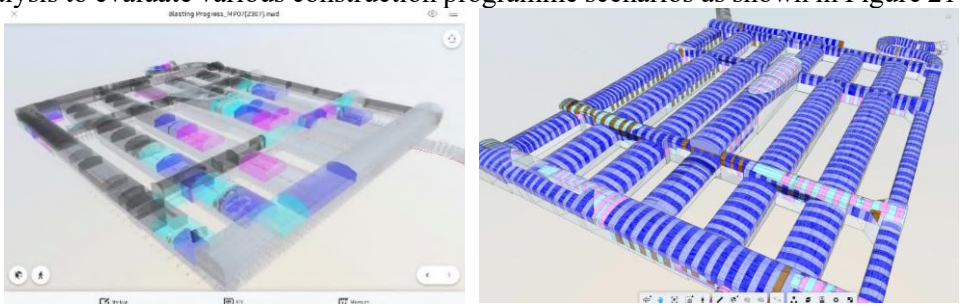

Figure 21: A Maximum of 13 Active Faces was Achieved, with up to Seven Blasts carried out per Day

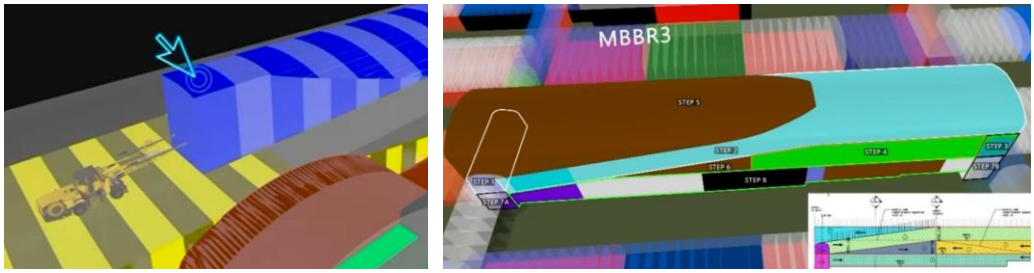

Figure 22: Holistic Review and Planning Process using BIM Analysis

4.5 Temporary Blasting Explosives Magazine (Mode A Store)

The excavation works were carried out over approximately 2.5 years, involving 2,488 blasts and producing about 2,100,000 m³ of excavated rock. At peak construction, up to 13 active blasting faces were in operation. To support operational flexibility, a temporary blasting explosives magazine (Mode A Store), as shown in Figure 23, was established on site for storage of limited quantities of explosives, including detonators and cartridges. This reduced reliance on daily deliveries from the Kau Shat Wan Explosives Depot and enabled contingency for multiple blasts to be conducted per day. The Mode A store was designed and operated in compliance with regulatory requirements, with a designated location, controlled capacity, and approved delivery route.

Figure 23: Temporary Blasting Explosives Magazine (Mode A Store)

Comprehensive safety and security measures were implemented, including CCTV surveillance, double-layer fencing, and 24-hour armed guarding. Access was restricted to authorised personnel, and the use of mobile phones or radio transmitting devices was prohibited. A three-key system was adopted for each compartment to ensure controlled access. All explosives handling, storage, and conveyance were carried out by authorised personnel, with only one class of explosive handled at any time. Explosives were issued under permit with proper documentation, and records were maintained in a stock register.

4.6 Handling on Excavated Rocks

The STC project transformed large-scale rock excavation into environmental value. A pre-contract rock handling plan was developed to identify designated areas for rock processing and reuse. Risk mitigation measures were implemented to avoid excessive stockpiling within the cavern. A rock crushing line was established to facilitate efficient sorting, processing, and reuse of excavated materials.

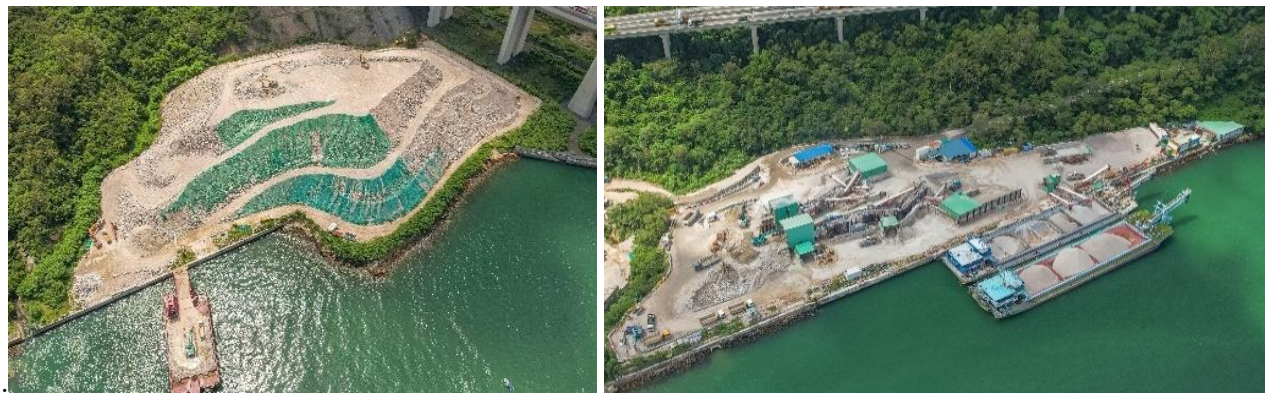

Figure 24: Rock Handling Facilities, including stockpiling, sorting, processing and transportation

4.7 Instrumentation & Monitoring

An instrumentation and monitoring system was implemented to assess ground response and the performance of permanent rock reinforcement during cavern excavation. Monitoring arrays as shown in Figure 25 included multipoint borehole extensometers (MPBX), load cells, strain gauges, optical prisms, vibrating wire

piezometers, and stress cells. The monitoring data were interpreted alongside the staged excavation sequence and enabled continuous evaluation of excavation-induced responses.

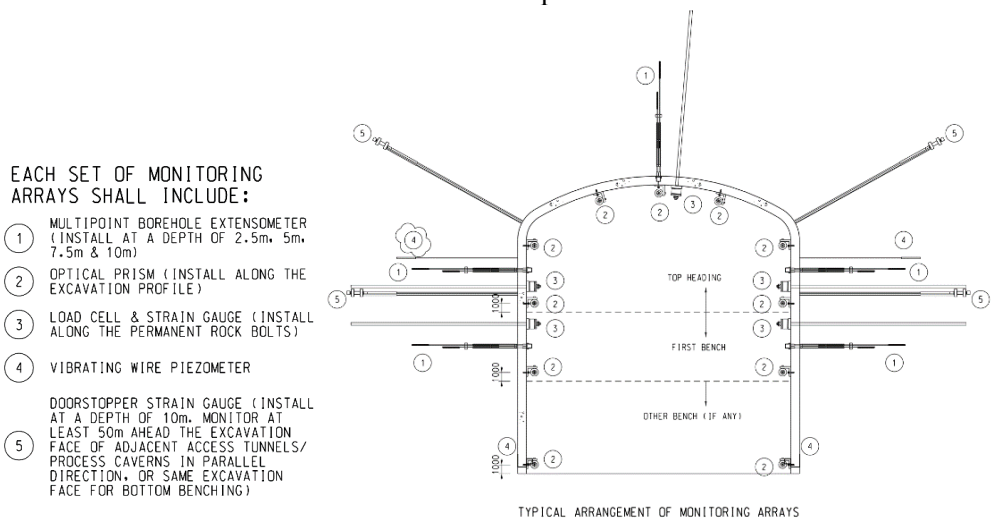

Figure 25: Monitoring Arrays at Caverns

Monitoring results confirmed that adjacent excavation activities influenced deformation and rock bolt forces. Measured displacements were small (generally within few mm) and stabilised after excavation, indicating controlled behaviour and effective support performance. Groundwater pressures remained low with minor seasonal variation, consistent with predominantly dry conditions and localised seepage. Overall, the monitoring results confirm that the excavation and support system performed satisfactorily with design assumptions.

4.8 Pilot Use of Vibration-Resistant Shotcrete (VRSC) in Hong Kong to achieve true Single-pass Lining

It is often considered that blast-induced vibrations could damage early-age sprayed concrete, leading to the conventional two-pass lining approach in Hong Kong, where the temporary shotcrete is treated as sacrificial. The VRSC was developed to withstand blasting impacts through bond strength enhancement, enabling a true single-pass lining system that serves both temporary and permanent support purposes. The pilot application in the STC project at benches excavation demonstrated its feasibility, supported by near-field vibration monitoring and confirmed that bond performance was not adversely affected by close-proximity blasting. Compared with conventional shotcrete, VRSC achieved reduction in sprayed concrete volume, rock excavation and time saving.

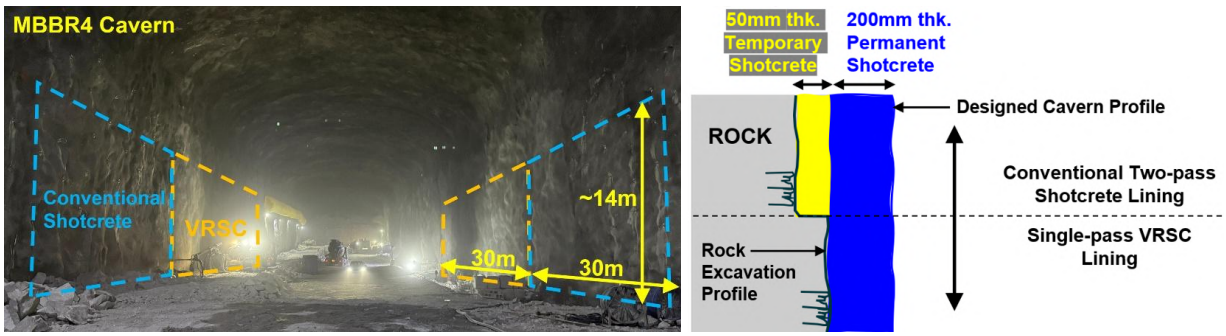

Figure 26: Pilot Application of VRSC at STC Project – Reduction in rock excavation and time saving

5 CONCLUSION AND RECOMMENDATIONS

This paper presents and showcases the STC project, the pilot government cavern project and the largest rock cavern development in Asia. It demonstrates the successful application of the RRA-based design approach for large-span cavern developments in Hong Kong, supported by comprehensive ground investigation, detailed design, and rigorous site supervision. The permanent rock reinforcement performed satisfactorily, with monitoring results confirming design assumptions and stable ground behaviour. The project provides valuable insights for performance enhancement in future large-scale cavern developments in Hong Kong.

ACKNOWLEDGEMENT
The authors gratefully acknowledge the Drainage Services Department, the Government of the Hong Kong Special Administrative Region, for permission to publish this paper.

REFERENCES
Barton N., Lien R. and Lunde J. 1974. *Engineering Classification of Rock Masses for the Design of Tunnel Support*. Rock Mechanics, vol. 6, pp 189-236.

Bischoff J.A. & Smart J.D. 1977. *A method of computing a rock reinforcement system which is structurally equivalent to an internal support system*. In Proceedings of the 16th US Symposium on Rock Mechanics, Minneapolis, MN, USA (Fairhurst C and Crouch SL (eds)). ASCE, New York, NY, USA, pp. 279–284

Grimstad E., and Barton N. 1993. *Updating of the Q-system for NMT*. Proceedings of the International Symposium on Sprayed Concrete, Fagernes, Oslo. pp46-66.

NGI. 2015. *Using the Q-system: Rock Mass Classifications and Support Design (handbook)*. Norwegian Geotechnical Institute, Oslo.

GEO. 2018. *Geoguide 4: Guide to Cavern Engineering, Second Edition (2018)*. Geotechnical Engineering Office, Hong Kong SAR.

To F.K.L., Bridges G.D.C. & Seto A.K.W. 2021. Design Optimization of Permanent Systematic Rock Bolts and Shotcrete Lining for Large-Span Caverns in Hard Rock. Proceedings of The HKIE Geotechnical Division. 41st Annual Seminar.

Test and Analysis of Confined Compressive Strength and Average Elastic Modulus of Metasedimentary Rocks in the Northern Metropolis of Hong Kong

Zhiqian Liu, Qi Zhao,Guoxu Chen, Pan Hu, Andy Y. F. Leung
The Hong Kong Polytechnic University, Hong Kong
Maggie H.Y. Suen & Cyrus C.F. Chow
AECOM Asia Company Limited, Hong Kong

ABSTRACT

Metasedimentary rocks are widely distributed in the Northern Metropolis of Hong Kong and exhibit pronounced variability in confined compressive strength (*CCS*) and average elastic modulus (*Avg. E*) due to well-developed foliations, fractures, and mineral fabric. To identify the controlling mechanisms and develop a practical prediction method, this study combined triaxial compression tests, pre- and post-test CT scanning, Cerchar abrasivity tests, slake durability tests, and petrographic thin-section analysis. CT results indicate that pre-existing fractures and structural integrity mainly control the lower bound of mechanical performance, whereas thin-section observations show that quartz skeleton continuity, quartz recrystallization, and the preferred orientation of platy minerals jointly affect load-bearing capacity and weak-plane development. Based on these observations, the controlling factors were classified into four physical dimensions: skeleton hardness, structural integrity and water sensitivity, loading angle, and confining pressure. Model comparisons show that the full-variable log-linear regression model improves *CCS* prediction over the single-variable model, and that reorganizing the variables according to mechanistic dimensions yields further improvement. The proposed framework provides a practical and interpretable approach for rapid estimation of the mechanical parameters of metasedimentary rocks in the Northern Metropolis of Hong Kong.

1 INTRODUCTION

The Northern Metropolis of Hong Kong is a key area for future urban expansion, cross-boundary infrastructure development, and underground space utilization. Metasedimentary rocks are widely distributed in this region. Owing to the pervasive development of foliation, bedding, joints, fractures, and mineral fabric, these rocks exhibit pronounced anisotropy and high variability. Existing confined compressive strength (*CCS*) test results (see Appendix Table 1) show that, under confining pressures ranging from 0 to 2000 kPa, the confined compressive strength of the samples varies from 1.95 to 199.64 MPa, while the average elastic modulus (average slope of the straight-line portion of the stress-strain curve in *CCS* test, *Avg. E*) ranges from 0.45 to 53.04 GPa, spanning several orders of magnitude. Such variability directly affects excavation method selection, support design, seismic analysis of underground structures, and slope stability assessment.

In engineering practice, *CCS* and *Avg. E* are two key parameters used to characterize the load-bearing capacity and deformation behavior of rock. The former is more directly related to peak load capacity and failure risk, whereas the latter governs rock mass deformation, stiffness compatibility with structures, and parameter selection in numerical analysis. However, both parameters are costly to determine experimentally and are highly sensitive to discontinuities, foliation orientation, pre-existing fractures, and water sensitivity. As a result, a limited number of direct tests often cannot reliably represent the characteristics of an entire rock mass section. Therefore, the rapid prediction of *CCS* and *Avg. E* using more readily obtainable indirect indices has become a critical issue in the engineering characterization of metasedimentary rocks.

Previous studies have shown that the strength and deformation parameters of foliation- or bedding-controlled rocks are highly sensitive to loading direction, with the most unfavorable orientation commonly occurring at intermediate angles between the loading axis and the weakness plane (Saroglou & Tsiambaos, 2008; Waqas et al., 2024). Meanwhile, tests on laboratory size samples including the Cerchar abrasivity test and the slake durability test provide rapid means of characterization from the perspectives of rock skeleton hardness, and structural integrity and water sensitivity, respectively. The Cerchar Abrasivity Index (*CAI*) is widely used to

reflect rock skeleton hardness and its relationship with strength and excavation performance (Alber et al., 2014; Gao et al., 2024; Jeong et al., 2023), whereas the Slake Durability Index (*SDI*) is a classical variable for evaluating the structural integrity and water sensitivity of weakly cemented rocks (Franklin & Chandra, 1972). However, for metasedimentary rocks that are jointly controlled by mineral skeleton, structural defects, foliation orientation, and water action, a single indirect index is usually insufficient to fully explain the high variability of their mechanical properties. Compared with purely empirical correlation analysis, CT scanning can directly reveal the initial fracture state of specimens before loading and the crack propagation path after loading, thereby providing structural evidence for the origin of strength and modulus variability. When combined with thin-section analysis and rapid tests such as Cerchar and slake durability, CT-based observations offer the potential to further identify the dominant mechanisms governing variations in the mechanical parameters of metasedimentary rocks.

To address this issue, the Rock Mechanics Laboratory of The Hong Kong Polytechnic University, in collaboration with the Geotechnical Engineering Office (GEO) of the Civil Engineering and Development Department (CEDD) and AECOM Asia Co. Ltd., established an integrated multi-technique characterization framework. This framework combines laboratory tests, including triaxial compression tests, pre- and post-test CT scanning, Cerchar abrasivity tests, slake durability tests, and petrographic thin-section analysis, to systematically identify the controlling mechanisms of the mechanical variability of metasedimentary rocks. On this basis, the present study takes *CCS* and *Avg. E* as the target parameters, develops prediction models, and compares them with a baseline model and a full-variable reference model, with the aim of exploring a prediction approach that is both practically convenient for engineering use and mechanistically interpretable. The results reported here represent one segment of a larger dataset derived from a comprehensive study of Hong Kong metasedimentary rocks, and our model will be improved continuously by incorporating more data points.

2 MATERIALS AND METHODS

2.1 Engineering Geological Background

The samples used in this study were collected from 12 boreholes at Sandy Ridge (SR) and Lok Ma Chau (LMC) in the Northern Metropolis of Hong Kong. The lithology is dominated by metasedimentary rocks. At the macroscopic scale, the samples generally exhibit varying degrees of foliation, layered structure, and jointing/fracturing, indicating strong structural anisotropy. Rather than emphasizing overall differences among boreholes or lithological groups, this study treats them as a single class of structurally complex and highly variable metasedimentary rock samples, with the focus placed on the common mechanisms controlling variations in *CCS* and *Avg. E*. The tested specimens were primarily intact laboratory-sized samples, with the exception of a few that appeared intact but contained pronounced pre-existing fractures.

2.2 Laboratory Testing and Characterization Scheme

To identify the sources of mechanical variability in metasedimentary rocks, an integrated multi-technique characterization scheme was adopted, including triaxial compression tests, pre- and post-test CT scanning, Cerchar abrasivity tests, slake durability tests, and petrographic thin-section analysis.

A total of 36 triaxial compression tests were conducted in accordance with ASTM D7012-23 (ASTM International, 2023) to obtain *CCS*, *Avg. E*, and failure modes; the detailed results are listed in Appendix Table 1. Five sets of pre- and post-test CT scans were performed to identify the initial fracture state and crack propagation paths within the specimens, thereby assessing the influence of pre-existing defects on strength and stiffness. A total of 31 Cerchar abrasivity tests were carried out in accordance with ASTM D7625-22 (ASTM International, 2022) to characterize rock skeleton hardness and abrasivity, with the *CAI* used as the quantitative measure of rock abrasivity. A total of 22 slake durability tests were conducted in accordance with ASTM D4644-16 (ASTM International, 2016), in which the initial moisture content (w) and the *SDI* were used to characterize structural integrity and water sensitivity. In addition, selected representative samples were subjected to petrographic thin-section analysis to identify quartz skeleton continuity, the preferred orientation of platy minerals, and recrystallization features, thereby providing microscopic evidence for interpreting skeleton load-bearing capacity and potential weak planes.

2.3 Data Matching and Selection of Modeling Samples

The samples used for model development were selected from borehole intervals for which *CCS* test results as well as Cerchar and slake durability test data were both available. It should be noted that the Cerchar and slake durability tests were not performed directly on the *CCS* specimens; instead, they were conducted on samples taken from nearby positions within the same borehole, with similar depths and lithologies. Therefore, sample matching was performed prior to modeling. The matching criteria prioritized consistency in borehole location, lithology, and depth proximity, so as to minimize errors introduced by sample substitution. The matching results are presented in Appendix Table 1.

3 RESULTS OF TRIAXIAL COMPRESSION TESTS AND MECHANISTIC INTERPRETATION

3.1 Relationship Between CCS and Avg. E

We first visualise compressive strength and *Avg. E* to obtain a rough understanding of their distributions and correlations in the samples we tested. For all test results, *Avg. E* generally increases with peak compressive strength, but the data are highly scattered, suggesting that *Avg. E* alone cannot determine *CCS*. For the unconfined specimens, *Avg. E* shows a clearer positive correlation with *UCS*. The fitted slope is close to the range of *Avg. E* ≈ 450–500 *UCS*, with $r = 0.851$ and $R^2 = 0.725$.

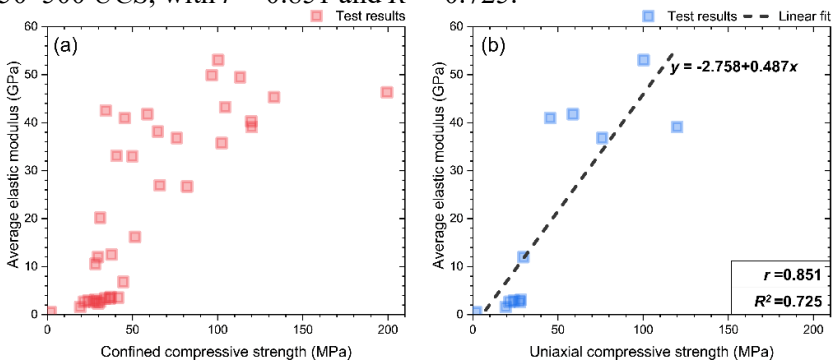

Figure 1: Relationships between *Avg. E* and compressive strength of the tested metasedimentary rocks: (a) *Avg. E* versus *CCS* for all triaxial test results under different confining pressures; (b) *Avg. E* versus uniaxial compressive strength (*UCS*) for the unconfined specimens, together with the best-fit linear regression line.

3.2 Initial Defects Revealed by CT Scanning and Their Mechanical Implications

Figure 2 presents the pre- and post-test CT scans of five representative specimens subjected to triaxial testing. The key value of CT scanning lies in its ability to identify the internal defect state prior to loading, thereby allowing assessment of whether pre-existing fractures provide preferential paths for subsequent failure. In general, specimens with more intact internal structures and fewer pre-existing fractures before testing tend to exhibit higher *CCS* and *Avg. E*, whereas specimens with more developed pre-existing fractures generally show lower strength and stiffness.

Among the specimens, T7 and T7a from SR-BH-B-137 (Figure 2a, Figure 2b) both appear relatively intact in the pre-test CT images, with the clear foliation pattern but no clearly identifiable pre-existing through-going fractures. After testing, localized through-going crack zones are observed. Their corresponding *CCS* and *Avg. E* values are 120.14 MPa and 39.06 GPa, and 113.34 MPa and 49.43 GPa, respectively, indicating that when no obvious pre-existing fractures are identifiable, the specimen can maintain relatively high overall load-bearing capacity and stiffness. Although the overall failure pattern still appears to follow the foliation (e.g., Figure 2b). In contrast, specimen T2 from SR-PD3-PO-02 (Figure 2c) shows a localized structural anomaly or vein-like feature in the pre-test CT image, and more pronounced crack propagation develops around this zone after testing. This specimen has a *CCS* of 64.97 MPa, while its *Avg. E* remains as high as 38.11 GPa, suggesting that even when overall stiffness is not low, peak strength may still be significantly reduced if pre-existing structural features provide preferential failure paths. Specimen T2 from LMC-VB1-2 (Figure 2d) already exhibits multiple pre-existing fractures in the pre-test CT image; after testing, these fractures further propagate and are accompanied by evident local block separation. Its *CCS* and *Avg. E* are only 19.37 MPa and 1.51 GPa,

respectively, indicating that both strength and stiffness decrease markedly when the specimen has poor initial integrity before loading. Specimen T5 from LMC-VB1-4 (Figure 2e) shows even more developed fractures and fragmented features in the pre-test CT image, followed by severe fragmentation and disintegration after testing. Its *CCS* and *Avg. E* are as low as 1.95 MPa and 0.45 GPa, respectively, representing a typical extremely weak specimen dominated by initial defects. These observations indicate that the more developed the pre-existing fractures are, the more weakened the specimen is.

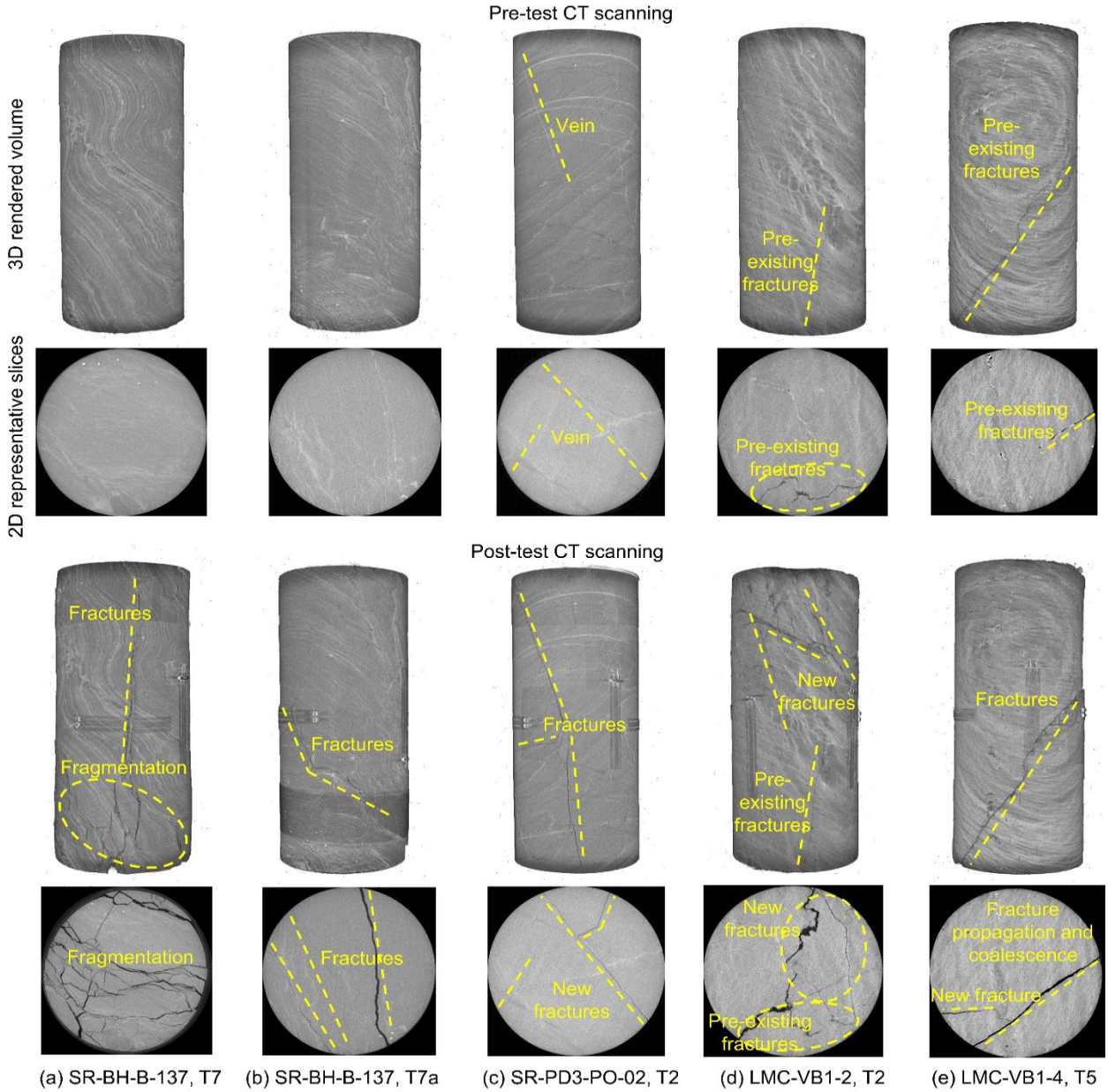

Figure 2: Pre- and post-test CT scanning results of five typical samples. Failures along foliation planes, joints, and fractures are commonly observed in the Metasedimentary Rocks in the Northern Metropolis of Hong Kong.

3.3 Thin-Section Features and Their Implications for Skeleton hardness and Weak Planes

Figure 3 presents petrographic thin-section images of six representative specimens. The main differences among these specimens are reflected in three aspects: the continuity of the quartz skeleton, the apparent degree of quartz recrystallization, and the prominence of the preferred orientation of platy minerals. These differences directly influence whether a specimen is more strongly governed by skeleton-dominated load bearing or is more prone to failure along weak planes.

In specimen CAI2 from SR-PD3-PO-02 (Figure 3b) and specimen T7 from SR-BH-B137 (Figure 3c), the quartz skeleton remains relatively distinct, and quartz forms a comparatively continuous load-bearing framework. These two specimens also appear to exhibit the strongest degree of quartz recrystallization among the six samples. In Figure 3b, this is reflected by the clearer quartz grain boundaries and intergranular contact relationships, whereas in Figure 3c the grain size is too fine to allow equally clear graphical annotation, although the overall texture still suggests a relatively high degree of recrystallization. Although the preferred orientation of platy minerals in T7 is still evident, the overall structure remains relatively dense, and the specimen is therefore more likely to maintain high skeleton hardness. By contrast, specimen T3 from SR-PD2-PO-01 (Figure 3a) is dominated by a fine-grained quartz–sericite–biotite assemblage. Its matrix is relatively compact, and some recrystallization features can also be identified, but both the continuity of the quartz skeleton and the apparent degree of recrystallization are weaker than those in Figures 3b and 3c, suggesting that its load-bearing capacity is likely at an intermediate level. In specimen SL3 from LMC-PD3-PD-01 (Figure 3d), quartz grains are embedded within more distinct weak bands, showing an alternating distribution of load-bearing skeleton and weak planes. In specimens T4 (Figure 3e) and T9 (Figure 3f) from LMC-PD3-PD-03, weak phases such as chlorite, biotite, and epidote are more strongly developed, the preferred orientation of platy minerals is more pronounced, and the continuity of the quartz skeleton is relatively poorer, making these specimens more likely to form continuous weak bands. For Figures 3d to 3f, no equally clear petrographic evidence of strong quartz recrystallization was identified.

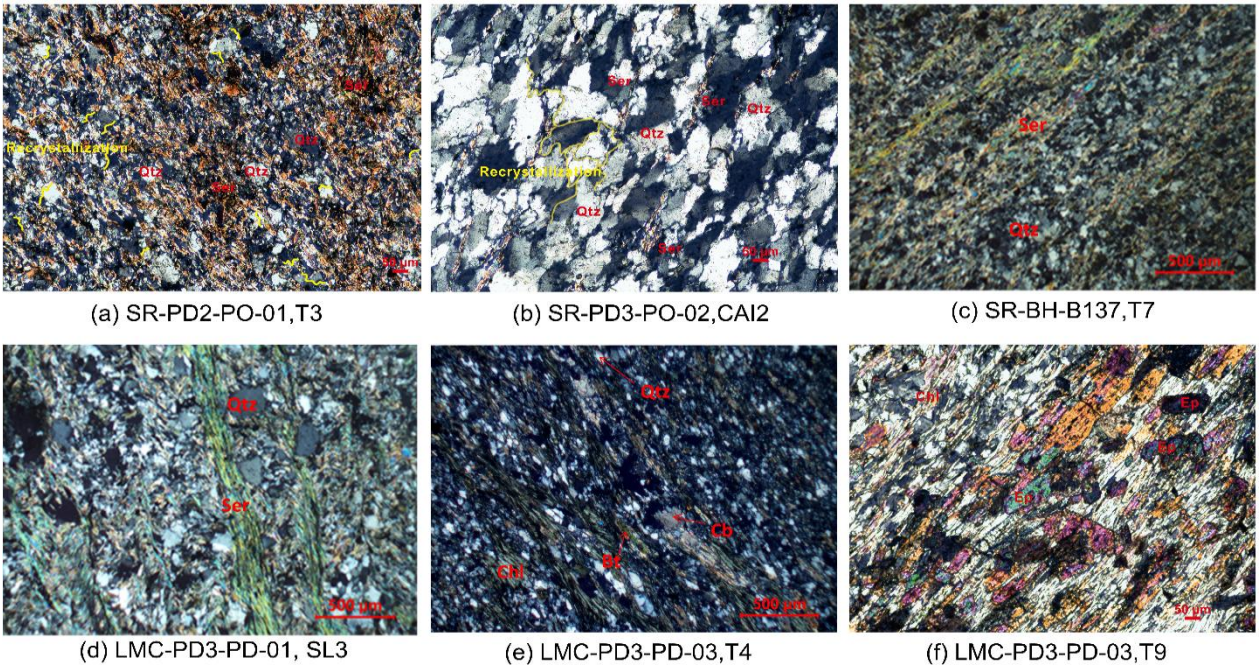

(a) SR-PD2-PO-01,T3 (b) SR-PD3-PO-02,CAI2 (c) SR-BH-B137,T7

(d) LMC-PD3-PD-01, SL3 (e) LMC-PD3-PD-03,T4 (f) LMC-PD3-PD-03,T9

Figure 3: Microscopic photos of rock thin sections of six typical samples

Overall, specimens with a more continuous quartz skeleton and more evident quartz recrystallization are more likely to exhibit higher strength and stiffness. In contrast, the stronger the preferred orientation of platy minerals and the more continuous the weak phases, the more easily the specimen tends to develop weak planes along foliation. In particular, specimens with more strongly developed weak phases such as chlorite also tend to exhibit looser structures and greater water sensitivity. These observations provide a microscopic basis for distinguishing between "skeleton hardness" and "structural weakening" in the subsequent analysis. The observed failure modes broadly support the petrographic interpretation. Bedding- or foliation-controlled shear failures are mainly associated with the preferred orientation of platy minerals and continuous weak bands, whereas axial splitting or shear failure not strictly following bedding suggests a stronger contribution from the intact quartz-bearing skeleton. Mixed failure modes reflect the combined effects of matrix cracking and foliation-controlled sliding. Thus, the variation in failure mode can be interpreted as a macroscopic manifestation of differences in mineral fabric, weak-phase continuity and pre-existing defects.

In that subsequent correlation framework, these thin-section features are treated as intrinsic material attributes, whereas confining pressure is considered separately as an external stress condition that directly affects the measured mechanical response, particularly *CCS*. Its influence on *Avg. E* is also examined, although its statistical contribution is relatively weak in the present dataset.

3.4 Mechanistic Motivation for Prediction Model Development

Figures 1 to 3 indicate that the mechanical variability of meta-sedimentary rocks in the Northern Metropolis of Hong Kong cannot be explained by any single factor. The CT results show that the more developed the initial fractures are, the more likely a specimen is weakened. The thin-section observations further indicate that differences in quartz skeleton continuity, degree of recrystallization, and preferred orientation of platy minerals determine whether a specimen is more strongly governed by skeleton-dominated load bearing or is more prone to instability along weak planes. Based on these observations, the controlling factors are subsequently grouped into four physical dimensions: skeleton hardness, structural integrity and water sensitivity, loading angle, and confining pressure. The specific proxy variables for each dimension and the results of their statistical screening are presented in the following section. As the dataset size is relatively limited, we report only the strength and quality of the correlations rather than the exact correlation parameters, in order to avoid potentially misleading engineering interpretations.

4 DEVELOPMENT OF PREDICTION MODELS FOR *CCS* AND *Avg. E*

4.1 Selection of Candidate Variables and Correlation Analysis

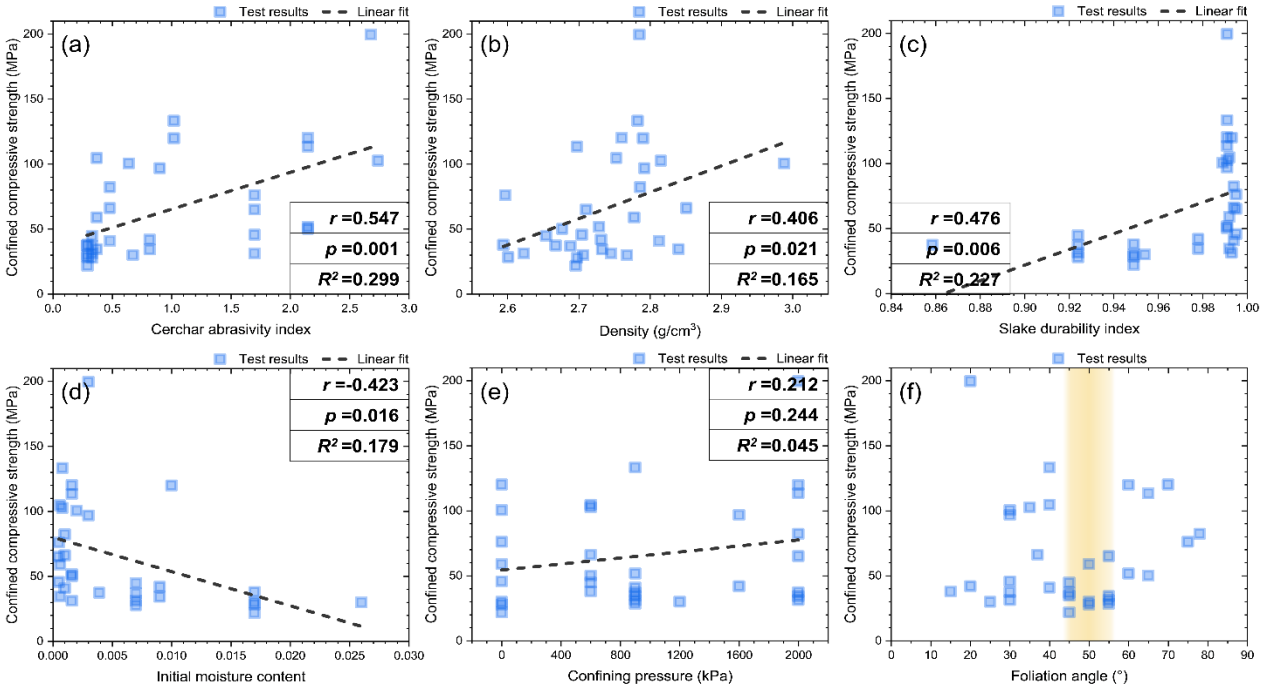

Figure 4: Correlation analysis between each candidate proxy variable and *CCS*

Based on the preceding test results and mechanistic interpretation, six candidate variables were selected for model development: Density (ρ), Confining pressure (σ_3), Initial moisture content (w), Slake Durability Index (*SDI*), Cerchar Abrasivity Index (*CAI*), and foliation dip angle (θ). Among them, *CAI* primarily reflects rock skeleton hardness and abrasivity and was therefore considered a candidate proxy for skeleton hardness. In this study, ρ is treated as a composite proxy more closely related to structural integrity and the degree of defect development. *SDI* and w characterize the structural integrity and water sensitivity of the specimens from the perspectives of resistance to slaking and water-sensitivity activity, respectively. θ describes the geometric relationship between the loading direction and foliation/bedding-related weak planes and is therefore treated as a candidate variable of loading angle ($90°-\theta$) effects. In most cases, σ_3 directly controls *CCS* and even *Avg. E*.

Figures 4 and 5 present the correlations between these candidate variables and *CCS* and *Avg. E*, respectively. Pearson's correlation coefficient r, the significance level p, and the coefficient of determination R^2 were used to evaluate variable relevance and model explanatory power. For *CCS*, *CAI* exhibits the strongest positive correlation, indicating the importance of skeleton hardness, while ρ, *SDI*, and w also show noticeable effects. For *Avg. E*, *SDI* shows the strongest correlation, and ρ and w also contribute, indicating that *Avg. E* is more

sensitive to structural integrity and internal defects compared to *CCS*. The statistical contribution of σ_3 to *Avg. E* is negligible and is therefore ignored in the *Avg. E* model.

The choice of θ is based on both the test observations and the angle–property distribution. *CCS* is lowest within an intermediate angle range rather than changing monotonically with angle. The unfavorable range is concentrated between 45° and 55°, and 50° is therefore taken as the representative most unfavorable angle in the *CCS* model. By contrast, the influence of foliation dip angle θ on the *Avg. E* is relatively weak and is considered in the *Avg. E* prediction model.

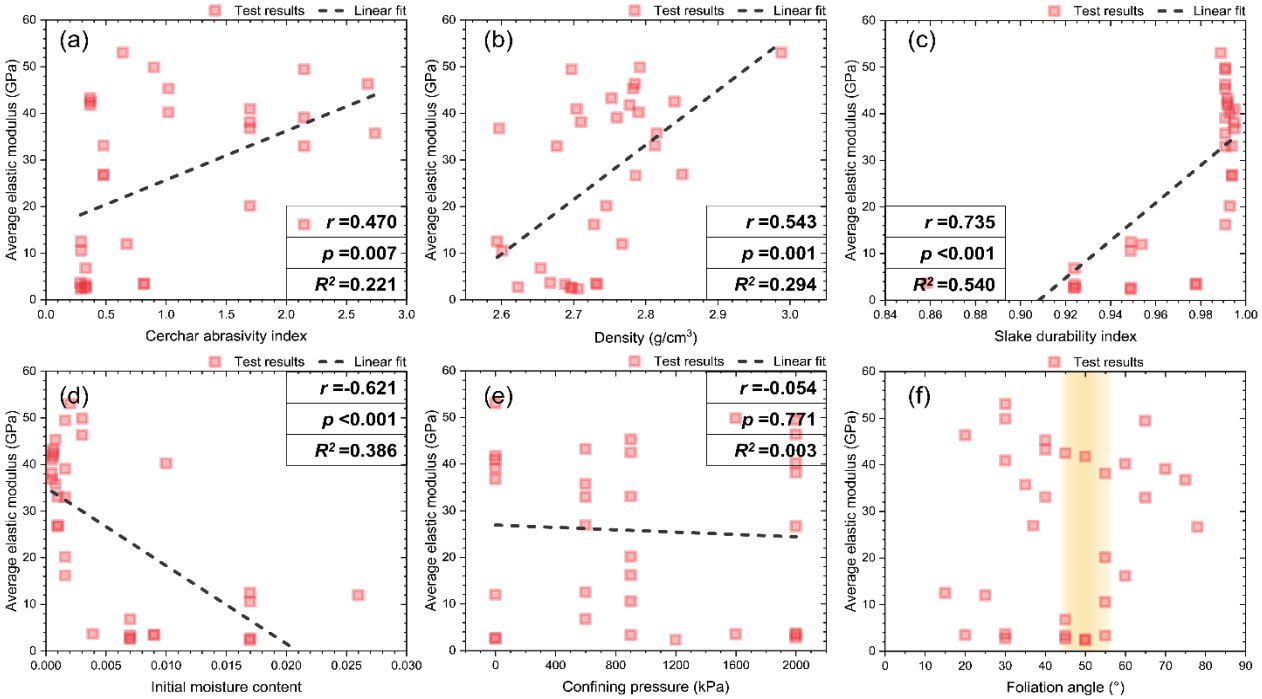

Figure 5: Correlation analysis between each candidate proxy variable and *Avg. E*

4.2 Data Preprocessing and Model Construction Method

Before model construction, the continuous variables were standardized to eliminate scale differences. For ρ, σ_3, w, *SDI*, and *CAI*, the standardized variable is defined as a function of the sample mean and standard deviation of variable. For foliation dip θ, its effect is usually not monotonic with angle but instead becomes most unfavorable within an intermediate angular range. Therefore, the angle value was not entered directly into the regression equation in a linear manner. Instead, it was transformed into an angle-effect function. In the *CCS* model, 50° was taken as the most unfavorable angle, and the corresponding angle function $f_{50}(\theta)$ was constructed using sine functions. The purpose of this process is to represent the basic pattern using a single scalar function. In this pattern, intermediate angles are the most unfavorable, whereas both end-member angles are relatively more favorable.

Because both *CCS* and *Avg. E* are strictly positive and span a wide range of values, log-linear regression was adopted to establish the prediction relationships. Log-linear regression was adopted for two reasons. First, it reduces the disproportionate influence of high-value samples on the fitting results. Second, it allows multiplicative effects of multiple variables on the target parameter to be expressed within a simple linear framework, making it more suitable for rock mechanical parameters that vary over a wide numerical range.

Three models were then constructed for comparison. The first was a baseline model using only the best-performing single variable. The second was a full-variable log-linear reference model using all candidate variables directly. The third was a mechanistically organized model based on rock skeleton hardness, structural integrity and water sensitivity, and loading angle, with confining pressure further incorporated as a correction term. Model performance was also evaluated using Pearson's correlation coefficient r, the corresponding p-value, the coefficient of determination R^2. To assess the generalization ability of the models for unseen samples, leave-one-out cross-validation (LOOCV) was further applied: one sample was left out as the validation set each time, while the remaining samples were used for model fitting, and this process was repeated until every sample

had been tested once. The cross-validated R^2 was then calculated accordingly. Compared with in-sample fitting results, LOOCV better reflects model robustness and practical predictive capability.

4.3 Baseline Model: Single-Variable Log-Linear Regression Model

The purpose of the baseline model is to provide the simplest prediction benchmark. It is used to show the extent to which *CCS* and *Avg. E* can be predicted when only a single variable is used. According to the correlation analysis results presented in Section 4.1, *CAI* was selected as the baseline variable for *CCS*, whereas *SDI* was selected as the baseline variable for *Avg. E*. Single-variable log-linear regression models were then established.

4.4 Reference Model: Full-Variable Log-Linear Regression Model

Building on the baseline model, a full-variable log-linear reference model was established. In this model, the candidate variables were entered directly into a single regression equation without imposing any predefined physical grouping. The purpose of this model is to represent the predictive performance of an empirical multivariable model. For *CCS*, the model includes ρ, σ_3, w, *SDI*, *CAI*, and $f_{50}(\theta)$. For *Avg. E*, the model includes ρ, w, *SDI*, and *CAI*.

The advantage of the full-variable reference model is that it makes full use of the available information. Its limitation is that all variables enter the model in parallel, so the physical meaning of the model remains relatively dispersed. As an empirical reference, it is used to evaluate the extent to which direct multivariable regression can achieve satisfactory in-sample fitting and cross-validation performance without mechanistic grouping.

4.5 Mechanistic Model Based on Three Composite Indicators with Confining Pressure Correction

Based on the baseline model and the full-variable reference model, this study further developed a mechanistic model. It was built on three composite indicators: skeleton hardness, structural integrity and water sensitivity, and loading angle. Confining pressure was included as a correction term. Unlike the previous models, this model does not simply place all variables in parallel. Instead, the variables are first grouped into several composite indicators according to their physical meanings, and the log-linear prediction relationship is then established.

The skeleton-strength indicator is directly represented by *CAI*. The structural integrity and water sensitivity indicator (I_d) is defined as a function of ρ, w, *SDI* and introduce three coefficients h_1, h_2, h_3 with a sum of 1 for constraint. The loading angle indicator is represented by the angle function $f_{50}(\theta)$. σ_3 is not an intrinsic material index but an external stress condition. It is therefore retained separately as a correction term in the *CCS* model.

The model coefficients were determined in two steps. In the first step, after the form of the composite indicators had been specified, different combinations of h_1, h_2, and h_3 were searched, and the optimal weights of the structural integrity and water sensitivity indicator were determined by maximizing the LOOCV R^2. In the second step, after the composite-indicator weights were fixed, the final log-linear regression equations were fitted using ordinary least squares.

For *CCS*, the resulting equation is defined as a function of *CAI*, I_d, $f_{50}(\theta)$ and σ_3.For *Avg. E*, the resulting equation is defined as a function of *CAI*, I_d. The physical meaning of this model can be summarized as follows: skeleton controls the mechanical strength, structural integrity and water sensitivity controls the degree of reduction, loading angle governs the additional weakening of *CCS*, and confining pressure provides an external correction to *CCS*. Compared with the full-variable reference model, this model does not introduce more original variables. However, by reorganizing them according to physical dimensions, it improves both interpretability and engineering readability.

5 COMPARISON OF PREDICTION RESULTS AND MODEL EVALUATION

5.1 Comparison of CCS Prediction Results

Figure 6 presents the in-sample prediction results of the three models for *CCS*. Overall, the data points of the baseline model (Figure 6a) deviate markedly from the 1:1 line, indicating that reliance on a single variable is insufficient to adequately capture the high variability of metasedimentary rock strength. The full-variable log-linear reference model (Figure 6b) shows a clear improvement over the baseline model, suggesting that the combined input of multiple variables enhances the predictive capability for strength. By contrast, the predicted

points of the mechanistic model (Figure 6c) are distributed more closely around the 1:1 line, indicating that, by incorporating skeleton hardness, structural integrity and water sensitivity, loading angle, and confining pressure correction, the model is able to more effectively capture the principal controlling factors governing *CCS*.

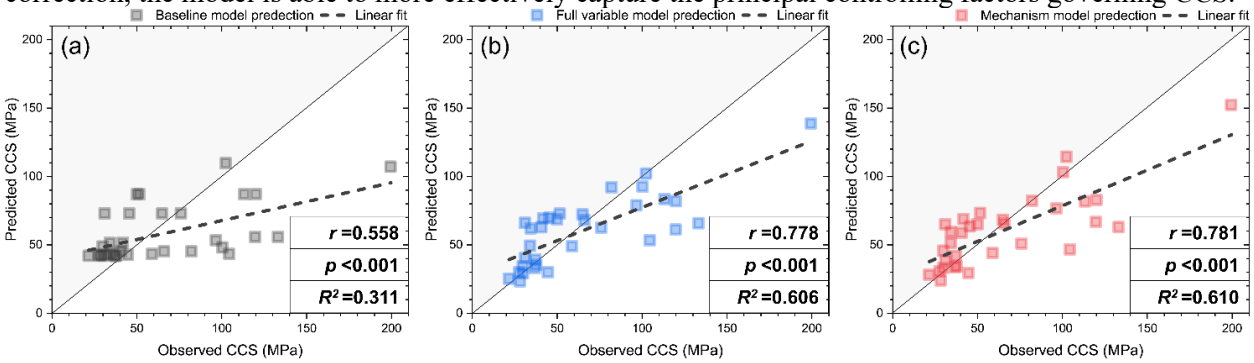

Figure 6: Comparison of in-sample *CCS* prediction results obtained from the three models.

5.2 Comparison of Avg. E Prediction Results

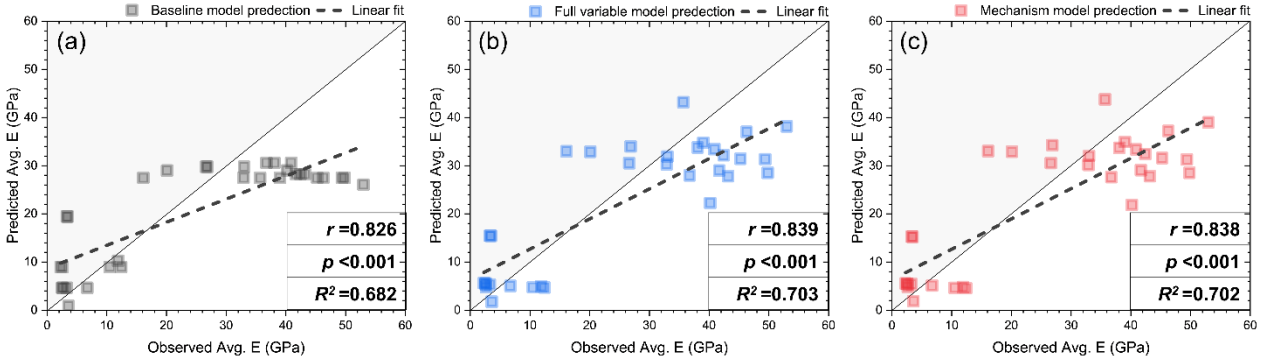

Figure 7: Comparison of in-sample *Avg. E* prediction results obtained from the three models.

Figure 7 presents the in-sample prediction results of the three models for *Avg. E*. Compared with *CCS*, the baseline model already shows a relatively good fitting performance for *Avg. E*, indicating that *Avg. E* is primarily controlled by structural integrity, and that a single integrity-related variable can already explain a large proportion of its variation. On this basis, both the full-variable reference model and the mechanistic model further improve the fitting results. This suggests that, for the present dataset, *Avg. E* is mainly governed by the internal condition of the rock, with structural integrity acting as the primary controlling factor and skeleton condition providing a secondary contribution. Because the statistical contributions of loading angle and confining pressure are weak, they were not retained in the final model.

5.3 Comparison of Leave-One-Out Cross-Validation (LOOCV) Results

Figures 8 and 9 present the LOOCV results of the three models for *CCS* and *Avg. E*, respectively. For *CCS*, the validation scatter of the baseline model is the most dispersed, indicating that a single variable has limited predictive capability for unseen samples. The full-variable reference model shows a clear improvement, whereas the mechanistic model performs best. According to the present calculations, the LOOCV R^2 values of the three models for *CCS* are 0.203, 0.408, and 0.483, respectively. For *Avg. E*, the baseline model already exhibits relatively high cross-validation accuracy, with a LOOCV R^2 of 0.639. By contrast, the full-variable reference model decreases slightly to 0.602, indicating that, under the current sample size and variable conditions, mechanically adding all variables does not necessarily improve predictive performance. The mechanistic model reaches 0.643, which is the best among the three, although its improvement over the baseline model is limited. Overall, the mechanistic model outperforms both the full-variable model and the baseline model in *CCS* prediction. For *Avg. E* prediction, the mechanistic model performs slightly better than the baseline model, and both outperform the full-variable model.

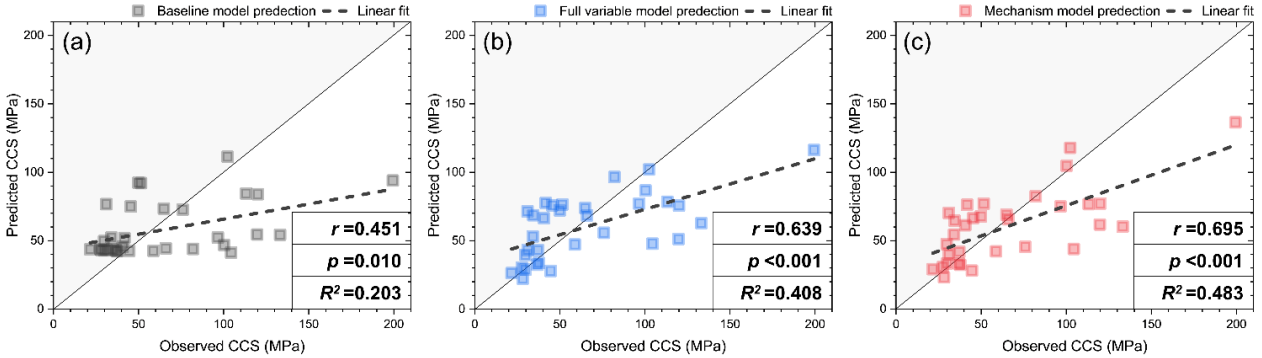

Figure 8: Comparison of LOOCV prediction results for *CCS* obtained from the three models.

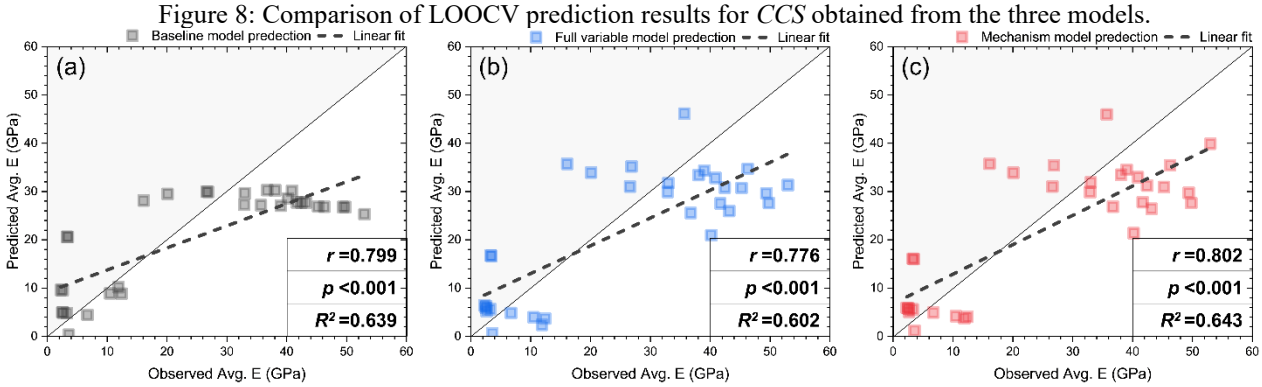

Figure 9: Comparison of LOOCV prediction results for *Avg. E* obtained from the three models.

5.4 Overall Evaluation of the Three Models

A comparison of Figures 6 to 9 shows that the baseline model is the simplest but reflects only one dominant factor, whereas the full-variable model uses more information but remains physically diffuse. By contrast, the mechanistic model organizes the variables into skeleton hardness, structural integrity and water sensitivity, and loading angle, with confining pressure correction further included in the *CCS* model, and therefore provides clearer interpretability and greater engineering readability. Although the mechanistic model can be regarded mathematically as a constrained special case of the full-variable model, the two models are not optimized toward the same objective. The full-variable model minimizes in-sample residuals by ordinary least squares, whereas the mechanistic model groups correlated variables into physically meaningful composite indicators and imposes coefficient constraints, thereby reducing model freedom and improving coefficient stability. In the present study, ρ, *SDI*, and w contain overlapping information related to structural integrity and structural integrity and water sensitivity. As a result, the full-variable model has greater in-sample flexibility but is also more sensitive to sample-specific fluctuations. The mechanistic model sacrifices some flexibility, but its physically constrained structure acts as a form of regularization and therefore shows better robustness in LOOCV. For structurally complex and highly variable metasedimentary rocks, such a mechanism-constrained approach is more effective for interpreting mechanical variability and supporting engineering applications.

6 CONCLUSIONS

Based on triaxial compression tests, pre- and post-test CT scanning, Cerchar abrasivity tests, slake durability tests, and petrographic thin-section analysis, this study investigated the prediction of *CCS* and *Avg. E* of metasedimentary rocks in the Northern Metropolis of Hong Kong. The main conclusions are as follows.

(1) The results show that the mechanical properties of these rocks exhibit pronounced variability. The poor *CCS–Avg. E* correlation indicates that their mechanical response cannot be explained by a single factor. CT observations show that pre-existing fractures and structural integrity are key factors controlling the lower bound of mechanical performance, whereas thin-section analysis indicates that quartz skeleton continuity, degree of recrystallization, and preferred orientation of platy minerals jointly influence load-bearing capacity and weak-plane development.

(2) The controlling factors were grouped into three physical dimensions, namely skeleton hardness, structural integrity and water sensitivity, and loading angle, while confining pressure was further incorporated as a

correction term in the *CCS* model. For *CCS*, the LOOCV R^2 values of the three models are 0.203, 0.408, and 0.483, respectively. For *Avg. E*, they are 0.639, 0.602, and 0.643, respectively. These results indicate that the mechanistic model outperforms both the full-variable model and the baseline model in *CCS* prediction. In *Avg. E* prediction, the mechanistic model performs slightly better than the baseline model, and both outperform the full-variable model. Compared with *Avg. E*, *CCS* is more sensitive to loading angle, whereas *Avg. E* is more strongly controlled by structural integrity and water sensitivity.

Overall, this study demonstrates that, by combining CT scanning, thin-section analysis, and rapid indirect tests, the complex mechanical variability of metasedimentary rocks can be organized into several physically meaningful controlling dimensions, and an interpretable yet practical prediction framework can be established accordingly. The data presented in this paper constitute a subset of a comprehensive experimental dataset on Hong Kong metasedimentary rocks. Our framework and model will be continuously improved with more data from the aforementioned tests, Direct structural indicators such as porosity, wave velocity, and quantitative CT-based fracture parameters, will also be integrated to enhance the accuracy and robustness of the model.

ACKNOWLEDGEMENTS

The indoor laboratory test samples of this study were provided by the Geotechnical Engineering Office (GEO) of the Civil Engineering and Development Department (CEDD), the Government of the Hong Kong Special Administrative Region, China. All supports from the GEO and AECOM Asia Co. Ltd are gratefully acknowledged.

REFERENCES

Alber, M., Yaralı, O., Dahl, F., Bruland, A., Käsling, H., Michalakopoulos, T. N., Cardu, M., Hagan, P., Aydin, H., Özarslan, A. (2014). ISRM suggested method for determining the abrasivity of rock by the CERCHAR abrasivity test. Rock Mechanics and Rock Engineering, 47(1), 261–266.

ASTM International. (2016). ASTM D4644-16: Standard test method for slake durability of shales and other similar weak rocks. ASTM International.

ASTM International. (2022). ASTM D7625-22: Standard test method for laboratory determination of abrasiveness of rock using the CERCHAR abrasiveness index method. ASTM International.

ASTM International. (2023). ASTM D7012-23: Standard test methods for compressive strength and elastic moduli of intact rock core specimens under varying states of stress and temperatures. ASTM International.

Franklin, J. A., Chandra, R. (1972). The slake-durability test. International Journal of Rock Mechanics and Mining Sciences & Geomechanics Abstracts, 9(3), 325–328.

Gao, K., Wang, X., Wei, H., Wang, S., Xu, W., Li, X., Sun, L., Jiang, H. (2024). Abrasivity database of different genetic rocks based on CERCHAR Abrasivity Test. Scientific Data, 11, 630.

Jeong, H., Choi, S., Lee, Y. K. (2023). Evaluation of cutting performance of a TBM disc cutter and Cerchar abrasivity index based on the brittleness and properties of rock. Applied Sciences, 13(4), 2612.

Li, G., Wang, H., Peng, J., Wang, L., Dai, B. (2023). Strength model of anisotropic rocks based on Hoek-Brown criterion. Rock and Soil Mechanics, 44(12), 3541–3550.

Saroglou, H., Tsiambaos, G. (2008). A modified Hoek–Brown failure criterion for anisotropic intact rock. International Journal of Rock Mechanics and Mining Sciences, 45(2), 223–234.

Waqas, U., Qureshi, M. U., Saqib, S., Rashid, H. M. A., Rasool, A. M. (2024). Evaluation of strength anisotropy in foliated metamorphic rocks: A review focused on microscopic mechanisms. Geosciences, 14(10), 253.

Appendix Table 1: Matched Dataset of *CCS* Test Results, Cerchar Abrasivity Test Results, and Slake Durability Test Results.

Drillhole No.	*CCS* test sample No.	Depth (m)	Confining Pressure (kPa)	Density (g/cm^3)	Strength (MPa)	Avg. *E* (GPa)	Foliation Dip angle (°)	Failure description*	Slake durability test Sample No.	Initial moisture content (*w*)	Slake durability Index (*SDI*)	CAI test sample No.	Cerchar Abrasivity Index (*CAI*)
LMC-VB1-4	T5	33.73-33.85	0	2.65	1.95	0.45	60	1	N/A	N/A	N/A	N/A	N/A
LMC-PD05	T1	24.82-24.94	600	2.68	24.19	2.84	50	1	N/A	N/A	N/A	N/A	N/A
LMC-VB1-1	T2	33.98-34.10	900	2.69	28.24	3.02	50	1	N/A	N/A	N/A	N/A	N/A
LMC-VB1-2	T2	32.97-33.08	2000	2.61	19.37	1.51	20	1	N/A	N/A	N/A	N/A	N/A
LMC-PD3-PD-01	T2	41.89-42.01	0	2.77	29.83	11.92	25	2	SL1	2.60%	95.40%	CAI3	0.67
LMC-PD3-PD-01	T4	46.94-47.06	2000	2.67	37.21	3.61	30	2	SL3	0.39%	85.85%	CAI1	0.29
LMC-PD3-PD-02	T5	19.64-19.75	0	2.70	27.70	2.53	50	4	SL1	0.70%	92.40%	CAI1	0.33
LMC-PD3-PD-02	T7	20.21-20.33	600	2.65	44.66	6.74	45	1	SL1	0.70%	92.40%	CAI1	0.33
LMC-PD3-PD-02	T12	23.96-24.08	900	2.69	36.80	3.3	45	2	SL1	0.70%	92.40%	CAI1	0.33
LMC-PD3-PD-02	T13	25.14-25.26	2000	2.62	31.14	2.66	30	1	SL1	0.70%	92.40%	CAI1	0.33
LMC-PD3-PD-03	T2	23.23-23.33	0	2.70	21.62	2.6	45	4	SL1	1.70%	94.90%	CAI1	0.29
LMC-PD3-PD-03	T4	24.53-24.65	600	2.59	37.75	12.44	15	2	SL1	1.70%	94.90%	CAI1	0.29
LMC-PD3-PD-03	T5	31.33-31.45	900	2.60	28.26	10.51	55	1	SL1	1.70%	94.90%	CAI1	0.29
LMC-PD3-PD-03	T6	31.83-31.95	1200	2.71	29.92	2.28	50	1	SL1	1.70%	94.90%	CAI1	0.29
LMC-PD3-PD-03	T8	44.16-44.28	1600	2.73	41.79	3.47	20	2	SL3	0.90%	97.80%	CAI3	0.82
LMC-PD3-PD-03	T9	44.28-44.40	2000	2.73	34.18	3.31	55	1	SL3	0.90%	97.80%	CAI3	0.82
SR-BH-B-137	T7	41.87-41.98	0	2.76	120.14	39.06	70	4	SL4	0.16%	99.10%	CAI4	2.15
SR-BH-B-137	T8	42.73-42.88	600	2.68	50.01	32.94	65	1	SL4	0.16%	99.10%	CAI4	2.15
SR-BH-B-137	T8a	42.58-42.73	900	2.73	51.58	16.13	60	1	SL4	0.16%	99.10%	CAI4	2.15
SR-BH-B-137	T7a	41.98-42.09	2000	2.70	113.34	49.43	65	2	SL4	0.16%	99.10%	CAI4	2.15
SR-PD1-PO-01	T1	25.67-25.79	0	2.99	100.44	53.04	30	2	SL2	0.20%	98.90%	CAI1	0.64
SR-PD1-PO-01	T2	30.12-30.23	600	2.82	102.51	35.72	35	3	SL1	0.08%	99.10%	CAI3	2.74
SR-PD1-PO-01	T4	33.74-33.85	900	2.78	133.28	45.29	40	2	SL1	0.08%	99.10%	CAI2	1.02
SR-PD1-PO-01	T7	39.47-39.59	2000	2.79	119.84	40.22	60	1	SL4	1.00%	99.30%	CAI2	1.02
SR-PD2-PO-01	T3a	30.99-31.01	0	2.78	58.86	41.74	50	3	SL1	0.06%	99.20%	CAI3	0.37
SR-PD2-PO-01	T3	31.11-31.24	600	2.75	104.56	43.22	40	1	SL1	0.06%	99.20%	CAI3	0.37
SR-PD2-PO-01	T4	31.39-31.51	900	2.84	34.40	42.48	45	1	SL1	0.06%	99.20%	CAI3	0.37
SR-PD2-PO-01	T6	37.74-37.84	1600	2.79	96.71	49.85	30	3	SL2	0.30%	99.10%	CAI5	0.90
SR-PD2-PO-01	T7a	37.01-37.13	2000	2.79	199.64	46.31	20	3	SL2	0.30%	99.10%	CAI4	2.68
SR-PD3-PO-01	T6a	55.53-55.64	600	2.85	66.06	26.89	37	1	SL2	0.10%	99.40%	CAI1	0.48
SR-PD3-PO-01	T6	55.40-55.52	900	2.81	40.70	33.04	40	1	SL2	0.10%	99.40%	CAI1	0.48
SR-PD3-PO-01	T3	52.67-52.78	2000	2.79	82.16	26.65	78	1	SL2	0.10%	99.40%	CAI1	0.48
SR-PD3-PO-02	T1	41.54-41.66	0	2.60	76.01	36.77	75	1	SL1	0.05%	99.50%	CAI2	1.70
SR-PD3-PO-02	T3	43.53-43.66	0	2.70	45.51	40.93	30	1	SL1	0.05%	99.50%	CAI2	1.70
SR-PD3-PO-02	T4	52.22-52.33	900	2.75	31.07	20.12	55	1	SL3	0.16%	99.30%	CAI2	1.70
SR-PD3-PO-02	T2	43.15-43.27	2000	2.71	64.97	38.11	55	2	SL1	0.05%	99.50%	CAI2	1.70

*Failure description: 1 Inclined shear fracture along bedding; 2 Inclined shear fracture not along bedding; 3 Axial splitting failure; 4 Inclined shear fracture and axial splitting failure.

Effective Health Diagnosis System for Underground Pipeline Networks Using Distributed Fiber Optic Sensing

YANG Wen-Tao & ZHANG Tian-Yu & FENG Wei-Qiang*
Department of Ocean Science and Engineering, Southern University of Science and Technology, Shenzhen, China
** Email: fengwq@sustech.edu.cn*

YANG Wen-Tao
Anchor Monitoring Technology (HK) Limited, Hong Kong

Ngai Kwok-Leung, Cheung Hoi-Yan
Electrical and Mechanical Services Department of HKSAR

Ng Wan-Lung Sean, Chan Chi-Ho Philip
Ove Arup Partners (HK) Limited

ABSTRACT

The safety of urban underground pipeline networks is identified as a critical factor for maintaining urban resilience and public safety. In this study, an integrated health diagnosis system based on Distributed Acoustic Sensing (DAS) and Distributed Temperature Sensing (DTS) is demonstrated for the real-time detection of pipeline leakages. Laboratory experiments were performed to characterize the acoustic and thermal responses under various leakage intensities and fluid temperatures. It is observed that the DAS system provides an immediate vibration-based response, with the vibration power spectral density (PSD) increasing from -50 dB to -20 dB upon the occurrence of a leak. This high-frequency spectral footprint, specifically identified in the 1.4 to 1.5 kHz range, allows for millisecond-level early warning and precise spatial localization. Concurrently, the DTS system provides thermal verification, showing a gradual temperature change with a detection delay of approximately 14 minutes in the tested insulation pipe. While DTS exhibits a temporal lag due to fluid seepage and heat conduction through the insulation layer, it remains significantly less susceptible to environmental noise, serving as a decisive criterion for event verification. The synergy between the high timeliness of DAS and the high confidence of DTS effectively resolves the trade-off between monitoring speed and accuracy, providing a robust technical solution for the proactive safety management of urban subsurface infrastructure. Looking forward, the integration of this dual-sensing optical framework with Internet of Things (IoT) devices holds great potential to establish a comprehensive, multi-parameter monitoring network, enabling an advanced analysis of both structural deformations and leakage events.

Keywords: Distributed Acoustic Sensing (DAS); Distributed Temperature Sensing (DTS); Pipeline leakage monitoring; Frequency band Analysis; Urban infrastructure safety.

1 INTRODUCTION

Urban underground pipeline networks, encompassing water supply, drainage, gas, heating, and industrial conduits, constitute the critical infrastructure essential for maintaining modern urban functions. With the continuous advancement of urbanization and the implementation of resilient city strategies, the scale and density of these networks have expanded significantly (Hoekstra et al. 2018; Zhu & Chang 2020; Sharma et al. 2021). Under the dual influence of complex corrosive environments and prolonged lack of systematic maintenance, structural defects such as internal rust, leakage, and pressure imbalances have become increasingly prominent (Tan & Long 2021; Hu et al. 2024; Li et al. 2025). The occurrence of pipeline leakage is identified as a primary induction factor for urban geological hazards, accounting for approximately 60% to 70% of ground collapse accidents (Wang & Xu 2022; Wang et al. 2022). The evolution of geological disasters induced by pipeline failures typically follows a chain-like process (Augarde et al. 2003; Shiau et al. 2021; Dai et al. 2024; Park et

al. 2024). This process is generally initiated by pipe defects and subsequent leakage, followed by high-velocity fluid injection, internal erosion of surrounding soils, the formation of underground cavities, and ultimately, the loss of surface structural stability. These cavities are often undetectable from the surface due to the arching effect of road structures, but once the dimensions exceed a critical threshold, instantaneous ground collapse is triggered (Li et al. 2023; Wang et al. 2023; Dai et al. 2024). Therefore, the precision sensing and real-time monitoring of leakage events are essential for mitigating the operational risks of urban geological hazards. Conventional monitoring technologies still have significant technical bottlenecks and application limitations. Ground Penetrating Radar (GPR) is primarily restricted to periodic inspections due to its reliance on manual operation and susceptibility to interference (Tong et al. 2020; Klewe et al. 2021). Similarly, traditional acoustic methods are constrained by rapid signal attenuation, limiting their effective coverage (Singh et al. 2021). Furthermore, traditional approaches often fail to provide continuous and long-range monitoring capabilities.

Given this limitation, the emergence of Distributed Fiber Optic Sensing (DFOS) provides a robust alternative for real-time health monitoring. Distributed Acoustic Sensing (DAS) and Distributed Temperature Sensing (DTS) offer continuous sensing capabilities over tens of kilometers with high spatial and temporal resolution (Barrias et al. 2016; Schenato 2017; Lu et al. 2019; Ashry et al. 2022). Concurrently, the Raman-based DTS system demodulates absolute temperature profiles by analyzing the intensity ratio between anti-Stokes and Stokes components (Dakin et al. 1985). Recent research has witnessed a transition in DTS applications from passive sensing toward active heating methods (ADTS) and ultra-high-resolution differential sensing (DdTS) to overcome sensitivity bottlenecks in identifying micro-leakages (Li et al. 2023). Concurrently, DAS systems, operating on the principle of phase-sensitive optical time-domain reflectometry (φ-OTDR), function as a continuous array of virtual sensors to quantify dynamic vibration signals (He & Liu 2021). The evolution of DAS technology has shifted from basic temporal-frequency analysis toward intelligent feature recognition powered by deep learning architectures, such as Convolutional Neural Networks (CNN) and Long Short-Term Memory (LSTM) networks, to enhance signal-to-noise ratios in high-noise environments (Zhang et al. 2023; Huang et al. 2024; Lang & Wang 2024).

Despite these advancements, several critical challenges persist in the engineering application of DFOS for pipeline safety. While these technologies are effective for qualitative leak identification, the high false alarm rate induced by complex urban environmental noise remains a significant operational burden (Zuo et al. 2020; Li et al. 2025). Furthermore, current monitoring schemes often lack the capability for the deep decoupling of multi-modal data, and a robust quantitative relationship between leakage intensity and multi-dimensional fiber optic signals has yet to be fully established (Xia et al. 2023). Additionally, the supporting foundation of underground pipelines is highly susceptible to differential settlement, horizontal displacement, or tilting driven by complex hydrogeological conditions. These structural deformations are often the underlying causes of stress concentration and eventual pipeline rupture (Hachiya et al. 2022; Zhang et al. 2024). This gap hinders the transition from simple event detection to precise, real-time quantitative assessment of pipeline health. Therefore, further investigation into the response characteristics of acoustic frequency bands and thermal gradients under varying leakage conditions is required to enhance the reliability and precision of integrated monitoring systems.

In this study, a comprehensive monitoring methodology for underground pipeline leakage is proposed based on the synergistic integration of DAS and DTS technology. The investigation is focused on characterizing the acoustic frequency band variations and temperature field responses under various leakage intensities and fluid temperatures. By analyzing the vibration signatures and thermal anomalies associated with escaping fluids, the sensing performance and localization accuracy of the integrated fiber optic system are rigorously evaluated. Laboratory experiments were performed to validate the effectiveness of these sensing techniques in capturing transient leakage events and identifying steady-state thermal gradients. It is demonstrated that the fusion of high-frequency vibration data and stable temperature profiles provides a reliable means for the timely detection of pipeline failures, effectively addressing the technical trade-offs between response time and measurement accuracy. This approach offers a significant technical basis for the proactive safety management of urban subsurface infrastructure and lays a crucial foundation for future synergistic integration with multi-dimensional IoT sensors.

2 METHODOLOGY AND PRINCIPLES

2.1 Distributed Temperature Sensing (DTS) Based on Raman Scattering

The implementation of DTS as a thermal monitoring tool leverages the sensing fiber as a continuous linear array, with its operational principle fundamentally rooted in the Raman scattering effect. This phenomenon is characterized by the inelastic scattering occurring between incident laser photons and optical phonons within the silica fiber core (Dakin et al. 1985; Ren et al. 2018; Zuo et al. 2020). The backscattered light is characterized by two distinct components, the Stokes and anti-Stokes lines. The intensity of the anti-Stokes component is observed to be highly sensitive to environmental temperature fluctuations, whereas the Stokes component remains relatively stable. By calculating the power ratio between these two components and applying time-of-flight analysis, absolute temperature profiles along the pipeline are demodulated. The DTS equipment used in this study is capable of identifying temperature anomalies with ±0.5 °C accuracy and 1 m spatial resolution.

In the context of pipeline leakage monitoring, Raman scattering is independent of the fiber strain state, thereby ensuring that thermal anomalies induced by leaking fluids are captured without interference from structural deformations or ground movements. This decoupling capability renders Raman-based DTS a more reliable choice for identifying localized cooling or heating effects associated with subsurface pipe leakages.

2.2 Distributed Acoustic Sensing (DAS) Based on Rayleigh Backscattering

DAS system based on Phase-Sensitive Optical Time-Domain Reflectometry (φ-OTDR) is implemented as the high-frequency vibration monitoring (Lu et al. 2010; He & Liu 2021; Wang et al. 2022). The sensing process is initiated by launching highly coherent laser pulses into a single-mode sensing fiber, where Rayleigh backscattering is induced by sub-wavelength refractive index inhomogeneities. These scattering centers form a stationary interference pattern along the fiber length. When acoustic waves or mechanical vibrations generated by fluid leakage impinge upon the fiber, dynamic axial strain is induced, which modifies the local optical path length through the photo-elastic effect. Unlike direct detection methods, the φ-OTDR system utilizes coherent detection schemes to demodulate the linear optical phase shift of the backscattered signal. This allows for the quantitative reconstruction of the amplitude, frequency, and precise spatial location of the acoustic field.

The DAS system operates with a broad bandwidth, enabling the capture of high-frequency jetting noises produced by high-pressure leakages. Because the sensing signals are acquired independently for each spatial interval, disturbances are not accumulated over distance, allowing for high-sensitivity vibration monitoring over ranges exceeding 40 km. The DAS equipment used in this study can offer a frequency response ranging from 0.1 Hz to 50 kHz and a spatial resolution of 1 m.

The integration of DAS-derived vibration signatures with DTS-derived thermal gradients establishes a multi-dimensional data framework for the identification of pipeline failures under varying operational intensities.

3 INDOOR PIPE LEAKAGE SYSTEM DESIGN AND TEST PROGRAM

A simulated monitoring system for urban water supply pipeline leakage was constructed in a laboratory setting to evaluate the feasibility of DAS technology. The physical model and the corresponding sensor layout are presented in Figure 1. This experimental platform utilizes a prefabricated direct-buried insulation pipe structure. This structure consists of an internal stainless steel working pipe, a middle layer made of rigid polyurethane foam for insulation, and an external anti-corrosion sheath composed of high-density polyethylene. To facilitate distributed monitoring, multiple sensing conduits are embedded within the insulation layer near the stainless-steel pipe to house the optical sensing fibers. A controllable valve is also installed on the pipeline section to simulate leakage events with different aperture sizes. The fluid environment is managed by connecting the pipeline ends with flexible hoses to a water pump, which creates a closed loop with adjustable water pressure. Furthermore, a heater is integrated into the system to increase the temperature of the circulating water, allowing for the simulation of various leakage scenarios. Optical sensing cables are installed both inside the conduits of the insulation pipe and along the exterior of the copper pipeline. Real-time vibration responses and temperature changes are monitored using a BL-DAS equipment from Brillnova and a FET8609D DTS equipment from PREMIER during both normal operation and leakage conditions.

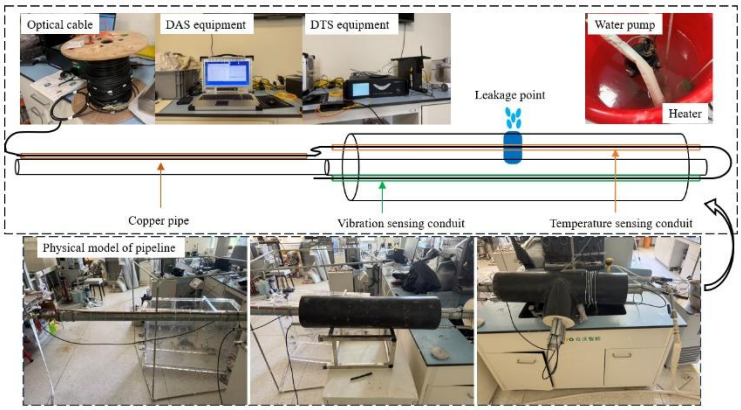

Figure 1: Schematic diagram of the pipeline model test system

Multiple controlled experiments were conducted on this platform to collect high-fidelity vibration signals under four typical states: static, normal operation, leakage, and noise interference (as shown in Table 1). The primary objective is to identify the relationship between the water flow state and changes in the vibration spectrum by comparing the frequency characteristics of these signals. Therefore, various experiments were performed to obtain steady-state vibration data under different conditions. The experimental procedure focuses on responses to transient events and system calibration. Initially, tapping was performed at a fixed point on the water supply pipeline between 19:46 and 19:50 while the water was either stationary or moving at a low speed. This action generated a wideband transient vibration source at a specific time and location to calibrate the spatial positioning and response accuracy of the DAS system. Following this, the system was operated in three consecutive states: normal operation from 19:50 to 19:54, a full leakage condition from 19:54 to 19:57, and a return to normal status from 19:57 to 20:00. Finally, the water pump was deactivated between 20:00 and 20:03. During this stage, the DAS system focused on capturing transient hydraulic vibrations as the water flow transitioned from a dynamic state to a static state.

Table 1: Pipeline leakage simulation test conditions and event records

Date	Time	Events
2025/10/23	19:46-19:50	Tap on the water supply pipeline
	19:50-19:54	Circulating water flow, start heating
	19:54-19:57	Circulating water flow, leakage valve fully open
	19:57-20:00	Circulating water flow, leakage valve closed
	20:00-20:03	Turn off the water pump

4 RESULTS AND DISCUSSION

4.1 Spatiotemporal Vibration Analysis

To intuitively analyze the spatiotemporal evolution characteristics of vibration signals, this study calculated the RMS intensity of the signals. Figure 2 shows the RMS intensity waterfall plot of DAS signals throughout the third test, which clearly distinguishes transient disturbances such as knocking from persistent events such as leakage. Different events display significant characteristic differences in both spatial and temporal dimensions. Specifically, periodic strong signals were observed near Channel 36 between 19:46 and 19:50, which matches the transient and incidental nature of knocking events. After 19:50, continuous water circulation signals appear near the leakage point at Channel 29. Crucially, when the leakage valve was opened at 19:54, the signal intensity of Channels 29 and 30 immediately shows a persistent step increase. This waterfall plot intuitively confirms the distinguishability between persistent leakage and transient disturbances in the temporal dimension.

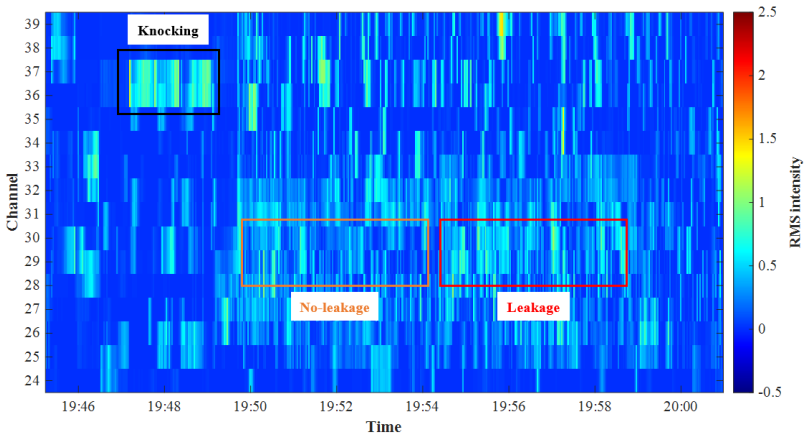

Figure 2: Schematic diagram of the pipeline model test system

4.2 Spectral Feature Identification and Spatial-Frequency Mapping

Although root-mean-square (RMS) analysis effectively captures the spatiotemporal energy evolution of signals at the macro level, it falls short in revealing the detailed spectral features hidden behind energy changes. To further explore the signal frequency components at the leakage point, this study carried out short-time Fourier transform (STFT) analysis on the data from Channel 29. Figure 3 compares the 2D time-frequency spectrograms of vibration signals before (a) and after (b) the leakage.

As shown in Figure 3(a), the background signal before leakage exhibited a low vibration amplitude, with its peak intensity generally below 0.015. Energy was mainly concentrated in the low-frequency band, with most of these frequencies falling below 800 Hz. This reflects the natural low-frequency characteristics of steady fluid flow in the pipeline. High-frequency components above 1 kHz were almost inactive, leaving the high-frequency region visually dominated by a dark blue background. In contrast, once the leakage valve was opened, the spectrogram underwent a significant transformation, as shown in Figure 3(b). A distinct broadband energy surge was observed. First, the vibration intensity increased sharply, with the peak amplitude exceeding 0.025. This magnitude is prominently indicated by the red regions in the heatmap, which verifies the step-like growth observed in the RMS analysis. More importantly, the signal bandwidth expanded greatly. The high-energy zone was no longer limited to the low-frequency band but extended to 1.4–1.5 kHz. The emergence of such high-frequency spectral components is a typical acoustic feature of high-pressure water jets.

This detailed spectral comparison proves that a leakage event not only elevates the overall energy level but also introduces specific high-frequency spectral features, fully demonstrating the ability of the DAS system to capture the fine acoustic characteristics of pipeline leakage. However, relying solely on the analysis of a single measuring point is insufficient. To ensure the robustness of detection, it is necessary to further investigate the spatial distribution of these spectral features, thereby confirming whether such high-frequency anomalies can be clearly distinguished from the background water flow noise monitored by other fiber-optic channels along the pipeline.

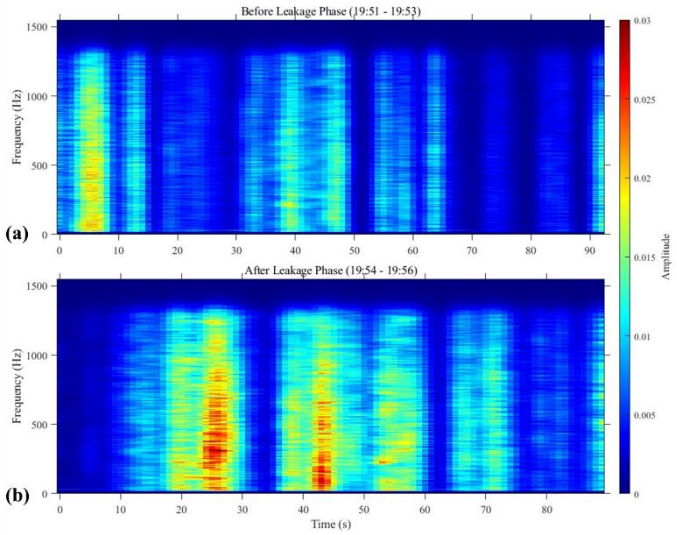

Figure 3: 3D time-frequency spectrogram of vibration signal (a) before leakage and (b) after leakage

The spatial distribution of spectral features was further examined using Power Spectral Density (PSD) analysis to ensure robust detection and localization. As illustrated in the 2D PSD difference heatmap (Figure 4), the energy variations between the leakage and non-leakage states are explicitly visualized. This differential approach effectively highlights a prominent energy concentration strictly localized at Channels 28 and 29, successfully separating the leakage-induced acoustic features from the background fluid noise. To precisely quantify these spectral anomalies, Figure 5 presents a smoothed PSD comparison for these two specific channels. Under normal operating conditions, the baseline fluctuations remain weak, with negligible energy distributed in the high-frequency band near 1.4 kHz. Conversely, during a leakage event, the spectral distribution undergoes a dramatic shift. The smoothed curves clearly demonstrate a high-intensity, broadband energy surge extending from several hundred hertz up to 1.4 kHz. This specific frequency expansion is a typical acoustic signature of high-pressure water jets. Ultimately, by isolating these unique high-frequency spectral features, this comparative analysis effectively filters out high-energy, low-frequency background interference, thereby ensuring accurate leakage positioning and reliable detection at Channels 28 and 29.

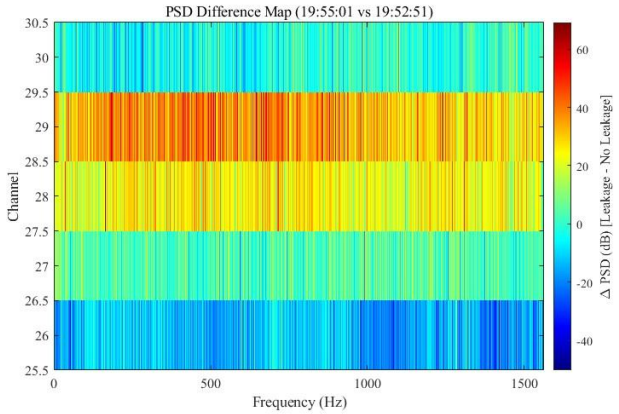

Figure 4: Heatmap of spatial-frequency energy variations (Δ PSD) between the leakage and non-leakage states

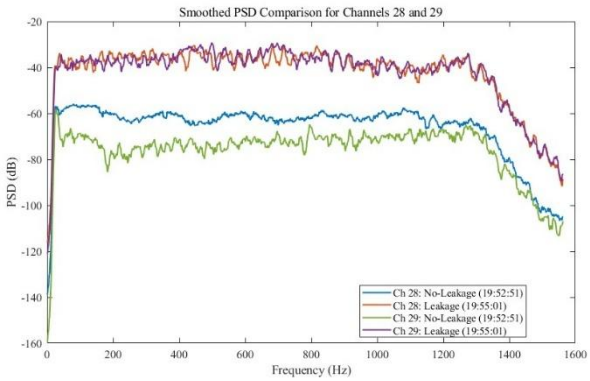

Figure 5: Smoothed PSD comparison curves for Channels 28 and 29

4.3 Thermal Verification and System Synergy

The leakage events were further corroborated from a thermal perspective using the Distributed Temperature Sensing (DTS) system, as illustrated in Figure 6. Before the leakage, the temperature profile along the optical fiber remained stable at a baseline ambient level of approximately 25 °C. Once the leakage started, pronounced thermal anomalies were recorded. The temperature elevation was most intense within a 1-meter radius of the leakage source, specifically between the 126.1 m and 127.1 m marks. The thermal response attenuated progressively as the distance from the leakage point increased, demonstrating high spatial sensitivity. These experimental results confirm that the DTS system can pinpoint the leakage location with a spatial precision of 1 m, providing critical accuracy for targeted maintenance in practical engineering applications.

Despite its spatial precision, a limitation in the temporal response of the DTS system was observed. The temperature rise manifested gradually rather than instantaneously. For instance, reaching a predefined detection threshold of 5 °C above the ambient temperature required approximately 14 minutes at the primary leakage point. This temporal delay is primarily attributed to the physical processes involved, namely the time required for the fluid to permeate the pipeline's insulation layer and the subsequent heat conduction to the sensing cable. Because of this inherent thermal lag, the integration of DAS and DTS technologies becomes indispensable. While the DAS system offers near-instantaneous, real-time alerts within seconds, it remains comparatively susceptible to environmental acoustic noise. Conversely, the DTS system provides a slower but highly reliable and interference-resistant verification of the event. The synergistic application of these two technologies effectively resolves the inherent trade-off between response speed and detection reliability, thereby establishing a robust and comprehensive monitoring framework for pipeline infrastructure.

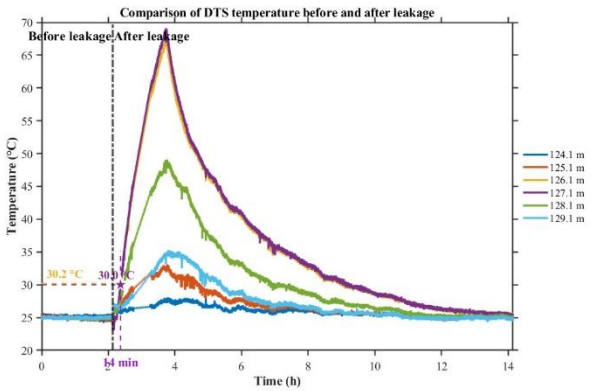

Figure 6: Comparison of DTS temperature before and after leakage

5 CONCLUSIONS

In this study, the integration of DAS and DTS is demonstrated as a robust and real-time monitoring solution for urban pipeline leakage detection. Based on the experimental results, the following conclusions are drawn:

(a) The implementation of DAS technology provides an immediate response to leakage events via vibration signals, with the vibration PSD observed to increase from -50 dB to -20 dB upon the occurrence of a leak. This sensitivity facilitates millisecond-level early warning and precise spatial localization through the identification of high-frequency spectral footprints.

(b) The thermal data obtained from DTS indicate that temperature changes associated with leakage are gradual rather than instantaneous, with a detection delay of approximately 14 minutes recorded in this investigation. However, DTS measurements are significantly less influenced by environmental noise compared to acoustic methods, allowing for the stable and reliable verification of leakage events.

(c) The synergistic application of DAS and DTS effectively resolves the technical trade-off between monitoring timeliness and detection accuracy. By combining the high-speed response of acoustic sensing with the high-confidence thermal field data, a comprehensive health diagnosis framework is established for the proactive safety management of underground infrastructure.

(d) To further enhance safety management, future work will integrate the proposed DAS-DTS framework with Internet of Things (IoT) sensors, such as Global Navigation Satellite System (GNSS) for three-dimensional displacement, tiltmeters for inclination, and soil moisture sensors. These will allow for a synergistic analysis of both structural deformations and subsurface leakage. This multi-parameter approach will facilitate earlier warning capabilities and a deeper understanding of pipeline failure mechanisms.

ACKNOWLEDGEMENTS

This study is financially supported by the innovation project of the Electrical and Mechanical Services Department, HKSAR Government (Contract No. 2852EM17A and 2283EM24A), a grant from Offshore Oil Engineering CO., LTD. (202518685939), Guangzhou Metro Design & Research Institute Co., Ltd (SWLBA-G-2025-011), Shenzhen Science and Technology Innovation Commission (JCYJ20230807093305011; JCYJ20210324105210028). It is acknowledged that the core methodology and primary datasets utilized in this study were originally developed for a more extensive research article titled *Real-Time Health Diagnosis System for Underground Pipeline Networks: Distributed Fiber Optic Sensing and GNSS Integrated Approach*, which is currently under review. This conference paper specifically emphasizes the engineering feasibility and the multi-dimensional signal response of Distributed Acoustic Sensing and Distributed Temperature Sensing for monitoring acoustic frequency band variations and temperature changes during pipeline leakage events.

REFERENCES

Ashry, I., Mao, Y., Wang, B. & et al. 2022. A review of distributed fiber–optic sensing in the oil and gas industry. Journal of Lightwave Technology, 40(5): 1407-1431.

Augarde, C.E., Lyamin, A.V. & Sloan, S.W. 2003. Prediction of undrained sinkhole collapse. Journal of Geotechnical and Geoenvironmental Engineering, 129(3): 197-205.

Barrias, A., Casas, J.R. & Villalba, S. 2016. A review of distributed optical fiber sensors for civil engineering applications. Sensors, 16(5): 748.

Dai, Z., Peng, L. & Qin, S. 2024. Experimental and numerical investigation on the mechanism of ground collapse induced by underground drainage pipe leakage. Environmental Earth Sciences, 83(1): 32.

Dakin, J.P., Pratt, D.J., Bibby, G.W. & et al. 1985. Distributed optical fibre Raman temperature sensor using a semiconductor light source and detector. Electronics letters, 21(13): 569-570.

Hachiya, M., Inoue, Y., Tohda, J., Takatsuka, Y. & Takagi, R. 2022. Response of buried pipelines subjected to differential ground settlement. In Physical Modelling in Geotechnics, 911-916.

He, Z. & Liu, Q. 2021. Optical fiber distributed acoustic sensors: A review. Journal of Lightwave Technology, 39(12): 3671-3686.

Hoekstra, A.Y., Buurman, J. & Van Ginkel, K.C.H. 2018. Urban water security: A review. Environmental research letters, 13(5): 053002.

Hu, Q., Zhang, Q., Liu, W. & et al. 2024. Mitigation of urban road collapses based on machine learning via integrating susceptibility assessment and geophysical detection validation. International Journal of Disaster Risk Reduction, 111: 104667.

Huang, X., Qu, W. & Xiao, L. 2024. Identification method of internal leakage in nuclear power plants valves using convolutional block attention module. Nuclear Engineering and Design, 424: 113239.

Klewe, T., Strangfeld, C. & Kruschwitz, S. 2021. Review of moisture measurements in civil engineering with ground penetrating radar–Applied methods and signal features. Construction and Building Materials, 278: 122250.

Lang, X. & Wang, Z. 2024. A multi-sensor feature fusion attention convolutional neural network for complex magnetic leakage. IEEE Transactions on Instrumentation and Measurement.

Li, D., Zhou, X., Yi, D. & et al. 2025. Frequency band feature extraction analysis of pipeline leakage in fiber optic DAS system. In Proc of Fourth International Computational Imaging Conference (CITA 2024). SPIE, 13542: 240-244.

Li, H.J., Zhu, H.H., Tan, D.Y. & et al. 2023. Detecting pipeline leakage using active distributed temperature Sensing: Theoretical modeling and experimental verification. Tunnelling and Underground Space Technology, 135: 105065.

Li, X., Cao, L., Li, Z. & et al. 2025. Influence of Leakage from Buried Drainage Pipes on Shallow Soil Settlement and Urban Road Collapse. Natural Hazards Review, 26(3): 04025017.

Li, X., Chen, R., Liu, L. & et al. 2023. A non-Darcy flow CFD–DEM method for simulating ground collapse induced by leakage through underground pipeline defect. Computers and Geotechnics, 162: 105695.

Lu, P., Lalam, N., Badar, M. & et al. 2019. Distributed optical fiber sensing: Review and perspective. Applied physics reviews, 6(4).

Lu, Y., Zhu, T., Chen, L. & et al. 2010. Distributed vibration sensor based on coherent detection of phase-OTDR. Journal of Lightwave Technology, 28(22): 3243-3249.

Park, K., Soliman, M., Kim, Y.J. & et al. 2024. Sinkhole stability chart for geotechnical investigation. Transportation Geotechnics, 45: 101191.

Ren, L., Jiang, T., Jia, Z. & et al. 2018. Pipeline corrosion and leakage monitoring based on the distributed optical fiber sensing technology. Measurement, 122: 57-65.

Schenato, L. 2017. A review of distributed fibre optic sensors for geo-hydrological applications. Applied Sciences, 7(9): 896.

Sharma, V.B., Singh, K., Gupta, R. & et al. 2021. Review of structural health monitoring techniques in pipeline and wind turbine industries. Applied System Innovation, 4(3): 59.

Shiau, J., Chudal, B., Mahalingasivam, K. & et al. 2021. Pipeline burst-related ground stability in blowout condition. Transportation Geotechnics, 29: 100587.

Singh, S., Agrawal, S., Sahu, T. & et al. 2021. iPipe: water pipeline monitoring and leakage detection. In Proc of 2021 IEEE International Symposium on Smart Electronic Systems (iSES). City: IEEE, 367-372.

Tan, Y. & Long, Y.Y. 2021. Review of cave-in failures of urban roadways in China: A database. Journal of Performance of Constructed Facilities, 35(6): 04021080.

Tong, Z., Gao, J. & Yuan, D. 2020. Advances of deep learning applications in ground-penetrating radar: A survey. Construction and Building Materials, 258: 120371.

Wang, F., Wang, F., Gong, X. & et al. 2023. Water erosion and extension of ground fissures in Weihe basin based on DEM-CFD coupled modeling. Water, 15(13): 2321.

Wang, K., Zhang, J., Gao, G. & et al. 2022. Causes, risk analysis, and countermeasures of urban road collapse in China from 2019 to 2020. Journal of Performance of Constructed Facilities, 36(6): 04022054.

Wang, X.W. & Xu, Y.S. 2022. Investigation on the phenomena and influence factors of urban ground collapse in China. Natural Hazards, 113(1): 1-33.

Wang, Y., Xu, R., Deng, Z. & et al. 2022. High-Performance Distributed Acoustic Sensing with Coherent Detection. In Proc of 2022 IEEE 10th International Conference on Information, Communication and Networks (ICICN). IEEE, 485-488.

Xia, B., Lyu, D., Wang, N. & et al. 2023. Development of a rapid and quantitative prediction model for assessing the leakage status of water pipeline systems. Journal of Civil Structural Health Monitoring, 13(2): 605-613.

Zhang, Y., Duan, L., Li, Y. & Gao, M. 2024. Study on deformation characteristics of underground pipeline corridors and uneven settlement factors of foundations in sandy chalky soil layer. Frontiers in Earth Science, 11: 1266559.

Zhang, Z., Xu, C., Xie, J. & et al. 2023. MFCC-LSTM framework for leak detection and leak size identification in gas-liquid two-phase flow pipelines based on acoustic emission. Measurement, 219: 113238.

Zhu, D. & Chang, Y.J. 2020. Urban water security assessment in the context of sustainability and urban water management transitions: An empirical study in Shanghai. Journal of Cleaner Production, 275: 122968.

Zuo, J., Zhang, Y., Xu, H. & et al. 2020. Pipeline leak detection technology based on distributed optical fiber acoustic sensing system. IEEE Access, 8: 30789-30796.

Geotechnical Instrumentation Monitoring – A Transition from 3A to 5A Approach

Arthur K O So & Roger J W Lee
Meinhardt Infrastructure and Environment Limited

ABSTRACT

The referenced project is a cut-and-cover tunnel constructed in a dense urban area with a long history of reclamation and aged buildings. A critical section encroached into a historic two-block premises that require enhanced protection. Block 1 is a reinforced-concrete frame on cast in-situ piles, while Block 2 is a brickwork structure on shallow footings. Although PNAP APP-18 and APP-137 prescribe traditional 3A monitoring levels, these were considered too rigid for a project of this scale and complexity. The project team therefore introduced a revised third A level before the second A level was triggered, using updated settlement predictions and mitigation measures to maintain control. Damage classifications by Skempton and MacDonald (1956) and Burland et al. (1977) guided interpretation of building response. PLAXIS was used to model pile–soil interaction and verify geotechnical safety factors, while SAP2000 assessed structural integrity under predicted movements. Regular instrumentation meetings ensured that monitoring data were reviewed alongside construction progress, allowing timely refinement of mitigation strategies and further adjustments to the revised third A levels. This adaptive, performance-driven approach anticipated the flexibility later formalized in the 5A framework of PNAP APP-137 (BD 2024), demonstrating that large projects can balance efficiency with robust engineering safety.

KEYWORDS: Damage Classifications of Buildings, Deformation Modes, Limiting Tensile Strains, Geotechnical Instrumentation Monitoring Systems, Response Levels, Preventive and Mitigation Measures

1 INTRODUCTION

In Hong Kong, statutory regulations require the submission of a monitoring plan when construction works may affect the nearby buildings, structures, land, streets, or utilities (BD 2004). Traditionally, monitoring checkpoints and instruments are evaluated against three triggering levels, known as the Alert Alarm Action or 3A system, which dictate the response actions approved by the Buildings Department (BD) and Geotechnical Engineering Office (GEO) or supervising officer. These levels are determined based on the site conditions, nature and proximity of sensitive receivers to the construction site. Before 2012, there is no guideline on specific response levels for the 3A monitoring system except the third A level for utilities, which required agreement with the relevant government department or utility provider to reflect the maximum tolerable movement for the service in question (BD 2004). Since these 3A values were not directly correlated with the predicted settlements, making their use as control levels appeared potentially misleading.

A significant change occurred in March 2011 when the West Kowloon Terminus (WKT) of the Express Rail Link project adopted an innovative instrumentation monitoring plan (So et al. 2013), which is inspired by the Generalized Plan of Action and the Detailed Plan of Action outlined in the MTR Standard Material and Workmanship Specification (MTR 2009) and Project Integrated Management System (MTR 2010). In February 2012, the BD formalized detailed monitoring requirements in the Practice Notes for Authorized Persons (PNAP) APP-18 (BD 2012a) and APP-137 (BD 2012b), closely resembling the WKT approach. The 3A levels were explicitly defined as Alert, Alarm, and Action. PNAP APP-18 (BD 2012a) outlined the reference contingency measures for piling works at each level, to be implemented by the Registered Structural Engineer (RSE) and Registered Specialist Contractor (RSC). Meanwhile, Appendix B in the PNAP APP-137 (BD 2012b) recommended ground settlement limits for piling and related operations, along with the reference 3A values for ground settlement markers, utility settlement markers and building tilt markers, based on serviceability criteria. As different structures can exhibit varying tolerances to their movement and foundation displacement, the acceptability of estimated ground settlements must be assessed case by case, considering their structural integrity, stability, and functionality.

While the 3A values and monitoring requirements in the PNAP APP-18 (BD 2012a) and APP-137 (BD 2012b)

are generally suitable for small-scale projects, they present limitations for larger, more complex developments. An example is the construction of a cut-and-cover tunnel underneath two operating flyovers in old reclaimed urban land surrounded by old buildings on piles or footings, and at a location partially encroached into a historic building premises. It pioneered a revision of the Action Level (third A) before the Alarm Level (second A) was triggered after in-depth building condition surveys, additional ground investigation, interpretation of monitoring data, implementation of mitigation measures, more rigorous design reviews and settlement predictions. Further adjustments to the mitigation strategies and revised Action Levels were implemented as needed.

In November 2024, PNAP APP-137 (BD 2024) was updated to introduce a refined 5A system, closely resembling this project's approach. This revision retains the Alert and Alarm Levels but subdivides the Action Level into Action Levels 1, 2 and 3. Unless sensitive structures or utilities are nearby, empirical limits provided may serve as provisional trigger values for pile foundations and ELS works. The Technical Guidance Note No. 54 (TGN 54) by GEO (2024) also provides similar guidelines on ground deformation control mechanism for geotechnical works. This enhanced framework aims to improve the risk management for large-scale projects while safeguarding surrounding infrastructure.

Thus, this project may serve as a case study for its pioneering and resemblance to the 5A system. It highlights critical factors such as site-specific constraints, geotechnical challenges, design rationale, preventive measures, preemptive mitigation strategies, construction execution, and with main focus on the engineering approach to revise the 3A triggering criteria to protect the surrounding buildings, in parallel with the project advancement.

2 DEFORMATIONS AND DAMAGE TO BUILDINGS ADJACENT TO EXCAVATIONS

2.1 Deformation Modes and Damage Classification

Literature about damage due to deformations usually relates to the curvature of building because more curvature means higher strains and more damage. Curvature κ can be calculated as a derivative of deformation, and radius $R = 1/\kappa$ is a similar indicator for possible damage. Curvature of a building can arise from various modes of deformation such as shear deformation, bending, extension, compression, and a combination of deformation modes generally occuring simultaneously. When evaluating potential damage to buildings, it is crucial to distinguish various deformation modes associated with the damage (Bonshor and Bonshor 1996). Most damage occurs from cracks, so that crack degree is the main indicator of damage to a building. However, they do not necessarily indicate the extent of damage if stand alone. Table 1 shows two common classification systems. Skempton and MacDonald (1956) classified the amount of damage based on deformation into three broad categories, while Burland et al. (1977) refined these broad categories based on cracks into six categories, numbered 0 to 5 with increasing severity based on the studies by Skempton and MacDonald (1956), Grant, Christian and Vanmarcke (1974). These data sets apply to what have been traditional types of structures in the past, mainly buildings with frames and block or brick walls, or older buildings. No further updated state-of-the art paper is published since then. Notwithstanding this, both systems are widely used for building damage assessment due to deep excavations and other causes. e.g. BRE (1981) and the Institution of Structural Engineers (1994).

Table 1: Damage Classification System for Buildings

Damage Description	Limiting Relative Rotation
Structural Damage	1/150
Cracking in Walls and Partitions	1/300
Safe Limit against Cracking	1/500

(a) Skempton and MacDonald (1956)

Category of Damage	Degree of Damage	Description of Typical Damage	Approximate Crack Width (mm)	Limiting Tensile Strain (%)
0	Negligible	Hairline cracks	< 0.1	< 0.05
1	Very Slight	Fine cracks easily treated during normal redecoration. Perhaps isolated slight fracture in building. Cracks in exterior visible upon close inspection.	0.1 – 1.0	0.05 – 0.075
2	Slight	Cracks easily filled. Redecoration probably required. Several slight fractures inside building. Exterior cracks visible. Some repainting may be required for weather-tightness. Doors and windows may stick slightly.	1.0 – 5.0	0.075 – 0.15
3	Moderate	Cracks may require cutting out and patching. Recurrent cracks can be masked by suitable linings. Tuck pointing and possible replacement of a small amount of exterior brickwork may be required. Doors and windows sticking. Utility services may be interrupted. Weather tightness often impaired.	5.0 – 15.0 Several closely spaced cracks > 3.0	0.15 – 0.3
4	Severe	Extensive repair required involving removal and replacement of walls especially over doors and windows. Window and door frames distorted. Floor slopes noticeably. Walls lean or bulge noticeably. Some loss of bearing in beams. Utility services disrupted.	15.0 – 25.0 Depending on the number of cracks	> 0.3
5	Very Severe	Major repair required involving partial or complete reconstruction. Beams lose bearing. Walls lean badly and require shoring. Windows broken by distortion. Danger of instability.	> 25.0 Depending on the number of cracks	> 0.3

(b) Burland's (1977)

2.2 Deformation-Based Approach based on Empirical Criteria for Damage

The limits for damage to buildings are available in various forms and can be derived either theoretically or from field observations. The simplest limits are in the form of maximum settlement of the structure or differential settlement; while others describe the maximum rotation of the building. More advanced damage assessment approaches consider the deflection ratio or relative rotation. The current state of the art for predicting building damage from expected deformations is to calculate the strains from deflection ratio or relative rotation coupled with finite element methods. Table 2 is a summary of empirical criteria of limiting deformations for frame building and unreinforced load bearing walls. Meyerhof (1953) estimated the total and differential settlements of foundations in relation to the soil and foundation characteristics and the structure stiffness. The settlement stresses in foundation and superstructure are considered, and the recent observations on brick walls and cladded building frames are analysed. Skempton and MacDonald (1956) are the first to describe the effect of building damage. They introduced the criterion Δ/L with Δ and L being the differential settlement and distance between two footings or points on a building, which was later defined by Burland (1977) as relative rotation β. Based on observations and theoretical study, Polshin and Tokar (1957) used 0.05% as the limiting tensile strain for brick buildings with $L/H > 3$ where L is the distance between two separating joints which is not the necessarily the whole building length, and H is the height of the building. Boscardin and Cording (1989) combined Δ/L and horizontal strain into a damage matrix of which tensile strain > 0.05% implies risk of cracking while $\Delta/L >$ 1/300 implies structural damage.

Table 2: Empirical Criteria for Damage (After Korff 2009)

Damage Description	Limiting Relative Rotation β	Source
Structural Damage	1/150	Skempton and MacDonald (1956)
Cracking in Walls and Partitions	1/300	
Safe Limit against Cracking	1/500	
Cracking to No Infill Structures or No Danger of Damage to Cladding	1/200	Polshin and Tokar (1957)
Cracking to Steel and Concrete Frame Infilled Structures	1/500	
Cracking in Open Frames	1/300	Meyerhof (1953)
Cracking in Infilled Frames	1/1000	
Cracking in Load Bearing walls or Continuous Brick Cladding	1/2000	

(a) Limiting Deformations for Frame Buildings

Damage Description	Limiting Δ/L	Source
Sagging $L/H \leq 3$	1/3300 – 1/2500	Polshin and Tokar (1957)
Sagging $L/H \geq 5$	1/2000 – 1/1400	
Sagging	1/2500	Meyerhof (1953)

(b) Limiting Deformations for Unreinforced Load Bearing Walls

2.3 Crack-Based Approach based on Limiting Tensile Strains

Burland and Wroth (1974) first introduced limiting tensile strain to relate the effect of ground displacement into the strain in a building. They assumed the building as a simple beam such that when settlements affect the building, direct tensile strains occur due to bending deformation and diagonal strains due to shear deformation. The load can be modelled by a central point load or a uniform load. The neutral axis for bending is assumed to be at the bottom of the beam or wall in hogging and at mid-sp

an in sagging. Boscardin and Cording (1989) expanded this model to include horizontal strains to the bending and shear deformations based on angular distortion because deformations caused by excavation and tunnelling cause horizontal strains as well. Mair et al. (1996) and Burland et al. (2004) further refined this by integrating Mohr's circle for combined bending and shear strains. Son and Cording (2005) improved their previous works and got a lateral strain independent of L/H, E/G and the position of neutral axis, where E is the elastic modulus and G is the shear modulus of the building. However, e.g. CIRIA (2003) reported that low rigidity buildings like brick walls are probably governed more in bending than shear. In cases where large openings exist, buildings will behave more flexible and shear might govern instead. Boone (2001) took a similar approach but assumed a uniform loaded beam with neutral axis at mid-span. He considered critical tensile strains to be the absolute minimum of 0%, noting pre-existing cracks may widen under strain.

2.4 Drawbacks of Deformation and Crack Based Approaches

Despite these two approaches being widely used, they have some drawbacks. The assumption of isotropic building behaviour is often unrealistic because real structures exhibit orthotropic properties, with varying ratios of bending to shear stiffness (E/G) (Burland and Wroth 1974). The distribution of shear strain over building height and long buildings is another concern because Netzel (2005) found that shear strain varies over height and ignoring unaffected sections in long building may lead to non-conservative strain predictions. The use of deflection ratio Δ/L or relative rotation β is contentious. CIRIA (2003) considered that Δ/L is better to describe bending strains and β is more suitable for shear deformation, while a building that bends rather than rotates usually experiences more damage. Netzel (2005) also demonstrated inconsistencies in strain estimation when applying these methods to real analysis, complicating their interchangeability. Finally, rigid body tilt introduces ambiguity. Although tilt is often excluded from strain calculations, it can indirectly induce damage through gravity-induced stresses, particularly in framed structures with isolated footings. Modern approaches will use finite element to simulate soil-structure interaction to predict deformation-induced damage and real time monitoring to provide building deformation data and surface crack movement. Notwithstanding these drawbacks, the tensile strain methods can provide a valuable framework to assess potential damage to building due to construction activities and is also adopted in this project.

3 SITE GEOLOGY

The said project is located on a reclaimed land with a complex history of reclamation and use over the past 2 centuries. As shown in Figure 1, the existing ground level is generally flat at +4mPD and groundwater level generally fluctuates from +0.5mPD to +2.8mPD. The ground comprises of reclamation Fill overlying Marine Deposits (MDs), Alluvium, Residual Soils and Granitic bedrock. Since reclamation in the old days is by end-tipping from trucks without dredging and is uncontrolled, the Fill can be very loose without compaction and is expected to be placed on in-situ large sea wall stones, cobbles, boulders, timber, dead vegetation, abandoned drainage pipes and debris which were not removed prior to reclamation. This will give rise to a fill layer ranging from a few meters to more than 10m with large variability in properties and conductivity. The MDs are soft to firm silty clay with inter-bedded deposits of Marine Sand. The reclamation can also give rise to disturbance to the MDs in the form of mud waves leading to locations of very soft disturbed MD which were apparent. The undrained strengths and thicknesses of the MDs were highly variable. The Alluvium is firm or dense but locally soft or very soft. The interface between the MDs and underlying Alluvium is irregular. Further below is varying thickness of completely to highly decomposed Granite and then bedrock with locally abrupt change of rockhead level ranging from -15mPD in the east to -60mPD in the west.

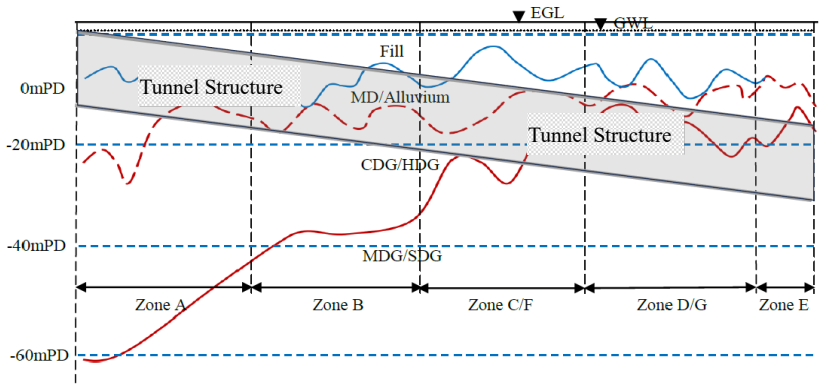

Figure 1: Geological Stratigraphy of the Site

4 DESIGN AND CONSTRUCTION

4.1 Original Engineer Design and Construction

The conforming excavation and lateral support (ELS) system is very robust in stability and hydraulic cut-off, adopting diaphragm wall panels as the vertical elements. These wall panels would penetrate sufficiently into bed rock. Top-down construction was adopted to minimize the impact to the surrounding environment and existing traffic. Basic construction sequence involved installation of diaphragm wall which serves as the permanent tunnel wall, construction of a temporary steel deck for temporary traffic diversion, excavation and lateral support, and construction of tunnel slabs as the excavation progressed in a top-down construction approach. The majority of the tunnel construction was carried out underneath existing flyover with continuous live traffic maintained, resulting in a significant headroom constraint.

4.2 Alternative Contractor Design and Construction – Challenges and Measures

Alternative designs were proposed to reduce rock excavation by trench cutter. Proposed was an underpinning wall in Zone E, temporary pipe pile wall embedded into rock with in-situ concrete wall for the part encroached into the historic premises and in high rock head locations. However, the alternative pipe pile wall design was subjected to risk of seepage at the wall openings that enabled utility crossings, the interface between the diaphragm wall panel and pipe pile, gaps between the pipe piles, at the pile toes and the rock joints if the rock quality is poor.

Figure 2 shows the alternative ELS design adjacent to the historic premises. As part of building Block 1 encroached into the tunnel alignment, a pipe pile wall with curtain grout was used instead of the diaphragm wall

panels to avoid clash with the existing building foundation, and affected foundation piles were also removed. The ground floor slab was removed, and pipe piles were installed under low head room conditions, limited by the ceiling of upper floor slab. Tube-a-manchette (TAM) grouting was designed between and at the back of pipe piles to stop seepage through the wall, which were strengthened with steel plankings as excavation progressed. Fissure grouting was proposed in rock with poor quality to stop seepage from the bottom of the excavation. Prior to bulk excavation works, preventive measures were also implemented. Polyurethane grout was injected through the holes drilled in the floor slab to stabilize the underlying ground and fill any potential voids to prevent building settlement. Temporary micro-piles with stitching to the existing building caps in the area within the tunnel footprint were first installed, then ground improvement was implemented using TAM grouting underneath footprint area of caps, to reinforce the building foundation and to prevent building settlement. Also, 406mm diameter socketed H-piles were proposed under low head room condition (less than 4m). Upon partial transfer of the existing building load to the new foundation system, the loading from the existing piles and associated temporary micro-piles could be neglected during tunnel excavation.

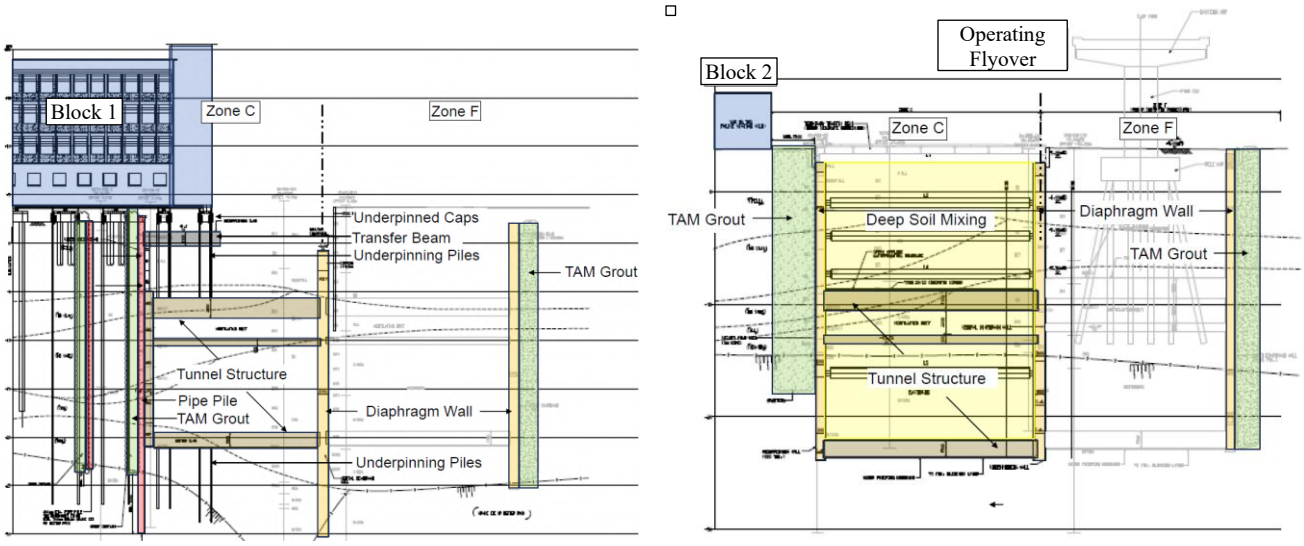

(a) Section across Block 1 (b) Section across Block 2

Figure 2 – Alternative ELS Design adjacent to the Historic Building

5 MONITORING AND RESPONSE ACTIONS – A CONVENTIONAL 3A APPROACH

Major diaphragm wall construction was started in mid-2018, followed by bulk excavation in phases. As the works progressed, the instrument readings were measured and monitoring data was made available online daily. Should there be any exceedance of the 3A values, a short message service (SMS) together with an email would be sent to the relevant persons. In addition to the statutory and contractual requirements, regular instrumentation monitoring meetings were set up. Instrument readings were reviewed and collated with construction activities. If the measured data exceeded any of the A levels, immediate review would be carried out and mitigation actions would be discussed and confirmed to implement in the meeting in accordance with the instrumentation monitoring system and reporting procedures established under the contract. Specific task force on this aspect had also been established during the critical stages to oversee the process. Minute as a record, and formal submissions were followed up as necessary. This collaboration with mutual respect enabled clarity of works and acquired practical and prompt decisions, avoiding communication in writing and dragging on submissions.

5.1 Excessive Drawdowns, Investigations and Remedial Measures

Initial settlements were generally within design predictions. However, progressive increase in settlements over a large area were observed after successful completion of pumping test and start of excavation in a zone. Thorough investigation found that the causes of increased settlement were due to slight water ingress through the cofferdam and bursting of a watermain at distant. Following the action plan in the alternative pipe pile wall

design, preempt remedial measures were implemented. Review was immediately carried out and tube-a-manchette (TAM) grouting enhancement measures was agreed as an appropriate scheme. TAM grouting was carried out using inclined holes from ground along the two blocks. Monitoring records showed that the ground water tables outside the cofferdam restored and the settlements were stabilized. Site inspection found that the excavation bottom was generally dry, and this indicated that the remedial grouting below excavated soil was effective. The effectiveness of remedial grouting was then verified by another pumping test without carrying out recovery phase to avoid flooding of the excavation, which was confirmed by a joint-inspection after submission of the pumping retest assessment report.

6 DESIGN REVIEW AND THIRD A REVISION – TRANSITION FROM 3A TO '5'A APPROACH

Besides the above, a task force involving some geotechnical experts was set up to conduct a holistic review and establish actions in controlling the settlement issue. In order to avoid any unrecoverable adverse effect to the concerned structures and potential interruption or suspension of works when the third A is reached, the allowable water drawdown and predicted building settlements were reviewed incorporating new observations and the triggering values were revised.

6.1 Resetting of Baseline Readings and Revision of Third A Values – A Step from 3A to '5'A

The instruments for the said project were installed as early as mid-2018. Since then, the site conditions had largely been changed due to different land use, site construction and traffic diversions. As such, a holistic review was conducted in December 2022. All unnecessary instruments were deleted and at some locations, where required instruments were added. Since soil is a particulate material, it can change in volume when it is loaded or unloaded due to changes in effective stress. Thus, lowering groundwater level will increase soil load causing compression along the λ-line, while rising groundwater level will reduce soil load leading to swelling along the κ-line. Given that the historic low groundwater level is 0mPD to -1mPD, settlement from drawdown to this range has already occurred, so that revisiting it would not cause further settlement. Ground settlements would diminish with distance from source and were predicted for further groundwater drawdown to -3mPD following Peck (1969) given in Figure 46 in the Review of Design Methods for Excavation (GEO Publication 1/90) by GEO 1990. Among them, the revising and updating of the third A levels at the historic premises is a notable example to discuss in details.

6.2 Block 1 – Reinforced Concrete Building on Cast In-situ Reinforced Concrete Piles

Block 1 is a 4-storey reinforced concrete building constructed in 1957, with a height of 14.5m and a footprint of 24.5m × 40.7m. The structural system consists of a beam-column frame with a core wall to resist lateral loads. Typical column grids are spaced at approximately 5.1m. The foundation features isolated pile caps connected by tie beams, supported by 80 number about 22m long 0.8m diameter cast-in-situ concrete piles. Appraisal was conducted to evaluate the building's structural adequacy under Ultimate Limit State (ULS) and Serviceability Limit State (SLS), incorporating the soil-structure interaction effects due to prescribed ground settlements. The assessment was focused on the structural capacity in bending and shear, pile-soil-structure interaction under differential settlement and stability against soil collapse using c'-ϕ reduction analysis.

In the pile-soil-structure interaction analysis, a two dimensional PLAXIS 2D model was developed as shown in Figure 3(a) to simulate the ground movement induced by tunnel construction, accounting for the limited stiffness of the existing ELS system. A 3 dimenional PLAXIS 3D model was also used to analyze the full foundation system, including piles, with c'-ϕ reduction analysis to determine the factor of safety against soil collapse. Predicted ground settlements were exported as contour plots. The original predicted settlement profile along the building, the current settlement profile and predicted settlement profile after updating with current monitoring data and design review is shown in Figure 3(b). A value of 45mm maximum settlement was predicted at the edge of the building.

For the structural analysis, a 3 dimensional SAP2000 model was used to analyze the load effects to the space frame of columns, beams and slabs under the imposed settlements. Critical elements such as the ground-floor columns and first/second floor beams were prioritized due to their higher stiffness demands under settlement-induced loading. The building was assumed to deform as the predicted ground settlemnt profile. The differential

settlement using angular distortion approach by Skempton & MacDonald (1957) in Table 1(a) was used to appraise the structure. The relative rotation or angular distortion was calculated as the ratio of differential settlement to the distance between two points, excluding the tilting effects. The computed angular distortion was equal to 1/450, which falls within the negligible to very slight structural damage range. Under these conditions, the utilization ratios of critical elements were assessed and were determined equal to 0.82 in hogging and 0.78 in sagging for first/second floors beams and 0.85 in axial/flexural for ground floor columns. All values remain below 1.0, confirming the adequacy under ULS. Furthermore, soil-structure interaction using c'-ϕ reduction analysis demonstrated that a FOS = 17.7 is obtained across all soil strata, significantly exceeding the minimum requirement of 3.0. This shows that soil collapse is not a governing factor, which implies that the settlement limits are driven by the structural tolerances rather than geotechnical failure. On integrating the above outcomes, the third A level was revised to 45mm total settlement with 1/450 angular distortion.

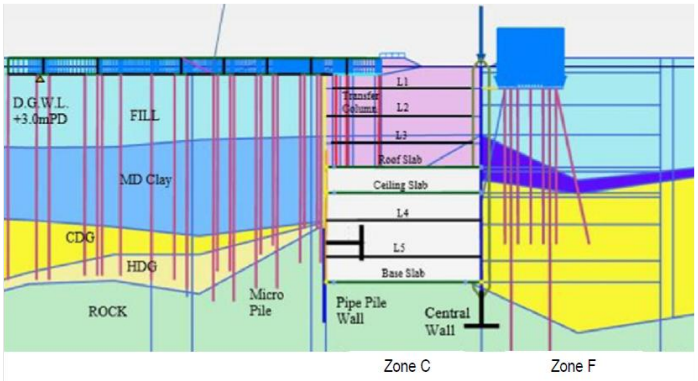

(a) Modeling for Excavation adjacent to Block 1

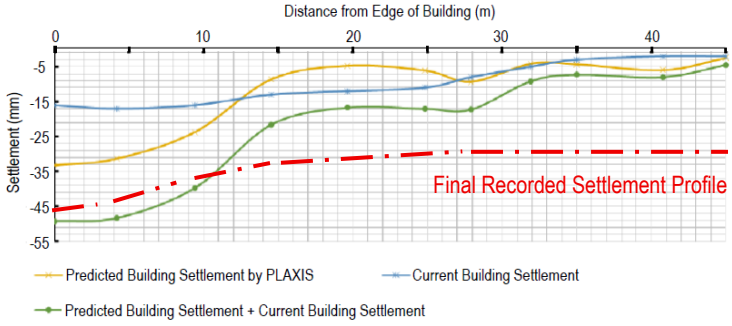

(b) Measured and Predicted Settlements

Figure 3: Prediction of Settlement Profile of Block 1

6.3 Block 2 – Historic Brick Building on Footings

Block 2 is a historic 3-storey brick building constructed in 1922. It stands 11.69m tall to the roof slab and 15.8m to the ridge of its tiled roof. The structure consists of two blocks measuring 46.8m × 16.5m and 34.7m × 15.4m, with a reinforced concrete beam-slab system supported by load-bearing brick piers and walls. As there were no piling records available, the foundation is assumed to be strip or pad footings of 300mm thick with top level at +3.09mPD based on trial pit survey findings. Condition survey conducted in 2018 showed that the conditions of the structure was basically satisfactory. Obvious visible defects such as cracks and concrete spalling for all structural elements were not observed.

Given the ongoing deep excavations adjacent to the building, an assessment was conducted to evaluate the potential ground movement effects. The methodology combines geotechnical analysis and structural calculation based on established engineering principles, particularly those outlined by Burland (2012). Three structural sections along the building were considered. In the geotechnical analysis, a two dimensional PLAXIS 2D model as shown in Figure 4(a) was developed to simulate the greenfield ground deformations and stress changes due to excavation. Building loads were modelled as plate elements and the resulting settlement profile was derived.

Of the structural assessment, the limiting tensile strain methods by Burland and Wroth (1974) and Boscardin and Cording (1989) were followed to estimate the building response. The structure was conservatively assumed to behave as a weightless elastic beam subject to full greenfield ground movements. Strains were calculated for sagging and hogging zones by analytical beam equations. Damage classification followed Burland's (1977) system in Table 1(b). This is also adopted by BRE (1981) and Institution of Structural Engineer (1978 and 1994). Due to limited as-built records, design practices for 1920s were inferred from the ICE Manual of Geotechnical Engineering (Burland et al. 2012) and the Settlement of Buildings and Associated Damage by Burland and Wroth (1974). Calculated settlement profile in Figure 4(b) shows that 34mm maximum settlement occurs at the southern edge of the building and hogging deformation dominates beyond 30m from the nearest building edge.

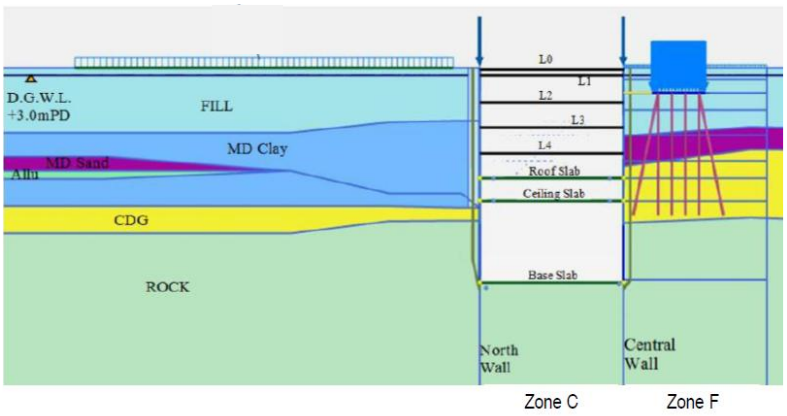

(a) Modeling for Excavation adjacent to Block 2

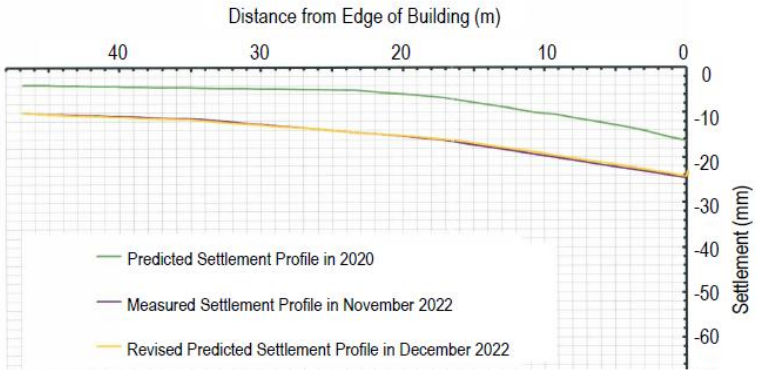

(a) Measured and Predicted Settlements

Figure 4: Prediction of Settlement Profile of Block 2

Structural responses are calculated giving 0.06% maximum tensile strain. This is in Category 1 (i.e. very slight damage with cracks ≤ 1mm) with angular distortion approximated to 1/500 differential settlement which is also within the safe limits given by Skempton and MacDonald (1956) (Table 1a). Based on these predictions, the third A level was revised to the maximum tensile strain limit = 0.08% (i.e. Category 2 with slight degree of damage) and differential settlement limit = 1/500 (i.e. safe limit against cracking), with 45mm maximum settlement. With these revisions, Block 2 was expected to experience "very slight damage" (Category 1) under the predicted ground movements. Notwithstanding these findings, extensive grouting was applied to ensure settlements remained below 45mm to prevent exceeding the angular limits.

However, larger settlements than the above predictions in Block 2 were observed in 2022 after start of excavation and later bursting of a watermain at distant. Sensitivity design checks by varying the soil stiffness and ground water level along the road in the geological model to mimic the measured settlements suggested that the bursting of watermain was likely the main cause of under-prediction. Additional boreholes considered that the adopted soil stiffness is appropriate while additional standpipes and piezometers revealed that extensive water drawdown occurred along the road. This is likely due to the large conductivity of the fill and probably

amplified by the damping effect after construction of the diaphragm walls and injection of extensive TAM grouting. Nevertheless, the geological model was revised with variation of ground water level extended to a larger distance to mimic the measured settlements. Further predictions showed that the differential settlement limit would remain at 1/400 with 0.09% maximum tensile strain and 64mm maximum settlement. The third A level was revised to 1/400 differential settlement limit (i.e. safe limit against cracking) with 0.09% maximum tensile strain limit (i.e. remain in Category 2 with slight degree of damage) and 80mm maximum settlement (Figure 5). Since the drawdown effects were distant and could extend to the left periphery of the building, further TAM grouting was applied in stages to this area to control the relative settlements/angular distortions.

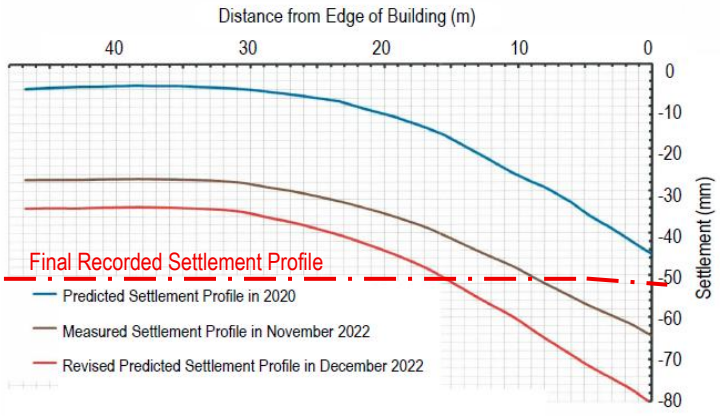

Figure 5: Revised Prediction of Settlement Profile of Block 2

7 DISCUSSIONS AND CONCLUSIONS

All excavations were basically completed in May 2025. Figure 6 shows the settlements of the historic premises continued to gradually increase but became stable in April/May 2024 when the base slabs started to construct. This proves that the new monitoring approach with the remedial measures and additional preventive measures are effective and appropriate. Despite the measured settlements are much smaller than the predicted maximum settlements, the settlements distant from the excavation are found much larger than the predicted settlements for Block 1 and Block 2. This is likely attributed to the long-term settlement arisen from the consolidation of underlying Marine Deposits due to fluctuation of ground water level during excavation.

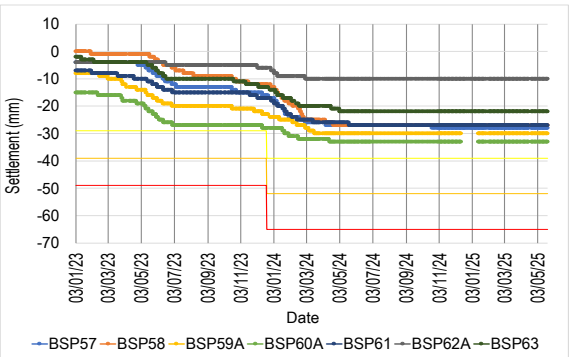

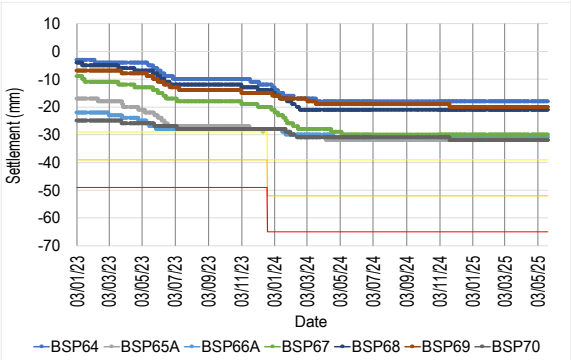

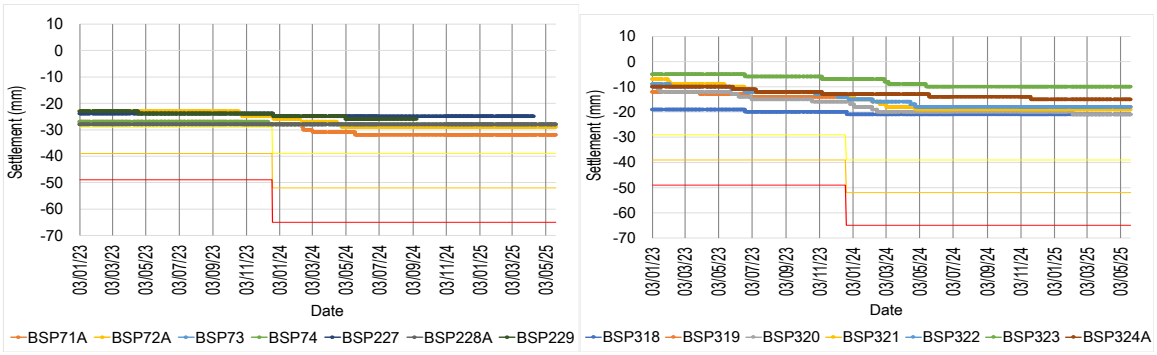

(a) Measured Settlements at Block 1

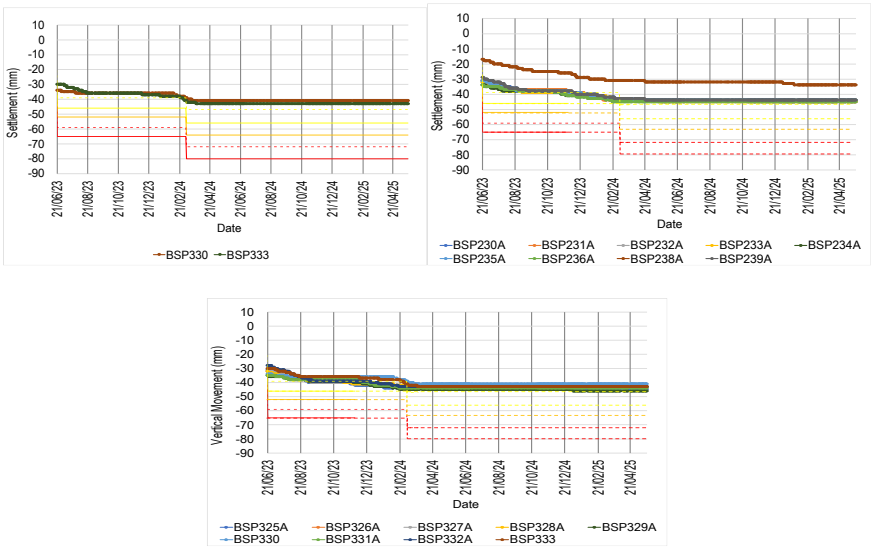

(b) Measured Settlements at Block 2

Figure 6: Measured Settlements of the Historic Premises to Completion of Excavation

Thus, the said project can serve as a notable example showing limitations of the 3A approach (BD 2012) and innovations to overcome the challenges in a large and complicated project before launching of the 5A approach (BD 2024). To avoid exceedance of the third A leading to project progress, a very robust ELS system was proposed along with additional preventive and enhancement measures such as TAM grout, polyurethane grout, DCM grout and underpinning of the existing building. It is no doubt that time-savings would be one of the benefits from this pro-active approach during design reviews and provides more suitable predictions of ground response to the satisfaction of the governing authorities. In this regard, the task force decided to execute all these actions in advance before the second A was reached, following the concept of Generalized Plan of Action by MTR (2009).

This action pioneered a new approach to review and reset the third A value based on sound engineering principles before the second or third A was reached, resembling the 5A approach promulgated by BD in 2024 (BD 2024). A holistic review such as building condition surveys, additional ground investigation, interpretations of monitoring data, implementation of mitigation measures, more rigorous design review and settlement prediction was required prior the revision of the third A. The interim trigger of the 5A approach provides an early warning and provide opportunity for early planning on preventative measures such that the critical SLS condition level does not occur. Particular focus in this paper is given to the protection of buildings, using a historic building with one block in reinforced concrete on cast in-situ piles and another block in brickwork on footings as an example. It explained how the controlling criteria, in terms of settlement, relative/differential settlement and angular distortion were established, and work approaches on how the triggering values for reinforced concrete and brickwork structures were revised based on the existing damage classification systems. Further adjustments to the mitigation strategies and revised Action Levels were implemented when needed and

mastered. This enhanced framework, resembling the 5A approach and requiring collaboration of the project team, can improve the risk management for large-scale projects while safeguarding surrounding infrastructure.

REFERENCES

BD. 2012a. PNAP APP-18 – Requirements for an Excavation and Lateral Support Plan Building (Administration) Regulation 8(1)(bc). Practice Notes for Authorized Persons, Registered Structural Engineers and Registered Geotechnical Engineers, Buildings Department, Hong Kong Government.

BD. 2012b, 2024. PNAP APP-137 –Ground-Borne Vibrations and Ground Settlements Arising from Pile Driving and Similar Operations. Practice Notes for Authorized Persons, Registered Structural Engineers and Registered Geotechnical Engineers, Buildings Department, Hong Kong Government.

Bonshor, R. B. and Bonshor, L. L. 1996. Cracking in buildings, Construction Research Communications Ltd.

Boone, S. J. 2001. Assessing Construction and Settlement-Induced Building Damage: A Return to Fundamental Principles. Underground Construction. London.

Boscardin, M. D. and Cording, E. J. 1989. Building Response to Excavation-Induced Settlement. Journal of Geotechnical Engineering 115(1), pp. 1-21.

BRE. 1981. Assessment of Damage in Low-Rise Buildings. Publisher BRE Archive Author BRE.

BRE. 2005. Concrete in Aggressive Ground. Special Digest 1: 2005. BRE Construction Division. The Concrete Centre. Publisher BRE Bookshop, Garston, Watford WD259XX.

Burland, J. B. and Wroth, C.P. 1974. Settlement of Buildings and Associated Damage. SOA Review. Conference on Settlement of Structures, Cambridge.

Burland, J.B., Broms, B.B., De Mello, V.F.B. 1977. Behaviour of Foundations and Structures. Ninth International Conference on Soil Mechanics and Foundation Engineering, Tokyo, Japan, pp. 495-546

Burland, J.B., Mair, R. J. and Taylor, R. N. 1996. Prediction of Ground Movements and Assessment of Risk of Building Damage due to Bored Tunnelling. The International Symposium of Geotechnical Aspects of Underground Construction in Soft Ground. Mair & Taylor. London, April 1996, Rotterdam, Balkema.

Burland, J. B., Mair, R. J. and Standing, J.R. 2004. Ground Performance and Building Response due to Tunnelling. Advances in Geotechnical Engineering - The Skempton Conference. London, ICE.

Burland, J, Chapman, T., Skinner, H. and Brown, M. 2012. Problematic Soils and Site Investigation. ICE Manual of Geotechnical Engineering, Volume I Geotechnical Engineering Principles, Author Burland J.B., Imperial College London, UK. (pp. 281-296)

CIRIA. 2003. Response of Buildings to Excavation-Induced Ground Movements. Proceedings of the International Conference (SP201), Imperial College, London, UK.

GEO. 1990. The Review of Design Methods for Excavation, GEO Publication 1/90, CEDD, Hong Kong Government.

GEO. 2024. The GEO Technical Guidance Note No. 54 (TGN 54), CEDD, Hong Kong Government.

Grant, R.; Christian, J. T.; Vanmarcke, E. H. 1974. Differential Settlement of Buildings. ASCE, Journal of Geotechnical Engineering Division 100(GT 9): 973-991.

Institution of Structural Engineers. 1994. Subsidence of Low-Rise Buildings – A guide for Consulting Engineers, Building Surveyors, Contractors and Builders, Insurers, Mortgage Lenders, Property Valuers, Loss Adjusters, Local Authorities, and Other Interested Parties. By Institution of Structural Engineers.

Korff, M. 2009. Deformations and Damage to Buildings Adjacent to Deep Excavations in Soft Soils. Literature Survey F531, Deltares.

Meyerhof, G. G. 1953. Some Recent Foundation Research and Its Application to Design. The Structural Engineer 31(June), pp. 151-167.

MTR. 2009. Section 23 – Geotechnical Instrumentation. Materials and Workmanship Specification for Civil Engineering Works, Volume 3, MTR Corporation Limited.

MTR. 2010. PIMS/PN/11-22/A1 – Reporting of Exceedances in Instrumentation Monitoring Readings to Senior Management. Project Inte-grated Management System PIM Practice Note, MTR Corporation Limited.

Netzel, H. D. 2005. Review of the Limiting Tensile Strain Method for Predicting Settlement Induced Building Damage. Geotechnical Aspects of Underground Construction in Soft Ground, Amsterdam, Taylor and Francis Group, London.

Peck, R. B. 1969. Deep Excavations and Tunneling in Soft Ground. 7th International Conference on Soil Mechanics and Foundation Engineering. Mexico City, Sociedad Mexicana de Mecanica de Suelos, A.C.

Polshin, D. E. and Tokar, R.A. 1957. Maximum Allowable Non-Uniform Settlement of Structures. Proceedings 4th International Conference on Soil Mechanics and Foundation Engineering. London, UK, Vol.1, Butterworth's Scientific.

Skempton, A. W. and McDonald, D.H. 1956. The Allowable Settlements of Buildings. Proceedings Institution of Civil Engineers Part III, 5(50), pp. 727-768.

So, A. K. O., Ko, P. W. L. and Man, V. K. W. 2013. Geotechnical Instrumentation Monitoring for the Construction of the West Kowloon Terminus of the Express Rail Link. Proceedings of the 4th International Symposium on Geotechnical Safety and Risk, 4-6 December 2013, Hong Kong. pp. 551-558.

Son, M. and Cording, E.J. 2005. Estimation of Building Damage due to Excavation-Induced Ground Movements. Journal of Geotechnical and Geoenvironmental Engineering (131), pp. 162- 177.

From Simplified Assumptions to Soil–Structure Interaction: A Paradigm Shift in Raft and Piled Raft Foundation Design

Ted Tse, Ryan Cheung and Bryan Zhu
Binnies Hong Kong Limited

ABSTRACT

Over the past two decades, foundation design software has advanced significantly, enabling the modelling of complex loading conditions and soil-structure interaction (SSI). With increasing automation and AI-assisted workflows, numerical models can now be developed more efficiently than ever. However, an important question remains: have these advances led to more reliable and optimized foundation design in practice? This paper reviews the evolution of foundation design from traditional hand calculations to comprehensive three-dimensional (3D) numerical modelling. While modern tools allow more rigorous simulation of SSI, their effectiveness depends on the validity of the underlying assumptions.
An alternative design framework for raft and piled raft foundations is presented, integrating geotechnical and structural analysis. In structural software such as SAFE, soil support is commonly represented by the modulus of subgrade reaction (k_s). Rather than relying on simplified empirical correlations, this study derives k_s from 3D finite element analyses using PLAXIS 3D. This approach captures complex subsurface conditions and interaction effects, allowing spatial variation of k_s across the foundation system.
The proposed methodology provides in a more realistic and technically robust estimation of foundation stiffness, improving prediction of load distribution, settlement and structural response. By integrating advanced numerical tools and AI-assisted modelling techniques, raft and piled raft systems can be designed with greater accuracy and efficiency, potentially enabling optimization of foundation solutions that would otherwise be considered overly conservative, costly, or time-consuming under conventional design practices.

1 INTRODUCTION

Traditionally, foundation design has been based on simplified analytical approaches in which system such as isolated footings or pile caps are idealized as rigid elements. These methods, commonly implemented using hand calculations or spreadsheets, assume simplified soil response and largely neglect soil deformability.

However, soil is inherently deformable, and the foundation behaviour is governed by soil-structure interaction (SSI). The relative stiffness between the structure, foundation, and supporting soil plays a critical role in determining load distribution, settlement and internal forces within the foundation system.

With advances in computational tools, modern design practice has shifted towards modelling foundations as flexible systems. Structural analysis software such as SAFE represents foundations as plates supported by elastic springs, where the soil behaviour is characterized by the modulus of subgrade reaction (k_s). In this approach, soil pressures develop in response to foundation deformation rather than being pre-assumed.

Nevertheless, k_s is not an intrinsic soil property but a system-dependent parameter influenced by foundation geometry, soil conditions, and structural stiffness. It should not be assumed uniform across a raft foundation. Therefore, despite advances in analysis tools, design reliability ultimately depends on the validity of the adopted assumptions and input parameters.

2 SIMPLIFIED DESIGN METHOD

2.1 Rigid Foundation Assumption

Although conventional rigid foundation assumptions are often regarded as simplified, they can, in certain cases, provide results closer to reality than flexible models based on oversimplified soil stiffness representations, particularly for relatively small foundations supporting one or a few columns.

Meyerhof (1953), classified foundation as rigid or flexible based on the ratio of structural stiffness to founding material stiffness. The relative stiffness factor, K_r is used to assess whether a foundation behaves as a rigid body:

$$K_r = \frac{EI_b}{E_s B^3} \qquad \text{Eq. (1)}$$

where E = Modulus of Elasticity of Structure; E_s = Modulus of Elasticity of Soil; B = Width of Foundation; and I_b = Moment of Inertia of Structure per unit length at right angles to B.

The American Concrete Institute (ACI) Committee 336 (1998) recommends that foundation with $K_r \geq 0.5$ may be treated as rigid, with soil pressure determined using simple statics. For $K_r < 0.5$, the foundation should be modelled as flexible system on elastic supports.

Figure 1 illustrates the variation of K_r with foundation size and thickness. Typical configurations such as 5x5m^2 (1m thick), 10x10m^2 (1.5m thick) and 15x15m^2 (2.5m thick) may still behave as rigid foundations, for which simplified design approaches remain applicable. Eq. (1) has not considered the stiffness of superstructure and as noted by Hain (1980), effective stiffness should consider the combined interaction of the superstructure, foundation and supporting soil.

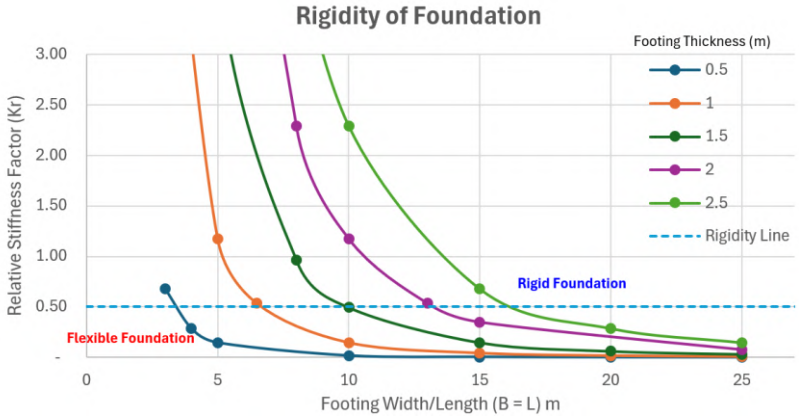

Figure 1: Rigidity of Foundation with varying Size and Thickness

2.2 Piled Raft Foundation

For raft foundations, particularly those of large plan dimensions, bearing capacity is rarely the governing design criterion. Instead, performance is typically controlled by total and differential settlements (GEO Pub. 1/2006). The concept of piled raft foundations is therefore to optimize pile layout to enhance overall system stiffness and control settlement, rather than to provide additional bearing capacity.

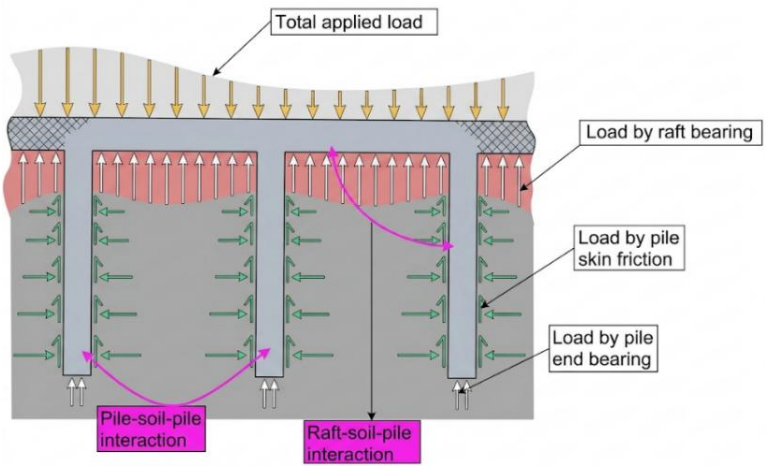

Figure 2: Load Transfer Mechanisms of Piled Raft Foundation System (Structville, 2024)

The load-sharing mechanism in piled raft systems remains an active area of research. As illustrated in Figure 2, the proportion of load carried by piles may range from approximate 50% to 80%, depending on soil conditions, pile length, spacing, and raft stiffness (Structville, 2024). Key influencing factors include:

- **Raft rigidity**: A stiffer raft promotes more uniform load distribution, while a flexible raft increases load transfer to piles
- **Soil properties**: Soil stiffness and compressibility govern load transfer behaviour
- **Pile characteristics**: Number, length, spacing, and stiffness of piles influence load sharing

Although piled raft foundations are widely adopted internationally, their use remains limited in some regions, such as in Hong Kong. In practice, neglecting the contribution of raft-soil contact is often considered a conservative simplification.

Poulos-Davis-Randolph (PDR) is a well-adopted simplified method for pile raft design. By this method, the load sharing ratio between raft and piled raft (X) can be determined using Randolph (1994) method and piled raft settlement (S) can be established using Polous and Davis (1980) method. The equations are as follows:

$$X = Q_r/Q_{pr} = \left[(1-\alpha_{rp})k_r\right]/\left[k_{pg} + (1-2\alpha_{rp})k_r\right] \quad \text{Eq. (2)}$$

$$S = Q_{pr}/k_{pr} \quad \text{Eq. (3)}$$

$$k_{pr} = \left[k_{pg} + (1-\alpha_{rp})k_r\right]/\left[1-\alpha_{rp}{}^2(k_r/k_{pg})\right] \quad \text{Eq. (4)}$$

$$\alpha_{rp} = 1 - [ln(r_c/r)/\varsigma] \quad \text{Eq. (5)}$$

$$r_c = \sqrt{(A/n\pi)} \quad \text{Eq. (6)}$$

$$\varsigma = ln(r_m/r) \quad \text{Eq. (7)}$$

$$r_m = \{0.25 + \xi[2.5\rho(1-\nu) - 0.25]\}L \quad \text{Eq. (8)}$$

$$\rho = G_{avg}/G_l \quad \text{Eq. (9)}$$

$$\xi = G_l/G_b \quad \text{Eq. (10)}$$

$$k_{pg} = k_p \cdot \sqrt{n} \quad \text{Eq. (11)}$$

where,
Q_r = Load carried by the raft
Q_{pr} = Load carried by piled raft
k_r = stiffness of the raft (Poulos & Davis, 1974)
k_p = stiffness of the single pile (Randolph, 1994)
k_{pg} = stiffness of the pile group,
k_{pr} = Stiffness of the piled raft
α_{rp} = Interaction factor
A = Raft area
n = Number of piles
L = length of piles
r_m = Maximum radius from pile axis
G_l = Shear modulus of soil along pile shaft
G_b = Shear modulus of soil at pile end
ν = Poisson's ratio of soil

In addition to the PDR method, the piled raft design should be checked against with Equivalent Raft Method. This method is for estimation of settlement of piled raft foundations in compressible soil as suggested by Tomlinson (2008). It assumes the piled raft foundation behaves as a raft foundation with its founding level at two-third of the average pile length underneath the pile cap. Determination of the size of the equivalent raft is assumed of load spread with 1 in 4 above the equivalent raft founding level and then 30° below as shown in Figure 3 which is extracted from Tomlinson (2008). The settlement of the equivalent raft can be estimated with the soil beneath the founding level treated as elastic materials.

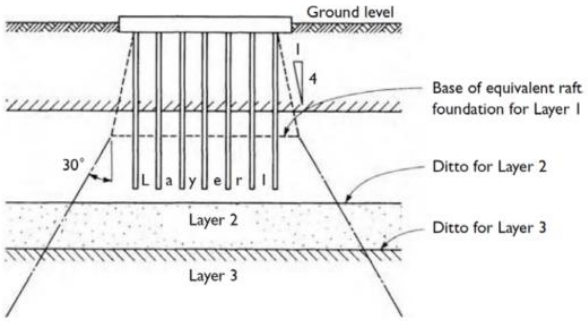

Figure 3: Principles of Equivalent Raft Method [Extracted from Tomlinson (2008)]

3 MYTH OF FLEXIBLE FOUNDATION

The application of finite element analysis using structural software such as SAFE, based on flexible foundation assumptions, has increasingly become a standard practice in foundation design. In such models, soil-structure interaction (SSI) is commonly represented using the Winkler Model (WM), where soil is idealized as a series of independent springs defined by the modulus of subgrade reaction (k_s).

However, designers must recognize that k_s is not an intrinsic soil property, but a system-dependent parameter influenced by foundation geometry, soil conditions, loading and structural stiffness. Simplified estimation of k_s may therefore lead to either overly conservative or unconservative designs, particularly for large raft or piled raft foundations. There are several critical limitations for applying WM with k_s as soil support for raft foundation design described by Tse (2025).

3.1 Myth of Uniform Springs of Modulus of Subgrade Reaction (ks)

In practical, flexible foundations are often modelled using a constant k_s, implying uniform soil stiffness across entire foundation. A widely adopted formula is Vesic (1961):

$$k_s = \frac{E_s}{B(1-\upsilon^2)} \quad \text{(Eq. 12)}$$

where Es = Young's modulus of soil, B = width of footing and υ = Poisson's ratio of soil.

However, k_s depends not only on soil properties but also on the foundation dimensions (Poulos, 2000). As foundation width increases, k_s decreases, often leading to exaggerated settlement predictions, particularly near edges and corners. To address this, Hans-Georg (2006) suggested multiplying k_s by factors of 1.75 and 3.5 at the edge and corner respectively.

More fundamentally, the WM treats soil as isolated springs with no interaction and the spring only deflects if a pressure is applied to it. Thus, unloaded areas in a Winkler soil model do not deflect, and hence there is no stress transmission or interaction within the soil (Poulos, 2000). In reality, soil behaviour involves stress redistribution and interaction between adjacent zones. The absence of these effects leads to inaccurate predictions of soil pressure and structural response, especially under non-uniform loads.

As a result, the so-called "flexible" model may fail to capture the true soil-structure interaction mechanisms if k_s values are not correctly input. This leads to what may be termed the myth of the flexible foundation – the belief that allowing structural flexibility alone is sufficient to produce realistic results. However, the accuracy of such models is governed not by the flexibility of the structural element, but by the validity of the soil representation. A flexible foundation model based on a uniform k_s may produce less reliable predictions than a simplified rigid foundation approach, which implicitly captures stress redistribution. Comparison results of rigid and flexible foundation are discussed in Section 3.3 below.

In order to prevent misuse of the WM, the writer suggests applying geotechnical finite element model (FEM) software, such as PLAXIS 3D or MIDAS GTS NX, allow for more rigorous simulation of soil-foundation interaction and derivation of spatially varying subgrade reaction parameters, which can then be incorporated into structural models. Details of the application are described in Section 6.

3.2 Myth of Conservative Design Using Reduced Modulus of Subgrade Reaction (k_s)

The k_s is often treated as a tuning parameter, which lower values are adopted under the assumption of conservatism. However, this assumption is not generally valid and may be misleading.

Reducing k_s increases settlement, which may appear conservative, but does not necessarily improve design reliability. Instead, it reflects increased structural demand within the limitations of the adopted model. In some cases, higher k_s values can result in larger bending moments and shear forces due to reduced foundation flexibility. This phenomenon can be explained by the relative stiffness factor as mentioned in Section 2.1 Eq. (1) above. A smaller relative stiffness factor, indicative of a lower value of modulus of k_s of the founding materials, may render the foundation more 'flexible', and so increase of the design forces.

In consideration of the uncertainties in k_s estimation, it is advisable to conduct sensitivity analyses for Ultimate Limit State (ULS) structural design to enhance the robustness of the design. It is recommended that sensitivity analyses cover a range of 50% to 150% of the estimated k_s for structural checking.

3.3 Comparison of Rigid and Flexible Foundation Results

A comparative study was conducted using four analysis methods:

(i) Rigid foundation with hand calculation [HC];
(ii) Flexible foundation by SAFE with uniform k_s [WM(Uniform)];
(iii) Flexible foundation by SAFE with spatially adjusted k_s from PLAXIS 3D [WM (Adj.)]; and
(iv) Flexible foundation by PLAXIS 3D FEM as the benchmark [FEM].

The results are presented in Table 1 and Figure 4:

Table 1: Comparison of Maximum Settlement, Bearing Pressure, and Bending Moment

Model	Size (B×L×D) (m)	Load Pattern	K_r (1)	Max. Settlement (mm)				Max. Bearing Pressure (2) (kPa)				Max. Bending Moment (kNm/m)							
				HC	WM (Uniform)	WM (Adj.)	FEM	HC	WM (Uniform)	WM (Adj.)	FEM	HC		WM (Uniform)		WM (Adj.)		FEM	
												Sag	Hog	Sag	Hog	Sag	Hog	Sag	Hog
A	5×5×1	4 x 625 kN	1.17	36	38	40	40	125	125	151	204	62	-78	69	-66	6	-51	7	-39
B	10×10×1	4 x 2500 kN	0.15	72	76	69	69	125	125	214	243	250	-312	430	-265	88	-144	68	-124
C	15×15×1	9 x 2500 kN	0.04	108	115	92	92	125	126	232	293	346	-175	406	-274	19	-1	83	-4
D	20×20×1	16 x 2500 kN	0.02	144	157	119	116	125	129	302	322	334	-227	396	-487	02	-2	84	-8
E	25×25×1	25 x 2500 kN	0.01	179	209	140	142	125	131	255	329	326	-165	383	-480	13	-1	09	-8
F	30×30×1	36 x 2500 kN	0.01	215	244	162	165	125	134	353	356	336	-226	387	-632	84	-1	082	-12

Remark:

(1) Relative stiffness factor, K_r, is estimated based on Grade C45 concrete and founding stiffness (Es ~ 150,000kN/m^2). If K_r is greater than 0.5, the foundation is categorized as rigid or else to be flexible.

(2) Even though FEM models show much higher max. bearing pressure (at the edges), the average bearing pressure for all four methods are similar.

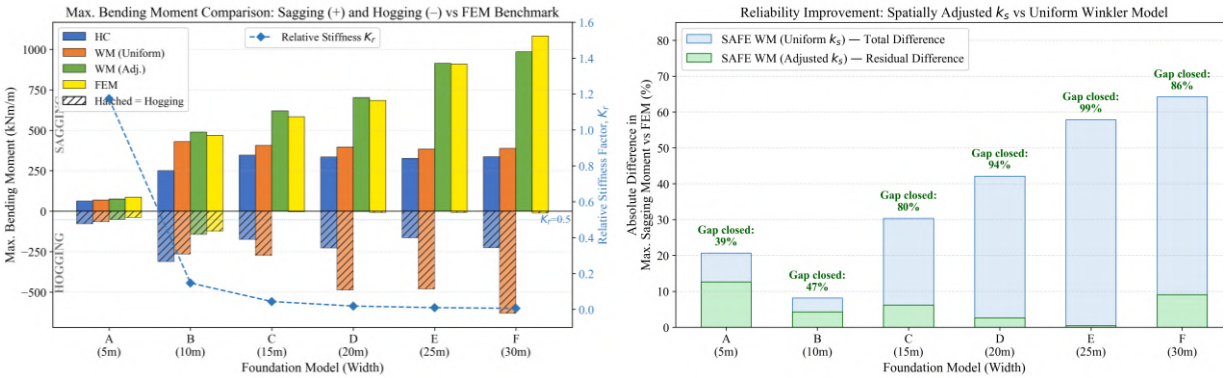

Figure 4: (Left) Bending Moment Comparison and (Right) Reliability Improvement by Spatially adjusted k_s

Key Observations are as follows:

- For small foundations (e.g. 5m×5m, K_r = 1.17), all methods produce similar settlements and bearing pressures. Differences in bending moments are relatively small and of limited design significance.
- As foundation size increases, both [HC] and [WM (Uniform)] become less accurate. Settlement is generally overestimated, while sagging moments are underestimated and hogging moments significantly overpredict comparing to [FEM].
- Notably, [HC] performs comparably to [WM (Uniform)] in terms of bearing pressure and bending moment and in some cases provides better settlement predictions.
- [WM(Adj.)] shows excellent agreement with [FEM] results across all foundation sizes, with bending moment differences typically within ±10%. [WM(Adj.)] and [FEM] should be recommended for design when raft foundation is greater than 10m in width.
- While [WM(Uniform)] loses accuracy as foundation size increases, the implementation of a spatially adjusted k_s effectively closes the performance gap. The "gap closure" percentage increases alongside foundation size, demonstrating that spatial variation in soil springs is essential for reliable large size foundation as shown in Figure 4.

Further sensitivity analyses were conducted to evaluate the influence of foundation stiffness on analysis accuracy. Model C was selected, with raft thickness varied from 1.0 m to 2.5 m. The results are summarized in Table 2.

Table 2: Effect of Raft Thickness on Analysis Accuracy - Bending moment, Settlement and Bearing Pressure comparison for 15 m × 15 m Raft with varying Thickness (Models C–C3)

Model	Size (B×L×D) (m)	Load Pattern	K_r	Max. Bending Moment (kNm/m)										
				HC		WM (Uniform)		WM (Adj.)		FEM		Difference Comparison for Sagging Moment With [FEM]		
				Sag	Hog	Sag	Hog	Sag	Hog	Sag	Hog	[HC]	[WM(Uniform)]	[WM(Adj.)]
C	15×15×1	9 x 2500 kN	0.04	346	-175	406	-274	619	-1	583	-4	−40.7%	−30.4%	+6.2%
C1	15×15×1.5	9 x 2500 kN	0.15	380	-192	405	-278	648	-1	619	-4	−38.6%	−34.6%	+4.7%
C2	15×15×2	9 x 2500 kN	0.35	414	-209	404	-280	669	0	640	-4	−35.3%	−36.9%	+4.5%
C3	15×15×2.5	9 x 2500 kN	0.68	448	-226	404	-280	683	0	656	-4	−31.7%	−38.4%	+4,1%

Bending Moment Accuracy:

- **[HC]:** Accuracy improves slightly in bending moment as Kr increases (-40.7% → -31.7%), reflecting the increasing validity of the rigid assumption. However, even as Kr = 0.68, the ~32% underestimate of sagging moment remains unacceptable for structural design.
- **[WM(Uniform)]:** Shows counterintuitive deterioration with increasing raft thickness. Errors worsen from -30.4% to -38.4% at Kr = 0.68, indicating that increased structural stiffness further amplifies the limitations of uniform ks assumption.
- **[WM(Adj.)]:** Demonstrates consistently high accuracy with sagging moment differences within +4 to -6% across all thicknesses. The SSI-calibrated ks distribution remains robust regardless of foundation rigidity.

Reinforcement Design Implications

- **Sagging (Bottom Face):** Both [HC] and [WM (Uniform)] present a significant risk of under-design. For t = 1.0 m, both methods suggest 0.13% reinforcement (1,300 mm²/m), approximately 20% lower than the [FEM] requirement (1,632 mm²/m).
- **Hogging (Top Face):** [FEM] and [WM (Adj.)] predict substantially lower hogging moments, leading to more efficient reinforcement design compared with [HC] and [WM (Uniform)]. This shows [HC] and [WM (Uniform)] may be over-design for hogging moment.

In summary, comparison across settlement, bearing pressure, and bending moment (sagging and hogging) reveals a critical paradox: a simplified rigid approach may outperform a more sophisticated flexible analysis when soil stiffness is oversimplified. In particular, a uniform k_s underestimates sagging and significantly overestimates hogging, resulting in a distorted moment envelope for large raft foundations. The issue, therefore, lies not in flexible modelling itself, but in the representation of soil behaviour. A more reliable approach is to adopt a spatially varying k_s that reflects continuum interaction, which can be derived through the PLAXIS 3D back-analysis workflow described in Section 4 below.

4 APPLICATION OF ADVANCED TECHNOLOGIES FOR SOIL STRUCTURE INTERACTION

Geotechnical finite element software such as PLAXIS 3D enables rigorous simulation of soil-structure interaction (SSI) by modelling the soil continuum, foundation, and piles as a coupled system. To translate these capabilities into practical design, two complementary approaches are adopted:

- **Design Approach 1: PLAXIS 3D + SAFE SSI Iteration –** PLAXIS 3D is used to derive spatially varying ks. which is then incorporated into SAFE for structural analysis and reinforcement design under multiple load combinations.
- **Design Approach 2: PLAXIS 3D Only** – PLAXIS 3D is used as a unified platform for both geotechnical and structural assessment, capturing full SSI behaviour within a single 3D continuum model.

4.1 Implementation of Design Approach 1: PLAXIS 3D → SAFE SSI Iteration

In this approach, k_s values in the Winkler Model (WM) are calibrated using results from PLAXIS 3D. A representative load case (typically dead load + live load) is first analyzed in PLAXIS 3D. The raft is discretized into grids (e.g. 1 m × 1 m), and k_s is back-calculated at each location from the ratio of applied pressure to corresponding settlement.

The derived spatially varying k_s distribution is then implemented in SAFE for structural analysis. This method significantly improves prediction accuracy (see Section 3.3) while retaining the efficiency of SAFE for handling multiple load combinations and reinforcement design.

This design approach is more acceptable under current situation. Majority of designers and approval authorities are more confident to adopt SAFE for structural design as PLAXIS 3D is less suitable to compute for large amount of load combinations and limited structural design capability. For each structural load combination, PLAXIS 3D will set up separate models for analysis. The modelling time and computational time for all these load combination models are very time consuming.

4.2 Implementation of Design Approach 2: Automation Design using PLAXIS 3D

PLAXIS 3D offers key advantages through advanced constitutive modelling and staged construction analysis. Nonlinear soil behaviour can be captured using models such as Hardening Soil or Soft Soil, allowing stiffness and strength to evolve with stress level. Construction sequencing can also be explicitly simulated, which is critical for realistic load transfer assessment.

The Design Approach framework enables implementation of limit state design in accordance with standards such as Eurocode 7, through systematic application of partial safety factors to loads and material parameters.

To improve efficiency for complex projects, Python-based scripting can be integrated via the PLAXIS API. This allows automation of:

- Load combinations and design approaches
- Parameter assignment and modification
- Generation of calculation phases
- Batch analysis and result extraction

Such automation significantly reduces modelling effort and improves consistency, particularly for parametric studies and large-scale design problems.

4.3 Comparison of PLAXIS 3D and SAFE Results

A comparative study was conducted to examine the accuracy of PLAXIS 3D and SAFE [WM(Adj.)] for structural design analysis. The two models are raft foundation with 27m x 23.25m x 1m as shown in the Figure 5. Bending moment and shear force obtained from the two models are compared in Figure 6.

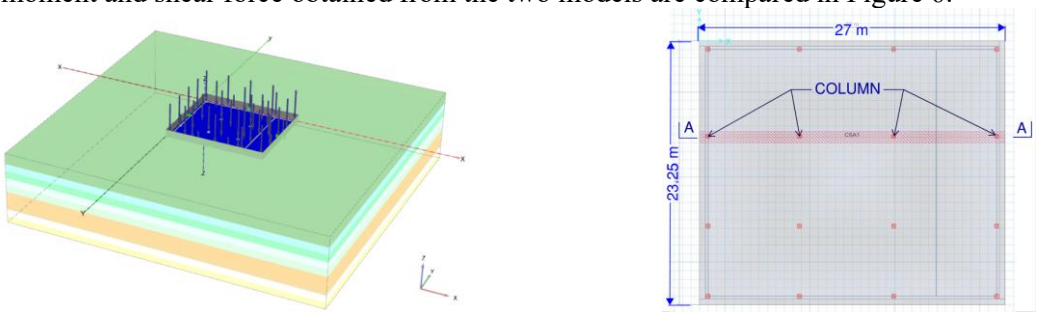

Figure 5: (Left) PLAXIS 3D Model and (Right) SAFE Model

The bending moment and shear force estimations derived from PLAXIS 3D exhibit a good level of agreement with the results obtained from SAFE. For bending moments, the maximum values (sagging moment) predicted by PLAXIS 3D are slightly higher while minimum values (hogging moment) are slightly lower than those obtained from SAFE. In terms of shear force, the PLAXIS 3D results exhibit sharp and odd changes at the locations of point loads, which may be due to potential numerical singularities and lack of physical smoothing. However, those abnormal shear force values are unlikely to affect the overall reinforced concrete (RC) design as no shear failure at columns/walls location under shear enhancement. Owing to limitations in scope and time, further investigation and optimization of PLAXIS 3D for application in RC design are deferred to future studies and are not discussed in detail herein.

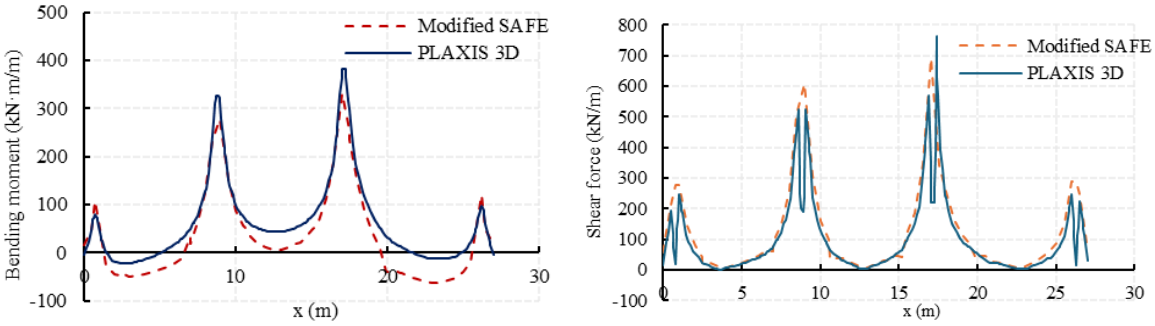

Figure 6: (Left) Bending Moment and (Right) Shear Force Comparison at Section A from SAFE and PLAXIS 3D

5 PARAMETIC STUDIES FOR PILED RAFT DESIGN

5.1 Raft Footing VS Piled Raft Foundation

In order to illustrate the advantages of a piled raft system against raft footing, a comparative analysis (Set M) was conducted between raft footing (Model M1) and piled raft foundation (Model M2). The results are presented in Table 3 and Figure 7.

Table 3: Comparison of Raft Footing and Piled Raft Foundation

Model No.	Footing/Raft Size (B x L x D) (m)	Pile			Load (kPa)	Founding E_s (kPa)	Max. Settlement (mm)	Bearing Pressure (kPa)
		Diameter (mm)	Length (m)	Number				
Model M1	20 x 20 x 1	None			70kPa+200kN	15,000	66	101
Model M2		0.6	30	6 x 6			29	31

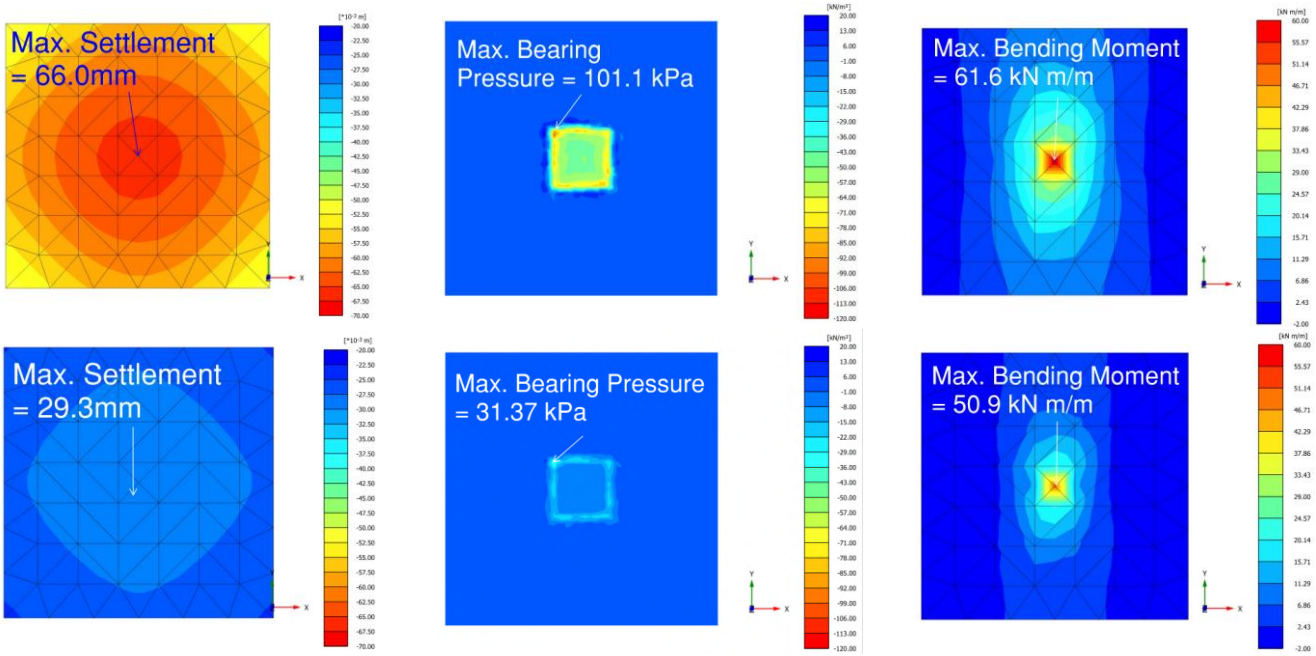

Figure 7: Results Comparison for (Top Row) Raft Footing and (Bottom Row) Pile Raft Foundation: (Left) Settlement, (Middle) Bearing Pressure and (Right) Bending Moment

The inclusion of floating piles significantly enhances foundation performance by reducing settlement and redistributing loads, thereby lowering bearing pressure on the founding soils. For a typical founding soil characterized by a friction angle of $\phi' = 33°$, the allowable bearing capacity for a 20m x 20m footing comfortably exceeds 200 kPa based on Code of Practices for Foundations 2017, even when conservatively neglecting

cohesive strength (c'). This indicates that bearing capacity is rarely the governing design criterion for raft foundation.

Instead, piled rafts are primarily adopted to control total and differential settlements through optimization of system stiffness. The role of piles is therefore not to prevent failure, but to improve serviceability performance via efficient load sharing between the raft and pile group.

5.2 Parametric Studies for Piled Raft Foundation Design

To identify the critical factors governing piled raft foundation performance, five sets of parametric studies were conducted. Specifically, these analyses compared the Poulos-Davis-Randolph (PDR) method with PLAXIS 3D [FEM]. The primary objective is twofold: to investigate the sensitivity of various design parameters and to evaluate the predictive accuracy and limitations of the PDR method concerning maximum settlement and load-sharing behaviour. The parameters considered in the study are summarized in

Table 4 to Table 8 and are described as follows:

- Pile length – from 10m to 30m, refer to Set A
- Pile number – from 3 x 3 to 7 x 7, refer to Set B
- Raft thickness – from 0.6m to 1.4m, refer to Set C
- Founding materials – Elastic Modulus from 15,000kPa to 50,000 kPa, refer to Set D
- Loading magnitude – Uniform Distributed Load (UDL) from 20kPa to 100kPa, refer to Set E

Design Groundwater level is taken as Ground Level.

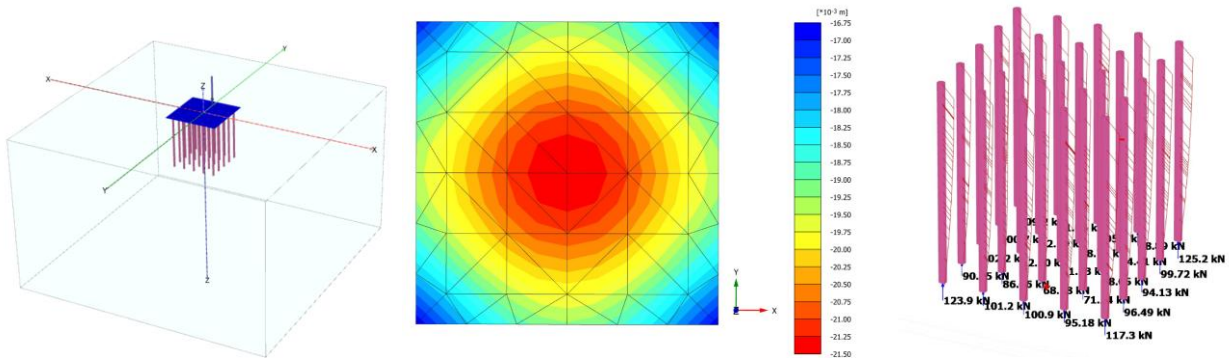

Figure 8: PLAXIS 3D – Model A3: (Left) Inputs Arrangement, (Middle) Settlement Profile and (Right) Pile Forces

Table 4: Inputs and Results for Set A Parametric Study – Pile length

Model No.	Raft Size (B x L x D) (m)	*Pile*			Uniform Load (kPa)	Founding E_s (kPa)	Pile Load Share Ratio		Max. Settlement (mm)	
		Diameter (mm)	*Length (m)*	Number			PDR	FEM	PDR	FEM
Model A1	20 x 20 x 1	0.6	*10*	5 x 5	40kPa	15,000	62.0%	58.1%	26.6	29.3
Model A2	20 x 20 x 1	0.6	*15*	5 x 5	40kPa	15,000	72.4%	74.5%	21.7	24.9
Model A3	20 x 20 x 1	0.6	*20*	5 x 5	40kPa	15,000	78.5%	83.4%	18.4	21.5
Model A4	20 x 20 x 1	0.6	*25*	5 x 5	40kPa	15,000	82.4%	85.3%	16.0	19.0
Model A5	20 x 20 x 1	0.6	*30*	5 x 5	40kPa	15,000	85.1%	86.5%	14.2	17.0

Table 5: Inputs and Results for Set B Parametric Study – Pile Number

Model No.	Raft Size (B x L x D) (m)	*Pile*			Uniform Load (kPa)	Founding E_s (kPa)	Pile Load Share Ratio		Max. Settlement (mm)	
		Diameter (mm)	Length (m)	*Number*			PDR	FEM	PDR	FEM
Model B1	20 x 20 x 1	0.6	10	*3 x 3*	40kPa	15,000	39.7%	32.8%	34.1	33.0
Model B2	20 x 20 x 1	0.6	10	*4 x 4*	40kPa	15,000	52.2%	47.8%	30.1	31.1
Model B3	20 x 20 x 1	0.6	10	*5 x 5*	40kPa	15,000	62.0%	58.1%	26.6	29.3
Model B4	20 x 20 x 1	0.6	10	*6 x 6*	40kPa	15,000	69.5%	65.5%	23.5	28.2
Model B5	20 x 20 x 1	0.6	10	*7 x 7*	40kPa	15,000	75.2%	81.7%	21.0	27.4

Table 6: Inputs and Results for Set C Parametric Study – Raft Thickness

Model No.	Raft *Size (B x L x D) (m)*	Pile			Uniform Load (kPa)	Founding E_s (kPa)	Pile Load Share Ratio		Max. Settlement (mm)	
		Diameter (mm)	Length (m)	Number			PDR	FEM	PDR	FEM
Model C1	*20 x 20 x 0.8*	0.6	10	5 x 5	40kPa	15,000	62.0%	59.0%	26.6	31.7
Model C2	*20 x 20 x 1.0*	0.6	10	5 x 5	40kPa	15,000	62.0%	58.1%	26.6	29.3
Model C3	*20 x 20 x 1.5*	0.6	10	5 x 5	40kPa	15,000	62.0%	58.0%	26.6	28.4
Model C4	*20 x 20 x 2.0*	0.6	10	5 x 5	40kPa	15,000	62.0%	57.8%	26.6	27.8
Model C5	*20 x 20 x 2.5*	0.6	10	5 x 5	40kPa	15,000	62.0%	57.1%	26.6	26.7

Table 7: Inputs and Results for Set D Parametric Study – Founding Material (E_s)

Model No.	Raft Size (B x L x D) (m)	Pile			Uniform Load (kPa)	*Founding E_s (kPa)*	Pile Load Share Ratio		Max. Settlement (mm)	
		Diameter (mm)	Length (m)	Number			PDR	FEM	PDR	FEM
Model D1	20 x 20 x 1	0.6	10	5 x 5	40kPa	*10,000*	62.2%	58.2%	39.7	42.8
Model D2	20 x 20 x 1	0.6	10	5 x 5	40kPa	*15,000*	62.0%	58.1%	26.6	29.3
Model D3	20 x 20 x 1	0.6	10	5 x 5	40kPa	*20,000*	61.8%	57.6%	20.0	22.4
Model D4	20 x 20 x 1	0.6	10	5 x 5	40kPa	*25,000*	61.7%	57.3%	16.1	18.2
Model D5	20 x 20 x 1	0.6	10	5 x 5	40kPa	*50,000*	60.8%	57.2%	8.2	10.1
Model D6	20 x 20 x 1	0.6	10	5 x 5	40kPa	*80,000*	59.8%	55.6%	5.2	6.5

Table 8: Inputs and Results for Set E Parametric Study – Loading

Model No.	Raft Size (B x L x D) (m)	Pile			*Uniform Load (kPa)*	Founding E_s (kPa)	Pile Load Share Ratio		Max. Settlement (mm)	
		Diameter (mm)	Length (m)	Number			PDR	FEM	PDR	FEM
Model E1	20 x 20 x 1	0.6	10	5 x 5	*20kPa*	15,000	62.0%	71.8%	13.3	14.2
Model E2	20 x 20 x 1	0.6	10	5 x 5	*40kPa*	15,000	62.0%	58.1%	26.6	29.3
Model E3	20 x 20 x 1	0.6	10	5 x 5	*60kPa*	15,000	62.0%	53.6%	39.9	44.6
Model E4	20 x 20 x 1	0.6	10	5 x 5	*80kPa*	15,000	62.0%	52.1%	53.1	60.1
Model E5	20 x 20 x 1	0.6	10	5 x 5	*100kPa*	15,000	62.0%	51.4%	66.4	75.8

5.3 Key Findings from Parametric Studies

- **Pile Length Effect** – Set A Model as shown in Table 4 and Figure 9 (Left)**:**

  Increasing pile length increases pile load-sharing and reduces settlement. However, the benefit diminishes beyond a threshold length, indicating that excessively long piles are neither efficient nor economical.

- **Pile Number Effect –** Set B Model as shown in
- Table 5 and Figure 9 (Right)**:**

  Increasing pile number enhances load-sharing but yields only modest settlement reduction. For example, increasing piles from 9 to 49 reduces settlement by less than 20%. This suggests diminishing returns due to the equivalent raft behaviour governing overall response.

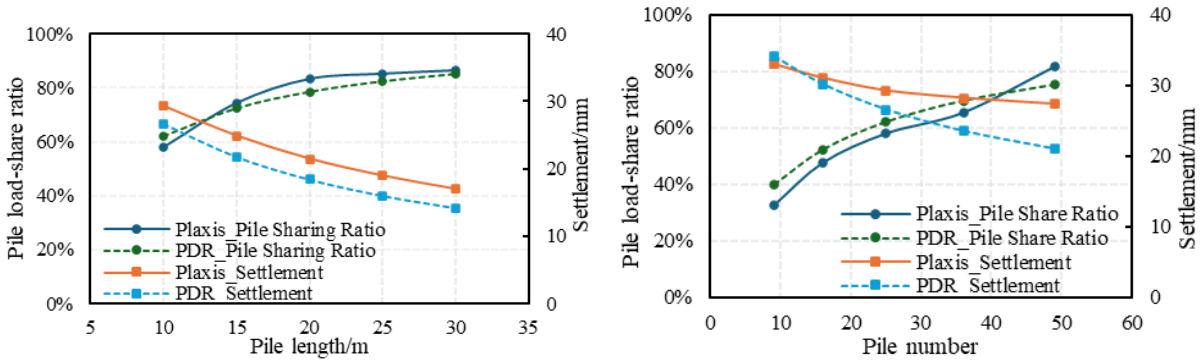

Figure 9: (Left) Parametric Study for Pile Length and (Right) Parametric Study for Pile Number

- **Raft thickness Effect** – Set C Model as shown in Table 6 and Figure 10 (Left):
  Raft thickness has limited influence on both settlement and load-sharing. While stiffness increases, the overall system response remains largely governed by soil–pile interaction.
- **Loading Effect –** Set E Model as shown in Table 8 and Figure 10 (Right):
  The PDR method assumes linear elastic behaviour and predicts constant load-sharing. In contrast, FEM results show decreasing pile load contribution with increasing load due to nonlinear soil behaviour. This highlights a key limitation of simplified methods.

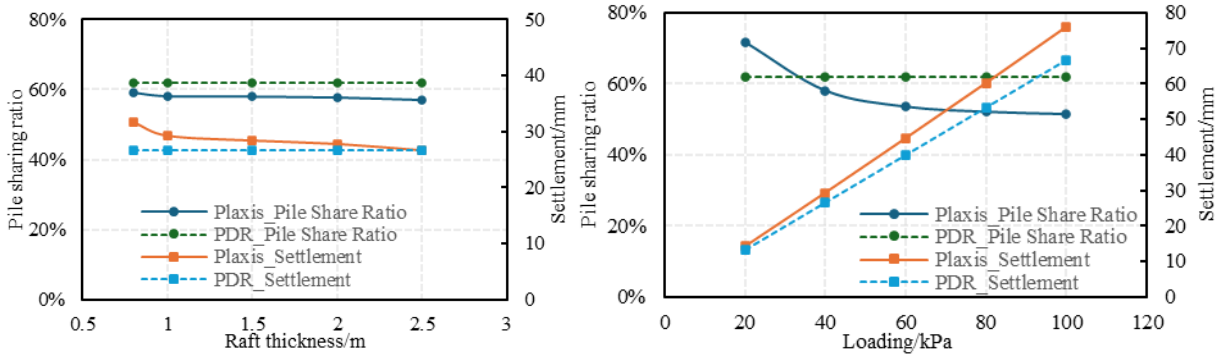

Figure 10: (Left) Parametric Study for Raft Thickness and (Right) Parametric Study for UDL Loading

- **Founding Young's Modulus E_s Effect** – Set D Model As shown in Table 7 and Figure 11 (Left):

The proportion of load carried by the pile group remains nearly unchanged with increasing E_s for both the PDR method and PLAXIS 3D. This trend indicates that increasing soil stiffness benefits both piles and raft in a similar manner, resulting in a relatively constant load-sharing ratio between the pile group and the raft. In contrast, the maximum settlement decreases nonlinearly as E_s increases, reflecting the enhanced stiffness of the soil–foundation system.

As illustrated by the k_s results in Figure 11 (Right), the k_s values at different areas of the raft exhibit distinct growth rates relative to the increase in E_s. Specifically, the k_s in the central area increases rapidly in a non-linear manner. In contrast, the edge area shows a linear and proportional growth, while the corner area experiences only a marginal increase as the soil E_s improves. This reinforces that k_s is not uniform and depends on both soil stiffness and position within the raft.

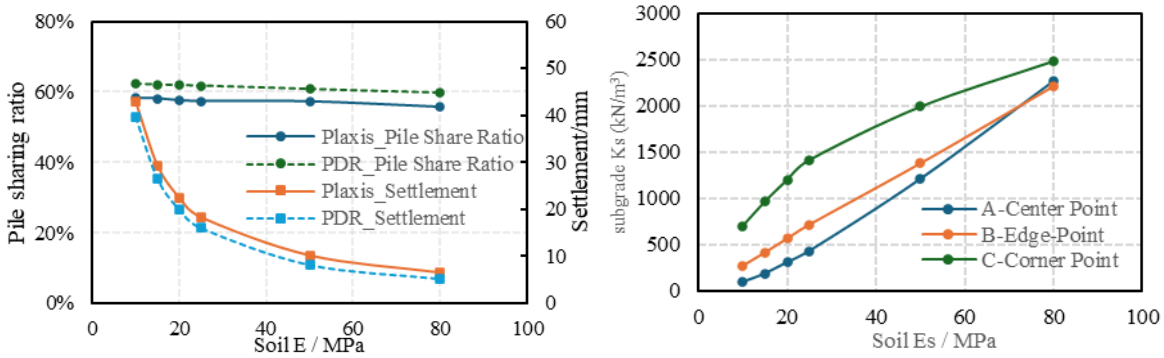

Figure 11: (Left) Parametric Study for Soil E_s and (Right) Dependence of Subgrade K_s to Soil E_s

6 SUGGESTED METHOD FOR PILED RAFT DESIGN

6.1 Design Approach 1 with PLAXIS 3D and SAFE

Based on the limitations identified in Section 3, a four-step integrated workflow is proposed for piled raft design. This approach combines simplified methods with advanced soil-structure interaction (SSI) modelling to achieve both efficiency and accuracy.

Step 1 – Preliminary design using PDR method

The Poulos-Davis-Randolph (PDR) method is used to estimate load sharing (X) and settlement (S). The equations are presented in Section 2.2. This step establishes the initial pile configuration (number, length, layout) and provides a preliminary settlement check against serviceability criteria.

Step 2 – PLAXIS 3D finite element analysis

A PLAXIS 3D model is developed under the governing SLS load case to:

- verify settlement, differential settlement, and bearing pressure;
- evaluate load sharing (X by FEM) against the preliminary estimate; and
- derive spatially varying raft stiffness (k_s) and pile spring stiffness (k_{paile}).

Step 3 – SAFE structural analysis with non-uniform subgrade

The derived k_s and k_{pile} values are imported into SAFE for analysis under full ULS and SLS load combinations. An iterative check (±10%) is performed to ensure consistency between settlement profiles from both models before extracting bending moment and shear envelopes for design.

Step 4 – Sensitivity analysis

To account for uncertainty in soil stiffness, k_s and k_{pile} are varied between 50% and 150%. The resulting bounding envelopes of bending moment and shear are adopted for final reinforced concrete design, ensuring robustness against SSI variability.

6.2 Application Example and Convergence Verification

To validate the 4-step workflow, a 20m×20m piled raft case study (6×6 pile grid with 30m pile length, 28,200kN total load) is evaluated. Spatially varying subgrade (k_s) and pile point springs (k_{pile}) are extracted from the PLAXIS 3D continuum benchmark under the dominant SLS load case and imported into the SAFE structural model. Example of spatially varying subgrade (k_s) is shown in Figure 12. The results are presented in Table 9 and key outcomes include:

- Load sharing ratio difference < 1%
- Maximum settlement difference ≈ 4%
- Consistent prediction of load distribution between raft and piles

This level of convergence confirms that the proposed workflow effectively bridges geotechnical and structural analyses, enabling reliable and practical design of piled raft foundations.

Table 9: Integrated Convergence Verification

Parameter	PDR Method	PLAXIS 3D	SAFE (Adj. Springs)	Difference (PLAXIS VS SAFE)	% Difference (PLAXIS VS SAFE)	Status
Load Carried by Piles	24,985kN	23,939kN	23,739kN	-200kN	-0.84%	PASS
Load Sharing Ratio (X)	88.6%	84.89%	84.18%	-0.71%	-	PASS
Maximum Settlement	21.3mm	30.7mm	31.8mm	+1.1mm	+3.64%	PASS

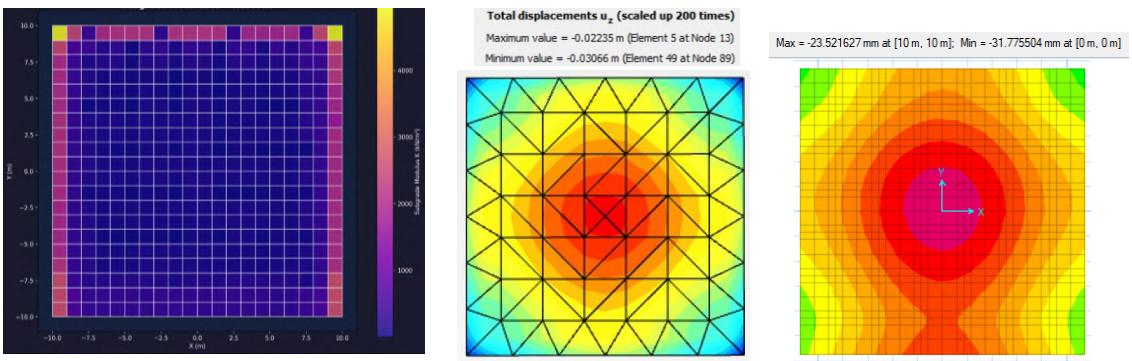

Figure 12: (Left) Spatially Varying Subgrade Modulus (ks) Map, (Center) Settlement Contour from PLAXIS 3D and (Right) Settlement Contour from SAFE

7 CONCLUSIONS

The evolution of foundation design from simplified analytical methods to advanced numerical modelling demonstrates that technological advancement alone does not guarantee improved reliability unless soil-structure interaction (SSI) is properly represented. This study highlights a key paradox where traditional "flexible" models based on a uniform modulus of subgrade reaction (k_s) may fail to capture actual continuum behaviour, particularly for large raft foundations where stiffness varies spatially, with higher resistance typically occurring at edges and corners.

A shift towards integrated design approaches is therefore essential. By combining geotechnical finite element modelling (e.g. PLAXIS 3D) with structural analysis platforms (e.g. SAFE), and by adopting spatially varying stiffness parameters, foundation behaviour can be represented more realistically. The proposed workflow demonstrates that such integration can achieve close agreement between geotechnical and structural models while maintaining practical efficiency for design.

Looking forward, a "PLAXIS 3D Only" approach is becoming increasingly viable, as a unified "source of truth". With the support of Python-based automation and design frameworks, it is now possible to handle complex load combinations and streamline reinforcement design within a single high-fidelity 3D environment.

Overall, the adoption of advanced numerical tools, combined with appropriate sensitivity analyses, enables engineers to move beyond conservative empirical assumptions towards more accurate, efficient, and performance-based foundation design.

REFERENCES

ACI Committee 336. 1998. *Design and Construction of Drilled Piers (ACI 336.3R-93, Reapproved 1998)*.

Farmington Hills, Michigan: American Concrete Institute.

Bentley Systems. 2024. *PLAXIS 3D 2024.3 Reference Manual*. Exton, PA: Bentley Systems, Incorporated.

Buildings Department. 2024. *Code of Practice for Foundations 2017 (2024 ed.)*. Hong Kong: The Government of the Hong Kong Special Administrative Region.

Geotechnical Engineering Office (GEO). 2006. *Foundation Design and Analysis (GEO Publication No. 1/2006)*. Hong Kong: Civil Engineering and Development Department.

Hain, S.J. 1980. *Analysis of piled raft foundations*. Ph.D. Thesis, University of New South Wales, Sydney, Australia.

Hans-Georg Kempfert, H.K. 2006 Chapter 5, Excavations and Foundations in Soft Soils: 337-347: Springer

Kempfert, H.G. 2006. *Recommendations on Piling (EA-Piles)*. Berlin: Ernst & Sohn.

Meyerhof, G.G. 1953. T*he bearing capacity of foundations under eccentric and inclined loads.* In Proc. 3rd International Conference on Soil Mechanics and Foundation Engineering. Zurich, 16-27 August 1953. Vol. 1: 440-445.

Poulos, H.G. & Davis, E.H. 1980. *Pile Foundation Analysis and Design*. New York: John Wiley & Sons.

Poulos, H. G., & Davis, E. H. 1974. *Elastic solutions for soil and rock mechanics*. John Wiley & Sons.

Poulos, H.G. 2000. *Practical design procedures for piled raft foundations*. In Geotechnical Engineering Conference. Melbourne: 425-433.

Randolph, M. F. 1994. *Design methods for pile groups and piled rafts*, *13th ICSMFE*, New Delhi, India, 61-82.

Structville. 2024. *Design of piled raft foundations*. Available at: https://structville.com/design-of-piled-raft-foundations (accessed 14 April 2026).

Tomlinson, M.J. & Woodward, J. 2008. *Pile Design and Construction Practice*. 5th edition. Abingdon: Taylor & Francis.

Tse, T., Lee, K.M. and Lam, J., 2025. *Overcoming limitations in raft footing design: Alternative approaches to uniform modulus of subgrade reaction analysis*. In: Proceedings of The HKIE Geotechnical Division 45th Annual Seminar 2025. Hong Kong: AIJR Proceedings, pp. 272-283.

Vesic, A.S. 1961. *Bending of beams on an elastic subgrade of finite depth*. Journal of the Engineering Mechanics Division, ASCE, 87(2): 35-53.

Yenginar, Y. & Olgun, M. 2013. *Designing piled raft foundations using simplified analysis methods.* Geotechnical and Geological Engineering, 31(5): 1541-1558.